Aromatic Interactions

Frontiers in Knowledge and Application

Published on 15 November 2016 on http://pubs.rsc.org | doi:10.1039/9781782626626-FP001

View Online

Published on 15 November 2016 on http://pubs.rsc.org | doi:10.1039/9781782626626-FP001

Monographs in Supramolecular Chemistry

Series Editors:
Professor Philip Gale, *University of Southampton, UK*
Professor Jonathan Steed, *Durham University, UK*

Titles in this Series:

1: Cyclophanes
2: Calixarenes
3: Crown Ethers and Cryptands
4: Container Molecules and Their Guests
5: Membranes and Molecular Assemblies: The Synkinetic Approach
6: Calixarenes Revisited
7: Self-assembly in Supramolecular Systems
8: Anion Receptor Chemistry
9: Boronic Acids in Saccharide Recognition
10: Calixarenes: An Introduction, 2nd Edition
11: Polymeric and Self Assembled Hydrogels: From Fundamental Understanding to Applications
12: Molecular Logic-based Computation
13: Supramolecular Systems in Biomedical Fields
14: Synthetic Receptors for Biomolecules: Design Principles and Applications
15: Polyrotaxane and Slide-Ring Materials
16: Boron: Sensing, Synthesis and Supramolecular Self-Assembly
17: Porous Polymers: Design, Synthesis and Applications
18: Pillararenes
19: Supramolecular Chemistry at Surfaces
20: Aromatic Interactions: Frontiers in Knowledge and Application

How to obtain future titles on publication:
A standing order plan is available for this series. A standing order will bring delivery of each new volume immediately on publication.

For further information please contact:
Book Sales Department, Royal Society of Chemistry, Thomas Graham House, Science Park, Milton Road, Cambridge, CB4 0WF, UK
Telephone: +44 (0)1223 420066, Fax: +44 (0)1223 420247
Email: booksales@rsc.org
Visit our website at http://www.rsc.org/Shop/Books/

View Online

Aromatic Interactions

Frontiers in Knowledge and Application

Published on 15 November 2016 on http://pubs.rsc.org | doi:10.1039/9781782626626-FP001

Edited by

Darren W. Johnson
University of Oregon, Eugene, Oregon, USA
Email: dwj@uoregon.edu

Fraser Hof
University of Victoria, Victoria, British Columbia, Canada
Email: fhof@uvic.ca

View Online

Published on 15 November 2016 on http://pubs.rsc.org | doi:10.1039/9781782626626-FP001

Monographs in Supramolecular Chemistry No. 20

Print ISBN: 978-1-78262-417-2
PDF eISBN: 978-1-78262-662-6
EPUB eISBN: 978-1-78262-959-7
ISSN: 1368-8642

A catalogue record for this book is available from the British Library

© The Royal Society of Chemistry 2017

All rights reserved

Apart from fair dealing for the purposes of research for non-commercial purposes or for private study, criticism or review, as permitted under the Copyright, Designs and Patents Act 1988 and the Copyright and Related Rights Regulations 2003, this publication may not be reproduced, stored or transmitted, in any form or by any means, without the prior permission in writing of The Royal Society of Chemistry or the copyright owner, or in the case of reproduction in accordance with the terms of licences issued by the Copyright Licensing Agency in the UK, or in accordance with the terms of the licences issued by the appropriate Reproduction Rights Organization outside the UK. Enquiries concerning reproduction outside the terms stated here should be sent to The Royal Society of Chemistry at the address printed on this page.

The RSC is not responsible for individual opinions expressed in this work.

The authors have sought to locate owners of all reproduced material not in their own possession and trust that no copyrights have been inadvertently infringed.

Published by The Royal Society of Chemistry,
Thomas Graham House, Science Park, Milton Road,
Cambridge CB4 0WF, UK

Registered Charity Number 207890

Visit our website at www.rsc.org/books

Printed in the United Kingdom by CPI Group (UK) Ltd, Croydon, CR0 4YY, UK

Published on 15 November 2016 on http://pubs.rsc.org | doi:10.1039/9781782626626-FP005

Preface

Aromatic rings are prevalent throughout nature, found in hydrocarbons, nucleic acids, proteins, metabolites, and drugs. Aromatic groups are also ubiquitous in materials science, where they are prized for their programmed reactivity and chemical stability.[1,2] The interactions of aromatic groups with their surroundings are central to their properties and functions in all of these settings. In this book we seek to introduce the reader to modern research on aromatic interactions. This monograph should not be viewed as a comprehensive review of all knowledge on aromatic systems, but rather we aspire to highlight topics of current interest that have emerged in the last several years. The scope of topics to be covered fits into three main categories, including: (i) new developments in our fundamental understanding of aromatic interactions (substituent effects, electronic effects, thermodynamics), (ii) discovery and characterization of new kinds of aromatic interactions (anion–π interactions, aromatic interactions on surfaces), and (iii) emerging applications of aromatic interactions (biological sciences, catalysis, organic electronics, and materials science).

The field of aromatic interactions has generated significant new content, and with it renewed controversy in recent years. The fundamental nature of substituent effects in aromatic interactions has been discussed, the term "π-stacking" itself has been reconsidered, the understanding of the nature of the interaction between ions and aromatic rings continues to evolve, and new theoretical frameworks have been developed and tested against experiment. Against this backdrop of an evolving basic knowledge, aromatic interactions have repeatedly appeared among the applied solutions found for problems in biology and materials science.

While many other weak interactions have been well understood for decades, our fundamental understanding of aromatic interactions has continued to evolve in the last 10 years. Early models for aromatic interactions

Monographs in Supramolecular Chemistry No. 20
Aromatic Interactions: Frontiers in Knowledge and Application
Edited by Darren W. Johnson and Fraser Hof
© The Royal Society of Chemistry 2017
Published by the Royal Society of Chemistry, www.rsc.org

View Online

Published on 15 November 2016 on http://pubs.rsc.org | doi:10.1039/9781782626626-FP005

were based primarily on electrostatics; however, in order to explain the observed strengths of interactions, van der Waals forces and desolvation were also highlighted as playing significant energetic roles.[3,4] When dealing with polarized aromatic systems, the early model by Hunter and Sanders broke the electrostatic contributions down into πσ–πσ (present in non-polarized systems), atom–atom (partial atomic charge attraction or repulsion), and atom–πσ (the interaction of the partial atomic charge of one molecule with the out-of-plane π electron cloud of another molecule). Such a model accurately predicts the strengths of benzene dimer interactions, as well as benzene–hexafluorobenzene, but breaks down with more complex systems.

Since this initial model, there have been many advances in understanding the phenomenon of "aromatic interactions" through detailed physical organic studies on solutions, solid-state investigations, and quantum mechanical computations. Such an understanding has enabled the rational design of new functional molecular systems relying on aromatic interactions.[5] Stoddart has made rotaxanes that depend on aromatic interactions to control molecular movements and locations;[6] Sharpless has utilized host ligands that bind aromatic guests in defined geometries that favor reactivity;[7] organic materials featuring π–π stacking are used in semiconducting charge-transfer materials,[8] just to name a few. Practical advances like these have progressed in lockstep with studies that reveal the fundamental nature of aromatic interactions.

Aromatic interactions remain a vibrant area of study because of their complexity. This book dives into further theoretical understanding of the nature of these interactions, with several chapters describing the latest approaches to arene–arene, cation–π, anion–π, and main group lone pair–π interactions. In Chapter 1, Lewis goes beyond the quadrupolar electrostatic distribution of aromatic systems and brings in aromatic polarizability, induction, dispersion, exchange, and substituent-dominated effects to improve the understanding of aromatic interactions. The strength of the contributing factors, as well as their individual contributions to the overall energy of the interaction, are further discussed for simple arene–arene interactions as well as cation–π. And in Chapter 2, Maji and Wheeler expand on how this fundamental understanding of aromatic interactions can be harnessed to direct organic reactions with new organocatalysts.

The list of canonical types of aromatic interactions is still expanding. Since the last publication of this Monographs series, anion–π (Chapters 2 and 3) and main group–π (Chapter 4) interactions have entered the scene. The strength of anion–π interactions is enhanced with an increase in electron deficiency of the out-of-plane π electron cloud; however, the strength is also increased by the anion's ability to induce a dipole in the π-electron cloud. Anion–π and related interactions have been found to be a powerful directing effect for organic reactions, and catalysis, as mentioned in Chapter 2 and highlighted in greater detail in Chapter 3. Harnessing the understanding of anion–π interactions led Frontera and Ballester to propose that extended π-systems should be used in anion–π complexes due to their increased polarizability.

View Online

Published on 15 November 2016 on http://pubs.rsc.org | doi:10.1039/9781782626626-FP005

Even more recently, main group element lone pair–π interactions have been defined, characterized, and exploited for self-assembly (Chapter 4). Many examples of such contacts have been discovered through searches of the Cambridge Structural Database (CSD). Much like cation–π interactions, the polarizability of the participating electrons is key for the interaction to take place. However, given the ambipolar-type nature of some main group complexes, the main group element can in some cases donate its electron as a π-base to a π-acidic aromatic ring, or alternately, serve as the Lewis acidic cation in a cation–π complex, thereby exhibiting features of both anion–π and cation–π interactions, sometimes even within the same complex.

Changes in the way the field has modeled aromatic interactions computationally, and the changes advanced by that understanding, are driven by trying to accurately predict what is experimentally observed in solution. This has driven work aimed at understanding how simple model systems can be used for quantitative measurement and the study of non-covalent interactions between aromatic rings in solution. In Chapter 5, Shimizu and Hwang describe a series of such systems carefully designed to control and understand different contributing factors such as electrostatics, dispersion, repulsion, and solvent effects. There are key challenges that must be overcome, such as defining a system where other weak forces such as dipole effects, sterics, and secondary interactions are not mistaken for aromatic interactions. The models that have been studied vary from simple fixed interactions of aromatics to adapting biomolecular frameworks for physical organic models. The combinations of these studies, both simple and complex, have and continue to contribute greatly to the fundamental understanding of these interactions. Paired with computational studies and single crystal X-ray diffraction, these solution state studies have benefitted biological understanding and biomimetic design of molecular structures and systems.

The inspiration for using subtle aromatic interactions to direct and/or catalyze organic reactions (Chapters 2 and 3) is derived in part from studying biological systems. We devote two chapters to biological examples of aromatic interactions: in Chapter 6, Bockus and Urbach describe aromatic interactions of amino acids and proteins; in Chapter 7, Koenig and Waters focus on cation–π interactions in biological chemistry. Both chapters describe efforts to understand the fundamental nature of interactions, while also describing the progression to creating synthetic molecules that can bind to and modulate natural, biological partners. A definitive fundamental lesson highlighted in Chapter 7 explores the use of isosteric R-NMe_3^+ and R-$C(Me)_3$ ligands to understand the role of cation–π interactions in natural protein–protein interactions. Chapter 6 highlights a seminal example of the type of synthetic recognition systems enabled by aromatic interactions in viologen-bound hosts that co-encapsulate aromatic side chains of amino acids, peptides, and whole proteins.

The principles that allow aromatic interactions to be utilized in molecular systems have also advanced into the realm of materials chemistry. This application in materials chemistry can take on different forms: aromatic

View Online

Published on 15 November 2016 on http://pubs.rsc.org | doi:10.1039/9781782626626-FP005

interactions can be used for functionalizing materials surfaces, molecular receptors can be applied to a surface, and favorable interactions with the surface can help facilitate organized self-assembly on the surface.[8–10] Applying aromatic molecules to metallic surfaces has afforded new characterization methods, as well as novel reactivity. In Chapter 8, Marangoni, Cloke and Fischer introduce such surface characterization methods, with a focus on the techniques that allow visualization at submolecular resolution. These methods are powerful tools in advancing the understanding of aromatic molecules and their interactions. The metallic substrates can also be utilized to control reactivity of the adsorbed aromatic compounds, including reactions that are unprecedented in the solution phase. By "building up" complexity on the surface, the creation of 2D and 3D molecules is now possible. This further advances extended π surfaces, with promise for improved electronic devices such as organic light emitting diodes, organic thin film transistors, and organic photovoltaics.

Structural investigations of aromatic molecules on crystalline surfaces has resulted in novel reactivity and new applications in materials chemistry. The designed use of predictive aromatic interactions has impacted fields ranging from catalysis (through conformational control), drug design (molecular recognition), and materials chemistry (surface functionalization), among others. Such designs would not be possible without the continued evolution of fundamental understandings furthered by computational chemistry informed by solution-state models—both synthetic and biological—as well as data from solid state structural investigations.

As can be seen from the content described above, this book does not aim to be a tutorial review on aromatic interactions. We have aimed instead to include content that describes the last 10 years of progress—the newest classes of interactions, latest ways of understanding interactions, and the cutting edge of experimental systems that exploit this knowledge to drive new science. It is clear that the field of Aromatic Interactions is not yet settled. We look forward to the next decade of discovery.

Kara M. Nell, University of Oregon, Eugene, USA
Fraser Hof, University of Victoria, Victoria, Canada
Darren W. Johnson, University of Oregon, Eugene, USA

References

1. K. A. Wilson, J. L. Kellie and S. D. Wetmore, *Nucleic Acids Res.*, 2014, **10**, 6726–6741.
2. C. A. Hunter, *J. Mol. Biol.*, 1993, **230**, 1025–1053.
3. C. A. Hunter and J. K. M. Sanders, *J. Am. Chem. Soc.*, 1990, **112**, 5525–5534.
4. C. A. Hunter, *Chem. Soc. Rev.*, 1994, **23**, 101–109.
5. C. A. Hunter, K. R. Lawson, J. Perkins and C. J. Urch, *J. Chem. Soc., Perkin Trans. 2*, 2001, 651–669.

View Online

6. R. A. Bissell, E. Cordova, A. E. Kaifer and J. F. Stoddart, *Nature*, 1994, **369**, 133.
7. M. R. Bryce, *Adv. Mater*, 1999, **11**, 11.
8. H. C. Kolb, P. G. Andersson and K. B. Sharpless, *J. Am. Chem. Soc.*, 1994, **116**, 1278.
9. K. M. Nell, S. A. Fontenot, T. G. Carter, M. G. Warner, C. L. Warner, R. S. Addleman and D. W. Johnson, *Environ. Sci.: Nano*, 2016, **3**, 138–145.
10. S. Lee, B. E. Hirsch, Y. Liu, J. R. Dobscha, D. W. Burke, S. L. Tait and A. H. Flood, *Chem.–Eur. J.*, 2016, **22**, 560–569.

Published on 15 November 2016 on http://pubs.rsc.org | doi:10.1039/9781782626626-FP005

Published on 15 November 2016 on http://pubs.rsc.org | doi:10.1039/9781782626626-FP011

Contents

Chapter 1 **Modern Computational Approaches to Understanding Interactions of Aromatics** **1**
Michael Lewis, Christina Bagwill, Laura Hardebeck and Selina Wireduaah

1.1 Introduction and Background 1
1.1.1 Arene–Arene Interactions 2
1.1.2 Cation–Arene Interactions 3
1.1.3 Beyond the Aromatic Quadrupole Moment 4
1.2 Computational Approaches to Understanding Arene–Arene Interactions 5
1.2.1 The Nature of Arene–Arene Interactions 5
1.2.2 Predicting the Strength of Arene–Arene Interactions 9
1.3 Computational Approaches to Understanding Cation–Arene Interactions 10
1.3.1 The Nature of Cation–Arene Interactions 10
1.3.2 Predicting the Strength of Cation–Arene Interactions 13
1.4 Summary 14
References 15

Chapter 2 **Role of Aromatic Interactions in Directing Organic Reactions** **18**
Rajat Maji and Steven E. Wheeler

2.1 Introduction and Background 18
2.2 Aromatic Interactions of Relevance to Organic Reactions 19

Monographs in Supramolecular Chemistry No. 20
Aromatic Interactions: Frontiers in Knowledge and Application
Edited by Darren W. Johnson and Fraser Hof
© The Royal Society of Chemistry 2017
Published by the Royal Society of Chemistry, www.rsc.org

View Online

Published on 15 November 2016 on http://pubs.rsc.org | doi:10.1039/9781782626626-FP011

2.3 Aromatic Interactions in Non-Catalytic Reactions 22
2.4 Aromatic Interactions in Transition-Metal Catalyzed Reactions 24
2.5 Aromatic Interactions in Organocatalysis 25
2.6 Aromatic Interactions in Cooperative Catalysis 31
2.7 Reactions Directed by Anion–π Interactions 31
2.8 Reactions Directed by π–π^+ Interactions 33
2.9 Concluding Remarks 34
Acknowledgements 34
References 34

Chapter 3 Anion–π Interactions: Theoretical Studies, Supramolecular Chemistry and Catalysis 39
A. Frontera and P. Ballester

3.1 Introduction 39
3.2 Physical Nature 41
3.3 Anion–π Interactions in Solution 46
3.3.1 Supramolecular Chemistry and Synthetic Receptors Involving Anion–π Interactions 46
3.3.2 Anion–π Interactions in Reaction Catalysis 65
3.3.3 Ionic Liquids 74
3.4 On the Importance of Anion–π Interactions in the Solid State 76
3.4.1 Charge Neutral π-Systems 76
3.4.2 Aromatic Ligands Coordinated to Metal Ions 83
3.4.3 Positively Charged or Protonated Aromatics 86
3.5 Outlook 88
Acknowledgements 88
References 89

Chapter 4 A New Non-Covalent Bonding Mode in Supramolecular Chemistry: Main Group Element Lone-Pair–π(arene) Interactions 98
Ignez Caracelli, Ionel Haiduc, Julio Zukerman-Schpector and Edward R. T. Tiekink

4.1 Introduction 98
4.2 Methodology 100
4.3 Overview of M(lp)···π(arene) Interactions 102
4.3.1 Indium(I) 102
4.3.2 Thallium(I) 102
4.3.3 Tin(II) 104
4.3.4 Lead(II) 105
4.3.5 Arsenic(III) 106
4.3.6 Antimony(III) 108
4.3.7 Bismuth(III) 108

View Online

4.3.8 Selenium(II, IV) 109
4.3.9 Tellurium(II, IV) 115
4.4 Biological Relevance 116
4.5 Conclusions and Outlook 118
Acknowledgements 119
References 119

Chapter 5 Solution-Phase Measurements of Aromatic Interactions 124
K. D. Shimizu, P. Li and J. Hwang

5.1 Introduction 124
5.2 Types of Model Systems 125
5.2.1 Bimolecular Model Systems 125
5.2.2 Unimolecular Model System 126
5.2.3 Thermodynamic Approach 126
5.2.4 Kinetic Approach 127
5.2.5 Analysis of Experiment Models 127
5.2.6 Isolation of the Interaction Energy 128
5.3 Case Studies of Solution-Phase Measurements of Aromatic Interactions 129
5.3.1 Aromatic Stacking Interactions 129
5.3.2 Aromatic Edge-to-Face Interactions 140
5.3.3 Aliphatic CH–π Interactions 145
5.3.4 Aromatic Cation–π Interactions 150
5.3.5 Anion–π Interaction 155
5.3.6 Lone Pair–π Interaction 159
5.4 Conclusion 162
Acknowledgements 163
References 163

Chapter 6 Molecular Recognition of Aromatic Peptides and Proteins in Nature and by Design 172
Andrew T. Bockus and Adam R. Urbach

6.1 Overview 172
6.2 Aromatic Amino Acids 173
6.3 Aromatic Residues in Biological Complexes 175
6.4 Designed Ligands 180
6.5 Efficiency of Aromatic Residues 182
6.6 Synthetic Receptors 183
6.7 Synthetic Receptors for Amino Acids 184
6.7.1 Aromatic Amino Acid Recognition by Viologen-Containing Receptors 184
6.7.2 Aromatic Amino Acid Recognition by Cyclodextrins 186
6.7.3 Aromatic Amino Acid Recognition by Cucurbiturils 188

Published on 15 November 2016 on http://pubs.rsc.org | doi:10.1039/9781782626626-FP011

View Online

Published on 15 November 2016 on http://pubs.rsc.org | doi:10.1039/9781782626626-FP011

6.7.4 Recognition of Non-Aromatic Amino Acids by Synthetic Receptors 189
6.8 Recognition of Aromatic Peptides by Synthetic Receptors 192
6.8.1 Early Receptors for Peptides 193
6.8.2 Peptide Recognition by Coordination Complexes 195
6.8.3 Peptide Recognition by Cucurbit[*n*]urils 197
6.9 Recognition of Aromatic Sites on Proteins by Synthetic Receptors 203
6.10 Lessons Learned and Challenges 206
Acknowledgements 208
References 208

Chapter 7 Cation–π Interactions in Biomolecular Recognition 214
Amber L. Koenig and Marcey L. Waters

7.1 The Nature of the Cation–π Interaction 214
7.2 Model Systems for Cation–π Interactions in Aqueous Solution 216
7.2.1 Applications of Synthetic Systems that Mediate Cation–π Interactions 218
7.3 Cation–π Interactions in Proteins 218
7.4 Cation–π Interactions in Nucleic Acids 225
7.5 Cation–π Interactions in Lipids 229
7.6 Conclusions 232
References 232

Chapter 8 Aromatic Molecules on Metallic Surfaces: Structure and Reactivity 238
Tomas Marangoni, Ryan R. Cloke and Felix R. Fischer

8.1 Introduction 238
8.2 Structural Investigations of Aromatic Molecules on Surfaces 240
8.2.1 General Surface Characterization Techniques 240
8.2.2 Visualization Techniques with Sub-Molecular Resolution: STHM and nc-AFM 241
8.3 Reactivity of Aromatic Molecules on Metallic Surfaces 247
8.3.1 Surface-Mediated Polymerization 248
8.3.2 Cyclodehydrogenation Reactions 255
8.3.3 Metal-Coordination Reactions 257
8.3.4 Graphene Nanoribbon Synthesis 261
8.4 Conclusions 269
References 269

Subject Index 277

Published on 15 November 2016 on http://pubs.rsc.org | doi:10.1039/9781782626626-00001

CHAPTER 1

Modern Computational Approaches to Understanding Interactions of Aromatics

MICHAEL LEWIS*[a], CHRISTINA BAGWILL[a], LAURA HARDEBECK[a] AND SELINA WIREDUAAH[a]

[a]Department of Chemistry, Saint Louis University, 3501 Laclede Avenue, Saint Louis, Missouri, 63103, USA
*E-mail: LewisM5@slu.edu

1.1 Introduction and Background

Two of the most common, and widely studied, interactions of aromatics are arene–arene and cation–arene interactions[1] and this chapter will focus on modern computational approaches aimed at understanding them. Two aromatic molecules generally interact to form one of the conformations shown in Figure 1.1(a): parallel face-to-face (**pff**), offset face-to-face (**osff**), edge-to-face (**etf**), or t-shaped (**tsh**).[2,3] Of course, each one of these conformations has an infinite number of possible structures, largely dependent on the angle between the planes of the aromatic rings, and the degree to which the molecules are offset. Cation–arene interaction[4] normally assume a conformation where the cation is over the π-density of the aromatic ring, as shown in Figure 1.1(b), and this has led to the interaction being termed cation–π. Depending on the nature of the aromatic, the cation may assume a position not directly

Monographs in Supramolecular Chemistry No. 20
Aromatic Interactions: Frontiers in Knowledge and Application
Edited by Darren W. Johnson and Fraser Hof
© The Royal Society of Chemistry 2017
Published by the Royal Society of Chemistry, www.rsc.org

View Online

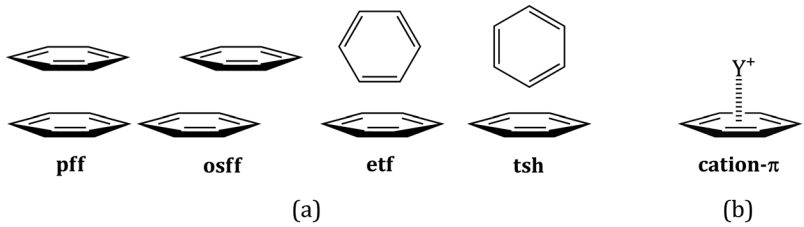

Figure 1.1 General conformations of: (a) arene–arene interactions; (b) cation–arene interactions.

above the center of the aromatic, and for certain polar aromatics the most stable cation–arene conformation has the cation binding to the negative end of the molecular dipole.[5]

A brief historical background on each of these interactions, largely focused on computational investigations, is given below, and this is followed by a review of current computational work aimed at understanding the nature of the interactions and predicting the strength of the interactions.

1.1.1 Arene–Arene Interactions

In the mid-1980s, Burley and Petsko reported one of the seminal studies showing that arene–arene interactions were distinct from typical hydrophobic interactions, showing that aromatic amino acid residues are predominantly found in the vicinity of other aromatic amino acid residues, and that the residues interact in an energetically favorable manner.[6] Subsequently, non-covalent interactions of aromatics have been shown to play a significant role in a wide range of biologically and chemically relevant systems and processes. Face-to-face arene–arene interactions are important in nucleic acid structure[1,7] and aromatic interactions are important in carbohydrate interactions[8,9] the structure of helical peptides[10] aromatic amino acid interactions,[11] DNA/RNA protein complexes[12] biological receptor interactions[13] and peptide formation.[14] In addition, due to the ubiquity of aromatics in biological systems, aromatic interactions are often a focus in drug development, and many pharmaceuticals contain an aromatic moiety.[15] In terms of chemical systems, a few areas where aromatic interactions have been shown to be important include molecular recognition[1,16] supramolecular complexes[17] molecular self-assembly[18] nanomaterials[19] and organic catalysis.[20,21]

Early computational investigations aimed at understanding arene–arene interactions focused on the aromatic quadrupole moment.[22] Figure 1.2(a) presents a pictorial view of the quadrupole moments of benzene and hexafluorobenzene. Benzene has a negative quadrupole moment[23] and this can be viewed as the π-electron density region being more electron-rich than the hydrocarbon σ-framework region. Conversely, hexafluorobenzene has a positive quadrupole moment[23] and the hydrocarbon σ-framework region with the fluorine atoms is more electron-rich than the π-electron region. Hunter

Published on 15 November 2016 on http://pubs.rsc.org | doi:10.1039/9781782626626-00001

View Online

Published on 15 November 2016 on http://pubs.rsc.org | doi:10.1039/9781782626626-00001

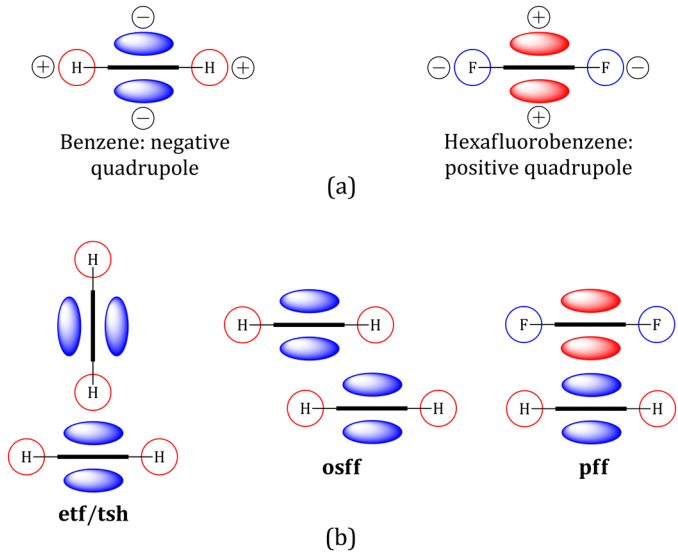

Figure 1.2 (a) The quadrupole moments of benzene (negative; −8.7 ± 0.5 DÅ) and hexafluorobenzene (positive; +9.5 ± 0.5 DÅ) are opposite in sign.[23] (b) The preferred **etf** and **osff** conformations of C_6H_6–C_6H_6 complexes, and the preferred **pff** conformations of C_6H_6–C_6F_6 complexes, can be explained *via* the aromatic quadrupole moments.

and Sanders discussed the nature of π–π interactions through a charge distribution model[2] the results of which dictate that two aromatics with the same quadrupole moment, such as benzene, would interact most favorably either by adopting an **etf** or **tsh** conformation or by having the negative ends of their quadrupole moments get out of each other's way *via* an **osff** conformation (Figure 1.2(b)). Conversely, aromatics that have quadrupole moments opposite in sign, such as benzene and hexafluorobenzene, would be expected to prefer the **pff** conformation (Figure 1.2(b)), and this was demonstrated in the solid state[24] and *via* computations.[25]

1.1.2 Cation–Arene Interactions

Kebarle and coworkers first reported the importance of the cation–arene interaction when they showed that the K^+-benzene dimer had slightly more binding ΔH and $\Delta G°$ values than the K^+-water dimer in the gas phase.[26] The result was quite surprising at the time, as it suggests a cation would prefer to bind to a nonpolar molecule, benzene, rather than the highly polar water molecule. Kebarle and coworkers suggested the cation–π conformation shown in Figure 1.1(b) to explain why the cation would be attracted to an aromatic ring. Subsequently, cation–π interactions have been shown to be important in a wide range of chemistry and biology[1] with significant early work being performed by the Dougherty group.[27]

View Online

Published on 15 November 2016 on http://pubs.rsc.org | doi:10.1039/9781782626626-00001

Similar to their work on the importance of arene–arene interactions in protein structures, Burley and Petsko also showed that amino acid residues with cationic side chains are preferentially found in the vicinity of aromatic amino acids.[28] In addition to being important in protein stability, notable areas where cation–π interactions have been shown to be important in biology include enzyme/protein-substrate recognition[29,30] and ion-transport processes.[31] In chemistry, cation–π interactions have been reported to play a role in organic reaction development[32] and in nanomaterials.[19]

As was the case for arene–arene interactions, early computational work aimed at understanding cation–π interactions focused on the aromatic quadrupole moment.[33] In general, cation–arene interactions were generally investigated for electron-rich aromatics, which have negative quadrupole moments (*i.e.*, benzene[23]), and the interaction can be described as a positive charge being attracted to the negative region of the arene quadrupole. Figure 1.3 shows this for Na^+-benzene. Related to understanding the cation–π interaction *via* the aromatic quadrupole moment, early computational studies also aimed to understand the interactions *via* the aromatic electrostatic potential, as reported by Dougherty and coworkers.[27,34]

1.1.3 Beyond the Aromatic Quadrupole Moment

The aromatic quadrupole moment proved useful as a model for predicting some aspects of the interactions of aromatics. As discussed above, it can be used to understand the preferred conformations for benzene–benzene and benzene–hexafluorobenzene dimers. In addition, it provides a good approach for understanding the cation–arene interactions of electron-rich aromatics such as benzene. However, the quadrupole moment describes the aromatic electron density distribution, and using it to describe arene–arene and cation–arene interactions suggests they can be understood in purely electronic/electrostatic terms. Recent computational approaches to understanding interactions of aromatics have highlighted the importance of aromatic polarizability, the importance of forces other than electrostatics such as induction, dispersion, and exchange, as well as substituent–substituent and ion–substituent effects. The findings of these modern computational approaches are discussed below, both in terms of understanding the interactions and in terms of predicting the relative strength of the interactions.

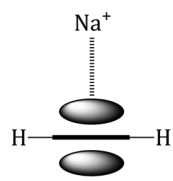

Figure 1.3 Prototypical cation–π complex of an aromatic: Na^+–C_6H_6. The attraction can be understood as the cation binding to the negative region of the aromatic quadrupole moment.

View Online

Published on 15 November 2016 on http://pubs.rsc.org | doi:10.1039/9781782626626-00001

1.2 Computational Approaches to Understanding Arene–Arene Interactions

1.2.1 The Nature of Arene–Arene Interactions

Following the early computational work of Hunter and Sanders focusing on the importance of the aromatic quadrupole moment in arene–arene interactions[2] many small-molecule models were experimentally investigated to determine the forces important in arene–arene interactions[35–39]. The small-molecule models generally focused on the interactions between substituted benzenes, and one such example is the 1,8-diarylnaphthalenes investigated by Cozzi and Siegel (Figure 1.4).[38,39] A common theme among this body of work is the reported relationship between the experimentally determined arene–arene binding energies and Hammett substituent constants, and the interpretation that this correlation suggested the interactions were due to polar/π electronic effects.

At the same time as experimental work showing correlations between arene–arene binding energies and Hammett constants continued to be reported[1] some experimental results began to appear suggesting forces other than electronic/electrostatic effects were important in understanding the nature of arene–arene interactions. Gung and coworkers showed that when one aromatic was electron-rich and the other aromatic was electron-poor (*i.e.*, hexafluorobenzene), the experimentally measured arene–arene binding energies did not correlate with the Hammett constants, and they suggested charge-transfer effects may be important in such arene–arene interactions.[40] In addition to these results, the early 2000s saw the beginning of a wealth of computational results showing there was no general relationship between arene–arene binding energies and Hammett constants, and suggesting that forces other than electronic/electrostatic effects were important in understanding the nature of these interactions. Primary among these studies was the work of Sherrill and coworkers employing the energy decomposition method symmetry adapted perturbation theory (SAPT). The SAPT method[41,42]

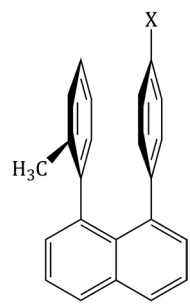

Figure 1.4 The 1,8-diarylnaphthalenes system is an example of a small-molecule model used to experimentally investigate arene–arene binding energies.[38,39]

View Online

Published on 15 November 2016 on http://pubs.rsc.org | doi:10.1039/9781782626626-00001

allows for the overall non-covalent binding energy E_{bind} to be broken down to the energies due to electrostatics (E_{ele}), induction (E_{ind}), dispersion (E_{disp}), and exchange (E_{exch}). Using the SAPT method to investigate mono-substituted benzene–benzene dimers, Sherrill's research group showed the energy due to dispersion (E_{disp}) is a greater contributor to the overall E_{bind} value than E_{ele} for both **pff** and **etf** conformations.[43] This result was also reported by Tsuzuki and coworker[44] using a different computational approach to determine E_{ele}, E_{ind}, and E_{disp}; they calculated E_{ele} and E_{ind} using the program ORIENT,[45] while E_{disp} was approximated as the energy contribution from electron correlation (E_{corr}) on E_{bind}. Tsuzuki and coworkers determined the E_{corr} value as the difference between the interaction energies calculated with electron-correlated levels and at the HF levels.[44] The Tsuzuki group computationally investigated arene–arene interactions in **pff**, and various **etf**, **tsh**, and **osff** conformations when two electron-rich aromatics were interacting (toluene–toluene, toluene–benzene)[46] when two electron-poor aromatics were interacting (nitrobenzene–nitrobenzene)[47] and when an electron-rich and electron-poor aromatic were interacting (nitrobenzene–benzene[47] and hexafluorobenzene–benzene[48]), and in all cases they found E_{disp} was the greatest contributor to E_{bind}. Kim and coworkers studied **tsh** mono-substituted benzene–benzene dimers where the substituted benzene could be either the vertical (Figure 1.5(a)) or horizontal (Figure 1.5(b)) aromatic in the dimer conformation.[49] Using SAPT calculations they showed that E_{disp} was the greatest contributor to E_{bind} regardless of the substituent or conformation. The examples from the Sherrill, Tsuzuki, and Kim research groups capture the beginning of using energy decomposition methods in computational chemistry to understand interactions of aromatics broadly, and arene–arene interactions in particular. The work provided the important insight that the energy due to electrostatics (E_{ele}) is not the major contributor to arene–arene binding energies (E_{bind}), and the use of energy decomposition methods continues to be important in modern computational approaches to understanding arene–arene interactions.

The fact that SAPT calculations showed E_{disp} to be the major contributor to E_{bind} values for arene–arene interactions suggested that Hammett constants

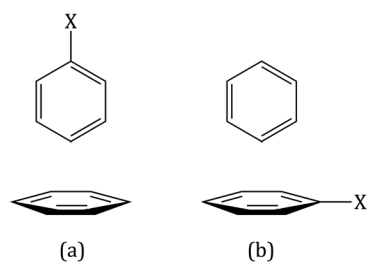

Figure 1.5 Arene–arene dimers between a substituted benzene and benzene, and in the t-shaped (**tsh**) conformation, can adopt two general conformations: (a) the substituted aromatic vertical; (b) the substituted aromatic horizontal.

View Online

Published on 15 November 2016 on http://pubs.rsc.org | doi:10.1039/9781782626626-00001

should not correlate to arene–arene binding energies, as was reported in most of the experimental work. Consistent with the emerging view from computational work that E_{disp} was important to understanding arene–arene interactions, Sherrill and coworkers showed that adding any substituent to one of the aromatics in a **pff** benzene–benzene dimer, regardless of whether the substituent is electron-withdrawing or electron-donating, led to the dimer having a stronger binding energy.[43,50] A natural outcome of this result is that E_{bind} values for substituted benzene–benzene dimers cannot correlate with Hammett substituent constants, and Sherrill and coworkers explicitly demonstrated this by computationally investigating **pff** substituted benzene–benzene dimers with an approximately equal number of electron-withdrawing (positive Hammett value) or electron-donating (negative Hammett value) groups.[51] The resulting graph of E_{bind} *versus* $\Sigma\sigma_m$ (multi-substituted benzenes were investigated, and thus $\Sigma\sigma_m$ was used) yielded a parabola; there was no linear correlation. Work by the Sherrill group[43] and Kim group[49] showed the same trend is not apparent for **tsh** substituted benzene–benzene dimers, and adding a substituent may make such a complex more or less binding than the parent **tsh** benzene–benzene dimer, depending on the conformation.

Further investigating **pff** substituted benzene–benzene dimers using SAPT calculations, Lewis and coworkers reported that adding any substituent to the substituted aromatic results in a more binding E_{ele} value.[52] This surprising result was explained by the Sherrill group as being the result of charge penetration.[53] The equilibrium distances for most arene–arene dimers, approximately 3.5–4.0 Å, brings the two aromatic monomers close enough such that the electron density of one aromatic monomer electrostatically interacts with the nuclei of the other aromatic monomer, and this is termed charge penetration. Replacing a hydrogen atom with any substituent results in a more electropositive nuclei, and increased electron density, thus increasing the electrostatic attraction due to charge penetration.

Just prior to the reports from the Sherrill and Lewis groups, Houk and Wheeler reported that the difference in substituted benzene–benzene **pff** dimer binding energies was due to the substituent of the substituted benzene interacting with the adjacent benzene ring, and not due to the substituent tuning the electrostatics of the substituted benzene.[54] Houk and Wheeler computationally demonstrated this important finding by comparing C_6H_5X–C_6H_6 E_{bind} values to the E_{bind} values of HX–C_6H_6 dimers where the X group in HX and the C_6H_5X mono-substituted benzene are the same (Figure 1.6). This comparison showed that the difference in E_{bind} values between the C_6H_5X–C_6H_6 dimers for various substituted benzenes (C_6H_5X) was the same as the E_{bind} differences for HX–C_6H_6 dimers with various HX. This supports the notion that the strength of substituted benzene–benzene interactions is dictated by the interaction between the substituent and the adjacent (unsubstituted) benzene ring.[54] This finding aligns very well with the role of charge penetration in arene–arene interactions.[53] Houk and Wheeler expanded their work to **etf** dimers, computationally demonstrating the importance of substituents interacting directly with the adjacent ring in understanding the nature of the interactions.[3]

View Online

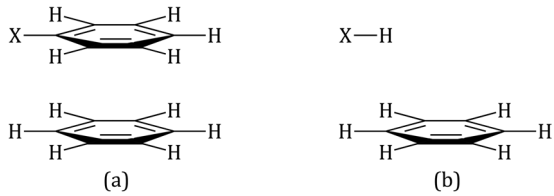

Figure 1.6 The E_{bind} values for C_6H_5X–C_6H_6 **pff** dimers (a) can be approximated very well as the E_{bind} values for HX–C_6H_6 complexes (b) where the X substituents in C_6H_5X and HX are the same. This supports the notion that the strength of substituted benzene–benzene interactions are dictated by the interaction between the substituent and the adjacent benzene ring.[54]

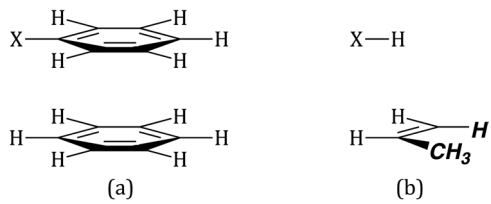

Figure 1.7 The E_{bind} values for C_6H_5X–C_6H_6 **pff** dimers (a) can be approximated very well as the E_{bind} values for HX–C_3H_6 complexes (b) where the X substituents in C_6H_5X and HX are the same. This supports the hypothesis that arene–arene interactions are best understood as local, through-space, interactions between proximal regions of the adjacent aromatics.[55]

Further computational work by Wheeler showed that arene–arene interactions can be understood *via* direct local interaction between the substituent and the region of the adjacent aromatic closest to the substituent (Figure 1.7).[55,56] For instance, the E_{bind} values for C_6H_5X–C_6H_6 interactions correlated very well with the E_{bind} values for HX–C_3H_6 dimers[55] supporting the idea that arene–arene interactions are best understood as local, through-space, interactions between proximal regions of the adjacent aromatics. Wheeler has also looked at the interactions of substituted benzenes with aromatics other than benzene, such as borazine and 1,3,5-triazine, and computationally demonstrated more generally that arene–arene interactions are best understood as through-space interactions between the substituents of the substituted benzene with the proximal region of the neighboring aromatic, be it benzene, borazine or 1,3,5-triazine.[57]

The recent advances in understanding arene–arene interactions underscore the notion that the term "π-stacking" has become outdated, and Martinez and Iverson highlighted this point a few years ago in an important perspective.[58] In this work they point out the emerging importance of considering direct interactions between substituents on the interacting rings in understanding arene–arene complexes. In the four years since they published their perspective, work by the Sherrill group and by Houk and

Published on 15 November 2016 on http://pubs.rsc.org | doi:10.1039/9781782626626-00001

View Online

Published on 15 November 2016 on http://pubs.rsc.org | doi:10.1039/9781782626626-00001

Wheeler, among others, has cemented the idea that understanding arene–arene interactions should not be approached from the lens of π–π stacking. Rather, while arene–arene interactions were initially understood in terms of the aromatic quadrupole moment, according to the Hunter–Sanders model,[2] modern computational approaches have shown the nature of these interactions are best understood *via* the substituents on one aromatic monomer interacting, through-space, with the proximal region of the adjacent aromatic monomer.[56] Furthermore, the attractive nature of arene–arene dimers can be understood as arising from charge penetration.[53]

1.2.2 Predicting the Strength of Arene–Arene Interactions

As described in various places throughout Section 1.2.1, a common theme in computational work aimed at understanding the nature of arene–arene interactions is correlating the E_{bind} values with physicochemical parameters, the most common being Hammett substituent constants.[59] While early experimental work showed that Hammett values, usually σ_p[38,39] correlated well with the E_{bind} values, computational work showed the correlations deteriorated when electron-donating substituents (with negative Hammett values) were included in the analysis.[51] Recent computational work by the Sherrill and Wheeler groups, respectively noting the importance of charge penetration in arene–arene interactions, and how the proximally close regions of the aromatics in an arene–arene dimer interact in a local, through-space manner, demonstrates the complexity of the interactions and suggests the E_{bind} values should not correlate with an electronic parameter such as the Hammett substituent constant. Not surprisingly, Sherrill and coworkers found the best approach to correlating the E_{bind} values for **tsh** benzene-substituted benzene dimers was with a multi-variable equation.[60] The parameters included in the equation were the Hammett σ_m, the molecular polarizability, and a term accounting for the interaction between the substituents on one arene and the H-atoms on the adjacent aromatic.[60] Lewis and coworkers performed SAPT calculations on a large set of substituted benzene–benzene dimers in the **pff** conformation, and they found that most of the variability in E_{bind} was due to variability in the energy due to electrostatics; the E_{ele} term.[52] The sum of the non-electrostatic terms ($E_{ind} + E_{disp} + E_{exch}$) was approximately constant regardless of the substitution pattern of the substituted aromatic. Still, the E_{bind} values did not correlate very well with the Hammett constants, and they too employed a multi-variable equation to best correlate the E_{bind} values; the terms in the equation were the Hammett constant σ_m and the molecular polarizability parameter M_r.[52]

It is worth noting that modern approaches to predicting the strength of arene–arene interactions are in line with Iverson's suggestion[58] that the terms "π-stacking" and "π–π interactions" do not convey the important forces at play in arene–arene binding. Both the Sherrill group[60] and Lewis group[52] have shown the need for multi-parameter equations to accurately predict the strength of arene–arene interactions involving substituted benzenes, and the

View Online

Published on 15 November 2016 on http://pubs.rsc.org | doi:10.1039/9781782626626-00001

Sherrill group explicitly uses a parameter that accounts for the interaction between the substituents on one arene and the H-atoms on the adjacent aromatic.[60] That the strength of arene–arene interactions involving substituted benzenes cannot simply be predicted *via* Hammett constants strongly suggests that the terms "π-stacking" and "π–π interactions" are, as Iverson suggests, outdated.[58]

1.3 Computational Approaches to Understanding Cation–Arene Interactions

1.3.1 The Nature of Cation–Arene Interactions

As noted in the Introduction, Section 1.1.2, early work on understanding cation–π interactions of aromatics centered around the aromatic quadrupole moment[33] and the aromatic electrostatic potential (ESP).[33,34] Dougherty and coworkers showed that the total cation-binding energy, E_{bind}, of a cation and negative quadrupole moment (Θ_{zz}) substituted aromatics correlates very well with the ESP of the substituted aromatic.[34] At about the beginning of the 2000s work by Cubero and coworkers[61] and Tsuzuki and coworkers[62] was disseminated showing the importance of π-electron polarizability in cation–π interactions. In both cases the groups demonstrated that cations induce polarization in the aromatic compound (Figure 1.8), and this induction contributes to the overall cation–π E_{bind}.

Shortly after the work illustrating the importance of π-electron polarizability in cation–π interactions, computational results were reported showing that positive Θ_{zz} aromatics bind cations[63] however, this was initially described as an anomaly due to the investigated aromatics having small positive Θ_{zz} values. Not long after, Lewis and Clements demonstrated that substituted aromatics with non-negligible positive Θ_{zz} values did bind cations.[64] This suggests that even though electrostatics is an important factor when describing the nature of cation–π interactions, other factors may also play important roles in the binding. The work of Cubero[61] and Tsuzuki[62] suggesting the importance of π-electron density polarizability in cation–π interactions of aromatics was offered as an explanation for why positive Θ_{zz} aromatics bind cations.

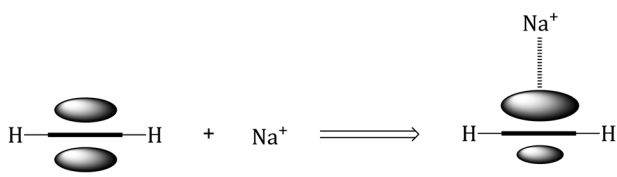

Figure 1.8 Work by Cubero and coworkers[61] and Tsuzuki and coworkers[62] suggested cations induce polarization in the aromatic compound, and this induction leads to an increase in the cation–π E_{bind}.

View Online

Published on 15 November 2016 on http://pubs.rsc.org | doi:10.1039/9781782626626-00001

The results reported by Lewis and Clements suggested cation–π interactions may, at least partially, be guided by direct interactions between the cation and the aromatic ring substituents,[64] and this idea has been expanded by Wheeler and Houk. In a similar fashion to their work demonstrating the importance of through-space interactions on arene–arene complexes (Figures 1.6 and 1.7), Wheeler and Houk showed that the E_{bind} value for a cation interacting with a substituted aromatic was reasonably approximated by adding the E_{bind} values for a cation interacting with benzene and the E_{bind} value of the cation interacting with the appropriate H–X.[65] They also included the E_{bind} value for the cation interacting with the H atoms of the substituted benzene, and an equation illustrating the relationship is shown in Figure 1.9.[65] This strongly suggests the E_{bind} values for cation–π interactions of substituted aromatics are dictated by through-space interactions between the cation and aromatic substituents, rather than being dictated by the substituents tuning the π-density of the aromatic ring. Suresh and Sayyed, taking a somewhat similar approach to Wheeler and Houk, looked at how cations interacted with different fragments of substituted aromatics and found that through-space cation–substituent interactions were most important for electron-withdrawing substituents.[66]

Recent computational work by Quinonero and coworkers suggests that cation–π interactions of aromatics are not entirely due to through-space interactions between the cation and the aromatic substituents.[67] Using the calculated quadrupole moment to approximate the energy due to electrostatics and the calculated dipole polarizabilities to approximate the energy due to polarizability, Quinonero and coworkers found the cation–π binding energies of 104 substituted benzenes and 67 heteroaromatics were best described by a combination of the electrostatic and polarizability parameters.[67] The dependence of the overall cation–π non-covalent binding energy on the aromatic dipole polarizabilities was interpreted by the authors as supporting the notion that π-electron cloud polarizability was important in cation–π binding energies, and the interactions weren't completely dictated by through-space interactions between the cation and the aromatic substituents. The authors concede that the polarizability term may reflect the polarizability

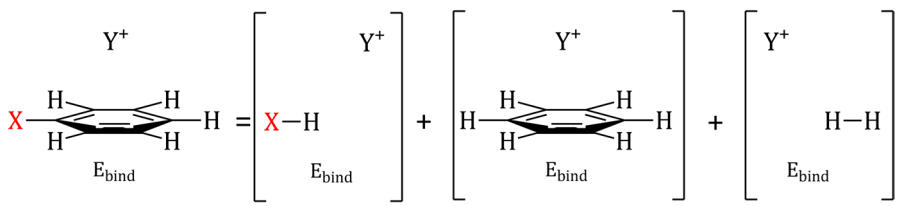

Figure 1.9 The E_{bind} value for a cation interacting with a substituted aromatic (C_6H_5X) can be reasonably approximated by adding the E_{bind} value for a cation interacting with benzene, the E_{bind} value of the cation interacting with the appropriate H–X, and the E_{bind} value for the cation interacting with the H atoms of the substituted benzene.[65]

View Online

Published on 15 November 2016 on http://pubs.rsc.org | doi:10.1039/9781782626626-00001

of the substituent in a through-space interaction; however, they show that the polarizability of the C atom at the *para* position of the mono-substituted benzenes correlates very well with the Hammett constant, σ_p, of the substituent, but not σ_m. Quinonero and coworkers suggest this supports the notion that the substituents are directly involved in the polarization of the aromatic ring, and that π-cloud polarizability and through-space interactions are both important in the cation–π interactions of aromatics.[67]

Recent work by Lewis and coworkers[68] and by Sastry and coworkers[69] applied energy decomposition methods to understand the cation–π binding of aromatics. Lewis and coworkers employed the SAPT approach with the CCSD/6-311++G** method and basis set to investigate the cation–π binding of substituted benzenes[68] and Sastry and coworkers employed both the reduced variational space (RVS) and the DFT-SAPT approaches to investigate the energy decomposition of cation–π complexes involving benzene, phenol, and a variety of heteroaromatics.[69] As noted above in the arene–arene section, the SAPT calculations allow for the total non-covalent binding energy to be decomposed into E_{ele}, E_{disp}, E_{ind}, and E_{exch}, and the results reported by Lewis and coworkers show that E_{ele} is the largest contributor to the overall cation–π binding of substituted benzenes. Furthermore, among the component energy terms, E_{ele} is most sensitive to the distance between the cation and aromatic ring.[68] The RVS method decomposes the overall non-covalent binding energy into E_{ele}, E_{exch}, E_{pol}, and E_{CT}, where E_{ele} and E_{exch} are the same as for the SAPT method, E_{pol} is the energy due to polarization, and E_{CT} is the energy due to charge transfer. The DFT-SAPT method decomposes the overall non-covalent binding energy into E_{ele}, E_{disp}, E_{ind}, and E_{exch}, $E_{exch-disp}$, $E_{exch-ind}$ and δ(HF), and this allows the polarization component of the overall binding energy to be determined *via* the equation $E_{pol}(\text{DFT-SAPT}) = E_{ind} + E_{exch\text{-}ind} + \delta(\text{HF})$. Using the RVS and DFT-SAPT energy decomposition methods, Sastry and coworkers showed the major contributors to the cation–π binding energy of benzene, phenol, and various heteroaromatics were the E_{ele} and E_{pol} terms.[69] It is worth noting that neither the energy decomposition work by Lewis and coworkers, nor the work by Sastry and coworkers, directly addresses the issue of whether cation–arene interactions are dictated by the cation interacting with the π-electron density, the substituent, or both. Cation–substituent and cation–π interactions can both be explained as owing their attraction to electrostatics and/or electron density polarization.

The medium in which cation–arene interactions are studied can have a significant effect on the strength of the interaction, and this has been widely disseminated experimentally.[27,70] Using the SM5.42R/HF/6-31+G* level of theory, Dougherty and Gallivan computationally showed that increasing solvent polarity led to a decrease in the cation–π E_{bind} value.[71] However, the decrease was found to be minimal compared to the calculated decrease in binding energy for salt bridges across solvents with different polarities. Sherrill and coworkers reported similar findings for cation–π interactions of benzene where the cation is Li^+, Na^+, K^+, or NH_4^+ using the polarizable continuum model (PCM) computational approach; increasing solvent polarity decreases

View Online

Published on 15 November 2016 on http://pubs.rsc.org | doi:10.1039/9781782626626-00001

the strength of the cation–π interaction.[72] Recently, Bania and coworkers showed that the same solvent polarity trends hold for substituted aromatics partaking in cation–π interactions with Li^+, Na^+, or K^+ using the PCM approach to model the solvents.[73] The issue of specific solvation of water molecules was computationally addressed by Sastry and coworkers and they reported that solvation of the cation in cation–π complexes decreases the overall E_{bind}, while solvation of the aromatic enhances the binding strength.[74]

While most studies of cation–π complexes of substituted aromatics have focused on the half-sandwich motif (Figure 1.1(b)), it is estimated that sandwich complexes (Figure 1.10), with alkali or alkaline earth metal cations, are at least as abundant in biology.[1] For instance, many of the studies that describe the importance of cation–π binding in protein folding, structure and function are in fact sandwich complexes.[75,76] Modern computational work has aimed to address the issue of the additivity of the E_{bind} values for the cation–π sandwich complexes ($E_{bind,S}$). The issue involves whether $E_{bind,S}$ is additive, and is equal to the sum of the binding energies of the two corresponding half-sandwich complexes ($E_{bind,HS}$), or whether $E_{bind,S}$ is non-additive, and $E_{bind,S} < 2 \times E_{bind,HS}$. Initial work on this issue by Jiang and coworkers suggested $E_{bind,S}$ was additive and $E_{bind,S} = 2 \times E_{bind,HS}$.[77] More recent calculations by Orabi and Lamoureux on the topic showed the binding energy of cation–π sandwich complexes was non-additive, and $E_{bind,S} < 2 \times E_{bind,HS}$.[78] Subsequent computational efforts by the Lewis group showed that a triple-ζ basis set was required to observe the non-additivity of cation–π sandwich complexes.[79] The Lewis group also showed that non-additivity was increased when less polarizable ions were included in the sandwich complex (for instance, when Li^+ is the ion rather than Na^+ or K^+).[79]

1.3.2 Predicting the Strength of Cation–Arene Interactions

Early work on predicting the binding strength of cation–π complexes of substituted aromatics focused on the electrostatic potential and Hammett substituent constants.[59] Dougherty and coworkers showed a correlation between the calculated electrostatic potential of 11 aromatics and the Na^+ binding energy.[34] These 11 aromatics included benzene, naphthalene, pyridine, and eight substituted benzenes. This early work by Dougherty and coworkers

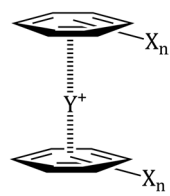

Figure 1.10 General structure of cation–π sandwich complexes for two substituted benzenes, where Y is any monovalent cation, X is any substituent, and $n = 1–6$.

View Online

Published on 15 November 2016 on http://pubs.rsc.org | doi:10.1039/9781782626626-00001

also suggested a correlation between the calculated Na^+-substituted benzene cation–π binding energies and the Hammett substituent constant σ_m.[34] Subsequent work by Jiang and coworkers investigated the cation–π binding of Li^+, Na^+, K^+, Be^{2+}, Mg^{2+}, and Ca^{2+} with aniline, toluene, phenol, benzene, fluorobenzene, 1,4-difluorobenzene, and 1,3,5-trifluorobenzene, and an excellent correlation was reported between the binding enthalpies and σ_{Total}, which the authors define as $\sigma_{Total} = (\Sigma\sigma_m + \Sigma\sigma_p)$.[80] This is the only example of using the σ_{Total} parameter to predict the relative cation–π binding of substituted benzenes, and Jiang and coworkers suggest it means both resonance and induction are important in cation–π binding.[80] More recently, Suresh and Sayyed showed that cation–π interaction energies correlated very well with the term ΔV_{min}, which is the difference between the calculated molecular electrostatic potential on the aromatic π-region for a substituted arene and the corresponding unsubstituted analog.[81] Suresh and Sayyed investigated multiple aromatic frameworks, cations, and substituents, and they found that the calculated ΔV_{min} performed very well in predicting the relative cation–arene binding energy.

Recent work by Quinonero—in response to the Houk and Wheeler work—suggesting that cation–arene interactions of substituted benzenes may be dictated by both cation–π interactions and cation–substituent interactions showed that a two-parameter equation involving a linear combination of the electrostatic energy and the polarization energy correlated very well with the cation–π binding energies of substituted aromatics.[67] As noted above, for the Quinonero and coworkers' study, the energy due to electrostatics was approximated using the calculated aromatic quadrupole moment, and the energy due to polarization was approximated *via* the calculated aromatic dipole polarizabilities. Another recent study noted above, by Lewis and coworkers investigating the energy decomposition energies of cation–π interactions of aromatics, showed a poor correlation between the binding energies/enthalpies and the $\Sigma(\sigma_m + \sigma_p)$, $\Sigma\sigma_p$, $\Sigma\sigma_m$, and Θ_{zz} values for a large number of substituted benzenes.[68] As a result, the researchers developed a cation–π binding constant, Π^+, from the cation-binding enthalpies of the mono-substituted aromatics. Specifically, the substituent constant was derived from the equation $\Pi^+ = -\log[(\Delta H_{298}(Na^+–C_6H_5X))/(\Delta H_{298}(Na^+–C_6H_6))]$, and the correlation with the cation–π binding energies of the larger group of substituted aromatics, mono-substituted and multi-substituted, was excellent.

1.4 Summary

Initial computational work on arene–arene and cation–arene non-covalent interactions focused on the aromatic quadrupole moments. Over time, Hammett substituent constants and aromatic electrostatic potentials were commonly employed to understand and describe arene–arene and cation–arene interactions. Modern computational efforts have focused on the importance of substituent–substituent interactions in the binding of arene–arene complexes, and cation–substituent interactions in the binding of cation–arene

View Online

Published on 15 November 2016 on http://pubs.rsc.org | doi:10.1039/9781782626626-00001

complexes. In addition, energy decomposition methods, such as SAPT, are becoming more widely employed to better understand the non-covalent interactions of aromatics. Future work will surely see energy decomposition methods applied to larger aromatic systems. Furthermore, the importance of π–π *versus* substituent–substituent interactions in understanding the nature of the attraction in arene–arene complexes, and the importance of cation–π *versus* cation–substituent interactions in understanding the nature of the attraction in cation–arene complexes, will certainly be investigated with larger, polyaromatic, systems. The concluding chapter of this book describes new directions in organic materials chemistry that are spawning this interest in larger, polyaromatic systems.

References

1. L. M. Salonene, M. Ellermann and F. Diederich, *Angew. Chem., Int. Ed.*, 2011, **50**, 4808.
2. C. A. Hunter and J. K. M. Sanders, *J. Am. Chem. Soc.*, 1990, **112**, 5525.
3. S. E. Wheeler and K. N. Houk, *Mol. Phys.*, 2009, **107**, 749.
4. D. A. Dougherty, *Acc. Chem. Res.*, 2013, **46**, 885.
5. M. Watt, J. Y. Hwang, K. W. Cormier and M. Lewis, *J. Phys. Chem. A*, 2009, **113**, 6192.
6. S. K. Burley and G. A. Petsko, *Science*, 1985, **229**, 23.
7. K. Riley and P. Hobza, *Acc. Chem. Res.*, 2013, **46**, 927.
8. Z. R. Laughrey, S. E. Kiehna, A. J. Riemen and M. L. Waters, *J. Am. Chem. Soc.*, 2008, **130**, 14625.
9. J. L. Asensio, A. Arda, F. J. Canada and J. Jimenez-Barbero, *Acc. Chem. Res.*, 2013, **46**, 946.
10. S. Aravinda, N. Shamala, C. Das, A. Sriranjini, I. L. Karle and P. Balaram, *J. Am. Chem. Soc.*, 2003, **125**, 5308.
11. C. J. Pace and J. Gao, *Acc. Chem. Res.*, 2013, **46**, 907.
12. K. A. Wilson, J. L. Kellie and S. D. Wetmore, *Nucleic Acids Res.*, 2014, **42**, 6726.
13. Y. An, J. W. G. Bloom and S. E. Wheeler, *J. Phys. Chem. B*, 2015, **119**, 14441.
14. N. Chaudhary and R. Nagaraj, *J. Pept. Sci.*, 2011, **17**, 115.
15. C. Bissantz, B. Kuhn and M. Stahl, *J. Med. Chem.*, 2010, **53**, 5061.
16. F.-G. Klarner and T. Schrader, *Acc. Chem. Res.*, 2013, **46**, 967.
17. H.-J. Schneider, *Acc. Chem. Res.*, 2013, **46**, 1010.
18. D. Ajami and J. Rebek, *Acc. Chem. Res.*, 2013, **46**, 990.
19. D. Umadevi, S. Panigrahi and G. N. Sastry, *Acc. Chem. Res.*, 2014, **47**, 2574.
20. E. H. Krenske and K. N. Houk, *Acc. Chem. Res.*, 2013, **46**, 979.
21. G. B. Jones, *Tetrahedron*, 2001, **57**, 7999.
22. J. H. Williams, *Acc. Chem. Res.*, 1993, **26**, 593.
23. M. R. Battaglia, A. D. Buckingham and J. H. Williams, *Chem. Phys. Lett.*, 1981, **78**, 421.
24. J. H. Williams, J. K. Cockcroft and A. N. Fitch, *Angew. Chem., Int. Ed.*, 1992, **31**, 1655.

View Online

25. S. Lorenzo, G. R. Lewis and I. Dance, *New J. Chem.*, 2000, **24**, 295.
26. J. Sunner, K. Nishizawa and P. Kebarle, *J. Phys. Chem.*, 1981, **85**, 1814.
27. J. C. Ma and D. A. Dougherty, *Chem. Rev.*, 1997, **97**, 1303.
28. S. K. Burley and G. A. Petsko, *FEBS Lett.*, 1986, **203**, 139.
29. K. D. Daze and F. Hof, *Acc. Chem. Res.*, 2013, **46**, 937.
30. D. A. Dougherty, *J. Nutr.*, 2007, **137**, 1504S.
31. K. Fujisawa, M. Humbert-Droz, R. Letrun, E. Vauthey, T. A. Wesolowski, N. Sakai and S. Matile, *J. Am. Chem. Soc.*, 2015, **137**, 11047.
32. K. Ishihara, M. Fushimi and M. Akakura, *Acc. Chem. Res.*, 2007, **40**, 1049.
33. D. A. Dougherty, *Science*, 1996, **271**, 163.
34. S. Mecozzi, A. P. West and D. A. Dougherty, *J. Am. Chem. Soc.*, 1996, **118**, 2307.
35. B. W. Gung, M. Patel and X. W. Xue, *J. Org. Chem.*, 2005, **70**, 10532.
36. F. J. Carver, C. A. Hunter, D. J. Livingstone, J. F. McCabe and E. M. Seward, *Chem. – Eur. J.*, 2002, **8**, 2848.
37. E.-i. Kim, S. Paliwal and C. S. Wilcox, *J. Am. Chem. Soc.*, 1998, **120**, 11192.
38. F. Cozzi, M. Cinquini, R. Annunziata, T. Dwyer and J. Siegel, *J. Am. Chem. Soc.*, 1992, **114**, 5729.
39. F. Cozzi, M. Cinquini, R. Annunziata and J. Siegel, *J. Am. Chem. Soc.*, 1993, **115**, 5330.
40. B. W. Gung and J. C. Amicangelo, *J. Org. Chem.*, 2006, **71**, 9261.
41. B. Jeziorski, R. Moszynski and K. Szalewicz, *Chem. Rev.*, 1994, **94**, 1887.
42. H. L. Williams, K. Szalewicz, B. Jeziorski, R. Moszynski and S. Rybak, *J. Chem. Phys.*, 1993, **98**, 1279.
43. M. O. Sinnokrot and C. D. Sherrill, *J. Am. Chem. Soc.*, 2004, **126**, 7690.
44. S. Tsuzuki, K. Honda, T. Uchimaru, M. Mikami and K. Tanabe, *J. Am. Chem. Soc.*, 2002, **124**, 104.
45. A. J. Stone, A. Dullweber, M. P. Hodges, P. L. A. Popelier and D. J. Wales, *Orient, a program for studying interactions between molecules*, University of Cambridge, 1995.
46. S. Tsuzuki, K. Honda, T. Uchimaru and M. Mikami, *J. Chem. Phys.*, 2005, **122**, 144323.
47. S. Tsuzuki, K. Honda, T. Uchimaru and M. Mikami, *J. Chem. Phys.*, 2006, **125**, 124304.
48. S. Tsuzuki, T. Uchimaru and M. Mikami, *J. Phys. Chem. A*, 2006, **110**, 2027.
49. E. C. Lee, B. H. Hong, J. Y. Lee, J. C. Kim, D. Kim, Y. Kim, P. Tarakeshwar and K. S. Kim, *J. Am. Chem. Soc.*, 2005, **127**, 4530.
50. M. O. Sinnokrot and C. D. Sherrill, *J. Phys. Chem. A*, 2003, **107**, 8377.
51. A. L. Ringer and C. D. Sherrill, *J. Am. Chem. Soc.*, 2009, **131**, 4574.
52. M. Watt, L. K. E. Hardebeck, C. C. Kirkpatrick and M. Lewis, *J. Am. Chem. Soc.*, 2011, **133**, 3854.
53. E. G. Hohenstein, J. Duan and C. D. Sherrill, *J. Am. Chem. Soc.*, 2011, **133**, 13244.
54. S. E. Wheeler and K. N. Houk, *J. Am. Chem. Soc.*, 2008, **130**, 10854.
55. S. E. Wheeler, *J. Am. Chem. Soc.*, 2011, **133**, 10262.
56. S. E. Wheeler, *Acc. Chem. Res.*, 2013, **46**, 1029.

Published on 15 November 2016 on http://pubs.rsc.org | doi:10.1039/9781782626626-00001

View Online

Published on 15 November 2016 on http://pubs.rsc.org | doi:10.1039/9781782626626-00001

57. R. K. Raju, J. W. G. Bloom and S. E. Wheeler, *J. Chem. Theory Comput.*, 2013, **9**, 2379.
58. C. R. Martinez and B. L. Iverson, *Chem. Sci.*, 2012, **3**, 2191.
59. M. Lewis, C. Bagwill, L. K. E. Hardebeck and S. Wireduaah, *Comput. Struct. Biotechnol. J.*, 2012, **1**, e201204004.
60. A. L. Ringer, M. O. Sinnokrot, R. P. Lively and C. D. Sherrill, *Chem.–Eur. J.*, 2006, **12**, 3821.
61. E. Cubero, F. J. Luque and M. Orozco, *Proc. Natl. Acad. Sci. U. S. A.*, 1998, **95**, 5976.
62. S. Tsuzuki, M. Yoshida, T. Uchimaru and M. Mikami, *J. Phys. Chem. A*, 2001, **105**, 769.
63. C. Garau, A. Frontera, D. Quinonero, P. Ballester, A. Costa and P. M. Deya, *Chem. Phys. Lett.*, 2004, **399**, 220.
64. A. Clements and M. Lewis, *J. Phys. Chem. A*, 2006, **110**, 12705.
65. S. E. Wheeler and K. N. Houk, *J. Am. Chem. Soc.*, 2009, **131**, 3126.
66. F. B. Sayyed and C. H. Suresh, *J. Phys. Chem. A*, 2011, **115**, 5660.
67. A. Bauza, P. M. Deya, A. Frontera and D. Quinonero, *Phys. Chem. Chem. Phys.*, 2014, **16**, 1322.
68. S. Wireduaah, T. M. Parker, C. Bagwill, C. C. Kirkpatrick and M. Lewis, *RSC Adv.*, 2014, **4**, 62061.
69. B. Sharma, H. K. Srivastava, G. Gayatri and G. N. Sastry, *J. Comput. Chem.*, 2015, **36**, 529.
70. R. A. Kumpf and D. A. Dougherty, *Science*, 1993, **261**, 1708.
71. J. P. Gallivan and D. A. Dougherty, *J. Am. Chem. Soc.*, 2000, **122**, 870.
72. M. S. Marshall, R. P. Steele, K. S. Thanthiriwatte and C. D. Sherrill, *J. Phys. Chem. A*, 2009, **113**, 13628.
73. K. K. Bania, A. K. Guha, P. K. Bhattacharyya and S. Sinha, *Dalton Trans.*, 2014, **43**, 1769.
74. J. S. Rao, H. Z. Zipse and G. N. Sastry, *J. Phys. Chem. A*, 2009, **113**, 7225.
75. S. C. Lummis, *Biochem. Soc. Trans.*, 2009, **37**, 1343.
76. S. C. Lummis, I. McGonigle, J. A. Ashby and D. A. Dougherty, *J. Neurosci.*, 2011, **31**, 12371.
77. T. Liu, W. Zhu, J. Gu, J. Shen, X. Luo, G. Chen, C. M. Puah, I. Silman, K. Chen, J. L. Sussman and H. Jiang, *J. Phys. Chem. A*, 2004, **108**, 9400.
78. E. A. Orabi and G. Lamoureux, *J. Chem. Theory Comput.*, 2012, **8**, 182.
79. S. Wireduaah, T. M. Parker and M. Lewis, *J. Phys. Chem. A*, 2013, **117**, 2598.
80. W. Zhu, X. Tan, J. Shen, X. Luo, F. Cheng, P. C. Mok, R. Ji, K. Chen and H. Jiang, *J. Phys. Chem. A*, 2003, **107**, 2296.
81. F. B. Sayyed and C. H. Suresh, *J. Phys. Chem. A*, 2012, **116**, 5723.

Published on 15 November 2016 on http://pubs.rsc.org | doi:10.1039/9781782626626-00018

CHAPTER 2

Role of Aromatic Interactions in Directing Organic Reactions

RAJAT MAJI[a] AND STEVEN E. WHEELER*[a]

[a]Department of Chemistry, Texas A&M University, College Station, TX 77842, USA
*E-mail: wheeler@chem.tamu.edu

2.1 Introduction and Background

Non-covalent interactions involving aromatic rings (π-stacking interactions, CH/π interactions, *etc.*; see Figure 2.1) abound in organic systems, and the last decade has witnessed a surge in interest in organic reactions directed by these aromatic interactions. This interest has accompanied a general shift in emphasis from a predominantly steric view of organic reactions to a more nuanced view in which the fate of a reaction hinges on the interplay of both attractive and repulsive non-covalent interactions. For instance, asymmetric reactions were long thought to result primarily from the destabilization of the disfavored pathway through repulsive steric interactions (*e.g.* the steric shielding of one face of a pro-chiral molecule to favor direct attack of the less hindered face).[1] More modern views, however, highlight the potential role of both stabilizing and destabilizing non-covalent interactions in determining the relative free energy of stereocontrolling transition states.[2–4] There have been a number of excellent recent reviews of non-covalent interactions in the context of organic reactions. For instance, Krenske and Houk[5] provided an overview of aromatic interactions as control elements in stereoselective organic reactions. More

Monographs in Supramolecular Chemistry No. 20
Aromatic Interactions: Frontiers in Knowledge and Application
Edited by Darren W. Johnson and Fraser Hof
© The Royal Society of Chemistry 2017
Published by the Royal Society of Chemistry, www.rsc.org

View Online

Published on 15 November 2016 on http://pubs.rsc.org | doi:10.1039/9781782626626-00018

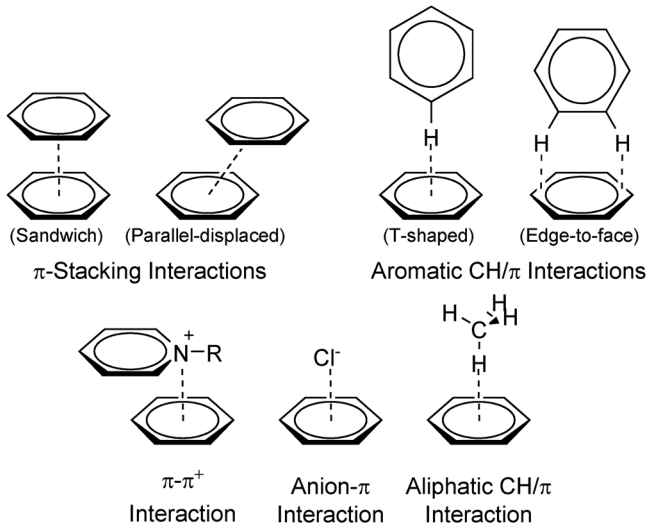

Figure 2.1 Prototypical non-covalent interactions involving aromatic rings.[8]

recently, Wagner and Schreiner[6] reviewed the role of dispersion effects, which are the drivers of many aromatic interactions, in everything from the structure and stability of organic molecules to reactivity, catalysis, and spectroscopy. Similarly, Matile and co-workers have very recently published a perspective on the intriguing world of anion–π catalyzed reactions.[7]

In order to harness the power of non-covalent interactions to control organic reactions, one needs to first understand both the nature of these non-covalent interactions and their role in existing organic transformations. Our understanding of aromatic interactions has seen tremendous advances in the last few years,[8] and continues to evolve. Concurrent with these changes in our understanding of aromatic interactions is a growing body of examples of organic reactions in which these non-covalent interactions appear to play key roles.

Herein, we proceed by first providing a brief overview of aromatic interactions, followed by selected examples of both catalytic and non-catalytic reactions in which these interactions play important roles. The aim is not to provide a comprehensive review of aromatic interactions in organic reactions, but instead to convey the breadth of systems in which non-covalent interactions appear to be operative. Our hope is that this overview will inspire other, novel uses of aromatic interactions in directing organic reactions, leveraging the power of supramolecular chemistry to advance the field of organic synthesis.

2.2 Aromatic Interactions of Relevance to Organic Reactions

There are a number of non-covalent interactions involving aromatic rings that play vital roles in many organic reactions, including π-stacking interactions, CH/π interactions, anion–π interactions, and π–π^+ interactions, among

View Online

Published on 15 November 2016 on http://pubs.rsc.org | doi:10.1039/9781782626626-00018

others (see Figure 2.1). Below, we summarize these main classes of interactions and direct the reader to recent reviews for more detailed discussions of their origin and nature.[8–13]

π-stacking interactions, which are generally defined as attractive interactions between aromatic rings, have long been known;[14] however, their origin and nature continues to be debated.[15–29] Indeed, even the utility of the term "π-stacking" has recently come into question.[11] The simplest system exhibiting π-stacking interactions is the benzene dimer, which is typically considered in four prototypical arrangements (see Figure 2.1). Among these, we consider the sandwich and parallel displaced configurations to be "π-stacked", whereas the interaction present in the T-shaped and edge-to-face dimers are examples of aromatic CH/π interactions (*vide infra*). This differentiation between the sandwich and parallel displaced configurations, on one hand, and the T-shaped and edge-to-face dimers on the other, is justifiable on both geometric grounds and physical grounds. For instance, while the interactions in the T-shaped and edge-to-face dimers are primarily electrostatic in nature, the π-stacking interactions in the sandwich and parallel displaced benzene dimers are due mostly to dispersion interactions.[30] For non-substituted arenes, the parallel-displaced configuration is strongly favored over sandwich-like stacking; the sandwich configuration, while still favorable relative to separated benzenes, is a saddle point on the potential energy surface.[30]

Although dispersion interactions are the primary drivers of π-stacking interactions, the ability of heteroatoms and substituents to tune the strength and geometry of these interactions is largely attributed to electrostatic effects. Traditionally, the impact of substituents on π-stacking interactions was explained in terms of resonance-based changes in the aryl π-electron density induced by the substituents.[15,17,18,31–35] That is, electron-withdrawing substituents (*e.g.* CN, NO_2, *etc.*) deplete the electron density of the substituted ring, rendering it "electron-deficient." This electron-deficient ring then interacts more favorably with the "electron-rich" π-electron cloud of the other ring. However, mounting computational data[25,28,36] suggests that, at least in the gas phase, the dominant effect of substituents in π-stacking interactions arises from local, direct interactions of the substituents on one ring with the nearby C–H bonds of the other ring. More recently, Raju *et al.*[26] have shown that substituent effects in sandwich dimers of diverse aromatic rings can be explained by the interaction of the local dipole moment associated with the substituents and the electric field of the other ring. One special case of substituent effects in π-stacking interactions concerns so-called arene–perfluoroarene interactions.[9,10] These interactions, typified by the sandwich-like dimer of benzene and hexafluorobenzene, are generally more favorable than aryl–aryl interactions between rings of comparable size. Moreover, perfluoroarene–arene interactions tend to favor sandwich-like stacking configurations, rather than the parallel-displaced stacking most often exhibited by non-fluorinated arenes.

View Online

Published on 15 November 2016 on http://pubs.rsc.org | doi:10.1039/9781782626626-00018

Aliphatic CH/π interactions,[37] in which a CH bond is directed toward the face of an arene, are also largely driven by dispersion interactions.[38,39] However, the relative contribution of dispersion and electrostatic effects varies with the hybridization of the carbon atom involved, with the importance of electrostatics decreasing with the increasing p-character of the carbon. For instance, Tsuzuki *et al.* showed[40,41] that sp-hybridized CH/π interactions (*i.e.* an acetylenic CH group directed toward the face of an arene) are largely electrostatic in nature, whereas the complex between methane and benzene is almost entirely dispersion-driven. Similarly, aromatic CH/π interactions are mostly electrostatic in origin. With regard to substituent effects, Bloom *et al.*[42] showed that for sp^3-hybridized CH/π interactions, substituent effects are driven primarily by dispersion effects. Consequently, the polarizability of the substituent is the primary predictor of the strength of interaction in model complexes of methane with substituted benzenes. On the other hand, the electronic character of the substituent will determine the strength of sp- and sp^2-hybridized CH/π interactions, including aromatic CH/π interactions. In these cases, substitution of the arene accepting the CH···π interaction with electron donating groups leads to more favorable interactions.

Anion–π interactions are typically defined as attractive interactions between atomic or polyatomic anions and the face of an electron-deficient ring. These interactions, often viewed as analogous to the more well-known cation–π interactions,[43–47] were proposed by theorists a dozen years ago and have rapidly shifted the supramolecular landscape.[48] As seen below, anion–π interactions have emerged as a potentially powerful means of both accelerating and steering organic reactions. Finally, π–π^+ interactions are attractive interactions between a cationic arene (*e.g.* pyridinium) and a neutral arene. While quite distinct from π-stacking and cation–π interactions, π–π^+ interactions combine some features of both of these more well-known interactions.[49,50] Pioneering work by Tsuzuki *et al.*[50] has shown that, in contrast to π-stacking interactions, π–π^+ interactions arise primarily from electrostatic interactions and induction.

Since many of these non-covalent interactions depend strongly on dispersion interactions, their computational description has long been a challenge. Correlated *ab initio* methods (*e.g.* MP2, CCSD, *etc.*) are able to capture dispersion interactions, but at considerable computational cost; moreover, MP2 tends to overestimate the impact of dispersion interactions. Traditional density functional theory (DFT) methods (*e.g.* B3LYP), on the other hand, fail to capture any substantial dispersion-like interactions. However, the last decade has witnessed tremendous advances in DFT-based methods to capture dispersion-like interactions, which has opened the door to robust computational studies of these interactions in the context of organic reactions. The most common methods used to capture dispersion-driven non-covalent interactions in organic systems are the empirical dispersion correction of Grimme (the so-called -D, -D2, and -D3 methods)[51–53] and the M05 and M06 families of functionals from Truhlar and co-workers.[54–56] Notably, the

View Online

Published on 15 November 2016 on http://pubs.rsc.org | doi:10.1039/9781782626626-00018

venerable B3LYP functional, which for many years was the workhorse of computational organic chemistry, fails to capture dispersion interactions, and results from this functional applied to systems in which dispersion interactions play key roles should be viewed with some skepticism.

2.3 Aromatic Interactions in Non-Catalytic Reactions

Aromatic interactions play key roles in many organic reactions, including non-catalytic processes, such as cycloadditions and macrocyclizations. Cycloadditions have long been a staple of physical organic chemistry, and the impact of stereoelectronic effects on their regiochemistry and reactivity is a common topic in the undergraduate and graduate organic chemistry curricula. However, in some cases, aromatic interactions provide an additional means of steering these reactions. For example, in 2006, McNeil, Swager, and co-workers[57] introduced a remarkably stereoselective and high-yielding Diels–Alder cycloaddition of anthracene with a substituted maleic anhydride in their synthesis of conjugated polymers incorporating π-stacking interactions along the polymer backbone (Figure 2.2). In unpublished work, McNeil *et al.* found that substituents (X) modulated the stereoselectivity of this reaction, which was tentatively attributed to differences in π-stacking interactions in the transition states for the two possible cycloadditions. Building on this work, Wheeler, McNeil, *et al.*[58] sought to quantify the role of π-stacking interactions in the stereoselectivity of these reactions, and, ultimately, to use

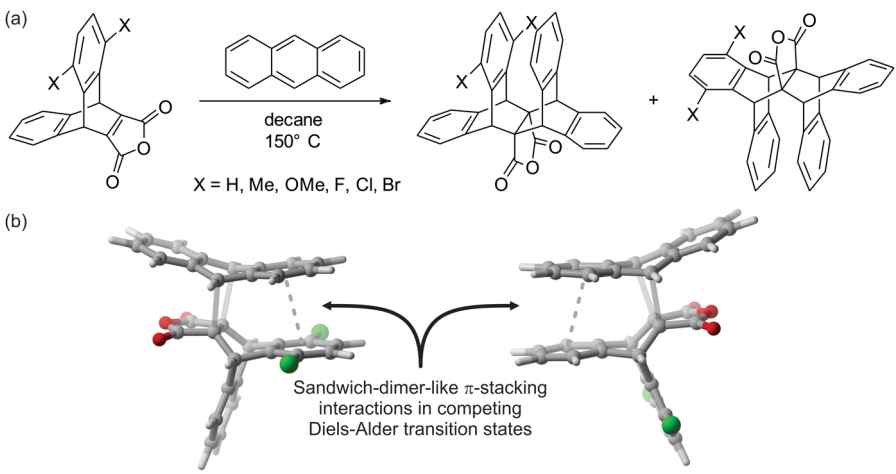

Figure 2.2 (a) Stereoselective Diels–Alder cycloaddition studied by Wheeler, McNeil, *et al.* in which π-stacking interactions in competing transition states modulate the stereoselectivity. (b) Computed TS structures from ref. 58.

View Online

Published on 15 November 2016 on http://pubs.rsc.org | doi:10.1039/9781782626626-00018

these reactions as an experimental probe of substituent effects in π-stacking interactions. Unlike π-stacking interactions in most unconstrained systems, which tend to adopt parallel-displaced arrangements, the nature of these Diels–Alder transition state structures places two phenyl rings in almost idealized stacked sandwich dimer configurations (see Figure 2.2(b)). Thus, these reactions provided a unique opportunity to probe the impact of substituent effects on model sandwich benzene dimers.

Experimental and computational data confirmed that substituent effects in π-stacking interactions could be used to control the stereoselectivity of this reaction,[58] guiding the addition of anthracene to one or the other face of the maleic anhydride. Ultimately, these data provided experimental confirmation of the importance of direct interactions in substituent effects in π-stacking interactions.[25,28,36] Moreover, this work provided one of the first confirmations of the utility of M05-2X as a suitable means of studying organic reactions in which π-stacking interactions play key roles.

In 2006, Collins and coworkers[59] exploited attractive aromatic interactions to promote macrocyclizations *via* ring closing metathesis (Figure 2.3). During preliminary studies, they noted that they could reduce the conformational flexibility of their acyclic diene precursor through stabilizing π-stacking interactions that favored a closed conformation, thereby increasing the probability of macrocyclization. This was supported by semi-empirical (AM1) and *ab initio* (MP2) computations that showed a clear preference for closed conformations featuring stacked aromatic rings over open conformations. Moreover, this conformational preference was strongly impacted by the use of a perfluorophenyl group, which led to even more favorable stacking interactions through perfluoroarene–arene interactions. Subsequently, Collins *et al.*[60] observed that replacing the pentafluorophenyl ring with a 3,5-(trifluoromethyl)phenyl ring provided even better yields for macrocyclizations *via* an ene–yne metathesis reaction. This can be attributed to the enhanced π-stacking afforded by the two CF_3 groups, in addition to possible lone-pair/π interactions in the low-lying conformers. In 2008, Collins *et al.*[61] found that replacing the ester linkage by an amide resulted in even greater macrocyclization yields (up to 27%), which was rationalized based on further enhanced π-stacking interactions based on computational studies. Finally, in 2010, Collins *et al.*[62] extended this concept to an intermolecular version

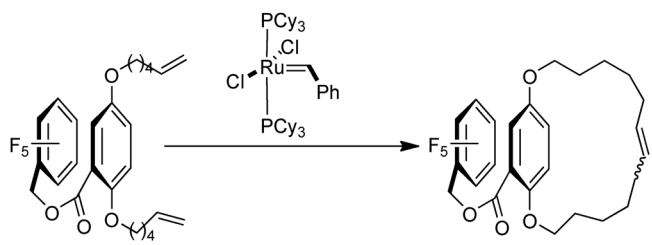

Figure 2.3 Macrocyclization scheme of Collins and co-workers.[59]

View Online

where a quinolinium salt additive acts as a conformation controlling element through π–π^+ interactions.

Published on 15 November 2016 on http://pubs.rsc.org | doi:10.1039/9781782626626-00018

2.4 Aromatic Interactions in Transition-Metal Catalyzed Reactions

Transition-metal catalyzed processes have long dominated the field of homogeneous catalysis, and are often impacted by aromatic interactions.[4] A seminal example of CH/π interactions in transition-metal catalyzed reactions was provided by Noyori and co-workers[63–66] during their study of the transfer hydrogenation of aromatic carbonyl compounds using chiral Ru^{III} complexes.[63–66] Intriguingly, Noyori *et al.* found that there was preferential formation of the (*S*)-isomer, despite the expected greater steric repulsion in the corresponding transition state. This was explained, based on computations at the MP2 level of theory, by the presence of favorable aromatic CH/π interactions (edge-to-face interactions) between the benzene complexed with the Ru and the pendant aryl group of the reacting ketone that preferentially stabilized the more sterically crowded (*S*)-transition state. This same trend persisted even after replacing the phenyl ring on Ru with a hexamethylphenyl ring. In this case, a favorable aliphatic CH/π interaction between one of the methyl groups of the hexamethylbenzene and the aryl group of the ketone still managed to outweigh the increasing unfavorable steric interactions in the TS leading to the (*S*)-isomer.

During their study of the C_3-symmetric Ti^{IV} amino trialkolate mediated enantioselective sulfoxidation reaction (Figure 2.4(a)), Santoni *et al.*[67]

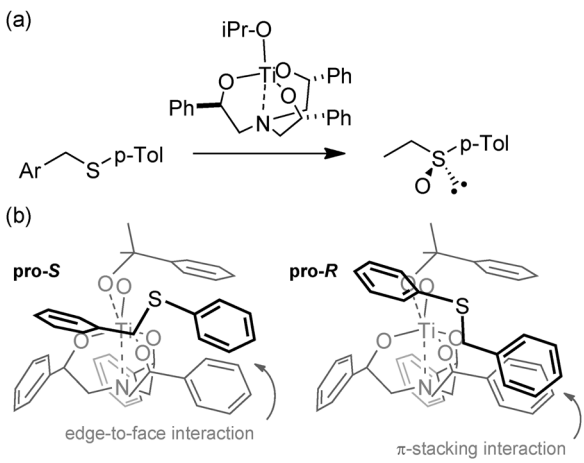

Figure 2.4 (a) Ti^{IV} mediated enantioselective sulfoxidation reaction of Santoni *et al.*,[67] along with their TS model (b), in which the stereoselectivity depends on the competition between edge-to-face and stacked aryl–aryl interactions.

View Online

Published on 15 November 2016 on http://pubs.rsc.org | doi:10.1039/9781782626626-00018

observed enhanced selectivity with catalysts containing aromatic rings. They used B3LYP to study the intermediate alkyl peroxo Ti^{IV} complex to unravel the origin of the selectivity for (*S*)-sulfoxides in this reaction. They identified two possible approaches of the substrate (see Figure 2.4(b)), which led to formation of the two enantiomeric sulfoxides. In these competing reaction pathways, the pro-*S* configuration features an edge-to-face interaction between phenyl rings on the substrate and catalyst; the pro-*R* configuration instead features π-stacking interactions between two rings. Santoni *et al.*[67] postulated that the former interaction is more favorable, explaining the preferential formation of the (*S*)-sulfoxide. This was corroborated by the fact that replacing one of the phenyl rings with either a perfluorophenyl ring or *p*-nitrobenzene, both of which should enhance the π-stacking interaction in the pro-*R* configuration, resulted in a drop in the observed stereoselectivity.

2.5 Aromatic Interactions in Organocatalysis

Aromatic interactions also play vital roles in myriad organocatalytic reactions, which often rely on subtle non-covalent interactions for both catalytic activity and stereoselectivity. For instance, proline-catalyzed aldol reactions form the foundation of modern organocatalysis, and there has been a long line of TS models explaining the stereoselectivity of these reactions in terms of various non-covalent interactions.[68] Intriguingly, even 13 years after the initial publication of the Houk–List model of proline-catalyzed intramolecular aldol reactions, computational studies continue to unveil additional subtleties regarding the non-covalent interactions responsible for the stereoselectivity of these transformations.[69,70]

In related work on substituent effects in proline-catalyzed aldol condensations in water (Figure 2.5), Houk *et al.*[71] identified π-stacking interactions as a key determinant of the catalytic activity of **1a**. In particular, catalyst **1a** was 43.5 times more reactive in water than **1f**, while these catalysts have similar rates in non-polar solvents (*e.g.* toluene). M06-2X computed activation energies were in general agreement. For instance, the energy difference between the rate-limiting transition states in a vacuum was very small (0.2 kcal mol^{-1}). Accounting for solvent led to a 2.6 kcal mol^{-1} difference in the predicted activation energies for catalysis by **1f** *vs.* **1a** in water. Ultimately, this difference in catalytic activity was attributed to a stabilizing edge-to-face interaction between the benzyl group of catalyst **1a** and the phenyl ring of the acceptor aldehyde (see Figure 2.5). Clearly, this stabilizing interaction is not possible in the analogous transition state with **1f**.

Asymmetric Diels–Alder reactions of α,β-unsaturated aldehydes in the presence of chiral imidazolidinones constitute another class of reactions in which aromatic interactions can play key roles. Pioneering work by Houk *et al.*,[72,73] as well as studies from Platts *et al.*[74] and Singleton *et al.*,[75] showed that stereoselectivity in these reactions is governed by the formation of a reactive iminium species for which the lowest energy conformer is stabilized by a CH/π interaction. More recently, Krenske *et al.*[76] offered insight into a

View Online

Published on 15 November 2016 on http://pubs.rsc.org | doi:10.1039/9781782626626-00018

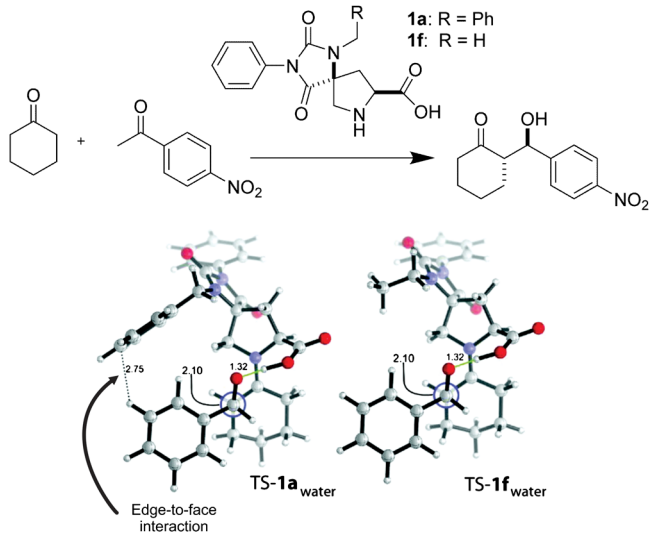

Figure 2.5 Proline-catalyzed aldol reaction of Houk *et al.* in water, along with their computed TS structures for the rate-limiting TS for catalysts **1a** and **1f**. Adapted with permission from *J. Org. Chem.*, 2012, **77**, 4784–4792. Copyright 2012 American Chemical Society.

similar enantioselective Diels–Alder reaction based on two camphor-derived catalysts developed by Ogilvie.[77–79] These reactions displayed markedly different stereoselectivities depending on the substituent R (see Figure 2.6). A detailed conformational search followed by TS optimization revealed a stabilizing CH/π interaction between hydrogens from the cyclopentadiene and the benzyl group in the case of catalyst **2a.** A fragment-based decomposition scheme was used to quantify the impact of this interaction on the stereoselectivity. Ultimately, it was shown that the (*R*)-transition state enjoys an additional 1.3 kcal mol^{-1} stabilization compared the (*S*)-transition state, which accounts for almost two thirds of the overall enantioselectivity.

Further examples of the central role of non-covalent interactions in iminium catalysis have been presented by Gilmour *et al.*,[80] who showed that the electronic modulation of the pendant aryl group controls the conformation and reactivity of α,β-unsaturated Macmillan type iminium salts. Similarly, Pihko and coworkers[81] ascribed the enantioselectivity of an iminium catalyzed Mukaiyama–Michael reaction to attractive CH/π interactions, rather than steric hindrance as initially conceived. However, we note that Mück-Lichtenfeld and coworkers[82] recently presented a different view regarding the positioning of the aryl side chain in iminium-catalyzed conjugated additions to α,β-unsaturated aldehydes and ketones. In particular, computational and crystallographic data indicate that the benzyl group in 2-benzylimidazolidinone iminium ions is freely rotating at ambient temperature due to the small rotational barriers between conformers. This free rotation effectively shields one particular face of the iminium–π system through an

View Online

Published on 15 November 2016 on http://pubs.rsc.org | doi:10.1039/9781782626626-00018

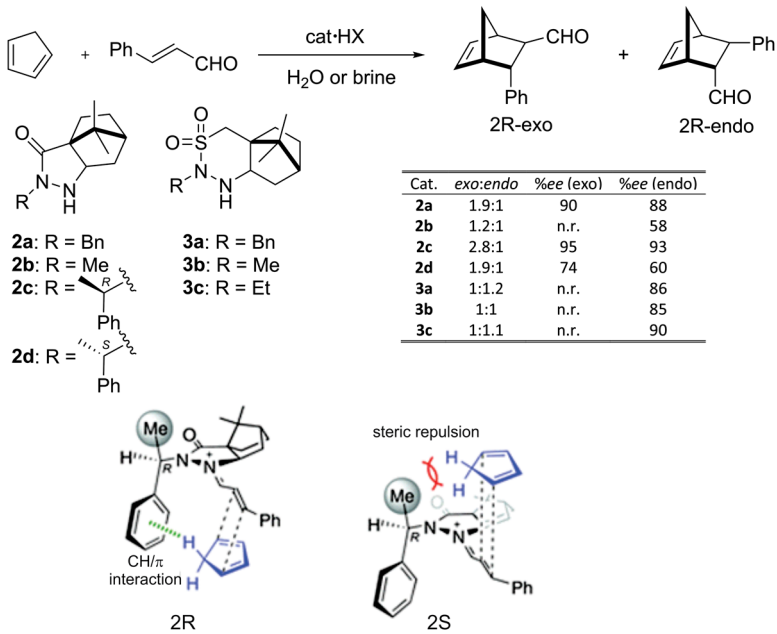

Figure 2.6 Enantioselective Diels–Alder cycloaddition studied by Krenske *et al.*, in which CH/π interactions help stabilize the TS structure leading to the favored stereoisomer. Adapted from ref. 76 with permission from the Royal Society of Chemistry.

effect they termed the "windshield-wiper effect," leading to the observed stereoselectivities.

N-heterocyclic carbene (NHC) catalyzed cross benzoin reactions have also been shown to involve stabilizing aromatic interactions. For instance, Legault and Gravel[83] disclosed a strong π-stacking interaction in alkyl–aryl cross benzoin and aryl–aryl homo benzoin reactions. The enantioselectivity of these reactions was traced to π-stacking interactions between the triazole of the catalyst and the aromatic moiety of the aldehyde, which preferentially stabilized one particular transition state relative to its diastereomers.

In 2012, Kozlowski *et al.*[84] studied the highly stereoselective γ,δ-unsaturated δ lactone formation by a NHC catalyzed [4+2] cycloaddition between an enolate derived from the α,β-unsaturated ketone and an enone (Figure 2.7). They found that a CH/π interaction between the terminal CH_2 of the enolate and the mesitylene ring was a key stabilizing feature of the TS leading to the major isomer. This view was supported by the observation that replacing the mesitylene ring with a perfluorophenyl ring, which is not expected to engage in CH/π interactions as strongly, resulted in a significant drop in ee both experimentally and computationally.

Phosphoric acids derived from chiral diols have emerged as a powerful platform for organocatalyst development,[85] and many chiral phosphoric acid catalyzed reactions benefit from stabilizing non-covalent interactions

View Online

Published on 15 November 2016 on http://pubs.rsc.org | doi:10.1039/9781782626626-00018

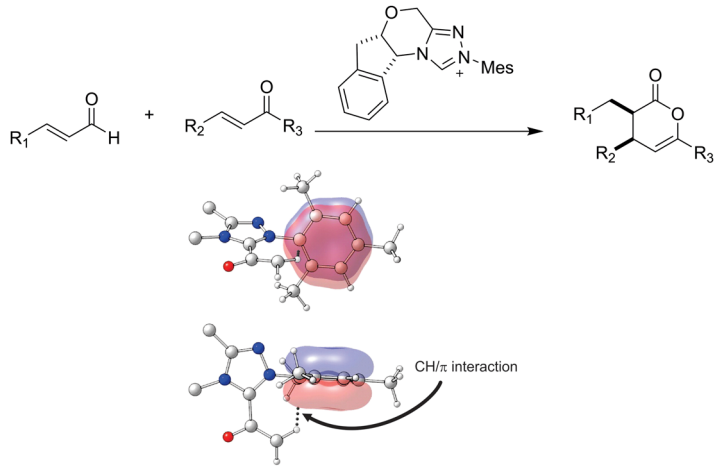

Figure 2.7 NHC-catalyzed [4+2] cycloaddition of Kozlowski and co-workers, along with a depiction of a key CH/π interaction in one of the transition states (the enone and indane ring were removed for clarity). Adapted with permission from *J. Am. Chem. Soc.*, 2012, **134**, 12098–12103. Copyright 2012 American Chemical Society.

between the substrates and aryl substituents of these catalysts. For example, Ess, Kürti, and coworkers[86] identified CH/π and π-stacking interactions as key determinants of stereoselectivity in their synthesis of axially chiral biaryls through a chiral phosphoric acid catalyzed atroposelective [3,3] rearrangement (Figure 2.8). Computations corroborated the experimental finding of reduced stereoselectivity upon replacement of aryl CF_3 substituents by CH_3, supporting the involvement of π-stacking interactions in the stereocontrolling TS.

Seguin *et al.*[87] also recently presented a study of the first catalytic asymmetric Fischer indole reaction, from List and co-workers.[88] Computations revealed that the stereoselectivity of this reaction hinged on the competition between π-stacking interactions, which preferentially stabilize the transition state leading to the (*R*)-isomer of the product, and CH/π interactions, which provide greater stabilization of the TS leading to the (*S*)-product. Ultimately, the CH/π interactions prevailed, and, when combined with hydrogen bonding interactions that also favor TS(*S*), the (*S*)-product was formed preferentially.

CH/π interactions have also proved pivotal in the realm of phase-transfer catalysis. In an elegant study of the phase-transfer catalyzed 5-*endo-trig* cyclization in the stereoselective synthesis of indanes, Paton, Smith, and co-workers[89] observed the importance of CH/π interactions in determining enantioselectivity (Figure 2.9). M06-2X computations revealed that the transition state leading to the major stereoisomer is preferentially stabilized by CH/π interactions in conjunction with an array of non-classical CH···O interactions.

View Online

Published on 15 November 2016 on http://pubs.rsc.org | doi:10.1039/9781782626626-00018

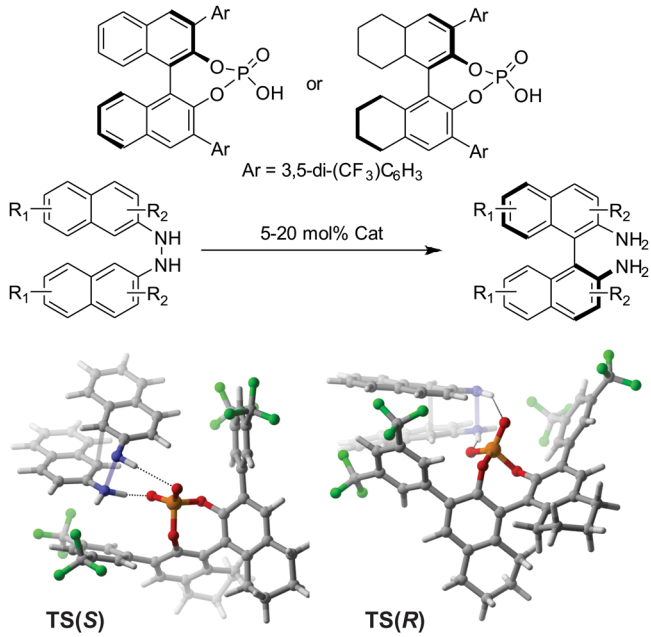

Figure 2.8 Chiral phosphoric acid catalyzed [3,3] sigmatropic rearrangement of Ess, Kürti, *et al.*,[86] along with their computed TS structures.[86]

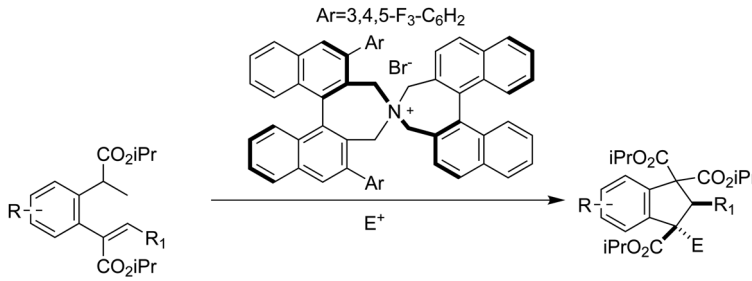

Figure 2.9 Enantioselective synthesis of indanes *via* a cation-directed 5-*endo-trig* cyclization, from Paton, Smith, *et al.*[89]

During their investigation of the TADDOL-catalyzed hetero-Diels–Alder reaction of benzaldehyde with 1-dimethylamino-3-*tert*-butyldimethylsiloxy butadiene, Houk *et al.*[90] identified CH/π interactions to be the key factor for stereoselectivity (Figure 2.10). A Monte-Carlo conformational search followed by mixed QM/QM calculations [ONIOM(B3LYP/6-31(d): AM1)] were employed to find the low lying TS. It was observed the lowest energy TS corresponding to *si*-facial *endo* addition (with respect to the aldehyde) is stabilized by a CH/π interaction between the aldehyde CH and the pseudoequatorial naphthyl group of the TADDOL catalyst. Computations predicted that this

View Online

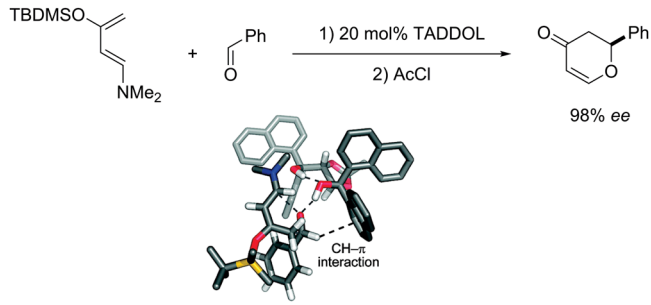

Figure 2.10 TADDOL-catalyzed hetero-Diels–Alder reaction of Houk *et al.*,[90] along with a key transition state stabilized by CH/π interactions. Adapted with permission from *Org. Lett.*, 2008, **10**, 2749–2752. Copyright 2008 American Chemical Society.

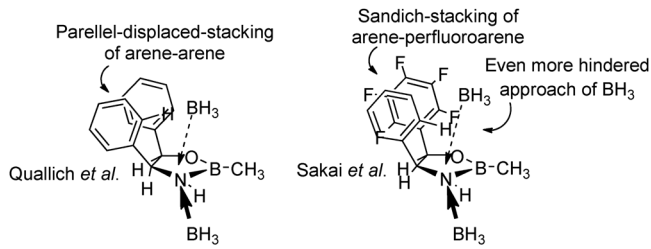

Figure 2.11 Chiral oxazaborolidines from Quallich *et al.*[91] and Sakai *et al.*[92] for asymmetric borane reductions of ketones. In the latter case, arene–perfluoroarene interactions are exploited to provide greater steric shielding of one face of the oxazaborolidine from complexation with BH_3.

TS is 1.5 kcal mol^{-1} more stable than the TS for *re*-facial attack, in reasonable agreement with the experimental ee. Notably, the TS for *re*-face attack lacks the CH/π interactions present in the competing TS, but instead features a π-stacking interaction. Thus, like the case of the phosphoric acid catalyzed Fischer indole reaction studied by Seguin *et al.*,[87] this TADDOL-catalyzed hetero-Diels–Alder reaction is an additional case in which CH/π interactions overwhelm the competing effects of π-stacking interactions in controlling stereoselectivity.

Finally, we highlight a case where understanding the nature of π-stacking interactions enabled the design of a more effective metal-free catalyst for asymmetric borane reductions. In particular, the oxazaborolidine from Quallich and Woodall[91] (Figure 2.11) has been shown to catalyze the borane reduction of ketones with a high degree of enantioselectivity. Quallich and Woodall[91] attributed this to the steric shielding of one face of the oxazaborolidine by the two stacked phenyl rings, which controls the coordination of BH_3 to the nitrogen. Sakai and coworkers[92] exploited the tendency of perfluoroarene–arene interactions to adopt more sandwich-like configurations,

Published on 15 November 2016 on http://pubs.rsc.org | doi:10.1039/9781782626626-00018

View Online

Published on 15 November 2016 on http://pubs.rsc.org | doi:10.1039/9781782626626-00018

compared to arene–arene stacking interactions, to design a more rigid chiral oxazaborolidine that provided an even more hindered approach of BH_3 to one face. The more sandwich-like configuration of these stacked rings was confirmed by both *ab initio* computations and a ^{1}H NMR study.

2.6 Aromatic Interactions in Cooperative Catalysis

There have been tremendous advances in our understanding of cooperative catalysis in recent years, and non-covalent interactions have been documented in many of these reactions. This topic was recently reviewed by Sunoj *et al.*;[93] here we present two representative examples in which aromatic interactions play key roles. The importance of non-covalent CH/π interactions in cooperative catalysis was highlighted by Xiao and coworkers[94] in the context of the enantioselective hydrogenation of imines using an achiral Ir-complex and a chiral phosphoric acid. Based on results from an extensive NMR study, they concluded that a ternary complex formed involving the achiral Ir-complex, phosphate anion, and iminium cation is responsible for stereocontrol. Comprehensive NOE, DFT, and semiempirical studies showed that the lowest-lying TS structure, which leads to the major product, is stabilized by multiple CH/π interactions.

Another key example of asymmetric cooperative catalysis in which non-covalent interactions play a central role was reported by Jacobsen and coworkers[95] during their study of an enantioselective Povarov reaction by the cooperative catalysis of a chiral bifunctional sulfamido urea with *o*-nitrobenzenesulfonic acid (Figure 2.12). Computational studies using both DFT and *ab initio* methods predicted that the lowest-lying TS, leading to the observed major product, is stabilized by both hydrogen-bonding and π-stacking interactions between the cationic aniline moiety of the substrate and the $(CF_3)_2$–C_6H_3N component of the catalyst. Notably, this stacking interaction is absent in the TS structures leading to the minor enantiomers, suggesting that it is important for the observed stereoselectivity.

2.7 Reactions Directed by Anion–π Interactions

Matile and co-workers recently introduced the potentially transformative concept of anion–π catalysis—the acceleration of reactions through favorable anion–π interactions.[96,97] During their initial study of the Kemp elimination of 5-nitrobenzisoxazole, Matile *et al.* synthesized two naphthalene diimide (NDI) based catalysts (**2** and **3**, Figure 2.13) with pendant carboxylates designed to stabilize the forming oxyanion in the rate-limited deprotonation of this base-catalyzed reaction. Matile *et al.*[96,97] observed marked rate accelerations using these NDI-based catalysts, which are expected to interact favorably with anions, whereas pyrene butyrate (**4**, which is not expected to stabilize anions) showed no catalytic activity. Further demonstrations of the concept of anion–π catalysis came in later work, in which they studied

View Online

Published on 15 November 2016 on http://pubs.rsc.org | doi:10.1039/9781782626626-00018

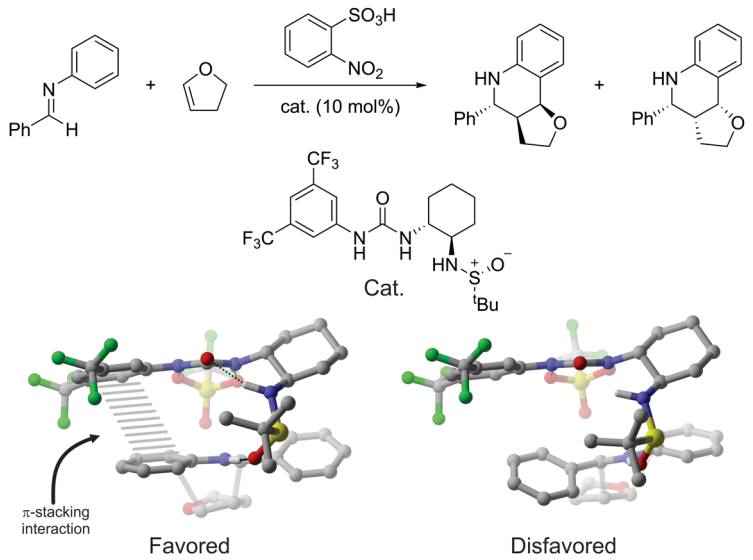

Figure 2.12 Model Povarov reaction studied by Jacobsen and co-workers along with the favored TS structure and one of the disfavored TS structures. Non-polar hydrogens omitted for clarity.

the deprotonation of a malonic acid covalently linked to an NDI, compared to free dimethyl malonic acid.[98,99] Overall, they observed a two-unit shift in pK_a for the acid linked to the NDI, providing direct experimental evidence of the stabilization of an enolate through anion–π interactions. For a detailed discussion on this work, the reader is also referred to Chapter 3—Anion–π Interactions: Theoretical Studies, Supramolecular Chemistry and Catalysis, by Ballester and Frontera.

Lu and Wheeler attempted to quantify the impact of anion–π interactions in Matile's anion–π catalyzed Kemp elimination reaction.[100] Computation results revealed that even though anion–π interactions were indeed stabilizing the rate-limiting transition state, they were stabilizing the catalyst–substrate complex to a greater extent. The result was that the *net effect* of anion–π interactions was to increase the overall reaction barrier. The problem was that with **2** and **3**, the negatively-charged catalytic carboxylate is stabilized to a greater extent than the partially anionic transition state. This is shown in Figure 2.13 for catalyst **2**. In this case, the electrostatic interactions of the substrate with the NDI are enhanced by 0.7 kcal mol^{-1} going from CS to TS. However, this is overshadowed by the 1.3 kcal mol^{-1} loss of stabilization of the carboxylate going from CS to TS. To remedy this, Lu and Wheeler devised modified versions of Matile's NDI-based catalysts in which the catalytic carboxylate was prevented from engaging in stabilizing anion–π interactions through the introduction of a rigid ethynyl linker (catalysts **4**–**6** in Figure 2.13). With these newly designed catalysts, the net effect of anion–π interactions was shown to significantly reduce the overall reaction barrier.

View Online

Published on 15 November 2016 on http://pubs.rsc.org | doi:10.1039/9781782626626-00018

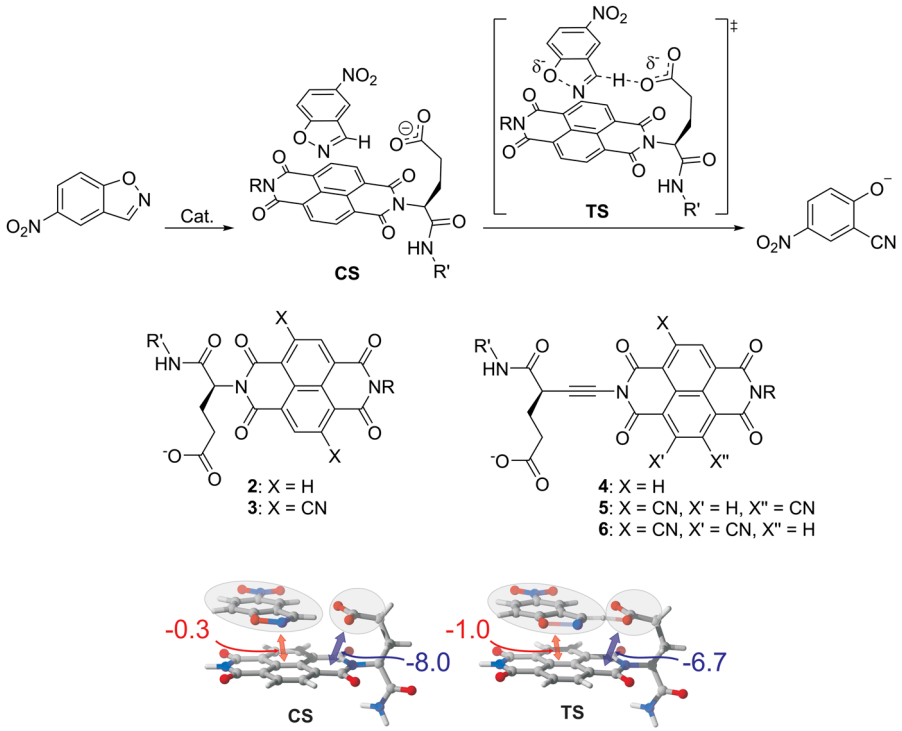

Figure 2.13 Kemp elimination of 5-nitrobenzisoxazole studied by Matile and co-workers,[7] along with an analysis of the electrostatic interactions occurring in the catalyst–substrate complex (CS) and transition state (TS) for this reaction from Lu and Wheeler.[100]

More recently, Matile and co-workers have showcased additional examples of anion–π catalysis. For instance, they exploited this strategy to selectively promote the conjugate addition of β-keto thioesters to nitroolefins over a more favorable decarboxylation reaction.[101] They observed that the extent to which these anion–π catalysts could accelerate the conjugate addition while suppressing the decarboxylation depended only on the π-acidity of the catalyst, not other external parameters. This further underscored the central role of anion–π interactions. In a similar vein, Matile *et al.*[102] also achieved stereoselective enamine addition to nitroolefins using a new NDI-based trifunctional organocatalyst. Ultimately, they concluded that while the enantioselectivity of this reaction is dependent on the π-acidity of the catalyst, the diastereoselectivity is determined primarily by the geometric matching of catalyst and substrate.

2.8 Reactions Directed by π–π$^+$ Interactions

Yamada and coworkers[103] have published extensively on the role of intramolecular non-covalent π–π$^+$ interactions involving pyridinium ions as conformational control elements in stereoselective reactions. In particular, based

View Online

Published on 15 November 2016 on http://pubs.rsc.org | doi:10.1039/9781782626626-00018

on NMR, CD, and analyses of crystal structures, they showed that these attractive π–π^+ interactions are able to conformationally lock fluxional systems into a single conformer that dictates the outcome of a number of enantioselective cyclopropanations,[104,105] kinetic resolutions,[106–108] and desymmetrizations.[109]

Intermolecular π–π^+ interactions, in which a cationic arene stacks with a neutral arene, are also prevalent in the literature. One of the most popular examples involves DMAP-mediated nucleophilic catalysis. For instance, Zipse and coworkers[110] showed that π–π^+ interactions serve as guiding elements in various acyl transfer catalyzed reactions. In a similar vein, Birman, Houk, *et al.*[111] reported stabilizing π–π^+ attractions between phenyl and pyridinium rings in a parallel-displaced geometry as the key factor in CF_3-PIP-catalyzed kinetic resolution of alcohols and enantioselective *N*-acylation of lactams and thiolactams.[112] π–π^+ interactions have also been identified as enantiocontrolling elements in recent work from Jacobsen *et al.*, including the enantioselective acylation of silyl ketene acetals through fluoride anion binding catalysis,[113] the enantioselective addition of indoles to pyrenes,[114] and enantioselective oxidopyrylium-based cycloadditions.[115]

2.9 Concluding Remarks

Aromatic interactions are potentially powerful control elements in organic reactions. Our ability to exploit these interactions has grown with our increased understanding of the factors that impact the strength and geometry of these non-covalent interactions. Above, we tried to survey a wide range of organic transformations in which aromatic interactions play key roles, demonstrating the breadth of systems for which such interactions have been identified to be pivotal for either reactivity or selectivity. Ultimately, the combination of experimental data and computation studies has proved invaluable in elucidating the role of these interactions, and will help drive the development of more efficient and selective organic reactions moving forward.

Acknowledgements

This work was supported in part by the National Science Foundation (Grant CHE-1266022) and the Welch Foundation (Grant A-1776).

References

1. G. B. Jones, *Tetrahedron*, 2001, **57**, 7999.
2. R. R. Knowles and E. N. Jacobsen, *Proc. Natl. Acad. Sci. U. S. A.*, 2010, **107**, 20678.
3. T. Lu and S. E. Wheeler, *Science*, 2015, **347**, 719.
4. G. T. Copeland and S. J. Miller, *J. Am. Chem. Soc.*, 2001, **123**, 6495.
5. E. H. Krenske and K. N. Houk, *Acc. Chem. Res.*, 2013, **46**, 979.

View Online

Published on 15 November 2016 on http://pubs.rsc.org | doi:10.1039/9781782626626-00018

6. J. P. Wagner and P. R. Schreiner, *Angew. Chem., Int. Ed.*, 2015, **54**, 12274.
7. Y. Zhao, Y. Cotelle, N. Sakai and S. Matile, *J. Am. Chem. Soc.*, 2016, **138**, 4270.
8. S. E. Wheeler and J. W. G. Bloom, *J. Phys. Chem. A*, 2014, **118**, 6133.
9. L. M. Salonen, M. Ellermann and F. Diederich, *Angew. Chem., Int. Ed.*, 2011, **50**, 4808.
10. E. A. Meyer, R. K. Castellano and F. Diederich, *Angew. Chem., Int. Ed.*, 2003, **42**, 1210.
11. C. R. Martinez and B. L. Iverson, *Chem. Sci.*, 2012, **3**, 2191.
12. R. K. Raju, J. W. G. Bloom, Y. An and S. E. Wheeler, *ChemPhysChem*, 2011, **12**, 3116.
13. S. E. Wheeler, *Acc. Chem. Res.*, 2013, **46**, 1029.
14. C. A. Hunter and J. K. M. Sanders, *J. Am. Chem. Soc.*, 1990, **112**, 5525.
15. C. A. Hunter, K. R. Lawson, J. Perkins and C. J. Urch, *J. Chem. Soc., Perkin Trans. 2*, 2001, 651.
16. F. J. Carver, C. A. Hunter, D. J. Livingstone, J. F. McCabe and E. M. Seward, *Chem.–Eur. J.*, 2002, **8**, 2848.
17. S. L. Cockroft, C. A. Hunter, K. R. Lawson, J. Perkins and C. J. Urch, *J. Am. Chem. Soc.*, 2005, **127**, 8594.
18. S. L. Cockroft, *et al.*, *Org. Biomol. Chem.*, 2007, **5**, 1062.
19. S. L. Cockroft and C. A. Hunter, *Chem. Commun.*, 2009, 3961.
20. M. O. Sinnokrot and C. D. Sherrill, *J. Phys. Chem. A*, 2003, **107**, 8377.
21. M. O. Sinnokrot and C. D. Sherrill, *J. Am. Chem. Soc.*, 2004, **126**, 7690.
22. A. L. Ringer, M. O. Sinnokrot, R. P. Lively and C. D. Sherrill, *Chem.–Eur. J.*, 2006, **12**, 3821.
23. A. L. Ringer and C. D. Sherrill, *J. Am. Chem. Soc.*, 2009, **131**, 4574.
24. J. W. G. Bloom and S. E. Wheeler, *Angew. Chem., Int. Ed.*, 2011, **50**, 7847.
25. S. E. Wheeler, *J. Am. Chem. Soc.*, 2011, **133**, 10262.
26. R. K. Raju, J. W. G. Bloom and S. E. Wheeler, *J. Chem. Theory Comput.*, 2013, **9**, 3479.
27. M. Watt, L. K. E. Hardebeck, C. C. Kirkpatrick and M. Lewis, *J. Am. Chem. Soc.*, 2011, **133**, 3854.
28. R. M. Parrish and C. D. Sherrill, *J. Am. Chem. Soc.*, 2014, **136**, 17386.
29. S. Grimme, *Angew. Chem., Int. Ed.*, 2008, **47**, 3430.
30. M. O. Sinnokrot and C. D. Sherrill, *J. Phys. Chem. A*, 2006, **110**, 10656.
31. F. Cozzi, M. Cinquini, R. Annunziata, T. Dwyer and J. S. Siegel, *J. Am. Chem. Soc.*, 1992, **114**, 5729.
32. F. Cozzi, M. Cinquini, R. Annunziata and J. S. Siegel, *J. Am. Chem. Soc.*, 1993, **115**, 5330.
33. F. Cozzi, F. Ponzini, R. Annunziata, M. Cinquini and J. S. Siegel, *Angew. Chem., Int. Ed.*, 1995, **34**, 1019.
34. F. Cozzi and J. S. Siegel, *Pure Appl. Chem.*, 1995, **67**, 683.
35. F. Cozzi, R. Annunziata, M. Benaglia, M. Cinquini, L. Raimondi, K. K. Baldridge and J. S. Siegel, *Org. Biomol. Chem.*, 2003, **1**, 157.
36. S. E. Wheeler and K. N. Houk, *J. Am. Chem. Soc.*, 2008, **130**, 10854.

View Online

Published on 15 November 2016 on http://pubs.rsc.org | doi:10.1039/9781782626626-00018

37. Y. Kodama, K. Nishihata, M. Nishio and N. Nakagawa, *Tetrahedron Lett.*, 1977, **18**, 2105.
38. S. Tsuzuki and A. Fujii, *Phys. Chem. Chem. Phys.*, 2008, **10**, 2584.
39. S. Tsuzuki, T. Uchimaru and M. Mikami, *J. Phys. Chem. A*, 2011, **115**, 11256.
40. K. Shibasaki, A. Fujii, N. Mikami and S. Tsuzuki, *J. Phys. Chem. A*, 2006, **110**, 4397.
41. S. Tsuzuki, K. Honda, T. Uchimaru, M. Mikami and K. Tanabe, *J. Am. Chem. Soc.*, 2000, **122**, 3746.
42. J. W. G. Bloom, R. K. Raju and S. E. Wheeler, *J. Chem. Theory Comput.*, 2012, **8**, 3167.
43. D. A. Dougherty, *Science*, 1996, **271**, 163.
44. S. Mecozzi, A. P. West Jr and D. A. Dougherty, *J. Am. Chem. Soc.*, 1996, **118**, 2307.
45. J. C. Ma and D. A. Dougherty, *Chem. Rev.*, 1997, **97**, 1303.
46. J. P. Gallivan and D. A. Dougherty, *Proc. Natl. Acad. Sci. U. S. A.*, 1999, **96**, 9459.
47. D. A. Dougherty, *Acc. Chem. Res.*, 2013, **46**, 885.
48. M. Giese, M. Albrecht and K. Rissanen, *Chem. Commun. (Cambridge, U. K.)*, 2016, **52**, 1778.
49. L. R. Rutledge, C. D. M. Churchill and S. D. Wetmore, *J. Phys. Chem. B*, 2010, **114**, 3355.
50. S. Tsuzuki, M. Mikama and S. Yamada, *J. Am. Chem. Soc.*, 2007, **129**, 8656.
51. S. Grimme, *J. Comput. Chem.*, 2004, **25**, 1463.
52. S. Grimme, *J. Comput. Chem.*, 2006, **27**, 1787.
53. S. Grimme, *Wiley Interdiscip. Rev.: Comput. Mol. Sci.*, 2011, **1**, 211.
54. Y. Zhao, N. E. Schultz and D. G. Truhlar, *J. Chem. Theory Comput.*, 2006, **2**, 364.
55. Y. Zhao and D. G. Truhlar, *J. Chem. Phys.*, 2006, **125**, 194101.
56. Y. Zhao and D. G. Truhlar, *Theor. Chem. Acc.*, 2008, **120**, 215.
57. A. J. McNeil, P. Müller, J. E. Whitten and T. M. Swager, *J. Am. Chem. Soc.*, 2006, **128**, 12426.
58. S. E. Wheeler, A. J. McNeil, P. Müller, T. M. Swager and K. N. Houk, *J. Am. Chem. Soc.*, 2010, **132**, 3304.
59. Y. El-azizi, A. Schmitzer and S. K. Collins, *Angew. Chem.*, 2006, **118**, 982.
60. S. K. Collins, Y. El-Azizi and A. R. Schmitzer, *J. Org. Chem.*, 2007, **72**, 6397.
61. Y. El-Azizi, J. E. Zakarian, L. Bouillerand, A. R. Schmitzer and S. K. Collins, *Adv. Synth. Catal.*, 2008, **350**, 2219.
62. P. Bolduc, A. Jacques and S. K. Collins, *J. Am. Chem. Soc.*, 2010, **132**, 12790.
63. M. Yamakawa, I. Yamada and R. Noyori, *Angew. Chem., Int. Ed.*, 2001, **40**, 2818.
64. R. Noyori, M. Yamakawa and S. Hashiguchi, *J. Org. Chem.*, 2001, **66**, 7931.

View Online

Published on 15 November 2016 on http://pubs.rsc.org | doi:10.1039/9781782626626-00018

65. M. Yamakawa, H. Ito and R. Noyori, *J. Am. Chem. Soc.*, 2000, **122**, 1466.
66. A. Matsuoka, C. A. Sandoval, M. Uchiyama, R. Noyori and H. Naka, *Chem.–Asian J.*, 2015, **10**, 112.
67. G. Santoni, M. Mba, M. Bonchio, W. A. Nugent, C. Zonta and G. Licini, *Chem.–Eur. J.*, 2010, **16**, 645.
68. S. Bahmanyar, K. N. Houk, H. J. Martin and B. List, *J. Am. Chem. Soc.*, 2003, **125**, 2475.
69. A. Armstrong, R. A. Boto, P. Dingwall, J. Contreras-Garcia, M. J. Harvey, N. J. Mason and H. S. Rzepa, *Chem. Sci.*, 2014, **5**, 2057.
70. B. W. Bakr and C. D. Sherrill, *Phys. Chem. Chem. Phys.*, 2016, **18**, 10297.
71. Q. Zhao, Y.-h. Lam, M. Kheirabadi, C. Xu, K. N. Houk and C. E. Schafmeister, *J. Org. Chem.*, 2012, **77**, 4784.
72. C. Allemann, R. Gordillo, F. R. Clemente, P. H.-Y. Cheong and K. N. Houk, *Acc. Chem. Res.*, 2004, **37**, 558.
73. R. Gordillo and K. N. Houk, *J. Am. Chem. Soc.*, 2006, **128**, 3543.
74. J. B. Brazier, G. Evans, T. J. K. Gibbs, S. J. Coles, M. B. Hursthouse, J. A. Platts and N. C. O. Tomkinson, *Org. Lett.*, 2009, **11**, 133.
75. O. M. Gonzalez-James, E. E. Kwan and D. A. Singleton, *J. Am. Chem. Soc.*, 2012, **134**, 1914.
76. E. H. Krenske, *Org. Biomol. Chem.*, 2013, **11**, 5226.
77. M. Lemay and W. W. Ogilvie, *Org. Lett.*, 2005, **7**, 4141.
78. M. Lemay and W. W. Ogilvie, *J. Org. Chem.*, 2006, **71**, 4663.
79. M. Lemay, L. Aumand and W. W. Ogilvie, *Adv. Synth. Catal.*, 2007, **349**, 441.
80. M. C. Holland, S. Paul, W. B. Schweizer, K. Bergander, C. Mück-Lichtenfeld, S. Lakhdar, H. Mayr and R. Gilmour, *Angew. Chem., Int. Ed.*, 2013, **52**, 7967.
81. E. K. Kemppainen, G. Sahoo, A. Piisola, A. Hamza, B. Kótai, I. Pápai and P. M. Pihko, *Chem.–Eur. J.*, 2014, **20**, 5983.
82. D. Seebach, U. Grošelj, W. B. Schweizer, S. Grimme and C. Mück-Lichtenfeld, *Helv. Chim. Acta*, 2010, **93**, 1.
83. S. M. Langdon, C. Y. Legault and M. Gravel, *J. Org. Chem.*, 2015, **80**, 3597.
84. S. E. Allen, J. Mahatthananchai, J. W. Bode and M. C. Kozlowski, *J. Am. Chem. Soc.*, 2012, **134**, 12098.
85. D. Parmar, E. Sugiono, S. Raja and M. Rueping, *Chem. Rev.*, 2014, **114**, 9047.
86. G.-Q. Li, H. Gao, C. Keene, M. Devonas, D. H. Ess and L. Kürti, *J. Am. Chem. Soc.*, 2013, **135**, 7414.
87. T. J. Seguin, T. Lu and S. E. Wheeler, *Org. Lett.*, 2015, **17**, 3066.
88. S. Müller, M. J. Webber and B. List, *J. Am. Chem. Soc.*, 2011, **133**, 18534.
89. C. P. Johnston, A. Kothari, T. Sergeieva, S. I. Okovytyy, K. E. Jackson, R. S. Paton and M. D. Smith, *Nat. Chem.*, 2015, **7**, 171.
90. C. D. Anderson, T. Dudding, R. Gordillo and K. N. Houk, *Org. Lett.*, 2008, **10**, 2749.
91. G. J. Quallich and T. M. Woodall, *Tetrahedron Lett.*, 1993, **34**, 4145.
92. T. Korenaga, K. Kadowaki and T. Sakai, *J. Fluorine Chem.*, 2007, **128**, 557.

View Online

93. G. Jindal, H. K. Kisan and R. B. Sunoj, *ACS Catal.*, 2015, **5**, 480.
94. W. Tang, S. Johnston, J. A. Iggo, N. G. Berry, M. Phelan, L. Lian, J. Bacsa and J. Xiao, *Angew. Chem., Int. Ed.*, 2013, **52**, 1668.
95. H. Xu, S. J. Zuend, M. G. Woll, Y. Tao and E. N. Jacobsen, *Science*, 2010, **327**, 986.
96. Y. Zhao, Y. Domoto, E. Orentas, C. Beuchat, D. Emery, J. Mareda, N. Sakai and S. Matile, *Angew. Chem., Int. Ed.*, 2013, **52**, 9940.
97. Y. Zhao, C. Beuchat, Y. Domoto, J. Gajewy, A. Wilson, J. Mareda, N. Sakai and S. Matile, *J. Am. Chem. Soc.*, 2014, **136**, 2101.
98. Y. Zhao, N. Sakai and S. Matile, *Nat. Commun.*, 2014, **5**, 3911.
99. F. N. Miros, Y. Zhao, G. Sargsyan, M. Pupier, C. Besnard, C. Beuchat, J. Mareda, N. Sakai and S. Matile, *Chem.–Eur. J.*, 2015, 2648.
100. T. Lu and S. E. Wheeler, *Org. Lett.*, 2014, **16**, 3268.
101. Y. Zhao, S. Benz, N. Sakai and S. Matile, *Chem. Sci.*, 2015, **6**, 6219.
102. Y. Zhao, Y. Cotelle, A.-J. Avestro, N. Sakai and S. Matile, *J. Am. Chem. Soc.*, 2015, **137**, 11582.
103. S. Yamada and J. S. Fossey, *Org. Biomol. Chem.*, 2011, **9**, 7275.
104. S. Kojima, K. Hiroike and K. Ohkata, *Tetrahedron Lett.*, 2004, **45**, 3565.
105. S. Kojima, K. Fujitomo, Y. Shinohara, M. Shimizu and K. Ohkata, *Tetrahedron Lett.*, 2000, **41**, 9847.
106. S. Yamada, T. Misono and S. Tsuzuki, *J. Am. Chem. Soc.*, 2004, **126**, 9862.
107. S. Yamada, T. Misono and Y. Iwai, *Tetrahedron Lett.*, 2005, **46**, 2239.
108. S. Yamada, T. Misono, Y. Iwai, A. Masumizu and Y. Akiyama, *J. Org. Chem.*, 2006, **71**, 6872.
109. S. Yamada and C. Morita, *J. Am. Chem. Soc.*, 2002, **124**, 8184.
110. Y. Wei, I. Held and H. Zipse, *Org. Biomol. Chem.*, 2006, **4**, 4223.
111. X. Li, P. Liu, K. N. Houk and V. B. Birman, *J. Am. Chem. Soc.*, 2008, **130**, 13836.
112. X. Yang, *et al.*, *J. Am. Chem. Soc.*, 2012, **134**, 17605.
113. J. A. Birrell, J.-N. Desrosiers and E. N. Jacobsen, *J. Am. Chem. Soc.*, 2011, **133**, 13872.
114. C. S. Yeung, R. E. Ziegler, J. A. Porco and E. N. Jacobsen, *J. Am. Chem. Soc.*, 2014, **136**, 13614.
115. N. Z. Burns, M. R. Witten and E. N. Jacobsen, *J. Am. Chem. Soc.*, 2011, **133**, 14578.

Published on 15 November 2016 on http://pubs.rsc.org | doi:10.1039/9781782626626-00018

Published on 15 November 2016 on http://pubs.rsc.org | doi:10.1039/9781782626626-00039

CHAPTER 3

Anion–π Interactions: Theoretical Studies, Supramolecular Chemistry and Catalysis

A. FRONTERA*[a] AND P. BALLESTER*[b,c]

[a]Universitat de les Illes Balears, Departament de Química, Crta. de Valldemossa km 7.5, 07122 Palma de Mallorca, Spain; [b]Institute of Chemical Research of Catalonia (ICIQ), The Barcelona Institute of Science and Technology, Av. Països Catalans, 16, 43007, Tarragona, Spain; [c]Catalan Institution for Research and Advanced Studies (ICREA), Passeig Lluís Companys, 23, 08018 Barcelona, Spain
*E-mail: toni.frontera@uib.es, pballester@iciq.es

3.1 Introduction

Supramolecular chemistry is certainly the most multidisciplinary field of chemical research. Its fast development and deep impact is related to the growing efficacy and success in the construction of supramolecular assemblies of different sizes, shapes and functionalities.[1,2] Chemists working in this discipline rely on the comprehension of non-covalent forces that are the basis of highly specific recognition processes. For instance, in rationally

Monographs in Supramolecular Chemistry No. 20
Aromatic Interactions: Frontiers in Knowledge and Application
Edited by Darren W. Johnson and Fraser Hof
© The Royal Society of Chemistry 2017
Published by the Royal Society of Chemistry, www.rsc.org

View Online

Published on 15 November 2016 on http://pubs.rsc.org | doi:10.1039/9781782626626-00039

designed receptors, interactions between hosts and guests drive the creation of assemblies with high affinities even in highly competitive media.[3–7] The correct description and understanding of the interactions that are established between molecules are essential for being successful in supramolecular chemistry. Strong and highly directional interactions such as hydrogen bonding and σ-hole bonding,[8–17] and less directional forces such as ion pairing are commonly used for this purpose. Moreover, interactions involving aromatic rings and other π-systems in general (quinones, nucleobases, cyanuric acid derivatives, *etc.*) are very relevant in supramolecular chemistry. For instance, a variety of well-established π-interactions (cation–π, π–π and C–H/π interactions) are important in protein structure and enzyme catalysis.[18–21] In the last 15 years, the naissance and consolidation of the anion–π interaction[22–26] (*i.e.*, the attractive interaction between an anion and an electron deficient π-system) has been established. As a matter of fact, a large number of theoretical[27–30] and experimental[31–35] investigations have been published substantiating the significance of this supramolecular bond. Recently, this interaction has also been defined as a subclass of π-hole bonding.[36] A π-hole is a region of positive electrostatic potential that is perpendicular to a portion of a molecular framework.[37] In the particular case of an anion–π interaction, this portion can be either an aromatic π system substituted with electron withdrawing groups or a heteroaromatic ring coordinated to a transition metal (or protonated). There are several fields where the importance of this interaction is noticeable, including medicine, environmental chemistry and understanding biochemical processes.[38–40] Moreover, their utilization in highly selective anion receptors, molecular carriers and transport channels confirms their extraordinary significance in the field of supramolecular chemistry.[41–43]

An especially relevant publication on this topic should be placed into perspective.[44] Woollins and collaborators in 1996 named the anion–π contact as a "π-facial interaction"[45] in their description of the close contact between chloride and the seven-membered aromatic $[S_4N_3]^+$ ring that they observed in the crystal packing of thiotrithiazylium chloride. Other pioneering publications from Schneider's[46,47] and Yamabe's groups[48,49] are also very important in understanding the naissance of this interaction.

This chapter is not intended to be a bibliographic review of the literature related to anion–π interactions since several surveys have been written for that purpose.[25,50–53] In its place, we emphasize herein the importance of this interaction both in solution and in the solid state, focusing our attention on the construction of new supramolecular assemblies, catalysts and anion receptors. We develop the discussion under three main headings. First, the physical nature of the interaction is explained for assimilation by a wide readership. Second, we select several examples of anion–π interactions in solution within host–guest systems, catalysis and ionic liquids. Third, we highlight recent examples from the literature where the anion–π interactions are very relevant for understanding the solid-state architecture of crystalline materials.

View Online

Published on 15 November 2016 on http://pubs.rsc.org | doi:10.1039/9781782626626-00039

3.2 Physical Nature

The physical nature of the anion–π interaction has been widely studied and rationalized using high level *ab initio* and DFT calculations and several partition energy schemes.[54,55] The general postulation is that electrostatic (charge-quadrupole) and ion-induced polarization (charge-induced dipole) are key forces that contribute to the anion–π interaction.[56–58] The electrostatic term in neutral arenes correlates well with the adequate component (perpendicular to the ring plane) of the quadrupole moment (Q_{zz}). The attachment of electron withdrawing substituents to benzene changes the Q_{zz} value from negative to positive (see Figure 3.1(A)) and the same effect occurs in pyridine upon its N-coordination to a metal centre. Therefore, the electrostatic interaction between an anion and the π-system becomes attractive either attaching electron-withdrawing substituents to the ring or coordinating metal ions in the case of heteroaromatic rings. Moreover, the anion polarizes the π-cloud of the arene inducing a dipole (see Figure 3.1(B)). Therefore, the polarization contribution to the binding energy is derived from the interaction of the anion with the induced dipole. This contribution has been used as to explain some unexpected issues related to this interaction. For instance, the electrostatic repulsion anticipated in the complex between the electron rich benzene and chloride is largely compensated by the favourable induced dipole interaction, resulting in nearly negligible interaction energy (2.4 kcal mol^{-1}).[59] Moreover, the induced polarization term explains the dual binding mode exhibited by arenes[60,61] featuring a negligible permanent quadrupole moment perpendicular to the ring plane, such as 1,3,5-trifluorobenzene (Q_{zz} = 0.57 B) and *s*-triazine (Q_{zz} = 0.90 B) that are able to interact with both anions and cations.

Recently the nature of the anion–π interaction has been revisited by Marek's group[62] by means of the quantum theory of atoms in molecules (QTAIM) and an energy decomposition scheme on the basis of interacting quantum atoms (IQA) theory.[63] It was concluded that these interactions benefit from what is defined as "multi-centre covalency" and that this phenomenon is more important than electrostatics. By comparing anion–π non-covalent complexes to covalent anion–σ complexes it was demonstrated that the anion–π systems exhibit an extensive degree of electron sharing between the anions and all atoms of the rings. Moreover, decomposition of the binding energy

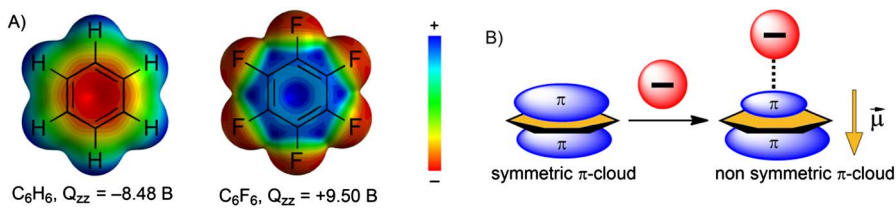

Figure 3.1 (A) Molecular electrostatic potential of benzene and hexafluorobenzene. (B) Schematic representation of the anion-induced dipole.

View Online

Published on 15 November 2016 on http://pubs.rsc.org | doi:10.1039/9781782626626-00039

into classical (electrostatics) and non-classical (exchange–correlation) components demonstrates that anion–π complexes are local minima exclusively if the non-classical contribution is greater than the classical. This suggests that stable anion–π complexes with the anions atop the π-rings should be prepared with extended π-systems since they have a higher exchange–correlation term. At this point, it should be kept in mind that a variety of so-called "energy decomposition analyses", or EDAs, are available in the literature.[64–85] Due to an inherent freedom in how the total energy is decomposed given an electronic wave function, there is an intrinsic arbitrariness in the generation of any EDA method (the different terms are not operators of the wave function).[86] Therefore, for a given anion–π complex, the magnitude of the electrostatic term is different depending on the EDA method selected for partitioning.

An unusual theory on the nature of anion–π interactions involving benzene rings was also offered by Wheeler and Houk,[87] who studied substituent effects in $Cl^{-}\cdots C_6H_{6-n}Y_n$ (Y = any substituent) complexes using both DFT and *ab initio* methods. The predicted interaction energies for a large number of model $Cl^{-}\cdots C_6H_{6-n}Y_n$ complexes show an excellent correlation (r = 0.99) with computed electrostatic potentials. In contrast to the aforementioned physical explanations of the anion–π interaction, which relies on substituent-induced changes in the π system in both polarizability and quadrupole moment, a model has been proposed where substituent effects in these systems are attributed basically to direct interactions between the anion and local C–Y dipoles. That is, interaction energies for $Cl^{-}\cdots C_6H_{6-n}Y_n$ complexes could be matched using a model system in which the substituents are isolated from the aromatic ring and π-resonance effects are impossible. From this point of view, when conceiving anion-binding motifs, phenyl rings are just simple scaffolds upon which appropriate substituents are placed to create the local dipoles.

The anion–π interaction has also been analysed in terms of molecular orbital analysis[61] and compared to the related cation–π interaction. As a result, a totally different picture of both interactions emerges from the comparison since the atomic orbitals of the cation do not participate in the molecular orbitals of the cation–π complex and, conversely, the atomic orbitals of the anion actively participate in the molecular orbitals of the anion–π complex.

Apart from the understanding of the physical nature of the interaction, the additivity of the anion–π interaction is obviously a very important aspect, since it is intended to be used for constructing supramolecular assemblies and anion receptors. This has been examined in halide complexes and demonstrated theoretically[88,89] using several *s*-triazine derivatives as examples. It has been shown that the interaction energy of a ternary "sandwich" complex ($\pi^{A}\cdots X^{-}\cdots\pi^{B}$) is essentially twice the interaction energies of the corresponding binary complexes ($X^{-}\cdots\pi^{A}$ and $X^{-}\cdots\pi^{B}$) for X = Cl and Br. It is quite evident that to be successful in the design of supramolecular assemblies based on the anion–π interaction, the π-binding units should have a large

View Online

Published on 15 November 2016 on http://pubs.rsc.org | doi:10.1039/9781782626626-00039

and positive quadrupole moment and a large molecular polarizability. Since the electrostatic term depends on the magnitude of the quadrupole moment (Q_{zz}) and the polarization term on the magnitude of the molecular polarizability (denoted as α_l), there is an obvious restriction for the first condition due to the limitation of strong electron withdrawing groups available for constructing the π-acidic binding blocks. Moreover, it is synthetically complicated to attach many of these groups to the same aromatic ring. As a matter of fact, the use of $-NO_2$ and −CN groups is required to have a large positive value of Q_{zz}, and it is complicated to attach more than three strong electron withdrawing groups. A suitable solution is the use of heteroaromatic rings, especially di-, tri- and tetrazines coordinated to transition metals. The coordination drastically increases the π-acidity of the ring, thus increasing the ability to bind anions.[90–92] Moreover, the metal coordination facilitates the formation of supramolecular assemblies in the solid state from smaller molecular components (ligands) in most cases with remarkably high yields. A clear example of this behaviour was reported by the Domasevitch group.[91] In particular, several X-ray crystal structures of *s*-tetrazine μ^4-coordinated to Ag^I were reported, exhibiting very close contacts between the anion and the *s*-tetrazine ring indicating strong anion–π interactions, in agreement with theoretical predictions. The effect on the electronic nature of the arene caused by the metal coordination is similar to the effect of protonation. For example, pyridine and related azines can be protonated by adjusting the pH of the medium increasing their ability to interact with anions through the π-system (anion–π^+ interactions). In this respect, the geometric and energetic features of anion–π^+ complexes of several aromatic cations (tropylium, quinolizinium) have been reported combining theoretical calculations and the analysis of the Cambridge Structural Database,[93–96] see Figure 3.2(A) and (B). Closely related, the importance of the anion–π^+ interaction in protonated purine and pyrimidine bases has been recently reviewed.[97] As an example, the solid state structure of N^1-hexylcytosine hydrobromide is shown in Figure 3.2(C). As expected, the interaction energies of these complexes are dominated by strong electrostatic effects exhibiting very large binding energies (>80 kcal mol^{-1}).

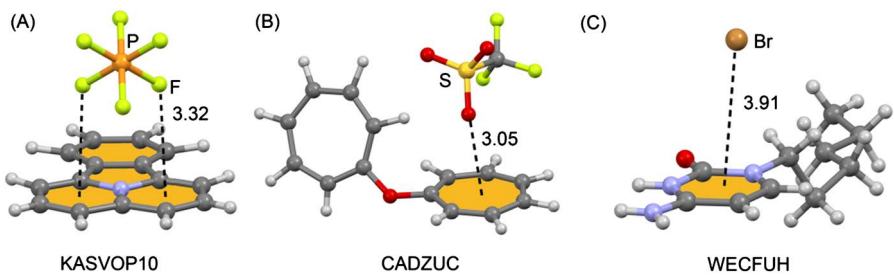

Figure 3.2 Fragments of the X-ray crystal structures containing quinolizinium (A), tropylium (B) and cytosinium (C) moieties. The relevant anion–π interactions are indicated by dashed lines (distances in Å). The CSD reference codes are indicated.

View Online

Published on 15 November 2016 on http://pubs.rsc.org | doi:10.1039/9781782626626-00039

Strong anion–π interactions involving electron rich π-systems are also feasible whenever the aromatic ring is simultaneously interacting with a cation on the opposite side of the ring. In fact, the concurrent interaction of anions and cations on opposite faces of the same arene has been studied theoretically[98–100] and the π-system is capable of acting as a charge insulator between the counterions. These ternary "inverse sandwich" anion–π–cation complexes exhibit large interaction energies and short ion–π distances (shorter than those in the corresponding binary cation–π and anion–π complexes). Noteworthy experimental work that corroborates these theoretical findings was reported by Atwood's group.[101–104] The solid state X-ray structures of calixarenes and cyclotriveratrylenes (see Figure 3.3) clearly demonstrate that the host–guest behaviour of these receptors is drastically altered in the presence of transition metal centres (Ru, Ir, Rh) since they recognize anionic guest species (instead of cationic) within the molecular cavity.

Apart from the coordination of the arenes to transition metals that drastically increase the π-acidity of the ring (see Figure 3.4(A)–(D)), another good

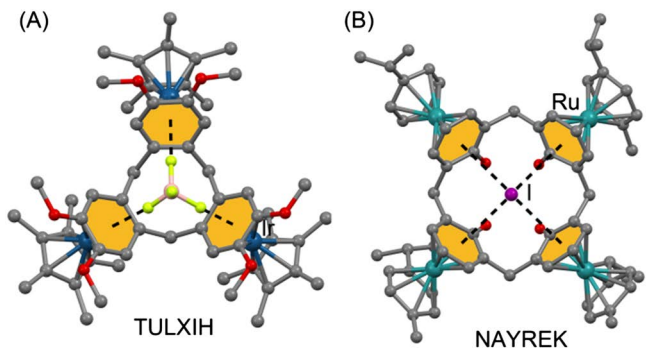

Figure 3.3 X-Ray crystal structures of transition-metal complexed cyclotriveratrylene (A) and calixarene (B) receptors exhibiting anion–π–cation bonding. The CSD reference codes are indicated.

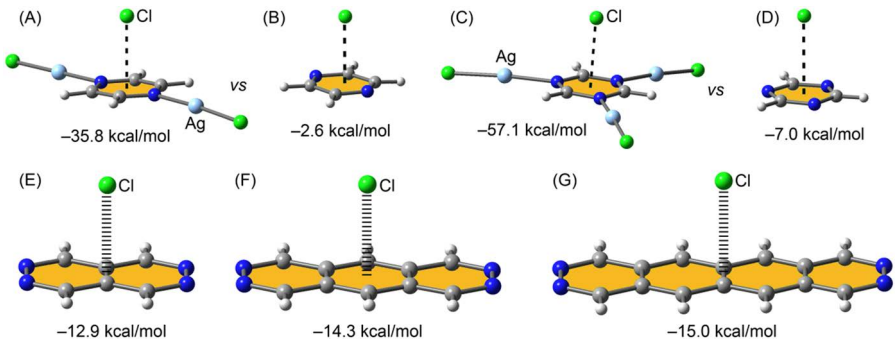

Figure 3.4 (A)–(D) Interaction energies of pyrazine and triazine anion–π complexes. (E)–(G) Interaction energies of Cl^-–π complexes of pyridazino[4,5-*d*]-pyridazine and related rings.

View Online

Published on 15 November 2016 on http://pubs.rsc.org | doi:10.1039/9781782626626-00039

strategy to build π-systems with strong anion binding ability is the utilization of polycyclic aromatic compounds comprising several fused rings. This allows us, on the one hand, to attach more electron withdrawing groups to the system, thus increasing the quadrupole moment. On the other hand, the molecular polarizability also increases due to the extended π-system, thus enhancing the charge-induced dipole contribution. This strategy has been used by Dunbar *et al.* to construct a neutral anion-receptor based on 1,4,5,8,9,12-hexaazatriphenylene (HAT) substituted with six cyano groups. This extended π-acidic system is able to interact with four anions simultaneously in the solid state.[105] Furthermore, anion–π complexes of $HAT(CN)_6$ have also been studied both theoretical and experimentally by us.[106] It has been demonstrated that the formation of anion–π non-covalent, charge-transfer or electron transfer adducts strongly depends on the type of anion (see next section for a more detailed explanation). Another remarkable example of polycyclic aromatic arenes is pyridazino[4,5-*d*]pyridazine since this system conserves the N-donor ability of pyridazine to form transition metal complexes and form strong π-acidic systems. Moreover, it can be easily obtained by a one-pot synthesis involving inverse electron demand Diels–Alder cycloaddition.[107] The ability to establish anion–π interactions of this ligand has been analysed theoretically[108,109] and it has been demonstrated that the interaction energies with several anions are more favourable that those of pyrazine. The theoretical work also included the study of larger polycyclic arenes based on pyridazino[4,5-*d*]pyridazine and it was also demonstrated that the anion–π interaction strengthens as the number of fused rings increases (see Figure 3.4(E)–(G)). As a matter of fact, pyridazino[4,5-*d*]pyridazine has been used as a ligand by Gural'skiy *et al.*[107] to investigate the ability of this extended π-system to establish anion–π interactions in the solid state.

Finally, the usefulness of an intermolecular interaction in supramolecular chemistry also relies on its directionality. Various theoretical studies revealed that a single anion–π interaction varies in strength from weak (−3.6 kcal mol^{-1} for 1,4-difluorobenzene···Cl^- complex) to strong (−24.0 kcal mol^{-1} for 1,3,5-trinitrobenzene···Cl^-). In light of such interaction energies it can be expected that anion–π interactions are directional. In the geometry that is preferred the anion is located above/below the centre of an aromatic ring at a ring plane–anion angle of 90°. However, the wide electropositive region above/below the aromatic implies that a deviation from this geometry has a small energy cost. To this respect, the directionality of the interaction has been analysed using the Cambridge Structure Database (CSD), since a proper statistical analysis of the CSD often unveils the geometric preferences of a given supramolecular interaction. Several CSD surveys have shown close proximity of electron rich/anionic entities above/below electron deficient (hetero) aromatics.[22,110–113] The directional character of anion–π[114,115] interactions has been demonstrated by a thorough CSD evaluation of interactions between anionic/electron rich atoms and a pentafluorophenyl *vs.* a phenyl ring.[114] The method used in these inquiries usually considers the non-spherical volume of the arene and takes into account the correction for a random

View Online

Published on 15 November 2016 on http://pubs.rsc.org | doi:10.1039/9781782626626-00039

scattering of the data. These studies undoubtedly showed that the directional anion–π binding mode is preferred for pentafluorophenyl rings, and the C–H···X^- H-bonding interaction is preferred with phenyl rings.[114,115]

3.3 Anion–π Interactions in Solution

3.3.1 Supramolecular Chemistry and Synthetic Receptors Involving Anion–π Interactions

In 2013 we overviewed the experimental efforts carried out by the scientific community to determine the binding energies of anion–π interactions in solution.[116] The reviewed examples centred around the use of uncharged synthetic receptors that bound anions, mainly halides, with the assistance or exclusive existence of anion–π interactions. Owing to the unique Lewis and Brönsted basicity properties of fluoride we refrained to comment on fluoride–π interactions. We concluded that anion–π interactions did indeed exist in solution, and the binding energy estimated for these attractive interactions was less than −1 kcal mol^{-1} when substituted phenyl groups were used as acceptors. As mentioned in the previous section, numerous reviews on anion–π interactions in supramolecular systems have been published by other authors in recent years.[22,23,26,52,117–119] They include relevant examples of solution studies addressing the quantification of anion–π interactions and we refer interested readers to these previous accounts. In this section, we will focus on solution studies for the quantification of anion–π interactions that were published since 2013 and were not included in our previous review of the field.

Wang and Wang systematically studied anion–π interactions using tetraoxaazacalix[2]arene[2]triazine **1** as a receptor/probe (Figure 3.5). They selected polyatomic anions with varied geometry that included linear thiocyanate (NCS^-), triangular nitrate (NO_3^-), tetrahedral tetrafluoroborate (BF_4^-) and octahedral hexafluorophosphate (BF_6^-). They probed the interactions of the anions with receptor **1** by means of spectrometric titrations (UV-vis and fluorescence).[120] The incremental addition of all tested anions to separated acetonitrile solutions of **1** did not induce noticeable changes in its

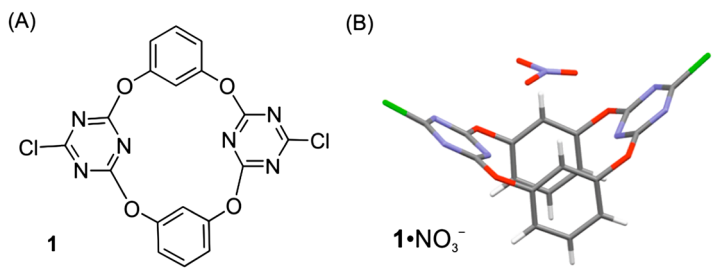

Figure 3.5 (A) Structure of tetraoxacalix[2]arene[2]triazine **1**; (B) X-ray crystal structure of **1**·NO_3^- complex, the Et_4N^+ was omitted for clarity.

View Online

Published on 15 November 2016 on http://pubs.rsc.org | doi:10.1039/9781782626626-00039

electronic spectrum. However, variations in the fluorescence spectrum of **1** were observed during the titration experiments. A new fluorescence band centred at 450 nm emerged and gradually increased upon the incremental addition of the anions. Job plots assigned a 1:1 stoichiometry to the complexes being formed. The fit of the titration data to a 1:1 binding model allowed the assessment of the magnitudes of the binding constant. The calculated values were $K(\mathbf{1}\cdot NO_3^-) = 16\,950 \pm 847\ M^{-1}$, $K(\mathbf{1}\cdot Cl^-) = 4246 \pm 83\ M^{-1}$,[121] $K(\mathbf{1}\cdot BF_4^-) = 673 \pm 34\ M^{-1}$, $K(\mathbf{1}\cdot PF_6^-) = 291 \pm 15\ M^{-1}$ and $K(\mathbf{1}\cdot NCS^-) = 239 \pm 12\ M^{-1}$. The association constant values varied significantly as a function of the anion. It is interesting to note that when the same interactions were probed using ^1H and ^{13}C NMR spectroscopy, negligible chemical shift changes were observed in the spectra of the receptor. This finding was used by the authors to exclude other possible non-covalent arene CH–anion interactions with the receptor on formation of the complex in solution. Mass spectrometry studies evidenced the formation of the anionic 1:1 complexes in the gas phase. The structures of the **1**·anion complexes formed in solution were inferred from the solid-state structures determined using X-ray diffraction analysis of single crystals. In all solid state 1:1 complexes, the bis-chloro tetraoxacalix[2]arene[2]triazine **1** nested the anion between the two π-electron deficient thiazine rings that defined a V-shaped cleft as is further explained below (Section 3.4.1).

Stoddart and co-workers designed and synthesized rigid chiral triangular prims, (−)-**2** and (+)-**2** featuring tubular cavities that are defined by three naphthaleneimide (NDI) units (Scheme 3.1).[122] As described above, the highly π-acidic nature of NDIs has been explored for the investigation and applications of anion–π interactions. The authors reasoned that the electronic communication existing between redox centres in the prisms, which was responsible for an increase in the electron-affinity of the NDI units, should also favour an enhancement of charge-transfer interactions with anions.

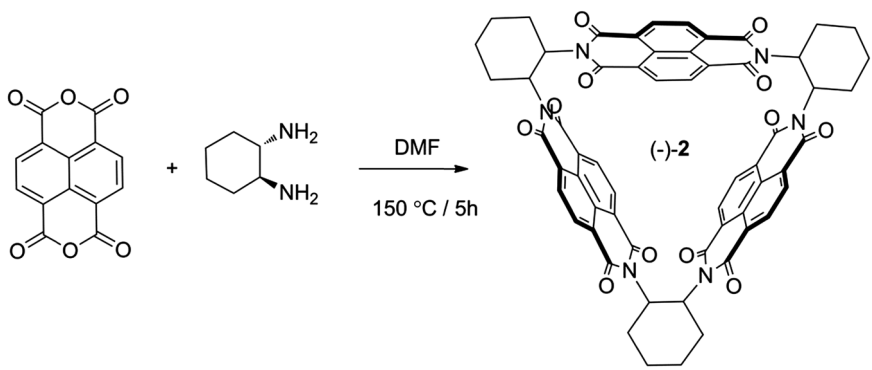

Scheme 3.1 Stereospecific synthesis of the triangular prims (−)-**2** from naphthalenediimide and the (*R,R*)-enantiomer of *trans*-1,2-diaminocyclohexane. The enantiomer (+)-**2** was synthesized using the same procedure starting from the (*S,S*)-enantiomer of the diamine.

View Online

Published on 15 November 2016 on http://pubs.rsc.org | doi:10.1039/9781782626626-00039

It was demonstrated that the tubular and electronic deficient cavities of (−)-**2** and (+)-**2** provided a perfect fit for the inclusion of the linear of I_3^- anion. By performing ^{1}H NMR titrations of (−)-**2** with [Bu4][I_3] in CD_2Cl_2 solution and by fitting the titration data to a 1:1 binding model, the authors determined the magnitude of the binding constant as K_a (I_3^-⊂(−)-**2**) = 25 ± 2 M^{-1}. Although the binding was weak, it demonstrated that the anion–π interactions with the neutral host (−)-**2** were enough to break-up the ion-pairing of the salt in a non-polar solvent. The structural evidence of the inclusion geometry assigned to the I_3^-⊂(−)-**2** complex formed in solution was derived from single-crystal X-ray diffraction results (see Section 3.4.1).

Dunbar and co-workers described the role of anion–π interactions in the unusual thermodynamic stability exhibited by Fe(II) metallacycles assembled in acetonitrile solution.[123] The authors embarked on a comprehensive study of anion-templated self-assembly processes involving solvated organometallic complexes [Fe(II)$(CH_3CN)_6$][X^-]$_2$ (X = [BF_4^-] and [SbF_6^-]) and the bis-pyridine ligand **3** (Figure 3.6). They described that an equimolar mixture of **3** and [Fe(II)$(CH_3CN)_6$][BF_4^-] in acetonitrile solution produced, after overnight stirring and standing for several days layered with toluene, an analytically pure dark blue solid. Single crystals suitable for X-ray diffraction analysis were grown by layering an acetonitrile solution of the obtained solid over toluene. The analysis of the diffraction data revealed the assembly of a molecular square [Fe_4(**3**)$_4(CH_3CN)_8$]$^{8+}$ in which each Fe(II) occupies a vertex and the ligand bridges two metal centres (Figure 3.6). The cavity of the square includes a disordered but tightly bound [BF_4^-] anion establishing C···F contacts with the C atoms of two tetrazine rings in opposing **3** ligands. The C···F distances were shorter than the sum of van der Waals radii. Under analogous conditions the assembly of **3** with [Fe(II)$(CH_3CN)_6$][SbF_6^-]$_2$ produced a pentameric assembly [Fe_5(**3**)$_5(CH_3CN)_{10}$]$^{10+}$ whose structure in the solid state was also solved by X-ray diffraction analysis. Two symmetrically related [SbF_6^-] anions in close proximity were located in the cavity of the pentamer. Each anion engaged in three short C···F contacts with the C atoms of the tetrazine rings of the ligands. Taken together, these results indicated that the π-acidic interiors of the tetrameric and the pentameric assemblies are excellent cavities for including anions. The included anions engage in C···F contacts with the tetrazine rings of the edge ligands. Moreover, the nature of the anion played a decisive role in the molecularity of the assembled polygon.

^{1}H NMR studies of the obtained solids dissolved in acetonitrile suggested that both assemblies remained intact in solution. Cyclic voltammetry results also corroborated this finding. The templating effect of the anion was also supported by solution studies that involved the interconversion between the square and the pentagonal Fe(II) metallacyles in the presence of an excess of the appropriate anion. These studies revealed that the pentagonal assembly was thermodynamically more stable than the square. Other hexafluoride anions, *i.e.* PF_6^- and AsF_6^-, were used to template the assembly of pentameric structures and to test their relative thermodynamic stability. The data derived from ^{1}H NMR studies of multiple interconversion processes between

View Online

Published on 15 November 2016 on http://pubs.rsc.org | doi:10.1039/9781782626626-00039

the square and pentamer aggregates lead to the following order of stability for the Fe(II) pentagons: $[Fe_5(\mathbf{3})_5(CH_3CN)_{10}][PF_6]_{10} \ll [Fe_5(\mathbf{3})_5(CH_3CN)_{10}][SbF_6]_{10} > [Fe_5(\mathbf{3})_5(CH_3CN)_{10}][AsF_6]_{10}$. Considering the different volumes of the anions, the authors concluded that the $[AsF_6^-]$ anions provide the optimal filling and anion–π contacts for the pentagonal cavity. They also indicated that the templation effect was not only a matter of size, shape and symmetry complementarity with the cavity but it also required the establishment of strong anion–π contacts. This conclusion was supported by the observation that despite the similarity of volumes of the $[CF_3SO_3^-]$ and the $[AsF_6^-]$ anions,

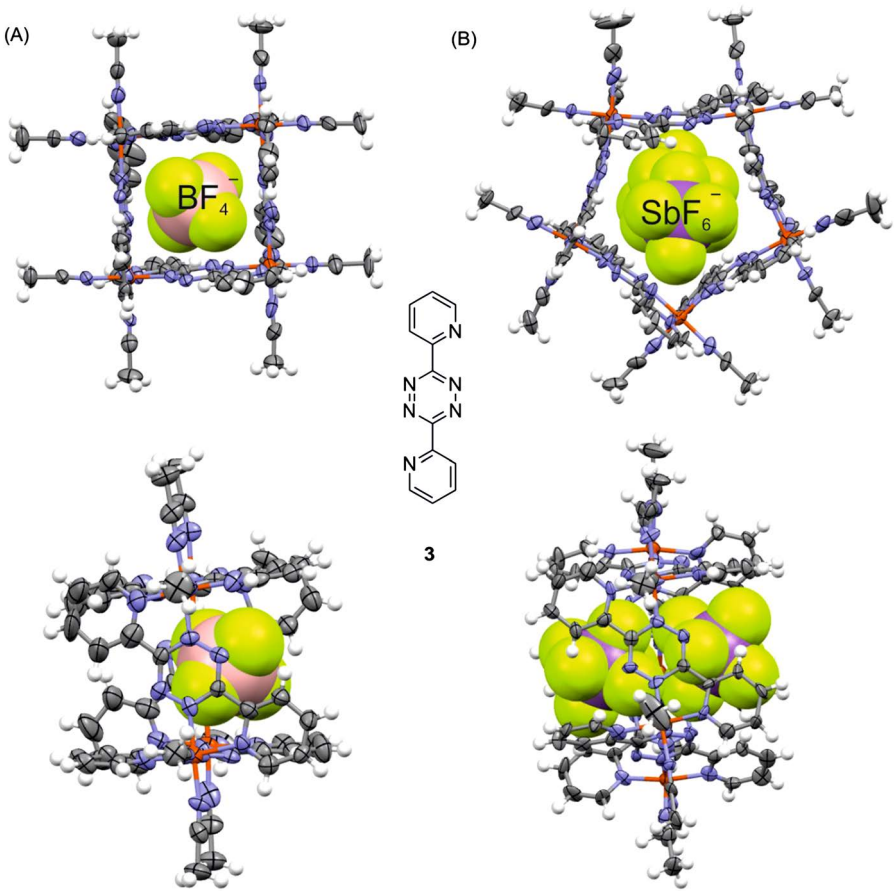

Figure 3.6 (Middle) Structural formula of the divergent and π-acidic ligand **3**. (Left and right) Top and side views of: (A) X-ray crystal structure of the molecular square $[Fe_4(\mathbf{3})_4(CH_3CN)_8]^{8+}$ showing the included BF_4^- anion; (B) X-ray structure of the pentameric assembly $[Fe_5(\mathbf{3})_5(CH_3CN)_{10}]^{10+}$ with two encapsulated SbF_6^- anions. In (A) and (B) thermal ellipsoids of the cationic units are set at 50% probability level and the H atoms as spheres of 0.3 Å. The included anions are depicted with space filling spheres.

View Online

Published on 15 November 2016 on http://pubs.rsc.org | doi:10.1039/9781782626626-00039

the former did not support the templation of a pentagon. Using variable temperature ^{19}F NMR experiments in solution, the authors were not able to identify the fluorine signals of the included $[BF_4^-]$ anion in the $[Fe_4(\mathbf{3})_4(CH_3CN)_8][BF_4]_8$ square. Conversely, similar experiments performed on the pentameric assembly $[Fe_5(\mathbf{3})_5(CH_3CN)_{10}][PF_6]_{10}$ allowed the observation of two separate fluorine signals. The one with lower intensity was assigned to the two included $[PF_6^-]$ anions. The rate of the anion exchange was calculated from the coalescence temperature and corresponded to an activation energy of $\Delta G^{\ddagger}$ = 11 kcal mol^{-1}. The determined low activation energy indicated that the exchange of the anion did not require the cleavage of Fe–N coordination bonds and occurred by the simple passage of the anions through the portals of the cage. The authors stated that the agreement between the determined activation energy value for the exchange process with the expected energy range for anion–π interactions (4.7–16.7 kcal mol^{-1})[22] corroborated the inclusion of the anion in the cage by non-covalent contacts. Apparently, this reasoning neglected the important coulombic interactions that existed between the anionic species and the cationic container in the stabilization of these inclusion complexes.

The groups of Johnson and Haley developed a tripodal receptor **4a** equipped with urea functionalities for the selective binding of nitrate in competitive hydrogen bonding solvents.[124] Simple molecular modelling studies performed by us suggested that due to geometrical constraints receptor **4a** was suitable for the multitopic binding of the nitrate anion but using only two of its three urea groups. The authors stated that nitrate can accommodate up to six hydrogen bonding interactions—two interactions per oxygen atom—and that ditopic hydrogen bonding donors such as urea groups are ideal binding partners.[125,126] We were unable to model energy minimized geometries for the NO_3^-·**4a** complex in which the three urea groups were simultaneously bound to the anion. The minimum energy structure we obtained for the NO_3^-·**4a** complex is shown in Figure 3.7.

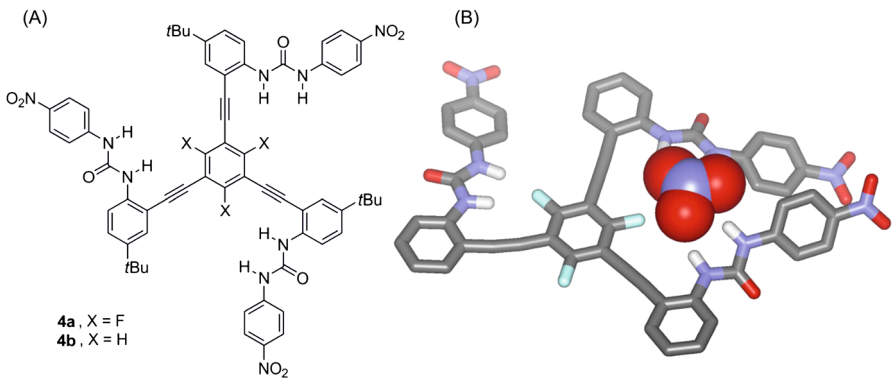

Figure 3.7 (A) Line drawing structures of tripodal receptors **4a,b**. (B) Energy minimized (MM3) structure obtained for a putative NO_3^-·**4a** complex.

View Online

Published on 15 November 2016 on http://pubs.rsc.org | doi:10.1039/9781782626626-00039

The nitrate anion forms four hydrogen bonds with two adjacent urea groups. One oxygen atom of the bound nitrate displays a bifurcated or three-centred hydrogen bond interacting with two NHs of the urea groups in different arms. The other two oxygen atoms of the nitrate are hydrogen bonded to only one urea NH. This binding geometry is reminiscent of the one observed by the authors in the solid-state for the NO_3^-·**4a** complex (Figure 3.8). However, in the solid-state the NO_3^- anions are bound to two urea groups belonging to different receptors. The authors suggested that the π-acidic central aryl ring in **4a** could provide additional binding interactions with the anion. Indeed, the solid-state structure of the NO_3^-·**4a** complex revealed the placement of the anion over the alkyne linker and the anionic π-system aligned in a parallel arrangement with the central π-system of the receptor. The intermolecular distances between the atoms of the nitrate and the carbon atoms of the alkyne linker and the aryl spacer were shorter than 3.7 Å.

In order to suppress self-aggregation of **4a** and possibly ion-pairing of the anion salts, the ^{1}H NMR titrations of the receptor with the tetrabutylammonium (TBA) salts of chloride and nitrate anions were performed in 10% DMSO–d_6-$CDCl_3$ solutions. In this solvent mixture, the monitored chemical shift changes nicely fit a 1:1 binding model. The largest association constant value was determined for the NO_3^- anion, K_a (NO_3^-·**4a**) = 24 100 M^{-1}. The stability constant for the chloride complex was reduced by half, K_a (Cl^-·**34**) = 12 200 M^{-1}. Tripodal receptor **4a** exhibited the strongest nitrate

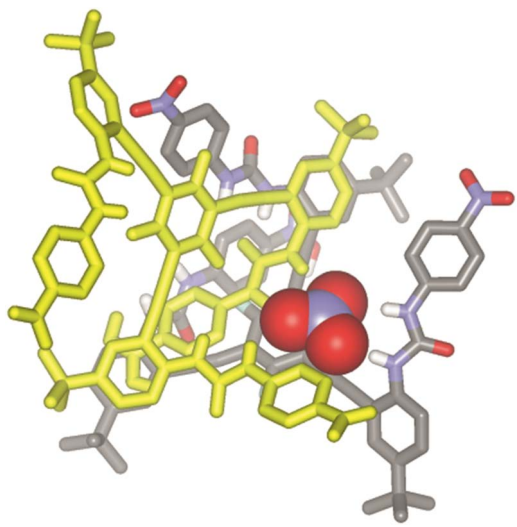

Figure 3.8 Section of the crystal packing for the NO_3^-·**4a** complex showing the hydrogen-bonding interactions of one nitrate anion (CPK model) with two urea groups belonging to arms of adjacent receptors (stick representation). The two **4a** receptors are shown in different colours for clarity. The anion shows anion–π interactions with the alkyne linker and the central aryl ring.

View Online

Published on 15 November 2016 on http://pubs.rsc.org | doi:10.1039/9781782626626-00039

binding for a neutral receptor in competitive solvents determined by that date, and anion–π interactions were claimed to assist the binding. A question that arises from this study is, why does the nitrate have stronger anion–π interactions than the chloride? The authors proposed that owing to the conjugate system of the nitrate, the anion–π interaction was assisted by π–π interactions. To further investigate this hypothesis, the unsubstituted and more electron-rich receptor **4b** was synthesized and studied (Figure 3.7). Changing the fluorine atoms by hydrogen atoms not only modified the electronic nature of the central aryl ring, but also added additional hydrogen bond donor sites. Receptor **4b** turned out to bind chloride stronger than nitrate. In comparison to **4a** the binding of chloride by **4b** was boosted, K_a (Cl^-·**4b**) = 63 700 M^{-1}, and that of nitrate reduced, K_a (NO_3^-·**4b**) = 11 800 M^{-1}. The change in the electronic nature of the central aryl was expected to provide weaker or repulsive anion–π interactions, leading to the observed reduction of binding affinity for NO_3^-. The unexpected increase in affinity determined for **4b** binding chloride was assigned to the presence of a hydrogen bond donor in the structure of receptor **4b** compared to **4a**. In fact, the formation of a hydrogen bond between the chloride and the aromatic proton of the central aryl ring was evidenced by the high downfield-shift experienced by its signal during the ^1H NMR titration. Remarkably, no significant chemical shift changes were observed for the same aromatic protons in the titration of **4b** with nitrate. Taken together, these results supported that in close analogy to **4a**, receptor **4b** binds nitrate by establishing anion–π interactions assisted by π–π interactions with the core aryl ring. On the contrary, **4b** binds chloride through hydrogen bonding with the aryl core protons instead of interacting with its π-system. This new binding mode effectively raises the stability constant of the Cl^-·**4b** complex compared to that of its counterpart Cl^-·**4a** reversing the NO_3^-/Cl^- selectivity featured by the later receptor.

Very recently, Stoddart and co-workers reported the template-assisted synthesis of a macrobicyclic cyclophane composed of six pyridinium rings fused with two triazine cores and separated by three paraxylene spacers, the so-called Blue-Cage^{6+} **5a**.[127] The authors' expectations were that due to the electron-poor triazine rings, Blue-Cage^{6+} would show more favourable interactions with polycyclic aromatic hydrocarbons, *i.e.* pyrene **6**, than the analogous Ex-Cage^{6+} **5b** having two central 1,3,5-substituted benzenoid rings (Figure 3.9). However, isothermal titration calorimetry (ITC) experiments performed in CH_3CN solution at 298 K revealed that the binding constant of the inclusion complex of pyrene and Ex-Cage^{6+}, K_a (**6**⊂**5b**) = 6.77 × 10^5 M^{-1} was slightly larger than that of the analogous complex with the Blue-Cage^{6+}, K_a (**6**⊂**5a**) = 4.93 × 10^5 M^{-1}.

The detailed examination of the enthalpic and entropic factors of the two inclusion complexes, **6**⊂**5a** and **6**⊂**5b**, shed some light on the unexpected finding. The Δ*H*s for the inclusion complexes of Blue-Cage^{6+}and Ex-Cage^{6+} with pyrene are −9.91 and −10.82 kcal mol^{-1}, respectively. This small difference indicated an energy penalty for the inclusion of the guest with Ex-Cage^{6+}. The authors observed one PF_6^- anion included in the aromatic cavity of the

View Online

Published on 15 November 2016 on http://pubs.rsc.org | doi:10.1039/9781782626626-00039

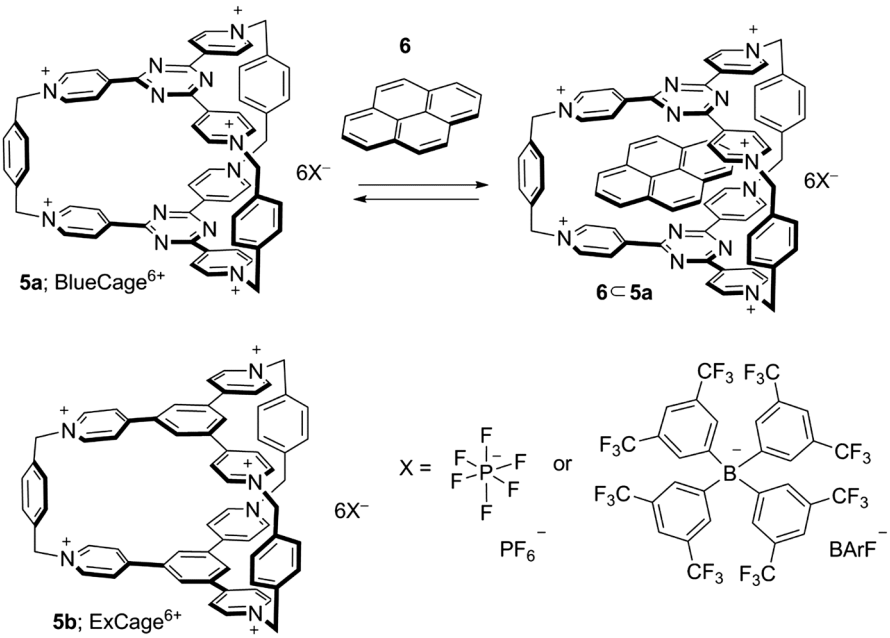

Figure 3.9 Structural formulae of BlueCage^{6+} **5**, pyrene **6**, Ex-Cage^{6+} **7**, PF_6^- and $BArF^-$ anions. The binding equilibrium for the formation of the **6⊂5** inclusion complex is shown at the top of the figure.

Blue-Cage^{6+}·$(PF_6^-)_6$ salt (Figure 3.10). The ion interacted more with the triazine units than with the pyridinium rings. The distances between the PF_6^- ion and the central rings were shorter than for typical anion–π interactions and the trigonal platforms of the Blue-Cage^{6+} bowed outward owing to the anion inclusion. Consequently, it was proposed that the above mentioned energy penalty (~1 kcal mol^{-1}) might be caused by the displacement of the included PF_6^-anion from the cavity of the Blue-Cage^{6+}. The analysis of the entropic terms for the inclusion processes also supported this hypothesis, that is the formation of the Blue-Cage^{6+} complex is entropically less demanding than that of the Ex-Cage^{6+}. The authors indicated that in the former case the inclusion process can be considered as a simple guest exchange (PF_6^- by pyrene) while in the latter case two entities are involved in forming one complex.

To substantiate this hypothesis, the PF_6^- anions of the Blue-Cage^{6+} salt were exchanged by $BArF^-$ anions. The $BArF^-$ ion is too large to be included in the cavity of Blue-Cage^{6+}. The ITC experiment of Blue-Cage^{6+}·$(BArF^-)_6$ salt with pyrene returned an association constant value of K_a (**6⊂5a**) = 3.95 × 10^6 M^{-1}. This value is one order of magnitude larger than the one measured for the PF_6^- salt of the Blue-Cage^{6+}. An analogous change of counter-ions for the Ex-Cage^{6+} resulted in a negligible effect in the stability constant value determined by ITC. The origin of the increase in binding affinity observed for the

View Online

Published on 15 November 2016 on http://pubs.rsc.org | doi:10.1039/9781782626626-00039

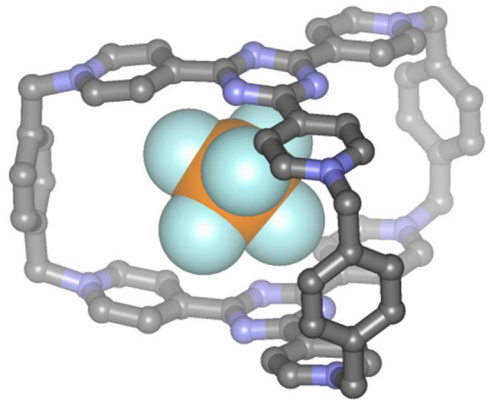

Figure 3.10 X-Ray structure showing the encapsulation of one PF_6^- anion inside the cavity of **5**. The other five anions are also involved in anion–π interactions but were removed for clarity. The Blue-Cage^{6+} is displayed in a ball and stick representation and the included anion as a CPK model. Hydrogen atoms were removed for clarity.

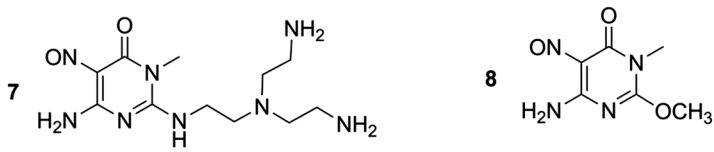

Figure 3.11 Line-drawing structure of the heterocyclic receptors **7** and **8** used to investigate SO_4^{2-}-π–π interactions in water.

Blue-Cage^{6+}·$(BArF^-)_6$ was largely entropic, whereas the enthalpy component of the inclusion process diminished, ΔH = 7.76 kcal mol^{-1}. These changes were attributed to the lack of anions in the cavity of the $BArF^-$ salt of **5a** that permitted solvent molecules to reside inside. The entropy increase reflects the release of the included solvent molecules. On the other hand, the reduction of enthalpy derives from the cost of desolvating the cavity prior to guest inclusion.

The thermodynamics of anion–π interactions in aqueous solution were investigated by Bianchi, Lopez-Garzón and co-workers using potentiometric titrations and ITC experiments. Using potentiometric (pH-metric) titrations, they showed that the successive protonated forms of the ligand **7** (Figure 3.11) were able to bind anions and form thermodynamically stable complexes in aqueous solution.[128] In the particular case of SO_4^{2-}, an anion that was not protonated in the investigated pH range, a nice linear correlation was obtained between the binding free energy and the receptor charge. From this linear relationship, the authors dissected the binding energy in two energetic contributions. One was related to the increment in free energy for the unitary addition of charge to the ligand (slope), the other was assigned

View Online

Published on 15 November 2016 on http://pubs.rsc.org | doi:10.1039/9781782626626-00039

to the residual free energy contribution at zero-ligand charge (intercept). This latter contribution was associated with the anion–π interaction and quantified as $\Delta G = -2.13$ kcal mol^{-1}. Later on,[129] new potentiometric titrations and ITC experiments were used to verify that neutral ligand **7** bound SO_4^{2-} with a free energy of binding in the range of $\Delta G = -2.2$ (pH-metric) and -2.4 (ITC) kcal mol^{-1}. The authors stated that these results provided support for the formation of anion complexes with neutral **7** in solution. The possibility that these complexes were stabilized by a pure anion–π interaction remained questionable in the absence of additional evidence and this point was clearly acknowledged by the authors, who also mentioned other non-specified forces as possible contributors to the complex formation. The X-ray structure of the complex formed by triprotonated pyrimidine derivative $[\mathbf{7}H_3]^{3+}$ and the $Co(CN)_6^{3-}$ anion was used as evidence that this and other studied anions were establishing anion–π interactions. In the solid state, the $Co(CN)_6^{3-}$ anion located the nitrogen atom of one of its cyanide ligands almost above the centroid of the pyrimidine ring of **7** at a distance of 2.786 Å. A weaker anion–π interaction with a second $Co(CN)_6^{3-}$ anion was also located. The observed binding geometries of the $Co(CN)_6^{3-}$ anions were also in agreement with previous examples reporting CN–π interactions in the solid state.

To further elaborate on the presence of anion–π interactions stabilizing the $SO_4^{2-}\cdot\mathbf{7}$ complex, binding studies in water using just the pyrimidine residue of **7**—*i.e.*, the aromatic heterocycle **8**—were performed. ITC experiments indicated that **8** formed a 1 : 1 complex with SO_4^{2-} in 0.1 M NMe_4Cl water solution at 298.1 K. Because **8** is deprived of the polyamine chain, it was deduced that no other interactions, except anion–π interactions could be effective for the binding of the anion. The thermodynamic stability of the $SO_4^{2-}\cdot\mathbf{8}$ complex ($\Delta G = -2.05$ kcal mol^{-1}) was only slightly reduced compared to that of the parent $SO_4^{2-}\cdot\mathbf{7}$ complex (*vide supra*). This finding was used to indicate that the contributions of the polyamine chain to the stability of the $SO_4^{2-}\cdot\mathbf{7}$ complex were almost irrelevant. Owing to the similar values obtained for the enthalpy and entropy terms in the binding of SO_4^{2-} with receptors **7** and **8**, it was concluded that solvation–desolvation processes were non-discriminant. The authors assigned the calculated thermodynamic parameters to the anion–π interactions established in water between the SO_4^{2-} anion and the heterocyclic ring in **7** and **8**. They ruled out the participation of other weak forces, in particular hydrogen-bonding, in the formation of these two complexes.

The energies derived from ITC experiments for the anion–π interactions stabilizing the complexes $SO_4^{2-}\cdot\mathbf{7}$ and $SO_4^{2-}\cdot\mathbf{8}$ were 2.4 and 2.0 kcal mol^{-1}, respectively. These values are 2–3 fold larger than those determined for the interaction of halides with substituted phenyl rings (π-acidic) in organic solvents.[116] Consequently, it was stated that **7** and **8** formed strong anion–π interactions in water with SO_4^{2-}. It is worth noting that the assigned anion–π interactions are almost athermic and were mainly driven by entropy. The authors reasoned that because the formation of the anionic complexes took place with *modest* charge neutralization (coulombic interactions are absent

View Online

Published on 15 November 2016 on http://pubs.rsc.org | doi:10.1039/9781782626626-00039

in neutral receptors), the entropy gain must be derived from the desolvation of the lyophilic aromatic surface of pyrimidine **8**. Interestingly, the thermodynamic signatures of the anion binding processes were consistent with classical hydrophobic binding. Finally, it was also mentioned that amino-pyrimidines exhibited strong polarization of their electronic structure[130–132] and, accordingly, the described anion–π interactions were ascribed to polarization effects despite the fact they were enthalpically disfavoured.

The synthesis of a family of receptors featuring a naphthalene spacer substituted with two arms equipped with triazolium rings as binding sites was recently reported by Molina and co-workers (Figure 3.12).[133] The anion-recognition properties of the receptor series were initially evaluated using ^{1}H NMR spectroscopy. The addition of an excess of several anions as TBA salts to separated solutions of the receptors in a 9 : 1 v/v mixture of CD_3CN–CD_3OD evidenced that F^- exclusively promoted their deprotonation and only $HP_2O_7^{3-}$ and $H_2PO_4^-$ anions induced significant changes in their ^{1}H NMR spectra. Significantly, the observed chemical shift changes for the hydrogen atoms of the receptors were dependent on the nature of the added anion and the electronic character of the terminal substituents of the 1,2,3-triazolium rings. For example, the addition of the dihydrogenphosphate anion produced analogous chemical shift changes in all receptors of the series. The hydrogen atom of the triazolium residues experienced a significant downfield shift ($\Delta\delta \sim 0.6$ ppm). The aromatic protons resonating as a singlet also moved downfield but to a lesser extent ($\Delta\delta \sim 0.4$ ppm). These complexation-induced changes suggested the involvement of these protons in the binding of the anion, as indicated in the inset of Figure 3.12. The Job plot analysis of the titration data revealed the formation of 2 : 1 complexes. The reported stability constants for the stepwise binding indicated that the formation of the 2 : 1 complex showed positive cooperativity ($2K_{2:1} > K_{1:1}/2$) for **9** and **10** and no cooperativity for **11** and **12**. However, an analogous *in–in* conformation of the receptor was assigned to the geometry of all 1 : 2 complexes with dihydrogenphosphate anions. The authors related the magnitude of $K_{1:1}$ to the electronic distribution in the triazolium cations that was quantified by computing the molecular electrostatic potential (MEP) values at the centre of the

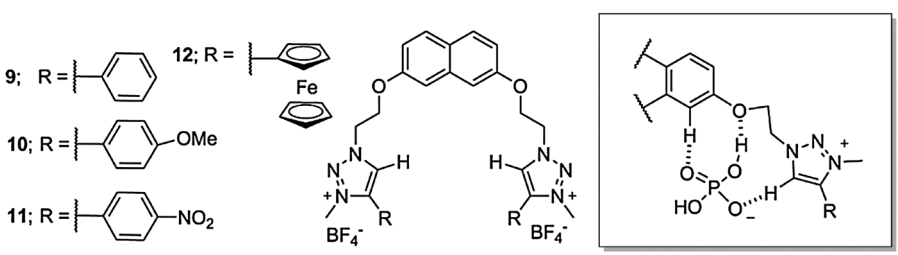

Figure 3.12 Line drawing structures of the receptors **9**–**12** equipped with triazolium rings as hydrogen-bond donors and anion–π binding sites. Inset: binding geometry for one-arm anion–receptor complex.

View Online

Published on 15 November 2016 on http://pubs.rsc.org | doi:10.1039/9781782626626-00039

ring and on the lobule of its C–H bond. The best correlation was obtained with the MEP values calculated for the π-systems, but the authors warned about making conclusions from this fact. In conclusion, the receptors series binds the mono-charged anion by establishing multiple hydrogen-bonding interactions (one classical X···H–X and two non-classical X···HC) assisted with charge–charge interactions.

A completely different scenario was observed in the binding studies with the triply-charged hydrogenpyrophosphate anion and this receptor series. On the one hand, for receptors **9**, **11** and **12** the addition of 0.5 equiv. of the anion produced the disappearance of the signal assigned to the CH of the triazolium rings in the free receptor and the observation of two separate signals in the downfield region of the spectra that were assigned to this proton in the complex. One signal was broad and resonated downfield with respect to the chemical shift of the triazolium CH in the unbound state, the other was sharp and appeared upfield-shifted with respect to the same reference. The addition of more than 0.5 equiv. of the anion induced downfield shifts to the broad signal but did not alter the chemical shift of the sharper one. Based on additional ^{1}H NMR experiments the authors concluded that receptors **9**, **11** and **12** formed 1 : 1 complexes with the triple charged anion in which one triazolium ring acted as a hydrogen-bond donor, whereas the other was involved in anion–π interactions[134] with the oxoanion also participating in CH···anion interactions with the inner aromatic protons of the naphthalene spacer (Figure 3.13). On the other hand, the binding of the triply-charged hydrogenpyrophosphate anion to receptor **10** produced the observation of two sharp and upfield-shifted signals for the CH protons of the triazolium units in the complex. In this case, it was suggested that the oxoanion established anion–π interactions with both triazolium binding units of the receptor that experienced different magnetic environments owing to conformational restrictions.

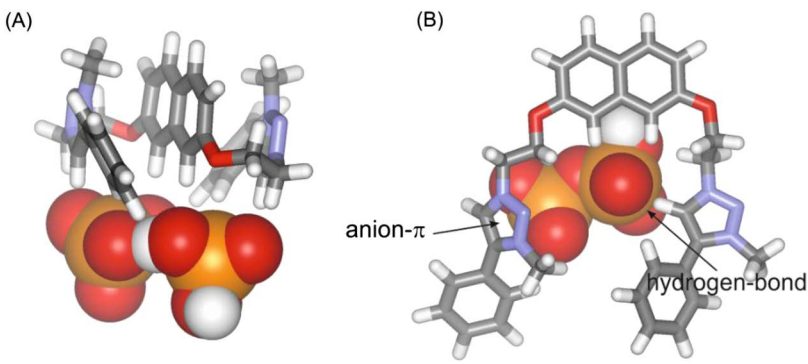

Figure 3.13 Reported optimized structures (B97D/6-31+G(d)) of: (A) the 1 : 2 complex **9**• $(H_2PO_4^-)_2$ showing a different hydrogen bonding pattern to the one proposed in the inset of Figure 3.13 and (B) the 1 : 1 complex **9**• $HP_2O_7^{3-}$ in which the oxoanion interacts *via* a CH···$^-$O hydrogen bond with one triazolium binding site and O^-···π interactions with the other.

View Online

Published on 15 November 2016 on http://pubs.rsc.org | doi:10.1039/9781782626626-00039

Surprisingly, the stability constants reported for the 1:1 complexes with the triply-charged anion are of the same order of magnitude (10^3 M^{-1}) as those of the mono-charged anion suggesting that the coulombic forces are not very effective in the stabilization of the complexes. However, a close examination of the titration curves provided in the supplementary information of the manuscript showed that the chemical shift changes of the receptors reached a plateau (saturation) by the addition of three or more equivalents of the mono-charged $H_2PO_4^-$ anion but required only one equivalent of the triply-charged $HP_2O_7^{3-}$ counterpart. This observation suggested that the binding constants for the complexes with triply-charged $HP_2O_7^{3-}$ anion were under-evaluated and should be estimated as larger than 10^4 M^{-1}. This value is more consistent with an increase of coulombic interactions provided by the triple negative charge of the anionic guest. The proposed structures for the different complexes and the receptor–anion interaction modes present in them are supported by extensive high-level electronic structure calculations, computation of MEP values and chemical shifts calculations (GIAO) that compare well with experiment.

Theoretical and experimental studies on anion–π interactions have shown that they are mainly dominated by electrostatic and anion-induced polarization contributions.[135,140,144] These studies also indicated that the magnitude of the anion–π interaction can be modulated by tuning the electronic nature of the aromatic system. This has been achieved by installing diverse and multiple electron-withdrawing substituents in the aromatic system, which in turns lowers its reduction potential.[41,136–138] As discussed above, anion–π interactions in solution are generally weak and difficult to assess with accuracy. Moreover, anion–π interactions may not perturb the energy levels of the aromatic systems' orbitals to the level required for the experimental observation of changes in their absorption and NMR spectra.[139] However, there are known examples of arenes possessing large positive quadrupole moments, which underwent significant changes of their absorption and emission spectra upon forming thermodynamically weak anion–π interactions.[140] The establishment of these anion–π interactions was associated with the observation of charge transfer (CT) bands that displayed Mulliken dependence.[141] CT bands are also typical of donor–acceptor complexes, in this particular case the anion will act as donor and the π-system as acceptor. The CT character of anion–π complexes seemed to provide additional thermodynamic stability.

It was postulated that anion–π complexes with electron-transfer (ET) character constituted one of the extremes of the energy continuum of CT complexes.[142,143] We consider it sensible to draw an analogy between the extremes provided by CT and ET anion–π complexes and the "weak σ" and "attack" structures derived from electronic structure calculations.[144] Anion–π complexes with formal ET nature are analogous to a radical pair in a solvent cage. As the CT character of the anion–π complexes evolves into ET, the electrostatic nature of the interaction decreases and the degree of covalent bonding increases. The dissociation of the solvent-caged radical pair resulting from

View Online

Published on 15 November 2016 on http://pubs.rsc.org | doi:10.1039/9781782626626-00039

anion–π complexes with strong ET character is equivalent to a net inner sphere ET process. Both radicals must be stable for the back-electron transfer to occur producing the intact binding partners for example in response to an external stimulus.[145] If this is not the case, the dissociation process becomes irreversible and one or both binding partners might be consumed. Aromatic radicals can be distinguished from anion–π complexes featuring CT/ET character because the absorption spectra of the former, not being supramolecular aggregates, must not display Mulliken dependence. Likewise, radicals are paramagnetic species and EPR active, while supramolecular or covalent (Messenheimer) anion–π complexes are usually diamagnetic.

Several authors have demonstrated that Lewis basic anions and NDIs featuring low reduction potentials are involved in irreversible, thermal ET processes.[143,146] It was also shown that NDIs and moderately Lewis basic anions underwent photoinduced ET (PET) processes, while strongly Lewis basic anions induced the exclusive formation of anion–π complexes with CT character.[147] The non-covalent interaction of NDIs with non-Lewis basic anions was described to produce non-chromogenic anion–π complexes.[148] As commented in the previous section, we became interested in studying the possibility of inducing related ET and PET processes from suitable anions to another π-acidic and strong electron acceptor aromatic system, the 2,3,6,7,10,11-hexacyano-1,4,5,8,9,12-hexaazatriphenylene *a.k.a.* $HAT(CN)_6$, **13** (Figure 3.14).[106] Prior to our work, Dunbar and co-workers had shown that

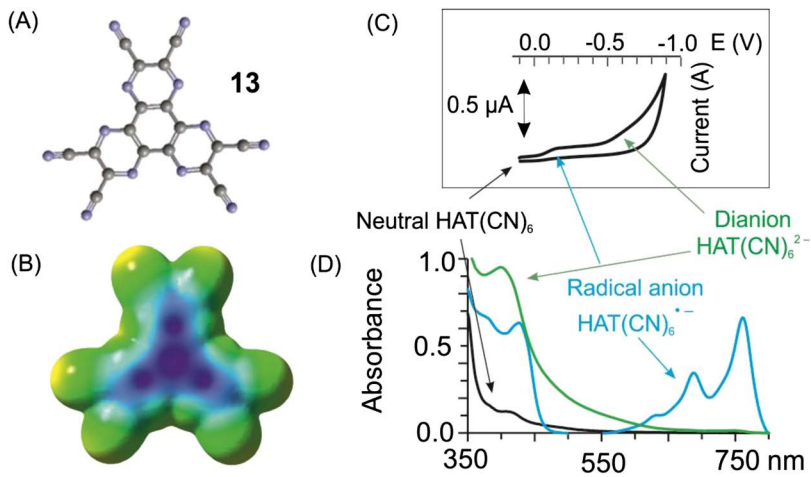

Figure 3.14 (A) Structural formula of **13**; (B) calculated MEP of **13**; (C) cyclic voltammetry of **13** displaying two half-wave potentials centred at −64 and −450 mV; (D) absorption spectra registered upon electrochemical reduction of **13**. An applied potential of −200 mV produced the radical anion $[\mathbf{13}]^{\bullet-}$. Its reoxidation proceeds uneventfully affording pure **13**. A higher negative potential of −700 mV produced the dianions $[\mathbf{13}]^{2-}$ as the main species in solution. Probably the dianion is not persistent in solution and its reoxidation did not produce pure **13**.

View Online

Published on 15 November 2016 on http://pubs.rsc.org | doi:10.1039/9781782626626-00039

the interaction of Cl^-, Br^- and I^- anions with **13** in THF solution produced CT bands.[105] Consequently, the resulting anion–π complexes were assigned with an obvious CT character. The mathematical analysis of the UV-vis titration data assigned extremely high binding constants to the complexes ($K_{CT}(X^-\cdot\mathbf{13})$ = 1–4 × 10^3 M^{-1}) when compared to related examples also featuring CT bands (K_{CT} = 1–10 M^{-1}).[142,143]

We demonstrated the different nature of the interactions established between a series of mono and polyatomic anions, featuring differing levels of Lewis base strengths, and **13**. We performed all our experiments in acetonitrile solution. The stronger Lewis basic anions (F^-, HO^- and ^-OCN) were involved in thermal ET processes involving the LUMO of **13** and the HOMO of the anion. The perfect agreement that existed between the spectroscopic features of the monoanion radical $[\mathbf{13}]^{\bullet-}$ and the dianion $[\mathbf{13}]^{2-}$ derived from the spectroelectrochemical study of **13**. The UV-vis spectra recorded during the titrations of **13** with the strong Lewis basic anions provided evidence for the existence of ET processes between the anions and the aromatic systems. NMR and EPR experiments also provided irrefutable evidence of the formation of radicals through the interaction of **13** and the strong Lewis basic anions (Figure 3.15). Less Lewis basic anions (Br^-, I^- and ^-SCN) interacted with **13** by producing mainly CT anion–π complexes with reduced thermodynamic stability. Some of these anions were involved in thermal ET processes but to a very reduced extent. In the cases where the thermal ET processes were turned off, they could be partially activated by photoexcitation of the aromatic acceptor. The Cl^- anion constituted a special case. It behaved as a weak Lewis basic anion under thermal conditions and produced an anion–π complex $Cl^-\cdot\mathbf{13}$ with CT character. However, the photoexcitation of the complex induced a quantitative PET process yielding dianion $[\mathbf{13}]^{2-}$. Computational results provided an explanation of the energetic requirements (HOMO/LUMO levels of anion donor and π-acceptor) that are necessary to achieve thermal ET.

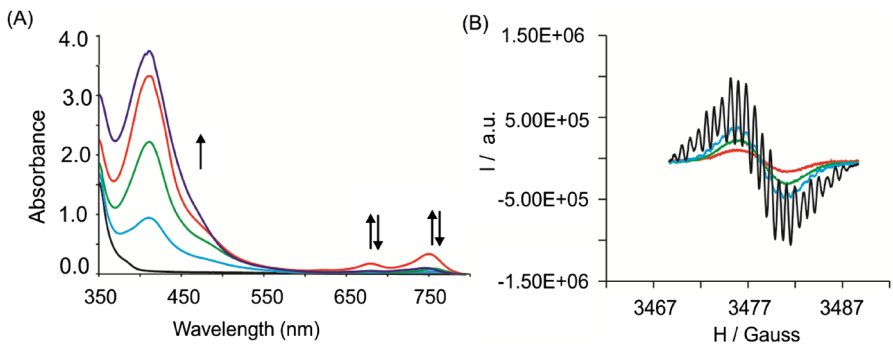

Figure 3.15 (A) UV-vis spectroscopic changes observed during the titration of **13** with TBAF (0, 0.8, 1.5, 4.5, and 10 equiv. added); (B) EPR spectral changes registered during an analogous titration. **13** is diamagnetic and EPR silent.

View Online

Published on 15 November 2016 on http://pubs.rsc.org | doi:10.1039/9781782626626-00039

We proposed that the Lewis basic characteristics of the anion determined the character of the initially formed anion–π complex (non-chromogenic, CT or ET). In turn, the nature of this complex controls the preferred mode of interaction: anion–π supramolecular complex or net ET, which after dissociation of the solvent caged radical pair produce the radical anion $[\mathbf{13}]^{\bullet-}$ and by further net ET the dianion $[\mathbf{13}]^{2-}$. This proposal is in agreement with the unifying ET mechanism that operates *via* donor–acceptor complexes.[142]

We are aware that the formation of the radical anion $[\mathbf{13}]^{\bullet-}$ is thermodynamically uphill but we attributed the driving force towards its massive formation to the sacrificial role played by the anion radical $\mathbf{X}^{\bullet}$ that is also generated. This prevents the back-electron transfer process and leads to irreversible formation of the aromatic radical $[\mathbf{13}]^{\bullet-}$ that is considerably stable in solution.

In 2008 we designed and synthesized a series of anion receptors based on α,α,α,α-isomers of aryl extended calix[4]pyrroles **14** (Figure 3.16).[138] These receptors featured four *meso*-phenyl substituents with different *para*-substituents to tune the electronic properties of the surface potentials on top of their π-systems[149] (density and charge distribution). The formation of four hydrogen bonds between the pyrrole NHs and the Cl^- anion locked the receptors in the cone conformation and arrested the anion in the deep aromatic cavity defined by the four *meso*-phenyl substituents in this conformation. The bound anion was forced to experience anion–π interactions with four aromatic panels. We showed that the complexation process was mainly driven by the formation of the strong hydrogen bonds, and that this strong interaction was attractively or repulsively modulated by the much weaker anion–π interactions. We used this "four wall" receptor series to quantify chloride–π(phenyl) interactions in acetonitrile solution demonstrating that only the interaction of Cl^- with a *p*-NO_2-substituted phenyl group was slightly attractive (~0.1 kcal mol^{-1}). We assessed this interaction energy value by subtracting and dividing by four the free energy of binding of Cl^- to the "no wall"

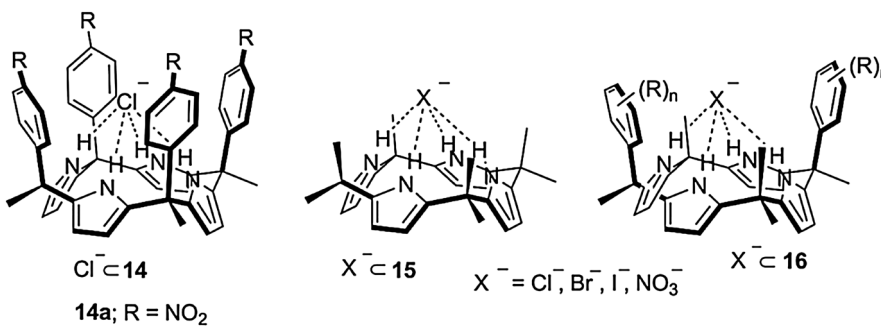

Figure 3.16 (Left and right) Molecular structures of the halide inclusion complexes with "four wall" **14**, and "two wall" **16** *meso*-phenyl substituted calix[4]pyrroles. (Middle) Halide inclusion complex of the "no wall" **15** octamethyl-calix[4]pyrrole receptor used as reference for the assessment of anion–π interactions.

View Online

Published on 15 November 2016 on http://pubs.rsc.org | doi:10.1039/9781782626626-00039

reference receptor, $\Delta G(Cl^- \subset \mathbf{15}) = -6.9$ kcal mol^{-1}, to that of the *p*-NO_2-substituted "four wall" complex, $\Delta G(Cl^- \subset \mathbf{14a}) = -7.2$ kcal mol^{-1} (Figure 3.16). To further study and quantify anion–π interactions in solution, more recently, we prepared an additional series of "two wall" aryl extended calix[4]pyrrole receptors **16**.[150] The new receptor series allowed the placement of multiple electron-withdrawing groups in the *meso*-phenyl substituents opening the range of aromatic surface potentials or quadrupole values that can be examined with respect to their interactions with anions. We also discovered that the deletion of two aromatic walls in series **16** provided a significant increase in the thermodynamic stability of the Cl^- complexes compared to the "four wall" series **14** counterpart. This allowed the "two wall" system **16** also to be applied to the investigation of anion–π interactions with Br^- and I^-. The complexes of these two later halides with the "four wall" receptors were too weak for accurate measurement of binding constants.

Using ^{1}H NMR titration experiments and X-ray diffraction studies of single crystals (Figure 3.17), it was demonstrated that in the complexes of the halides with the "two wall" receptor series **16**, the anion was hydrogen-bonded to the pyrrole NHs and wedged in the cleft defined by the two *meso*-phenyl substituents. The sandwiched anions were forced to establish two simultaneous halide–π interactions.

Halide binding became increasingly attractive as the number and electron-withdrawing character of the aromatic substituents increased (Figure 3.18). This result was taken as evidence of the existence of halide–π interactions in solution and their important electrostatic nature. Again using the "no wall" receptor **15** as reference, a coarse quantification of the various halide–π interactions in solution was assessed. The measured strength of the interaction for Cl^- and Br^- with the different aromatic systems was very similar in strength and reached a maximum of −0.7. kcal mol^{-1} for pentafluoro and dinitro phenyl substituted rings. In general, I^- experienced stronger anion–π interactions with the studied phenyl systems. The maximum determined energy was −1.0 kcal mol^{-1} for both pentafluoro and dinitro phenyl substituted rings. This observation was ascribed to the larger polarizability of I^- with respect to the smaller halides.

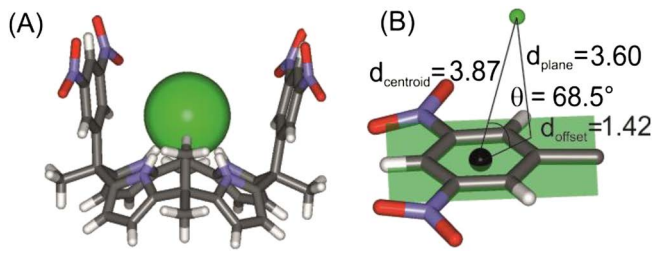

Figure 3.17 (A) X-Ray structure of the inclusion complex of Cl^- with α,α-dinitrophenyl-calix[4]pyrrole receptor; (B) expansion of one region of the complex relevant for the Cl^-–π interactions with indication of important geometrical parameters.

View Online

Published on 15 November 2016 on http://pubs.rsc.org | doi:10.1039/9781782626626-00039

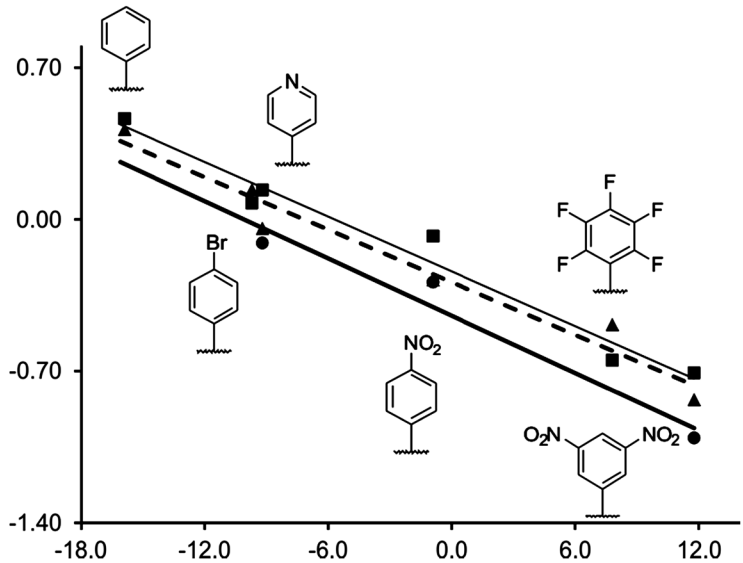

Figure 3.18 Plot of the statistically corrected experimental values $\Delta\Delta G$ (kcal mol^{-1}) for the halide–π interactions *vs.* ESP values (kcal mol^{-1}) calculated at the centroid of the phenyl ring: chloride (triangle), bromide (square) and iodide (circle).

The binding processes were analysed in detail with respect to the enthalpy and entropic components using ITC experiments. Surprisingly, in acetonitrile solution the observed increase in free energy of biding (ΔG) of halides with the "two wall" receptor series correlated well with a more favourable entropic term (Figure 3.19). On the contrary, the enthalpic component showed a reduced, inverted trend. This phenomenon was assigned to solvation effects and the "two wall "system was reinvestigated in chloroform solution using methyl trioctylammonium chloride (MTOACl) instead of TBACl. Upon changing to the less polar chloroform solvent, the binding data displayed the expected enthalpy/free energy relationship typically observed in the formation of complexes in non-polar organic solvents, that is the increase in free energy is reflected by an increase in binding enthalpy. Nevertheless, the expected entropy–enthalpy compensation was not observed even in chloroform. Probably, the entropy gain related to the solvent molecules that are released to the bulk over-compensates the entropy associated with the complex formation. The presented results indicated that halide–π-phenyl interactions in polar and non-polar organic solvents can be weakly attractive (−0.7 to 1 kcal mol^{-1}) when electron withdrawing substituents are introduced. Moreover, in striking contrast to the reports of anion–π interactions in water,[129] the attractive halide–π interactions measured with the "two wall" calix[4]pyrrole system **16** in organic solvents are mainly driven by enthalpy.

The "two wall" series of receptors was also used to quantify NO_3^-–π interactions.[150] As was observed with the halide anions, the receptors featuring

View Online

Published on 15 November 2016 on http://pubs.rsc.org | doi:10.1039/9781782626626-00039

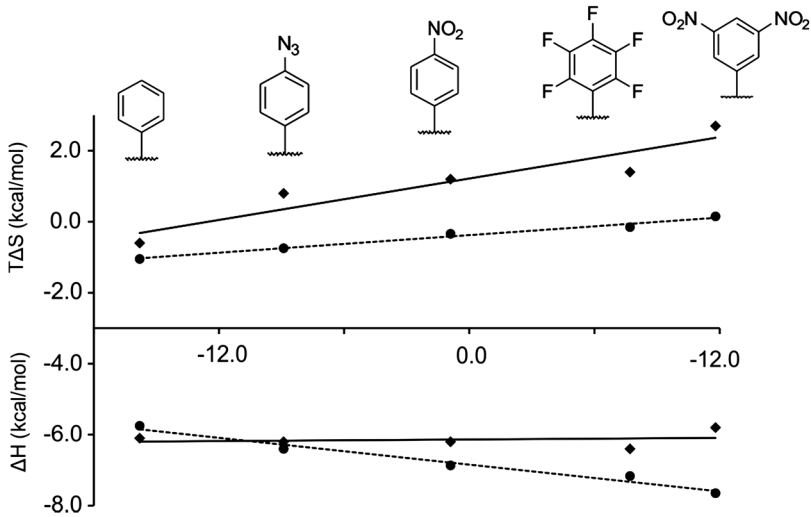

Figure 3.19 Plot of the experimental thermodynamic contributions ΔH (kcal mol^{-1}) and TΔS (kcal mol^{-1} at 298 K) to the total free energy of binding for the inclusion complexes of the "two wall" series **16** with chloride in acetonitrile (circle) and chloroform (diamonds) solutions. The salts used as chloride precursors were TBACl for acetonitrile and MTOACl for chloroform. In acetonitrile solution, anionic complexes are formed. However, in chloroform solution, receptor-separated ion-paired complexes are produced.

the more electron-poor aromatic walls were the ones that showed stronger binding for the nitrate anion. The energetic estimate for the interaction of the nitrate and the dinitro phenyl substituted ring was −0.9 kcal mol^{-1}. The preferred binding geometry of the nitrate anion when sandwiched between the two aromatic *meso*-phenyl substituents was revealed from the X-ray structure of the NO_3^- anion included in the dinitrophenyl calix[4]pyrrole derivative (Figure 3.20). Only one oxygen atom accepts the four hydrogen bond donors of the calix[4]pyrrole core. The other two oxygen atoms of the nitrate interacted with the aromatic walls displaying O···C distances shorter than the sum of the van der Walls radii. Notably, the "two wall" calix[4]pyrrole series of receptors turned out to be excellent carriers for ion transport through lipid-based lamellar membranes. The most active transporters were the *p*-nitro and the dinitro-derivatives probably functioning *via* an anion–anion antiport mechanism. They also exhibited a remarkable selectivity for nitrate transport over all other anions tested. Recently, Wang and co-workers also demonstrated that oxacalix[2]arene[2]triazine receptors, previously used to investigate anion–π interactions in solution and in the solid state,[120] mentioned at the beginning of this section, were good ion-pair transporters (transmembrane carriers *via* a symport mechanism).[151]

"Two wall" calix[4]pyrroles bearing *meso*-2-thiophenyl substituents were reported by Sripadi and co-workers for the investigation of anion–π

View Online

Published on 15 November 2016 on http://pubs.rsc.org | doi:10.1039/9781782626626-00039

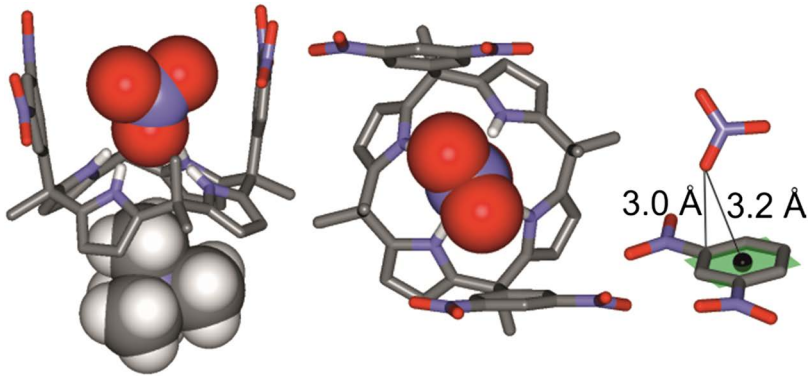

Figure 3.20 Side and top views of one of the binding geometries observed in the solid state for the inclusion complex of nitrate with α,α-dinitrophenyl-calix[4]pyrrole receptor.

interactions in solution.[152] The authors conclude that the α,α-isomer showed stronger binding with F^- and Cl^- than the α-β-isomer. The results suggested that the thiophene rings were involved in anion–π interactions.

3.3.2 Anion–π Interactions in Reaction Catalysis

A generally accepted method for catalysis relies on the binding of an elusive target: the transition state.[153] The ability of anion–π interactions[52] to assist in the binding[116] and transport[154] of anions has been demonstrated and some of the more relevant results briefly mentioned in the previous section. The application of anion–π interactions to catalysis by stabilization of anionic transitions states derived from these findings. It was also inspired by the well-known and widespread use of the complementary cation–π interactions to catalyze reactions in biology and chemistry. Until very recently, there were no reports of the use of anion–π interactions in catalysis. This lack of examples also derived from the limited availability of the required π-acids, aromatic surfaces with positive quadrupole moments. Matile and co-workers published the first examples of catalysis based on anion–π interactions (*vide infra*). In 2013, they reported experimental evidence on the contribution of anion–π interactions in the catalysis of the Kemp elimination reaction. The Kemp elimination is a well-established tool for the elaboration and study of innovative catalysis in multiple areas. The key step of the reaction is the deprotonation of an aromatic carbon in the benzisoxazole substrate **17** by a general base. The reaction proceeds through a single anionic transition state (TS) affording the nitrophenolate. The anionic nature of the transition state made this simple reaction an ideal model to study the putative contribution of anion–π interactions to catalysis.

Matile and co-workers prepared π-acidic naphthalenediimides (NDIs) **18**–**19** (Figure 3.21) having a covalently attached carboxylate at one end and a

View Online

Published on 15 November 2016 on http://pubs.rsc.org | doi:10.1039/9781782626626-00039

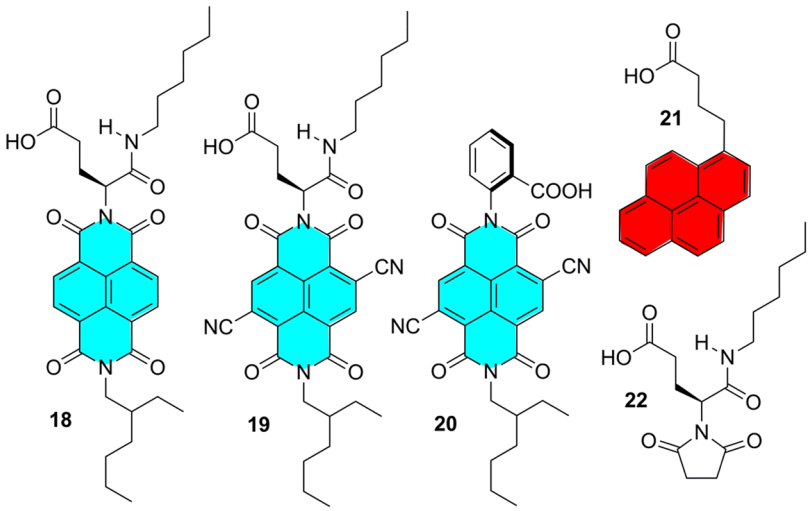

Figure 3.21 Line drawing structures of the functional NDI catalysts **18–19** and the control molecules **20–22** used in Matile's study of the anion–π interactions for reaction catalysis.

lipophilic solubilizing residue at the other end. They also prepared suitable controls **20–22** (Figure 3.21) to further elaborate on the effects provided by the anion–π interactions in the catalysis of the reaction. When benzisoxazole **17** (13 mM) was dissolved with NDI **18** (5 mM) in CD_3OD solution and 0.5 equivalents of tetrabutylammonium hydroxide were added, the formation of nitrophenol **23** (v_{ini} ~ 60 μM min^{-1}), monitored by ^1H NMR spectroscopy, was clearly faster than in the presence of controls **20** (v_{ini} ~ 10 μM min^{-1}) or **21** (v_{ini} ~ 15 μM min^{-1}). In addition, from the three substrates tested as potential catalysts, **18**, **20** and **21**, only NDI **18** showed a dramatic reaction rate enhancement upon increasing concentration.

From these results, the authors concluded that **20** did not possess the right arrangement of the π-basic surface and the carboxylate group to attain the optimum geometry in both the substrate–catalyst complex and the transition state, while **21** was ineffective owing to the π-basic nature of the pyrene aromatic substituents.

A study of the substrate concentration dependence (0–180 mM), using constant catalyst concentration (8.3 mM), revealed saturation kinetics for **18** but not for control **22** lacking the π-acidic NDI aromatic unit. This result supported the formation of the catalyst–substrate ground state complex **18·17** and indicated that under the same concentration regimes, the analogous **22·17** complex was too weak to be formed in detectable amounts. The Michaelis–Menten analysis of the kinetic data obtained using NDI **18** as catalyst allowed the calculation of the stabilization energy for the ground state complex **18·17** ($\Delta\Delta G_{GS}$ = −1.5 ± 0.1 kcal mol^{-1}), as well as that of the transition state **TS18·17** ($\Delta\Delta G_{TS}$ = 6.8 ± 0.1 kcal mol^{-1}) with respect to the uncatalysed process.

View Online

Published on 15 November 2016 on http://pubs.rsc.org | doi:10.1039/9781782626626-00039

The use of NDI **19**, bearing two cyano groups in the NDI core, as catalyst had a profound impact on the magnitudes determined for the stabilization energies of both the ground state complex **19·17** ($\Delta\Delta G_{GS} = -1.7 \pm 0.1$ kcal mol^{-1}; 0.2 kcal mol^{-1} increase with respect to **18·17**) and the transition state complex **TS19·17** ($\Delta\Delta G_{TS} = 7.2 \pm 0.1$ kcal mol^{-1}; increase of 0.4 kcal mol^{-1} with respect to **TS18·17**). The catalytic proficiency calculated for NDI **19** more than doubled that of NDI **18**. Molecular modelling carried out at a high level of theory for the elimination reaction of benzisoxazole **17** catalyzed by NDI **19** showed that distance between the *p*-nitro phenyl ring and the π-acidic surface decreased when moving from the GS to the TS and finally to the reactive intermediate (RI) (Scheme 3.2). This finding was in complete agreement with operational anion–π interactions in catalysis. The formation of the carbanion in the isoxazole ring was assigned as the rate determining step of the reaction. The formed carbanion was stabilized by being placed on top of one of the aromatic rings of the NDI. In conclusion, this study provided solid and unprecedented experimental evidence for the involvement of anion–π interactions in catalysis and encouraged Matile and co-workers to further investigate the topic.

A complete experimental and theoretical account of the role of anion–π interactions in the Kemp elimination reaction catalyzed by a larger series of

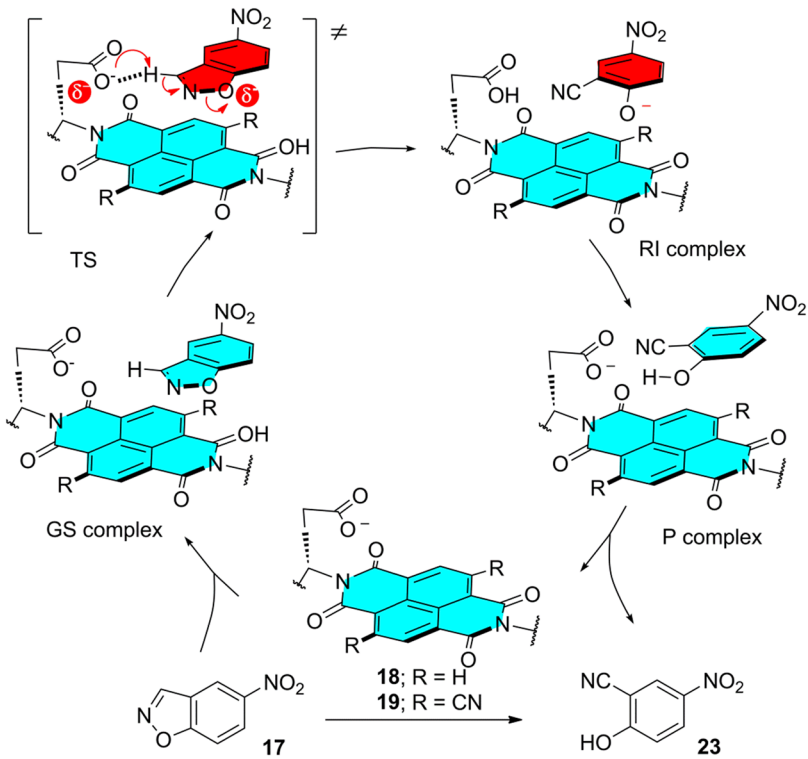

Scheme 3.2 Catalysis of the Kemp elimination using π-acidic naphthalenediimide carboxylate as a catalyst.

View Online

Published on 15 November 2016 on http://pubs.rsc.org | doi:10.1039/9781782626626-00039

naphthalene imides appeared recently.[155] The dependence of anion–π catalysis on π-acidity was investigated by using sulfide oxidation chemistry (Scheme 3.3). The NDI derivative **24**, equipped with two sulfides, was oxidized with *m*-chloroperbenzoic acid (MCPBA) at 0 °C to afford the strong π-acid **25** with two sulfoxides in the NDI core. In NDI **25** the sulfoxides exist as a mixture of stereoisomers.[156] Further MCPBA oxidation of **25** at room temperature produced sulfone **26** with maximal π-acidity. Using this methodology, the π-acidity of the NDI core was tuned without significant structural changes. Unfortunately, sulfone **26** could not be used as a catalyst owing to competing and unidentified secondary reactions.

Compared to the parent NDI **18**, the introduction of the two sulfides stabilized further the GS complex **17·24** ($\Delta\Delta G_{GS} = -8.3 \pm 0.1$ kcal mol^{-1}; 0.5 kcal mol^{-1} with respect to **18·17**). This anticatalytic effect was assigned to the existence of additional hydrophobic interactions between the ethyl groups at the periphery of **24** and the benzisoxazole **17**, which were sufficient to compensate the reduced π–π interactions owing to the Lewis acidity loss of NDI **24** compared to **18**. Based on this result, the authors claimed that π–π interactions seemed to be less affected by π-acidity changes than anion–π counterparts. The hypothesis was nicely substantiated by the fact that, compared to NDI **18**, the 0.4 kcal mol^{-1} stabilization energy measured for the **TS17·24** complex ($\Delta\Delta G_{TS} = 7.1 \pm 0.1$ kcal mol^{-1}) was somewhat smaller than that determined for the corresponding GS.

The increase of π-acidity when moving from the disulfide NDI catalysts **24** to the sulfoxide derivatives **25** provoked an additional stabilization of the TS in *ca.* 0.5 kcal mol^{-1} ($\Delta\Delta G_{TS} = -7.6 \pm 0.1$ kcal mol^{-1}). This increase in TS stabilization paralleled the results obtained using the parent NDI catalyst **18** and the dicyano derivative **19** reinforcing the idea that anion–π interactions were functional in reaction catalysis. Remarkably, NDIs **24** (sulfide) and **25**

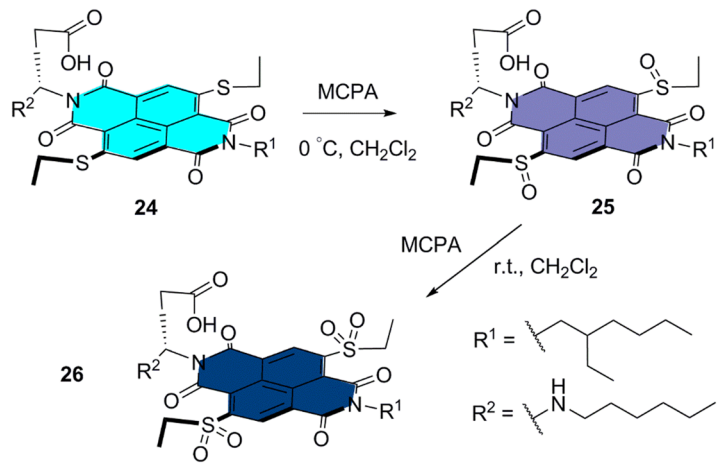

Scheme 3.3 Synthesis of sulfoxide **25** and sulfone **26** from sulfide **24**.

View Online

Published on 15 November 2016 on http://pubs.rsc.org | doi:10.1039/9781782626626-00039

(sulfoxide) stabilized their GS complexes, **17**·**24** and **17**·**25**, respectively, to a comparable extent (0.5 kcal mol^{-1}, compared to **17**·**18**). This result was in striking contrast with the previously reported data for **18** and **19**, in which an increase of 0.5 kcal mol^{-1} in TS stabilization was mirrored by an increase of 0.2 kcal mol^{-1} in GS stabilization energy. The authors explained these results indicating that NDIs **24** and **25** possessed nearly identical global structures; however, this was not the case for **18** and **19** for which peripheral contacts with the added cyano substituents were possible. So far, the best NDI carboxylate derivative assayed as an anion–π catalyst in the Kemp elimination of benzisoxazole **17** was bis-sulfoxide **25**.

In this work, the authors also assessed the dependence of the anion–π catalysis on the length and substitution of the alkyl spacer that connected the π-surface with the carboxylate base. A series of NDI anion–π catalysts **27**–**34** containing simple alkyl linkers of increasing length were synthesized (Figure 3.22). The butyric acid NDI **28** with a pure Leonard linker[157] (a trimethylene bridge) corresponds to the linker length in the original NDI **18** and provided nearly identical GS and TS stabilizations to the latter. This result demonstrated that the branching of the spacer in **18** was irrelevant and that the catalytic inactivity of **21** (Figure 3.21) must have derived from repulsive anion–π interactions with the pyrene ring and not from lacking substituents on the spacer.

The results obtained with the series of NDIs having alkyl linkers of increasing size **27**–**32** showed that anion–π catalysis had a reduced sensitivity to linkers longer than four methylene carbons and suggested that the adequate

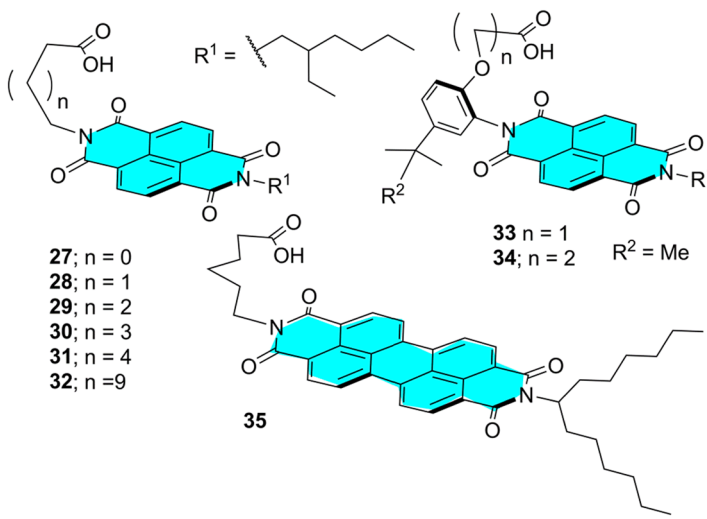

Figure 3.22 Structures of the carboxylic NDI acids **27**–**34** used as catalysts to investigate the effect of the spacer length and substitution on the anion–π catalysis. The structure of the perylene diimide (PDI) **35** used in this study is also shown.

View Online

Published on 15 November 2016 on http://pubs.rsc.org | doi:10.1039/9781782626626-00039

positioning of the carboxylate and the π-surface in these cases could result from an induced-fit binding mechanism. They also indicated that the length of three methylene carbons displayed by the Leonard linker in NDI **28** did not have a preorganising effect, because longer and conformationally more flexible linkers gave similar results. This latter interpretation was also corroborated by the use of NDIs **33** and **34** with conformationally more rigid linkers as catalysts. While in NDI **33** the linker length of four atoms is equivalent to that of **29**, the catalytic properties of the former were significantly worse than those of the latter. The homologous NDI **34**, containing an extra carbon atom in the linker, produced better catalytic results.

The inclusion in this study of perylenediimide (PDI) **35** as a putative anion–π catalyst allowed the dissection of the contribution of π–π and anion–π interactions to reaction catalysis. The enlargement of the aromatic surface in PDI **35** favored π–π interactions. In contrast, PDIs are less π-acidic than their NDI counterparts. PDI **35** was equipped with a five methylene spacer as NDI **30**, which was a fully operational catalyst. However, the use of PDI **35** as catalyst for the Kemp elimination reaction did not show saturation kinetics. The poor performance of PDI **35** as catalyst was assigned to the fact that the contribution of π–π interactions is completely irrelevant in stabilizing the corresponding anionic-like **TS17·35**.

Enolate chemistry is particularly attractive for the investigation of anion–π interactions. Matile *et al.* provided convincing experimental evidence of the stabilization of the ground-state of enolates on π-acidic surfaces using the covalent macrocyclic model system **36** (Figure 3.23).[158] In ^{1}H NMR titrations with 1,1,3,3-tetramethylguanidine (TMG), the methylene protons of the malonyl unit in **36** disappeared with much less TMG added than for diethylmalonate **37**. From these experiments a pK_a = 14.5 was assigned to the macrocycle **36**. This represented an increase of acidity by the aromatic surface of ΔpK_a = 1.9 and demonstrated that the macrocyclic malonyl enolate **38** was thermodynamically more stable than the free enolate **39** ($\Delta\Delta G$ = 1.1 kcal mol^{-1}).

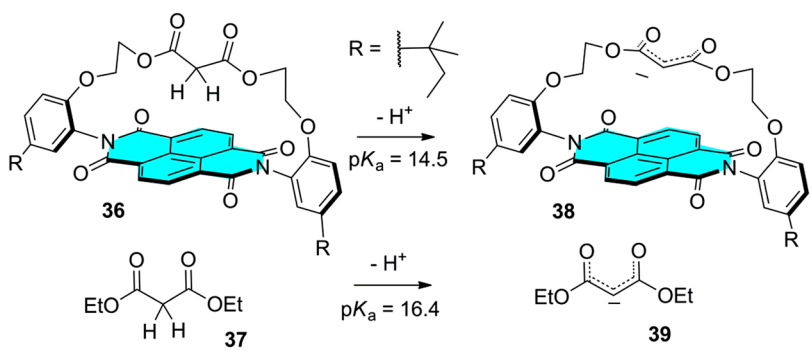

Figure 3.23 Line drawing structures of macrocycle **36** featuring a bridging diester malonate unit and of diethyl malonate **37**. The formation of the corresponding enolates induced by base deprotonation and the assigned pK_a values are also indicated.

View Online

Published on 15 November 2016 on http://pubs.rsc.org | doi:10.1039/9781782626626-00039

This finding provided robust evidence for the potential stabilization of reactive enolates by anion–π interactions.

The significance of the anion–π interaction in the macrocycle enolate **38** was evaluated in the Michael addition to α,β-unsaturated enone **40**. The reaction was performed in a 1 : 1 mixture of CD_3CN–$CDCl_3$, the concentrations of the macrocyclic malonate **36** and the enone **40** were 50 mM, and 1,8-diazabicycloundec-7-ene (DBU) was used as base in a 5 mM concentration. Diethyl malonate **37** was used as control under identical reaction conditions. The analysis of the kinetic data revealed that on the aromatic surface the Michael addition was 86-fold faster than in the control. This corresponds to a stabilization of the negative charge in the transition state by $\Delta\Delta G^{\#}$ = 2.6 kcal mol^{-1} through the presence of effective anion–π interactions. The scope of this finding was evaluated by reacting the enolate **38** with nitro-olefin **41** (Figure 3.24). The analysis of the kinetic data assigned a transition state stabilization energy provided by anion–π interactions of $\Delta\Delta G^{\#}$ = 1.5 kcal mol^{-1}.

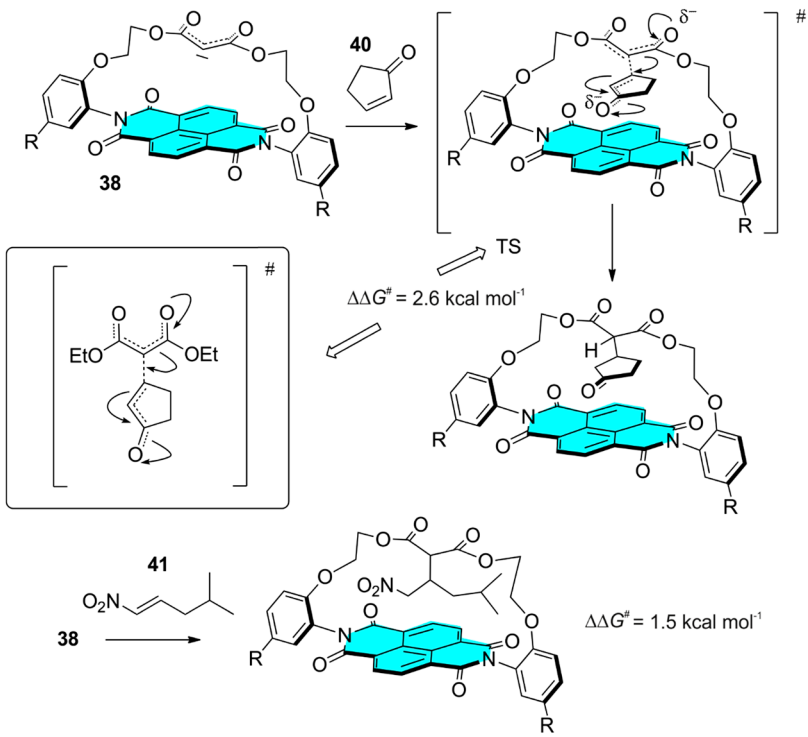

Figure 3.24 (Top) Michael addition of enolate **38** to enone **40**. The transition states for the catalyzed and uncatalyzed reaction are also shown. The differences in initial velocity implied that anion–π interactions stabilized the TS for the enolate **38** by 2.6 kcal mol^{-1}. (Bottom) 1,4-Addition of enolate **38** to the nitroolefin **41** as Michael acceptor affording adduct **42**, the TS is stabilized by 1.5 kcal mol^{-1} from comparison to initial rate of the analogous reaction with diethyl malonate.

View Online

Published on 15 November 2016 on http://pubs.rsc.org | doi:10.1039/9781782626626-00039

Very recently, Matile *et al.* have used closely related anion–π interactions in molecular tweezer catalysts in the selective acceleration of disfavored enolate addition reactions.[159]

Anion–π interactions have also been invoked in the catalysis of asymmetric enamine additions to nitroolefins.[160] NDIs were selected to construct the catalyst. A proline derivative was placed at one side of the π-surface for enamine formation. A suitable spacer located the proline unit slightly apart from the π-surface in order to leave space for the nitroolefin intercalation and also to place the iminium intermediate far away from the π-acidic surface to avoid repulsive interaction (Figure 3.25). A carboxylic acid was placed at the distal position of the π-surface making use of the well-established Leonnard spacer and following Wennemers' design of bifunctional catalysts for asymmetric additions of enamine to nitroolefins.[161] Sulfide oxidation was also employed as discussed above to tune the π-acidity of the NDI aromatic surface. The obtained results provided experimental evidence of functional anion–π interactions in the catalysis of asymmetric enamine additions to nitroolefins. The increase in enantioselectivity and reaction rate observed by increasing the π-acidity in two almost isostructural catalysts were key to support the existence and relevance of anion–π catalysis. The relationship between the diastereoselectivity and π-acidity of stereoisomeric catalysts was more difficult to rationalize.

Anion binding catalysis is also a relatively new concept in the field of organocatalysis. In this methodology, the catalyst—a receptor for anion binding—facilitates the release from one of the starting materials of an anion by binding it reversibly. A paradigmatic example was reported by Jacobsen *et al.* in 2008 for the catalysis of the reaction between 1-chloroisochroman **42** and the silyl ketene acetal **43** (Figure 3.26). Hydrogen bonds were used as the driving force for the binding of the anion with the thiourea receptor/catalyst **44**.[162] There are well-known alternatives to hydrogen-bonds for anion binding,

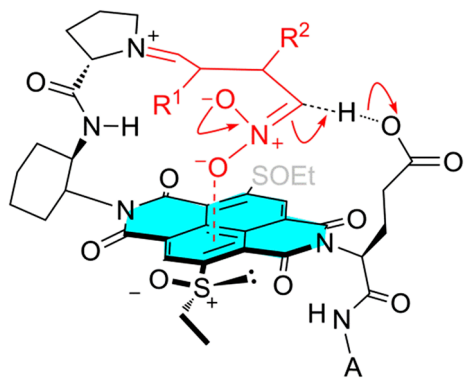

Figure 3.25 Possible stabilization of the TS of adding enamines (from aldehydes) to nitro olefins using the organocatalyst used by Matile and co-workers acting through anion–π catalysis in the protonation step of the nitronate.

View Online

Published on 15 November 2016 on http://pubs.rsc.org | doi:10.1039/9781782626626-00039

i.e. halogen bonds, anion–π interactions, and coulombic interactions. In 2013, Huber *et al.* demonstrated the use of the neutral double halogen-bond receptor **45** to catalyze the same reaction.[163] It was assumed that the excision of the chloride from **42** to form the oxonium cation **46** was assisted by binding to the neutral halogen-bond donor catalyst **45**. This mode of action is related to the interaction of substrate **42** with Jacobsen's thiourea **44** but the hydrogen-bond interactions are substituted by halogen-bond interactions.

Berkessel *et al.* exploited coulombic interactions for the design of receptors able to perform anion–binding catalysis.[164,165] They focused on the use of pyridinium ions owing to their well-known halide-binding abilities, which in the solid state had provided structural evidence of anion–π interactions.[166] Their initial attempts to alkylate 1-chloroisochroman **42** with ketene **43** using pyridinium ions substituted with one **47**·BPh_4 or two **48**·BPh_4 electron-withdrawing substituents were unsuccessful (Figure 3.27). In an effort to increase the π-acidity of the pyridinium ring, a third electron-withdrawing substituent was attached. This methodology produced a new generation of triply substituted pyridinium ions **49a–c**·BPh_4 that did promote the alkylation of **42**. In the particular case of organocatalyst **49a**·BPh_4, the binding (excision) of the chloride was achieved by combining coulombic and anion–π interactions.

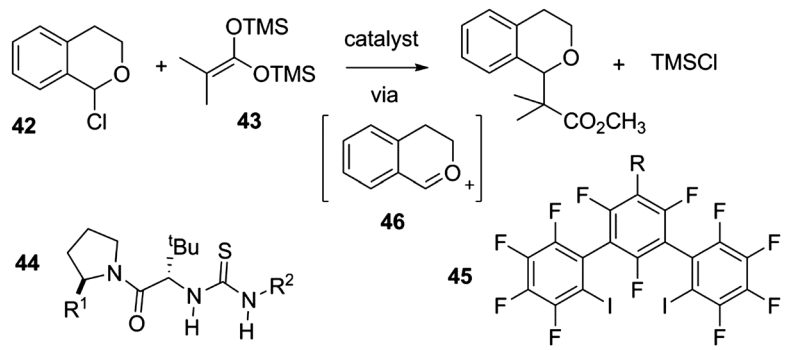

Figure 3.26 (Top) Organo-catalytic α-haloether alkylation. (Bottom) Organocatalysts used in the reaction featuring hydrogen-bonding binding motif **44** and halogen-bonding binding motif **45**.

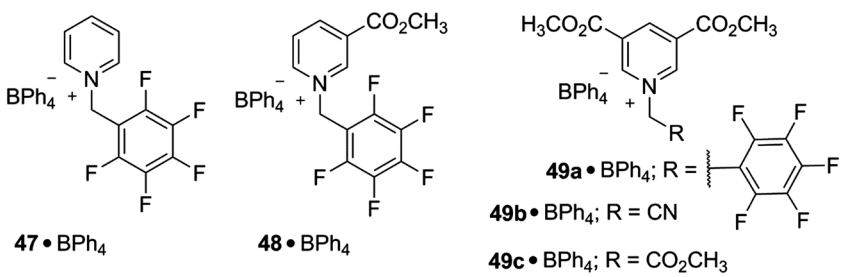

Figure 3.27 Molecular structures of electron-deficient pyridinium salts **47–49**.

View Online

Published on 15 November 2016 on http://pubs.rsc.org | doi:10.1039/9781782626626-00039

The X-ray structure of the **49**·Br salt demonstrated that as with other pyridinium halides the interaction is dominated by charge–charge (coulombic) interactions (Figure 3.28). However, an additional interaction between the bromide and the centroid of the pentafluorophenyl ring—an anion–π interaction—was evidenced in the solid-state from the observation of a distance between them shorter than the sum of their van der Waals radii. The isostructural pyridinium salt with chloride **49**·Cl was also prepared and characterized both in solution and the solid state. The use of the pyridinium salts as organocatalysts for the alkylation of **42** required the metathesis of the halides by non-coordinative tetraphenylborate anions. ^{1}H NMR titration experiments showed a thermodynamic preference of pyridinium **49** for the binding of chloride over tetraphenylborate (formal K_a = 200 M^{-1}). The triply substituted organocatalyst **49**·BPh_4 exceeded halogen bonding catalysts **45** with regard to reaction rate and represented the first example of catalysis promoted by anion-binding that combined coulombic and anion–π interactions. For additional information on anion-binding organocatalysis, the interested reader is advised to consult a recently published review by Gale *et al.* on applications of supramolecular anion recognition.[167]

3.3.3 Ionic Liquids

Ionic liquids (ILs) are interesting and complex fluids composed of ions that exhibit special physicochemical properties. ILs have been proposed as potential substitutes for conventional solvents,[168] leading to a continuously growing number of IL applications. They comprise, among others, carbon dioxide capture,[169] treatment and dissolution of lignocellulose biomass,[170–172] fuel storage, energy devices[173–175] and lubricants.[176–179]

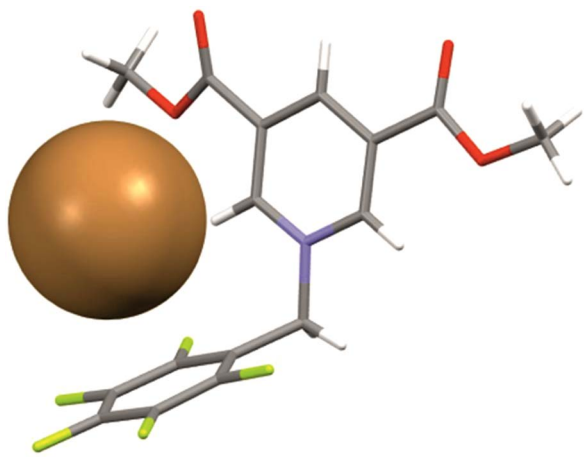

Figure 3.28 X-Ray crystal structure of **49**·Br.

View Online

Published on 15 November 2016 on http://pubs.rsc.org | doi:10.1039/9781782626626-00039

The optimisation and increased utilization of ILs for a variety of applications is dependent on the comprehension of the fundamental interactions present in these liquids. Clearly, coulombic forces dominate in ILs, however, the non-directional nature of pure electrostatic charge–charge interactions allows other directional secondary intermolecular interactions to have a role facilitating additional stabilisation and directing to some extent the chemistry of ILs. In this respect, π-type interactions are found to co-exist alongside H-bonding within imidazolium based ILs. In particular, Matthews *et al.*[180] have studied theoretically the importance of hydrogen bonding and π-interactions (π^+–π^+ and anion–π^+) in imidazolium-chloride ionic liquid clusters using several ion pair (IP) dimers. Interestingly, the clusters form non-directional charge quadrupolar arrangements, but retain structural fluidity for both cation and anion. This allows for large conformational changes at little energy cost, which is facilitated by the varying strengths of distant dependent primary (electrostatic) and secondary H-bond interactions, coupled with anion–π^+ and π^+–π^+ interactions. Both interactions (primary and secondary) decrease as a function of distance, however, the latter interactions play a more significant role in structuring imidazolium chloride ILs because the energy of primary interactions decreases more rapidly with the distance than secondary H-bond, anion–π^+ and π^+–π^+ interactions.

In this particular field of research, a remarkable and unprecedented series of experimental studies should be emphasized.[181] The first magnetic phase of an ionic liquid with anion–π interactions has been reported, which displays a three-dimensional (3D) magnetic ordering below the Néel temperature (T_N = 7.7 K). The X-ray structure of this material, see Figure 3.29, reveals a monoclinic phase and it is characterized by layers of imidazolium cations $[Dimim]^+$ and tetrabromoferrate ions $[FeBr_4]^-$ that change the orientation

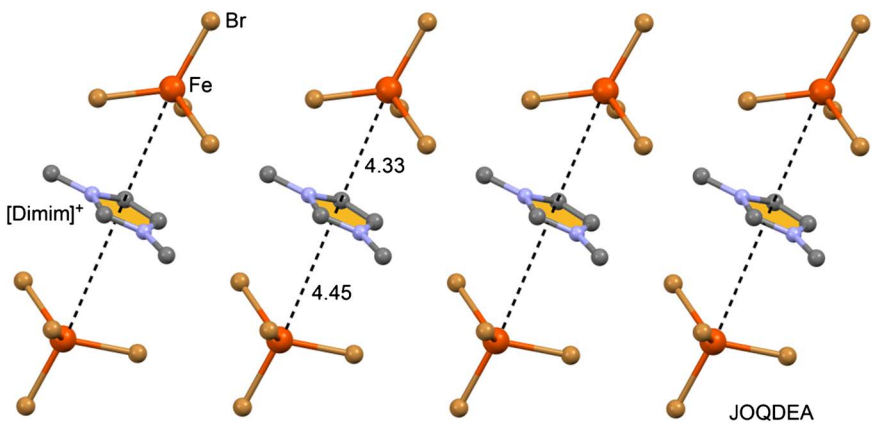

Figure 3.29 Fragment of the X-ray crystal structure containing imidazolium cations $[Dimim]^+$ and tetrabromoferrate ions $[FeBr_4]^-$. The relevant anion–π interactions are indicated by dashed lines. The CSD reference code is indicated.

View Online

Published on 15 November 2016 on http://pubs.rsc.org | doi:10.1039/9781782626626-00039

from layer to layer. Magnetization measurements show the presence of 3D antiferromagnetic ordering below T_N with the presence of a remarkable magneto-crystalline anisotropy. Using low-temperature neutron diffraction it was demonstrated that the antiferromagnetic order is originated by the antiparallel ordering of ferromagnetic layers of the $[FeBr_4]^-$ metal complex along the *b* direction and the magnetic moments are aligned along the *c* direction. The fundamental role of the anion–π interaction has also been demonstrated by means of the projected density of states (PDOS) of the imidazolium with the bromines of the $[FeBr_4]^-$ metal complex.

3.4 On the Importance of Anion–π Interactions in the Solid State

3.4.1 Charge Neutral π-Systems

As aforementioned, the use of polycyclic aromatic compounds comprising several fused arene rings is a good strategy to generate neutral π-systems with strong anion binding ability, as exemplified by 1,4,5,8,9,12-hexaazatriphenylene (HAT) substituted with six cyano groups.[123] A different strategy is the use of *N*-oxides of diazines or triazines. These compounds are formally neutral, however, they are strongly π-acidic due to the high degree of polarization of the N^+–O^- bonds. For instance, *s*-triazine-*N*, *N*′,*N*″-trioxide has a molecular electrostatic potential value over the ring centre that is 15 kcal mol^{-1} higher than that of trinitrobenzene (see Figure 3.30). As a matter of fact, pyrazine-*N*,*N*′-dioxide has been recently used as a linker in the design and synthesis of hybrid octacyanotungstenate-based networks.[182] These compounds reveal supramolecular assemblies in the solid state where the electron deficient pyrazine-*N*,*N*′-dioxide linker plays a significant role. One selected example is shown in Figure 3.31, where two binding modes are observed. First, a face-to-face interaction between the pyrazine-*N*,*N*′-dioxide aromatic ring plane and one N_4 square face of the $[W(CN)_8]^{3-}$ anion and end-to-face interactions between the pyrazine ring and a single N_{CN} atom of the anionic moiety. These intermolecular arrangements showing anion–π interactions are unprecedented in octacyanometalate chemistry.

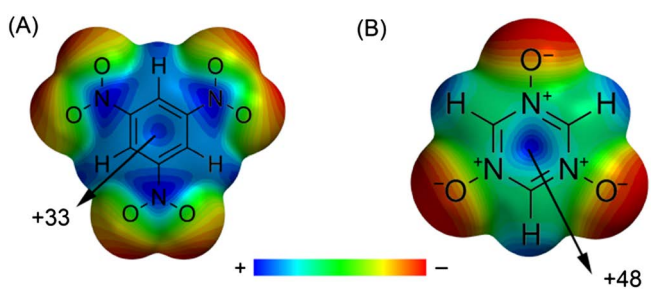

Figure 3.30 MEP surfaces of 1,3,5-trinitrobenzene (A) and 1,3,5-triazine 1,3,5-trioxide (B), values of MEP over the centre of the ring are indicated in kcal mol^{-1}.

View Online

Published on 15 November 2016 on http://pubs.rsc.org | doi:10.1039/9781782626626-00039

As commented above, tetraoxacalix[2]arene[2]triazine macrocyclic hosts have been systematically used by Wang *et al.*[120] and using several techniques (electrospray ionization mass spectrometry, fluorescence titration and X-ray crystallography), it has been shown that they form 1 : 1 complexes with several monoatomic and polyatomic anions of different geometries and shapes. In the solid state, the anion–π complexes show two convergent triazine rings that act as a pair of tweezers to interact with the anions through cooperative anion–π interactions (see Figure 3.32) in polyatomic anions such as NO_3^-, BF_4^-, PF_6^- and SCN^-. Remarkably, in less bulky monoatomic anions such as Cl^- and Br^-, a water molecule is also involved in the anion binding and the tweezers interact with the guests through cooperative anion–π and

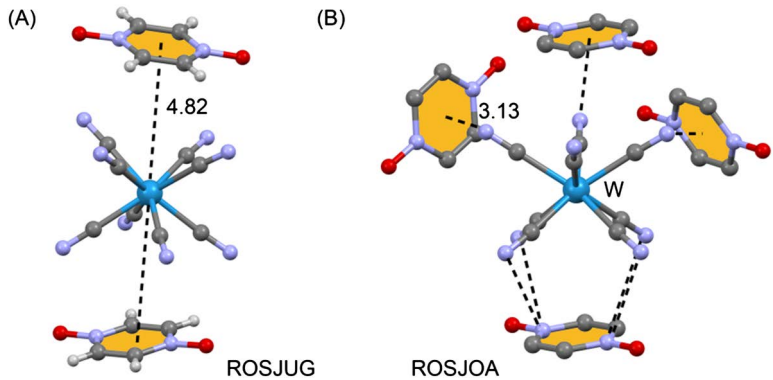

Figure 3.31 Fragments of the X-ray crystal structures (A,B) containing pyrazine-*N*,*N*′-dioxide moieties. The relevant anion–π interactions are indicated by dashed lines. The CSD references codes are indicated. Distances in Å.

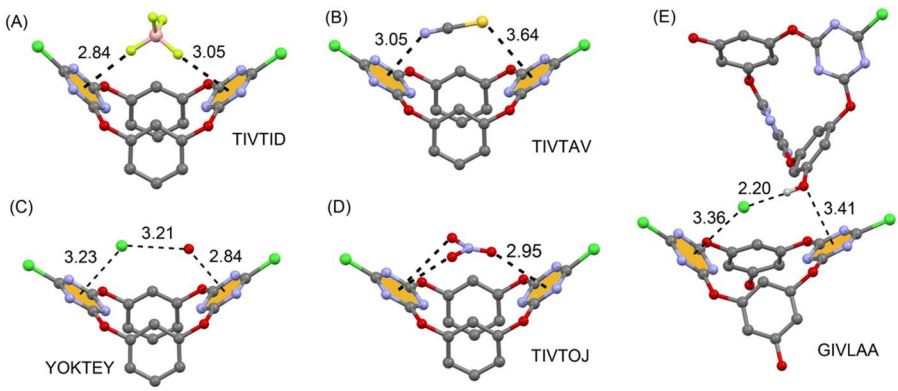

Figure 3.32 X-Ray solid state crystal structures of tetraoxacalix[2]arene[2]triazine hosts exhibiting anion–π interactions with tetrafluoroborate (A), thiocyanate (B), chloride (C), nitrate (D). (E) X-ray structure of a tetraoxacalix[2]arene[2]triazine dimer. The CSD reference codes are indicated. Distances in Å.

View Online

Published on 15 November 2016 on http://pubs.rsc.org | doi:10.1039/9781782626626-00039

lone pair–π interactions (see Figure 3.32(C)).[121] Taking advantage of this behaviour, a new receptor was envisaged and synthesized. That is, the simple introduction of a hydroxyl group (mimicking the role of the water) on the larger rim of the tetraoxacalix[2]arene[2]triazine host rendered the macrocyclic molecule as a unique donor–acceptor functional building block.[183] As a result, infinite self-assemblies were obtained in the solid state dominated by cooperative anion–π, lone-pair interactions and intermolecular hydrogen bonding (see Figure 3.32(E)). This investigation is an interesting example where the anion–π interaction directed a self-assembled structure previously designed through the rational fabrication of building blocks.

The naphthalenediimide (NDI) core amply used in anion–π receptors[41] and anion–π catalysts[160] in solution has also been used by several authors to construct fascinating assemblies in the solid state, and some of them are highlighted in this section. For instance, Liu *et al.*[184] have generated a panchromatic hybrid crystal that is characterized by the existence of long-lived charge-separated states even upon irradiation from indoor lighting. Thus, this investigation opens the door to research fields as important as solar cells and photocatalysis. The organic–inorganic photoactive hybrid is constituted of anionic iodoplumbate nanowires that strongly bind to the NDIs by means of charge-assisted anion–π interactions (see Figure 3.33). A differentiating feature of this crystal is that the colour is black, much darker than other reported hybrids based on iodoplumbate nanowires.[185,186] Actually, the solid-state UV-vis diffuse reflectance spectral analysis showed that it is a panchromatic hybrid with a broad absorption band from 200 nm to 800 nm. It is worth mentioning that the long-lived charge separation in this hybrid material is basically due to the intense and panchromatic absorption and the close contacts between organic and inorganic units through anion–π interactions that are beneficial to the electron transfer (see Figure 3.33).

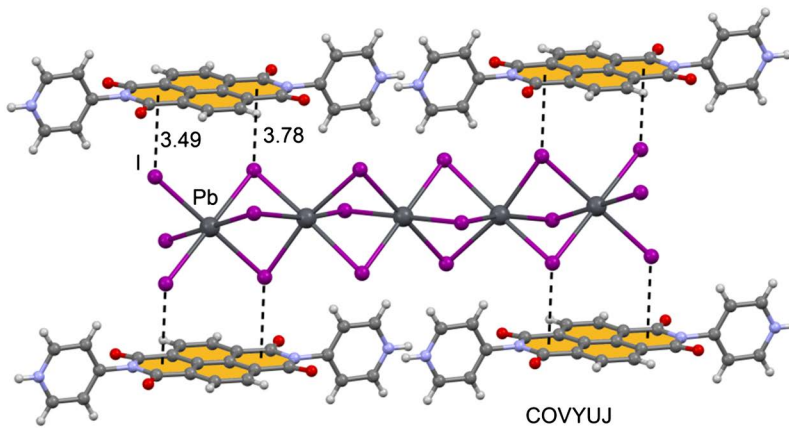

Figure 3.33 X-Ray structure of the hybrid crystal of iodoplumbate nanowire and NDIs. The CSD reference code is indicated. Distances in Å.

View Online

Published on 15 November 2016 on http://pubs.rsc.org | doi:10.1039/9781782626626-00039

NDIs have also been used by Kumar *et al.*[187] to demonstrate the unusual stability of the naphthalenediimide radical anion and its extraordinary π-acidic precursor. They used the phosphonium group to stabilize for the first time a naphthalenediimide-based radical ion $[(NDI^{\bullet+})BPh_4^-]$ (see Figure 3.34(A)), allowing its isolation, purification and X-ray characterization under ambient conditions. Furthermore, it is the first example of a radical ion that resists unaltered silica-gel chromatography. This study is extremely attractive from the point of view of synthetic radical/radical ion chemistry. Furthermore, the X-ray structure of the "ultra-electron-deficient" system also provided direct evidence of interactions between the BF_4^- and the NDI core $[(NDI^{2+})BF_4^-]$ (see Figure 3.34(B)). Polyoxometalates (POMs) and NDIs have also been used[188] to construct an unusual non-interpenetrated three-dimensional hydrogen-bonded supramolecular framework. It contains POM guest molecules that efficiently control the geometry and the interpenetration of the hydrogen-bonded supramolecular framework *via* directional anion–π interactions (see Figure 3.34(C)). This investigation demonstrates for the first time that anion–π interactions are appropriate for the stabilization and immobilization of functional polyoxometalate anions and, moreover, directly affect to a major extent the final structure of host–guest supramolecular materials. An intelligent combination of anion–π and H-bonding interactions with *N*,*N*′-di(4-pyridyl)-1,4,5,8-naphthalenediimide tectons assists the self-assembly process and controls the structures of polyoxometalate-based host–guest materials and their solid state architectures.

The combination of NDIs, POMs, Zn(II) and several coligands has been recently used[189] to synthesize a very rare radical-doped POM-based host–guest crystalline material. Interestingly, it has fast-responsive reversible photochromic properties and photo-controlled and tunable luminescence. In addition, this POM-based host–guest photochromic material is able to oxidize efficiently benzylic alcohols to aldehydes acting as a green and recyclable

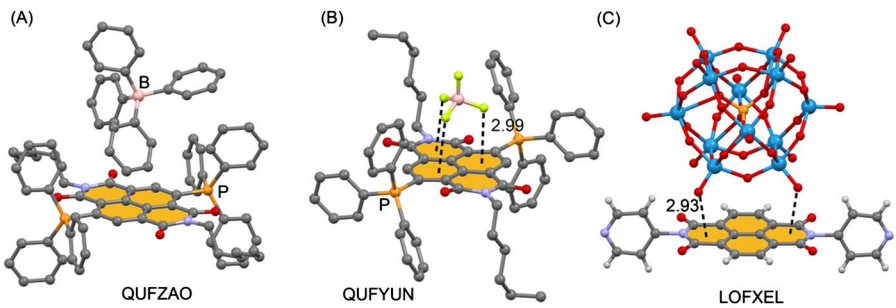

Figure 3.34 (A) and (B) Fragments of the X-ray crystal structures containing NDI π-acidic moieties. The relevant anion–π interactions are indicated by dashed lines. (C) Fragment of the X-ray crystal structures containing POM and NDI moieties. The relevant anion–π interactions are indicated by dashed lines. The CSD reference codes are indicated. Distances in Å.

View Online

Published on 15 November 2016 on http://pubs.rsc.org | doi:10.1039/9781782626626-00039

photocatalyst under air as the catalyst re-oxidant. Of particular importance is that the trapped POM anions interact with functional NDIs *via* directional anion–π contacts. The anion–π interactions stabilize and immobilize the functional POM anions and also promote the charge transfer and exchange among components leading to interesting properties of the crystalline material (*i.e.*, reversible photochromism, photocontrolled tunable luminescence, and photocatalytic activity). This is a very promising investigation since it demonstrates that it is possible to design and construct photochromic and photocatalytic crystalline materials based on POMs and π-acidic NDIs by forming anion–π interactions.

As commented above, NDI building blocks have also been used by Stoddart's group[122] to build molecular triangular prisms to encapsulate anions. Apart from the solution phase studies (NMR) detailed in Section 3.3.1, they have used both theory and experiment to demonstrate orbital interactions and electron transfer between the anion and the π-acidic surface of the NDI in their synthesized redox-active prisms (see Figure 3.35). The presence of three NDI moieties symmetrically distributed leads to a large number of individually accessible redox states in the triangular prisms, opening the door to potential applications in the molecular electronics field. The electron deficient interior of the molecular prism is perfect for studying anion–π interactions. This ability is evidenced by the trapping of linear I_3^- anions inside the receptor cavity, causing a significant change in the packing of the prisms in the extended solid-state architecture. The encapsulation of I_3^- anions provokes π–π stacking of the chiral prisms into supramolecular helices (see Figure 3.35), providing an extraordinary example of anion-induced self-assembly. In addition, the chirality provided by the six stereogenic centres of the cyclohexane corners in the occupied prisms dictates either right- or left-handed helices associated with their packing in the solid state.

Apart from the strong ability of NDIs to establish anion–π interactions in the solid state, the electron deficient pentafluorophenyl group[52] is also a good binding block for constructing anion receptors. In this respect, Giese *et al.*[166,190,191] have analysed in depth the importance of anion–π interactions in the solid state focusing on purely organic and charge-neutral fluorophenyl groups bearing a positive charge located at a side chain. The detailed

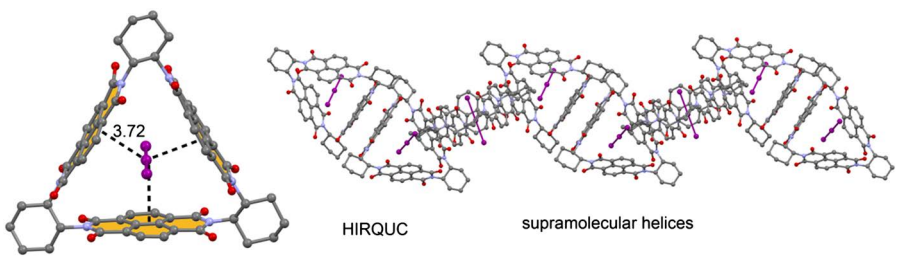

Figure 3.35 The X-ray crystal structure of the NDI-based triangular prism. The CSD reference code is indicated. H-atoms are omitted for clarity.

View Online

Published on 15 November 2016 on http://pubs.rsc.org | doi:10.1039/9781782626626-00039

statistical analysis of a series of structural data sets demonstrates the geometrical variability of anion–π bonding in the solid state. Moreover, the substituents of the arene are key elements that control the final position of the anions above π-systems. The hapticity concept is used to classify the structural variety of the interaction between anions and electron-deficient arenes. The high variability of the anion position is caused by the interplay of various non-covalent forces that coexist in the solid state. Two remarkable systems are selected to illustrate the ability of the pentafluorophenyl group to establish anion–π interactions and their influence in the crystal structure. First, *N*-(pentafluorobenzyl)pyridinium salts have been used to investigate the anion size dependence in solid state structures exhibiting anion–π interactions. In this particular system, both π-acidic rings (C_6F_5 and pyridinium moieties) are involved in the anion–π contacts (see Figure 3.36).[190] In the solid-state structures, the anion is embedded in a number of hydrogen bonds (C–H···X) and anion–π contacts. The supramolecular complexes are different depending on the size of the anion. That is, the crystal structures of *N*-(pentafluorobenzyl)pyridinium salts of I_3^- and PF_6^- show a cooperative anion–π interaction between the two electron-deficient arenes and the anion located

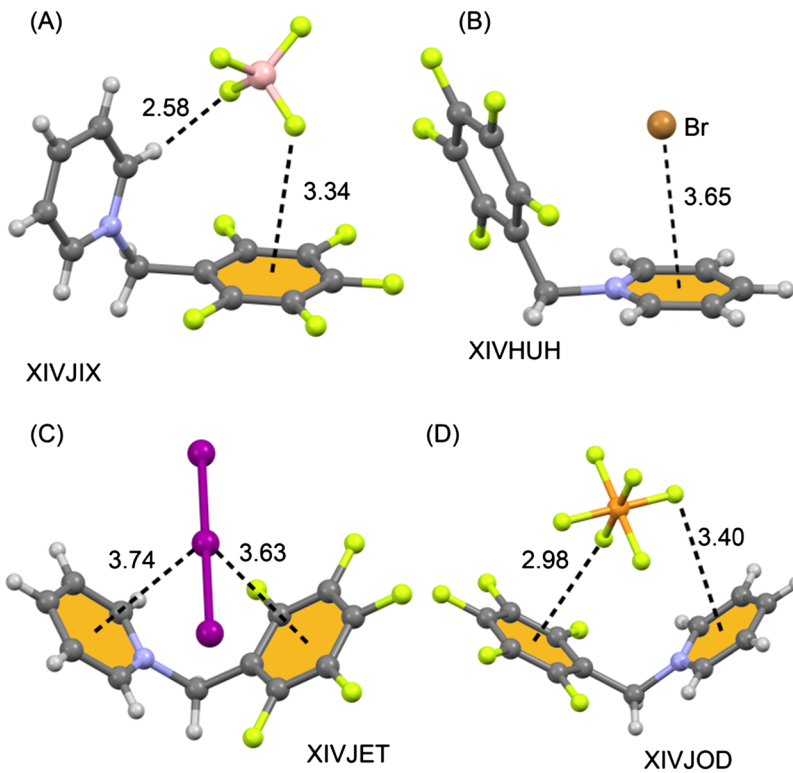

Figure 3.36 (A–D) X-Ray crystal structures of pentafluorophenyl derivatives. The CSD reference codes are indicated. Distances in Å.

View Online

Published on 15 November 2016 on http://pubs.rsc.org | doi:10.1039/9781782626626-00039

between them (see Figure 3.36(C) and (D)). In contrast, this cooperativity is not observed for other anions like bromide or BF_4^- (see Figure 3.36(A) and (B)). In the second investigation related to the suitability of the C_6F_5 binding block to construct anion receptors,[191] the authors use simple triphenyl(pentafluorobenzyl)-phosphonium (see Figure 3.37(A) and (B)) and bis(pentafluorobenzyl)-phosphonium (see Figure 3.37(C)–(E)) salts. The X-ray structures provided crucial data on the influence of anion size on the molecular structure of cations containing two adjacent electron-deficient rings (see Figure 3.37(C)–(E)). In particular, whereas bromide anions interact by means of anion–π interactions in a 1:1 mode with the pentafluorobenzene unit *anti*-configured (Figure 3.37(E)), the bulkier anions iodide, tetrafluoroborate (Figure 3.37(D)), and hexafluorophosphate (Figure 3.37(C)) result in a 1:2 tweezer-like *syn*-configuration in which one anion interacts simultaneously with two pentafluorobenzene units. When the spatial separation of the two electron-deficient rings matches the size of the anion, the formation of two concurrent anion–π interactions induces a conformational change from the *anti*-form observed for the smaller anion to the tweezer-like *syn*-form for the greater one.

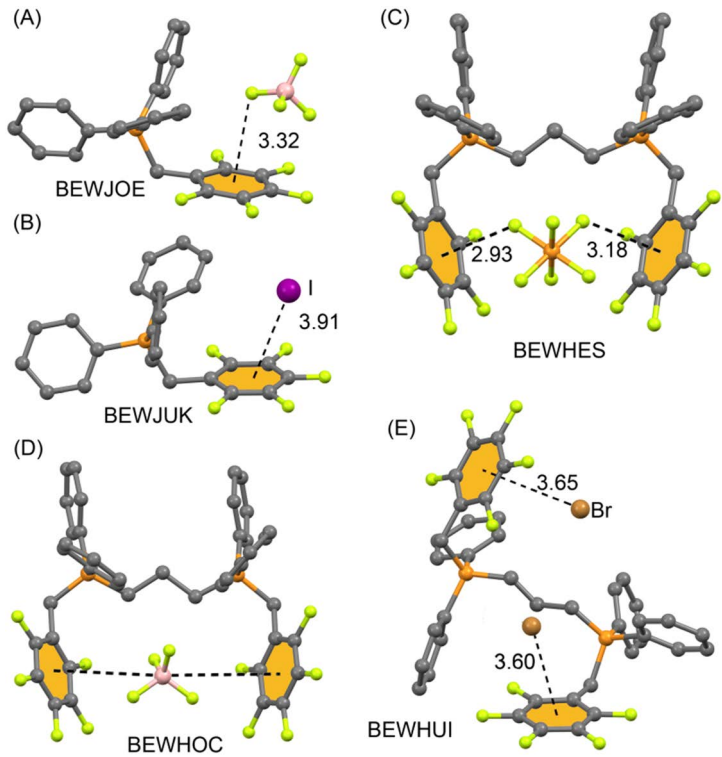

Figure 3.37 (A–E) X-Ray crystal structures of pentafluorophenyl derivatives. The CSD reference codes are indicated. Distances in Å.

View Online

Published on 15 November 2016 on http://pubs.rsc.org | doi:10.1039/9781782626626-00039

3.4.2 Aromatic Ligands Coordinated to Metal Ions

As aforesaid, a convenient strategy to dramatically increase the π-binding ability of heteroarenes is their coordination to metal centres. One of the most successful research studies in this regard has been carried out by Dunbar's group.[192–194] The crucial role of the anion–π interaction in the formation of self-assembled metallacycles is a clear example (see also Section 3.3.1). That is, taking advantage of the structural versatility of metal ions and the directionality of metal–ligand interactions,[195–200] the spontaneous assembly of elegant supramolecular architectures with unusual properties and applications or intriguing host–guest behaviour was recently described.[123] They provided unambiguous evidence that anion–π interactions are the main driving force in the templation process leading to the formation of Fe(II) metallacycles with π-acidic cavities, using 3,6-bis(2-pyridyl)-1,2,4,5-tetrazine as a chelating ligand in the solid state. As commented above, the anions play a decisive role in the formation and size of the supramolecular polygons (square or pentagon), establishing multiple anion–π interactions with the electron deficient walls (see Figure 3.7).

POMs and NDIs complexed to transition metals have also been used to construct interesting supramolecular structures.[201] In fact the assembly and photochromism of POM-based host–guest compounds are controlled by anion–π interactions. That is, a different photoresponsive reversible visible light photochromism is obtained as a result of a combination of different functional components, NDI tectons and POMs. A minor adjustment of the substituent of the diimide nitrogens results in different modes of anion–π interactions, which lead to different structures and different sensitivities to visible light. The anion–π interactions adjust the structures of the compounds and, to some extent, the ability to gain or lose electrons of the NDIs of the compounds, which is evident from subtle changes in photochromic sensitivity and reduction potentials. The distance between NDI tectons (mean plane) and the POM is ~3.50 Å in panel B (see Figure 3.38), which is much longer than that of the anion–π interactions in panel A. Interestingly, the weaker anion–π interaction in panel B makes the NDI core easier to reduce.

Other interesting examples are the anion–induced Ag^{I} self-assemblies with electron deficient aromatic ligands reported by Safin *et al.*[202] The anion–π interaction is the driving force for templated 1D, 2D and 3D supramolecular coordination networks. The π-acidic aromatic moieties in the 3,6-bis(2′-pyrimidyl)-1,2,4,5-tetrazine and 2,4,6-tris(2-pyrimidyl)-1,3,5-triazine ligands coordinated to Ag^{I} provide an ideal platform to induce anion–π interactions. Moreover, the multiple coordination sites in the ligands promote multidimensional growth. Interestingly, the selective use of PF_6^-, ClO_4^- and TfO^- anions leads to the formation of different solid state architectures, providing clear evidence of the pivotal role played by different anions (size and shape) and their interactions with the ligand. Figure 3.39 shows two fragments of the X-ray structures: (a) in the TUNDAJ structure the ClO_4^- is sandwiched between two central rings of the 2,4,6-tris(2-pyrimidyl)-1,3,5-triazine ligand;

View Online

Published on 15 November 2016 on http://pubs.rsc.org | doi:10.1039/9781782626626-00039

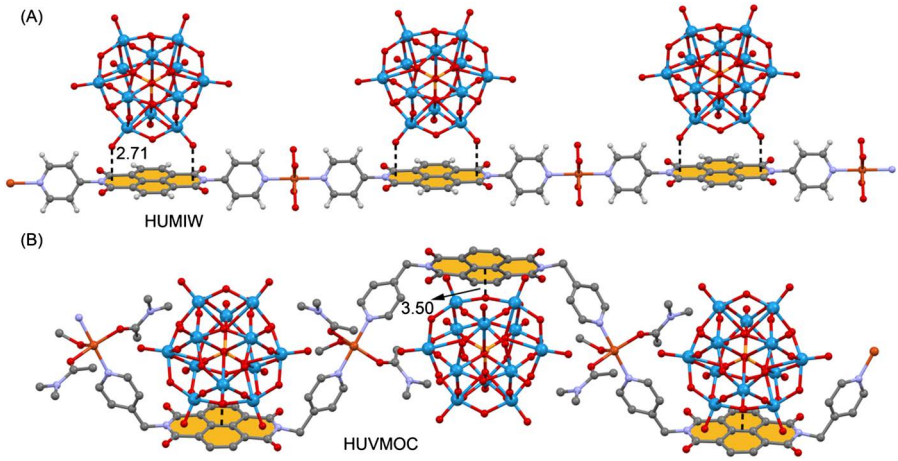

Figure 3.38 (A,B) Fragments of the X-ray crystal structures containing NDI-based polymers and POM moieties. The relevant anion–π interactions are indicated by dashed lines. The CSD reference codes are indicated. Distances in Å.

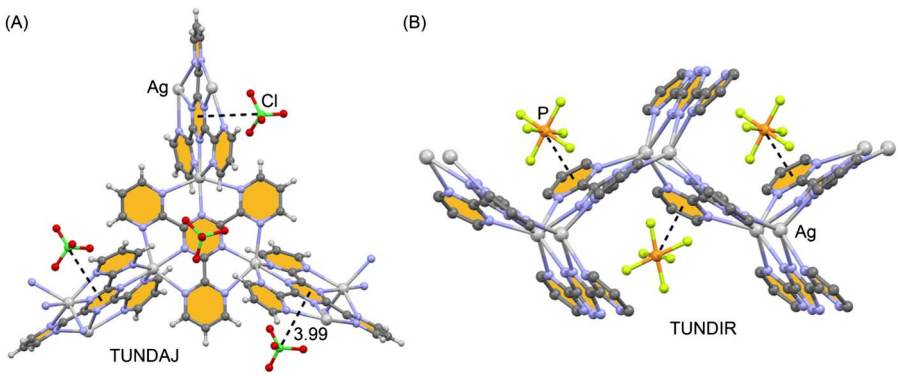

Figure 3.39 Fragments of the X-ray crystal structures containing 2,4,6-tris(2-pyrimidyl)-1,3,5-triazine (A) and 3,6-bis(2′-pyrimidyl)-1,2,4,5-tetrazine ligands (B) coordinated to Ag. The relevant anion–π interactions are indicated by dashed lines. The CSD reference codes are indicated. Distances in Å.

(b) in the TUNDIR structure, the PF_6^- anion interacts with three central tetrazine rings of the 3,6-bis(2′-pyrimidyl)-1,2,4,5-tetrazine ligand. Another clear example of this strategy using Ag^I as a metal centre has been reported by Domasevitch's group.[91] In particular, several X-ray crystal structures of *s*-tetrazine μ^4–coordinated to Ag^I exhibit very close contacts between the anion and the *s*-tetrazine ring indicating strong anion–π interactions.

The phenanthroline ligand presents a high polarizability (three fused rings) and it is an excellent bidentate ligand, thus it is a convenient binding

View Online

Published on 15 November 2016 on http://pubs.rsc.org | doi:10.1039/9781782626626-00039

block for constructing supramolecular assemblies. As a matter of fact, an interesting investigation reported by Qin *et al.*[203] evidences the formation of anion–π contacts involving BF_4^- anions and coordinated phenanthroline ligands. They reported the aqueous synthesis of an octanuclear macrocycle that includes fluorescent carbazole-based dipyrazole ligands, which coordinate to dipalladium corners. The X-ray diffraction analysis (see Figure 3.40) reveals that this hybrid metallomacrocycle traps BF_4^- anions in the dipalladium–phenanthroline clips through short anion–π contacts.

Cooperativity effects between the anion–π interactions and several noncovalent bonds such as hydrogen and halogen bonds have been studied theoretically.[108,204,205] Particularly relevant is the interplay between π–π and anion–π interactions, which has been investigated combining theoretical studies and searches in the CSD.[206–208] It has been shown that the mutual influence between ion–π and π–π interactions can lead to strong cooperativity effects. Experimental and theoretical studies[209,210] have shown the formation of similar anion–π/π–π/π–anion assemblies in the solid state structures of several Cu(II) and Zn(II) complexes with a tetradentate Schiff base (see Figure 3.41 for two selected examples). These assemblies are crucial to explain the 3D architecture of the complexes in the solid state and, moreover, the mutual reinforcement of both anion–π and π–π interactions has been demonstrated computationally. Similar anion–π/π–π/π–anion assemblies in the solid state have been also found in N^6-decyladenine hydrochloride salts and bisadenine derivatives.[211]

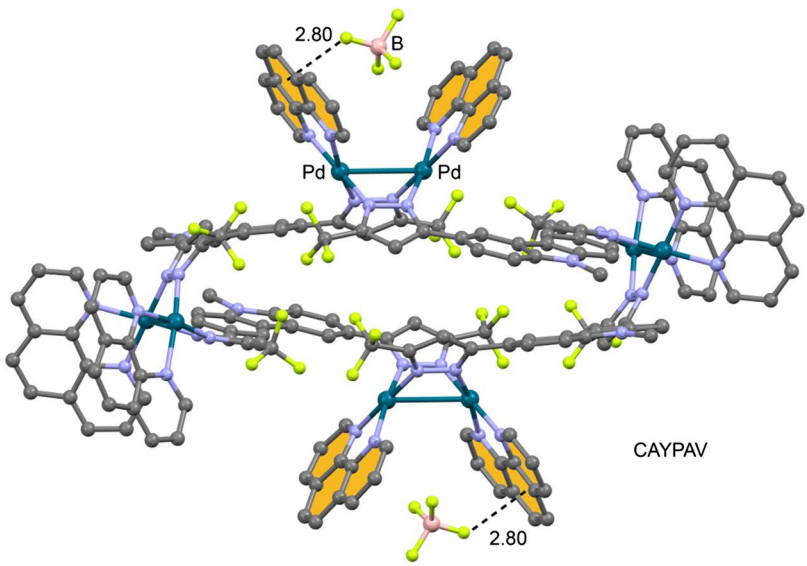

Figure 3.40 Fragment of the X-ray crystal structure showing the anions trapped in the dipalladium clips through anion–π interactions. The relevant anion–π interactions are indicated by dashed lines. The CSD reference code is indicated. Distance in Å.

View Online

Published on 15 November 2016 on http://pubs.rsc.org | doi:10.1039/9781782626626-00039

3.4.3 Positively Charged or Protonated Aromatics

As stated above, aromatic cations form very strong anion–π^+ complexes due to the large component of the electrostatic term. In pyridine and related azines, the π^+ motif can be easily generated by protonation by simply adjusting the pH of the medium. As a matter of fact, interesting supramolecular assemblies in the solid state architecture of two new pH-dependent 4′-(4-pyridyl)-2,2′:6′,2″-terpyridine (PTP) salts have been reported recently by Manna *et al.*[212] The structural architecture depends on the type of anion (mononuclear or trinuclear). In the X-ray structures the pyridine rings participate in hydrogen-bonding (N–H···Br^-) and anion–π interactions (see Figure 3.42). In both compounds, the anions are in close proximity to the electron-deficient PTP cores, forming characteristic anion–π interactions thus generating interesting supramolecular anion–π/π–π/π–anion assemblies. In this experimental work, the role of the anion–π interaction in the solid state has also been investigated theoretically, providing additional evidence to its role as a valuable supramolecular force in building the multidimensional structures.

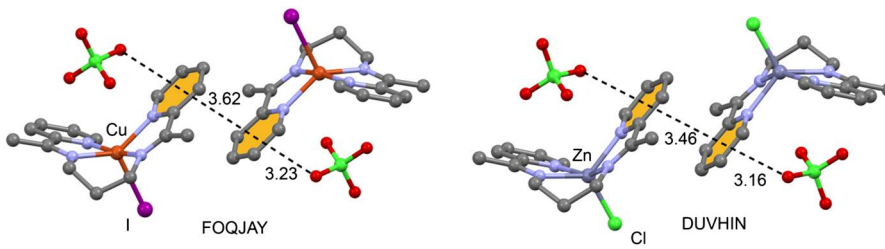

Figure 3.41 Fragments of the X-ray crystal structure exhibiting anion–π/π–π/π–anion assemblies with Cu (A) and Zn (B). The CSD references codes are indicated. Distances in Å.

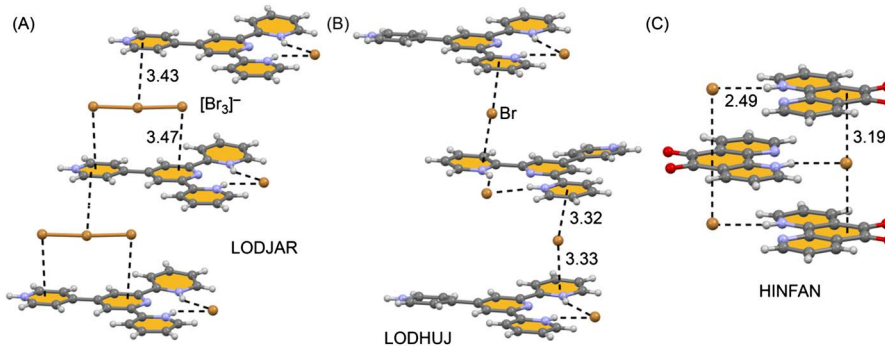

Figure 3.42 Fragments of the X-ray crystal structures containing 4′-(4-pyridyl)-2,2′:6′,2″-terpyridine (A), 4′-(4-pyridyl)-3,2′:6′,3″-terpyridine (B) and 5,6-dioxo-1,10-phenanthrolinium (C) moieties. The relevant anion–π interactions are indicated by dashed lines. The CSD reference code are also indicated. Distances in Å.

View Online

Published on 15 November 2016 on http://pubs.rsc.org | doi:10.1039/9781782626626-00039

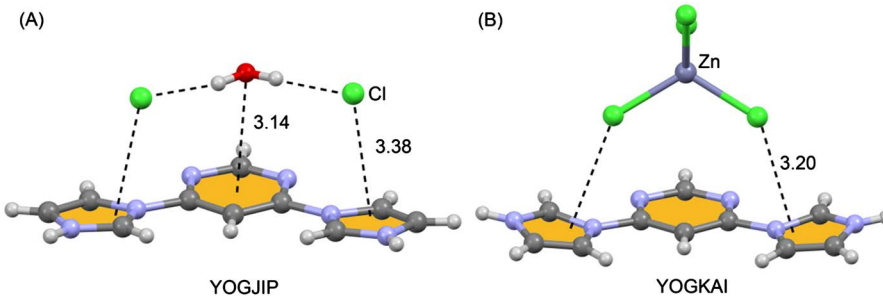

Figure 3.43 (A,B) Fragments of the X-ray crystal structures containing 4,6-di(1*H*-imidazol-1-yl)pyrimidine moieties. The relevant anion–π interactions are indicated by dashed lines. The CSD reference codes are shown. Distances in Å.

The same research group[213] has further investigated the role of the anion–π interactions in the generation of supramolecular assemblies using a similar ligand, *i.e.* the triply protonated 4′-(4-pyridyl)-3,2′:6′,3″-terpyridine molecule and perchlorate as counterion in order to analyse the influence of a tetrahedral anion on the final solid state structure and the formation of the assemblies. As a result, combined X-ray crystallographic and theoretical studies reveal that π^+–π^+, π^+–π, and various anion–π interactions are the major driving forces in the stabilization of the assemblies observed in the solid state structure. Other groups[214] have reported similar supramolecular assemblies. For instance, the X-ray structure of 5,6-dioxo-1,10-phenanthrolinium bromide (see Figure 3.42(C)) where the anions induce the formation of sandwich complexes in the solid state, forming two symmetrically equivalent anion–π interactions with the dioxo ring. The anion is further stabilized by the formation of charge-assisted hydrogen bonds.

Similarly, García-Raso's group[215] has designed, synthesized and structurally characterized five proton transfer compounds using 4,6-di(1*H*-imidazol-1-yl)pyrimidine and different counterions. In the crystal structures of the five salts, anion–π interactions involving the aromatic rings play a fundamental role for the generation of three-dimensional supramolecular frameworks in the solid state. Two selected examples are illustrated in Figure 3.43. The first one (YOGJIP) is characterized by the formation of a remarkable supramolecular architecture through two anion–π (chloride ions) and one lp–π (water molecule) interactions involving all three aromatic rings of the diprotonated 4,6-di(1*H*-imidazol-1-yl)pyrimidine moiety. That is, an oxygen atom lone pair of the water molecule is oriented toward the π-cloud of the pyrimidine ring forming a strong lp–π interaction. In addition, two chloride ions interact with the imidazolium rings forming two anion–π^+ interactions. In the second one (YOGJOV), two chlorine atoms of the $[ZnCl_4]^{2-}$ anion interact with two imidazolium moieties in the solid state (see Figure 3.43).

In the examples shown above, the positive charge in the heteroarene was simply generated by protonation adjusting the pH. Another possibility is the alkylation of the arene as recently used by Albrecht and co-workers.[216]

View Online

Published on 15 November 2016 on http://pubs.rsc.org | doi:10.1039/9781782626626-00039

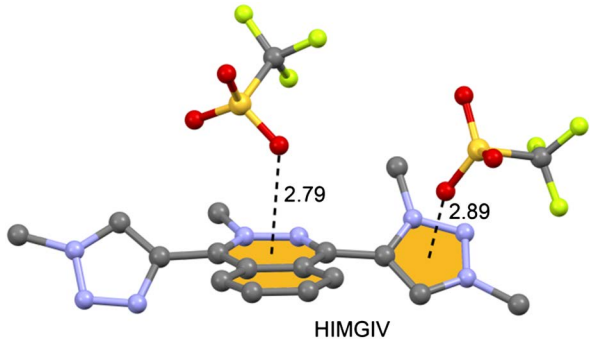

Figure 3.44 Fragment of the X-ray crystal structures containing dimethylated (1,4-bis(1-methyl-1*H*-1,2,3-triazol-4-yl)phthalazine). The relevant anion–π interactions are indicated by dashed lines. The CSD reference code is indicated. Distances in Å.

The synthesis and characterization of a novel phthalazine-triazole ligand (1,4-bis(1-methyl-1*H*-1,2,3-triazol-4-yl)phthalazine) was reported with the purpose to generate new ruthenium(II) complexes. However, the reactivity of the ligand in several methylation reactions was also studied. Particularly, when the ligand was reacted with MeOTf (OTf = trifluoromethyl sulfonate), a double methylation was observed and the resulting product was characterized by X-ray analysis (see Figure 3.44). Interestingly, the double methylated ligand exhibits anion–π interactions with both the six and five membered rings that are positively charged in the solid state.

3.5 Outlook

The purpose of this chapter is to showcase the fascinating bonding relationship between anions and π systems by describing experimental and theoretical investigations at the forefront of this interaction. The exceptional potential of the anion–π interaction to impact the field of supramolecular science and catalysis is evident. Moreover, the anion–π interaction is increasingly taken into consideration by the scientific community and will provide new opportunities for the design of novel sensors, hosts, catalysts, and materials. The utilization of this interaction in the field of ionic liquids is in its naissance. Taking into consideration these perspectives, we anticipate that some relevant physico–chemical processes will only be possible in the near future thanks to the rational utilization of the anion–π interaction.

Acknowledgements

The continuous financial support of our research from MINECO of Spain (projects CTQ2014-57393-C2-1-P, CTQ2014-56295-R, Severo Ochoa Excellence Accreditation 2014–2018 SEV-2013-0319 and CONSOLIDER INGENIO 2010 CSD2010-00065, FEDER funds) and the ICIQ Foundation is gratefully acknowledged.

View Online

Published on 15 November 2016 on http://pubs.rsc.org | doi:10.1039/9781782626626-00039

References

1. H. J. Schneider, *Angew. Chem., Int. Ed.*, 2009, **48**, 3924.
2. H. J. Schenider and A. Yatsimirski, *Principles and methods in supramolecular chemistry*, Wiley, Chichester, 2000.
3. J. M. Lehn, *Supramolecular chemistry concepts and perspectives*, Wiley–VCH, Weinheim, 1995.
4. F. Vögtle, *Supramolecular chemistry: an introduction*, Wiley, New York, 1993.
5. P. D. Beer, P. A. Gale and D. K. Smith, *Supramolecular chemistry*, Oxford University Press, Oxford, 1999.
6. W. Steed and J. L. Atwood, *Supramolecular chemistry*, Wiley, Chichester, 2000.
7. H. Destecroix, C. M. Renney, T. J. Mooibroek, T. S. Carter, P. F. N. Stewart, M. P. Crump and A. P. Davis, *Angew. Chem., Int. Ed.*, 2015, **54**, 2057.
8. P. Murray-Rust and W. D. S. Motherwell, *J. Am. Chem. Soc.*, 1979, **101**, 4374.
9. P. Murray-Rust, W. C. Stallings, C. T. Monti, R. K. Preston and J. P. Glusker, *J. Am. Chem. Soc.*, 1983, **105**, 3206.
10. N. Ramasubbu, R. Parthasarathy and P. Murray-Rust, *J. Am. Chem. Soc.*, 1986, **108**, 4308.
11. P. Metrangolo, H. Neukirch, T. Pilati and G. Resnati, *Acc. Chem. Res.*, 2005, **38**, 386.
12. P. Politzer and J. S. Murray, *ChemPhysChem*, 2013, **14**, 278.
13. P. Politzer, J. S. Murray and T. Clark, *Phys. Chem. Chem. Phys.*, 2013, **15**, 11178.
14. P. Politzer, J. S. Murray and T. Clark, *Phys. Chem. Chem. Phys.*, 2010, **12**, 7748.
15. A. Bundhun, P. Ramasami, J. S. Murray and P. Politzer, *J. Mol. Model.*, 2013, **19**, 2739.
16. A. Bauzá, T. J. Mooibroek and A. Frontera, *Angew. Chem., Int. Ed.*, 2013, **52**, 12317.
17. A. Bauzá and A. Frontera, *ChemPhysChem*, 2015, **16**, 3108.
18. J. C. Ma and D. A. Dougherty, *Chem. Rev.*, 1997, **97**, 1303.
19. N. Zacharias and D. A. Dougherty, *Trends Pharmacol. Sci.*, 2002, **23**, 281.
20. N. S. Scrutton and A. R. C. Raine, *Biochem. J.*, 1996, **319**, 1.
21. J. P. Gallivan and D. A. Dougherty, *Proc. Natl. Acad. Sci. U. S. A.*, 1999, **96**, 9459.
22. A. Frontera, P. Gamez, M. Mascal, T. J. Mooibroek and J. Reedijk, *Angew. Chem., Int. Ed.*, 2011, **50**, 9564.
23. B. L. Schottel, H. T. Chifotides and K. R. Dunbar, *Chem. Soc. Rev.*, 2008, **37**, 68.
24. C. Caltagirone and P. A. Gale, *Chem. Soc. Rev.*, 2009, **38**, 520.
25. P. Gamez, T. J. Mooibroek, S. J. Teat and J. Reedijk, *Acc. Chem. Res.*, 2007, **40**, 435.
26. B. P. Hay and V. S. Bryantsev, *Chem. Commun.*, 2008, 2417.

View Online

Published on 15 November 2016 on http://pubs.rsc.org | doi:10.1039/9781782626626-00039

27. D. Quinonero, C. Garau, C. Rotger, A. Frontera, P. Ballester, A. Costa and P. M. Deya, *Angew. Chem., Int. Ed.*, 2002, **41**, 3389.
28. M. Mascal, A. Armstrong and M. D. Bartberger, *J. Am. Chem. Soc.*, 2002, **124**, 6274.
29. I. Alkorta, I. Rozas and J. Elguero, *J. Am. Chem. Soc.*, 2002, **124**, 8593.
30. D. Y. Kim, N. J. Singh and K. S. Kim, *J. Chem. Theory Comput.*, 2008, **4**, 1401.
31. B. L. Schottel, J. Bacsa and K. R. Dunbar, *Chem. Commun.*, 2005, 46.
32. B. Han, J. Lu and J. K. Kochi, *Cryst. Growth Des.*, 2008, **8**, 1327.
33. M. Mascal, I. Yakovlev, E. B. Nikitin and J. C. Fettinger, *Angew. Chem., Int. Ed.*, 2007, **46**, 8782.
34. R. J. Götz, A. Robertazzi, I. Mutikainen, U. Turpeinen, P. Gamez and J. Reedijk, *Chem. Commun.*, 2008, 3384.
35. M. Albrecht, M. Muller, O. Mergel, K. Rissanen and A. Valkonen, *Chem.–Eur. J.*, 2010, **16**, 5062.
36. A. Bauzá, T. J. Mooibroek and A. Frontera, *ChemPhysChem*, 2015, **16**, 2496.
37. J. S. Murray, P. Lane, T. Clark, K. E. Riley and P. Politzer, *J. Mol. Model.*, 2012, **18**, 541.
38. C. Estarellas, A. Frontera, D. Quinonero and P. M. Deya, *Angew. Chem., Int. Ed.*, 2011, **50**, 415.
39. S. Chakravarty, Z.-Z. Sheng, B. Iverson and B. Moore, *FEBS Lett.*, 2012, **586**, 4180.
40. D. D. Jenkins, J. B. Harris, E. E. Howell, R. J. Hinde and J. Baudry, *J. Comput. Chem.*, 2013, **34**, 518.
41. R. E. Dawson, A. Hennig, D. P. Weimann, D. Emery, V. Ravikumar, J. Montenegro, T. Takeuchi, S. Gabutti, M. Mayor, J. Mareda, C. A. Schalley and S. Matile, *Nat. Chem.*, 2010, **2**, 533.
42. N. Sakai, J. Mareda, E. Vauthey and S. Matile, *Chem. Commun.*, 2010, **46**, 4225.
43. K. E. Ranaghan, J. E. Hung, G. J. Bartlett, T. J. Mooibroek, J. N. Harvey, D. N. Woolfson, W. A. van der Donk and A. J. Mulholland, *Chem. Sci.*, 2014, **5**, 2191.
44. A. Bauza, D. Quinonero, P. M. Deya and A. Frontera, *New J. Chem.*, 2013, **37**, 2636.
45. J.-R. Galan-Mascaros, A. M. Z. Slawin, J. Derek Woollins and D. J. Williams, *Polyhedron*, 1996, **15**, 4603.
46. H.-J. Schneider, F. Werner and T. Blatter, *J. Phys. Org. Chem.*, 1993, **6**, 590.
47. H.-J. Schneider, *Angew. Chem., Int. Ed. Engl.*, 1991, **30**, 1417.
48. K. Hiraoka, S. Mizuse and S. Yamabe, *J. Phys. Chem.*, 1987, **91**, 5294.
49. K. Hiraoka, S. Mizuse and S. Yamabe, *J. Chem. Phys.*, 1987, **86**, 4102.
50. P. Ballester, *Recognition of Anions*, Springer, Berlin Heidelberg, 2008.
51. A. Frontera, *Coord. Chem. Rev.*, 2013, **257**, 1716.
52. M. Giese, M. Albrecht and K. Rissanen, *Chem. Rev.*, 2015, **115**, 8867.
53. A. Bauzá, T. J. Mooibroek and A. Frontera, *CrystEngComm*, 2016, **18**, 10.
54. D. Kim, P. Tarakeshwar and K. S. Kim, *J. Phys. Chem. A*, 2004, **108**, 1250.

View Online

Published on 15 November 2016 on http://pubs.rsc.org | doi:10.1039/9781782626626-00039

55. D. Y. Kim, N. J. Singh, J. W. Lee and K. S. Kim, *J. Chem. Theory Comput.*, 2008, **4**, 1162.
56. C. Garau, A. Frontera, D. Quinonero, P. Ballester, A. Costa and P. M. Deya, *ChemPhysChem*, 2003, **4**, 1344.
57. D. Quinonero, C. Garau, A. Frontera, P. Ballester, A. Costa and P. M. Deya, *Chem. Phys. Lett.*, 2002, **359**, 486.
58. A. Bauza, P. M. Deya, A. Frontera and D. Quinonero, *Phys. Chem. Chem. Phys.*, 2014, **16**, 1322.
59. C. Garau, D. Quinonero, A. Frontera, P. Ballester, A. Costa and P. M. Deya, *New J. Chem.*, 2003, **27**, 211.
60. C. Garau, D. Quinonero, A. Frontera, P. Ballester, A. Costa and P. M. Deya, *Org. Lett.*, 2003, **5**, 2227.
61. C. Garau, A. Frontera, D. Quinonero, P. Ballester, A. Costa and P. M. Deya, *J. Phys. Chem. A*, 2004, **108**, 9423.
62. C. Foroutan-Nejad, Z. Badri and R. Marek, *Phys. Chem. Chem. Phys.*, 2015, **17**, 30670.
63. E. Francisco, A. Martín Pendás and M. A. Blanco, *J. Chem. Theory Comput.*, 2006, **2**, 90.
64. K. Kitaura and K. Morokuma, *Int. J. Quantum Chem.*, 1976, **10**, 325.
65. I. Mayer, *Chem. Phys. Lett.*, 2003, **382**, 265.
66. A. Krapp, F. M. Bickelhaupt and G. Frenking, *Chem.–Eur. J.*, 2006, **12**, 9196.
67. M. v. Hopffgarten and G. Frenking, *Wiley Interdiscip. Rev.: Comput. Mol. Sci.*, 2012, **2**, 43.
68. P. S. Bagus, K. Hermann and C. W. Bauschlicher, *J. Chem. Phys.*, 1984, **80**, 4378.
69. P. S. Bagus, K. Hermann and C. W. Bauschlicher, *J. Chem. Phys.*, 1984, **81**, 1966.
70. W. J. Stevens and W. H. Fink, *Chem. Phys. Lett.*, 1987, **139**, 15.
71. E. D. Glendening and A. Streitwieser, *J. Chem. Phys.*, 1994, **100**, 2900.
72. E. D. Glendening, *J. Am. Chem. Soc.*, 1996, **118**, 2473.
73. E. D. Glendening, *J. Phys. Chem. A*, 2005, **109**, 11936.
74. J. Korchowiec and T. Uchimaru, *J. Chem. Phys.*, 2000, **112**, 1623.
75. I. Mayer and A. Hamza, *Int. J. Quantum Chem.*, 2005, **103**, 798.
76. S. F. Vyboishchikov and P. Salvador, *Chem. Phys. Lett.*, 2006, **430**, 204.
77. K. Szalewicz, *Wiley Interdiscip. Rev.: Comput. Mol. Sci.*, 2012, **2**, 254.
78. G. Jansen, *Wiley Interdiscip. Rev.: Comput. Mol. Sci.*, 2014, **4**, 127.
79. B. Jeziorski, R. Moszynski and K. Szalewicz, *Chem. Rev.*, 1994, **94**, 1887.
80. T. Baba, M. Takeuchi and H. Nakai, *Chem. Phys. Lett.*, 2006, **424**, 193.
81. H. Nakai, Y. Kurabayashi, M. Katouda and T. Atsumi, *Chem. Phys. Lett.*, 2007, **438**, 132.
82. S. Liu, *J. Chem. Phys.*, 2007, **126**, 244103/1.
83. R. Z. Khaliullin, E. A. Cobar, R. C. Lochan, A. T. Bell and M. Head-Gordon, *J. Phys. Chem. A*, 2007, **111**, 8753.
84. P. R. Horn, E. J. Sundstrom, T. A. Baker and M. Head-Gordon, *J. Chem. Phys.*, 2013, **138**, 134119/1.

View Online

Published on 15 November 2016 on http://pubs.rsc.org | doi:10.1039/9781782626626-00039

85. Y. Mo, P. Bao and J. Gao, *Phys. Chem. Chem. Phys.*, 2011, **13**, 6760.
86. M. Rahm and R. Hoffmann, *J. Am. Chem. Soc.*, 2015, **137**, 10282.
87. S. E. Wheeler and K. N. Houk, *J. Phys. Chem. A*, 2010, **114**, 8658.
88. C. Garau, D. Quinonero, A. Frontera, P. Ballester, A. Costa and P. M. Deya, *J. Phys. Chem. A*, 2005, **109**, 9341.
89. C. Garau, A. Frontera, D. Quinonero, N. Russo and P. M. Deya, *J. Chem. Theory Comput.*, 2011, **7**, 3012.
90. D. Quinonero, A. Frontera and P. M. Deya, *ChemPhysChem*, 2008, **9**, 397.
91. I. A. Gural'skiy, D. Escudero, A. Frontera, P. V. Solntsev, E. B. Rusanov, A. N. Chernega, H. Krautscheid and K. V. Domasevitch, *Dalton Trans.*, 2009, 2856.
92. A. Bauzá, D. Quiñonero, P. M. Deyà and A. Frontera, *Theor. Chem. Acc.*, 2012, **131**, 1219.
93. C. Estarellas, A. Frontera, D. Quinonero and P. M. Deya, *J. Chem. Theory Comput.*, 2008, **4**, 1981.
94. D. Quinonero, A. Frontera, D. Escudero, P. Ballester, A. Costa and P. M. Deya, *ChemPhysChem*, 2007, **8**, 1182.
95. A. Das, S. R. Choudhury, B. Dey, S. K. Yalamanchili, M. Helliwell, P. Gamez, S. Mukhopadhyay, C. Estarellas and A. Frontera, *J. Phys. Chem. B*, 2010, **114**, 4998.
96. A. Das, S. R. Choudhury, C. Estarellas, B. Dey, A. Frontera, J. Hemming, M. Helliwell, P. Gamez and S. Mukhopadhyay, *CrystEngComm*, 2011, **13**, 4519.
97. J. J. Fiol, M. Barcelo-Oliver, A. Tasada, A. Frontera, A. Terron and A. Garcia-Raso, *Coord. Chem. Rev.*, 2013, **257**, 2705.
98. I. Alkorta and J. Elguero, *J. Phys. Chem. A*, 2003, **107**, 9428.
99. I. Alkorta, D. Quinonero, C. Garau, A. Frontera, J. Elguero and P. M. Deya, *J. Phys. Chem. A*, 2007, **111**, 3137.
100. D. Quinonero, A. Frontera, P. M. Deya, I. Alkorta and J. Elguero, *Chem. Phys. Lett.*, 2008, **460**, 406.
101. J. W. Steed, R. K. Juneja and J. L. Atwood, *Angew. Chem., Int. Ed. Engl.*, 1995, **33**, 2456.
102. M. Staffilani, K. S. B. Hancock, J. W. Steed, K. T. Holman, J. L. Atwood, R. K. Juneja and R. S. Burkhalter, *J. Am. Chem. Soc.*, 1997, **119**, 6324.
103. K. T. Holman, M. M. Halihan, S. S. Jurisson, J. L. Atwood, R. S. Burkhalter, A. R. Mitchell and J. W. Steed, *J. Am. Chem. Soc.*, 1996, **118**, 9567.
104. M. Staffilani, G. Bonvicini, J. W. Steed, K. T. Holman, J. L. Atwood and M. R. J. Elsegood, *Organometallics*, 1998, **17**, 1732.
105. H. T. Chifotides, B. L. Schottel and K. R. Dunbar, *Angew. Chem., Int. Ed. Engl.*, 2010, **49**, 7202.
106. G. Aragay, A. Frontera, V. Lloveras, J. Vidal-Gancedo and P. Ballester, *J. Am. Chem. Soc.*, 2013, **135**, 2620.
107. I. A. Gural'skiy, P. V. Solntsev, H. Krautscheid and K. V. Domasevitch, *Chem. Commun.*, 2006, 4808.
108. D. Escudero, A. Frontera, D. Quinonero and P. M. Deya, *J. Comput. Chem.*, 2009, **30**, 75.

View Online

Published on 15 November 2016 on http://pubs.rsc.org | doi:10.1039/9781782626626-00039

109. X. Lucas, C. Estarellas, D. Escudero, A. Frontera, D. Quinonero and P. M. Deya, *ChemPhysChem*, 2009, **10**, 2256.
110. T. J. Mooibroek and P. Gamez, *Inorg. Chim. Acta*, 2007, **360**, 381.
111. T. J. Mooibroek, C. A. Black, P. Gamez and J. Reedijk, *Cryst. Growth Des.*, 2008, **8**, 1082.
112. C. Murcia-García, A. Bauzá, A. Frontera and R. Streubel, *CrystEngComm*, 2015, **17**, 6736.
113. C. Murcia-García, A. Bauzá, G. Schnakenburg, A. Frontera and R. Streubel, *CrystEngComm*, 2015, **17**, 1769.
114. T. J. Mooibroek and P. Gamez, *CrystEngComm*, 2012, **14**, 1027.
115. T. J. Mooibroek and P. Gamez, *CrystEngComm*, 2013, **15**, 1802.
116. P. Ballester, *Acc. Chem. Res.*, 2013, **46**, 874.
117. H. T. Chifotides and K. R. Dunbar, *Acc. Chem. Res.*, 2013, **46**, 894.
118. P. Gamez, *Inorg. Chem. Front.*, 2014, **1**, 35.
119. M. M. Watt, M. S. Collins and D. W. Johnson, *Acc. Chem. Res.*, 2013, **46**, 955.
120. D. X. Wang and M. X. Wang, *J. Am. Chem. Soc.*, 2013, **135**, 892.
121. D. X. Wang, Q. Y. Zheng, Q. Q. Wang and M. X. Wang, *Angew. Chem., Int. Ed.*, 2008, **47**, 7485.
122. S. T. Schneebeli, M. Frasconi, Z. C. Liu, Y. L. Wu, D. M. Gardner, N. L. Strutt, C. Y. Cheng, R. Carmieli, M. R. Wasielewski and J. F. Stoddart, *Angew. Chem., Int. Ed.*, 2013, **52**, 13100.
123. H. T. Chifotides, I. D. Giles and K. R. Dunbar, *J. Am. Chem. Soc.*, 2013, **135**, 3039.
124. M. M. Watt, L. N. Zakharov, M. M. Haley and D. W. Johnson, *Angew. Chem., Int. Ed.*, 2013, **52**, 10275.
125. B. P. Hay, M. Gutowski, D. A. Dixon, J. Garza, R. Vargas and B. A. Moyer, *J. Am. Chem. Soc.*, 2004, **126**, 7925.
126. B. P. Hay, D. A. Dixon, J. C. Bryan and B. A. Moyer, *J. Am. Chem. Soc.*, 2002, **124**, 182.
127. N. Hafezi, J. M. Holcroft, K. J. Hartlieb, E. J. Dale, N. A. Vermeulen, C. L. Stern, A. A. Sarjeant and J. F. Stoddart, *Angew. Chem., Int. Ed.*, 2015, **54**, 456.
128. P. Arranz, A. Bianchi, R. Cuesta, C. Giorgi, M. L. Godino, M. D. Gutierrez, R. Lopez and A. Santiagot, *Inorg. Chem.*, 2010, **49**, 9321.
129. P. Arranz-Mascaros, C. Bazzicalupi, A. Bianchi, C. Giorgi, M. L. Godino-Salido, M. D. Gutierrez-Valero, R. Lopez-Garzon and M. Savastano, *J. Am. Chem. Soc.*, 2013, **135**, 102.
130. J. Garcia-Martin, R. Lopez-Garzon, M. L. Godino-Salido, R. Cuesta-Martos, M. D. Gutierrez-Valero, P. Arranz-Mascaros and H. Stoeckli-Evans, *Eur. J. Inorg. Chem.*, 2005, 3093.
131. A. Quesada, A. Marchal, M. Melguizo, M. Nogueras, A. Sanchez, J. N. Low, D. Cannon, D. M. M. Farrell and C. Glidewell, *Acta Crystallogr., Sect. B: Struct. Sci.*, 2002, **58**, 300.
132. J. N. Low, A. Quesada, C. Glidewell, M. A. Fontecha, P. Arranz, M. L. Godino and R. Lopez, *Acta Crystallogr., Sect. E: Struct. Rep. Online*, 2002, **58**, o942.

View Online

Published on 15 November 2016 on http://pubs.rsc.org | doi:10.1039/9781782626626-00039

133. F. Zapata, L. Gonzalez, A. Caballero, I. Alkorta, J. Elguero and P. Molina, *Chem.–Eur. J.*, 2015, **21**, 9797.
134. A. Caballero, F. Zapata, L. Gonzalez, P. Molina, I. Alkorta and J. Elguero, *Chem. Commun. (Cambridge, U. K.)*, 2014, **50**, 4680.
135. M. G. Chudzinski, C. A. McClary and M. S. Taylor, *J. Am. Chem. Soc.*, 2011, **133**, 10559.
136. M. Giese, M. Albrecht, C. Bannwarth, G. Raabe, A. Valkonen and K. Rissanen, *Chem. Commun.*, 2011, **47**, 8542.
137. M. Giese, M. Albrecht, S. Steike, A. Ackermann, A. Valkonen and K. Rissanen, *Inorg. Chem.*, 2013, **52**, 7666.
138. G. Gil-Ramirez, E. C. Escudero-Adan, J. Benet-Buchholz and P. Ballester, *Angew. Chem., Int. Ed.*, 2008, **47**, 4114.
139. D. X. Wang, Q. Q. Wang, Y. C. Han, Y. L. Wang, Z. T. Huang and M. X. Wang, *Chem.–Eur. J.*, 2010, **16**, 13053.
140. Y. S. Rosokha, S. V. Lindeman, S. V. Rosokha and J. K. Kochi, *Angew. Chem., Int. Ed.*, 2004, **43**, 4650.
141. S. V. Rosokha and J. K. Kochi, *Struct. Bonding (Berlin)*, 2008, **126**, 137.
142. S. V. Rosokha and J. K. Kochi, *Acc. Chem. Res.*, 2008, **41**, 641.
143. S. Guha, F. S. Goodson, L. J. Corson and S. Saha, *J. Am. Chem. Soc.*, 2012, **134**, 13679.
144. O. B. Berryman, V. S. Bryantsev, D. P. Stay, D. W. Johnson and B. P. Hay, *J. Am. Chem. Soc.*, 2007, **129**, 48.
145. J. S. Park, E. Karnas, K. Ohkubo, P. Chen, K. M. Kadish, S. Fukuzumi, C. W. Bielawski, T. W. Hudnall, V. M. Lynch and J. L. Sessler, *Science*, 2010, **329**, 1324.
146. Y. J. Zhao, Y. J. Li, Z. H. Qin, R. S. Jiang, H. B. Liu and Y. L. Li, *Dalton Trans.*, 2012, **41**, 13338.
147. F. S. Goodson, D. K. Panda, S. Ray, A. Mitra, S. Guha and S. Saha, *Org. Biomol. Chem.*, 2013, **11**, 4797.
148. S. Guha, F. S. Goodson, R. J. Clark and S. Saha, *CrystEngComm*, 2012, **14**, 1213.
149. S. E. Wheeler and J. W. G. Bloom, *Chem. Commun.*, 2014, **50**, 11118.
150. L. Adriaenssens, C. Estarellas, A. Vargas Jentzsch, M. Martinez Belmonte, S. Matile and P. Ballester, *J. Am. Chem. Soc.*, 2013, **135**, 8324.
151. X. D. Wang, S. Li, Y. F. Ao, Q. Q. Wang, Z. T. Huang and D. X. Wang, *Org. Biomol. Chem.*, 2016, **14**, 330.
152. C. D. Kumar, K. Sirisha, D. K. Dhaked, P. Lokesh, A. V. S. Sarma, P. V. Bharatam, S. Kantevari and P. Sripadi, *J. Org. Chem.*, 2015, **80**, 1746.
153. J. Chen and J. Rebek, *Org. Lett.*, 2002, **4**, 327.
154. A. V. Jentzsch, A. Hennig, J. Mareda and S. Matile, *Acc. Chem. Res.*, 2013, **46**, 2791.
155. Y. J. Zhao, C. Beuchat, Y. Domoto, J. Gajewy, A. Wilson, J. Mareda, N. Sakai and S. Matile, *J. Am. Chem. Soc.*, 2014, **136**, 2101.
156. N.-T. Lin, A. V. Jentzsch, L. Guenee, J.-M. Neudoerfl, S. Aziz, A. Berkessel, E. Orentas, N. Sakai and S. Matile, *Chem. Sci.*, 2012, **3**, 1121.
157. D. T. Browne, J. Esinger and N. J. Leonard, *J. Am. Chem. Soc.*, 1968, **90**, 7302.

View Online

Published on 15 November 2016 on http://pubs.rsc.org | doi:10.1039/9781782626626-00039

158. Y. J. Zhao, N. Sakai and S. Matile, *Nat. Commun.*, 2014, **5**, 3911.
159. Y. J. Zhao, S. Benz, N. Sakai and S. Matile, *Chem. Sci.*, 2015, **6**, 6219.
160. Y. J. Zhao, Y. Cotelle, A. J. Avestro, N. Sakai and S. Matile, *J. Am. Chem. Soc.*, 2015, **137**, 11582.
161. J. Duschmale, J. Wiest, M. Wiesner and H. Wennemers, *Chem. Sci.*, 2013, **4**, 1312.
162. S. E. Reisman, A. G. Doyle and E. N. Jacobsen, *J. Am. Chem. Soc.*, 2008, **130**, 7198.
163. F. Kniep, S. H. Jungbauer, Q. Zhang, S. M. Walter, S. Schindler, I. Schnapperelle, E. Herdtweck and S. M. Huber, *Angew. Chem., Int. Ed.*, 2013, **52**, 7028.
164. A. Berkessel, S. Das, D. Pekel and J.-M. Neudörfl, *Angew. Chem., Int. Ed.*, 2014, **53**, 11660.
165. S. Das, D. Pekel, J. M. Neudorfl and A. Berkessel, *Angew. Chem., Int. Ed.*, 2015, **54**, 12479.
166. M. Giese, M. Albrecht, T. Repenko, J. Sackmann, A. Valkonen and K. Rissanen, *Eur. J. Org. Chem.*, 2014, **2014**, 2435.
167. N. Busschaert, C. Caltagirone, W. Van Rossom and P. A. Gale, *Chem. Rev.*, 2015, **115**, 8038.
168. T. Welton, *Chem. Rev.*, 1999, **99**, 2071.
169. X. Zhang, X. Zhang, H. Dong, Z. Zhao, S. Zhang and Y. Huang, *Energy Environ. Sci.*, 2012, **5**, 6668.
170. R. P. Swatloski, S. K. Spear, J. D. Holbrey and R. D. Rogers, *J. Am. Chem. Soc.*, 2002, **124**, 4974.
171. A. Brandt, M. J. Ray, T. Q. To, D. J. Leak, R. J. Murphy and T. Welton, *Green Chem.*, 2011, **13**, 2489.
172. A. Brandt, J. Gräsvik, J. P. Hallett and T. Welton, *Green Chem.*, 2013, **15**, 550.
173. P. Simon and Y. Gogotsi, *Nat. Mater.*, 2008, **7**, 845.
174. Y. Bai, Y. Cao, J. Zhang, M. Wang, R. Li, P. Wang, S. M. Zakeeruddin and M. Grätzel, *Nat. Mater.*, 2008, **7**, 626.
175. M. Armand, F. Endres, D. R. MacFarlane, H. Ohno and B. Scrosati, *Nat. Mater.*, 2009, **8**, 621.
176. A. Somers, P. Howlett, D. MacFarlane and M. Forsyth, *Lubricants*, 2013, **1**, 3.
177. F. Zhou, Y. Liang and W. Liu, *Chem. Soc. Rev.*, 2009, **38**, 2590.
178. C. Ye, W. Liu, Y. Chen and L. Yu, *Chem. Commun.*, 2001, 2244.
179. S. Perkin, T. Albrecht and J. Klein, *Phys. Chem. Chem. Phys.*, 2010, **12**, 1243.
180. R. P. Matthews, T. Welton and P. A. Hunt, *Phys. Chem. Chem. Phys.*, 2015, **17**, 14437.
181. A. Garcia-Saiz, I. de Pedro, P. Migowski, O. Vallcorba, J. Junquera, J. A. Blanco, O. Fabelo, D. Sheptyakov, J. C. Waerenborgh, M. T. Fernandez-Diaz, J. Rius, J. Dupont, J. A. Gonzalez and J. R. Fernandez, *Inorg. Chem.*, 2014, **53**, 8384.
182. R. Podgajny, D. Pinkowicz, B. Czarnecki, M. Koziel, S. Chorazy, M. Wis, W. Nitek, M. Rams and B. Sieklucka, *Cryst. Growth Des.*, 2014, **14**, 4030.

View Online

Published on 15 November 2016 on http://pubs.rsc.org | doi:10.1039/9781782626626-00039

183. W. Liu, Q. Q. Wang, Y. Y. Wang, Z. T. Huang and D. X. Wang, *RSC Adv.*, 2014, **4**, 9339.
184. J.-J. Liu, Y.-F. Guan, C. Jiao, M.-J. Lin, C.-C. Huang and W.-X. Dai, *Dalton Trans.*, 2015, **44**, 5957.
185. J.-i. Fujisawa, N. Tajima, K. Tamaki, M. Shimomura and T. Ishihara, *J. Phys. Chem. C*, 2007, **111**, 1146.
186. T. Fukumoto, M. Hirasawa and T. Ishihara, *J. Lumin.*, 2000, **87–89**, 497.
187. S. Kumar, M. R. Ajayakumar, G. Hundal and P. Mukhopadhyay, *J. Am. Chem. Soc.*, 2014, **136**, 12004.
188. J. Z. Liao, X. J. Dui, H. L. Zhang, X. Y. Wu and C. Z. Lu, *CrystEngComm*, 2014, **16**, 10530.
189. J.-Z. Liao, H.-L. Zhang, S.-S. Wang, J.-P. Yong, X.-Y. Wu, R. Yu and C.-Z. Lu, *Inorg. Chem.*, 2015, **54**, 4345.
190. M. Giese, M. Albrecht, A. Valkonen and K. Rissanen, *Eur. J. Org. Chem.*, 2013, 3247.
191. M. Giese, M. Albrecht, A. Valkonen and K. Rissanen, *Chem. Sci.*, 2015, **6**, 354.
192. C. S. Campos-Fernández, B. L. Schottel, H. T. Chifotides, J. K. Bera, J. Bacsa, J. M. Koomen, D. H. Russell and K. R. Dunbar, *J. Am. Chem. Soc.*, 2005, **127**, 12909.
193. B. L. Schottel, H. T. Chifotides, M. Shatruk, A. Chouai, L. M. Pérez, J. Bacsa and K. R. Dunbar, *J. Am. Chem. Soc.*, 2006, **128**, 5895.
194. P. S. Szalay, J. R. Galan-Mascaros, B. L. Schottel, J. Bacsa, L. M. Perez, A. S. Ichimura, A. Chouai and K. R. Dunbar, *J. Cluster Sci.*, 2004, **15**, 503.
195. R. Chakrabarty, P. S. Mukherjee and P. J. Stang, *Chem. Rev.*, 2011, **111**, 6810.
196. M. Fujita, M. Tominaga, A. Hori and B. Therrien, *Acc. Chem. Res.*, 2005, **38**, 369.
197. M. Fujita, K. Umemoto, M. Yoshizawa, N. Fujita, T. Kusukawa and K. Biradha, *Chem. Commun.*, 2001, 509.
198. M. D. Pluth, R. G. Bergman and K. N. Raymond, *Acc. Chem. Res.*, 2009, **42**, 1650.
199. R. A. Bilbeisi, J. K. Clegg, N. Elgrishi, X. de Hatten, M. Devillard, B. Breiner, P. Mal and J. R. Nitschke, *J. Am. Chem. Soc.*, 2012, **134**, 5110.
200. J. Rebek, *Acc. Chem. Res.*, 2009, **42**, 1660.
201. J. Z. Liao, X. Y. Wu, J. P. Yong, H. L. Zhang, W. B. Yang, R. M. Yu and C. Z. Lu, *Cryst. Growth Des.*, 2015, **15**, 4952.
202. D. A. Safin, A. Pialat, A. A. Leitch, N. A. Tumanov, I. Korobkov, Y. Filinchuk, J. L. Brusso and M. Murugesu, *Chem. Commun.*, 2015, **51**, 9547.
203. L. Qin, L.-Y. Yao and S.-Y. Yu, *Inorg. Chem.*, 2012, **51**, 2443.
204. C. Estarellas, A. Frontera, D. Quinonero and P. M. Deya, *ChemPhysChem*, 2011, **12**, 2742.
205. C. Estarellas, A. Frontera, D. Quinonero, I. Alkorta, P. M. Deya and J. Elguero, *J. Phys. Chem. A*, 2009, **113**, 3266.
206. A. Frontera, D. Quinonero, C. Garau, A. Costa, P. Ballester and P. M. Deya, *J. Phys. Chem. A*, 2006, **110**, 9307.

View Online

207. D. Quinonero, A. Frontera, C. Garau, P. Ballester, A. Costa and P. M. Deya, *ChemPhysChem*, 2006, **7**, 2487.
208. A. Frontera, D. Quinonero, A. Costa, P. Ballester and P. M. Deya, *New J. Chem.*, 2007, **31**, 556.
209. A. Bhattacharyya, P. K. Bhaumik, A. Bauzá, P. P. Jana, A. Frontera, M. G. B. Drew and S. Chattopadhyay, *RSC Adv.*, 2014, **4**, 58643.
210. M. Roy, A. Bauzá, A. Frontera, S. Banerjee, S. Halder and A. Saha, *Polyhedron*, 2015, **102**, 764.
211. A. Garcia-Raso, F. M. Alberti, J. J. Fiol, A. Tasada, M. Barcelo-Oliver, E. Molins, D. Escudero, A. Frontera, D. Quinonero and P. M. Deya, *Inorg. Chem.*, 2007, **46**, 10724.
212. P. Manna, S. K. Seth, A. Bauzá, M. Mitra, S. Ray Choudhury, A. Frontera and S. Mukhopadhyay, *Cryst. Growth Des.*, 2014, **14**, 747.
213. P. Manna, S. K. Seth, M. Mitra, S. R. Choudhury, A. Bauza, A. Frontera and S. Mukhopadhyay, *Cryst. Growth Des.*, 2014, **14**, 5812.
214. M.-H. Chen, S.-F. Xue and Z. Tao, *Hecheng Huaxue*, 2009, **17**, 722, Reference to CSD code HINFAN.
215. F. Orvay, A. Bauzá, M. Barcelo-Oliver, A. Garcia-Raso, J. J. Fiol, A. Costa, E. Molins, I. Mata and A. Frontera, *CrystEngComm*, 2014, **16**, 9043.
216. J. Aguiló, A. Naeimi, R. Bofill, H. Mueller-Bunz, A. Llobet, L. Escriche, X. Sala and M. Albrecht, *New J. Chem.*, 2014, **38**, 1980.

Published on 15 November 2016 on http://pubs.rsc.org | doi:10.1039/9781782626626-00039

CHAPTER 4

A New Non-Covalent Bonding Mode in Supramolecular Chemistry: Main Group Element Lone-Pair–π(arene) Interactions

IGNEZ CARACELLI[a], IONEL HAIDUC[b], JULIO ZUKERMAN-SCHPECTOR[c] AND EDWARD R. T. TIEKINK*[d]

[a]Departamento de Física, Universidade Federal de São Carlos, C. P. 676, São Carlos, SP, 13565-905, Brazil; [b]Departamento de Química, Universidade Federal de São Carlos, C. P. 676, São Carlos, SP, 13565-905, Brazil; [c]Facultatea de Chimie, Universitatea Babes-Bolyai, Cluj-Napoca, RO-400028, Romania; [d]Research Centre for Crystalline Materials, Faculty of Science and Technology, Sunway University, 47500 Bandar Sunway, Selangor Darul Ehsan, Malaysia
*E-mail: edwardt@sunway.edu.my

4.1 Introduction

As "*the chemistry of molecular assemblies and of the intermolecular bond*",[1] supramolecular chemistry exploits a variety of non-covalent intermolecular forces to connect and organise chemical architectures constructed of

Monographs in Supramolecular Chemistry No. 20
Aromatic Interactions: Frontiers in Knowledge and Application
Edited by Darren W. Johnson and Fraser Hof
© The Royal Society of Chemistry 2017
Published by the Royal Society of Chemistry, www.rsc.org

molecules as building blocks (called "tectons").[2] The most common type of intermolecular interactions are hydrogen bonds,[3] donor–acceptor or dative-coordinate bonds,[4] secondary bonds or "soft–soft" interactions,[5] halogen bonds,[6] π···π stacking[7] and metal π-bonds.[8] Metal···π(arene) bonds are well documented for transition metals with complexes such as bis(benzene) chromium, $Cr(C_6H_6)_2$, and benzenechromium tricarbonyl, $C_6H_6Cr(CO)_3$, now being historical landmarks. The bond between a transition metal atom and an arene ring is formed by donation of the π-electrons from the ring into the d-orbitals of the metal. This is not possible in the case of main group (post-transition) elements. However, compounds of the main group elements non-covalently bonded to benzene or other arenes have been discovered and structurally characterised by X-ray diffraction, challenging puzzled chemists for a rational explanation. Examples are the so-called Menschutkin (Menšutkin) complexes of antimony and bismuth[9] including $C_6H_6{\cdot}SbCl_3$, $C_6Me_6{\cdot}2SbX_3$ (with X = Cl, Br) and $C_6H_6{\cdot}BiCl_3$ or $C_6Me_6{\cdot}BiX_3$ (with X = Cl or Br). Metal–aryl interactions were also discovered in the dimeric tin(II) dithiophosphate, $[Sn\{S_2P(OPh)_2\}_2]_2$,[10] and in the dimeric lead(II) dithiophosphonate, $[Pb\{S_2P(OPr^i)(C_6H_4OMe\text{-}4)\}]_2$.[11] Tellurium···π(arene) interactions were suggested in two compounds and their formation proposed as involving the lone-pairs of electrons interacting with the ring.[12] Thus, it was noted "*We tentatively suggest that the lone-pair is located between the π-bonded phenyl ring and the central tellurium atom. It is quite possible that similar weak π-interactions between tellurium atoms and aromatic groups are present in other organotellurium compounds and passed unnoticed so far*".[12] This prompted the first systematic search of the Cambridge Crystallographic Database (CSD),[13] where lone-pair···π(arene) interactions were proposed as being important in molecular packing. This search revealed a significant number of tellurium compounds displaying such interactions in the solid-state, but not identified as so in the original reports.[14] More recently, a new search was undertaken and the stereochemical influence of the tellurium lone-pair interaction with the π-systems investigated.[15] The data mining of the CSD[13] was extended to practically all post-transition metals,[16] *i.e.* gallium, indium and thallium,[17] tin,[18] lead,[19] arsenic,[20] antimony and bismuth,[21] and selenium.[22] In related bibliographic studies, organometallic metal carbonyl compounds were also found to form M–CO···π(arene) complexes, with intermolecular bonds leading to supramolecular associations and recognisable supramolecular architectures;[23] a more recent survey of DMSO-O(lp)···π(arene) interactions reinforces the importance of this type of contact in supramolecular chemistry.[24]

The lone-pair···π(arene) interaction[14] is now recognised as a valid bond type, both intramolecular and intermolecular, leading in the last case to supramolecular self-assembly.[14–24] DFT calculations with an exchange hole dipole moment (XDM) dispersion correction on some arsenic(III) species showed these interactions may be described as lone pair(As)···π but, interestingly, in some examples these were best described as being of the type donor(π)–acceptor(As).[25] Clearly, there is scope for further

theoretical investigations in this area as this has proven highly informative in the cases of halogen[26] and chalcogen bonding.[27] This being stated, in the literature, attention is mostly concentrated on anion···π(arene)[28] and cation···π(arene)[29] interactions rather than those involving main group elements, with the possible exception of alkali metal cations.[30] Attention is also directed towards oxygen (*e.g.* water) and halogen lone-pair···π(arene) interactions.[31] In addition to the aromatic hydrocarbons (benzene, naphthalene, *etc.*), the π-system can be aromatic heterocycles (pyridine, triazene, *etc.*) and even some chelate rings[32] or pseudo-chelates.[33] Recently, inorganic rings, *e.g.* borazine, were also considered as potential candidates for lone-pair···π(arene) ring interactions, and some theoretical calculations were performed on the assumption that the carbon-free heterocycles may display some aromatic character.[34]

The intention here is to highlight the relevance of main group element lone-pair···π(arene) interactions, abbreviated hereafter as M(lp)···π(arene), as a new non-covalent bonding mode in supramolecular chemistry. In so doing, the diversity the supramolecular aggregates sustained by these interactions will be revealed, most of which remained hidden until an appropriate analysis of the available information from the CSD[13] was performed. Most of the earlier literature reports only the molecular structures, but the analysis of their molecular packing often reveals supramolecular associations through M(lp)···π(arene) interactions.

4.2 Methodology

The Cambridge Structural Database (CSD)[13] was employed as the primary resource in data mining studies searching for M(lp)···π(arene) interactions. The CSD was searched using the program CONQUEST[35] in accord with the structural protocols shown in Figure 4.1(a). Thus, two key geometric restrictions were applied. Firstly, *d*, the distance between the main group element atom (M) and the centroid (Cg) of the arene ring was based on the sum of the half-thickness of a phenyl ring, taken as 1.9 Å, being the upper value for half the centroid–centroid distance in parallel arene rings,[7a] and the respective van der Waals radii of M,[36] plus 10% to enable the capture of all putative contacts.[37] The second criterion relates to the angle, α, which is defined as the angle between the normal to the plane through the arene ring (V_1) and the vector passing through Cg to M (V_2). The α angle was restricted to be less than 30° to ensure that only delocalised M···π(arene) interactions were extracted. Referring to Figure 4.1(b), a delocalised interaction corresponds to the M atom sitting plumb or close to plumb over the ring centroid.[38] By contrast, a localised interaction would see the lone-pair directed towards a specific atom of the ring and a semi-localised interaction would have the lone-pair directed towards one bond of the ring. Preliminary screening was applied so that structures with disorder or unresolved errors were omitted along with those having other heavy metal atoms. Manual sorting of each individual "hit" ensued, employing the programs PLATON[39] and DIAMOND.[40]

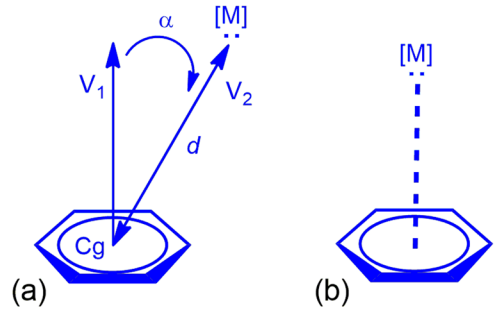

Figure 4.1 (a) Search protocols for the identification of M(lp)···π(arene) interactions in structures included in the Cambridge Structural Database: *d* is the distance between the main group element (M) and the centroid (Cg) of the arene ring, and the angle, α, is defined as the angle between the normal to the plane through the arene ring (V_1) and the vector passing through Cg to M (V_2), and (b) a representation of a delocalised M(lp)···π(arene) interaction whereby the main group element (M) sits plumb to the plane of the arene ring or deviates from the vertical by no more than 30°.

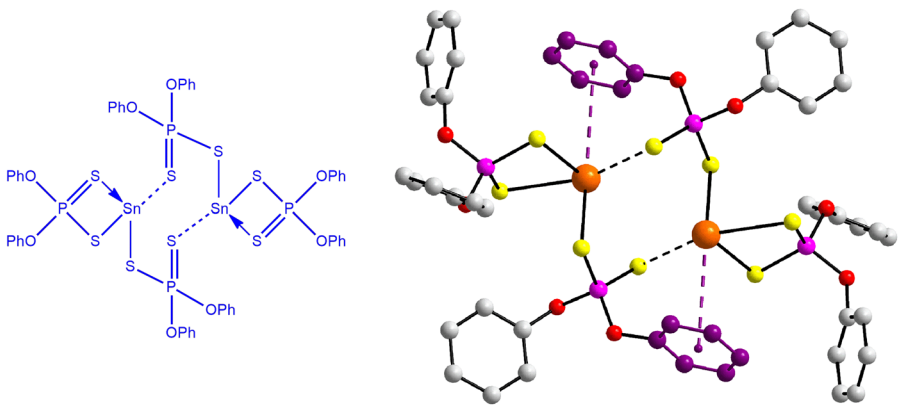

Figure 4.2 Chemical diagram and molecular structure of supramolecular dimer $[Sn\{S_2P(OPh)_2\}_2]_2$, (**1**), being an example of a structure excluded from consideration as having an independent Sn(lp)···π(arene) interaction because the dimer is also sustained by Sn···S secondary bonding (black dashed lines). Colour code: orange, main group element; yellow, sulfur; pink, phosphorus; red, oxygen; grey, carbon; purple, carbon of the interacting arene ring; purple dashed line, the M(lp)···π(arene) interaction.

The manual inspection of each structure enabled the confirmation that the M(lp)···π(arene) interaction was operating in isolation of other intermolecular interactions. An example of this concept is illustrated in Figure 4.2. Referring to this figure, in binuclear and centrosymmetric $\{Sn[S_2P(OPh)_2]_2\}_2$,[10] one phenyl ring of each bidentate bridging dithiophosphate ligand is directed over the centrosymmetrically-related tin atom enabling a putative Sn(lp)···π(arene)

interaction. Here, d = 3.66 Å and α = 19.6°, fulfilling the standard geometric restrictions mentioned above. However, along with the Sn(lp)···π(arene) interaction, secondary interactions,[5] of the type Sn···S [3.04 Å] also occur so that the Sn(lp)···π(arene) interactions are not "stand-alone", but operate in concert with the Sn···S contacts, and therefore the structure was not regarded as having independent Sn(lp)···π(arene) interactions and therefore, is not included herein. On this basis, a good number of the initial "hits" from the CSD searches were excluded often owing to the presence of the aforementioned secondary interactions and to hydrogen bonding. Finally, it should be noted that the putative Sn(lp)···π(arene) interaction in $[Sn\{S_2P(OPh)_2\}_2]_2$ [10] is recognised, on geometric grounds, as a contact by the ubiquitous structure analysis program, PLATON.[39] Despite this, it is still rare for M(lp)···π(arene) interactions to be commented upon in the primary literature.

In the ensuing sections, selected examples of M(lp)···π(arene) points of contact found in indium(I),[17] thallium(I),[17] tin(II),[18] lead(II),[19] arsenic(III),[20] antimony(III),[21] bismuth(III),[21] selenium(II and IV)[22] and tellurium(II and IV)[15] crystal structures are presented, in this order. Examples were selected on the basis of novelty and aesthetics: the interested reader is referred to the original exhaustive reviews for full details for each element. Diagrams were drawn/redrawn with the aid of DIAMOND,[40] with all hydrogen atoms omitted, and the accompanying chemical structure diagram only includes the species participating in the M(lp)···π(arene) interaction, *i.e.* typically counter-ions, solvents, *etc.* are not included.

4.3 Overview of M(lp)···π(arene) Interactions

4.3.1 Indium(I)

The chemistry of gallium and indium with the element in the +I oxidation state is not very well developed,[41] there being relatively few examples, certainly when compared with the far-ranging chemistry of thallium(I). There is in fact only one example of an indium(I) structure featuring an In(lp)···π(arene) interaction, namely $[In\{OC_6H_2(CF_3)_3\text{-}2,4,6\}]_2$, (**2**).[42] The molecule is binuclear with each of the crystallographically independent indium atoms forming an In(lp)···π(arene) interaction [d = 3.87 Å and α = 7.6°; 4.22 Å, 18.0°]. The supramolecular aggregation sustained by these interactions is a zigzag chain as illustrated in Figure 4.3.

4.3.2 Thallium(I)

The centrosymmetric binuclear aggregate illustrated in Figure 4.4(a) and found in the structure of [2-(2′,6′-diisopropylphenylamido)-4-(2′,6′-diisopropylphenylimino)-2-pentene] thallium(I),[43] (**3**), and supported by a pair of Tl(lp)···π(arene) interactions [d = 3.92 Å and α = 11.0°] is a common motif found for thallium(I) and indeed other main group elements. Higher nuclearity, zero-dimensional aggregates are also known. For example, in the crystal

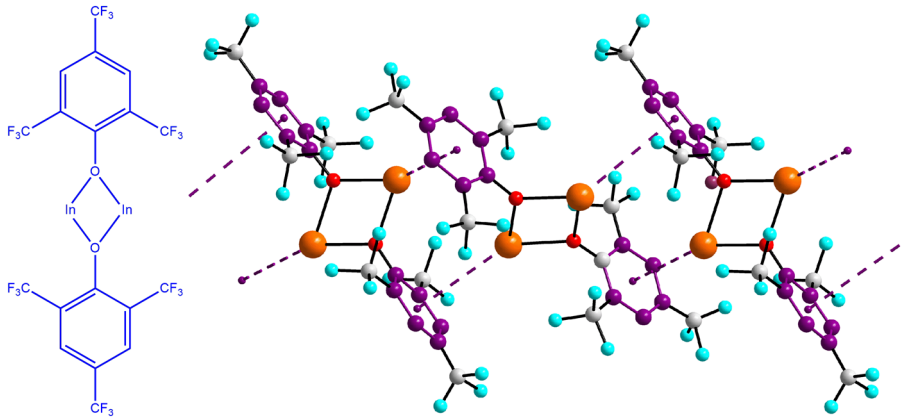

Figure 4.3 Chemical diagram of $[In\{OC_6H_2(CF_3)_3\text{-}2,4,6\}]_2$, (**2**), and the supramolecular chain sustained by In(lp)···π(arene) interactions. Additional colour code: aqua, fluoride or other halide.

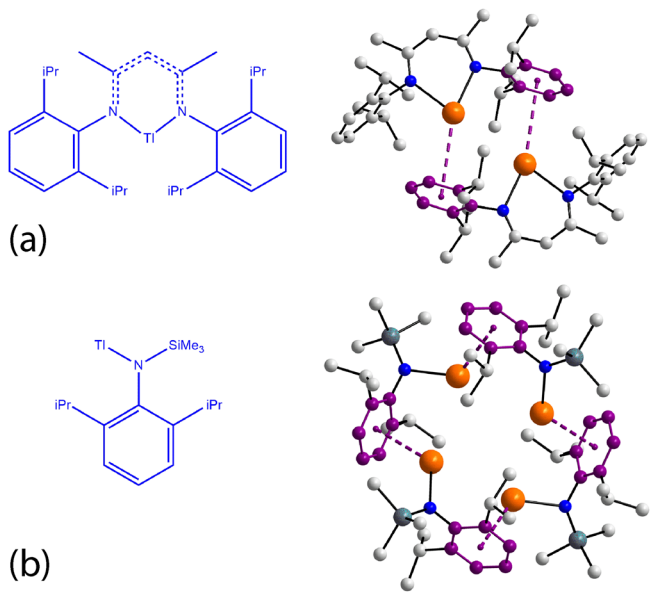

Figure 4.4 Chemical diagrams of (a) [2-(2′,6′-diisopropylphenylamido)-4-(2′,6′-diisopropylphenylimino)-2-pentene]thallium(I), (**3**), and (b) $Tl[N(SiMe_3)C_6H_3(iPr)_2\text{-}2,6]$, (**4**), and supramolecular aggregates sustained by Tl(lp)···π(arene) interactions. Additional colour code: hunter green, silicon; blue, nitrogen.

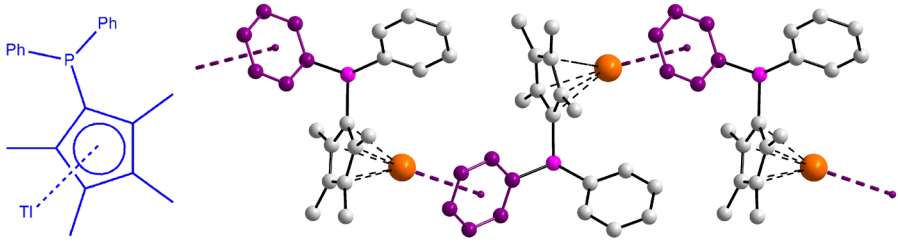

Figure 4.5 Chemical diagram of {(η^5-diphenylphosphanyl-tetramethyl-cyclopentadienyl)thallium(I), (**5**), and the supramolecular chain sustained by Tl(lp)···π(arene) interactions.

structure of Tl[N(SiMe$_3$)C$_6$H$_3$(iPr)$_2$-2,6],[44] (**4**), centrosymmetric tetranuclear aggregates involving both crystallographically independent molecules are formed and feature four Tl(lp)···π(arene) interactions [d = 3.11 Å and α = 11.7°; 3.12 Å, 9.6°], Figure 4.4(b).

One-dimensional aggregation is found for {(η^5-diphenylphosphanyl-tetramethyl-cyclopentadienyl)thallium(I),[45] (**5**), with each molecule accepting and donating a Tl(lp)···π(arene) interaction [d = 3.60 Å and α = 19.6°]. The topology of the chain is zigzag, Figure 4.5.

4.3.3 Tin(II)

The centrosymmetric dimeric motif features prominently among tin(II) compounds forming Sn(lp)···π(arene) interactions.[18] An example, [Sn{N(Ph)=C(Me)C(H)=C(Me)N(Ph)}Cl],[46] (**6**), where the pyramidal N$_2$Cl donor set is capped by an arene ring [d = 3.46 Å and α = 4.9°], is illustrated in Figure 4.6.

The mixed oxidation state tetranuclear compound, [{Sn(O$_2$CMe)$_2$}$_2$O]$_2$, crystallises as a mono-benzene solvate (**7**) with the benzene located about a two-fold axis of symmetry.[47] The exocyclic tin(II) atoms form Sn(lp)···π(arene) interactions [d = 3.32 Å and α = 6.1°] to generate a somewhat twisted supramolecular

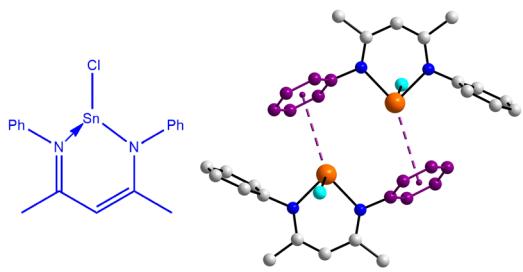

Figure 4.6 Chemical diagram of [Sn{N(Ph)=C(Me)C(H)=C(Me)N(Ph)}Cl], (**6**), and the supramolecular dimer sustained by Sn(lp)···π(arene) interactions.

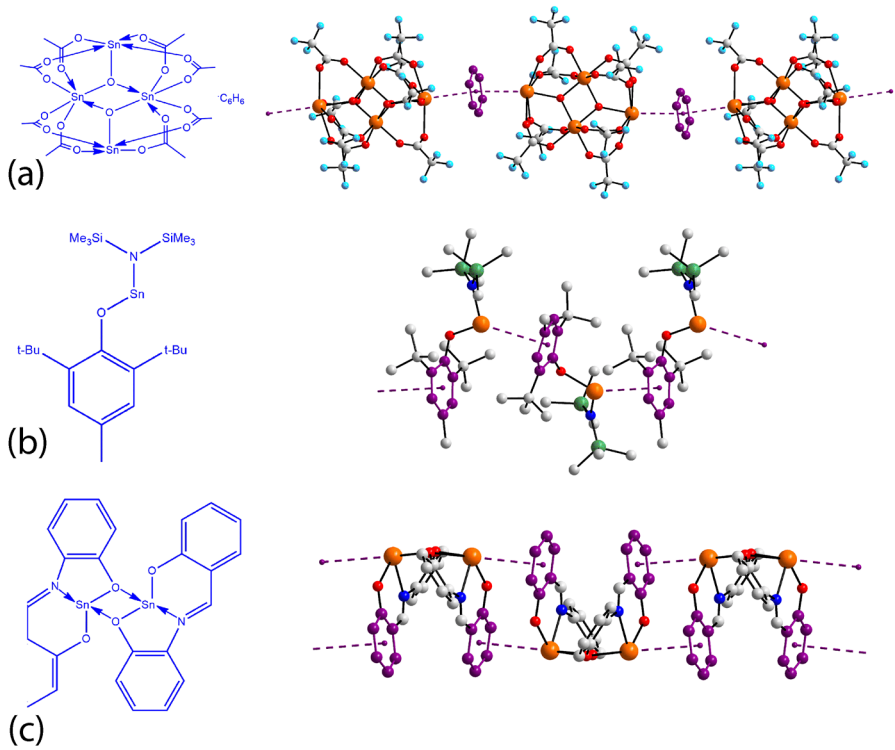

Figure 4.7 Chemical diagrams of (a) $[\{Sn(O_2CMe)_2\}_2O]_2{\cdot}C_6H_6$, (7), (b) $(Me_3Si)_2NSn[OC_6H_2(tBu_2)$-2,6-Me-4], (**8**), and (c) bis(μ_2-*N*-(2-oxidophenyl)salicylideneiminato)-di-tin(II), (**9**), and supramolecular chains sustained by Sn(lp)···π(arene) interactions.

chain, Figure 4.7(a). In $(Me_3Si)_2NSn[OC_6H_2(tBu_2)$-2,6-Me-4],[48] (**8**), with two-coordinate tin(II) atoms, a supramolecular zigzag chain is formed as shown in Figure 4.7(b) [d = 3.76 Å and α = 1.2°]. Binuclear bis(μ_2-*N*-(2-oxidophenyl) salicylideneiminato)-di-tin(II),[49] (**9**), has crystallographically imposed two-fold symmetry and features a tetra-coordinated tin(II) centre within a NO_3 donor set. The flat portions of centrosymmetrically-related molecules face each other to facilitate the formation of Sn(lp)···π(arene) interactions [d = 3.53 Å and α = 5.6°], with the two donor and two acceptor interactions per molecule leading to a supramolecular chain with a twisted topology, Figure 4.7(c).

4.3.4 Lead(II)

As mentioned above in Section 4.3.2, the zero-dimensional dimeric aggregate illustrated in Figure 4.4(a) is a common motif. A variation on this motif is found for $Pb(SC_6H_3Me_2$-2,6)$_2(NC_5H_4NMe_2$-4),[50] (**10**), where the dimeric aggregate sustained by two Pb(lp)···π(arene) interactions [d = 3.52 Å and α = 12.7°] has two-fold symmetry, Figure 4.8(a). The asymmetric unit of $Pb(C_6H_4Br$-4)$_2$,[51]

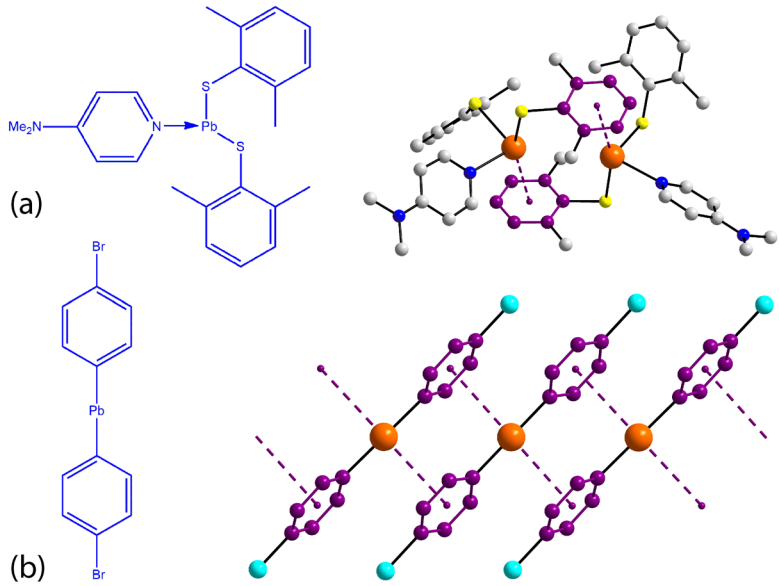

Figure 4.8 Chemical diagrams of (a) $Pb(SC_6H_3Me_2\text{-}2,6)_2(NC_5H_4NMe_2\text{-}4)$, (**10**), and (b) $Pb(C_6H_4Br\text{-}4)_2$, (**11**), and supramolecular aggregates sustained by Pb(lp)···π(arene) interactions.

(**11**), contains two independent molecules and each is located on a crystallographic centre of inversion. A linear supramolecular chain is formed as both independent lead(II) atoms form two apparent Pb(lp)···π(arene) interactions [d = 3.62 Å and α = 6.5°; d = 3.67 Å and α = 8.0°], Figure 4.8(b). The formation of two Pb(lp)···π(arene) interactions is perhaps unexpected and the nature of these still unclear. It is possible that the lone-pair of electrons is arranged spherically around the lead(II) centre. Another view is that one of the interactions is of the type Pb(lp)···π(arene) and the other is a transition metal-like π(arene)···Pb interaction.

The two-coordinate lead(II) atom in (*N*,*N*′-di-neopentyl-1,2-phenylenediamino)lead(II),[52] (**12**), lies on a crystallographic mirror plane. Again, each lead(II) atom forms two apparent Pb(lp)···π(arene) interactions with one being significantly longer than the other [d = 3.18 Å and α = 6.1°; d = 3.97 Å and α = 10.1°]. The arene ring accepts both interactions and the result is a two-dimensional arrangement as illustrated in Figure 4.9. The topology of the layer is flat with the neopentyl groups lying to either side.

4.3.5 Arsenic(III)

One-dimensional supramolecular chains sustained by As(lp)···π(arene) interactions are often observed in the crystal structures of arsenic(III) compounds.[20] An exception is found in the centrosymmetric dimeric aggregate in the structure of $[(2,6\text{-}Me_2C_6H_3N)AsCl]_3$,[53] (**13**), Figure 4.10(a) [d = 3.78 Å

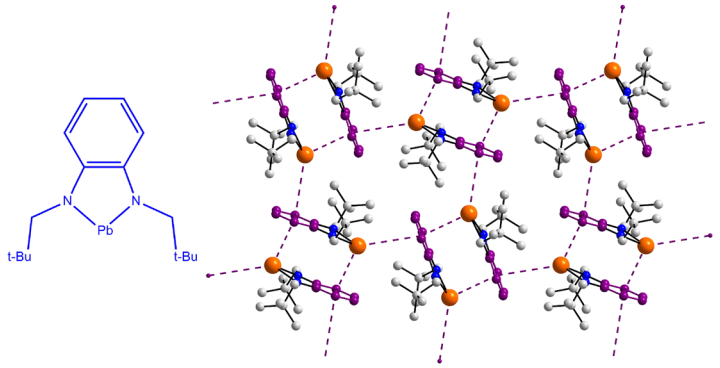

Figure 4.9 Chemical diagram of (*N*,*N*′-di-neopentyl-1,2-phenylenediamino)lead(II), (**12**), and the supramolecular layer sustained by Pb(lp)···π(arene) interactions.

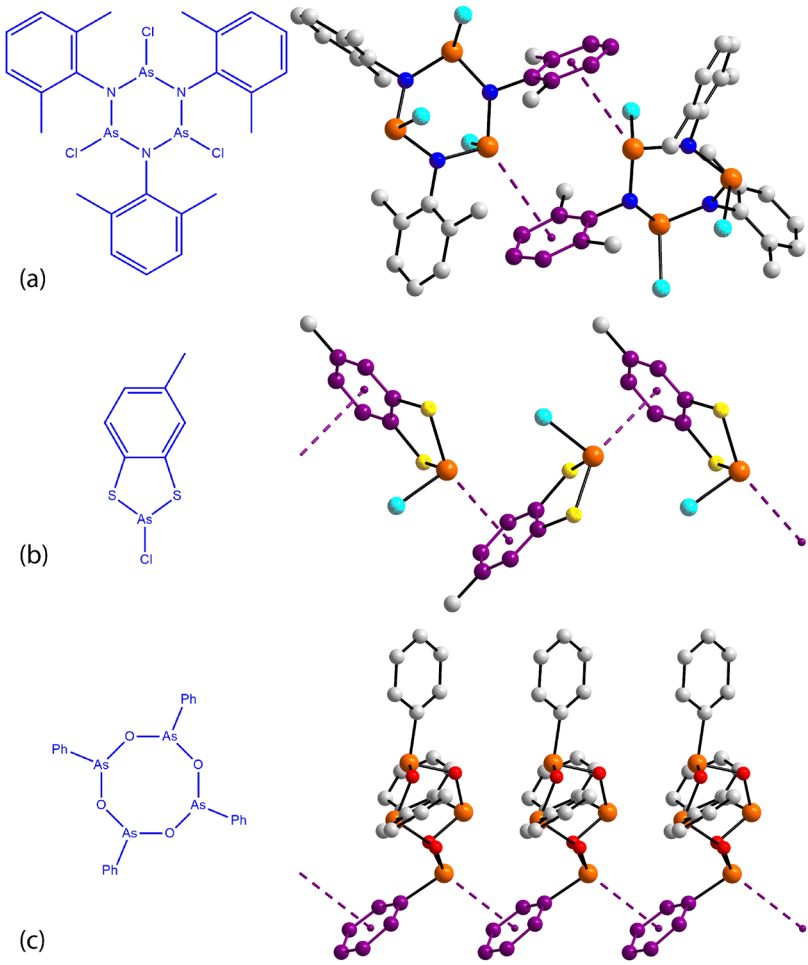

Figure 4.10 Chemical diagrams of (a) $[(2,6\text{-}Me_2C_6H_3N)AsCl]_3$, (**13**), (b) chloro-(toluene-3,4-dithiolato)arsenic(III), (**14**), and (c) $(PhAsO)_4$, (**15**), and supramolecular aggregates sustained by As(lp)···π(arene) interactions.

and α = 14.2°]. A truly remarkable supramolecular association is found in the structure of chloro-(toluene-3,4-dithiolato)arsenic(III),[54] (**14**), Figure 4.10(b). Here, the supramolecular chain, with a zigzag topology, is stabilised by As(lp)···π(arene) interactions [d = 3.30 Å and α = 3.6°]. This occurs despite there being both chloride and sulfur in the compound, each capable of forming As···Cl and/or As···S secondary interactions;[5] the closest As···Cl separation of 3.82 Å is beyond the sum of their respective van der Waals radii.[36] A supramolecular chain is also found in the structure of $(PhAsO)_4$,[55] (**15**). Here, only one of the four arsenic(III) atoms of the eight-membered ring compound forms As(lp)···π(arene) interactions [d = 3.52 Å and α = 11.8°]; the chain has a linear topology, Figure 4.10(c). The three examples mentioned here have the common feature of a pyramidal coordination geometry with a capping arene ring.

4.3.6 Antimony(III)

A full range of supramolecular architectures sustained by Sb(lp)···π(arene) interactions exists.[21] Zero-dimensional aggregates are well-known and are exemplified by dimeric and centrosymmetric (p-tol)$SbCl_2$,[56] (**16**), Figure 4.11(a) [d = 3.30 Å and α = 11.5°]. In dichloro-(8-(dimethylamino)naphthyl) antimony(III),[57] (**17**), a supramolecular chain with a helical topology is formed as a result of Sb(lp)···π(arene) interactions [d = 3.88 Å and α = 15.7°], Figure 4.11(b). A zigzag supramolecular chain is formed in the structure of $Sb(SC_6H_3Me_2\text{-}3,5)_3$,[58] (**18**), mediated by Sb(lp)···π(arene) interactions [d = 3.29 Å and α = 8.0°], Figure 4.11(c). As with the arsenic(III) structures cited above, no secondary Sb···S contacts are formed in the crystal structure of **18**.

A flat supramolecular layer with Sb(lp)···π(arene) interactions is found in the crystal structure of $[(t\text{-BuN})Sb(C_6H_3Me_2\text{-}2,6)]_2$,[59] (**19**), Figure 4.12. The four-membered cyclic molecule is disposed about a two-fold axis of symmetry. Each antimony(III) atom donates a lone-pair of electrons and each ring accepts an interaction, meaning four points of contact per molecule [d = 3.92 Å and α = 1.2°] contributing to the layer assembly.

4.3.7 Bismuth(III)

A wide range of zero-dimensional aggregates sustained by Bi(lp)···π(arene) interactions have been noted.[21] Centrosymmetric dimeric units are found in the structure of bis-[2-(dimethylaminomethyl)phenyl]-iodido-bismuth(III), (**20**),[60] Figure 4.13(a) [d = 3.92 Å and α = 18.4°]. A higher nuclearity aggregate is found in (2.2.2)paracyclophane tris[trichlorido-bismuth(III)],[61] (**21**), in which each arene ring accepts a Bi(lp)···π(arene) interaction. As the molecule lacks symmetry, there are three independent contacts [d = 2.98 Å and α = 10.5°; d = 2.99 Å, α = 5.6°; d = 3.08 Å, α = 3.5°], Figure 4.13(b).

Examples of linear and helical supramolecular chains are found in the crystal structures of Ph_3Bi,[62] (**22**), and $Bi(OC_6H_3Me_2\text{-}2,6)_3$,[63] (**23**), respectively, Figure 4.14(a) and (b). Each molecule of each chain participates in an

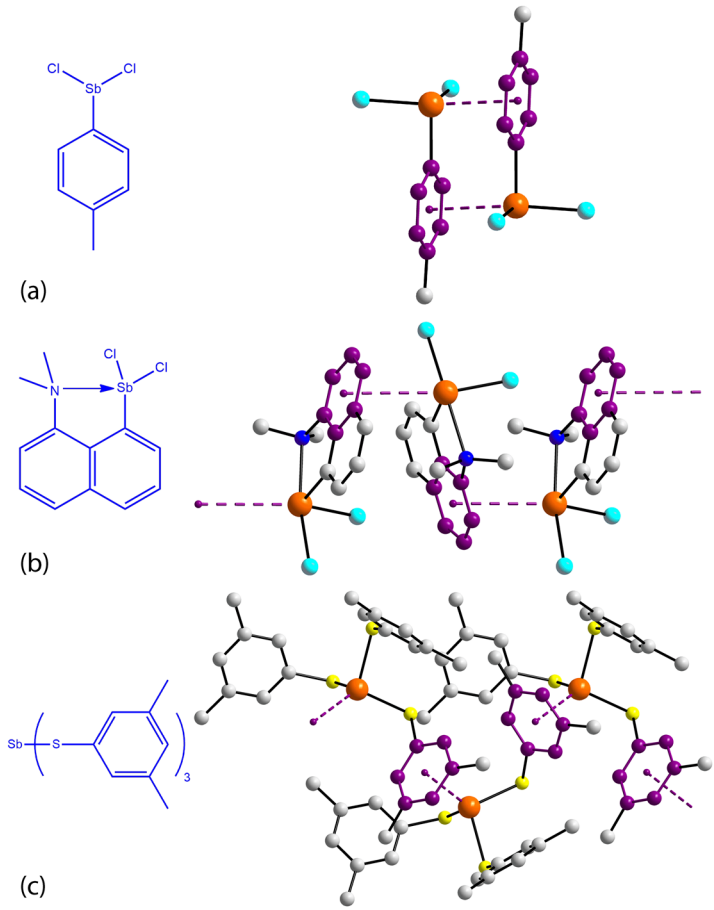

Figure 4.11 Chemical diagrams of (a) (*p*-tol)$SbCl_2$, (**16**), (b) dichloro-(8-(dimethylamino)naphthyl)antimony(III), (**17**), and (c) $Sb(SC_6H_3Me_2\text{-}3,5)_3$, (**18**), and supramolecular aggregates sustained by Sb(lp)···π(arene) interactions.

acceptor and donor Bi(lp)···π(arene) interaction [**22:** d = 3.76 Å and α = 11.0°; **23:** d = 2.99 Å, α = 3.3°].

In a compound closely related to **19** (see Figure 4.12), *i.e.* [(*t*-BuN)BiPh]$_2$,[64] (**24**), the centrosymmetric binuclear molecules participate in four Bi(lp)···π(arene) interactions [d = 3.92 Å and α = 10.1°] to form a supramolecular layer with a flat topology, Figure 4.15.

4.3.8 Selenium(II, IV)

The familiar zero-dimensional dimeric aggregate is found in the structure of the $[MeSeC(=CH_2)CH_2N^+(H)Me_2]$ cation,[65] (**25**), with the exception being there is no crystallographic symmetry relating the molecules so there are

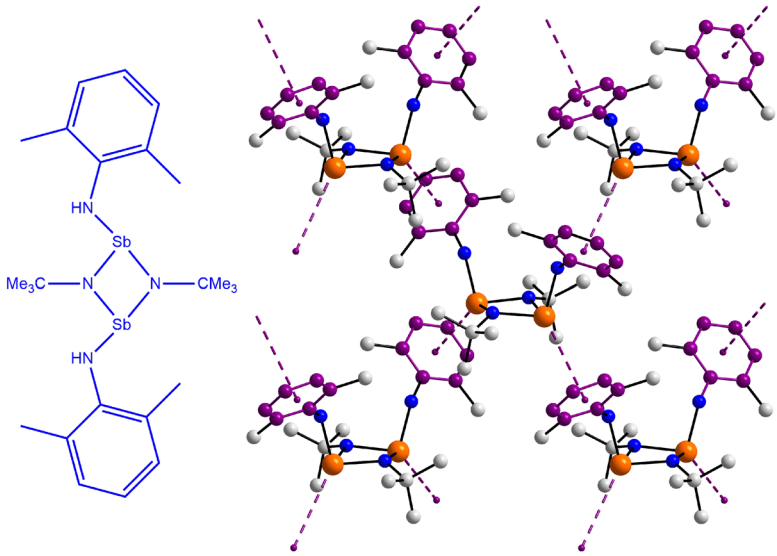

Figure 4.12 Chemical diagram of $[(t\text{-BuN})Sb(C_6H_3Me_2\text{-}2,6)]_2$, (**19**), and the supramolecular layer sustained by Sb(lp)···π(arene) interactions.

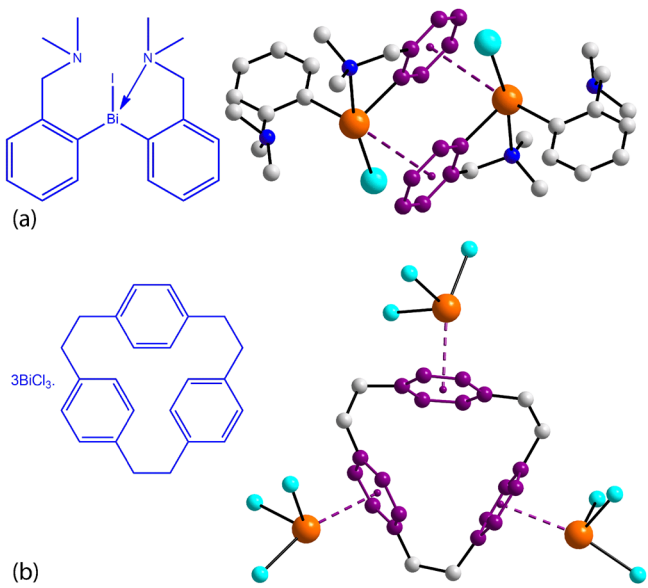

Figure 4.13 Chemical diagrams of (a) bis-[2-(dimethylaminomethyl)phenyl]-iodido-bismuth(III), (**20**), and (b) (2.2.2)paracyclophane tris[trichlorido-bismuth(III)], (**21**), and their supramolecular aggregates sustained by Bi(lp)···π(arene) interactions.

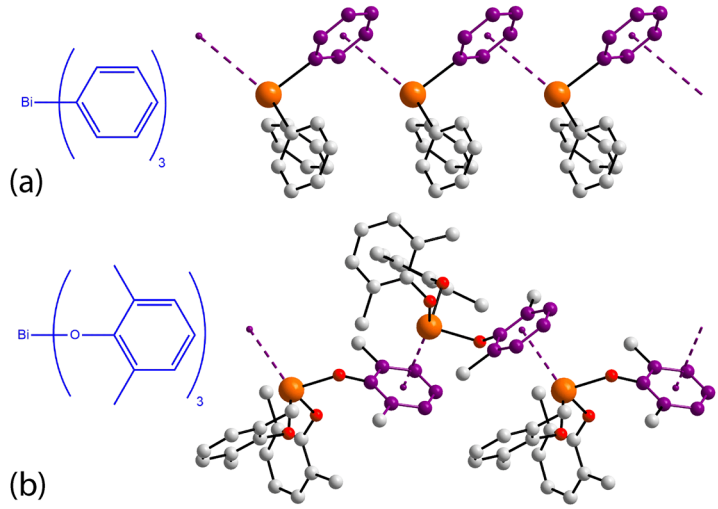

Figure 4.14 Chemical diagrams of (a) Ph_3Bi, (**22**), and (b) $Bi(OC_6H_3Me_2\text{-}2,6)_3$, (**23**), and their supramolecular chains sustained by Bi(lp)···π(arene) interactions.

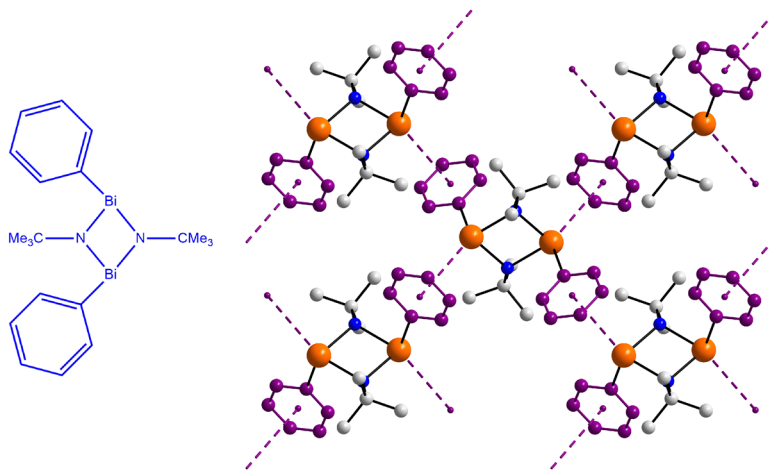

Figure 4.15 Chemical diagram of $[(t\text{-BuN})BiPh]_2$, (**24**), and the supramolecular layer sustained by Bi(lp)···π(arene) interactions.

two independent Se(lp)···π(arene) interactions supporting the aggregate, Figure 4.16(a). The parameters describing these interactions are equivalent, *i.e.* d = 3.82 Å and α = 26.5°, suggesting a pseudo centrosymmetric arrangement. The selenium(II) atom may be embedded within a ring, as in 5-phenyl-selenazolidine-2,4-dione,[66] (**26**), and still form a Se(lp)···π(arene) interaction. In the case of **26**, this interaction [d = 3.53 Å and α = 4.6°]

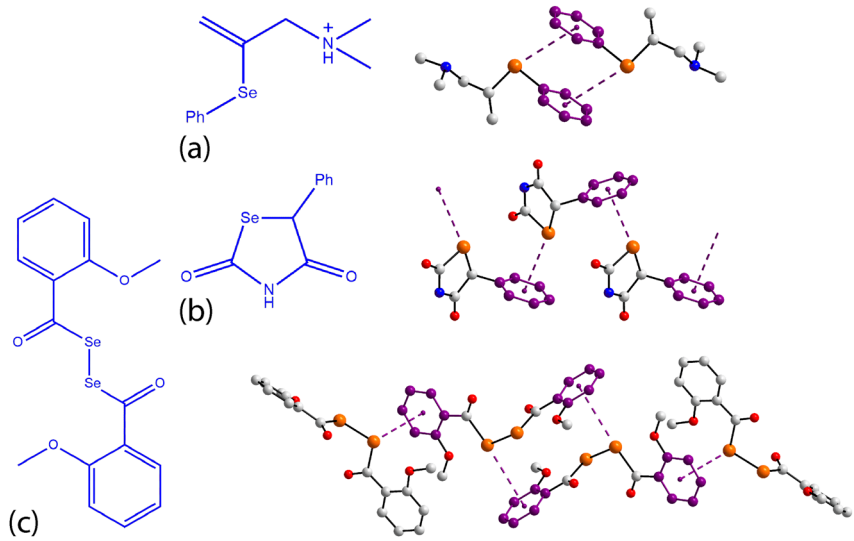

Figure 4.16 Chemical diagrams of (a) [MeSeC(=CH_2)CH_2N^+(H)Me_2], (**25**), (b) 5-phenyl-selenazolidine-2,4-dione, (**26**), and (c) [2-$MeOC_6H_4C$(=O)Se]$_2$, (**27**), and their supramolecular aggregates sustained by Se(lp)···π(arene) interactions.

results in a supramolecular chain with a helical topology, Figure 4.16(b). An example of an unusual aggregate results when the selenium atoms are directly connected as in the diselenide derivative [2-$MeOC_6H_4C$(=O)Se]$_2$,[67] (**27**). There are two independent diselenide molecules in the crystallographic asymmetric unit. One selenium(II) atom in each molecule forms a Se(lp)···π(arene) interaction [d = 3.90 Å and α = 26.4°; d = 3.93 Å and α = 12.7°]. The shorter interactions occur between centrosymmetrically-related molecules, and the resulting dimeric aggregate accepts two Se(lp)···π(arene) interactions from a second set of symmetry-related independent molecules with the result that a four-molecular aggregate is formed, Figure 4.16(c). Viewed from another perspective, both arene rings of one independent molecule participate in Se(lp)···π(arene) interactions while the arene rings of the second molecule participate in no such interactions.

In binuclear molecules where the selenium atoms are well separated, if each participates in a Se(lp)···π(arene) interaction, higher aggregation patterns will ensue. This is realised in the structure of [PhSe(Cl)C=C(Cl)SePh],[68] (**28**). Here, the molecule is centrosymmetric, and forms two interactions [d = 3.80 Å and α = 24.4°] resulting in a linear supramolecular chain, Figure 4.17(a). A variation is found in the structure 1,2,4,5-tetrafluoro-3,6-bis(phenylseleno) benzene,[69] (**29**), for which two independent molecules comprise the crystallographic asymmetric unit, each of which is disposed about a centre of inversion. Only one of the molecules forms Se(lp)···π(arene) interactions [d = 3.99 Å

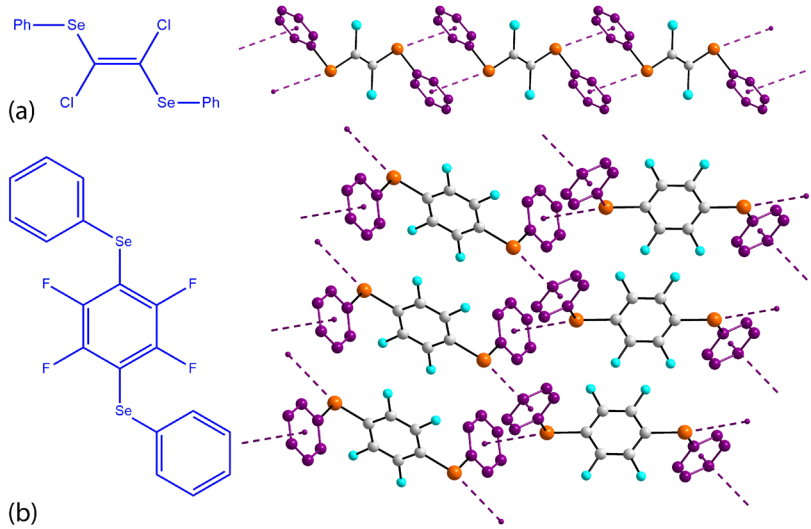

Figure 4.17 Chemical diagrams of (a) [PhSe(Cl)C=C(Cl)SePh], (**28**), and (b) 1,2,4,5-tetrafluoro-3,6-bis(phenylseleno)benzene, (**29**), and their supramolecular aggregates sustained by Se(lp)···π(arene) interactions.

and α = 27.2°] to lead to a supramolecular layer with a flat topology, Figure 4.17(b).

Selenium in the form of doubly-bonded selenide can also form Se(lp)···π(arene) interactions. An example of this is found in the structure of 2-phenyl-2,3-dihydro-1,3,2-benzothiazaphosphole 2-selenide,[70] (**30**), with the interactions [d = 3.52 Å and α = 17.6°] leading to a zigzag supramolecular chain, Figure 4.18(a). Se(lp)···π(arene) interactions have been found to occur between charged species as for example in the bicyclic salt $[Ph_4P]_2[As_4Se_6]$,[71] (**31**). As shown in Figure 4.18(b), two selenium(II) atoms form Se(lp)···π(arene) interactions [d = 3.63 Å and α = 11.6°; d = 3.96 Å and α = 22.6°], bridging one of the independent Ph_4P^+ anions to form a linear supramolecular chain.

Selenium(IV), with one lone-pair of electrons, rather than the two found in selenium(II) compounds, can also form Se(lp)···π(arene) interactions. This is illustrated for PhSe(=O)OH,[72] (**32**), where these interactions [d = 3.50 Å and α = 17.2°] lead to linear supramolecular chains, Figure 4.18(c).

The final compound to be discussed in this section is also a salt, namely $[PhN^+Me_3][SeBr_4]\{2[Se_2Br_2]\cdot 2Br^-\}$,[73] (**33**), bearing both selenium(II) and selenium(IV) centres. The selenium(IV) atom, located on a crystallographic centre of inversion, is coordinatively saturated precluding its participation in Se(lp)···π(arene) interactions. One of the selenium(II) atoms forms two independent Se(lp)···π(arene) interactions [d = 3.51 Å and α = 4.7°; d = 3.93 Å and α = 25.1°] with the same arene ring to form a flat supramolecular layer, Figure 4.19.

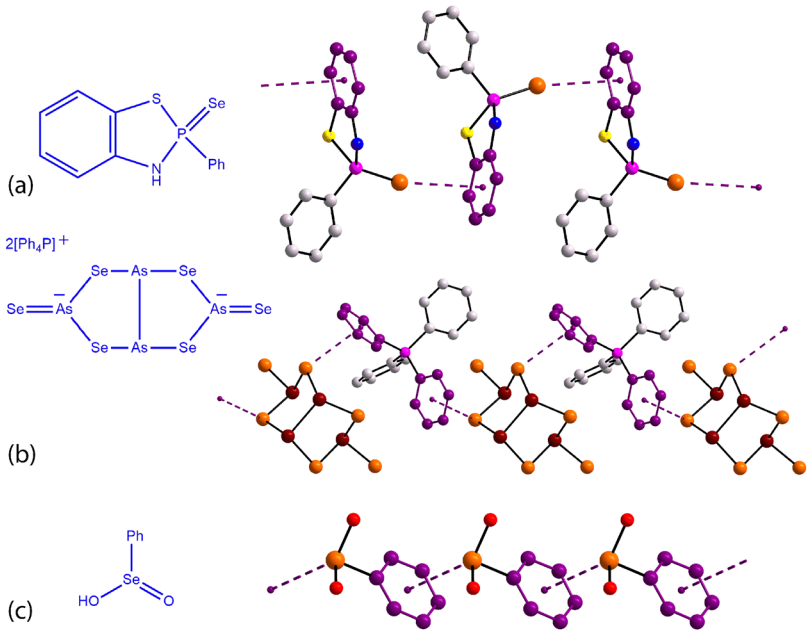

Figure 4.18 Chemical diagrams of (a) 2-phenyl-2,3-dihydro-1,3,2-benzothiazaphosphole 2-selenide, (**30**), (b) $[Ph_4P]_2[As_4Se_6]$, (**31**), and (c) PhSe(=O)OH, (**32**), and their supramolecular chains sustained by Se(lp)···π(arene) interactions.

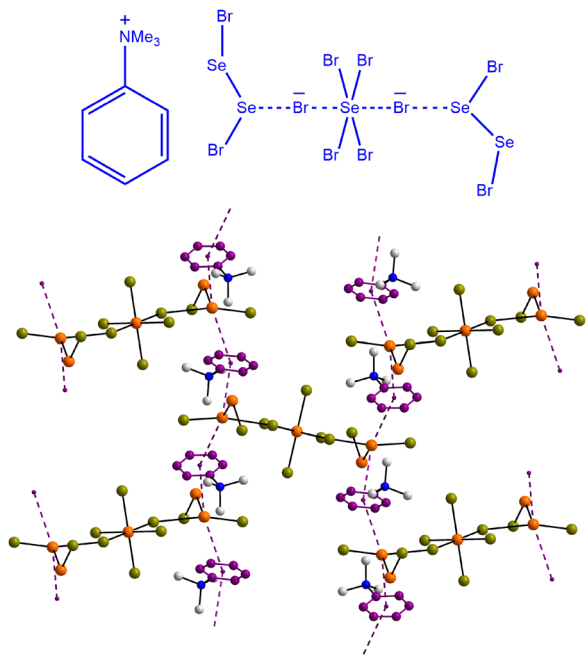

Figure 4.19 Chemical diagram of $[PhN^+Me_3][SeBr_4]\{2[Se_2Br_2]\cdot 2Br^-\}$, (**33**), and the supramolecular layer sustained by Se(lp)···π(arene) interactions.

4.3.9 Tellurium(II, IV)

Despite not being isomorphous, the supramolecular aggregation sustained by Te(lp)···π(arene) interactions in the crystal structure of [PhTeC(Cl)=C(Cl)TePh],[74] (**34**), matches that of the selenium(II) analogue, *i.e.* **28**, Figure 4.17(a). The Te(lp)···π(arene) interactions [d = 3.76 Å and α = 12.4°] lead to a linear supramolecular chain as shown in Figure 4.20.

A rare example of a three-dimensional architecture sustained by M(lp)···π(arene) interactions is found in the structure of [4-ClC_6H_4Te-$TeC_6H_4Cl_4$-4],[75] (**35**), Figure 4.21. The ditelluride molecule lacks symmetry but each tellurium(II) atom forms a Te(lp)···π(arene) interaction [d = 3.67 Å and α = 9.5°; d = 3.81 Å and α = 19.6°]. The molecule has the approximate shape of the letter L with four points of contact involving Te(lp)···π(arene) interactions resulting in the stabilisation of a three-dimensional structure.

The final three structures to be described feature tellurium(IV) centres. The centrosymmetric dimeric aggregate motif is found in the crystal structure of (4-$MeOC_6H_4$)Te[(Ph)C=C(H)SPh]Cl_2,[76] (**36**), Figure 4.22(a), stabilised by Te(lp)···π(arene) interactions [d = 3.41 Å and α = 0.9°]. Another example of a supramolecular aggregate sustained by Te(lp)···π(arene) interactions is the zigzag chain in the crystal structure of $[Ph(Cl)C{=}CH]_2TeCl_2$,[77] (**37**), Figure 4.22(b); [d = 3.76 Å and α = 12.4°].

The last structure to be described poses a dilemma in the assignment of the putative Te(lp)···π(arene) interactions akin to that noted in the structures of $Pb(C_6H_4Br\text{-}4)_2$,[51] (**11**), Figure 4.8(b), and (*N*,*N*′-di-neopentyl-1,2-phenylenediamino)lead(II),[52] (**12**), Figure 4.9. The tellurium(IV) centre in bis(2,2′-biphenylylene)-tellurium(IV),[78] (**38**), forms two almost identical interactions with two arene rings as illustrated in Figure 4.22(c). The parameters associated with these interactions are d = 3.72 Å and α = 11.1°, and d = 3.72 Å and α = 11.6°. The resulting assembly is a supramolecular linear chain.

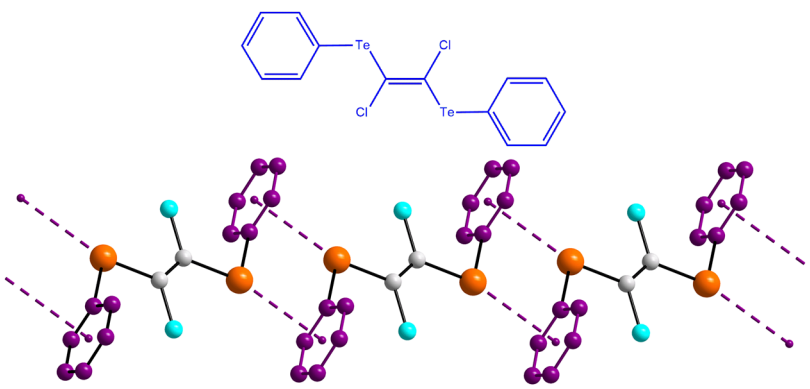

Figure 4.20 Chemical diagram of [PhTeC(Cl)=C(Cl)TePh], (**34**), and the supramolecular chain sustained by Te(lp)···π(arene) interactions.

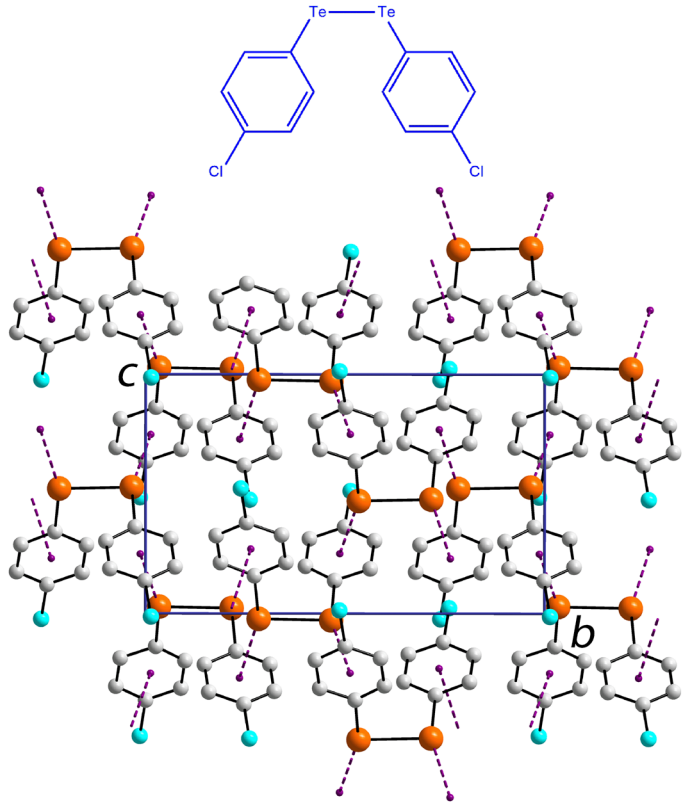

Figure 4.21 Chemical diagram of [4-$ClC_6H_4TeTeC_6H_4Cl_4$-4], (**35**), and a view of the three-dimensional supramolecular architecture sustained by Te(lp)···π(arene) interactions.

4.4 Biological Relevance

While the recognition of M(lp)···π(arene) interactions in main group element systems is a relatively recent phenomenon, it is likely that the first report of such an interaction was in the macromolecular literature.[79] Referring to Figure 4.23, the cytidine-sugar oxygen atom, O4′, interacts with the pyrimidine ring of a guanine residue, *i.e.* representing an O(lp)···π(pyrimidine) interaction similar to the M(lp)···π(arene) interactions described. By contrast to many of the structural papers on molecular main group element chemistry, the original authors of this work highlighted the role of the O(lp)···π(pyridimidine) interactions as being important in stabilising the Z-DNA conformation.[79] In several of the previous surveys of M(lp)···π(arene) interactions, analogous interactions operating in macromolecular systems were also noted.[17,21,22]

While a comprehensive survey of M(lp)···π(arene) interactions in macromolecular structures is not appropriate here, one structure is particularly

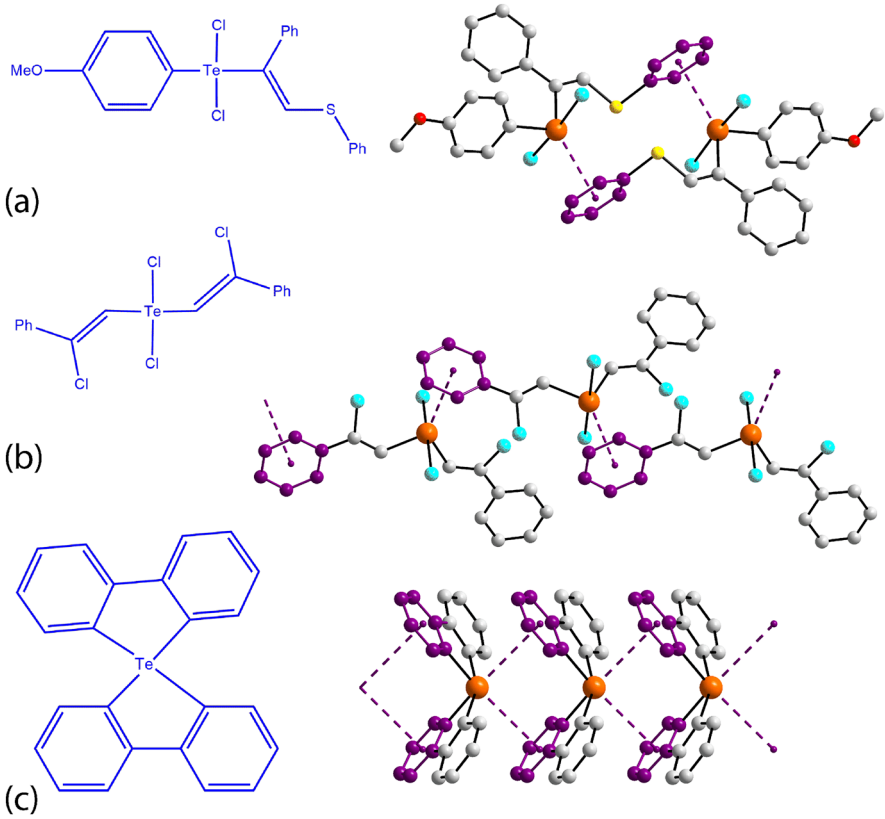

Figure 4.22 Chemical diagrams of (a) (4-MeOC$_6$H$_4$)Te[(Ph)C=C(H)SPh]Cl$_2$, (**36**), (b) [Ph(Cl)C=CH]$_2$TeCl$_2$, (**37**), and (c) bis(2,2′-biphenylylene)-tellurium(IV), (**38**), and their supramolecular aggregates sustained by Te(lp)···π(arene) interactions.

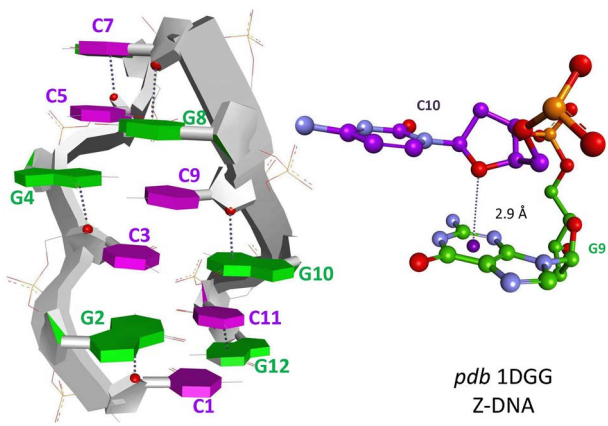

Figure 4.23 Images highlighting the O(lp)···π(ring) interaction between the cytidine-sugar-O(lp) and the pyrimidine ring of a guanine residue in left-handed Z-DNA.

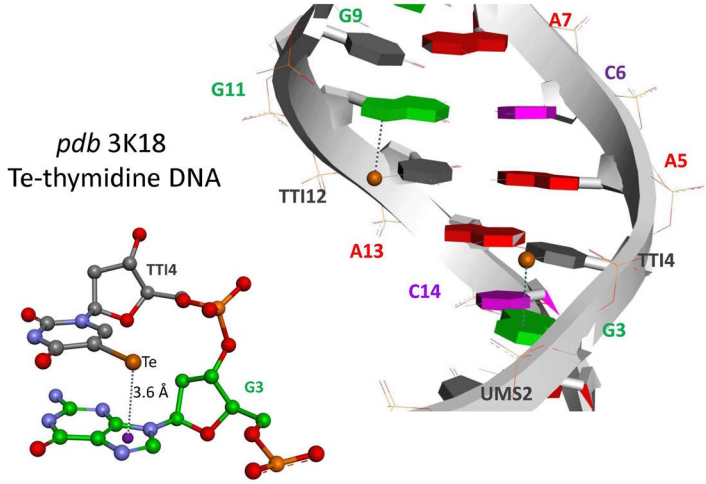

Figure 4.24 Images highlighting the Te(lp)···π(ring) interaction of a doubly-bonded telluride atom interacting with the five-membered ring of a guanidine ring.

worth highlighting. As shown in Figure 4.24, an interaction of a telluride atom incorporated within the five-membered ring of a guanidine residue occurs in a synthetic oligonucleotide.[80] This Te(lp)···π(arene) [d = 3.56 Å and α = 12.7°] interaction does not have a precedent in the molecular chemistry of tellurium; selenium examples are known, however; see Section 4.3.8.

4.5 Conclusions and Outlook

The foregoing discussion indicates that M(lp)···π(arene) interactions exercise a very real role in the supramolecular chemistry of the main group elements, leading to well-defined zero-, one- and more rarely, two- and three-dimensional supramolecular assemblies.[16–22] Thallium(I) compounds are the most likely to form these types of interactions, being found in nearly 14% of thallium(I)-containing structures. This number is greater than the 9% probability for bismuth(III) to form Bi(lp)···π(arene) interactions which in turn is higher than 6% for antimony(III), selenium(II, IV) and tellurium(II, IV) compounds. The least likely elements to form M(lp)···π(arene) interactions are arsenic(III) (4%), and tin(II) and lead(II) (2–3%) compounds. As noted previously,[16–22] no correlations exist between d and α. In some bismuth(III) series of compounds, systematic variations in d were successfully correlated to differences in electronegativity of bismuth(III) centres as well as the π-systems.[21]

A complete theoretical understanding of M(lp)···π(arene) interactions is a work in progress. However, there appears to be some consensus that the attributes leading to halogen bonding may be relevant in this context. Thus, there is polarity in the electron distribution of the lone-pair of electrons so that there is an electron deficiency at the tip of the lone-pair of electrons and a build-up of

electron density around the girth. The electron-rich π-system thereby interacts with the electropositive region at the tip of the lone-pair.[81,82] However, as noted in the Introduction, dispersion-corrected DFT calculations reveal that these interactions may be sometimes described as donor(π)–acceptor(As) interactions,[25] consistent with the aforementioned "additional" contacts mentioned for (**11**),[51] (**12**)[52] and (**38**).[78] The latter observations indicate more theoretical work is required to fully appreciate the nature of these interactions.

Clearly, M(lp)···π(arene) interactions may participate in the stabilisation of crystal structures and their presence should be identified during any crystal structure analysis. Future work will be devoted to fully understanding the chemical nature of the bonding behind these interactions, investigation of the relative importance of semi-localised and localised M(lp)···π(arene) interactions, and expanding the range of aromatic systems that can participate in M(lp)···π(arene) interactions, perhaps being inspired by macromolecular structures.

Acknowledgements

The Brazilian National Council for Scientific and Technological Development-CNPq (305626/2013-2 to JZS; 306121/2013-2 to IC) and CAPES are acknowledged for financial support.

References

1. J.-M. Lehn, *Supramolecular Chemistry. Concepts and Perspectives*, VCH, Weinheim, 1995.
2. (a) S. Simard, D. Su and J. D. Wuest, *J. Am. Chem. Soc.*, 1991, **113**, 4696; (b) M. C. T. Fyfe and J. F. Stoddart, *Acc. Chem. Res.*, 1997, **30**, 393.
3. (a) C. B. Aäkeroy, A. M. Beatty and D. S. Leinen, *Angew. Chem., Int. Ed.*, 1999, **38**, 1815; (b) A. M. Beatty, *CrystEngComm*, 2001, **3**, 1; (c) D. Braga, F. Grepioni and G. R. Desiraju, *Chem. Rev.*, 1998, **98**, 1375; (d) D. Braga and F. Grepioni, *Coord. Chem. Rev.*, 1999, **183**, 19.
4. (a) M. Fujita, *Chem. Soc. Rev.*, 1998, **27**, 417; (b) A. J. Blake, N. R. Champness, P. Hubberstey, W. S. Li, A. Withersby and M. Schröder, *Coord. Chem. Rev.*, 1999, **183**, 117; (c) J. A. R. Navarro and B. Lippert, *Coord. Chem. Rev.*, 1999, **185/186**, 653; (d) S. Leininger, B. Olenyuk and P. J. Stang, *Chem. Rev.*, 2000, **100**, 853; (e) R. Robson and J. Chem. Soc., *Dalton Trans.*, 2000, 3735; (f) M. J. Zaworotko, *Chem. Commun.*, 2001, 1.
5. (a) N. W. Alcock, *Adv. Inorg. Chem. Radiochem.*, 1972, **15**, 1; (b) I. Haiduc, in *Encyclopedia of Supramolecular Chemistry*, ed. J. Steed and J. Atwood, M. Dekker, Inc., New York, 2004, p. 1224.
6. (a) P. Metrangolo, F. Meyer, T. Pilati, G. Resnati and G. Terraneo, *Angew. Chem., Int. Ed.*, 2008, **47**, 6114; (b) G. Berger, J. Soubhye, A. van der Lee, C. Van de Velde, R. Wintjens, P. Dubois, S. Clément and F. Meyer, *ChemPlusChem*, 2014, **79**, 5529.

7. (a) C. Janiak and J. Chem. Soc., *Dalton Trans.*, 2000, 3885; (b) D. B. Amabilino and J. F. Stoddart, *Chem. Rev.*, 1995, **95**, 2725.
8. I. Haiduc and F. T. Edelmann, *Supramolecular Organometallic Chemistry*, Wiley-VCH, Weinheim, New York, 1999.
9. H. Schmidbaur and A. Schier, *Organometallics*, 2008, **27**, 2361.
10. J. L. Lefferts, K. C. Molloy, M. B. Hossain, D. van der Helm and J. J. Zuckerman, *Inorg. Chem.*, 1982, **21**, 1410.
11. I. P. Gray, A. M. Z. Slawin and J. D. Woollins, *Dalton Trans.*, 2004, 2477.
12. J. Zukerman-Schpector and I. Haiduc, *Phosphorus, Sulfur Silicon*, 2001, **171**, 73.
13. C. R. Groom and F. H. Allen, *Angew. Chem., Int. Ed.*, 2014, **53**, 662.
14. J. Zukerman-Schpector and I. Haiduc, *CrystEngComm*, 2002, **4**, 178.
15. I. Haiduc, E. R. T. Tiekink and J. Zukerman-Schpector, in *The Importance of Pi-Interactions in Crystal Engineering, Frontiers in Crystal Engineering*, ed. E. R. T. Tiekink and J. Zukerman-Schpector, John Wiley & Sons, Ltd., New York, 2012, p. 301.
16. E. R. T. Tiekink and J. Zukerman-Schpector, *CrystEngComm*, 2009, **11**, 2701.
17. I. Caracelli, I. Haiduc, J. Zukerman-Schpector and E. R. T. Tiekink, *Coord. Chem. Rev.*, 2014, **281**, 50.
18. I. Haiduc, E. R. T. Tiekink and J. Zukerman-Schpector, in *Tin Chemistry – Fundamentals, Frontiers and Applications*, ed. A. G. Davies, M. Gielen, K. H. Pannell and E. R. T. Tiekink, John Wiley & Sons, Ltd., Chichester, 2008, p. 392.
19. E. R. T. Tiekink and J. Zukerman-Schpector, *Aust. J. Chem.*, 2010, **63**, 535.
20. J. Zukerman-Schpector, A. Otero-de-la-Roza, V. Luaña and E. R. T. Tiekink, *Chem. Commun.*, 2011, **47**, 7608.
21. I. Caracelli, I. Haiduc, J. Zukerman-Schpector and E. R. T. Tiekink, *Coord. Chem. Rev.*, 2013, **257**, 2863.
22. I. Caracelli, I. Haiduc, J. Zukerman-Schpector and E. R. T. Tiekink, in *The Chemistry of Organic Selenium and Tellurium Compounds*, ed.Zvi Rappoport, John Wiley & Sons, Ltd., Chichester, 2013, p. 973.
23. (a) J. Zukerman-Schpector, I. Haiduc and E. R. T. Tiekink, *Chem. Commun.*, 2011, **47**, 12682; (b) J. Zukerman-Schpector, I. Haiduc and E. R. T. Tiekink, in *Advances in Organometallic Chemistry*, ed. A. F. Hill and M. J. Fink, Academic Press, Burlington, 2012, vol. 60, p. 49.
24. J. Zukerman-Schpector and E. R. T. Tiekink, *CrystEngComm*, 2014, **16**, 6398.
25. A. Otero-de-la-Roza, V. Luaña, E. R. T. Tiekink and J. Zukerman-Schpector, *J. Chem. Theory Comput.*, 2014, **10**, 5010.
26. G. Cavallo, P. Metrangolo, R. Milani, T. Pilati, A. Priimagi, G. Resnati and G. Terraneo, *Chem. Rev.*, 2016, **116**, 2478.
27. A. F. Cozzolino, P. J. W. Elder and I. Vargas-Baca, *Coord. Chem. Rev.*, 2011, **255**, 1426.
28. (a) M. M. Watt, M. S. Collins and D. W. Johnson, *Acc. Chem. Res.*, 2013, **46**, 955; (b) P. Gamez, T. J. Mooibroek, S. J. Teat and J. Reedijk, *Acc. Chem. Res.*, 2007, **40**, 435.

29. (a) B. P. Hay and R. Custelcean, *Cryst. Growth Des.*, 2009, **9**, 2539; (b) P. Gamez, *Inorg. Chem. Front.*, 2014, **1**, 35; (c) D.-X. Wang and M.-X. Wang, *J. Am. Chem. Soc.*, 2012, **135**, 892; (d) M. Giese, M. Albrecht and K. Rissanen, *Chem. Commun.*, 2016, **52**, 1778; (e) O. B. Berryman, V. S. Bryantsev, D. P. Stay, D. W. Johnson and B. P. Hay, *J. Am. Chem. Soc.*, 2007, **129**, 48; (f) H. T. Chifotides and K. R. Dunbar, *Acc. Chem. Res.*, 2013, **46**, 894.
30. (a) J. C. Ma and D. A. Dougherty, *Chem. Rev.*, 1997, **97**, 1303; (b) T. C. Dinadayalane, D. Afanasiev and J. Leszczynski, *J. Phys. Chem. A*, 2008, **112**, 7916.
31. (a) B. W. Gung, Y. Zou, Z. Xu, J. C. Amicangelo, D. G. Irwin, S. Ma and H.-C. Zhou, *J. Org. Chem.*, 2008, **73**, 689; (b) J. C. Amicangelo, D. G. Irwin, C. J. Lee, N. C. Romano and N. L. Saxton, *J. Phys. Chem. A*, 2013, **117**, 1336.
32. E. R. T. Tiekink and J. Zukerman-Schpector, *Chem. Commun.*, 2011, **47**, 6623.
33. (a) C. I. Yeo, S. N. A. Halim, S. W. Ng, L. T. Seng, J. Zukerman-Schpector, M. A. B. Ferreira and E. R. T. Tiekink, *Chem. Commun.*, 2014, **50**, 5984; (b) J. Zukerman-Schpector, C. I. Yeo and E. R. T. Tiekink, *Z. Kristallogr.*, 2016, **231**, 55.
34. (a) R. Miao, G. Yang, C. Zhao, J. Hong and L. Zhu, *J. Mol. Struct.: THEOCHEM*, 2005, **715**, 91; (b) H. Zhuo, Q. Li, W. Li and J. Cheng, *Phys. Chem. Chem. Phys.*, 2014, **16**, 159.
35. I. J. Bruno, J. C. Cole, P. R. Edgington, M. Kessler, C. F. Macrae, P. McCabe, J. Pearson and R. Taylor, *Acta Crystallogr.*, 2002, **B58**, 389.
36. A. Bondi, *J. Phys. Chem.*, 1964, **68**, 441.
37. A. Mukherjee and G. R. Desiraju, *IUCrJ*, 2014, **1**, 49.
38. (a) D. Schollmeyer, O. V. Shishkin, T. Rühl and M. O. Vysotsky, *CrystEngComm*, 2008, **10**, 715; (b) O. V. Shishkin, *Chem. Phys. Lett.*, 2008, **458**, 96.
39. A. L. Spek, *J. Appl. Crystallogr.*, 2003, **36**, 7.
40. K. Brandenburg, *DIAMOND. Visual Crystal Structure Information System, version 3.1*, Crystal Impact, Bonn, Germany, 2006.
41. C. Jones and A. Stash, in *The Group 13 Metals Aluminium, Gallium, Indium and Thallium. Chemical Patterns and Peculiarities*, ed. S. Aldridge and A. J. Down, John Wiley & Sons, Chichester, 2011, p. 285.
42. M. Scholz, M. Noltemeyer and H. W. Roesky, *Angew. Chem., Int. Ed.*, 1989, **28**, 1383.
43. M. S. Hill, P. B. Hitchcock and R. Pongtavornpinyo, *Dalton Trans.*, 2005, 273.
44. S. D. Waezsada, T. Belgardt, M. Noltemeyer and H. W. Roesky, *Angew. Chem., Int. Ed.*, 1994, **33**, 1351.
45. H. Schumann, T. Ghodsi, L. Esser and E. Hahn, *Chem. Ber.*, 1993, **126**, 591.
46. A. Akkari, J. J. Byrne, I. Saur, G. Rima, H. Gornitzka and J. Barrau, *J. Organomet. Chem.*, 2001, **622**, 190.
47. T. Birchall and J. P. Johnson, *J. Chem. Soc., Dalton Trans.*, 1981, 69.
48. H. Braunschweig, R. W. Chorley, P. B. Hitchcock and M. F. Lappert, *Chem. Commun.*, 1992, 1311.

49. A. M. van den Bergen, J. D. Cashion, G. D. Fallon and B. O. West, *Aust. J. Chem.*, 1990, **43**, 1559.
50. G. G. Briand, A. D. Smith, G. Schatte, A. J. Rossini and R. W. Schurko, *Inorg. Chem.*, 2007, **46**, 8625.
51. M. B. Hursthouse, D. E. Hibbs and M. Moloney, Private Communication to CSD, 2003.
52. F. E. Hahn, D. Heitmann and T. Pape, *Eur. J. Inorg. Chem.*, 2008, 1039.
53. N. Burford, J. C. Landry, M. J. Ferguson and R. McDonald, *Inorg. Chem.*, 2005, **44**, 5897.
54. J. M. Kisenyi, G. R. Willey, M. G. B. Drew and S. O. Wandiga, *J. Chem. Soc., Dalton Trans.*, 1985, 69.
55. I. M. Muller and J. Muhle, *Z. Anorg. Allg. Chem.*, 1999, **625**, 336.
56. P. L. Millington and D. B. Sowerby, *J. Organomet. Chem.*, 1994, **480**, 227.
57. C. J. Carmalt, A. H. Cowley, R. D. Culp, R. A. Jones, S. Kamepalli and N. C. Norman, *Inorg. Chem.*, 1997, **36**, 2770.
58. W. Clegg, M. R. J. Elsegood, L. J. Farrugia, F. J. Lawlor, N. C. Norman and A. J. Scott, *J. Chem. Soc., Dalton Trans.*, 1995, 2129.
59. D. J. Eisler and T. Chivers, *Inorg. Chem.*, 2006, **45**, 10734.
60. H. J. Breunig, L. Konigsmann, E. Lork, M. Nema, N. Philipp, C. Silvestru, A. Soran, R. Varga and R. Wagner, *Dalton Trans.*, 2008, 1831.
61. T. Probst, O. Steigelmann, J. Riede and H. Schmidbaur, *Chem. Ber.*, 1991, **124**, 1089.
62. P. G. Jones, A. Blaschette, D. Henschel and A. Weitze, *Z. Kristallogr.*, 1995, **210**, 377, D. M. Hawley and G. Ferguson, *J. Chem. Soc. A*, 1968, 2059.
63. W. J. Evans, H. J. Hain Jr and J. W. Ziller, *Chem. Commun.*, 1989, 1628.
64. G. G. Briand, T. Chivers and M. Parvez, *Can. J. Chem.*, 2003, **81**, 169.
65. V. P. Ananikov, D. A. Malyshev, I. P. Beletskaya, G. G. Aleksandrov and I. L. Eremenko, *J. Organomet. Chem.*, 2003, **679**, 162.
66. O. Niyomura, S. Kato and S. Inagaki, *J. Am. Chem. Soc.*, 2000, **122**, 2132.
67. Z. Garcia-Hernandez, B. Wrackmeyer, M. Herberhold, T. Irrgang and R. Kempe, *Z. Kristallogr.–New Cryst. Struct.*, 2006, **221**, 419.
68. V. N. Panov, V. A. Igonin, A. V. Goncharov, Yu. T. Struchkov, A. V. Martinov and A. N. Mirskova, *Zh. Strukt. Khim.*, 1992, **33**, 153.
69. M. Sato and Y. Kanatomi, *J. Sulfur Chem.*, 2009, **30**, 469.
70. G. Hua, A. L. Fuller, Y. Li, A. M. Z. Slawain and J. D. Woollins, *New J. Chem.*, 2010, **34**, 1565.
71. M. A. Ansari, J. A. Ibers, S. C. O'Neal, W. T. Pennington and J. W. Kolis, *Polyhedron*, 1992, **11**, 1877.
72. J. H. Bryden and J. D. McCullough, *Acta Crystallogr.*, 1954, **7**, 833.
73. S. Hauge, V. Janickis and K. Maroy, *Acta Chem. Scand.*, 1998, **52**, 1104.
74. G. Le Guillanton, A. V. Martynov, J. Delaunay, N. Mercier and A. Riou, *J. Chem. Res.*, 1998, 681.
75. G. Van den Bossche, M. R. Spirlet, O. Dideberg and L. Dupont, *Acta Crystallogr.*, 1984, **C40**, 1011.
76. J. Zukerman-Schpector, I. Caracelli, M. J. Dabdoub, V. B. Dabdoub and M. A. Pereira, *Acta Crystallogr.*, 1996, **C52**, 2772.

77. J. Zukerman-Schpector, I. Haiduc, M. J. Dabdoub, J. C. Biazzotto, A. L. Braga, L. Dornelles and I. Caracelli, *Z. Kristallogr.*, 2002, **217**, 609.
78. S. Sato, N. Kondo and N. Furukawa, *Organometallics*, 1994, **13**, 3393.
79. M. Egli and R. V. Gessner, *Proc. Natl. Acad. Sci. U. S. A.*, 1995, **92**, 180.
80. J. Sheng, A. E. Hassan and Z. Huang, *Chem.–Eur. J.*, 2009, **15**, 10210.
81. A. Priimagi, G. Cavallo, P. Metrangolo and G. Resnati, *Acc. Chem. Res.*, 2013, **46**, 2686.
82. A. Bauzá, D. Quiñonero, P. M. Deyà and A. Frontera, *Phys. Chem. Chem. Phys.*, 2012, **14**, 14061.

CHAPTER 5

Solution-Phase Measurements of Aromatic Interactions

K. D. SHIMIZU*[a], P. LI[a] AND J. HWANG[a]

[a]University of South Carolina, Department of Chemistry and Biochemistry, Columbia, SC 29208, USA
*E-mail: Shimizu@mail.chem.sc.edu

5.1 Introduction

The non-covalent interactions of aromatic surfaces are important components of many chemical and biological solution-based processes.[1–9] Examples include: reaction selectivity and catalysis,[10–18] supramolecular assembly,[19–22] drug–protein interactions,[23] and structure and function of biomacromolecules.[24–30] Theoretical models of these interactions provide some guidance in predicting their relative strengths and stability trends.[31–48] However, the accuracy of these calculations is still limited due to their relatively weak interaction energies and the complexity of their contributing terms.[49–53] The non-covalent interactions of aromatic surfaces, unlike hydrogen bonds, dipole–dipole, or electrostatic interactions, are not dominated by the electrostatic term. Instead, aromatic interactions are typically made up of multiple contributing terms of similar magnitude such as electrostatic, dispersion, repulsion, and solvent effects. The dispersion and solvent terms are particularly challenging, as methods to accurately model them are still being developed. Thus, the accurate experimental measurements of the strengths and stability trends for aromatic interactions in solution have significant value

Monographs in Supramolecular Chemistry No. 20
Aromatic Interactions: Frontiers in Knowledge and Application
Edited by Darren W. Johnson and Fraser Hof
© The Royal Society of Chemistry 2017
Published by the Royal Society of Chemistry, www.rsc.org

in aiding the development of fundamental models and in guiding the design of practical applications of these interactions. The goal of this chapter is to provide a tutorial review of current experimental studies of aromatic interactions in the solution phase. Illustrative systems from the literature were selected to provide practical examples on how different experimental strategies can be used to measure and analyze these weak non-covalent interactions and to highlight advantages and disadvantages of each approach.

The study and measurement of aromatic interactions in solution pose a number of challenges. First, the non-covalent interactions formed by aromatic surfaces are usually even weaker in solution due to solvent screening and dampening effects on the dispersion and electrostatic terms. Therefore, sensitive strategies are required to accurately measure sub-kilocalorie differences in these interaction energies. Second, isolating the contribution of individual aromatic interactions within a complex supramolecular system requires careful experimental design and rigorous data analysis. Aromatic interaction energies can be easily obscured by, or mistaken for, other weak forces such as other non-covalent interactions, dipole effects, sterics, solvophobic effects, and secondary interactions. Third, many aromatic interactions do not have a strong directional or geometric preference due to the lack of a dominant electrostatic term. Thus, an ideal model system would fix the interacting surfaces into a single interaction geometry. However, this is often synthetically and structurally challenging. Finally, the strength and geometric preferences of aromatic interactions are sensitive to their solvent environment. Understanding the impacts of solvent effects on aromatic interactions is critical to understanding the fundamental nature of the interaction and also in providing accurate stability trends for theorists. Therefore, an ideal model system would be able to measure aromatic interaction energy in a range of different solution environments.

5.2 Types of Model Systems

The model systems that have been used to observe and quantitatively assess the strength of aromatic interactions in solution can be grouped into four different categories (Figure 5.1). These categories are based on two criteria. The first is the classification of the model systems as bimolecular (Types **a** and **c**) or unimolecular (Types **b** and **d**). The second is the classification of the model systems by whether they measure the influence of the non-covalent interaction on a thermodynamic (Types **a** and **b**) or a kinetic (Types **c** and **d**) process.

5.2.1 Bimolecular Model Systems

The bimolecular model systems (Types **a** and **c**) place the interacting recognition groups on separate molecules. This has the advantage of reducing the complexity and synthetic effort to prepare each molecule. In addition, the interaction energies of a recognition surface on one component can be

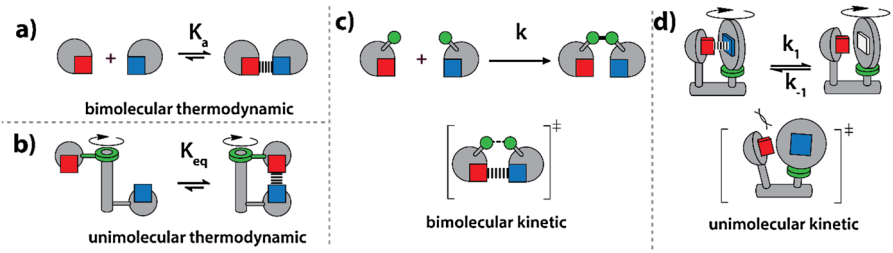

Figure 5.1 Schematic representations of the *four* types of model systems: bimolecular thermodynamic (a), unimolecular thermodynamic (b), bimolecular kinetic (c), and unimolecular kinetic (d).

quickly screened against a series of complementary components by constructing different pairs or mixtures of components together. A limitation of the thermodynamic bimolecular models (Type **a**) is that they usually require the presence of a second non-covalent interaction to reinforce or augment the association event, as the aromatic interaction is usually too weak and non-directional to form a coherent bimolecular complex. The presence of this supporting interaction limits the types of solvent environments that can be measured, as the solvent must be compatible with both the primary and supporting interactions. There are also some examples of multimolecular thermodynamic systems for probing aromatic interactions in solution, such as small molecule gelators with aromatic surfaces[54–56] or self-assembling planar dye molecules,[9,21] other supramolecular assemblies,[57–60] as well as direct calorimetric measurement of dissolution energies of small molecules.[61,62] However, these systems are typically much more difficult to analyze due to the many components and the cooperative nature of the assembly processes.

5.2.2 Unimolecular Model System

Unimolecular model systems have complementary advantages and disadvantages to bimolecular model systems. Unimolecular model systems (Types **b** and **d**) have the two recognition groups covalently linked together. This allows for greater control over the geometry of the intramolecular aromatic interaction. In addition, the covalent linker eliminates the necessity for the supporting interaction and thus, the unimolecular systems are more easily studied in different solvent environments. The main disadvantage of unimolecular model systems is the additional synthetic effort necessary to construct the linking framework and to vary the interacting recognition groups.

5.2.3 Thermodynamic Approach

The two basic strategies for measuring the interaction energies within a model system involve assessing the influence of the aromatic interactions on a thermodynamic equilibrium or a kinetic reaction. The thermodynamic

models are the most common types, involving a bimolecular complexation equilibrium (Type **a**) or an intramolecular conformational equilibrium (Type **b**). Small variations in the aromatic interaction energy can be observed from changes in the equilibrium (K_a or K_{eq}) due to the logarithmic relationship between the interaction energy and the equilibrium constant: $\Delta G = -RT\ln(K)$. For example, an energy change of 0.1 kcal mol^{-1} would be easily observable as K changes from 50 : 50 to 55 : 45 at room temperature. This sensitivity of thermodynamic systems comes at the cost of a limited dynamic range. The maximum changes in the interaction energy that can be accurately measured are approximately 5.4 and 3.0 kcal mol^{-1} for bimolecular and unimolecular thermodynamic models, respectively. This is due to difficulties in accurately measuring association constants above 10^4 M^{-1} and equilibrium constants greater than 100 : 1 by common NMR methods. Readers are referred to recent tutorials on determining association constants *via* titration experiments for more technical details.[63]

5.2.4 Kinetic Approach

Aromatic interaction energies can also be measured in solution by quantifying their impacts on the rate of a chemical or biological transformation. These variations in a reaction kinetic profile are measured as changes in the rate constant (k) or product selectivity factors such as diastereomeric (dr) or enantiomeric ratio (er). Kinetic models have similar levels of sensitivity as thermodynamic models due to the analogous logarithmic relationship between the interaction energy and the kinetic rate constants: $\Delta\Delta G^{\ddagger} = -RT\ln(k/k')$. However, the kinetic approach has the potential to measure a much wider range of interaction energies because rate constants can be accurately measured over many orders of magnitudes simply by varying the observation window. Finally, the quantification of product ratios is not limited to *in situ* methods as the products are usually stable structures. The main limitation of kinetic approaches is that it is often unclear exactly what is being measured. Ideally, the non-covalent interaction would change either the energy of the ground-state (GS) or the transition-state (TS) and thus, the variation in the rate constant would provide a direct measure of the interaction energy. However, in many kinetic models, the non-covalent interaction influences both the GS and TS often to different degrees and in different directions. Thus, it is difficult to definitively assess the relationship between the change in the energy barrier ($\Delta\Delta G^{\ddagger}$) and the non-covalent interaction energy.

5.2.5 Analysis of Experiment Models

The experimental methods for quantitatively monitoring model systems vary by model type. Association constants (K_a) for the bimolecular model systems are measured *via* titration experiments using NMR,[64] UV/vis,[65] or fluorescence[66] or by isothermal calorimetry titration.[67] Conformational equilibria (K_{eq}) for unimolecular model systems are most commonly measured by NMR. Quantitative NMR is used when conformers are in slow exchange,

whereas chemical shift and coupling constant analysis is used if conformers are in fast exchange. For bimolecular kinetic models, product distributions and selectivity factors are determined either by quantitative NMR or through analytic chromatography of the crude reaction mixture. For unimolecular kinetic models, isomerization barriers are measured using dynamic NMR experiments, such as lineshape analysis and exchange spectroscopy.

5.2.6 Isolation of the Interaction Energy

Rarely are the non-covalent aromatic interactions the only factor influencing the equilibrium ratios or reaction rates in the model systems. Therefore, most model systems require a series of well-designed control molecules to isolate the aromatic interaction of interest by subtracting out the influence of these other factors such as solvent, dipole, steric, and secondary as well as supporting non-covalent interactions (Figure 5.2(a)). Therefore, aromatic interaction energies are calculated from the difference between two or more measurements and are expressed as $\Delta\Delta G$ or $\Delta\Delta G^{\ddagger}$. The most systematic and accurate method of isolating interaction energies is the double mutant cycle (DMC) analysis, which was first developed to isolate the influence of individual residue changes (or mutations) within protein active sites.[68,69] This analysis isolates the interaction energy of interest ($E_{X\cdot\cdot Y}$) between two recognition groups, X and Y (A in Figure 5.2(b)), *via* the subtraction and addition of the equilibrium energies of three control systems (B, C, and D). The enhanced accuracy of DMC over a simple pairwise analysis (Figure 5.2(a)) is the ability to remove secondary interactions (broken lines in Figure 5.2(b)). The

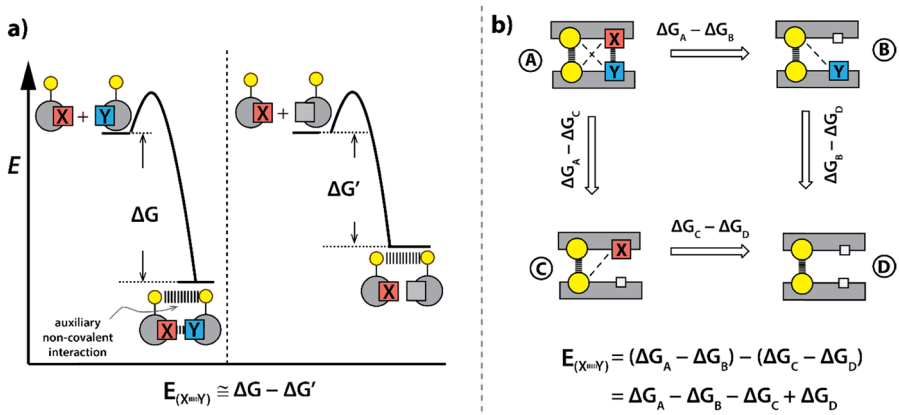

Figure 5.2 Schematic representation of two thermodynamic strategies for isolating a non-covalent interaction energy ($E_{X\cdot\cdot Y}$) between X and Y recognition groups in bimolecular complexes: (a) by a pairwise comparison against a control lacking the X··Y interaction and (b) through a double mutant cycle analysis of four analogues that systematically delete the X··Y interaction.

control systems B and C subtract out the secondary interactions of the functional groups X and Y, respectively. Control system D takes into account the framework effects (shown as the dashed broken line between the two yellow groups). Furthermore, variations in solubility and conformation of the models can be cancelled out by the pairwise parallel mutations.

The DMC analysis is commonly applied to bimolecular thermodynamic systems as shown in Figure 5.2(b) and to unimolecular thermodynamic systems as will be shown in examples below. Some concerns have been raised about the additivity of free energies in experimental systems,[70,71] which is a key premise in DMC analyses. They are warranted in cases where there are large variations in conformation or entropy between functional group mutations, especially when cooperative behaviors are evident.[72,73] However, the DMC analyses of most synthetic model systems for quantifying aromatic interactions appear to be valid due to the relative simplicity and high degree of reorganization (*vide infra*).[74] This can be seen by the self-consistency of more values taken from parallel thermodynamic mutant cycles in some of these systems.[75–78] Still, experimentalists should be aware of the assumptions being made when conducting the DMC analyses and when possible try to verify the additivity of free energies for a particular system by comparing the values from parallel thermodynamic cycles.

5.3 Case Studies of Solution-Phase Measurements of Aromatic Interactions

The body of this chapter is comprised of a series of examples from the literature that were designed to measure or study different types of aromatic non-covalent interactions in solution. These examples were chosen to provide an overview of each methodology. At least one example from each of the four types of model systems in Figure 5.1 is presented. In addition, specific characteristics, advantages, and disadvantages of each approach and model system are highlighted. The examples are organized by the type of non-covalent aromatic interactions being studied such as aromatic stacking, edge-to-face aromatic–aromatic interactions, aliphatic CH–π interactions, cation–π interactions, anion–π interactions, and lone pair–π (lp–π) interactions.

5.3.1 Aromatic Stacking Interactions

Non-covalent aromatic–aromatic interactions can be classified by the relative geometry of the two aromatic surfaces. The archetypical interaction geometries are shown in Figure 5.3 for the benzene dimer. Aromatic–aromatic interactions do not typically have a strong geometric preference. The off-set stacking, aligned stacking (sandwich), and edge-to-face geometries have all been observed in solution. The off-set stacking interaction is probably the most commonly recognized geometry. This interaction geometry is a compromise between the repulsion of the π-faces and the attractive dispersion

and electrostatic terms.[79] In polar solvents, the stacking geometry is further stabilized by solvophobic effects.

5.3.1.1 *Hunter's Supramolecular Zipper Complex*

In early 2000s, Hunter developed an elegant bimolecular thermodynamic model system to study aromatic stacking interactions in organic solution (Figure 5.4).[76,80,81] This "supramolecular zipper" is comprised of two complementary curved molecules, which are held together by an array of noncovalent interactions. These interactions included three hydrogen bonds, two aromatic edge-to-face interactions of the central aromatic rings, and aromatic stacking interactions of the terminal aromatic rings. The three hydrogen bonds are necessary to provide the majority of the complexation energy and also to fix the two molecules in the proper orientation to form an

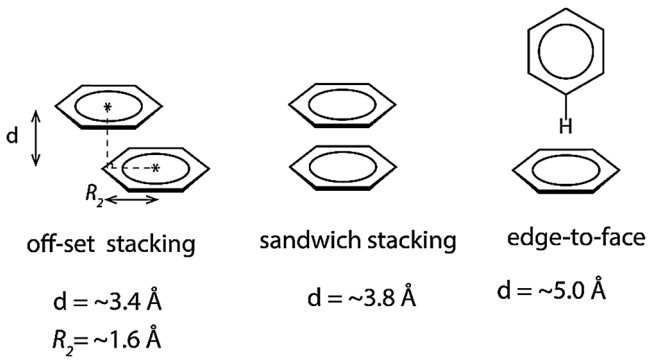

Figure 5.3 Schematic representation of the three archetypical interaction geometries for the benzene dimer: off-set stacking (left), sandwich stacking (middle), and edge-to-face (right). Two geometric parameters are provided to describe the relative positioning of two benzene rings: centroid-to-plane distance (d) and horizontal displacement (R_2).[31]

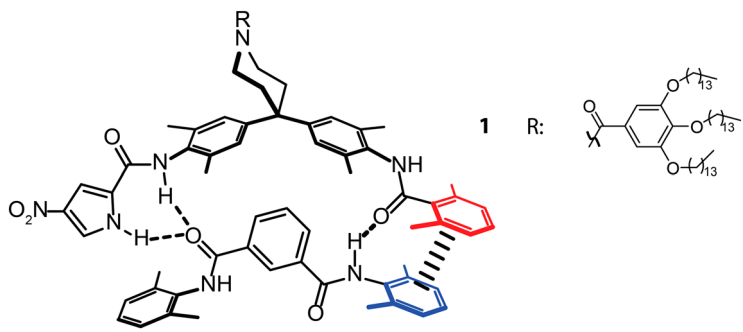

Figure 5.4 Hunter's supramolecular zipper model designed to measure aromatic stacking interactions in solution.

aromatic stacking interaction between the terminal aromatic rings. Another key design feature of the supramolecular zipper is the preorganized orthogonal geometry of the terminal aromatic groups that enables the simultaneous formation of the H-bonds and aromatic stacking interactions. This twisted geometry arises from the steric effects of the *o*,*o*′-dimethyl groups on the terminal aromatic rings, which force them out of plane with the adjacent hydrogen bonding amide groups. Without these preorganizing design features, the aromatic–aromatic interaction geometry of the terminal rings would be ill-defined as aromatic rings can adopt a continuum of geometries with similar interaction energies.[39]

The 1:1 association constants for the molecular zipper complexes were measured in chloroform by ^{1}H NMR titration experiments by following the complexation-induced changes in chemical shift. The formation of an aromatic stacking interaction between the terminal aromatic groups was confirmed by chemical shift analyses and ROESY. A double mutant cycle analysis was used to isolate the energetic contribution ($E_{\pi-\pi}$) of the relatively weak aromatic stacking interactions from the stronger hydrogen bonding and secondary interactions (Figure 5.5(a)). This required the preparation and measurement of three additional control complexes (**B**, **C**, and **D**) for each aromatic interaction being studied. Despite the complexity and large number of recognition groups, systematic structural modifications were readily achieved due to the modular design and the bimolecular nature of the zipper complex. The control molecules systematically replace the terminal aromatic rings with alkyl groups, eliminating the aromatic stacking interactions of interest. The DMC analysis found that the aromatic stacking interaction between the two unsubstituted phenyl rings was +0.07 kcal mol^{-1}. Thus, the stacking interaction of the unsubstituted zipper complex was actually slightly destabilizing. This could be due to the steric interactions between the four *ortho*-methyl groups that were used to help fix the geometry of the stacking complex. Alternatively, this positive stacking energy could be due to the control complexes (**B** and **C** in Figure 5.5(a)) forming aliphatic CH–π interactions of similar magnitude to the stacking interaction in complex **A**.

The presence of the aromatic stacking interactions in this system was more evident from the electrostatic substituent effect studies. Again, these studies were facilitated by the modular design and bimolecular nature of the system that allowed the rapid preparation of the substituted zippers and all of the control zippers. The substituent studies demonstrated that the electrostatic term of the stacking interaction could be used to systematically modulate the strength of the interaction (Figure 5.5(b)). When electron withdrawing groups (EWGs) were introduced on the bottom ring, the aromatic stacking interaction became predictably stronger (Figure 5.5(b), blue line). Good linear trends (R^2 = 0.86 to 0.98) were observed when correlating the measured stacking interaction energies with the Hammett σ_m parameters of the substituents. Conversely, when electron donating groups (EDGs) were introduced on the bottom ring, the aromatic stacking interactions became weaker. Interestingly, the opposite substituent trend was observed for the

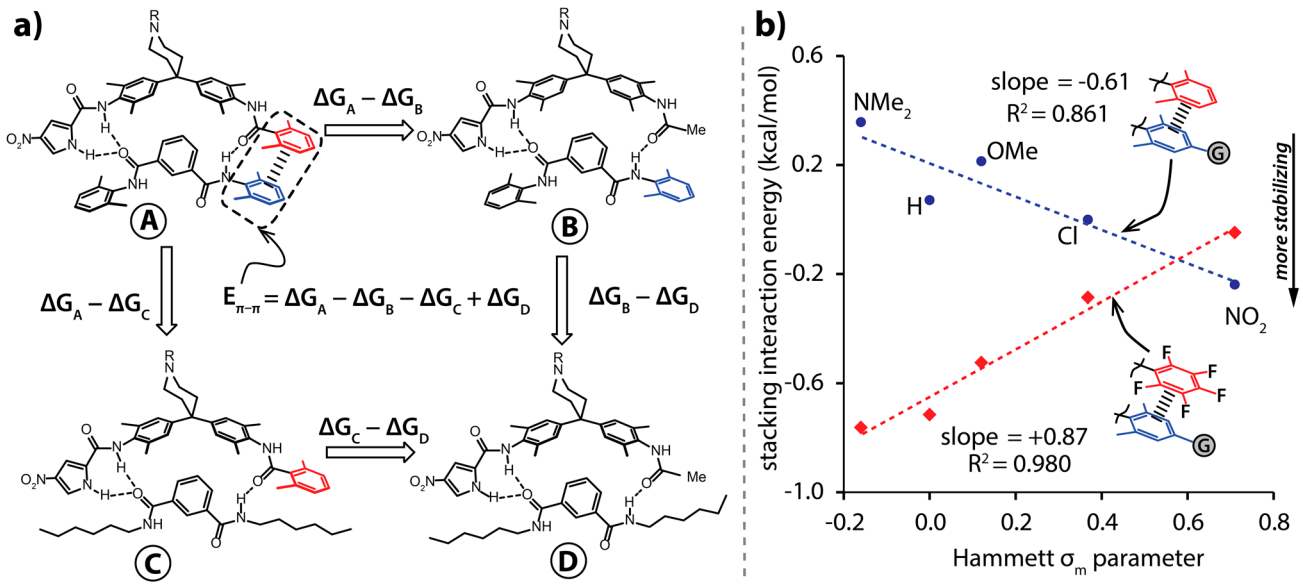

Figure 5.5 (a) Double mutant cycle analysis of the supramolecular zipper complex to isolate the energy of the aromatic stacking interactions ($E_{\pi-\pi}$) between the two terminal phenyl rings (highlighted in dashed line box) in complex A: $E_{\pi-\pi} = \Delta G_A - \Delta G_B - \Delta G_C + \Delta G_D$; (b) correlation of the aromatic stacking interaction energies ($E_{\pi-\pi}$) in chloroform with the Hammett σ_m parameter of the substituent G.

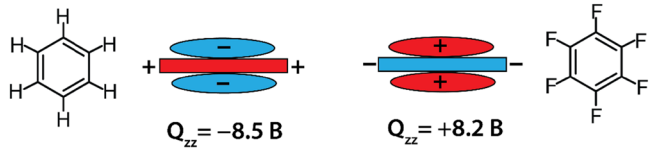

Figure 5.6 Schematic representation of the quadrupoles of benzene (left) and perfluorobenzene (right).

stacking interactions of an electron-poor perfluorinated top ring (Figure 5.5(b), red line), as EDGs stabilized and EWGs destabilized the stacking interactions.

These substituent effects were consistent with the electrostatic interactions of the benzene quadrupoles (Figure 5.6). The benzene ring has an electronegative region above and below the six-membered ring corresponding to the π-clouds and an electropositive region on the rim of the ring corresponding to the ring protons. EWGs are electronegative and form attractive interactions with the electropositive rim of the opposing ring in the stacking geometry. Conversely, EDGs are electropositive and form repulsive interactions with the electropositive rim of the opposing ring. In perfluorinated aromatic rings, the quadrupole moment is inverted. Thus, the electrostatic substituent trends are also inverted. The inverted quadrupole of the perfluorinated ring also has a much stronger electrostatic attraction to a non-perfluorinated ring.[11,82,83] This preference was observed in the zipper complexes as the stacking energy between a perfluorinated and non-perfluorinated ring (red line in Figure 5.5(b)) was consistently lower than that between two non-perfluorinated rings (blue line in Figure 5.5(b)) except for the case of the NO_2 substituent.

This zipper model system demonstrated that weak aromatic stacking interactions can be quantified and systematically evaluated within a complex bimolecular non-covalent system containing an array of non-covalent forces. A double mutant cycle analysis was able to isolate and measure the stacking interaction energy from the supporting H-bonds. This study was facilitated by the modular design and bimolecular complexation process, which allowed rapid variation of the aromatic surfaces and preparation of the many control molecules and complexes necessary for the DMC analysis. One limitation of this bimolecular model system was that the stacking interactions could not be studied in more polar solvent systems in which the supporting hydrogen bonding interactions would be disrupted.

5.3.1.2 Shimizu's Atropisomeric N-Arylimide Aromatic Stacking Balance

More recently, Shimizu developed a unimolecular thermodynamic model system to study aromatic stacking interactions in solution within a conformationally dynamic bicyclic *N*-arylimide framework (Figure 5.7(a)).[84–87] This

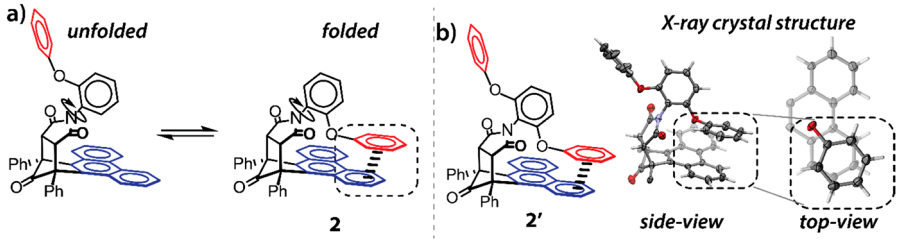

Figure 5.7 (a) Schematic representation of the *unfolded–folded* conformational equilibrium of the Shimizu aromatic stacking balance **2** designed to measure off-set aromatic stacking interactions in solution; (b) side- and top-views of the X-ray crystal structure of symmetrically two-armed stacking balance **2′**, highlighting the well-defined intramolecular stacking interaction between the arm and shelf six-membered rings (in dashed box) in the *folded* conformational region.

"molecular balance"[88] is based on an atropisomeric *N*-phenylimide rotor that is in equilibrium between two distinct conformational states. In the *folded* conformation, the aromatic surfaces on the rotor and on the framework form a well-defined intramolecular off-set stacking interaction. In the *unfolded* conformation, the two aromatic surfaces are held apart and cannot form an intramolecular stacking interaction. Thus, the aromatic stacking interaction energy can be measured by its influence on the equilibrium *folded–unfolded* ratios. The conformers were in slow exchange on the NMR timescale at room temperature. Thus, the *folded–unfolded* ratio could be measured by integration of the separate peaks for each conformer in the ^{1}H NMR spectra.

This example highlights one of the key advantages of unimolecular model systems, which is the precise control over the geometry of the interacting surfaces. The rigid C-shaped framework holds interacting aromatic surfaces at short interplanar distances <4 Å. This distance constraint is optimal for an intramolecular off-set stacking geometry and precludes the formation of the ETF geometry, which requires a larger centroid-to-centroid distance (Figure 5.3). The other key advantage is that additional supporting interactions are not required to form the weak stacking interaction. The covalent scaffold overcomes the entropy of binding, greatly enhancing the probability and stability of the aromatic interaction. The entropic stabilization and enhanced conformational control was verified by X-ray crystallography studies (Figure 5.7(b)) that clearly showed the formation of the off-set stacking interaction in the *folded* conformation of the balances. In fact, the ability to consistently form and characterize intramolecular interactions of the unimolecular balances systems in the solid-state *via* X-ray crystallography provides additional evidence for the greater stability and geometric control of the unimolecular approach. By comparison, only a small fraction of the bimolecular model systems have been characterized *via* X-ray crystallography due to the greater entropic cost and thus probability of forming the desired complex in the solid-state.

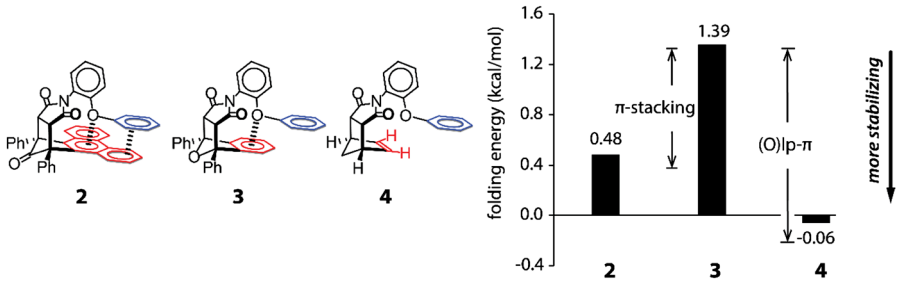

Figure 5.8 Measured folding energies of the aromatic stacking (**2**) and two control balances (**3** and **4**) in chloroform.

Although supporting interactions were not purposely incorporated into this molecular balance, a series of control balances was still necessary to isolate the stacking interaction (Figure 5.8). Of specific concern were the repulsive lp–π interactions formed by the oxygen linker and the aromatic shelf that destabilized the *folded* conformation. Other potential factors that could bias the folding equilibrium included differences in dipole and solvation energies between the *folded* and *unfolded* conformers. Thus designed was control balance **3** (Figure 5.8), which had the same aromatic surfaces connected to the rotor but with a smaller benzene shelf that could form the repulsive lp–π interactions but not the intramolecular stacking interaction. In addition, control balance **4**, which completely lacked an aromatic shelf and thus could not form attractive stacking or repulsive lp–π interactions, was designed to provide an estimate of the influence of the other factors on the conformational equilibrium.

Pairwise comparisons of the folding energies (Figure 5.8) of control balance **3** with control balance **4** confirmed that the lp–π interaction was a significant contributor in destabilizing the *folded* conformer by +1.5 kcal mol^{-1}. On the other hand, the near zero (−0.06 kcal mol^{-1}) folding energy of control balance **4** showed that the differences in dipole and steric biases of the bicyclic framework had little or no effect on the folding equilibrium. Together, these control balances enabled the isolation of the aromatic stacking interaction energy in balance **2** from the difference in folding energy of **2** and **3**, which was −0.9 kcal mol^{-1}. The magnitude of this weakly stabilizing interaction was consistent with previous estimates of the aromatic stacking interaction in solution.[89,90]

As in Hunter's model systems, the substituent effects of the aromatic stacking interactions were investigated, and these studies provided fundamental insights into the nature of the interaction. Electron withdrawing and donating substituents were introduced on the top aromatic ring attached to the rotor, and the expected stabilizing and destabilizing effects were observed for the stacking interactions. More importantly, the additivity of the substituent effects was investigated.[85] A new theoretical model from Wheeler and Houk about the origins of the substituent effects predicted

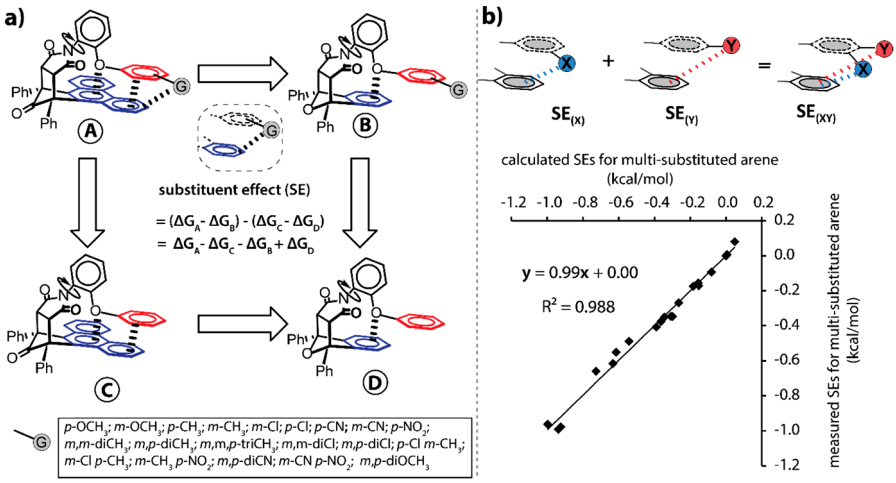

Figure 5.9 (a) DMC analysis isolating the substituent effects (SE) for the aromatic stacking interactions (dashed line box) in balance A; (b) schematic representations of the substituent effect additivity scheme (top) and correlation plot (bottom) of the measured multi-substituent effects with the calculated values based on an additive model.

that the substituent effects should be additive.[35,36] To test this hypothesis, a series of mono-, di-, and tri-substituted balances and control balances were prepared and their folding energies were measured. Five substituents (CH_3, OCH_3, Cl, CN, and NO_2) with varying electronic properties were used to yield 11 di- and tri-substituted stacking balances, and the substituent effects were isolated using DMC analyses. The measured substituent effects for the 11 multi-substituted balances showed excellent correlation with the values predicted by an additive model based on the sum of the corresponding individual substituent effects to an accuracy of ±0.03 kcal mol^{-1}. For example, the substituent effects for the disubstituted *p*-Cl,*m*-Me balance was estimated to be −0.34 kcal mol^{-1} from the sum of the measured mono-substituent effects of *p*-Cl (−0.15 kcal mol^{-1}) and *m*-Me (−0.19 kcal mol^{-1}). This was very similar to the experimentally measured substituent effect of −0.30 kcal mol^{-1} for the di-substituted balance. The generality and fidelity of the additive effects were also demonstrated by the strong linear correlation between the measured and predicted substituent effects (Figure 5.9). Not only did the verification of the additivity of the substituent effects provide support for the Wheeler–Houk stacking model, it also enables experimentalists to accurately predict the effect of substituents of new systems that rely on aromatic stacking interactions.

This stacking model system demonstrates many of the advantages of unimolecular thermodynamic models. Connecting the interacting surfaces *via* a rigid covalent framework precisely positions the aromatic surfaces which otherwise would not have a strong geometric preference. In addition, the

intramolecular nature of the non-covalent interactions yields a simpler system without additional supporting non-covalent interactions. These attractive design traits have facilitated additional studies using this model system to investigate the effects of polarizability,[87] *N*-heteroatoms, and charge[86] on the stacking interactions and also to study the aliphatic CH–π interaction.[91–95] Finally, the unimolecular nature of this model system allowed it to be readily studied in different solvents. For example, the aromatic stacking energy was found to stay relatively constant.[84] One limitation of the rigid covalent framework was the introduction of repulsive steric interactions, which necessitated the use of control molecules for pairwise or DMC analyses. Repulsive interactions are less likely or are of lower magnitude in bimolecular systems due to their greater flexibility in interaction geometry.

5.3.1.3 *Swager and Houk's Diels–Alder Reaction Aromatic Stacking Model System*

Swager and Houk employed the stereoselectivity of a Diels–Alder cycloaddition to study the substituent effects of the aromatic stacking interaction (Figure 5.10).[96] This bimolecular kinetic model was based on the formation of stacking interactions in the transition state between the aromatic rings of an anthracene diene and maleic anhydride dienophile. An asymmetrically substituted dienophile yielded two diastereomeric products that arose from transition states involving a stacking interaction with a substituted (product **A**) or unsubstituted ring (product **B**). These types of kinetic selectivity studies

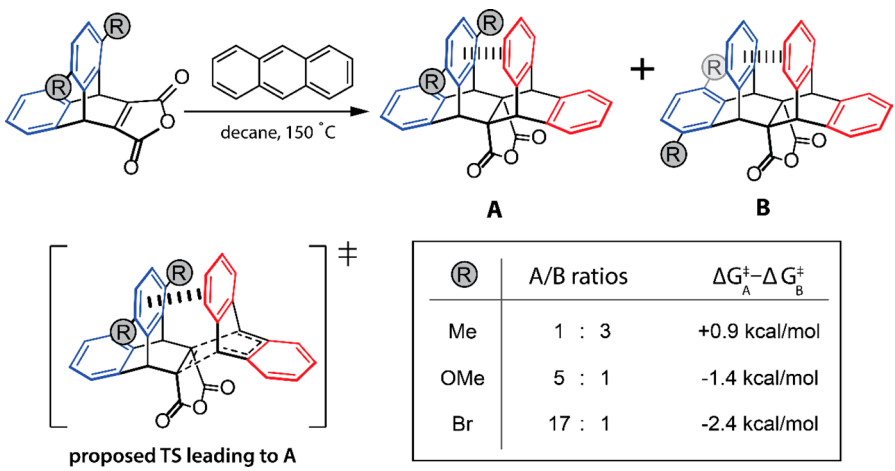

R	A/B ratios	$\Delta G^{\ddagger}_{A} - \Delta G^{\ddagger}_{B}$
Me	1 : 3	+0.9 kcal/mol
OMe	5 : 1	-1.4 kcal/mol
Br	17 : 1	-2.4 kcal/mol

Figure 5.10 Schematic representation of Houk–Swager's stereoselective Diels–Alder reaction model (top) for quantifying the aromatic stacking substituent effects (bottom right). A representation of the proposed TS structure (bottom left) that leads to product A highlighting the aromatic stacking interaction between diene (red) and dienophile (blue).

have the advantage that a single measurement is effectively a pairwise comparison performed under identical conditions.

The selectivity of the dienophiles with three different substituents (Me, OMe, and Br) was measured. The differences in TS energy ($\Delta\Delta G^{\ddagger}$) were calculated from the product ratios and found to correlate well with the Hammett σ_m parameter of the substituents. Interestingly, the slope from the Hammett plot was much steeper than those reported for previous thermodynamic stacking model systems.[80,81,90] This could be due to the presence of two substituents on the dienophile, which should double the magnitude of the substituent effects. In addition, as pointed out by the authors, the aligned as opposed to the off-set stacking geometry of the aromatic rings in the TS may give rise to a stronger substituent effect because the substituents are much closer to the opposing ring. Finally, it is interesting to note that the OMe group had a stabilizing effect despite being an EDG. This experimental observation is consistent with theoretical studies by Sherrill[33] and Houk,[35] which predicted that OH and OMe substituents have a stabilizing effect on aromatic stacking interactions due to attractive dispersion interactions.

This Diels–Alder model system demonstrates that aromatic stacking interactions can be used to tailor the rate and selectivity of a chemical transformation. Like earlier studies, measuring the electrostatic substituent effects assisted in verifying the formation of the stacking interactions. This kinetic system was also able to study the aligned stacking geometry which would be very difficult using thermodynamic models as this configuration typically does not correspond to an energy minimum. However, due to the fleeting nature of transition states, the analysis of kinetic model systems often requires parallel computational studies to help confirm and understand the role of non-covalent interactions on the energy barrier.

5.3.1.4 *Cozzi and Siegel's 1,9-Diarylnaphthalene π-Cofacial Model*

Cozzi and Siegel designed a unimolecular kinetic model system based on a 1,8-diarylnaphthalene framework (Figure 5.11(a)) to quantitatively assess the substituent effects for the aromatic stacking interaction.[97–99] Aromatic rings at the 1- and 8-positions were held by the rigid naphthalene scaffold in a parallel stacking geometry in the ground state. Their stacking interaction energies were assessed by measuring the rates of rotation of the phenyl rings. The stacking interaction only formed in the GS and not in the twisted TS. The rotational barriers were measured by NMR lineshape analysis or 2D EXSY. Alternatively, the rate of rotation could be measured from the kinetic rate of interconversion of enriched samples of the *cis*- or *trans*-rotamers formed by the restricted rotation of the 1,8-diphenyl rings. This system also had a small simple framework, which could be easily constructed by the coupling reaction between 1,8-dibromonaphthalene and various *o*-tolyl halides. This

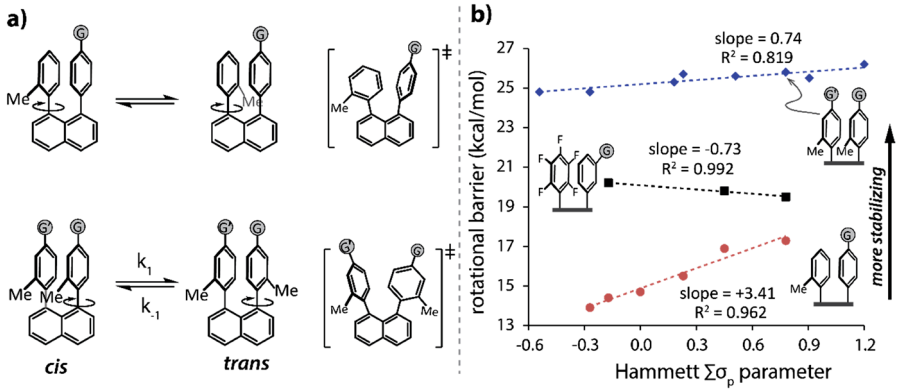

Figure 5.11 (a) Schematic representation of the conformational isomerism of Cozzi–Siegel's kinetic 1,8-diarylnaphthalene models with one (top) and two *o*-methyl phenyl rings (bottom) designed to measure aromatic stacking interactions; (b) correlation of the measured rotational barriers in DMSO with the sum of Hammett σ_p parameters of the G′ and G substituents. For the di-*o*-tolyl series, the *trans*→*cis* barriers were used. This corresponding *cis*→*trans* barriers were consistently lower by ~1 kcal mol^{-1} and gave a nearly identical slope.

modular framework has also been used by other researchers to explore the influences of charge and heteroatoms on aromatic interactions.[100–104]

A variety of substituents (Me, OMe, F, Cl, CO_2Me, and NO_2) with different electronic properties were introduced at the *meta*- and *para*-positions of one or both phenyl rings to probe the substituent effects on the rotational barrier ($\Delta G^{\ddagger}$). In each case, the Hammett plots showed a linear correlation. When a single substituent was positioned at the *para*-position (Figure 5.11(a), top), the EDGs lowered the rotational barrier and EWGs raised the rotational barrier (red line in Figure 5.11(b)). The EDGs destabilized the stacking interactions in the GS, which lowered the rotational barrier, while the EWGs stabilized the stacking interactions in the GS, which raised the rotational barrier. Thus, the observed electrostatic substituent trends in this kinetic system were consistent with those observed in the thermodynamic model systems.

Interestingly, when the substituents were placed at the *para*-positions of both phenyl rings (Figure 5.11(a), bottom), the electrostatic trend was much smaller (blue line in Figure 5.11(b)). This could be explained by a weakening of the GS aromatic stacking interaction due to the greater steric-driven splaying of the two *o*-methyl phenyl rings attenuating the substituent effects. This hypothesis was confirmed by a later study of an analogous 1,8-diarylbiphenylene model system with a larger inter-ring distance (3.8 Å), which showed similar reduced electrostatic substituent trends.[105] A negative slope was observed in the Hammett plot when one of the rings was perfluorinated

(black line in Figure 5.11(b)). Again, this is consistent with the inverted quadrupole of the perfluorinated ring leading to the opposite electrostatic substituent trends.

Cozzi and Siegel's 1,8-diarylnaphthalene model systems illustrate that unimolecular kinetic models can be used to effectively measure and study non-covalent aromatic interactions. A key aspect of this design was that the introduction of substituents only changed the energy of the GS and not the TS. One limitation of this system was that the rigidity and the close proximity of the 1- and 8-positions may impose additional repulsive forces on the stacking GS and the substituent effects that are not found in bimolecular or more flexible unimolecular systems where the aromatic surfaces and substituents have sufficient mobility to avoid severe steric interactions. Finally, the Hammett σ_p parameter was used in this early study as a measure of the electrostatic substituent effects. However, more recent studies have used the Hammett σ_m parameter or the calculated electrostatic potential of the ring because they provide a more direct measure of the inductive electrostatic substituent effects.

5.3.1.5 Other Model Systems for Studying Aromatic Stacking Interactions in Solution

Other model systems that have been developed to quantify aromatic stacking interactions in solution include: (a) the bimolecular thermodynamic models: Iverson's DAN–NDI complex,[106] Colquhoun's supramolecular tweezer,[107] Schneider's porphyrin-based host–guest system,[108] Gao's stacked fluoroaromatic α_2D protein,[109] Diederich's Rebek amide-based stacking complex,[110] Cockroft's naphthyridine-urea-based stacking complex,[111] Carey's benzoylleucine amide stacking dimer;[112] (b) the unimolecular thermodynamic models: Gellman's folding amide,[113] Gung's off-set stacking triptycene balance,[89,90] Shimizu's atropisomeric NDI stacking balance;[114] (c) the unimolecular kinetic models: Waters's flexible benzyl pyridinium,[115] Cozzi and Siegel's spiral polycyclic diol/dione.[116]

5.3.2 Aromatic Edge-to-Face Interactions

The other common aromatic–aromatic interaction geometry is the T-shape or edge-to-face geometry (ETF) (Figure 5.3).[28,30] In this geometry, the planes of the two aromatic rings are perpendicular with a larger centroid to centroid distance (~5 Å). The ETF geometry is roughly isoenergetic with the stacking geometry, and the more favorable geometry will depend upon the solvent or ring systems. The ETF geometry has a much larger electrostatic component due to better electrostatic complementarity of the aromatic quadrupoles and smaller dispersion and solvophobic components due to reduced surface area contact.

5.3.2.1 Wilcox's ETF Molecular Torsional Balance

In the late 1990s, Wilcox designed the first example of a "molecular torsional balance" based on the curved Troger's base (TB) framework to quantitatively study ETF aromatic interactions in solution (Figure 5.12(a)).[88,117] This seminal unimolecular thermodynamic model system was based on the conformational equilibrium of a phenyl rotor attached to the TB framework resulting in distinct *folded* and *unfolded* conformational states. In the *folded* conformation, a phenyl ring attached to the rotor is held on the concave face of the TB framework enabling formation of an intramolecular ETF interaction with a phenyl ring on the opposite end of the TB framework. The formation of an intramolecular ETF interaction in the *folded* conformation was confirmed by an X-ray crystal structure (Figure 5.12(b)), which showed the edge of the phenyl ester in contact with the face of the framework aromatic ring. In the *unfolded* conformation, the phenyl ester group is held on the convex side of the TB framework and cannot form an intramolecular ETF interaction. Thus, the conformational equilibrium energy provided a measure of the strength of the intramolecular ETF interaction. Due to the presence of two *ortho*-substituents (methyl and ester groups), the phenyl rotor rotates slowly at room temperature on the NMR timescale allowing the conformer ratios to be measured by quantitative ^{1}H NMR. This unimolecular model is relatively free of additional supporting interactions or biasing effects between the *folded* and *unfolded* conformers. This was confirmed by the near-unity *folded–unfolded* ratios of control balance **6** (Figure 5.12(c)), which had a small methyl ester that could not form intramolecular interactions with the opposing aromatic shelf. The strength of the ETF interaction (−0.2 kcal mol^{-1}) in chloroform was quantified by the difference in folding energy ($\Delta\Delta G$) between the phenyl and control methyl ester balances. While this initial interaction energy was small, the ETF interaction

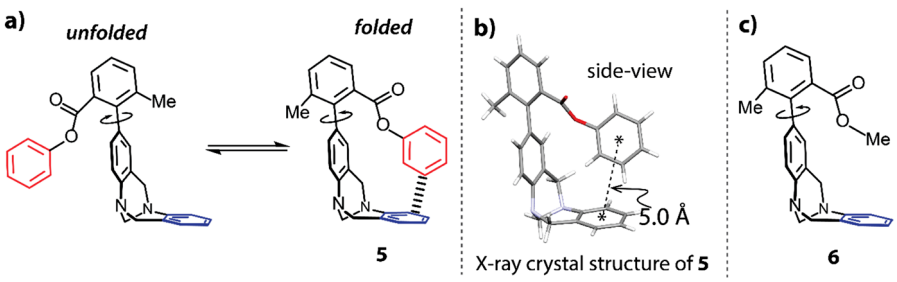

Figure 5.12 (a) Schematic representation of the *unfolded–folded* conformational equilibrium of Wilcox's ETF balance **5** with a phenyl ester arm for quantitatively measuring the aromatic ETF interaction; (b) side-view of the X-ray crystal structure of **5** (CCDC 1029982) highlighting the centroid-to-centroid distance of 5.0 Å between the two aromatic rings forming the ETF interaction; (c) structure of the *folded* control balance **6** that cannot form an intramolecular aromatic interaction.

could be greatly strengthened by increasing the electrostatic term *via* the introduction of appropriate substituents.

The electrostatic substituent effects in Wilcox's torsional molecular balance have been investigated by several groups.[117–120] A series of balances containing substituents with different electronic properties on the top ester phenyl and the bottom aromatic rings were synthesized and studied. The magnitude and direction of the substituent effects were found to depend on the types of substituents on the opposing ring. When the ester phenyl ring contained a strong EWG substituent such as a *p*-F or *p*-CF_3 group (green and blue lines in Figure 5.13(a)), a strong electrostatic effect was observed. EWGs on the bottom aromatic ring in the framework destabilized and EDGs stabilized the ETF interaction. The direction of this trend was consistent with the Hunter–Sanders quadrupole model for ETF interactions where the face of the bottom ring is electronegative because of its π-clouds and the edge of the top ring is electropositive. Thus, EDG substituents enhance and EWG substituents reduce the electron donating ability of the face ring. Interestingly, in the absence of a substituent on the ester phenyl ring (red line in Figure 5.13(a)), a very weak substituent effect in the opposite direction was observed for the bottom face ring. This suggests that the magnitude and sign of the electrostatic term of the ETF interaction varies greatly depending upon the

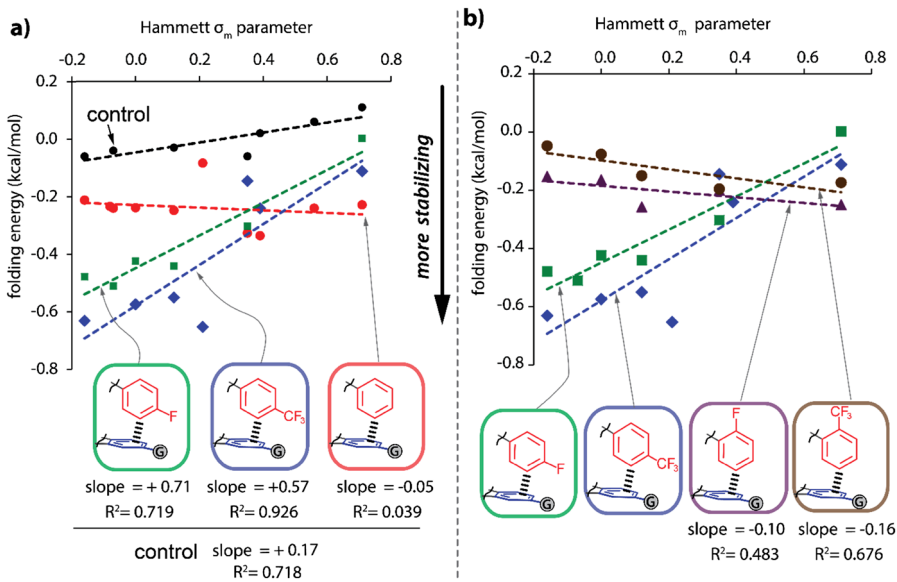

Figure 5.13 (a) Correlation plots of the folding energies of Wilcox's ETF molecular balances with the Hammett σ_m parameter of the face ring substituent (*G*) in chloroform for balances with *p*-F (green square), *p*-CF_3 (blue diamond), and unsubstituted phenyl ester (red dot), and methyl ester arms (black dot); (b) comparison of electrostatic effect trends between balances with *p*-F (green square), *p*-CF_3 (blue diamond), *o*-F (purple triangle), and *o*-CF_3 (brown dot) substituted phenyl ester arms.

relative electrostatic character of the interacting rings. The electrostatic term of the ETF interaction can actually be very small or negligible if the electrostatic surfaces of the interacting rings are very similar.

Recently, Diederich reported a detailed study of the substituent effects in the Wilcox ETF balances, pointing out a possible contribution of direct substituent-to-substituent interactions between opposing rings. When EWGs (F and CF_3) were positioned on the *ortho*-position of the top ring, the expected electrostatic substituent effects were observed with EWGs on the bottom ring stabilizing and EDGs destabilizing the *folded* conformation (purple and brown lines in Figure 5.13(b)). However, when F and CF_3 EWGs were positioned at the *para*-position of the top ring, the opposite trend was observed. This was explained by the formation of attractive or repulsive substituent-to-substituent interactions. The EDGs on the face ring formed strong attractive interactions with the *p*-F or *p*-CF_3 groups on the edge ring, presumably due to the complementarity in local electrostatic interactions, stabilizing the *folded* structure (blue and green lines in Figure 5.13(b)). The EWGs on the face ring, on the other hand, formed unfavorable interactions with the *p*-F or *p*-CF_3 groups on the edge ring diminishing the folding energy. These studies also demonstrated that the position of the substituents can have a strong influence on their stability trends.[33,121]

Wilcox's elegant ETF balances demonstrated the potential of molecular devices in quantifying weak non-covalent interactions in solution. Their successful design clearly inspired many later unimolecular model systems based on restricted rotation.[122] Wilcox's ETF balances also highlighted the potential of small unimolecular models to precisely control the interaction geometry. We would like to point out that analyses of this early aromatic interaction model that led in some cases to incorrect conclusions was *not* due to any design flaw in this system. Rather, the analyses were conducted at a time when there was not as good an understanding of the contributing terms in aromatic interactions as present. Reanalyses of the early studies[123,124] on the Wilcox molecular balance together with its later innovative use to probe new aspects of aromatic interactions[125–129] demonstrate the continued utility of a well-designed unimolecular model.

5.3.2.2 Hsung's 4+3 Cycloaddition ETF Model System

Hsung and Houk reexamined the stereoselectivity of the 4+3 cycloaddition reactions of oxazolidinone enolates and furans with respect to the possible formation of edge-to-face aromatic interactions in the transition state.[130,131] The cycloaddition of the 4-benzyl oxazolidinone *E*-enolate (Figure 5.14, left) gave the expected diastereomeric product B based on the repulsive steric mechanism of the benzyl group directing cycloaddition to the opposite face. However, similar steric arguments could not explain the opposite facial selectivity of the 4-phenyl oxazolidinone enolate (Figure 5.14, right). Computational studies suggested that this selectivity was due to an attractive ETF aromatic interaction between the furan substrate and the 4-phenyl

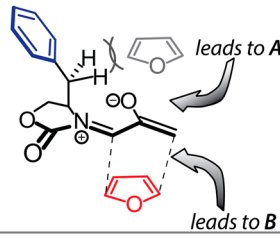

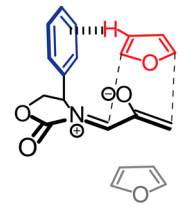

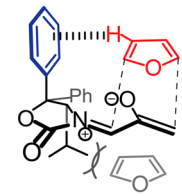

driving force	sterics	ETF	ETF & sterics
selectivity	*A : B = 23:77*	*A : B = 82:18*	*A : B = 94:6*
exp. $\Delta G^{\ddagger}_{A} - \Delta G^{\ddagger}_{B}$	0.55	-0.68	-1.24
calc. $\Delta H^{\ddagger}_{A} - \Delta H^{\ddagger}_{B}$ (kcal/mol)	0.1	-0.2	-2.3

Figure 5.14 Schematic representations of the stabilizing ETF and destabilizing steric interactions in Hsung's 4+3 cycloaddition TSs together with the observed product selectivities, experimentally measured TS free energy differences, and calculated TS enthalpy differences.

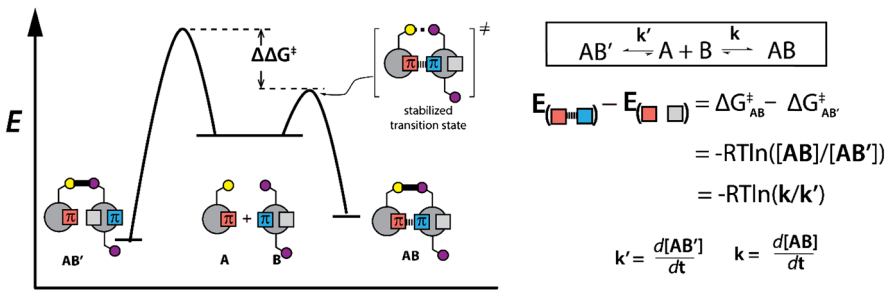

Figure 5.15 Schematic representation of a bimolecular kinetic model containing two reaction pathways (AB′ ← A + B → AB) designed to quantitatively measure aromatic interactions *via* the TS stabilization energy ($\Delta\Delta G^{\ddagger}$), which can be monitored by the product distribution ([AB]/[AB′]) or the rate constant ratio (k/k').

ring of the oxazolidinone. Without further controls, it is difficult to assess the fraction of the differentiation energy that can be directly attributed to the ETF interactions in TS. However, the observation for a third oxazolidinone substrate with 4- and 5-substituents (Figure 5.14, right) suggests that attractive ETF and repulsive steric interactions from the first two substrates may be additive. Thus, the enhanced selectivity of this reaction (94 : 6) can be attributed to a combination of the repulsive steric interactions from the 4-isopropyl group disfavoring pathway **B** and the attractive ETF interactions of the 5-phenyl ring favoring pathway **A**.

The main goal of this study was to develop a predictive mechanistic model for this cycloaddition reaction. Nevertheless, this study could also be adapted to measure the aromatic interaction energies (Figure 5.15) in the TSs *via* the observed reaction selectivity.

5.3.2.3 Other Model Systems for Studying Aromatic ETF Interactions in Solution

Other model systems used to quantify edge-to-face aromatic interactions in solution include: (a) the bimolecular thermodynamic models: Hunter's ETF supramolecular zipper complex;[74,75,132] (b) the unimolecular thermodynamic models: Jennings's imino torsional balance,[133,134] Waters's ETF β-hairpin peptide,[135] (c) the unimolecular kinetic models: Cozzi and Mazzanti's metaparacyclophanes.[136,137]

5.3.3 Aliphatic CH–π Interactions

Aromatic surfaces also form weak attractive interactions with aliphatic CH units.[4] These interactions are generally considered weaker than aromatic–aromatic interactions due their smaller electrostatic term as the C–H bonds in aliphatic systems are typically only weakly polarized.[38,48] Therefore, the interaction is considered to be dominated by dispersion and solvophobic terms.[138]

5.3.3.1 Asensio's Imine/Hemiaminal CH–π Model

Asensio recently reported a dynamic combinatorial chemistry (DCC)[139] model system to quantitatively evaluate the influence of CH–π interactions on the association of cyclic alkanes to aromatic surfaces in water (Figure 5.16).[140] Although this system contains multiple reactants and involves a covalent imine bond forming reaction, it is classified as a bimolecular thermodynamic model for two reasons. First, the aliphatic CH–π interaction is formed between structural units on two distinct species: the aldehyde and amine. The amine unit carries a cyclic alkyl group (**A** to **C** in Figure 5.16) bearing multiple CH bonds, and the aldehyde group carries various sized aromatic surfaces (**D** to **F** in Figure 5.16). Second, the reversible nature of the imine or hemiaminal forming reaction ensures that the product distribution is under thermodynamic control with the strength of the intramolecular CH–π interactions providing the main source of variation in the product distributions. Thus, DCC models differ from bimolecular kinetic models because the product distribution reflects the relative GS rather than TS energies.

Dynamic combinatorial chemistry has a number of unique advantages in measuring weak aromatic interactions.[141] First, the DCC approach allows the simultaneous measurement of multiple non-covalent interactions of interest with one experiment. For example in Figure 5.17, three reactants, W, Y, and Z react with one common reactant X in a reversible process to yield three different products. The product distribution ([XY]/[XZ]/[XW]) reflects the relative stabilities of the products including the energy of the intramolecular non-covalent interactions ($E_{x–y} - E_{x–z}$, $E_{x–y} - E_{x–w}$ and $E_{x–w} - E_{x–z}$). Second, since the products are covalent species, the analysis of DCC models is often much easier than measuring the concentrations of fragile non-covalent complexes. For instance, the relative concentrations of DCC reaction products can be

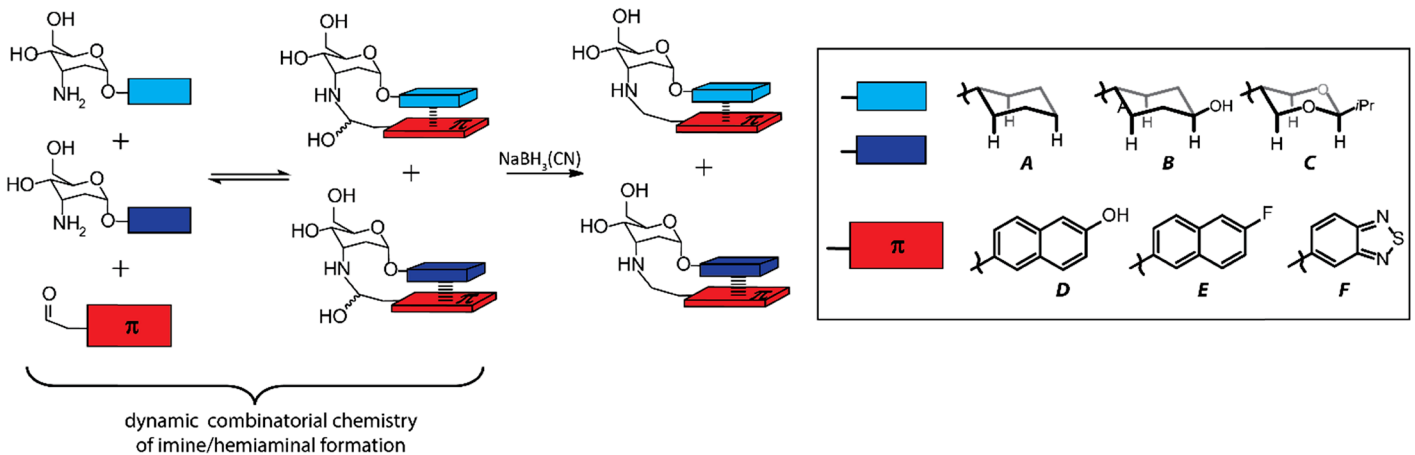

Figure 5.16 Schematic representation of Asensio's CH–π DCC model system using the reversible imine/hemiaminal formation (left) between various 3-amino-α-D-allopyranose derivatives bearing a cyclic alkyl group (**A–C**) with various 2-arylacetaldehydes (**D–F**) (right).

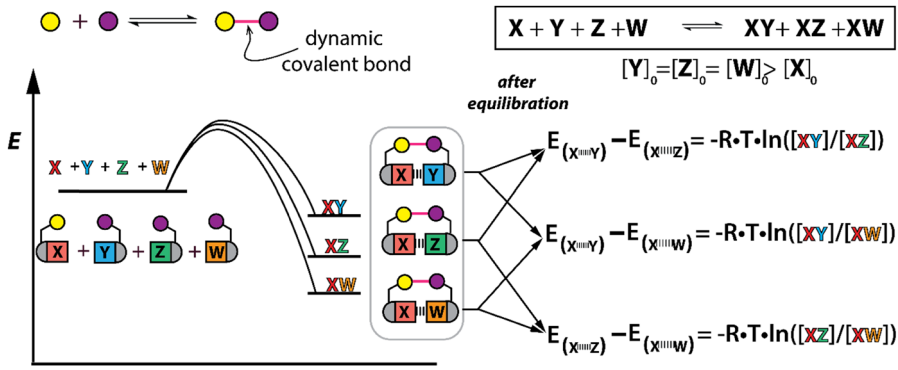

Figure 5.17 Schematic representation of a DCC model system based on a series of reversible reactions (X + Y + Z + W ⇋ XY + XZ + XW) for simultaneously quantifying three non-covalent interactions from the equilibrium product ratio [XY]/[XZ]/[XW].

measured by GC or HPLC, which would not be viable methods for non-covalent complexes.

Asensio's DCC reaction conditions involved mixing equimolar concentrations of two or more amines bearing different six-membered alkyl rings and a substoichiometric amount of a 2-arylacetaldyhyde in aqueous buffer. After equilibration, the thermodynamic hemiaminal/imine mixture was kinetically trapped by reduction to yield stable amine derivatives. The amine product ratios were quantified by ^{1}H NMR *via* their characteristic anomeric proton peaks. Note that the 3-amino-α-D-allopyranose scaffold of the amine was intentionally designed to allow only one face of the cyclic alkyl group to form in the intramolecular aliphatic CH–π interaction with the aromatic residue in the product.[142] The strength of the aliphatic CH–π interactions for the six-membered alkyl rings was calculated from the differences in the product ratios with a control amine bearing a smaller methyl group. In addition, the strength of the aromatic interactions for a particular pair could be estimated from a series of different mixtures of reactants providing a means of validating the values (Figure 5.18(a)). For example, the difference in strength between the aliphatic CH–π interactions in complexes **AD** and **CD** could be measured by analyzing two pairwise yields forming **AD** and **CD**, respectively, *versus* **BD**, which serves as a reference state or *via* a DCC reaction involving direct competition between reactants **A**, **C** and **D**.

Three six-membered cyclic alkyl groups (**A**, **B**, and **C**) with varying numbers of oxo units were analyzed to probe their influence on aliphatic CH–π interactions. The polarized CH units with adjacent oxygens were found to form significantly stronger aliphatic CH–π interactions with three different aromatic surfaces (Figure 5.18(b)). For example, the CH–π interaction between cyclohexyl group **A** (with no polarized CH units) and the aromatic

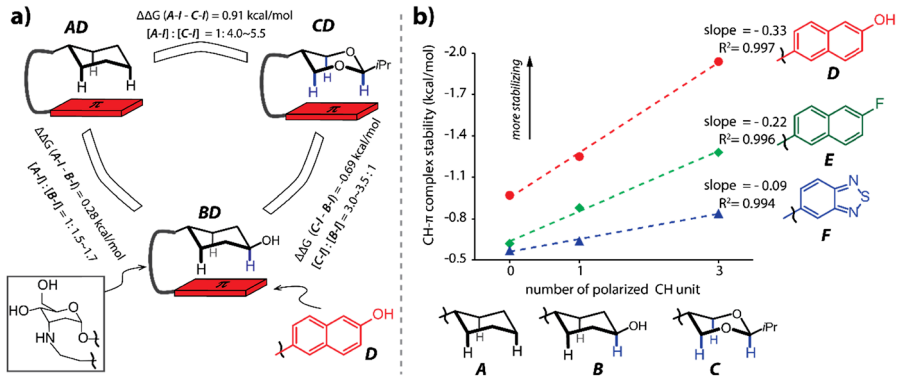

Figure 5.18 (a) Schematic diagram of the relative stabilities of various CH–π complexes *via* pairwise competition experiments; (b) correlation of the CH–π interactions (in D_2O phosphate buffer) of various six-membered cycloalkyl groups with various bicyclic aromatic groups with the number of polarized CH units in the cycloalkyl group; for each type of aromatic surface, a control complex containing a smaller methyl group was used as the reference state for quantifying CH–π interaction energies.

6-hydroxynaphth-2-yl group **D** were estimated to be −0.97 kcal mol^{-1}, while the interactions involving the 4-hydroxycyclohex-2-yl **B** (with one polarized CH unit) and the 3,5-dioxocyclohexyl group (with three polarized CH units) **C** were found to have stronger interaction energies of −1.25 and −1.94 kcal mol^{-1}, respectively. This trend was attributed to the increase in electrostatic attraction due to the greater partial positive charge on these polarized CH units. The added stabilization of polarizing one CH unit was estimated to be −0.3 kcal mol^{-1} in the corresponding CH–π interactions with the 6-hydroxynaphthyl group. It is noteworthy that the enhanced electrostatic contributions accounted for 47% of the aliphatic CH–π interactions between the 3,5-dioxocyclohexyl group **C** and the 6-hydroxynaphth-2-yl group **D** even in an aqueous medium. As expected, the CH–π polarization effect was smaller for a more electron poor aromatic surface, such as the 6-fluoronaphth-2-yl group **E** (−0.2 kcal mol^{-1} enhancement per polarized CH unit) and the benzo[*c*][1,2,5] thiadiazol-5-yl group **F** (−0.1 kcal mol^{-1} enhancement per polarized CH unit). Hydrophobic effects were found to be a significant component of the CH–π interaction energies in water, as adding organic co-solvents, such as acetonitrile, noticeably destabilized the CH–π complexes.

This CH–π DCC model system highlights the potential of the DCC approach for rapidly quantifying weak aromatic interactions under demanding biologically relevant conditions.[143,144] Under thermodynamic control, the equilibrium product population reflects the relative stabilities of the individual products in the mixture, which in turn could be used to evaluate the intramolecular interactions in each product. In this example, the reversible

chemical bond can be viewed as a stronger version of the non-covalent supporting interactions used in more conventional bimolecular thermodynamic models, such as Hunter's supramolecular zipper complexes.

5.3.3.2 Zondlo's Proline Tetrapeptide CH–π Model

Zondlo has adapted a flexible tetrapeptide model to measure the aliphatic CH–π interactions between the aliphatic protons in the prolyl group and neighboring aromatic residues (Figure 5.19).[145,146] This unimolecular thermodynamic model is based on the slow *cis–trans* isomerization of the peptidyl–prolyl bond that forms two distinct conformational states. In the *cis*-conformer, the aromatic side chain of the residue preceding Pro is folded towards the prolyl α-CH unit and forms a stabilizing intramolecular aliphatic CH–π interaction. In the *trans*-conformer, the aromatic residue and prolyl motif are far apart and cannot interact with each other. Variations in the intramolecular aliphatic CH–π interaction energy therefore are directly reflected as changes in the equilibrium *cis–trans* conformer ratio. The *cis–trans* ratio was measured by quantitative ^{1}H NMR, and the identity of the major and minor conformers was assigned through ROESY experiments.

Aromatic groups with varying electronic properties were incorporated to the side-chain of the residue adjacent to the Pro to probe the electrostatic character of the aliphatic CH–π interaction in aqueous solution. Tetrapeptides containing an electron rich aromatic group, such as hydroxyphenyl and indolyl, displayed a higher *cis–trans* ratio; while those containing electron poor aromatic groups, such as protonated pyridyl and nitrophenyl, displayed a lower *cis–trans* ratio. A more systematic study quantitatively measured

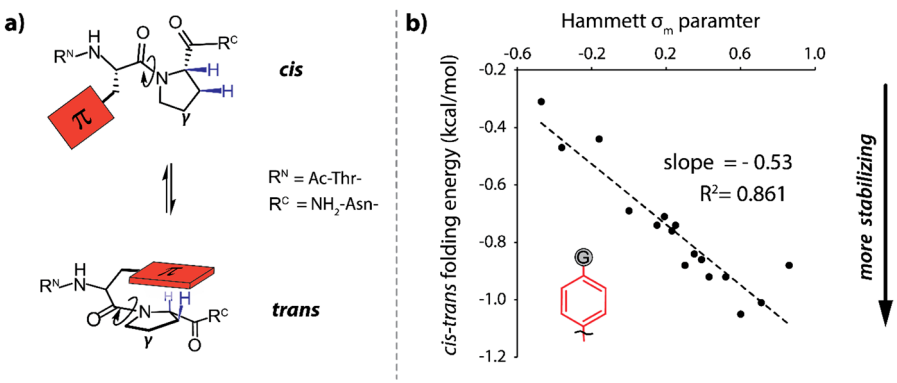

Figure 5.19 (a) Schematic representation of the amide *cis–trans* isomerism of Zondlo's folding tetrapeptide models for quantitatively assessing CH–π interactions of a prolyl group with its neighboring aromatic residue; (b) correlation of the folding energy of the tetrapeptide (in aqueous buffer) with the electrostatic Hammett σ_m parameter of the substituents on the phenyl alanine side-chain.

the electronic effects of substituents at the *para*-position of the interacting phenyl ring. An excellent linear correlation was found with the Hammett σ_m parameter (Figure 5.19(b)).

This and the previous DCC studies demonstrated that the strength of aliphatic CH–π interactions can be electrostatically modulated even in highly competitive aqueous environments. This was surprising as CH–π interactions typically have a small electrostatic term as the C–H bond in most alkyl groups is only weakly polarized. However, the CH bond of the α-carbon in proline is more strongly polarized due to the adjacent C=O. This leads to a larger than normal electrostatic term for this aliphatic CH–π interaction. This appears to be a general trend. For example, polarization of the γH in the Pro with a geminal fluoro group likewise stabilized the intramolecular CH–π interaction by −0.3 to −0.6 kcal mol^{-1}. Particularly surprising was the magnitude of this electrostatic trend. The slope of the electrostatic substituent effects correlation in the Hammett plot for this proline model was similar to that observed for stacking and ETF aromatic interactions in organic solvents. This folding tetrapeptide model also demonstrated the advantages of quantifying aromatic interactions within a biological construct. These biological or biomimetic systems can often be efficiently assembled using established synthetic methodologies, which in this case were peptide synthesis protocols. In addition, these biomolecular models can be directly studied under biologically relevant environments without further modification.

5.3.3.3 *Other Model Systems for Studying Aliphatic CH–π Interactions in Solution*

Other model systems that have been developed to quantify aliphatic CH–π interactions in solution include: (a) the bimolecular thermodynamic models: Morales's carbohydrate–π dangling-ended DNA model,[147,148] Gao's cyclohexyl–phenyl stacking α_2D protein;[149] (b) the unimolecular thermodynamic models: Wilcox's aliphatic CH–π balance,[88,117,150] and similar models by others,[127,128] Waters's carbohydrate–π stacking β-hairpin model,[151] Shimizu's atropisomeric *N*-arylimide CH–π molecular balance[91,93–95] and similar models by others,[152–154] and Gung's CH–π triptycene balance.[155]

5.3.4 Aromatic Cation–π Interactions

Aromatic surfaces also form attractive interactions with cationic metal or organic species, which are generally stronger than neutral species.[5,6,156] Cation–π interactions feature a geometry in which the cationic species approaches the π-face of the aromatic surface. The nature of cation–π interactions varies depending on the cationic species involved. The interactions between alkali or alkali earth metal ions and aromatic surfaces are dominated by large electrostatic and inductive terms. In contrast, cation–π interactions involving organic cations, such as NH_4^+ and NMe_4^+, often contain a significant dispersion component in addition to the electrostatic term.[47]

Note that cation–π interactions are not limited to aromatic π-systems. Other non-aromatic π-systems, such as ethylene and acetylene, also engage in cation–π interactions, however, these will not be discussed in this chapter. Interested readers are referred to reviews by Dougherty[5] and Sastry.[6]

5.3.4.1 Dougherty's Cyclophane Cation–π Model

Dougherty studied the ability of a water-soluble cyclophane host to bind organic cations in aqueous environments (Figure 5.20).[157,158] This pioneering bimolecular thermodynamic model forms multiple cation–π/aromatic interactions between the cyclic host and encapsulated small molecule cation guests. The cyclophane has four aromatic walls that create a concave interior within a rigid macrocyclic framework. Upon entering the cyclophane, the cationic aromatic guest is held in close proximity to the four aromatic walls, potentially forming multiple stabilizing aromatic stacking, cation–π, and hydrophobic interactions.

Dougherty's cyclophane model provided one of the first examples of the stability of cation–π interactions in an aqueous medium. Specifically, cationic guests generally showed larger binding energies than neutral ones of similar size and shape. For example, cationic *N*-methyl quinolinium had a binding constant (K_a) of 1.6×10^6 M^{-1} ($\Delta G = -8.4$ kcal mol^{-1}) with cyclophane host **7** in aqueous solution, which was markedly stronger than neutral isosteric 4-methyl quinoline with a K_a of 2.1×10^4 M^{-1} ($\Delta G = -5.9$ kcal mol^{-1}). The −2.5 kcal mol^{-1} stronger interaction energy of the cationic guest was interpreted as arising from the stabilizing cation–π interactions. However, the strong binding energies for cyclophane host **7** in an aqueous medium arose largely from the hydrophobic effect. This was evident from the significantly lower binding energies in organic solvents (chloroform) for the same guests with an organic soluble version of cyclophane host **8**.

The aromatic interior of the cyclophane host was also varied to probe the influence of the electronic properties of the aromatic side walls on the

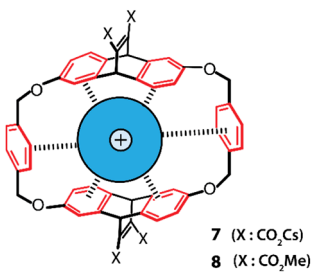

association energy (kcal/mol)	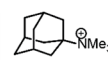			
7 in D_2O (borate buffer)	-6.7	-8.4	-5.9	-5.4
8 in $CDCl_3$	-2.1	-3.5	n/a	0.0

Figure 5.20 Schematic representation of Dougherty's cyclophane host binding a cation guest *via* cation–π interactions (left) together with the measured association energies for cationic and neutral guests in aqueous (D_2O buffer) and organic ($CDCl_3$) solvents.

cation–π interactions. Surprisingly, electron-rich aromatic surfaces, such as furan and thiophene, did not promote stronger cation–π interactions. This was attributed to an absence of a strongly negative electrostatic potential over the center of these aromatic rings.[5] In this regard, this was one of the first studies that used electrostatic potential surfaces to predict the stability trends for cation–π interactions.[159] In addition to thermodynamic binding studies, the cyclophane hosts were also used to probe the utility of cation–π interactions in catalysis. Both the alkylation reaction of quinoline and the dealkylation reaction of dimethyl(*p*-nitrophenyl)sulfonium were accelerated within the cyclophane host, revealing the ability of cation–π interactions to stabilize cationic transition states.[160]

5.3.4.2 Waters's β-Hairpin Peptide Cation–π Model

Waters designed a 12-residue β-hairpin peptide model system to quantitatively assess the cation–π interactions of cationic Lys or trimethylated Lys with Trp residues in water (Figure 5.21).[161–163] This unimolecular thermodynamic model utilized the dynamic folding process of a β-sheet structure to establish a two-state conformational equilibrium. The β-hairpin structure of the Asn–Gly sequence at positions 6 and 7 was stabilized by cation–π interactions between the ammonium and indole side-chains of Lys2 and Trp9. The formation of this bridging interaction was confirmed *via* NOEs and shielding-induced chemical shift changes. Thus, the cation–π interaction energy could be quantitatively measured from the folding equilibrium, as measured by the folding-induced chemical shift changes in the ^{1}H NMR spectra. Through a DMC analysis using Val2 and Ser9 as control residues, the cation–π interaction between a primary alkyl ammonium and aromatic indolyl group was measured to be −0.4 kcal mol^{-1} ($\Delta\Delta G$). The hydrophobic contribution to this cation–π interaction was assessed by replacing the cationic Lys

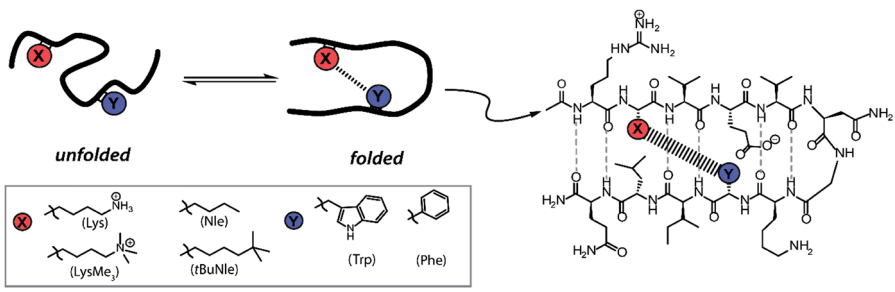

Figure 5.21 Schematic representation of the *unfolded–folded* equilibrium of Waters's β-hairpin peptide model for quantitatively evaluating cation–π interactions between the cationic residues in Lys or Lys(Me)$_3$ and the aromatic residues in Trp or Phe; a representation of the *folded* β-hairpin peptide (right) highlighting the cross-strand cation–π interactions and the array of supporting H-bonds.

with a neutral near isosteric Nle, and was found to be −0.2 kcal mol^{-1} ($\Delta\Delta G$). Thermal denaturation studies revealed that the Lys···Trp cation–π interaction was enthalpically more stabilizing by −1.5 kcal mol^{-1} ($\Delta\Delta H$) than the Nle···Trp hydrophobic interaction. The Lys···Phe and Lys(Me_3)···Trp cation–π interactions were also measured to be stabilizing by −0.2 and −1.0 kcal mol^{-1} ($\Delta\Delta G$), respectively.

This β-hairpin peptide model is another adroit illustration of the adaptation of a biomolecular framework for physical organic studies. Particularly impressive was the ability to observe and accurately measure weak attractive interactions of side-chains that were six residues apart. This cross-strand interaction was facilitated by the conserved β-sheet structure which contained an array of supporting hydrogen bonding and hydrophobic interactions. Again, the study of non-covalent interactions within this peptide scaffold had the advantage that the results had immediate biological relevance to protein stability, structure, and activity. For example, the cation–π interactions in this peptide model system were also measured *via* a protein–ligand binding assay.[163]

5.3.4.3 *Jacobsen's Enantioselective Polycyclization Cation–π Model*

Jacobsen developed a series of aromatic thiourea-based catalysts to investigate the role of cation–π interactions in facilitating and directing the enantioselectivity of a polycyclization reaction (Figure 5.22(a)).[14] The reaction proceeds through a cationic TS that could be stabilized by cation–π interactions with aromatic groups on the catalyst. In the mechanism, γ-hydroxylactam **9** in the presence of HCl is first transformed into a chlorolactam. Next, the thiourea motif of the catalyst facilitates the formation of an *N*-acyliminium intermediate *via* H-bond-mediated ionization of the chloride leaving group.

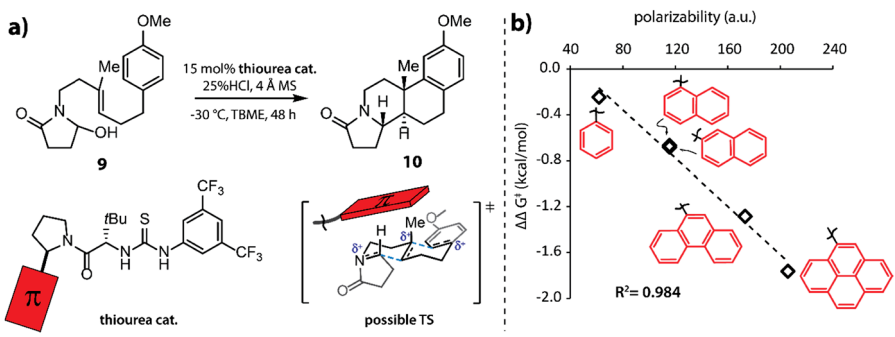

Figure 5.22 (a) Jacobsen's thiourea-catalyzed enantioselective cationic polycyclization for quantitatively evaluating the cation–π interaction *via* selective TS stabilization; (b) correlation of the measured TS stabilization with the polarizability of the aromatic groups (insets) in the thiourea catalysts.

This positions the cationic intermediate adjacent to an asymmetrically positioned aromatic group on the catalyst, which directs the stereoselectivity of the cyclization reaction. Thus, the enantioselectivity of the cyclization reaction provided a measure of the cation–π interactions in the TS.

Aromatic surfaces of varying sizes were incorporated into the thiourea-based catalyst. Larger aromatic surfaces were found to promote both higher enantioselectivities and yields. The simultaneous increase in the yield and selectivity signaled the involvement of a stabilizing cation–π interaction in the TS as opposed to repulsive steric effects, which would have slowed down the reaction. A quantitative linear correlation was observed between the TS stabilization energy ($\Delta\Delta G^{\ddagger}$) calculated from the enantioselectivity of the reaction and the polarizability of the aromatic groups (Figure 5.22(b)), which further confirmed the role of cation–π interactions in this stereoselective reaction. While the primary goal of this study was not to measure cation–π interactions, it was an excellent bimolecular kinetic model for quantitatively assessing cation–π interactions. In turn, this study demonstrated the utility of systematically optimizing aromatic interactions to guide catalyst design.

5.3.4.4 Waters's Benzyl Pyridinium Cation–π Model

Waters also developed a small molecule model system to evaluate the orientational preferences of cation–π interactions in aqueous media (Figure 5.23(a)).[164] This unimolecular kinetic model examined the influence of an intramolecular cation–π interaction on the rotational dynamics of a pyridinium ring connected to a biaryl framework. In the GS, the pendant pyridinium surface forms an intramolecular cation–π stacking interaction with the biphenyl framework lowering the GS energy. In the TS, the pyridinium moiety and the phenyl ring of the biphenyl framework adopted a splayed conformation, and thus the cation–π interaction is broken. Therefore, variations in

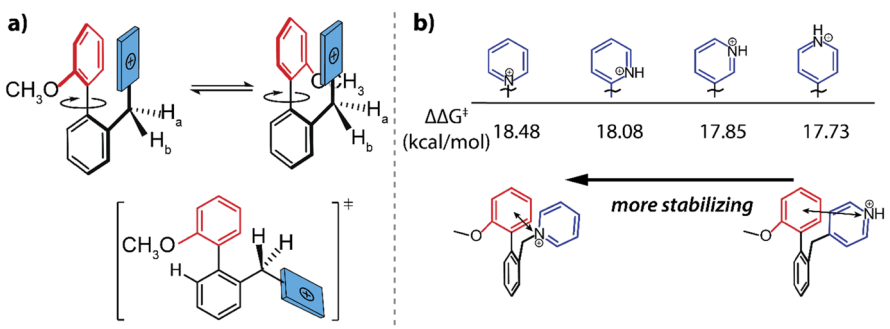

Figure 5.23 (a) Schematic representation of the isomerization process (top) of Waters's small molecule model for quantitatively assessing the orientational preferences in the cation–π interactions and the TS of isomerization (bottom); (b) measured isomerization barriers (in D_2O) together with the corresponding cationic pyridine ring.

the rotational barriers with different pyridinium groups could be correlated with the strength of the stabilizing cation–π interactions in the GS. In this study, the rotational barriers were measured by ^{1}H NMR *via* lineshape analysis of the diastereotopic methylene protons, H_a and H_b (Figure 5.23(a)).

A series of analogues were prepared with the pyridinium nitrogens positioned at different distances from the complementary ring in the biphenyl scaffold. The isomerization barrier was found to gradually increase as the pyridinium nitrogen was moved closer (*para* < *meta* < *ortho* < *ipso*) relative to the methylene linker (Figure 5.23(b)). The observed stability trends suggested a clear electrostatic-driven orientational preference for the stacking interactions of the charged pyridine rings. The closer the positive charge got to the opposing π-surface, the more stable the stacking interaction. This model system highlights the value of a simple design. First, the system could be quickly synthesized and varied. Second, the minimalistic framework was readily rendered water-soluble with a single cationic charge. Third, computational simulations could be performed at higher levels of accuracy due to its small size, providing better guidance in interpreting the observed trends. These were necessary due to the complexity of the isomerization process, which involved a number of intermediates, TS structures, and pathways. Another challenge was separating the stabilizing hydrophobic effect and cation–π interaction in the GS. Once again, the electrostatic cation–π interaction formed even in polar aqueous media. One explanation is that larger more polarizable organic cations such as pyridiniums and ammoniums are poorly solvated by hard polar solvents such as water. Thus, the desolvation penalty upon complexation of the organic cations is less severe.

5.3.4.5 Other Model Systems for Studying Cation–π Interactions in Solution

Other model systems that have been developed to quantify aromatic cation–π interactions include: (a) the bimolecular thermodynamic models: Schneider's cationic cyclophane host,[165,166] Shinkai's calixarene-based hosts[167–169] and similar systems by others,[170] Collet's cryptophane host,[171] Diederich's factor Xa ligand,[172,173] Hunter's supramolecular zipper complex;[174,175] (b) the unimolecular thermodynamic models: Yamada's seesaw balance,[176] Zoltewicz's 1,8-diarylnaphthalene cation–π cofacial model.[103,104]

5.3.5 Anion–π Interaction

Aromatic surfaces can also form stabilizing interactions with anions under specific conditions.[177,178] These anion–π interactions are typically characterized by the negatively charged ions approaching the face of an electron deficient aromatic surface.[179] The main driving force for anion–π interactions is the attractive electrostatic interaction between the anion and the electropositive face of a highly electron deficient arene.[177,180] Note that aromatic

surfaces normally have an electronegative π-cloud face and thus will form repulsive interactions with anions. The strength of anion–π interactions varies greatly depending on the anion, aromatic surface, and solvent environment. Experimental measurements of anion–π interactions in solution have been particularly challenging due to the difficulty in controlling the interaction geometry of the anion as well as in isolating the interaction energy from other competing non-covalent interactions. For example, the majority of anion–π studies employed bimolecular thermodynamic models because of the difficulty in connecting anions, such as halides, to a covalent framework. Many anion–π complexes also display a charge-transfer band that can be used to monitor their binding equilibria.[181,182] Readers are referred to recent reviews and accounts on anion–π interactions[7,8,179] and additional chapters in this volume.

5.3.5.1 *Wang's Calix[2]arene[2]triazine Anion–π Model*

Wang developed a V-shaped calix[2]arene[2]triazine receptor to quantitatively measure anion–π interactions in solution (Figure 5.24(a)).[183,184] This anion receptor preorganizes two electron-deficient triazine rings into a V-shaped anion binding pocket. Depending on its size, atomic anion guests can engage in anion–π interactions with one or both pyrazine rings. A binding-induced enhancement in fluorescent emission was used to measure the anion–receptor association constants. Job plot analyses confirmed that the receptor bound anions with a 1:1 stoichiometry in solution. Fluoride and chloride showed similar binding affinities in acetonitrile (4000 and 4300 M^{-1}), which corresponds to a binding energy of −4.9 kcal mol^{-1}. The anion–π interaction geometry was confirmed in the solid-state by X-ray crystal structures. The larger bromide did not appear to bind measurably under these conditions.

An intriguing observation from these studies was the highly organized role of solvent molecules in the halide–receptor complexes. The halide formed a

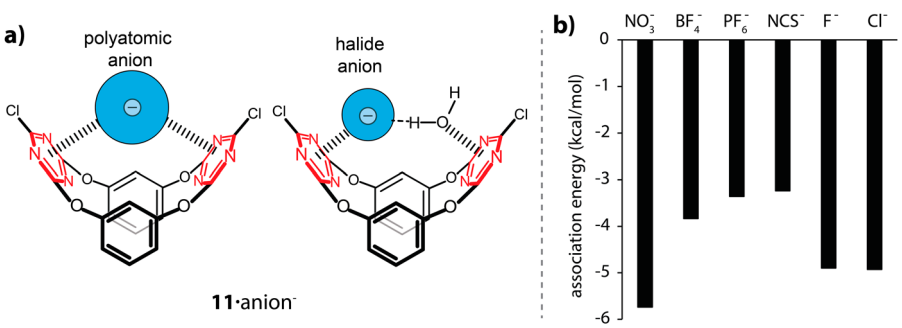

Figure 5.24 (a) Schematic representation of Wang's calix[2]arene[2]triazine host binding polyatomic (left) and halide (right) guests *via* anion–π interactions; (b) measured association energies in CH_3CN between calix[2]arene[2]triazine receptor and various anions.

direct anion–π interaction with only one of the pyrazine units. A second indirect halide–receptor interaction was formed *via* a bridging water molecule. The water molecule was bound into the cavity forming an H-bond with the halide and, at the same time, a lp–π interaction with the other pyrazine ring.

In addition to spherical halides, the binding of polyatomic anions (NCS^-, NO_3^-, BF_4^-, PF_6^-) of varying geometries was investigated in acetonitrile. Surprisingly, NO_3^- was found to have the highest affinity ($K_a = 1.7 \times 10^4\ M^{-1}$) in comparison to others ($K_a \leq 1000\ M^{-1}$). When converted to interaction energies, the anion–π interaction for NO_3 (−5.7 kcal mol^{-1}) was about −1 to −2 kcal mol^{-1} more stabilizing than those for other anions tested (−3.2 to −3.9 kcal mol^{-1}). X-Ray crystal structures revealed that these polyatomic anions formed anion–π interactions with both pyrazine rings upon binding. Interestingly, the linear and planar anions did not adopt a stacking-type of alignment upon forming the anions–π interactions in the V-shaped cavity.

5.3.5.2 *Ballester's Calix[4]pyrrole Anion–π Model*

Ballester developed a calix[4]pyrrole-based anion receptor to study anion–π interactions in solution (Figure 5.25(a)).[185] This receptor utilized supporting H-bond interactions from four pyrrole NHs to hold the anion guests at the bottom of a cone-shaped cavity with four aromatic walls. The contribution of the H-bond interactions to the anion–receptor association energy was assessed using a control receptor, which lacked the four aromatic groups. Association constants were measured by tracking the chemical shift change of the pyrrole NHs in the ^1H NMR spectra or by isothermal calorimetry titration (ITC).

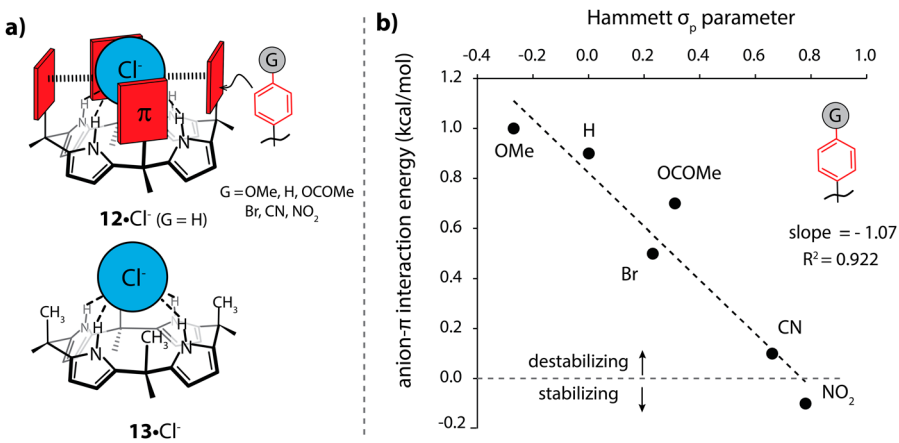

Figure 5.25 (a) Schematic representation of Ballester's "four-walled" calix[4]pyrrole host (top) and a control (**13**) that lacks aromatic walls (bottom) binding a chloride guest; (b) correlation of the measured anion–π interaction energies in CH_3CN with the Hammett σ_p parameter of the substituents.

Using chloride as the prototypical anion guest, the electrostatic effects of the anion–π interactions were studied by varying substituents at the *para*-position of the four phenyl rings (Figure 5.25(b)). The differences in binding energies of the tetraphenyl calix[4]pyrrole and control receptors provided an estimate of the cooperative effect of the four anion–π interactions. The electrostatic nature of the interaction was evident from the strong linear correlation between the measured anion–π interaction energies and the Hammett σ_p parameters of the substituents with the EDGs strongly destabilizing and the EWGs weakly destabilizing to weakly stabilizing the anion–π interactions. The anion–π interactions were destabilizing for all substituents except for NO_2, which was weakly stabilizing. Presumably, all of the substituents except for NO_2 were not sufficiently electron withdrawing to make the face of the phenyl rings electrostatically attractive to the chloride anion.

Ballester later improved the calix[4]pyrrole-based receptors by deleting two of the *meso*-aromatic rings, which created a larger anion binding cavity and allowed the introduction of multiple substituents on the two remaining phenyl rings (Figure 5.26(a)).[186] The two-walled receptors bound a broader range of anionic guests and with higher affinities than the previous four-walled version. For example, the two-walled receptor **14** bound Cl^- with a K_a with Cl^- (26.5×10^3 M^{-1}) that was two orders of magnitude larger than that of the four-walled receptor **12** (0.25×10^3 M^{-1}). This increased affinity could partially be due to the lower desolvation penalty of the anionic guests in the more open two-walled binding site. Larger bromide and iodide anions also bound with the two-walled receptor when sufficiently electron withdrawing groups were positioned on the two phenyl rings. Electrostatic and dispersion

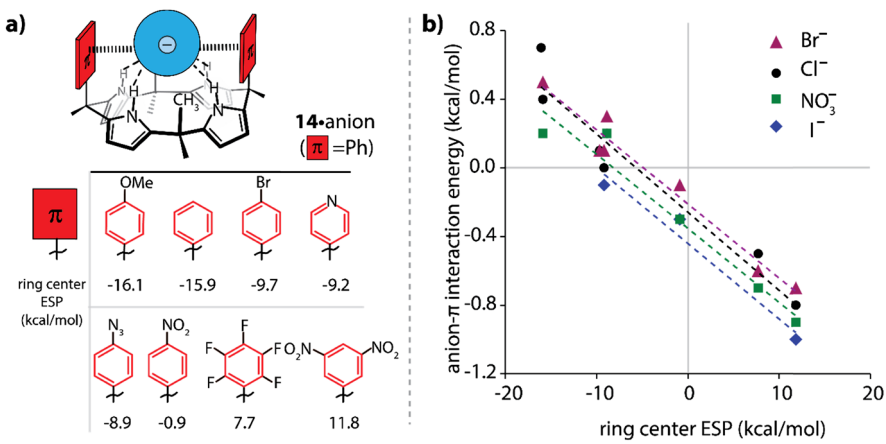

Figure 5.26 (a) Schematic representation of Ballester's "two-walled" calix[4]pyrrole host binding an anion guest; (b) correlation of measured anion–π interaction energies (in acetonitrile) between the two-walled receptor and various anions against the calculated ESP at the center of the aromatic group.

driven substituent trends were observed for the three halides Cl^-, Br^-, and I^- (Figure 5.26(b)). The more electronegative chloride formed a slightly more stabilizing anion–π interaction than bromide, which was consistent with the smaller harder anions forming stronger electrostatic interactions. However, the larger iodide anion consistently formed a stronger anion–π interaction than bromide, suggesting that anion polarizability is also important for anion–π interactions. The anion–π interactions of NO_3^- were also investigated and found to show a similar electrostatic trend on the correlation plot as the aforementioned halides (Figure 5.26(b)).[187]

5.3.5.3 Other Model Systems for Studying Anion–π Interactions in Solution

Other bimolecular thermodynamic model systems that have been developed to quantify aromatic anion–π interactions include: Dunbar's HATCN6 halide receptor,[182] Ghosh's tripodal perflurophenyl anion receptors,[188–191] Furuta's *N*-confused porphyrin anion receptor,[192,193] Johnson's *N*-aryl sulfonamide perfluoroaromatic anion receptor,[194] Taylor's urea-based perfluoroaromatic anion receptor.[195] Interested readers are referred to a recent review on the experimental measurements of anion–π interactions.[196]

5.3.6 Lone Pair–π Interaction

Crystal structure database studies have suggested that aromatic surfaces can form weak stabilizing interactions with sulfur and oxygen lone pairs under certain circumstances.[197,198] Typically, the π-faces of aromatic rings are predicted to form repulsive interactions with oxygen and sulfur lone pairs due to unfavorable electrostatic interactions.[199] However, as with anions, lone pairs have been observed to form stabilizing interactions with strongly electron deficient aromatic surfaces;[200–204] for example, the oxygen lone pair of water in the crystal structure of Wang's anion receptors (Figure 5.24(a)).[183] There is also some evidence that the lp–π interaction (*vide infra*) can be stabilizing even if the participating aromatic surfaces are unsubstituted or are only modestly electron deficient.[205,206] Thus, this is a topic that requires further study.

5.3.6.1 Gung's Oxygen lp–π Triptycene Balance

Gung designed a triptycene-based molecular balance to quantitatively assess oxygen lp–π interactions in solution (Figure 5.26(a)).[206] This unimolecular thermodynamic model was based on the rotation of a benzyl group at the 9-position of a 1,4-disubstituted triptycene framework, which leads to two *syn*- and one *anti*-conformations. In the *syn*-conformers, the benzyl group is held near an ether oxygen at the 1-position of the triptycene platform potentially forming an intramolecular lp–π interaction. In the *anti*-conformer, the

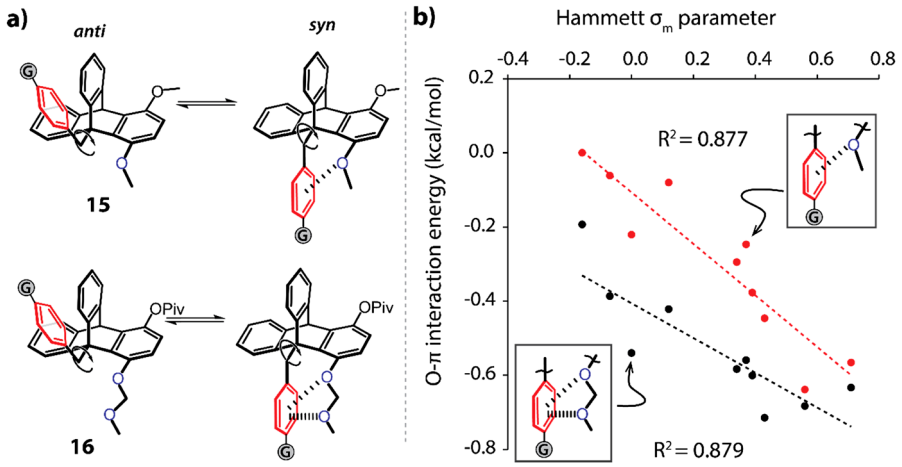

Figure 5.27 (a) Schematic representation of the *anti*⇋*syn* equilibrium of Gung's triptycene-based molecular balances for quantifying oxygen lp–π interactions; (b) correlation of the quantified oxygen lp–π interaction energies with the Hammett σ_m parameter of the *para*-substituent.

9-benzyl ring is held far from the substituent at the 1-position. Thus, the *syn–anti* equilibrium ratios can quantitatively measure the stabilizing or destabilizing influence of the lp–π interactions. One complication was the statistical 2 : 1 *syn–anti* ratio of the reference state in the absence of any intermolecular interactions between the groups at the 1- and 9-positions. Another complication was that the benzyl group rotated rapidly at room temperature. Therefore, the equilibrium ratios were determined at low temperatures (−40 to −50 °C) where the *syn*- and *anti*-conformers were in slow exchange and gave distinct signals in the ^{1}H NMR spectra.

A methyl ether at the triptycene 1-position formed a weakly stabilizing interaction (−0.17 kcal mol^{-1}) with the unsubstituted phenyl ring. Modeling predicted that the oxygen of the methyl ether was over the *ipso* position of the benzyl ring (Figure 5.27(b), inset) and could form an off-center lp–π interaction. The strength of this interaction was modulated by the introduction of EWGs and EDGs at the *para*-position of the 9-benzyl group. The observed stability trends were consistent with the EWGs stabilizing the oxygen lp–π interaction and EDGs destabilizing the interaction. The authors tried to rule out the possibility that the trends were due to the influences of the CH–π interaction from the methyl group and the C–O bond dipole. First, the negative slope of the Hammett plot was opposite to that expected for a polarized CH–π interaction[155] that would be stabilized by EDGs on the phenyl ring. Second, replacement of the methyl group with a COEt group, which had a greater C–O dipole, displayed a shallower trendline in the Hammett plot.

Gung later developed an improved triptycene balance with a methoxymethoxyl (MOMO) group in the 1-position, which contained a second oxygen that was better positioned above the center of the 9-benzyl ring upon forming

the lp–π interaction (Figure 5.26(a), bottom).[205] The intramolecular oxygen lp–π interaction involving MOMO was estimated to be −0.1 to −0.3 kcal mol^{-1} stronger than the interactions of the methyl ether. Similar electrostatic substituent effects of the interacting phenyl ring were observed with EWGs stabilizing and EDGs destabilizing the interaction. A significantly stronger oxygen lp–π interaction (<−1.2 kcal mol^{-1}) was observed when the 9-benzyl ring was perfluorinated, suggesting a magnification of the electrostatic term for this electron deficient ring.[207]

5.3.6.2 Motherwell's lp–π Seesaw Balance

Motherwell developed a seesaw molecular balance based on the dynamic bicyclic dibenzobicyclo[3,2,2]nonan (DBN) framework to study oxygen lp–π interactions in solution (Figure 5.27).[208] This unimolecular thermodynamic model followed the ring flip of a propylene bridge, which adopted two distinct conformers in which the bridge substituents, Z and Y, were alternatively positioned against an aromatic shelf. The two conformers were denoted as U or D according to whether the Z substituent was pointed "up" and away from or "down" and towards the aromatic shelf. The equilibrium U–D ratios, therefore, reflected the differences in strength of the Z-aromatic and Y-aromatic interactions in solution in each seesaw balance.[78,209] Due to the low isomerization barrier (<6.4 kcal mol^{-1}), the equilibrium U–D ratios were measured *via* coupling constant analysis of the diastereotopic methylene protons of the propylene bridge.

Oxygen and sulfur-containing groups were incorporated as the Z or Y substituent to evaluate the oxygen and sulfur lp–π interactions (Figure 5.28, right). The intramolecular oxygen lp–π interaction was first quantitatively evaluated against a counterweight methyl group, which formed intramolecular CH–π interactions. Surprisingly, the ether oxygen formed a −0.5 kcal mol^{-1} more stabilizing interaction than the "counter balancing" CH–π interactions

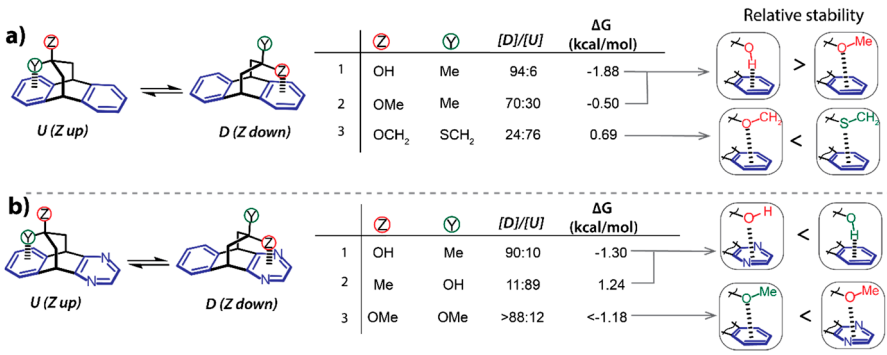

Figure 5.28 Schematic representation of the U–D conformational equilibrium of Motherwell's seesaw balances for quantifying the oxygen lp–π, sulfur lp–π (a) and oxygen lp–heterocycle (b) interactions.

of the methyl group in chloroform. Benchmarked against the same counter balancing interaction, the OH group formed a noticeably more stabilizing H-bond interaction with the electronegative π-cloud (by −1.4 kcal mol^{-1}) than the ether oxygen lp–π interactions.

The differences between the oxygen and sulfur lp–π interactions were also probed. The sulfur lp–π interaction was found to be modestly more stabilizing by −0.7 kcal mol^{-1} than the oxygen lp–π interaction, presumably due to a stronger dispersion contribution from the more polarizable sulfur atom. The oxygen lp–π interaction also became much stronger when the interacting aromatic shelf was changed into a heterocycle.[204] The lp–π interaction of an ether oxygen with a pyrazine shelf was more stabilizing by −1.2 kcal mol^{-1} than with a benzene shelf. The stronger stabilizing lp–π interactions with heteroaromatic surfaces were also evident from the change in the interaction type for the OH group, as the OH substituent preferred to form an lp–π interaction rather than H-bond with the electron deficient pyrazine shelf.

5.4 Conclusion

This chapter has provided a short overview of the different approaches to measure aromatic interactions in solution. These studies have contributed greatly to the recent acceleration in the fundamental understanding of these interactions and also to applications in biology and synthetic organic chemistry. In all of the examples, a model system with a preorganized molecular framework was utilized to position interacting groups and surfaces in specific geometries and orientations to form non-covalent interactions of interest. These model systems were classified into four types using two criteria: bimolecular *versus* unimolecular and thermodynamic *versus* kinetic. Each type of aromatic interaction can be or has been studied by all four types of model systems in solution. The bimolecular thermodynamic and the unimolecular thermodynamic models are the most commonly seen in the literature. However, each model type has its unique advantages as well as limitations, which deserve attention when selecting a model type for a particular study. Bimolecular and unimolecular model systems have complementary strengths and weaknesses. Bimolecular model systems have the advantage of ease in synthesis and testing because the recognition units are on separate molecules. The disadvantage of bimolecular model systems is their imprecise control over the interaction geometries. Conversely, the strength of unimolecular systems is their ability to precisely and predictably control the geometry of the non-covalent interaction both in the solid-state and in solution. This control comes at the cost of added synthetic effort as each pair of recognition units have to be covalently connected together by a rigid or highly preorganized framework.

Finally, we would like to close with some general observations and comments about the challenges in studying the weak aromatic interactions in solution. Surveying the results of the various studies described in this chapter, one common thread is the importance of electrostatics in modulating

the strength of aromatic interactions. This might be somewhat surprising as aromatic groups are generally considered to be non-polar or weakly polarized. However, it is clear that charged species, such as cations, anions, and molecules with strong dipoles, display some of the strongest affinities for aromatic surfaces. Even aromatic interactions with small or negligible electrostatic components, such as aliphatic CH–π interactions, can be greatly strengthened by the introduction of strongly EWG substituents. Another common thread is the importance of control models and measurements. In most cases, the accuracy and utility of a study are limited by the quality of its controls. Even in model systems that appear simple and straightforward, the analysis of control systems revealed the presence of other interactions that were of similar magnitude as the aromatic interactions being measured. In this regard, the DMC analysis was particularly helpful in isolating the non-covalent interaction energy even in very complex systems with many additional interactions. The most convincing studies were those employing multiple methods to probe the aromatic interactions, such substituent effects, solvent effects, X-ray crystallography, and computational studies. Finally, the study of weak aromatic interactions within biologically relevant frameworks or synthetic organic reactions can be more challenging but also has the benefit of practical utility and applications in these respective fields.

Acknowledgements

The support from NSF grant CHE 1310139 is acknowledged.

References

1. E. A. Meyer, R. K. Castellano and F. Diederich, *Angew. Chem., Int. Ed.*, 2003, **42**, 1210–1250.
2. L. M. Salonen, M. Ellermann and F. Diederich, *Angew. Chem., Int. Ed.*, 2011, **50**, 4808–4842.
3. E. Persch, O. Dumele and F. Diederich, *Angew. Chem., Int. Ed.*, 2015, **54**, 3290–3327.
4. O. Takahashi, Y. Kohno and M. Nishio, *Chem. Rev.*, 2010, **110**, 6049–6076.
5. J. C. Ma and D. A. Dougherty, *Chem. Rev.*, 1997, **97**, 1303–1324.
6. A. S. Mahadevi and G. N. Sastry, *Chem. Rev.*, 2013, **113**, 2100–2138.
7. B. L. Schottel, H. T. Chifotides and K. R. Dunbar, *Chem. Soc. Rev.*, 2008, **37**, 68–83.
8. M. Giese, M. Albrecht and K. Rissanen, *Chem. Rev.*, 2015, **115**, 8867–8895.
9. Z. Chen, A. Lohr, C. R. Saha-Moller and F. Wurthner, *Chem. Soc. Rev.*, 2009, **38**, 564–584.
10. M. Yamakawa, I. Yamada and R. Noyori, *Angew. Chem., Int. Ed.*, 2001, **40**, 2818–2821.

11. Y. El-Azizi, A. Schmitzer and S. K. Collins, *Angew. Chem., Int. Ed.*, 2006, **45**, 968–973.
12. P. Bolduc, A. Jacques and S. K. Collins, *J. Am. Chem. Soc.*, 2010, **132**, 12790–12791.
13. S. Yamada and C. Morita, *J. Am. Chem. Soc.*, 2002, **124**, 8184–8185.
14. R. R. Knowles, S. Lin and E. N. Jacobsen, *J. Am. Chem. Soc.*, 2010, **132**, 5030–5032.
15. R. Carrillo, M. Lopez-Rodriguez, V. S. Martin and T. Martin, *Angew. Chem., Int. Ed.*, 2009, **48**, 7803–7808.
16. Y. Zhao, Y. Domoto, E. Orentas, C. Beuchat, D. Emery, J. Mareda, N. Sakai and S. Matile, *Angew. Chem., Int. Ed.*, 2013, **52**, 9940–9943.
17. Y. Zhao, N. Sakai and S. Matile, *Nat. Commun.*, 2014, **5**, 3911.
18. Y. Zhao, Y. Cotelle, A. J. Avestro, N. Sakai and S. Matile, *J. Am. Chem. Soc.*, 2015, **137**, 11582–11585.
19. S. Fleming and R. V. Ulijn, *Chem. Soc. Rev.*, 2014, **43**, 8150–8177.
20. M. Kumar, K. V. Rao and S. J. George, *Phys. Chem. Chem. Phys.*, 2014, **16**, 1300–1313.
21. A. Das and S. Ghosh, *Angew. Chem., Int. Ed.*, 2014, **53**, 2038–2054.
22. J. K. Klosterman, Y. Yamauchi and M. Fujita, *Chem. Soc. Rev.*, 2009, **38**, 1714–1725.
23. C. Bissantz, B. Kuhn and M. Stahl, *J. Med. Chem.*, 2010, **53**, 5061–5084.
24. M. Brandl, M. S. Weiss, A. Jabs, J. Suhnel and R. Hilgenfeld, *J. Mol. Biol.*, 2001, **307**, 357–377.
25. G. B. McGaughey, M. Gagne and A. K. Rappe, *J. Biol. Chem.*, 1998, **273**, 15458–15463.
26. J. L. Asensio, A. Arda, F. J. Canada and J. Jimenez-Barbero, *Acc. Chem. Res.*, 2013, **46**, 946–954.
27. K. E. Riley and P. Hobza, *Acc. Chem. Res.*, 2013, **46**, 927–936.
28. S. K. Burley and G. A. Petsko, *Science*, 1985, **229**, 23–28.
29. C. A. Hunter, J. Singh and J. M. Thornton, *J. Mol. Biol.*, 1991, **218**, 837–846.
30. S. K. Burley and G. A. Petsko, *Adv. Protein Chem.*, 1988, **39**, 125–189.
31. M. O. Sinnokrot, E. F. Valeev and C. D. Sherrill, *J. Am. Chem. Soc.*, 2002, **124**, 10887–10893.
32. M. O. Sinnokrot and C. D. Sherrill, *J. Phys. Chem. A*, 2004, **108**, 10200–10207.
33. M. O. Sinnokrot and C. D. Sherrill, *J. Am. Chem. Soc.*, 2004, **126**, 7690–7697.
34. S. A. Arnstein and C. D. Sherrill, *Phys. Chem. Chem. Phys.*, 2008, **10**, 2646–2655.
35. S. E. Wheeler and K. N. Houk, *J. Am. Chem. Soc.*, 2008, **130**, 10854–10855.
36. S. E. Wheeler, *J. Am. Chem. Soc.*, 2011, **133**, 10262–10274.
37. S. E. Wheeler and J. W. G. Bloom, *J. Phys. Chem. A*, 2014, **118**, 6133–6147.
38. S. Tsuzuki, K. Honda, T. Uchimaru, M. Mikami and K. Tanabe, *J. Am. Chem. Soc.*, 2000, **122**, 3746–3753.

39. S. Tsuzuki, T. Uchimaru, K. Sugawara and M. Mikami, *J. Chem. Phys.*, 2002, **117**, 11216–11221.
40. S. Tsuzuki, K. Honda, T. Uchimaru, M. Mikami and A. Fujii, *J. Phys. Chem. A*, 2006, **110**, 10163–10168.
41. S. Tsuzuki, K. Honda, A. Fujii, T. Uchimaru and M. Mikami, *Phys. Chem. Chem. Phys.*, 2008, **10**, 2860–2865.
42. S. Tsuzuki, T. Uchimaru and M. Mikami, *J. Phys. Chem. B*, 2009, **113**, 5617–5621.
43. S. Tsuzuki, T. Uchimaru and M. Mikami, *J. Phys. Chem. A*, 2011, **115**, 11256–11262.
44. D. Kim, S. Hu, P. Tarakeshwar, K. S. Kim and J. M. Lisy, *J. Phys. Chem. A*, 2003, **107**, 1228–1238.
45. K. S. Kim, P. Tarakeshwar and J. Y. Lee, *Chem. Rev.*, 2000, **100**, 4145–4185.
46. D. Kim, P. Tarakeshwar and K. S. Kim, *J. Phys. Chem. A*, 2004, **108**, 1250–1258.
47. N. J. Singh, S. K. Min, D. Y. Kim and K. S. Kim, *J. Chem. Theory Comput.*, 2009, **5**, 515–529.
48. A. L. Ringer, M. S. Figgs, M. O. Sinnokrot and C. D. Sherrill, *J. Phys. Chem. A*, 2006, **110**, 10822–10828.
49. S. Ehrlich, J. Moellmann and S. Grimme, *Acc. Chem. Res.*, 2013, **46**, 916–926.
50. C. D. Sherrill, *Acc. Chem. Res.*, 2013, **46**, 1020–1028.
51. S. E. Wheeler, *Acc. Chem. Res.*, 2013, **46**, 1029–1038.
52. Y. Cho, W. J. Cho, I. S. Youn, G. Lee, N. J. Singh and K. S. Kim, *Acc. Chem. Res.*, 2014, **47**, 3321–3330.
53. S. R. Gadre, S. D. Yeole and N. Sahu, *Chem. Rev.*, 2014, **114**, 12132–12173.
54. S. S. Babu, V. K. Praveen and A. Ajayaghosh, *Chem. Rev.*, 2014, **114**, 1973–2129.
55. S.-M. Hsu, Y.-C. Lin, J.-W. Chang, Y.-H. Liu and H.-C. Lin, *Angew. Chem., Int. Ed.*, 2014, **53**, 1921–1927.
56. W. Liyanage and B. L. Nilsson, *Langmuir*, 2016, **32**, 787–799.
57. M. Roman, C. Cannizzo, T. Pinault, B. Isare, B. Andrioletti, P. van der Schoot and L. Bouteiller, *J. Am. Chem. Soc.*, 2010, **132**, 16818–16824.
58. M. K. Chung, S. J. Lee, M. L. Waters and M. R. Gagne, *J. Am. Chem. Soc.*, 2012, **134**, 11430–11443.
59. M. Xue, Y. Yang, X. Chi, Z. Zhang and F. Huang, *Acc. Chem. Res.*, 2012, **45**, 1294–1308.
60. D. Ajami and J. Rebek, *Nat. Chem.*, 2009, **1**, 87–90.
61. L. Bautista-Ibanez, K. Ramirez-Gualito, B. Quiroz-Garcia, A. Rojas-Aguilar and G. Cuevas, *J. Org. Chem.*, 2008, **73**, 849–857.
62. K. Ramirez-Gualito, R. Alonso-Rios, B. Quiroz-Garcia, A. Rojas-Aguilar, D. Diaz, J. Jimenez-Barbero and G. Cuevas, *J. Am. Chem. Soc.*, 2009, **131**, 18129–18138.
63. P. Thordarson, *Chem. Soc. Rev.*, 2011, **40**, 1305–1323.
64. L. Fielding, *Tetrahedron*, 2000, **56**, 6151–6170.

65. K. Hirose, *J. Inclusion Phenom. Macrocyclic Chem.*, 2001, **39**, 193–209.
66. C. A. Parker and W. T. Rees, *Analyst*, 1960, **85**, 587–600.
67. M. W. Freyer and E. A. Lewis, *Methods Cell Biol.*, Academic Press, 2008, vol. 84, pp. 79–113.
68. P. J. Carter, G. Winter, A. J. Wilkinson and A. R. Fersht, *Cell*, 1984, **38**, 835–840.
69. A. Horovitz, *Folding Des.*, 1996, **1**, R121–R126.
70. A. E. Mark and W. F. Vangunsteren, *J. Mol. Biol.*, 1994, **240**, 167–176.
71. K. A. Dill, *J. Biol. Chem.*, 1997, **272**, 701–704.
72. A. Whitty, *Nat. Chem. Biol.*, 2008, **4**, 435–439.
73. C. A. Hunter and H. L. Anderson, *Angew. Chem., Int. Ed.*, 2009, **48**, 7488–7499.
74. H. Adams, F. J. Carver, C. A. Hunter, J. C. Morales and E. M. Seward, *Angew. Chem., Int. Ed. Engl.*, 1996, **35**, 1542–1544.
75. F. J. Carver, C. A. Hunter, P. S. Jones, D. J. Livingstone, J. F. McCabe, E. M. Seward, P. Tiger and S. E. Spey, *Chem.–Eur. J.*, 2001, **7**, 4854–4862.
76. H. Adams, C. A. Hunter, K. R. Lawson, J. Perkins, S. E. Spey, C. J. Urch and J. M. Sanderson, *Chem.–Eur. J.*, 2001, **7**, 4863–4877.
77. C. A. Hunter, P. S. Jones, P. Tiger and S. Tomas, *Chem.–Eur. J.*, 2002, **8**, 5435–5446.
78. A. E. Aliev, J. R. T. Arendorf, I. Pavlakos, R. B. Moreno, M. J. Porter, H. S. Rzepa and W. B. Motherwell, *Angew. Chem., Int. Ed.*, 2015, **54**, 551–555.
79. C. R. Martinez and B. L. Iverson, *Chem. Sci.*, 2012, **3**, 2191–2201.
80. S. L. Cockroft, C. A. Hunter, K. R. Lawson, J. Perkins and C. J. Urch, *J. Am. Chem. Soc.*, 2005, **127**, 8594–8595.
81. S. L. Cockroft, J. Perkins, C. Zonta, H. Adams, S. E. Spey, C. M. R. Low, J. G. Vinter, K. R. Lawson, C. J. Urch and C. A. Hunter, *Org. Biomol. Chem.*, 2007, **5**, 1062–1080.
82. W. J. Gaw and F. L. Swinton, *Trans. Faraday Soc.*, 1968, **64**, 2023–2034.
83. G. W. Coates, A. R. Dunn, L. M. Henling, D. A. Dougherty and R. H. Grubbs, *Angew. Chem., Int. Ed. Engl.*, 1997, **36**, 248–251.
84. W. R. Carroll, P. Pellechia and K. D. Shimizu, *Org. Lett.*, 2008, **10**, 3547–3550.
85. J. Hwang, P. Li, W. R. Carroll, M. D. Smith, P. J. Pellechia and K. D. Shimizu, *J. Am. Chem. Soc.*, 2014, **136**, 14060–14067.
86. P. Li, C. Zhao, M. D. Smith and K. D. Shimizu, *J. Org. Chem.*, 2013, **78**, 5303–5313.
87. J. Hwang, B. E. Dial, P. Li, M. E. Kozik, M. D. Smith and K. D. Shimizu, *Chem. Sci.*, 2015, **6**, 4358–4364.
88. S. Paliwal, S. Geib and C. S. Wilcox, *J. Am. Chem. Soc.*, 1994, **116**, 4497–4498.
89. B. W. Gung, M. Patel and X. W. Xue, *J. Org. Chem.*, 2005, **70**, 10532–10537.
90. B. W. Gung, X. W. Xue and H. J. Reich, *J. Org. Chem.*, 2005, **70**, 3641–3644.
91. W. R. Carroll, C. Zhao, M. D. Smith, P. J. Pellechia and K. D. Shimizu, *Org. Lett.*, 2011, **13**, 4320–4323.
92. C. Zhao, R. M. Parrish, M. D. Smith, P. J. Pellechia, C. D. Sherrill and K. D. Shimizu, *J. Am. Chem. Soc.*, 2012, **134**, 14306–14309.

93. P. Li, T. M. Parker, J. Hwang, F. Deng, M. D. Smith, P. J. Pellechia, C. D. Sherrill and K. D. Shimizu, *Org. Lett.*, 2014, **16**, 5064–5067.
94. C. Zhao, P. Li, M. D. Smith, P. J. Pellechia and K. D. Shimizu, *Org. Lett.*, 2014, **16**, 3520–3523.
95. P. Li, J. Hwang, J. M. Maier, C. Zhao, D. V. Kaborda, M. D. Smith, P. J. Pellechia and K. D. Shimizu, *Cryst. Growth Des.*, 2015, **15**, 3561–3564.
96. S. E. Wheeler, A. J. McNeil, P. Muller, T. M. Swager and K. N. Houk, *J. Am. Chem. Soc.*, 2010, **132**, 3304–3311.
97. F. Cozzi, M. Cinquini, R. Annunziata, T. Dwyer and J. S. Siegel, *J. Am. Chem. Soc.*, 1992, **114**, 5729–5733.
98. F. Cozzi, M. Cinquini, R. Annuziata and J. S. Siegel, *J. Am. Chem. Soc.*, 1993, **115**, 5330–5331.
99. F. Cozzi, F. Ponzini, R. Annunziata, M. Cinquini and J. S. Siegel, *Angew. Chem., Int. Ed. Engl.*, 1995, **34**, 1019–1020.
100. J. A. Zoltewicz, N. M. Maier and W. M. F. Fabian, *J. Org. Chem.*, 1996, **61**, 7018–7021.
101. J. A. Zoltewicz, N. M. Maier and W. M. F. Fabian, *J. Org. Chem.*, 1997, **62**, 3215–3219.
102. J. A. Zoltewicz, N. M. Maier and W. M. F. Fabian, *J. Org. Chem.*, 1997, **62**, 2763–2766.
103. J. A. Zoltewicz, N. M. Maier and W. M. F. Fabian, *J. Org. Chem.*, 1998, **63**, 4985–4990.
104. J. A. Zoltewicz and S. Lavieri, *J. Org. Chem.*, 2001, **66**, 7227–7230.
105. F. Cozzi, R. Annunziata, M. Benaglia, K. K. Baldridge, G. Aguirre, J. Estrada, Y. Sritana-Anant and J. S. Siegel, *Phys. Chem. Chem. Phys.*, 2008, **10**, 2686–2694.
106. M. S. Cubberley and B. L. Iverson, *J. Am. Chem. Soc.*, 2001, **123**, 7560–7563.
107. Z. Zhu, C. J. Cardin, Y. Gan and H. M. Colquhoun, *Nat. Chem.*, 2010, **2**, 653–660.
108. H. J. Schneider and M. Wang, *J. Org. Chem.*, 1994, **59**, 7464–7472.
109. C. J. Pace and J. Gao, *Acc. Chem. Res.*, 2013, **46**, 907–915.
110. M. Harder, M. A. C. Corrales, N. Trapp, B. Kuhn and F. Diederich, *Chem.–Eur. J.*, 2015, **21**, 8455–8463.
111. L. Yang, J. B. Brazier, T. A. Hubbard, D. M. Rogers and S. L. Cockroft, *Angew. Chem., Int. Ed.*, 2016, **55**, 912–916.
112. S. E. Snyder, B.-S. Huang, Y. W. Chu, H.-S. Lin and J. R. Carey, *Chem.–Eur. J.*, 2012, **18**, 12663–12671.
113. R. R. Gardner, L. A. Christianson and S. H. Gellman, *J. Am. Chem. Soc.*, 1997, **119**, 5041–5042.
114. Y. S. Chong, W. R. Carroll, W. G. Burns, M. D. Smith and K. D. Shimizu, *Chem.–Eur. J.*, 2009, **15**, 9117–9126.
115. M. J. Rashkin and M. L. Waters, *J. Am. Chem. Soc.*, 2002, **124**, 1860–1861.
116. F. Cozzi, R. Annunziata, M. Benaglia, M. Cinquini, L. Raimondi, K. K. Baldridge and J. S. Siegel, *Org. Biomol. Chem.*, 2003, **1**, 157–162.
117. E. Kim, S. Paliwal and C. S. Wilcox, *J. Am. Chem. Soc.*, 1998, **120**, 11192–11193.

118. T. Ren, Y. Jin, K. S. Kim and D. H. Kim, *J. Biomol. Struct. Dyn.*, 1997, **15**, 401–405.
119. F. R. Fischer, W. B. Schweizer and F. Diederich, *Chem. Commun.*, 2008, 4031–4033.
120. H. Gardarsson, W. B. Schweizer, N. Trapp and F. Diederich, *Chem.–Eur. J.*, 2014, **20**, 4608–4616.
121. A. L. Ringer, M. O. Sinnokrot, R. P. Lively and C. D. Sherrill, *Chem.–Eur. J.*, 2006, **12**, 3821–3828.
122. I. K. Mati and S. L. Cockroft, *Chem. Soc. Rev.*, 2010, **39**, 4195–4205.
123. S. L. Cockroft and C. A. Hunter, *Chem. Commun.*, 2006, 3806–3808.
124. S. L. Cockroft and C. A. Hunter, *Chem. Commun.*, 2009, 3961–3963.
125. L. Yang, C. Adam, G. S. Nichol and S. L. Cockroft, *Nat. Chem.*, 2013, **5**, 1006–1010.
126. L. Yang, C. Adam and S. L. Cockroft, *J. Am. Chem. Soc.*, 2015, **137**, 10084–10087.
127. M. R. Ams, M. Fields, T. Grabnic, B. G. Janesko, M. Zeller, R. Sheridan and A. Shay, *J. Org. Chem.*, 2015, **80**, 7764–7769.
128. B. Bhayana and M. R. Ams, *J. Org. Chem.*, 2011, **76**, 3594–3596.
129. B. Bhayana, *J. Org. Chem.*, 2013, **78**, 6758–6762.
130. E. H. Krenske, K. N. Houk, A. G. Lohse, J. E. Antoline and R. P. Hsung, *Chem. Sci.*, 2010, **1**, 387–392.
131. J. E. Antoline, E. H. Krenske, A. G. Lohse, K. N. Houk and R. P. Hsung, *J. Am. Chem. Soc.*, 2011, **133**, 14443–14451.
132. F. J. Carver, C. A. Hunter, D. J. Livingstone, J. F. McCabe and E. M. Seward, *Chem.–Eur. J.*, 2002, **8**, 2848–2859.
133. W. B. Jennings, N. J. P. McCarthy, P. Kelly and J. F. Malone, *Org. Biomol. Chem.*, 2009, **7**, 5156–5162.
134. W. B. Jennings, N. O'Connell, J. F. Malone and D. R. Boyd, *Org. Biomol. Chem.*, 2013, **11**, 5278–5291.
135. C. D. Tatko and M. L. Waters, *J. Am. Chem. Soc.*, 2002, **124**, 9372–9373.
136. R. Annunziata, M. Benaglia, F. Cozzi and A. Mazzanti, *Chem.–Eur. J.*, 2009, **15**, 4373–4381.
137. J. Xia, S. Liu, F. Cozzi, M. Mancinelli and A. Mazzanti, *Chem.–Eur. J.*, 2012, **18**, 3611–3620.
138. S. Tsuzuki and A. Fujii, *Phys. Chem. Chem. Phys.*, 2008, **10**, 2584–2594.
139. P. T. Corbett, J. Leclaire, L. Vial, K. R. West, J. L. Wietor, J. K. M. Sanders and S. Otto, *Chem. Rev.*, 2006, **106**, 3652–3711.
140. E. Jimenez-Moreno, A. M. Gomez, A. Bastida, F. Corzana, G. Jimenez-Oses, J. Jimenez-Barbero and J. L. Asensio, *Angew. Chem., Int. Ed.*, 2015, **54**, 4344–4348.
141. J. Li, P. Nowak and S. Otto, *J. Am. Chem. Soc.*, 2013, **135**, 9222–9239.
142. T. Vacas, F. Corzana, G. Jimenez-Oses, C. Gonzalez, A. M. Gomez, A. Bastida, J. Revuelta and J. L. Asensio, *J. Am. Chem. Soc.*, 2010, **132**, 12074–12090.
143. A. G. Santana, E. Jimenez-Moreno, A. M. Gomez, F. Corzana, C. Gonzalez, G. Jimenez-Oses, J. Jimenez-Barbero and J. L. Asensio, *J. Am. Chem. Soc.*, 2013, **135**, 3347–3350.

144. E. Jimenez-Moreno, G. Jimenez-Oses, A. M. Gomez, A. G. Santana, F. Corzana, A. Bastida, J. Jimenez-Barberodef and J. L. Asensio, *Chem. Sci.*, 2015, **6**, 6076–6085.
145. K. M. Thomas, D. Naduthambi and N. J. Zondlo, *J. Am. Chem. Soc.*, 2006, **128**, 2216–2217.
146. N. J. Zondlo, *Acc. Chem. Res.*, 2013, **46**, 1039–1049.
147. J. C. Morales, J. J. Reina, I. Diaz, A. Avino, P. M. Nieto and R. Eritja, *Chem.–Eur. J.*, 2008, **14**, 7828–7835.
148. R. Lucas, I. Gomez-Pinto, A. Avino, J. J. Reina, R. Eritja, C. Gonzalez and J. C. Morales, *J. Am. Chem. Soc.*, 2011, **133**, 1909–1916.
149. C. J. Pace, D. Kim and J. Gao, *Chem.–Eur. J.*, 2012, **18**, 5832–5836.
150. C. S. Wilcox and B. Bhayana, *Angew. Chem., Int. Ed.*, 2007, **46**, 6833–6836.
151. Z. R. Laughrey, S. E. Kiehna, A. J. Riemen and M. L. Waters, *J. Am. Chem. Soc.*, 2008, **130**, 14625–14633.
152. K. Kishikawa, K. Yoshizaki, S. Kohmoto, M. Yamamoto, K. Yamaguchi and K. Yamada, *J. Chem. Soc., Perkin Trans. 1*, 1997, 1233–1239.
153. G. Grossmann, M. J. Potrzebowski, S. Olejniczak, N. E. Ziolkowska, G. D. Bujacz, W. Ciesielski, W. Prezdo, V. Nazarov and V. Golovko, *New J. Chem.*, 2003, **27**, 1095–1101.
154. L. Raimondi, M. Benaglia and F. Cozzi, *Eur. J. Org. Chem.*, 2014, 4993–4998.
155. B. W. Gung, B. U. Emenike, M. Lewis and K. Kirschbaum, *Chem.–Eur. J.*, 2010, **16**, 12357–12362.
156. D. A. Dougherty, *Acc. Chem. Res.*, 2013, **46**, 885–893.
157. M. A. Petti, T. J. Shepodd and D. A. Dougherty, *Tetrahedron Lett.*, 1986, **27**, 807–810.
158. P. C. Kearney, L. S. Mizoue, R. A. Kumpf, J. E. Forman, A. Mccurdy and D. A. Dougherty, *J. Am. Chem. Soc.*, 1993, **115**, 9907–9919.
159. S. Mecozzi, A. P. West and D. A. Dougherty, *Proc. Natl. Acad. Sci. U. S. A.*, 1996, **93**, 10566–10571.
160. S. M. Ngola and D. A. Dougherty, *J. Org. Chem.*, 1996, **61**, 4355–4360.
161. C. D. Tatko and M. L. Waters, *J. Am. Chem. Soc.*, 2004, **126**, 2028–2034.
162. R. M. Hughes and M. L. Waters, *J. Am. Chem. Soc.*, 2005, **127**, 6518–6519.
163. R. M. Hughes, K. R. Wiggins, S. Khorasanizadeh and M. L. Waters, *Proc. Natl. Acad. Sci. U. S. A.*, 2007, **104**, 11184–11188.
164. M. J. Rashkin, R. M. Hughes, N. T. Calloway and M. L. Waters, *J. Am. Chem. Soc.*, 2004, **126**, 13320–13325.
165. H. J. Schneider and T. Blatter, *Angew. Chem., Int. Ed. Engl.*, 1988, **27**, 1163–1164.
166. H. J. Schneider, T. Blatter, S. Simova and I. Theis, *Chem. Commun.*, 1989, 580–581.
167. K. Araki, H. Shimizu and S. Shinkai, *Chem. Lett.*, 1993, 205–208.
168. K. N. Koh, K. Araki, A. Ikeda, H. Otsuka and S. Shinkai, *J. Am. Chem. Soc.*, 1996, **118**, 755–758.
169. P. Lhoták and S. Shinkai, *J. Phys. Org. Chem.*, 1997, **10**, 273–285.
170. G. Arena, A. Casnati, A. Contino, G. G. Lombardo, D. Sciotto and R. Ungaro, *Chem.–Eur. J.*, 1999, **5**, 738–744.

171. L. Garel, B. Lozach, J. P. Dutasta and A. Collet, *J. Am. Chem. Soc.*, 1993, **115**, 11652–11653.
172. K. Scharer, M. Morgenthaler, R. Paulini, U. Obst-Sander, D. W. Banner, D. Schlatter, J. Benz, M. Stihle and F. Diederich, *Angew. Chem., Int. Ed.*, 2005, **44**, 4400–4404.
173. L. M. Salonen, C. Bucher, D. W. Banner, W. Haap, J. L. Mary, J. Benz, O. Kuster, P. Seiler, W. B. Schweizer and F. Diederich, *Angew. Chem., Int. Ed.*, 2009, **48**, 811–814.
174. C. A. Hunter, C. M. R. Low, C. Rotger, J. G. Vinter and C. Zonta, *Proc. Natl. Acad. Sci. U. S. A.*, 2002, **99**, 4873–4876.
175. C. A. Hunter, C. M. R. Low, C. Rotger, J. G. Vinter and C. Zonta, *Chem. Commun.*, 2003, 834–835.
176. S. Yamada, N. Yamamoto and E. Takamori, *Org. Lett.*, 2015, **17**, 4862–4865.
177. I. Alkorta, I. Rozas and J. Elguero, *J. Am. Chem. Soc.*, 2002, **124**, 8593–8598.
178. O. B. Berryman, V. S. Bryantsev, D. P. Stay, D. W. Johnson and B. P. Hay, *J. Am. Chem. Soc.*, 2007, **129**, 48–58.
179. A. Frontera, P. Gamez, M. Mascal, T. J. Mooibroek and J. Reedijk, *Angew. Chem., Int. Ed.*, 2011, **50**, 9564–9583.
180. D. Quinonero, C. Garau, C. Rotger, A. Frontera, P. Ballester, A. Costa and P. M. Deya, *Angew. Chem., Int. Ed.*, 2002, **41**, 3389–3392.
181. Y. S. Rosokha, S. V. Lindeman, S. V. Rosokha and J. K. Kochi, *Angew. Chem., Int. Ed.*, 2004, **43**, 4650–4652.
182. H. T. Chifotides, B. L. Schottel and K. R. Dunbar, *Angew. Chem., Int. Ed.*, 2010, **49**, 7202–7207.
183. D.-X. Wang, Q.-Y. Zheng, Q.-Q. Wang and M.-X. Wang, *Angew. Chem., Int. Ed.*, 2008, **47**, 7485–7488.
184. D.-X. Wang and M.-X. Wang, *J. Am. Chem. Soc.*, 2013, **135**, 892–897.
185. G. Gil-Ramirez, E. C. Escudero-Adan, J. Benet-Buchholz and P. Ballester, *Angew. Chem., Int. Ed.*, 2008, **47**, 4114–4118.
186. L. Adriaenssens, G. Gil-Ramirez, A. Frontera, D. Quinonero, E. C. Escudero-Adan and P. Ballester, *J. Am. Chem. Soc.*, 2014, **136**, 3208–3218.
187. L. Adriaenssens, C. Estarellas, A. V. Jentzsch, M. M. Belmonte, S. Matile and P. Ballester, *J. Am. Chem. Soc.*, 2013, **135**, 8324–8330.
188. P. S. Lakshminarayanan, I. Ravikumar, E. Suresh and P. Ghosh, *Inorg. Chem.*, 2007, **46**, 4769–4771.
189. P. S. Lakshminarayanan, I. Ravikumar, E. Suresh and P. Ghosh, *Chem. Commun.*, 2007, 5214–5216.
190. R. Dutta and P. Ghosh, *Eur. J. Inorg. Chem.*, 2012, 3456–3462.
191. S. Saha, B. Akhuli, I. Ravikumar, P. S. Lakshminarayanan and P. Ghosh, *CrystEngComm*, 2014, **16**, 4796–4804.
192. H. Maeda, A. Osuka and H. Furuta, *J. Inclusion Phenom. Macrocyclic Chem.*, 2004, **49**, 33–36.
193. H. Maeda, T. Morimoto, A. Osuka and H. Furuta, *Chem.–Asian J.*, 2006, **1**, 832–844.

194. O. B. Berryman, F. Hof, M. J. Hynes and D. W. Johnson, *Chem. Commun.*, 2006, 506–508.
195. M. G. Chudzinski, C. A. McClary and M. S. Taylor, *J. Am. Chem. Soc.*, 2011, **133**, 10559–10567.
196. M. Giese, M. Albrecht and K. Rissanen, *Chem. Commun.*, 2016, **52**, 1778–1795.
197. T. J. Mooibroek, P. Gamez and J. Reedijk, *CrystEngComm*, 2008, **10**, 1501–1515.
198. T. J. Mooibroek and P. Gamez, *CrystEngComm*, 2012, **14**, 1027–1030.
199. M. Egli and S. Sarkhel, *Acc. Chem. Res.*, 2007, **40**, 197–205.
200. M. Egli and R. V. Gessner, *Proc. Natl. Acad. Sci. U. S. A.*, 1995, **92**, 180–184.
201. J. P. Gallivan and D. A. Dougherty, *Org. Lett.*, 1999, **1**, 103–106.
202. Y. Danten, T. Tassaing and M. Besnard, *J. Phys. Chem. A*, 1999, **103**, 3530–3534.
203. J. C. Amicangelo, D. G. Irwin, C. J. Lee, N. C. Romano and N. L. Saxton, *J. Phys. Chem. A*, 2013, **117**, 1336–1350.
204. I. Pavlakos, T. Arif, A. E. Aliev, W. B. Motherwell, G. J. Tizzard and S. J. Coles, *Angew. Chem., Int. Ed.*, 2015, **54**, 8169–8174.
205. B. W. Gung, Y. Zou, Z. G. Xu, J. C. Amicangelo, D. G. Irwin, S. Q. Ma and H. C. Zhou, *J. Org. Chem.*, 2008, **73**, 689–693.
206. B. W. Gung, X. W. Xue and H. J. Reich, *J. Org. Chem.*, 2005, **70**, 7232–7237.
207. J. C. Amicangelo, B. W. Gung, D. G. Irwin and N. C. Romano, *Phys. Chem. Chem. Phys.*, 2008, **10**, 2695–2705.
208. W. B. Motherwell, J. Moise, A. E. Aliev, M. Nic, S. J. Coles, P. N. Horton, M. B. Hursthouse, G. Chessari, C. A. Hunter and J. G. Vinter, *Angew. Chem., Int. Ed.*, 2007, **46**, 7823–7826.
209. A. E. Aliev, J. Moise, W. B. Motherwell, M. Nic, D. Courtier-Murias and D. A. Tocher, *Phys. Chem. Chem. Phys.*, 2009, **11**, 97–100.

Published on 15 November 2016 on http://pubs.rsc.org | doi:10.1039/9781782626626-00172

CHAPTER 6

Molecular Recognition of Aromatic Peptides and Proteins in Nature and by Design

ANDREW T. BOCKUS[a] AND ADAM R. URBACH*[a]

[a]Department of Chemistry, Trinity University, 1 Trinity Place, San Antonio, TX 78212, USA
*E-mail: aurbach@trinity.edu

6.1 Overview

The complex structures of proteins enable their many biological functions, most of which include selective interactions with other molecules, *i.e.*, molecular recognition. The variety of recognition motifs, the range of binding affinities, and the fidelity of recognition displayed by proteins are truly remarkable and enable biological processes as diverse as cellular respiration, transport, signaling, metabolism, and the immune response, to name a few. In parallel with the efforts to characterize biomolecular recognition mechanisms, chemists have attempted to mimic them using designed small molecules and selected biological molecules (*e.g.*, monoclonal antibodies, nucleic acid aptamers, display peptides). Indeed, the molecular recognition of proteins has been a challenge in chemistry for several decades

Monographs in Supramolecular Chemistry No. 20
Aromatic Interactions: Frontiers in Knowledge and Application
Edited by Darren W. Johnson and Fraser Hof
© The Royal Society of Chemistry 2017
Published by the Royal Society of Chemistry, www.rsc.org

View Online

Published on 15 November 2016 on http://pubs.rsc.org | doi:10.1039/9781782626626-00172

and has led to the fields of drug design, biosensors, clinical diagnostics, bioseparations, biomaterials, and other areas of chemical biology.[1–8] Despite the extensive efforts and many successes to date, much remains to be understood about the interactions within and between the surfaces of proteins and the principles by which synthetic agents can be designed to efficiently imitate them. There are many reviews on this subject. The current chapter focuses on the unique properties of aromatic amino acids that have enabled their recognition by biological and synthetic receptors. Inquiries into the nature of aromatic interactions and the roles they play in biological recognition have been reviewed extensively elsewhere.[9–15] Select examples will be discussed here to illustrate the roles of aromatic residues in biological recognition before discussing in greater detail the development of synthetic receptors for proteins and peptides, and the lessons learned from those studies.

6.2 Aromatic Amino Acids

The twenty genetically encoded amino acids can be divided into the following groups according to the properties of their side chains (Figure 6.1): (1) acidic residues, including aspartic acid (Asp) and glutamic acid

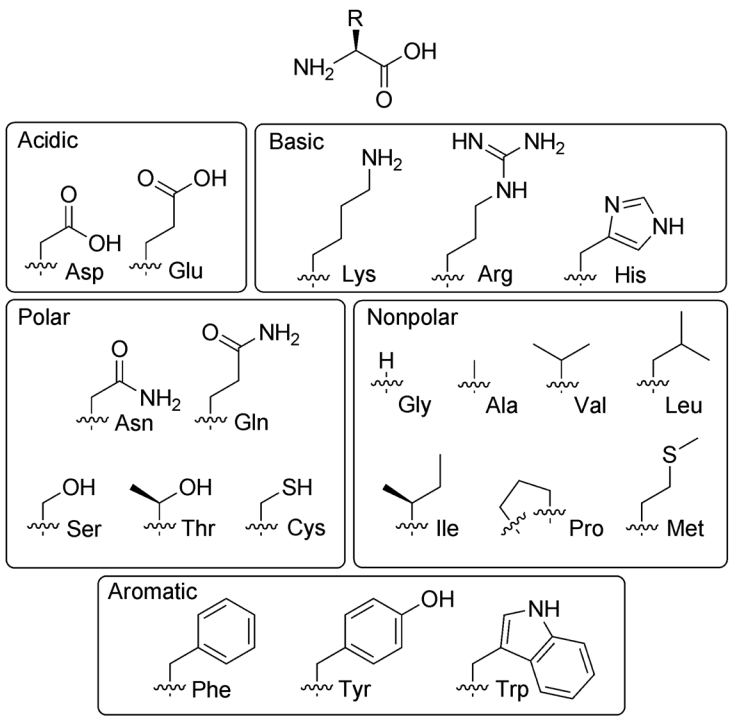

Figure 6.1 Chemical formulas of the twenty amino acids.

View Online

Published on 15 November 2016 on http://pubs.rsc.org | doi:10.1039/9781782626626-00172

(Glu); (2) basic residues, including lysine (Lys), arginine (Arg), and histidine (His). Although the imidazole side chain of His is aromatic, the behavior of this residue is primarily dictated by its basic character, and thus it is not grouped with the other aromatic amino acids in this review; (3) other polar residues, including asparagine (Asn), glutamine (Gln), serine (Ser), threonine (Thr), and cysteine (Cys); (4) hydrophobic aliphatic residues, including glycine (Gly), alanine (Ala), valine (Val), leucine (Leu), isoleucine (Ile), proline (Pro), and methionine (Met); and (5) aromatic residues, including phenylalanine (Phe), tyrosine (Tyr), and tryptophan (Trp). The behavior of the 10 polar residues is dominated by electrostatic interactions (ion–ion, ion–dipole, and dipole–dipole, including hydrogen bonding), which compete significantly with the solvent. The binding of hydrophobic aliphatic residues is driven by dispersion interactions and hydrophobic effects.

Aromatic residues have several structural features that make them particularly versatile for intermolecular interactions. The aromatic quadrupole moment drives binding to cations, hydrogen-bond donors, and other aromatic groups. The hydrophobicity, rigidity, and relatively large surface area of the ring facilitate desolvation from bulk water and the formation of extensive van der Waals contacts while mitigating the entropic cost of binding. These structural properties make it possible for aromatic interactions to be driven by electrostatic, dispersion, and/or hydrophobic effects depending on the context.[9,16,17] Trp, Tyr, and Phe occupy a unique physicochemical space as the most hydrophobic among the 20 natural amino acids. Aromatic residues have the largest side chains,[18] and therefore they have the largest possible interaction interfaces, which, when optimized, can drive strong and selective interactions with other molecules. The hydrophobicities of the amino acid side chains have been measured as the transfer energies of side chain analogs (*e.g.*, propane for Val; toluene for Phe; 3-methylindole for Trp) from cyclohexane to aqueous solution (Figure 6.2(a)),[19] and as the transfer energy of whole amino acids from a lipid bilayer to aqueous solution (Figure 6.2(b)).[20] These studies make the case for Trp, Phe, and Tyr as a combination of the largest and most hydrophobic amino acids. Aromatic side chains provide a simple means (*i.e.*, *via* a single residue) to display relatively large, flat, and hydrophobic surfaces on a protein surface, either within a cavity or on the exterior. These unique structural characteristics of aromatic residues help to explain their prevalence at key contact points in protein–protein and protein–peptide complexes in biological systems. Several examples of these complexes are discussed below in order to get a sense for the different ways in which aromatic residues contribute to these complexes. Electrostatic interactions with aromatic residues, especially cation–pi interactions, are prevalent in biological systems and are discussed in Chapter 7 of this book and in reviews.[10,13,21] This chapter concentrates on the hydrophobic nature of aromatic residues because that is where the greatest progress has been made in designing synthetic receptors.

View Online

Published on 15 November 2016 on http://pubs.rsc.org | doi:10.1039/9781782626626-00172

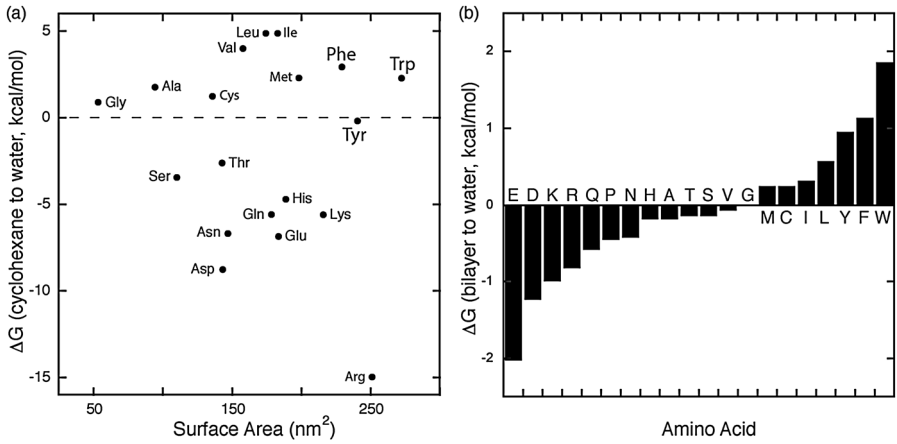

Figure 6.2 (a) Plot of the free energy of transfer from dilute cyclohexane solution to dilute aqueous solution, pH 7, *versus* the solvent-exposed surface area of the side chains of the 20 genetically encoded amino acids. The transfer energies were reported by Radzicka and Wolfenden for side chain analogues, *e.g.*, methane for alanine and 3-methylindole for tryptophan.[19] The surface areas were calculated by Chothia for tripeptides Gly-X-Gly.[18] Adapted by permission from Springer, ref. 62, ©2008. (b) Calculated whole-residue interfacial hydrophobicity (pH 8 for all residues except Arg and Lys, which were at pH 2). Notably, the extremes on this plot are dominated by charged residues at the negative end and aromatic residues at the positive end. Reprinted by permission from Macmillan Publishers Ltd., ref. 20, ©1996.

6.3 Aromatic Residues in Biological Complexes

Aromatic residues are highly prevalent in protein cavities, in which the vast majority of enzymatic catalysis and ligand binding occur. In a survey of 4000 protein–ligand complexes from the Protein Data Bank, Gallina and coworkers found that the aromatic residues Phe, Trp, and Tyr, along with His and Met, accounted for 26% of the residues found in binding pockets, while the same residues accounted for only 10.6% of the total number of amino acids in proteins. Aromatic interactions are also common at protein–protein interfaces (PPIs). The edge-to-face pi-stacking of aromatic residues is observed at the interfaces of homodimers of glutathione transferase, epidermal growth factor pathway substrate 8, and many others.[22,23] The high degree of conservation associated with these aromatic residues suggests that the role they play in recognition is significant.[22] Phe–Phe pi stacking has also been reported to be important in the anchoring of intrinsically disordered proteins.[24] Nearly 40% of a set of 77 protein–protein complexes was found to include at least one intermolecular pair of aromatic residues. Phe was found twice as frequently as Tyr and six times more than Trp at PPIs. Phe–Phe and Phe–Tyr pairings accounted for 60% of the pi–pi interactions, and the overwhelming majority of these were in the edge-to-face

View Online

Published on 15 November 2016 on http://pubs.rsc.org | doi:10.1039/9781782626626-00172

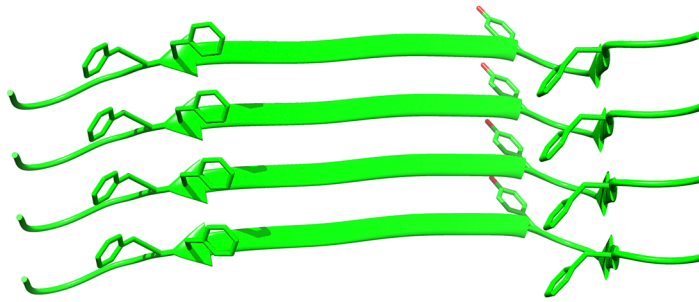

Figure 6.3 Rendering of the NMR structure of an amyloid beta fibril showing residues 1–26 (PDB: 2MVX). The aromatic residues are rendered as stick models.[25]

orientation. Computational alanine scanning suggests that 95% of the Phe residues and 85% of Tyr residues were important contributors to the free energy of binding. Trp was involved in only 10% of the pi–pi interactions, but in 80% of those cases, each Trp side chain contributed over 4 kcal mol^{-1} to the binding energy.[24]

Interchain pi-stacking interactions have also been observed to stabilize misfolded proteins and their resulting fibrils. For example, the fibrillation of amyloid beta(1–40) peptide, which occurs in response to the deltaE22 Osaka mutation, has been observed to have extensive pi-stacking interactions. The solid-state NMR structure of an assembly of these fibrils was recently solved (Figure 6.3).[25] It shows the four aromatic residues (Phe4, Tyr10, Phe19, and Phe20) of each peptide chain stacking in displaced face-to-face mode to mediate interstrand recognition.

Since the discovery from alanine scanning experiments that the majority of the stability in a protein–protein complex can derive from only a few residues,[26] such "hot spots" have received significant attention.[27] Bogan and Thorn analyzed 2325 alanine mutants for which the free energy of binding had been measured.[28] They found that hot spots are enriched in Trp, Tyr, and Arg residues, with Trp and Tyr accounting for 33% of the residues, and they proposed that occlusion of solvent by neighboring residues is likely to be an important factor in establishing strong interaction in the center of the hot spot (*i.e.*, the O-ring effect). Based on their work, hot spot residues are widely defined as those contributing at least 2.0 kcal mol^{-1} to the stability of the complex. Nussinov and coworkers found a correlation between the hot spot residues determined by alanine scanning and those that are conserved structurally.[29,30] They found that some residues, in particular Trp, are conserved at hot spots to a greater extent than at other surface-exposed sites, and they found that conserved residues tend to cluster in the center of hot spots, surrounded by less conserved residues. Aromatic residues are highly conserved, they contribute significantly to binding energy, and they are important for excluding water in order to maximize the energy of electrostatic interactions. Moreira and coworkers further studied the importance of aromatic residues

View Online

Published on 15 November 2016 on http://pubs.rsc.org | doi:10.1039/9781782626626-00172

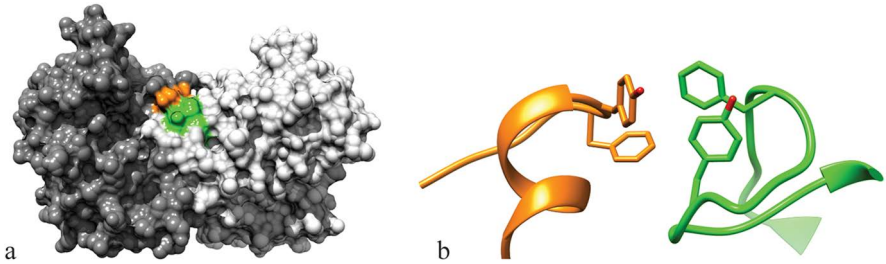

Figure 6.4 Rendering of the crystal structure (PDB: 1YDV) of the homodimeric TPI complex: (a) TPI dimer with the aromatic cluster darkened; (b) the aromatic cluster of Phe69 and Tyr74 (green) and Tyr101 and Phe102 (orange).[35]

at hot spots and found that these residues tend to cluster and form dimers that contribute significantly to binding.[31]

Sometimes a single aromatic residue can be responsible for mediating the homodimerization and resulting activation of a dimeric enzyme. The protein trypanosomal triosephosphate isomerase (TPI) forms a highly stable homodimeric complex, with an equilibrium association constant (K_a) value on the order of 10^{11} M^{-1}.[32] The monomers associate *via* a large but shallow hydrophobic interface. Mutation studies have shown that the conserved Tyr74 residue of TPI is essential to the stability of the homodimer.[33] Although the Tyr74Gly mutation did not appear to alter the secondary structure of the protein, it did increase the amount of the catalytically inactive monomer relative to the dimer.[33,34] Structural studies show that Tyr74 forms an aromatic cluster with Phe69, Tyr101, and Phe102 near the catalytic site and serves as an essential anchor point for dimerization (Figure 6.4).[35] The geometries of loops 1 and 3 are stabilized by interactions with Phe69, Tyr101, and Phe102, thereby preserving the motion required for catalysis.[34]

We provide here a cross-species sequence homology analysis of TPI (Table 6.1) with data from Uniprot.[36] Among this group of ten diverse species, the sequences surveyed retained either a Tyr74 or Phe74 residue, even in cases where the overall sequence homology was less than 40% (*i.e. P. falciparum vs.* Human, 36.9%). The other residues in the aromatic clusters, however, are variable across species. Tyr101 and Phe102 are replaced by aliphatic or charged residues in a few cases. The identity of residue 69 is highly variable and only conserved as an aromatic residue in the Plasmodium species. These data further demonstrate the essential role of the aromatic residue at position 74.

In addition to homodimeric protein complexes, heterodimeric complexes can also be mediated to a significant extent by aromatic residues. For example, ligase MDM2 binds the tumor suppressor protein p53 *via* an extensive interface and with high affinity ($K_a = 2.0 \times 10^6$ M^{-1}). Based on the crystal structure (Figure 6.5), the amphipathic alpha helix of p53 fits into the long hydrophobic cleft of MDM2.[37] Alanine mutation studies on p53

View Online

Table 6.1 Conservation of residues in the aromatic cluster of TPI.

Species	Identity of residue aligned with *P. falciparum*[a]			
P. falciparum	Phe69	Tyr74	Tyr101	Phe102
P. vivax	Phe	Tyr	Tyr	Phe
P. yoelii	Phe	Tyr	Tyr	Phe
T. gondii	Thr	Phe	Tyr	Tyr
N. frontalis	Lys	Tyr	Tyr	Phe
H. sapiens	Val	Phe	Val	Phe
E. coli	Asn	Phe	Tyr	His
M. musculus	Val	Phe	Val	Phe
S. cerevicea	Lys	Phe	Tyr	Phe
T. aestivum	Gly	Phe	Val	Ile

[a]Sequence alignments were performed with Uniprot.[36]

Published on 15 November 2016 on http://pubs.rsc.org | doi:10.1039/9781782626626-00172

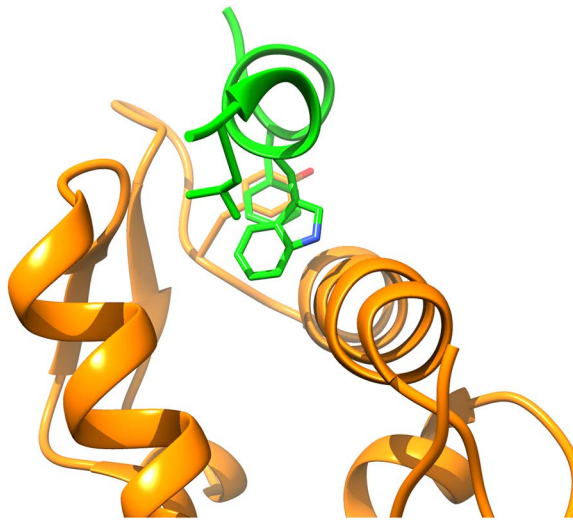

Figure 6.5 The alpha helix of p53 (green) associated with the deep hydrophobic cleft of MDM2 (orange). The residues with dominant energetic contributions to this interaction, Phe19, Trp23, and Leu26, are displayed. Tyr63 of MDM2 is observed in an off-set pi–pi interaction with Phe19 of p53 (PDB: 1YCQ).[37]

have identified the hydrophobic residues Trp19, Phe23, and Leu26 as the primary energetic contributors to binding.[38] Interestingly, the aromatic residues contribute more than hydrophobic character to the helix–cleft interface. Phe23 is engaged in a displaced face-to-face interaction with Tyr63 of MDM2, and the indole side-chain of Trp19 donates an intermolecular H-bond to the MDM2 helix.

Aromatic residues can also facilitate recognition events at interfaces between proteins and cell membranes. For example, the cluster of aromatic residues at one end of the protein equinatoxin II (illustrated in grey in Figure 6.6) facilitates the association with sphingomyelin lipids on the outer surface

View Online

Published on 15 November 2016 on http://pubs.rsc.org | doi:10.1039/9781782626626-00172

Figure 6.6 Equinatoxin II interacts with biological membranes *via* an aromatic-rich patch (PDB: 1IAZ).[39]

of the cell membrane.[39–41] Once associated, the N-terminal alpha helix is then inserted into the membrane to form an octameric pore complex.

Aromatic residues can also play key roles in the interactions of *peptides*. Antibodies are the proteins responsible for identifying foreign entities, typically by binding to specific peptide fragments. Martineau and coworkers surveyed 227 antibody–antigen complexes and found that Tyr was by far the most abundant residue in the hypervariable region (*i.e.*, the antigen binding site) of the antibodies, followed by Gly, Ser, Trp, and Asp.[42] Interestingly, they also found that among these residues, Tyr and Trp contributed the most energy per residue. Conversely, an aromatic residue in the peptide can provide the basis for selectivity. This process is exemplified in endopeptidases such as chymotrypsin and thermolysin, which can selectively recognize aromatic residues in a peptide and cleave the neighboring peptide bond.[43–45] The enkephalins, of sequence Tyr-Gly-Gly-Phe-Met and Tyr-Gly-Gly-Phe-Leu, are well characterized opioid peptides present in all eukaryotes. A semiempirical modeling study of the enkephalin–opioid receptor complex shows the lowest energy conformations of the relatively disordered enkephalin to involve stacking of the two aromatic residues with each other and with aromatic residues in the active site of the opioid receptor (Figure 6.7).[46]

The examples presented here demonstrate different ways in which Nature exploits the physicochemical properties of aromatic residues to enable strong and selective molecular recognition. It is clear from these examples

View Online

Published on 15 November 2016 on http://pubs.rsc.org | doi:10.1039/9781782626626-00172

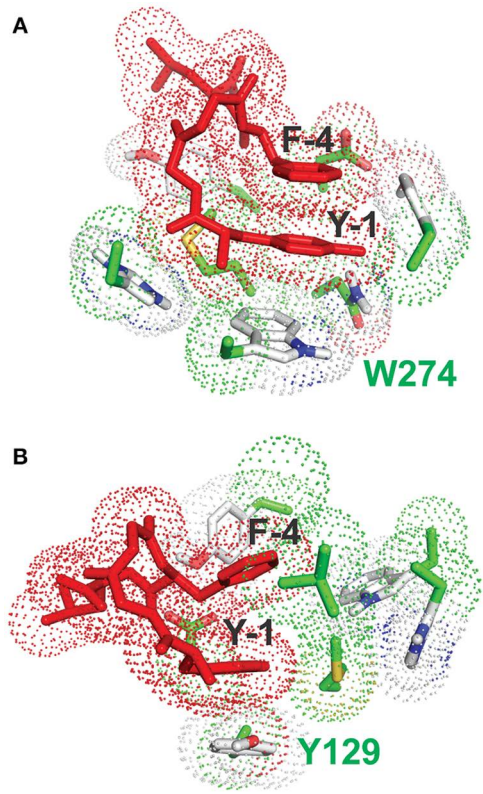

Figure 6.7 Lowest energy conformations for the binding of Leu-enkephalin (red) to the opioid receptor (green). Conformer A involves stacking of enkephalin Tyr[1] with the Trp side chain of receptor W274. Conformer B involves the stacking of enkephalin Tyr[1] with the Phe side chain of receptor F129.[46] Reprinted by permission from Frontiers Media *via* a Creative Commons License, ref. 46, 2014.

that aromatic residues contribute in diverse ways and to diverse processes, they contribute significant energy per residue, they are often conserved, they tend to cluster together at interfaces, and they exclude solvent from binding sites. Therefore, aromatic residues are excellent targets for ligands designed to interfere with protein interactions.

6.4 Designed Ligands

Molecules that bind strongly and selectively to desired biological targets (*i.e.*, "ligands") have been used to advance virtually all areas of basic and applied science at the interface of chemistry and biology. Ligands are used to study and control biological processes, to detect and quantify specific agents, and to isolate targets from complex mixtures. The most common ligands, drugs

View Online

Published on 15 November 2016 on http://pubs.rsc.org | doi:10.1039/9781782626626-00172

and antibodies, are discovered by selection from large libraries, whether synthetic or biological. For example, drug leads are selected from assays of many thousands of compounds. Antibodies are selected from the massive library available in a living organism.

As an alternative to the selection of ligands from libraries, chemists have long endeavored to *design* ligands and to prepare them using organic synthesis. Design, as an approach, has the advantage that it progresses our understanding of the relationship of a molecule's structure to its biological activity. Moreover, the ability to design a ligand implies the ability to predictively bind a target, and predictability is the key. Another important advantage of designed molecules is that they are typically small organic compounds (MW < 2000). Such compounds are preferable to proteins as ligands because, in general, they are less expensive to produce, easier to synthesize on large scale, easier to tailor, more stable, and better defined structurally.

Some of the most successful ligand designs have involved the predictive recognition of double-stranded DNA. The work of Dervan and coworkers in particular has demonstrated the power of modular design for binding DNA in a sequence-specific manner.[47,48] This example is discussed here because it contrasts in informative ways with the problem of protein recognition. Each molecule of genomic DNA contains myriad functional sites (*e.g.*, the binding site of a transcription factor), each comprising a specific sequence of nucleotides. Due to the structural regularity of the double helix, the overall shape of the DNA molecule at each site is approximately the same. Different nucleotide sequences, however, present different patterns of hydrogen bond donors and acceptors at the edges of the nucleobases, which are exposed to solution on the floor of the helical grooves. Therefore, it is possible to design ligands for DNA such as triple-helix-forming oligonucleotides, which bind in the major groove,[49] and pyrrole-imidazole polyamides,[48] which bind in the minor groove, such that the overall structure of the ligand matches the canonical curvature of the double helix, regardless of the sequence of base pairs. In these designs, each module of the ligand aligns with and recognizes a corresponding module (*i.e.*, base pair) of the DNA. The recognition of a specific sequence of base pairs can therefore be accomplished by composing a sequence of modules in the ligand.

This approach is an elegant demonstration of the power of design for the recognition of a biological polymer. It also helps to illustrate several important issues with regard to the design of protein ligands. In contrast to DNA, which contains many functional sites per molecule, each protein usually has only one function, and so we think about targeting one specific protein *versus* other proteins. Also in contrast to DNA, protein structures are often irregular and unpredictable. The amino acid sequence composition, which can be predicted from genomic data, determines the folded tertiary structure of the protein, but this relationship remains difficult to predict, even with the help of homology modeling. Therefore, the modular design approach applied to DNA recognition does not apply to proteins. That said, if it were possible to

View Online

Published on 15 November 2016 on http://pubs.rsc.org | doi:10.1039/9781782626626-00172

predictively recognize proteins on the basis of the amino acid sequence, it could be a powerful approach to designing ligands for proteins. The remainder of this chapter explores this possibility and the important role played by aromatic residues.

6.5 Efficiency of Aromatic Residues

One important consideration for the design of ligands for proteins involves the binding energy per amino acid residue, *i.e.*, the residue efficiency. High affinity ligands for proteins, including pharmaceuticals,[3] helix mimics,[50] aptamers,[51] and antibodies[52] interact by contacting multiple amino acid residues (Figure 6.8), either *via* an extended interface or with the ligand buried in a pocket. Although the multiple contacted residues are proximal in the *folded* structure of the protein, they are not typically neighbors in the linear amino acid sequence. Therefore, in contrast to DNA, it would be difficult, if not impossible, to predict these interactions on the basis of the amino acid sequence. Due to the protein folding problem, predictive recognition on the basis of amino acid sequence would require the target binding site to be extraordinarily small, say 2–3 neighboring residues. This site would be part of a larger protein and exposed to solvent on the protein surface. Alternatively, a small peptide could present this site; the peptide may be a model of the protein site, or it may be the desired target itself. In any event, such a small site would require each residue to contribute substantially to both the affinity and the specificity of binding; in other words, each residue would need to be highly efficient. Interestingly, this situation is already somewhat familiar. As described in Section 6.3, it is often the case that one residue or a few residues are crucial to protein–protein complexation, and that aromatic residues are often conserved and provide significant binding energy per residue. It follows that aromatic residues could also be efficient residues for the binding of designed ligands.

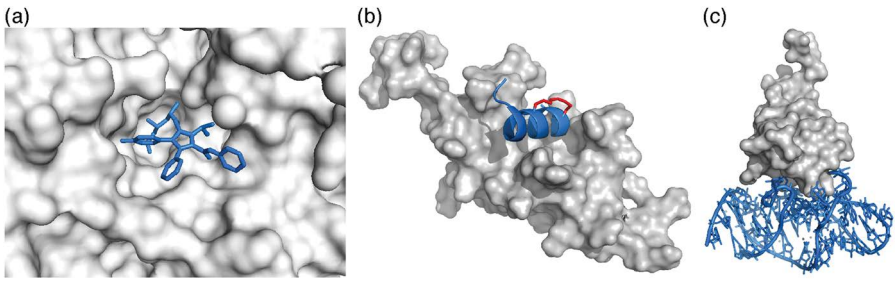

Figure 6.8 Illustrations of crystal structures of (a) atorvastatin bound to HMG CoA reductase,[53] (b) a staple helix bound to the HIV 1 capsid protein,[54] and (c) a nucleic acid aptamer bound to the protein CCL2.[55] Proteins are rendered in grey as their solvent-exposed surface; designed molecules are blue. These very different types of molecules all interact with their protein targets *via* contact with numerous amino acid residues.

View Online

Published on 15 November 2016 on http://pubs.rsc.org | doi:10.1039/9781782626626-00172

6.6 Synthetic Receptors

From a ligand design standpoint, one of the most basic and important considerations is maximizing the interfacial surface area in the complex. Small molecules accomplish this by binding within cavities; the interfacial surface area is maximized with the convex surface of the small molecule directed outward toward the larger concave cavity. If, however, the target site were a short sequence of amino acids, then that structure itself would be unlikely to form a stable cavity. Therefore, to maximize the interfacial surface area, a designed ligand for a short peptide sequence should wrap around the binding site. Synthetic receptors (*i.e.*, "hosts") are best suited for this purpose because they have well defined internal cavities designed to encapsulate smaller entities (*i.e.*, "guests"). For example, Figure 6.9 shows several lysine side chains on the surface of cytochrome *c* encapsulated by calixarene synthetic receptors.[56]

Synthetic receptors were discovered in the late 1960s to bind to metal cations.[57] Over the subsequent decades, the development of a broad range of hosts that bind to a broader range of guests developed into the multidisciplinary field of supramolecular chemistry, with applications in biology, medicine, hygiene, materials science, environmental science, energy, and defense.[57] The ability of synthetic receptors to mimic the activity of biological receptors has gained increasing attention in recent years due to the increasing number of synthetic receptors that function in purely aqueous solution.[58] Compared to biological receptors, synthetic receptors are more readily tunable in size, shape, valency, stability, and other physicochemical properties.[4,57,58] Many have preorganized binding sites (*e.g.*, macrocycles and cages) with a correspondingly low entropic cost of binding. Many are commercially available (*e.g.*, crown ethers, calixarenes, cyclodextrins, cucurbiturils), and virtually all are less expensive and more stable than their protein-based counterparts. With structural simplicity, however, comes limitations. Whereas biomolecules often have deep cavities and complex surface topologies that provide large binding interfaces with a broad range of

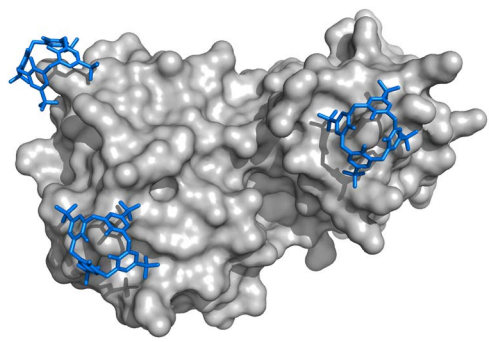

Figure 6.9 Crystal structure of cytochrome *c* (grey, showing solvent-exposed surface) with three calixarenes (blue, rendered as sticks) bound to surface-exposed lysine residues.[56]

View Online

Published on 15 November 2016 on http://pubs.rsc.org | doi:10.1039/9781782626626-00172

possible targets, the small size and repetitive structures of synthetic receptors limit their interactions to small molecules or to small protrusions from larger structures, with relatively limited capacity to discriminate subtle features of the target surface. The cavities of most synthetic receptors are sufficiently large to accommodate only one or two amino acid residues, and thus they require greater ligand efficiency than protein or nucleic acid-based receptors. Synthetic receptors also differ from biological receptors in that they can have especially hydrophobic cavities that do not allow water molecules to hydrogen bond to the walls of the cavity or to form stable hydrogen-bond networks. The hydrophobic effect in these systems involves the release of water upon guest binding that is strongly enthalpically driven.[9,59] These properties suggest that the strongest complexes of synthetic receptors in aqueous solution may be driven by hydrophobic interactions. As discussed in the section above on protein interactions, aromatic residues are particularly well suited to these conditions.

6.7 Synthetic Receptors for Amino Acids

In order to consider the possibility of recognizing sites on peptides and proteins, it is necessary first to consider binding to the constituent amino acids. This section reviews the binding of amino acids by several classes of synthetic receptors, which were selected to represent the strongest binders and the most highly characterized classes of synthetic receptors. The recognition of aromatic residues is the primary focus, but some examples of the recognition of non-aromatic residues are included to illustrate the breadth of binding modes. Only studies performed in purely aqueous solution have been included so that the binding phenomena, which depend heavily on solvent, may be related to those with peptides and proteins under physiologically relevant conditions. For each class of receptor, attention should be paid to the amino acid preference and the molecular basis for this preference.

6.7.1 Aromatic Amino Acid Recognition by Viologen-Containing Receptors

Viologen-containing receptors (Figure 6.10, Table 6.2) have been studied extensively.[57] The electron-deficient viologen (*N*,*N*-dialkyl-4,4′-bipyridinium) group can interact with guests through electrostatic interactions as well as through pi stacking. As a built-in sensor, viologen can form an excited state charge-transfer complex by stacking with relatively electron-rich aromatics. This phenomenon results in the growth of a visible absorbance and the quenching of any fluorescence of the electron-rich aromatic.

Kaifer, Stoddart, and coworkers reported the binding of cyclobis(viologen-*p*-phenylene) (*i.e.*, "blue box") with racemic amino acids using visible spectroscopic titration in 50 mM sodium phosphate, pH 7.[60] They observed selective binding to Trp ($K_a = 1.1 \times 10^3$ M^{-1}), with a two-fold preference over Tyr and 30-fold preference over Phe. Binding affinity was measured by the

View Online

Published on 15 November 2016 on http://pubs.rsc.org | doi:10.1039/9781782626626-00172

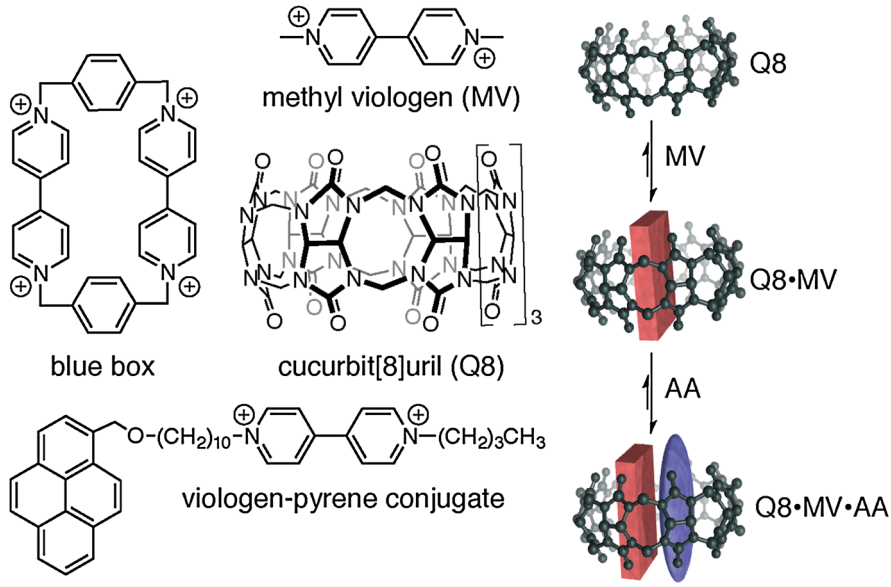

Figure 6.10 (left) Formulas of viologen-containing receptors; (right) ternary equilibrium for the formation of Q8·MV·AA (AA = amino acid).[60–62,65]

Table 6.2 Equilibrium binding data for viologen-containing receptors with amino acids.[60–62,65]

Receptor	Amino acid[a]	K_a[b] (M^{-1})
Blue box	Trp	1.1×10^3
	Tyr	5.8×10^2
	Phe	3.7×10^1
	His	n.d.[c]
	Ala	n.d.
Viologen–pyrene	Trp	1.3×10^3
	Phe	7.3×10^1
	Tyr	5.2×10^1
	Leu	n.d.
	His	n.d.
	Gly	n.d.
Q8·MV	Trp	4.3×10^4
	Phe	5.3×10^3
	Tyr	2.2×10^3
	All 17 others	n.d.

[a]Amino acids were racemic in the blue box studies, of unspecified enantiomeric composition in the viologen–pyrene studies, and L-isomers in the Q8·MV studies.
[b]Equilibrium association constant values were derived from fluorescence titrations at 298 K in 50 mM sodium phosphate, pH 7, for blue box; from fluorescence titrations at unknown temperature and in unspecified "aqueous solution" for the viologen–pyrene conjugate; and from isothermal titration calorimetry at 300 K in 10 mM sodium phosphate, pH 7.0 for the Q8·MV complex.
[c]n.d. indicates that the study was performed, but binding was not detected.

View Online

Published on 15 November 2016 on http://pubs.rsc.org | doi:10.1039/9781782626626-00172

growth of a visible charge-transfer absorbance. No binding was detected for His or Ala, which cannot form a charge-transfer complex. Binding selectivity was attributed to the greater electron donating ability of the side chains of Trp and Tyr *versus* that of Phe. NMR data confirmed the inclusion of the aromatic side chains within the cavity of the receptor.

Ramaiah and coworkers reported the synthesis and amino acid binding properties of a viologen–pyrene conjugate.[65] The intramolecular charge-transfer complex between the two aromatic groups is disrupted to various degrees upon binding to guests. Fluorescence titration experiments revealed a ~20-fold preference for binding Trp ($K_a = 1.3 \times 10^3$ M^{-1}) *versus* Phe and Tyr. Again, selectivity was rationalized on the basis of the side chain of Trp being more electron rich than those of Tyr and Phe.

Urbach and coworkers reported the binding of amino acids by the complex comprising cucurbit[8]uril (Q8, discussed in greater detail below) and methyl viologen (MV).[61,62] The Q8·MV complex forms with a binding constant of 8.5×10^5 M^{-1} in neutral 10 mM phosphate buffer,[61] and the large cavity of Q8 is able to accommodate the binding of a second guest (Figure 6.10).[63,64] Using isothermal titration calorimetry, they observed that Q8·MV binds preferentially to Trp with a K_a value of 4.3×10^4 M^{-1}, with eight-fold selectivity over Phe and 20-fold selectivity over Tyr.[61] No binding was observed to the other 17 amino acids; this method had a lower limit of detection of approximately 10^3 M^{-1}.[62] Taken together, these studies show a consistent preference for Trp by viologen-containing receptors and exemplify the utility of viologen for optical detection and Trp as an intrinsic fluorophore.

6.7.2 Aromatic Amino Acid Recognition by Cyclodextrins

Cyclodextrins are a class of macrocyclic cavitands (container-shaped molecules) composed of repeating units of α-D-glucose connected *via* 1,4-glycosidic linkages (Figure 6.11).[66] Cyclodextrins are among the most studied classes of synthetic receptor and have been included in a range of commercial applications,[67] including as excipients for drug delivery,[68] for reversing the rocuronium-induced neuromuscular blockade in anesthesia (*e.g.*, Bridion™ from Merck),[69] for environmental remediation,[70] and as an odor controlling agent (*e.g.*, Febreze™ from Procter & Gamble).[71] Several cyclodextrins are available commercially. The α-, β-, and γ-cyclodextrins are composed of 6, 7, and 8 glucose units respectively. These structures contain hydrophobic cavities that bind preferentially to nonpolar guests.[72] Kahle and Holzgrabe studied the binding of α- and β-cyclodextrin with amino acids using potentiometric titration in 0.15 M KCl, pH 7.0 (Table 6.3).[73] They observed the binding of α-cyclodextrin to L-Trp and L-Leu with equilibrium association constant (K_a) values of approximately 2×10^2 M^{-1}, but no binding was observed for L-Ala, L-Val, L-Ile, L-His, L-Phe, or L-Tyr. β-Cyclodextrin bound to L-Trp, L-Leu, L-Tyr, and L-Phe with binding constants in the range 4.1×10^1 to 4.5×10^2, but no binding was observed for L-Ala, L-Val, L-Ile, or L-His. Based on these data, they concluded that Leu and Trp bind well to both receptors due to their bulky hydrophobic side chains. It is not clear why Phe and Tyr bind measurably to

View Online

Published on 15 November 2016 on http://pubs.rsc.org | doi:10.1039/9781782626626-00172

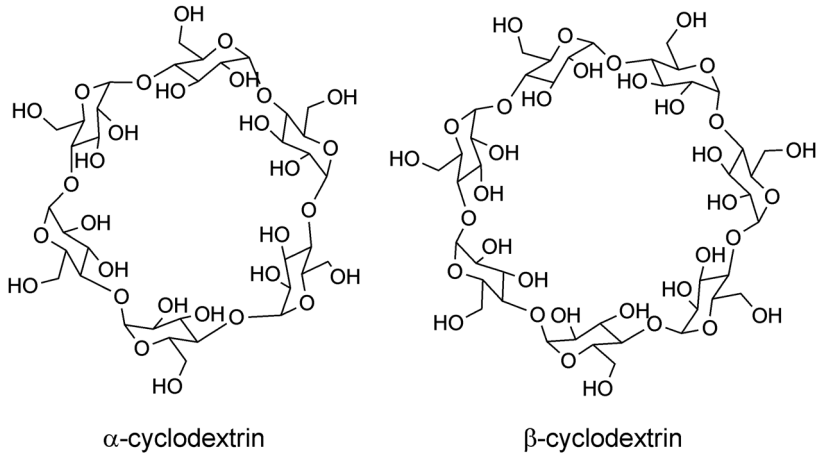

Figure 6.11 Chemical formulas of α- and β-cyclodextrin.

Table 6.3 Equilibrium binding data for α- and β-cyclodextrins with amino acids.[c,73]

Receptor	Amino acid[a]	K_a[b] (M^{-1})
α-Cyclodextrin	Trp	1.9×10^2
	D-Trp	8.1×10^2
	Leu	2.7×10^2
	D-Leu	1.4×10^2
	Phe	n.d.
	Tyr	n.d.
	His	n.d.
	Ile	n.d.
	Val	n.d.
	Ala	n.d.
β-Cyclodextrin	Trp	4.5×10^2
	D-Trp	8.8×10^1
	Leu	2.6×10^2
	D-Leu	2.0×10^2
	Phe	8.5×10^1
	Tyr	4.1×10^1
	His	n.d.
	Ile	n.d.
	Val	n.d.
	Ala	n.d.

[a]Amino acids were the L enantiomer unless otherwise indicated.
[b]Equilibrium association constant values were derived from potentiometric titrations at unspecified temperature in 0.15 M aqueous KCl.
[c]n.d. indicates that the study was performed, but binding was not detected.

β-cyclodextrin but not to α-cyclodextrin. They also observe some selectivity for D-Trp *vs.* L-Trp for α-cyclodextrin and L-Trp *vs.* D-Trp for β-cyclodextrin. These studies illustrate what has been observed more generally for cyclodextrins, which is preferential binding based on a combination of hydrophobicity and the ability to fit within the receptor cavity.[72]

View Online

Published on 15 November 2016 on http://pubs.rsc.org | doi:10.1039/9781782626626-00172

6.7.3 Aromatic Amino Acid Recognition by Cucurbiturils

Cucurbit[*n*]urils (Qn's, Figure 6.12) are an important class of cavitands that bind a wide range of guests in aqueous solution, with K_a values that extend upward to 10^{17} M^{-1} and with applications including drug delivery, anesthesia, environmental remediation, spectroscopic analysis, biosensing, catalysis, enzyme assays, high-affinity binding, polymers, and nanotechnology.[74–77] Cucurbit[*n*]urils are composed of *n* bis(methylene)-linked glycoluril units that create a rigid, hydrophobic cavity with constricted, ureido-carbonyl-lined entrances. These receptors bind to nonpolar guests *via* the release of high-energy water from the host cavity,[59] and they prefer guests containing both nonpolar and cationic groups, such as organic amines. Several cucurbiturils are available commercially. Numerous groups have studied the binding of various Qn homologues, derivatives, and acyclic analogues to amino acids.[62,78–84]

The recognition properties of Qn receptors depend heavily on the size of the cavity, with smaller hosts, such as cucurbit[5]uril and cucurbit[6]uril (Q6), capable of forming only exclusion complexes (guest binding outside the cavity). Buschmann and coworkers studied the binding of Q6 to amino acids in 50% aqueous formic acid;[78] this is not a purely aqueous solution, but it is included here for the sake of a more complete treatment of Qn recognition. Q6 bound Phe, Val, and Ala with similar affinity ($K_a \sim 10^3$ M^{-1}), and no binding was detected for Gly. This affinity and lack of specificity is consistent with the formation of exclusion complexes between the protonated amine groups of the amino acids and the carbonyl oxygens of Q6.

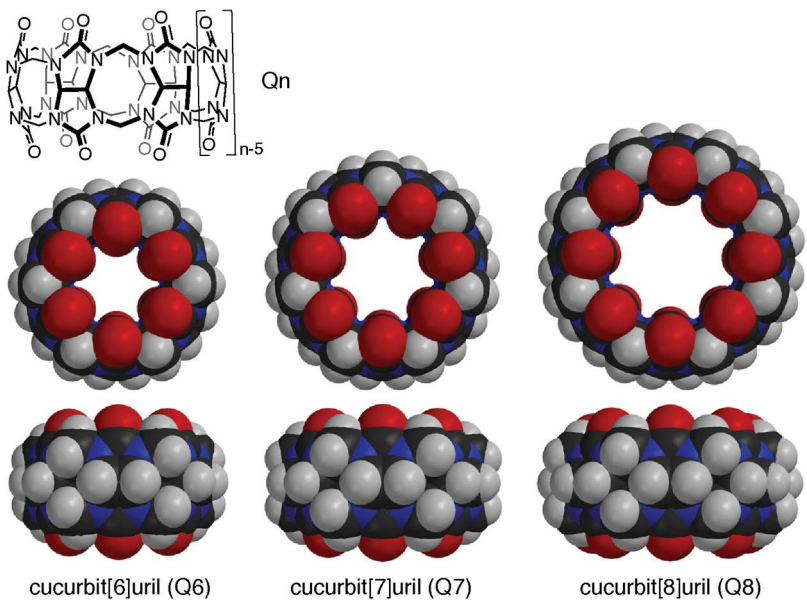

Figure 6.12 Chemical formulas and space-filling models of Q6, Q7, and Q8.

View Online

Published on 15 November 2016 on http://pubs.rsc.org | doi:10.1039/9781782626626-00172

The larger cavity size and greater solubility of cucurbit[7]uril (Q7) have encouraged several groups to explore the binding of Q7 to amino acids.[79,80,82–84] Table 6.4 compares the K_a values measured using different methods and/or under different conditions. In general, Q7 prefers Phe, followed by Tyr, then Trp, then the nonaromatic amino acids. NMR and crystallographic data support a binding mechanism in which the aromatic side chain binds within the Qn cavity, and the protonated amine group interacts with the carbonyl groups of the Qn.[79,80,84–86] Based on this binding mode, the observed amino acid selectivity can be rationalized by comparing the available size of the Q7 cavity with the sizes and hydrophobicities of the amino acid side chains. The aromatic amino acids release the most water upon inclusion within the cavity; Phe fits the best.

The binding of amino acids by the Q8·MV complex was discussed in Section 6.7.1. In the absence of MV, Q8 binds selectively to Trp and Phe *versus* the other 18 amino acids, and the complex stoichiometry is 2 : 1 (amino acid–Q8).[62] The values reported in Table 6.4 are for the formation of ternary complexes and are given in units of M^{-2}; the square root of this value approximates the order of magnitude of the binary K_a value of each amino acid. NMR experiments confirm that the side chains of both aromatic amino acids are bound simultaneously within the Q8 cavity in the 2 : 1 complex.

Isaacs and coworkers reported the synthesis and binding properties of an elongated analogue of Q6.[81] The intrinsic fluorescence of the host enabled binding measurements by fluorescence spectroscopy, and the large size of the internal cavity enabled the binding of larger guests to this host than to Q6. The Q6 analogue bound preferentially to Trp ($K_a = 3.2 \times 10^6$ M^{-1}) with 56-fold selectivity over Tyr and 145-fold selectivity over Phe. No binding was observed for His, likely due to its high polarity. Taken together, these studies demonstrate the capacity of Qn's to bind with high affinity and selectivity to the aromatic amino acids, with selectivity that depends on the size of the inner cavity.

6.7.4 Recognition of Non-Aromatic Amino Acids by Synthetic Receptors

A few examples of the recognition of non-aromatic amino acids will be described here to illustrate two important classes of synthetic receptors and their novel modes of recognition. Calix[*n*]arenes are cavitands composed of *n* repeating units of phenol, resorcinol, or pyrogallol. Their aromatic composition forms an excellent binding site for inorganic and organic cations. Their rims are readily derivatizable to modulate binding and solubility properties. Calixarenes have been studied for several decades and have found broad application as surfactants, as receptors for waste remediation (including nuclear), and in the fields of biosensors and drug discovery.[87–89] Several calixarenes are available commercially. Buschmann measured the binding of the water-soluble *p*-sulfonatocalix[4]arene (Figure 6.13) to eight amino acids

View Online

Published on 15 November 2016 on http://pubs.rsc.org | doi:10.1039/9781782626626-00172

Table 6.4 Equilibrium binding data for cucurbit[*n*]uril-type receptors with amino acids.[62,78,80–83]

Receptor	Amino acid[a]	K_a [b] (M^{-1})
Q6	Phe	1.4×10^3 [c]
	Val	1.4×10^3 [c]
	Ala	1.0×10^3 [c]
	Gly	n.d.[k]
Q7	Trp	3.7×10^5 [d]
	Trp	1.9×10^3 [e]
	Trp	1.6×10^3 [f]
	Phe	8.2×10^5 [d]
	Phe	1.5×10^5 [g]
	Phe	1.8×10^6 [h]
	Phe	1.1×10^5 [i]
	Tyr	2.3×10^5 [d]
	Tyr	2.2×10^4 [e]
	Tyr	2.4×10^4 [f]
	His	8.0×10^1 [d]
	His	4.0×10^2 [f]
	Lys	8.0×10^2 [e]
	Lys	8.7×10^2 [f]
	Arg	3.3×10^2 [e]
	Arg	3.1×10^2 [f]
	Leu	1.5×10^2 [d]
	Val	4.4×10^2 [d]
	Ala	3.6×10^1 [d]
	Met	2.7×10^2 [d]
	Glu	1.0×10^2 [d]
Q8	Trp	6.9×10^7 [i] M^{-2}
	Phe	1.1×10^8 [i] M^{-2}
	All 18 others	n.d.[k]
Q6 Analogue	Trp	3.2×10^6 [j]
	Tyr	5.7×10^4 [j]
	Phe	4.2×10^4 [j]
	His	n.d.[k]

[a]All amino acids were the L-isomer, except Gly.
[b]K_a values were for binary (1 + 1) equilibria and are reported in units of M^{-1} except for the studies with Q8, for which 2 : 1 (amino acid–Q8) stoichiometry was observed and K values are reported for the overall 2 + 1 reaction in units of M^{-2}.
[c]Isothermal titration calorimetry at 298 K in 50% aqueous formic acid.[78]
[d]K_a values for Trp, Tyr, and Phe were derived from UV-vis titrations at 298 K in water; K_a values for the others were derived from NMR titrations at 300 K in water.[80]
[e]Isothermal titration calorimetry at 303 K in 10 mM ammonium acetate, pH 6.0.[83]
[f]Competitive fluorescence titrations at 298 K in 10 mM ammonium acetate, pH 6.0.[83]
[g]Competitive NMR titrations at 298 K in water.[79]
[h]Isothermal titration calorimetry at 298 K in water.[82]
[i]Isothermal titration calorimetry at 300 K in 10 mM sodium phosphate, pH 7.0.[62,84]
[j]Fluorescence titrations at 298 K in 50 mM sodium acetate, pH 4.74.[81]
[k]n.d. indicates that the study was performed, but binding was not detected.

View Online

Published on 15 November 2016 on http://pubs.rsc.org | doi:10.1039/9781782626626-00172

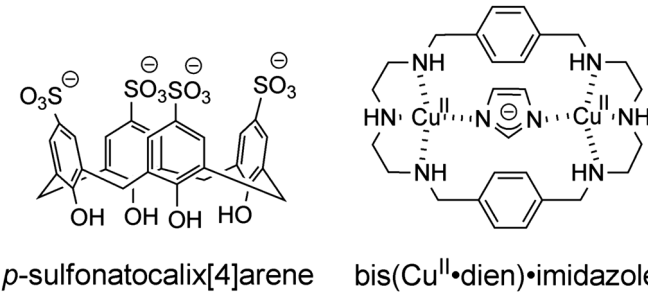

Figure 6.13 Chemical formulas of *p*-sulfonatocalix[4]arene and the bis(Cu^{II}·dien) complex with imidazole.[90,92,93]

Table 6.5 Equilibrium binding data for calixarene and Cu-complex hosts.[90,92,93]

Receptor	Amino acid[a]	K_a (M^{-1})
p-Sulfonatocalix[4]arene	Phe	1.4×10^{3} [b]
p-Sulfonatocalix[4]arene	Trp	1.3×10^{3} [b]
p-Sulfonatocalix[4]arene	Gly	5.5×10^{2} [b]
p-Sulfonatocalix[4]arene	Ala	1.7×10^{3} [b]
p-Sulfonatocalix[4]arene	Leu	1.2×10^{3} [b]
p-Sulfonatocalix[4]arene	Val	1.6×10^{3} [b]
p-Sulfonatocalix[4]arene	Thr	1.5×10^{3} [b]
p-Sulfonatocalix[4]arene	Lys	6.8×10^{3} [b]
p-Sulfonatocalix[4]arene	Lys	5.2×10^{2} [c]
p-Sulfonatocalix[4]arene	Lys(Me)	4.0×10^{3} [c]
p-Sulfonatocalix[4]arene	$Lys(Me_2)$	1.6×10^{4} [c]
p-Sulfonatocalix[4]arene	$Lys(Me_3)$	3.7×10^{4} [c]
Bis(Cu^{II}-dien) complex	His	1.6×10^{7} [d]
Bis(Cu^{II}-dien) complex	Gly	7.9×10^{5} [d]
Bis(Cu^{II}-dien) complex	Ala	6.3×10^{4} [d]
Bis(Cu^{II}-dien) complex	Phe	1.3×10^{4} [d]
Bis(Cu^{II}-dien) complex	Val	5.0×10^{3} [d]
Bis(Cu^{II}-dien) complex	Leu	3.2×10^{3} [d]
Bis(Cu^{II}-dien) complex	Pro	1.0×10^{3} [d]

[a]All amino acids were the L-isomer, except Gly.
[b]Isothermal titration calorimetry at 298 K in water.[92]
[c]NMR titrations at 298 K in 40 mM sodium phosphate, pH 7.0.[90]
[d]Fluorescence titrations at unspecified temperature in 50 mM HEPES, pH 7.[93]

using isothermal titration calorimetry and found similar binding affinities (~10^3 M^{-1}) among the entire group (Table 6.5).[92] In an interesting application, Hof discovered that this compound can differentiate among methylation states of lysine, which are post-translational modifications involved in gene regulation and developmental signaling.[90] This differentiation occurs over a range of 70-fold enhancement in equilibrium constant. They recently developed this observation into a chromatography technique capable of separating peptides with different extents of lysine methylation.[91] Synthetic transition metal complexes can be used to coordinate to biological ligands,

View Online

Published on 15 November 2016 on http://pubs.rsc.org | doi:10.1039/9781782626626-00172

similarly to natural transition metal complexes. Fabbrizzi and coworkers demonstrated the use of a bis-Cu^{II} complex (Figure 6.13) to bind with extraordinary affinity to His ($K_a = 1.6 \times 10^7$), with 20-fold selectivity *versus* Gly and up to 16 000-fold selectivity *versus* other amino acids.[93] The strong affinity is explained in light of the coordination of the imidazole side chain of His to the metal center(s).

6.8 Recognition of Aromatic Peptides by Synthetic Receptors

The studies described in the previous section for amino acid binding by synthetic receptors in aqueous solution illustrate several approaches to the recognition of a specific type of amino acid, each highly dependent on the structure of the receptor. Although it is possible to recognize certain amino acid residues, such as His, with very high affinity, K_a values in excess of 10^5 M^{-1} have been observed most often when targeting aromatic residues. These studies illustrate, from the point of view of synthetic receptors, that aromatics bind relatively efficiently. The current section will focus on the binding of aromatic residues in peptides.

A significant body of published work describes efforts to design synthetic receptors to recognize peptides in aqueous solution.[1,7,94,95] As short chains of amino acids, peptides contrast with proteins in that they are relatively less structured and relatively more solvent exposed. As described in Section 6.3, peptides can be important biological targets. From a design standpoint, we will also consider peptides as models for small protein binding sites comprising 2–3 neighboring amino acid residues. In this regard, it may be possible to use peptide studies to assess the possibility of recognizing small sites on proteins in a predictive manner. From a practical perspective, peptides are much easier than proteins to synthesize, tailor, and characterize using spectroscopic and crystallographic methods, and peptides often have higher aqueous solubilities than proteins, which facilitates binding studies. These are some the reasons there are so many more reports describing the binding of synthetic receptors to peptides than to proteins. Additional considerations are discussed in Section 6.9.

The presence of multiple amino acid residues in a peptide target causes a major problem for selective recognition. There are only 20 amino acids in most natural targets, and so a synthetic receptor that binds tightly to Trp will likely bind Trp in the context of any peptide. Moreover, larger peptides and proteins may present multiple copies of an amino acid on the surface (see Figure 6.9), and so it may not be possible to bind a specific site on the target. In order to discriminate between target peptides and proteins, there must be strategies for discriminating between residues of the same type (*e.g.*, Trp) in different contexts. The most obvious method is to bind simultaneously to multiple neighboring residues. If a receptor can discriminate the sequence X–Y or X–Y–Z from other possible dipeptide and tripeptide sequences, then

View Online

Published on 15 November 2016 on http://pubs.rsc.org | doi:10.1039/9781782626626-00172

selectivity for 1 out of 20 possible amino acids increases to as much as 1 out of 400 possible dipeptide sequences and 1 out of 8000 possible tripeptide sequences.

6.8.1 Early Receptors for Peptides

Among the earliest reports of designed ligands for sequence-specific peptide recognition in aqueous solution was a classic study involving monovalent and divalent β-cyclodextrin.[96] A library of 24 389 unique tripeptides (from 29 amino acids) was produced by split-and-mix combinatorial synthesis on Tentagel, and a colorimetric selection was carried out with the receptors. The remarkable observation was made that all of the peptides selected by the divalent cyclodextrin and most (85%) of the peptides selected by the monovalent cyclodextrin contained the sequence L-Phe-D-Pro or D-Phe-L-Pro. NMR studies of L-Phe-D-Pro and D-Phe-L-Pro dipeptides in complex with β-cyclodextrin revealed that the *s-trans* proline configuration is preferred, and computational modeling placed the aromatic side chain of Phe within the hydrophobic cavity of the cyclodextrin and the proline ring capping the opening to the cavity. The binding constant of L-Phe-D-Pro for β-cyclodextrin was reported as 180 M^{-1}. A follow-up study by Breslow and coworkers measured peptide binding by divalent β-cyclodextrin with a variety of linkers connecting the cyclodextrins *via* the primary face.[97] One compound, β-CD_2 (Figure 6.14(a)), bound preferentially to peptides containing one or two L-Phe-D-Pro sites

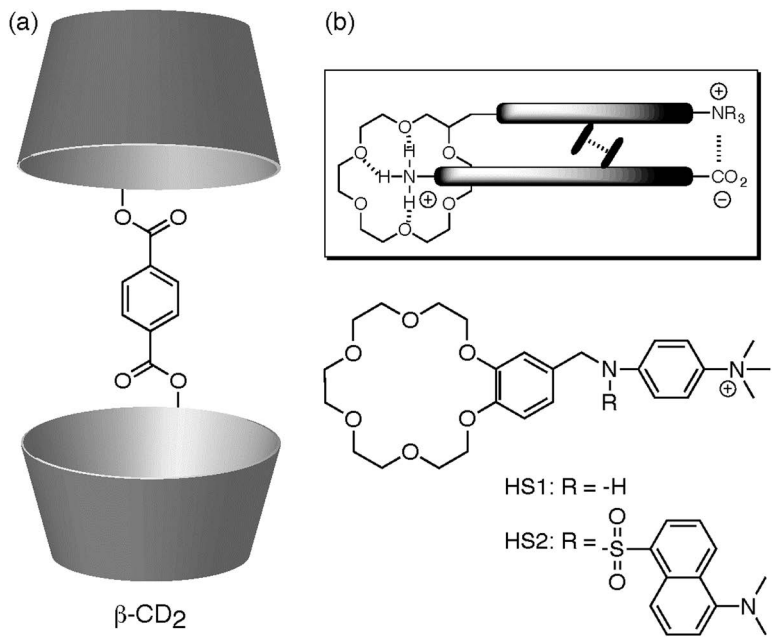

Figure 6.14 Chemical formulas for early peptide receptors.[97,99]

View Online

Published on 15 November 2016 on http://pubs.rsc.org | doi:10.1039/9781782626626-00172

in the context of cyclic hexapeptides or a linear, *N*-acetylated octapeptide ($K_a \sim 10^3$, Table 6.6), with ~10-fold selectivity *versus* tripeptides of sequence X-Gly-X (X = Trp or Phe) and the peptide Trp–Trp. Interestingly, β-CD_2 binds about 10-fold better than β-cyclodextrin to the cyclic hexapeptide of sequence c-(Phe-D-Pro-Asp-Phe-D-Pro-Asp), suggesting the enhancement of binding affinity *via* a multivalent interaction.[98]

An acyclic peptide has an ammonium group at the first position in the polypeptide chain (*i.e.*, the N-terminus) and a carboxylate group at the last position (the C-terminus). In addition to targeting one or more residue side chains, it is also possible to target the unique functional group(s) at the N- and/or C-termini to increase the selectivity of binding. When binding a dipeptide or tripeptide, those terminal groups are always nearby, and they may influence binding significantly. It is important to note that selective recognition of the terminal amino acid, if possible, would be predictable from the sequence of amino acids. The terminal residues are uniquely positioned in a polypeptide chain, and they present unique structures for binding, structures that include both the side chain of the terminal residue and the proximal, terminal ionic group. Although not mentioned in the 1996 paper by Breslow and Still, their β-cyclodextrin monomer bound preferentially to tripeptides containing the L-Phe-D-Pro or D-Phe-L-Pro sequence at the N-terminus (*e.g.*, L-Phe-D-Pro-X) *versus* at the C-terminus (*e.g.*, X-L-Phe-D-Pro).[96] This observation suggests the terminal functional group(s) may have played a role in recognition.

Hossain and Schneider also reported an early study on the sequence-selective recognition of aromatic peptides, and they designed a ligand to recognize both N- and C-terminal ionic groups as well as intervening side chains.[99] Their ligands were composed of a benzocrown ether (to bind the N-terminal ammonium group) conjugated to a trimethylaniline moiety (to bind the C-terminal carboxylate group) *via* a short linker that either contained (HS1) or did not contain (HS2) a dansylamide group (Figure 6.14(b)). Although their receptors bound peptides with relatively low affinity in water (K_a up to 2×10^3), they observed a remarkable degree of sequence selectivity (Table 6.6). In particular, HS2 bound to Gly-Phe-Gly with a K_a value of 1.7×10^3 M^{-1} and with eight-fold preference *versus* Phe-Gly-Gly and Gly-Gly-Phe. HS2 also bound selectively to Gly-Trp-Gly ($K_a = 2.2 \times 10^3$) with seven–eight-fold preference *versus* Trp-Gly-Gly and Gly-Gly-Trp. Most other peptides studied bound to HS2 with affinities in the range 200–900 M^{-1}. Overall, peptides bound less tightly and specifically to HS1 than to HS2. These results suggest that the observed differences in selectivity between HS1 and HS2 are based on interactions between the aromatic side chain and the aromatic dansyl group. The authors also suggest that flexibility in the terminal amino acids may be needed in order to optimize interaction of all groups simultaneously. It is worth noting that this approach to recognition of aromatic peptides involves electrostatic interactions to a significant extent, whereas other approaches involve primarily the hydrophobic effect.

View Online

Published on 15 November 2016 on http://pubs.rsc.org | doi:10.1039/9781782626626-00172

Table 6.6 Equilibrium binding data for peptides with early receptors.[97,99]

Host	Peptide[a]	K_a[b] (M^{-1})
β-CD_2	c(Phe-D-Pro-Asp-Phe-D-Pro-Asp)	2.6×10^3 [c]
β-CD_2	Ac-Trp-Gly-Trp-OH	1.3×10^2 [c]
β-CD_2	Ac-Phe-Gly-Phe-OH	9.1×10^1 [c]
β-CD_2	Ac-(Asp-Phe-D-Pro)$_2$-Gly_2-NH_2	1.1×10^3 [c]
β-CD_2	c(Phe-D-Pro-Asp-Val-D-Ala-Ala)	9.3×10^2 [c]
β-CD_2	H-Trp-Trp-OH	8.4×10^1 [c]
β-Cyclodextrin	c(Phe-D-Pro-Asp-Phe-D-Pro-Asp)	2.2×10^2 [c]
HS2	H-Phe-Gly-Gly-OH	2.2×10^2 [d]
HS2	H-Gly-Phe-Gly-OH	1.7×10^3 [d]
HS2	H-Gly-Gly-Phe-OH	2.2×10^2 [d]
HS2	H-Trp-Gly-Gly-OH	2.6×10^2 [d]
HS2	H-Gly-Trp-Gly-OH	2.2×10^3 [d]
HS2	H-Gly-Gly-Trp-OH	3.1×10^2 [d]
HS2	H-Gly-Leu-Gly-OH	8.5×10^2 [d]
HS2	H-Gly-Ala-Gly-OH	5.4×10^2 [d]
HS2	H-Gly-Gly-Gly-OH	2.1×10^2 [d]
HS1	H-Phe-Gly-Gly-OH	1.4×10^2 [e]
HS1	H-Gly-Phe-Gly-OH	1.8×10^2 [e]
HS1	H-Gly-Gly-Phe-OH	1.7×10^2 [e]
HS1	H-Gly-Gly-Gly-NH_2	2.0×10^2 [e]

[a]H- indicates an unprotected amino group at the N-terminus; Ac- indicates an acetylated N-terminus; c( ) indicates a cyclic peptide; -OH indicates a carboxylic acid at the C-terminus; -NH_2 indicates a primary amide at the C-terminus.
[b]All complexes had a stoichiometry of 1 : 1 receptor–peptide.
[c]Determined by isothermal titration calorimetry at 298 K in 0.2 M sodium acetate, pH 9.0.[97]
[d]Determined by fluorimetric titration at 298 K in water at pH 7.0.[99]
[e]Determined by NMR titration at 298 K in D_2O at pH 7.0.[99]

6.8.2 Peptide Recognition by Coordination Complexes

Fujita and coworkers have reported the use of coordination complexes to recognize aromatic peptides in a sequence-selective fashion (Table 6.7).[100] A self-assembled coordination cage (Figure 6.15) binds selectively to tripeptides containing at least two aromatic residues with K_a values in excess of 10^3 M^{-1}. The peptides were acetylated at their N-termini and had primary amides at their C-termini, thereby eliminating the ionic groups at the termini. Binding affinity in water was dependent on both the type and the sequence of amino acids. Trp was preferred, but the lack of binding observed for Trp-His-Ala *versus* high affinity binding for Trp-Tyr-Ala ($K_a = 5.3 \times 10^4$ M^{-1}) and Trp-Trp-Ala ($K_a > 10^6$ M^{-1}) suggests that the high polarity of His may hinder binding. Remarkably, binding was also dependent on the third residue, such that Trp-Trp-Ala bound at least 13-fold more tightly than Trp-Trp-Gly, and Trp-Trp-Ala was preferred in several sequence contexts. Further studies revealed inclusion of the Trp-Trp-Ala peptide within the cage, showing stacking of each electron-rich indole ring with the electron-deficient walls of the cage. This study records one of the highest affinity synthetic receptors for peptides. This group also described the use of a self-assembled coordination bowl (Figure 6.15) to induce alpha helix formation in linear peptides containing aromatic

View Online

Table 6.7 Equilibrium binding data for peptides with coordination complexes.[102,103]

Host	Peptide[a]	K_a[b] (M^{-1})
Cage	Ac-Trp-Trp-Ala-NH_2	$>10^6$ [c]
Cage	Ac-Trp-Ala-Trp-NH_2	2.5×10^5 [c]
Cage	Ac-Ala-Trp-Trp-NH_2	2.1×10^4 [c]
Cage	Ac-Trp-Trp-Gly-NH_2	7.4×10^4 [c]
Cage	Ac-Trp-Tyr-Ala-NH_2	5.3×10^4 [c]
Cage	Ac-Gly-Gly-Ala-NH_2	n.d.[d]
Cage	Ac-Trp-His-Ala-NH_2	n.d.[d]
Cage	Ac-Tyr-Tyr-Ala-NH_2	4.7×10^3 [c]
Cage	Ac-Ala-Trp-Trp-Ala-NH_2	$>10^6$ [c]
Cage	Ac-Ser-Gly-Ala-Trp-Trp-Ala-NH_2	$>10^6$ [c]
Bowl	Ac-(Ala-Glu-Ala-Ala)$_2$-Trp-Ala-Glu-Ala-Phe-Ala-Ala-Glu-NH_2	3.5×10^5 [e]
Bowl	Ac-Trp-Ala-Glu-Ala-Ala-Glu-Ala-Trp-NH_2	2.4×10^5 [e]
Bowl	Ac-Trp-Ala-Glu-Ala-Gly-Ala-NH_2	1.0×10^4 [e]
Bowl	Ac-Trp-Ala-Glu-Ala-Ala-Ala-NH_2	1.0×10^4 [e]
Bowl	Ac-Trp-Ala-Glu-Ala-Leu-Ala-NH_2	3.1×10^4 [e]
Bowl	Ac-Trp-Ala-Glu-Ala-Phe-Ala-NH_2	1.6×10^5 [e]
Bowl	Ac-Trp-Ala-Glu-Ala-Trp-Ala-NH_2	3.1×10^5 [e]
Bowl	Ac-Trp-Ala-Glu-Ala-Trp-Glu-Ala-Ala-NH_2	5.5×10^5 [e]

[a]Ac- indicates an acetylated N-terminus; -NH_2 indicates a primary amide at the C-terminus.
[b]All complexes had a stoichiometry of 1 : 1 host–peptide.
[c]Determined by UV-visible spectroscopic titration at 273 K in water.[103]
[d]n.d. indicates that the study was performed, but binding was not detected.
[e]Determined by UV-visible spectroscopic titration in water at an unspecified temperature.[102]

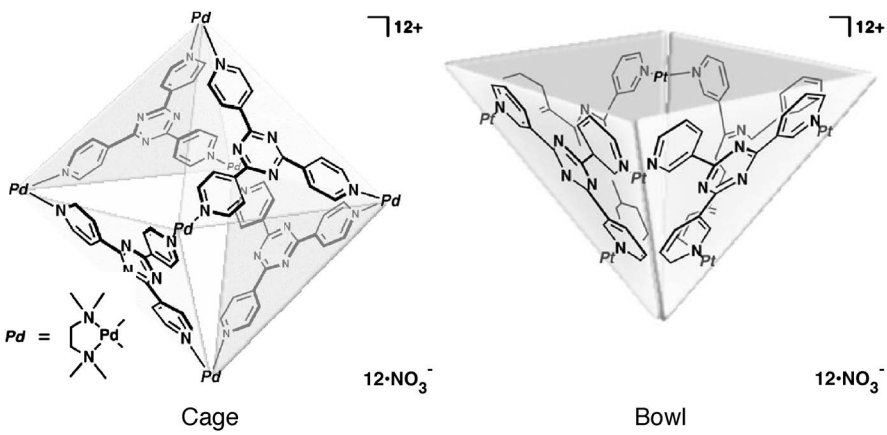

Figure 6.15 Chemical formulas of the self-assembled coordination cage and bowl.[101–103] Adapted by permission from ref. 100, ©2005 American Chemical Society and ref. 102, ©2010 American Chemical Society.

residues at the *i* and *i* + 7 positions in a 9-mer.[101] Remarkably, they were able to induce alpha helix formation in an 8-mer containing Trp residues at *i* and *i* + 7 using a single equivalent of the bowl.[102] Circular dichroism spectroscopy was particularly useful for following the change in secondary structure. Binding constant determination in phosphate buffer, pH 7 (Table 6.7),

Published on 15 November 2016 on http://pubs.rsc.org | doi:10.1039/9781782626626-00172

View Online

revealed a preference for peptides containing two aromatic residues at *i* and *i* + 4 positions.

Published on 15 November 2016 on http://pubs.rsc.org | doi:10.1039/9781782626626-00172

6.8.3 Peptide Recognition by Cucurbit[*n*]urils

Perhaps the most studied class of synthetic receptors for aromatic peptide recognition in aqueous solution is the cucurbit[*n*]urils.[95] Like amino acids, peptides primarily form exclusion complexes with cucurbit[6]uril (Q6), with the N-terminal or side chain ammonium group(s) binding to the carbonyl oxygens of Q6. K_a values are in the range 10^2–10^3 M^{-1}, and there is little sequence-selectivity. The larger cavity volumes and portal diameters of cucurbit[7]uril (Q7) and cucurbit[8]uril (Q8) allow them to accommodate guests and portions of guests that are larger than simple linear alkyl groups and small cycloalkyl groups, including the side chains of the aromatic amino acids.[74]

Early work by Kim, Inoue, and coworkers describes the binding of Q7 to dipeptides containing phenylalanine.[104] Binding constants range from 10^4–10^7 M^{-1} (Table 6.8). Selectivity depends primarily on the second residue, with Leu, Phe, and Ala preferred over Pro. In the case of Phe–Leu, 12-fold selectivity was observed for Phe–Leu *versus* its diasteromer D-Phe-Leu. A subsequent study examined the binding of Q7 to peptides containing a single aromatic residue at the N-terminal *vs.* C-terminal positions.[105] Binding constants ranged from 10^2–10^7 M^{-1}. N-terminal aromatic residues were preferred by 3–4 *orders of magnitude versus* C-terminal aromatic residues. This observation stands as the largest measured difference in binding selectivity between peptide sequence isomers. For N-terminal aromatic peptides, there was a clear preference for Phe > Tyr > Trp, but only Phe is preferred in the C-terminal series.

Subsequent studies by Urbach and coworkers examined the differences in Q7 binding between N-terminal Phe and nonterminal Phe, and between peptides that have carboxylic acid (–OH) *vs.* primary amide ($-NH_2$) groups at the C-terminus (Table 6.8).[84,86,106] They found 10-fold tighter binding to N-terminal Phe-containing peptides Phe-Leu-NH_2 *vs.* Phe-Leu-OH, but only a two-fold preference for nonterminal Phe-containing peptides Thr-Gly-Ala-Phe-Leu-NH_2 *vs.* Thr-Gly-Ala-Phe-Leu-OH. The identity of the C-terminal functional group also appears to impact sequence selectivity. Q7 binds Phe-Gly-Gly-OH 100-fold more tightly than Gly-Phe-Gly-OH, but only a 10-fold preference was observed for Phe-Gly-Gly-NH_2 *vs.* Gly-Phe-Gly-NH_2. When the N-terminal residue is the non-natural 4-aminomethyl phenyalanine (Amf), there is a 550-fold preference for Amf-Gly-Gly-NH_2 *vs.* Gly-Amf-Gly-NH_2.[84] These data reveal the subtle differences in sequence-selectivity due to the identity of the residue and the structure of the N- and C-termini.

In addition to binding aromatic amino acids, the Q8·MV complex (Figure 6.10) also binds to peptides containing aromatic residues. In 2005, Urbach and coworkers reported the binding of Q8·MV to tripeptides containing Trp, with a modest preference for Trp at the N-terminal > nonterminal > C-terminal

View Online

Table 6.8 Equilibrium binding data for cucurbit[7]uril (Q7) with peptides.[84,86,104–106]

Peptide[a]	K_a[b] (M^{-1})
H-Phe-Ala-OH	7.9×10^5 [c]
H-D-Phe-Ala-OH	1.3×10^6 [c]
H-Phe-Pro-OH	2.9×10^4 [c]
H-D-Phe-Pro-OH	5.0×10^4 [c]
H-Phe-Phe-NH_2	5.3×10^6 [c]
H-D-Phe-Phe-NH_2	1.3×10^6 [c]
H-Phe-Leu-NH_2	1.4×10^7 [c]
H-D-Phe-Leu-NH_2	1.7×10^6 [c]
H-Phe-Gly-OH	3.0×10^7 [d]
H-Gly-Phe-OH	1.3×10^3 [d]
H-Tyr-Gly-OH	3.6×10^6 [d]
H-Gly-Tyr-OH	2.0×10^2 [d]
H-Trp-Gly-OH	5.6×10^5 [d]
H-Gly-Trp-OH	2.8×10^2 [d]
H-Phe-Leu-OH	2.1×10^6 [e]
H-Phe-Leu-NH_2	2.7×10^7 [e]
H-Thr-Gly-Ala-Phe-Leu-OH	1.8×10^3 [e]
H-Thr-Gly-Ala-Phe-Leu-NH_2	3.5×10^3 [e]
H-Phe-Gly-Gly-OH	2.8×10^6 [f]
H-Gly-Phe-Gly-OH	2.2×10^4 [f]
H-Phe-Gly-Gly-NH_2	3.2×10^6 [f]
H-Gly-Phe-Gly-NH_2	2.3×10^5 [f]
H-Amf-Gly-Gly-NH_2[g]	1.1×10^9 [f]
H-Gly-Amf-Gly-NH_2	2.0×10^6 [f]

[a]H- indicates an unprotected amino group at the N-terminus; -OH indicates a carboxylic acid at the C-terminus; -NH_2 indicates a primary amide at the C-terminus.
[b]All complexes had a stoichiometry of 1:1 Q7–peptide.
[c]Determined by isothermal titration calorimetry at 298 K in 0.1 M NaCl.[104]
[d]Determined by isothermal titration calorimetry at 298 K in H_2O.[105]
[e]Determined by competitive fluorescence titrations at 310 K in 10 mM ammonium acetate, pH 7.2.[106]
[f]Determined by isothermal titration calorimetry at 300 K in 10 mM sodium phosphate, pH 7.0.[84,86]
[g]Amf is 4-aminomethyl phenylalanine.[84]

position (Table 6.9).[61] Studies with singly charged analogues of Trp support a mechanism of sequence selectivity based on simultaneous interaction of the indole side chain and the N-terminal ammonium group. The simultaneous inclusion of MV and the indole side chain of Trp within the cavity of Q8 yields a new visible charge-transfer absorbance and induces the quenching of Trp fluorescence. This optical property is akin to that of the complex of Q8·MV with 2,6-dihydroxynaphthalene reported by Kim and coworkers in 2001.[64] MBBI (Figure 6.16) was tested as an alternative to MV as an auxiliary for Q8.[107] MBBI is more chemically and thermally stable than MV, and MBBI is intrinsically fluorescent, thus offering the possibility of sensing guests that are not intrinsically fluorescent. The binding constants of Q8 to MV and to MBBI are similar (~10^6 M^{-1}), and the binding constants of Q8·MV and Q8·MBBI to Trp-Gly-Gly, Gly-Trp-Gly, and Gly-Gly-Trp are also strikingly similar. Therefore, MBBI promises to be a good alternative to MV for peptide studies.

Published on 15 November 2016 on http://pubs.rsc.org | doi:10.1039/9781782626626-00172

View Online

Published on 15 November 2016 on http://pubs.rsc.org | doi:10.1039/9781782626626-00172

Table 6.9 Equilibrium binding data for Q8·auxiliary complexes with peptides.[a,61,107]

Peptide	Auxiliary = MV (M^{-1})	Auxiliary = MBBI (M^{-1})
H-Trp-Gly-Gly-OH	1.3×10^{5} [b]	1.2×10^{5} [b]
H-Gly-Trp-Gly-OH	2.1×10^{4} [b]	1.7×10^{4} [b]
H-Gly-Gly-Trp-OH	3.1×10^{3} [b]	4.1×10^{3} [b]

[a]H- indicates an unprotected amino group at the N-terminus; -OH indicates a carboxylic acid at the C-terminus.
[b]All complexes had a stoichiometry of 1 : 1 Q8·auxiliary–peptide. K_a values were determined by isothermal titration calorimetry at 300 K in 10 mM sodium phosphate, pH 7.0.[61,107]

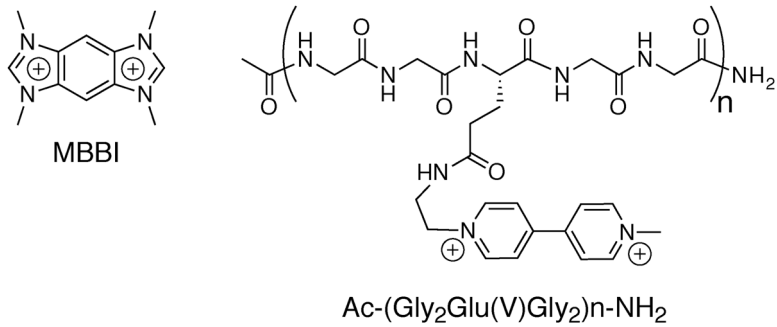

Figure 6.16 Chemical formulas of MBBI and the viologen-modified peptides for mono- and multivalent binding.[107–109]

In an effort to increase the affinity of peptide binding, Urbach and coworkers reported the design of multivalent receptors based on the Q8·MV complex (Figure 6.16).[109] Viologen groups were conjugated to the side chain of Glu residues, *i.e.*, Glu(V), and the resulting peptide-based receptors recruited one equivalent of Q8 per viologen group with noncooperative binding. This self-assembly approach circumvents the synthetic challenge of covalently linking multiple Q8 groups (Figure 6.17). The assembled monovalent, divalent, and trivalent complexes bound to peptides containing single Trp residues in a noncooperative fashion (Table 6.10), with K_a values of ~2×10^4 M^{-1} per site. The divalent receptors bound peptides containing two Trp residues in a divalent fashion with K_a values of ~5×10^5 M^{-1}. The induced charge-transfer upon inclusion of the indole groups of each Trp within the cavity of each Q8·viologen complex was used to quantify the valency of binding. The lengths of the linkages between Glu(V) groups in the receptor and between Trp residues in the target peptide were four or six Gly residues; remarkably, there was no significant difference in the divalent binding constants. Ideal multivalent binding would predict an approximately additive increase in free energy as a function of valency.[98] Additive favorable binding enthalpies were observed as a function of valency, but the unfavorable binding entropies were more than additive, and thus only modest gains in binding affinity were observed for divalent (30-fold) and trivalent (300-fold) *versus* monovalent binding.[109]

View Online

Published on 15 November 2016 on http://pubs.rsc.org | doi:10.1039/9781782626626-00172

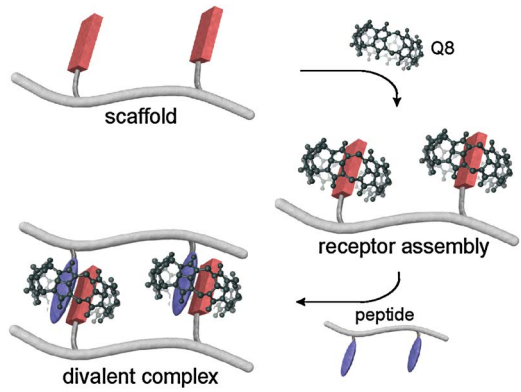

Figure 6.17 Schematic illustration of a self-assembled divalent receptor. A peptide modified with two viologen groups (red rectangles) recruits two equivalents of Q8 and then binds in a divalent fashion to a peptide containing two Trp residues (blue ovals).[109] Adapted by permission from ref. 109, © 2009 American Chemical Society.

Table 6.10 Equilibrium binding data for mono- and multivalent Q8·viologen receptors with peptides.[109]

Receptor[a]	Peptide[a]	K_a [b] (M^{-1})
Ac-$(Gly)_2$-Glu(V)-$(Gly)_2$-NH_2	Ac-$(Gly)_2$-Trp-$(Gly)_2$-NH_2	2.2×10^4 [c]
Ac-$(Gly)_2$-Glu(V)-$(Gly)_2$-NH_2	Ac-$(Gly)_3$-Trp-$(Gly)_3$-NH_2	2.2×10^4 [c]
Ac-$(Gly)_3$-Glu(V)-$(Gly)_3$-NH_2	Ac-$(Gly)_2$-Trp-$(Gly)_2$-NH_2	1.9×10^4 [c]
Ac-$(Gly)_3$-Glu(V)-$(Gly)_3$-NH_2	Ac-$(Gly)_3$-Trp-$(Gly)_3$-NH_2	2.2×10^4 [c]
Ac-$[(Gly)_2$-Glu(V)-$(Gly)_2]_2$-NH_2	Ac-$(Gly)_2$-Trp-$(Gly)_2$-NH_2	1.7×10^4 [d]
Ac-$[(Gly)_2$-Glu(V)-$(Gly)_2]_2$-NH_2	Ac-$(Gly)_3$-Trp-$(Gly)_3$-NH_2	1.5×10^4 [d]
Ac-$[(Gly)_3$-Glu(V)-$(Gly)_3]_2$-NH_2	Ac-$(Gly)_2$-Trp-$(Gly)_2$-NH_2	1.8×10^4 [d]
Ac-$[(Gly)_3$-Glu(V)-$(Gly)_3]_2$-NH_2	Ac-$(Gly)_3$-Trp-$(Gly)_3$-NH_2	1.4×10^4 [d]
Ac-$[(Gly)_2$-Glu(V)-$(Gly)_2]_2$-NH_2	Ac-$[(Gly)_2$-Trp-$(Gly)_2]_2$-NH_2	5.0×10^5 [e]
Ac-$[(Gly)_2$-Glu(V)-$(Gly)_2]_2$-NH_2	Ac-$[(Gly)_3$-Trp-$(Gly)_3]_2$-NH_2	4.6×10^5 [e]
Ac-$[(Gly)_3$-Glu(V)-$(Gly)_3]_2$-NH_2	Ac-$[(Gly)_2$-Trp-$(Gly)_2]_2$-NH_2	5.5×10^5 [e]
Ac-$[(Gly)_3$-Glu(V)-$(Gly)_3]_2$-NH_2	Ac-$[(Gly)_3$-Trp-$(Gly)_3]_2$-NH_2	5.0×10^5 [e]
Ac-$[(Gly)_2$-Glu(V)-$(Gly)_2]_3$-NH_2	Ac-$(Gly)_2$-Trp-$(Gly)_2$-NH_2	1.7×10^4 [f]
Ac-$[(Gly)_2$-Glu(V)-$(Gly)_2]_3$-NH_2	Ac-$[(Gly)_2$-Trp-$(Gly)_2]_3$-NH_2	4.7×10^6 [g]

[a] Ac- indicates an acetylated N-terminus; -NH_2 indicates a primary amide at the C-terminus; Glu(V) is the viologen-modified Glu residue shown in Figure 6.16.
[b] K_a values were determined by isothermal titration calorimetry at 300 K in 10 mM sodium phosphate, pH 7.0.
[c] Monovalent complexes; the stoichiometry was 1 : 1 receptor–peptide.
[d] Monovalent complexes; the stoichiometry was 1 : 2 receptor–peptide; the K_a value is given per independent binding site.
[e] Divalent complexes; the stoichiometry was 1 : 1 receptor–peptide.
[f] Monovalent complex; the stoichiometry was 1 : 3 receptor–peptide; the K_a value is given per independent binding site.
[g] Trivalent complex; the stoichiometry was 1 : 1 receptor–peptide.[109]

View Online

Published on 15 November 2016 on http://pubs.rsc.org | doi:10.1039/9781782626626-00172

Table 6.11 Equilibrium binding data for cucurbit[8]uril (Q8) with peptides.[85,108,110]

Peptide[a]	*K*
H-Phe-Gly-Gly-OH	$1.5 \times 10^{11\,b}$ M^{-2}
H-Gly-Phe-Gly-OH	n.d.[c]
H-Gly-Gly-Phe-OH	n.d.[c]
H-Trp-Gly-Gly-OH	$3.6 \times 10^{9\,b}$ M^{-2}
H-Gly-Trp-Gly-OH	n.d.[c]
H-Gly-Gly-Trp-OH	n.d.[c]
H-Ala-Gly-Phe-Arg-His-NH_2	$3.7 \times 10^{10\,d}$ M^{-2}
H-Lau-Val-Phe-Ile-Ala-NH_2	$7.7 \times 10^{9\,d}$ M^{-2}
H-Val-Ile-Phe-Ala-Glu-NH_2	$1.6 \times 10^{13\,d}$ M^{-2}
H-Tyr-Leu-Ala-NH_2	$1.4 \times 10^{8\,e}$ M^{-1}
H-Tyr-Ala-Leu-NH_2	$2.9 \times 10^{4\,e}$ M^{-1}
H-Ala-Tyr-Leu-NH_2	$3.2 \times 10^{5\,e}$ M^{-1}
H-Tyr-Lys-Ala-NH_2	$5.0 \times 10^{6\,e}$ M^{-1}
H-Tyr-Tyr-Ala-NH_2	$1.4 \times 10^{6\,e}$ M^{-1}
H-Tyr-Phe-Ala-NH_2	$3.5 \times 10^{6\,e}$ M^{-1}
H-Phe-Leu-Ala-NH_2	$2.3 \times 10^{6\,e}$ M^{-1}

[a]H- indicates an unprotected amino group at the N-terminus; -OH indicates a carboxylic acid at the C-terminus; -NH_2 indicates a primary amide at the C-terminus.
[b]Determined by isothermal titration calorimetry at 300 K in 10 mM sodium phosphate, pH 7.0. The observed stoichiometry was 1 : 2 Q8–peptide.[85]
[c]n.d. indicates that the study was performed, but binding was not detected.[85]
[d]Determined by isothermal titration calorimetry at 298 K in 10 mM sodium phosphate, pH 7.4.[110]
[e]Determined by isothermal titration calorimetry at 300 K in 10 mM sodium phosphate, pH 7.0. The observed stoichiometry was 1 : 1 Q8–peptide.[108]

In the absence of an auxiliary guest, Q8 can bind two equivalents of peptide.[85] The binding affinity per peptide is similar in magnitude to the Q8·auxiliary·peptide complexes, but the corresponding sequence-selectivity is orders of magnitude higher in the absence of the auxiliary (Tables 6.9 and 6.11). An early paper from the Urbach group reported crystal structures of the Q8·(Phe-Gly-Gly)$_2$ complex and the Q8·Trp-Gly-Gly complex (Figure 6.18(a) and (b)). The dimer complex revealed staggered face-to-face stacking of the Phe side chains of the two respective peptides within the cavity of Q8. Both crystal structures showed the N-terminal aromatic ammonium group chelated by the three proximal carbonyl oxygens on the respective portal of Q8. These structures provide a molecular basis for the high selectivity for the N-terminal aromatic residue *via* recognition of the unique structural epitope comprising the aromatic side chain and N-terminal ammonium group. More recently, Scherman and coworkers found that Q8 can bind to nonterminal Phe residues with high affinity, and that the binding affinity depends significantly on the sequence context.[110] The high affinity and selectivity of Q8 for peptide dimers has led several groups to apply this system to the noncovalent homodimerization of proteins and polymers in aqueous solution.[111–118]

The importance of sequence context on the binding of Qn's to peptides was mentioned briefly above. Urbach and coworkers undertook a more comprehensive investigation of the binding of Q8·MV to peptides containing an

View Online

Published on 15 November 2016 on http://pubs.rsc.org | doi:10.1039/9781782626626-00172

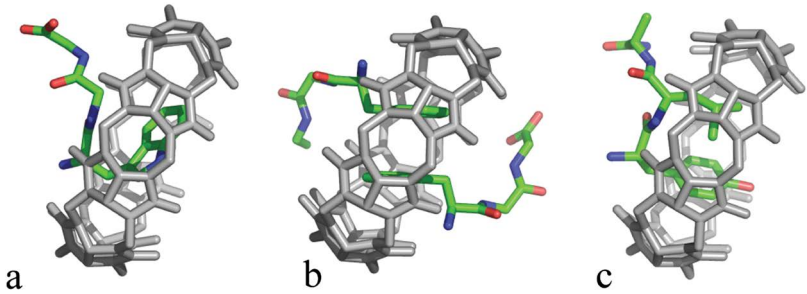

Figure 6.18 Crystal structures of Q8 in complex with (a) one equivalent of Trp-Gly-Gly and (b) two equivalents of Phe-Gly-Gly.[85] (c) Semiempirical model of Q8 bound to one equivalent of Tyr-Leu-Ala.[108]

N-terminal Phe or a nonterminal Phe.[119] Variation of the neighboring residues showed no significant impact on the binding affinity, and therefore Q8·MV should bind Trp in any sequence context. Taking advantage of the intrinsic fluorescence of MBBI to monitor the binding of nonfluorescent peptides,[107] the binding of Q8·MBBI to a series of peptides containing N-terminal Trp, Phe, or Tyr with variation at the two neighboring positions was measured.[108] This study revealed two interesting results. The first was that MBBI as an auxiliary can sense peptide binding in two ways: (1) the binding of a second guest causes the quenching of MBBI fluorescence, and (2) the displacement of MBBI by the analyte causes an enhancement in MBBI fluorescence. The second interesting result involved the Tyr-terminated peptides. For certain neighboring residues, the fluorescence increased if the neighbor was immediately adjacent to the N-terminal Tyr, but the fluorescence decreased if the neighbor was two residues away from the Tyr. Further investigation revealed that certain peptides (Tyr-Leu-Ala, Tyr-Phe-Ala, Tyr-Tyr-Ala) bind to Q8 in a 1:1 Q8–peptide stoichiometry. NMR studies, including a semiempirical model based on ROESY data (Figure 6.18(c)), showed that the side chains of Tyr and its immediate neighbor insert simultaneously into the cavity of Q8. Tyr-Leu-Ala showed the highest affinity (1.4×10^8 M^{-1}), with a 400-fold loss in affinity if the Tyr-Leu sequence is moved away from the N-terminus (*i.e.*, Ala-Tyr-Leu), and a 5000-fold loss in affinity if the Tyr and Leu are separated by one residue (*i.e.*, Tyr-Ala-Leu) (Table 6.11). These experiments, which reveal the highest affinity and second-highest sequence-selectivity reported to date, demonstrate the value of binding simultaneously to two neighboring residues *and* the terminal functional group.

The many studies described here of peptide binding by synthetic receptors in aqueous solution provide a few valuable design principles. First, as with biological systems, aromatic residues can provide highly efficient binding per residue. Second, simultaneous interaction of the receptor with multiple residues can increase the affinity and selectivity of binding. Third, the terminal residue provides a unique structural epitope comprising the side chain in proximity to the unreacted terminal functional group; simultaneous

View Online

Published on 15 November 2016 on http://pubs.rsc.org | doi:10.1039/9781782626626-00172

binding of the receptor to both parts of this epitope can increase the binding affinity and can be a powerful approach to distinguishing that residue from others. Finally, the simultaneous recognition of neighboring residues *and* the terminal functional group can yield additive benefits of both individual approaches. The affinity and selectivity demonstrated for cucurbit[*n*]uril·peptide complexes, in particular, have inspired many applications of this system.

6.9 Recognition of Aromatic Sites on Proteins by Synthetic Receptors

Peptides have clear practical advantages over proteins for studies of molecular recognition, but the extent to which peptide studies translate to proteins remains to be fully understood. One area in which excellent progress has been made is the study of peptides with well-defined secondary structure.[50,120,121] In particular, alpha helices, coiled coils, and beta hairpins have taught us invaluable lessons about intramolecular and intermolecular interactions in the context of structured peptides. Alpha helices and helix mimics have also been used as effective mimics of protein domains to inhibit protein–protein interactions.[50,122]

Side chains that are neighbors on the surface of proteins and structured peptides, however, are often not neighbors in the amino acid sequence. In the case of peptides with well-defined secondary structure, there are design principles for predicting the secondary structure from the amino acid sequence,[50,120,121] and therefore the presentation of side chains on the surface of the peptide can be reasonably estimated. For most natural proteins, however, the structure is difficult to predict from the sequence. Therefore, several approaches to targeting the surface of proteins have been based on simple electrostatic attraction.[7,123,124] Electrostatic interactions can be powerful for increasing the affinity of interaction, but they suffer from poor selectivity.

An alternative approach to protein recognition is to target individual side chains that are accessible on the surface. Molecular tweezers (Figure 6.19)

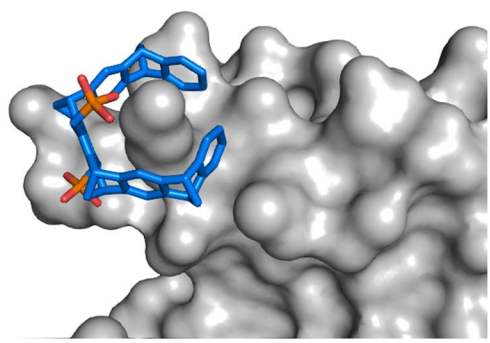

Figure 6.19 Crystal structure of a molecular tweezer bound to a lysine residue on the surface of 14-3-3σ (PDB ID: 4HQW).[125]

View Online

Published on 15 November 2016 on http://pubs.rsc.org | doi:10.1039/9781782626626-00172

and calixarenes (Figure 6.9) have been used to target to target lysine and methylated lysine residues on proteins *via* electrostatic interactions.[56,125,126] Cyclodextrins have also been used to target individual residues on the surface of proteins. In some cases, cyclodextrins form inclusion complexes with nonpolar side chains.[127] Wimmer and coworkers reported a structural study of the interactions of β-cyclodextrin with insulin and ubiquitin. NMR studies revealed interaction of the host with surface-exposed Phe residues on insulin but not on ubiquitin. Further investigation revealed limited solvent-exposure at the ubiquitin sites.[127] On the whole, these studies reveal two major drawbacks to targeting individual residues on the surface of proteins: (1) structured polypeptides present side chains in a sterically crowded environment, thereby limiting access by a synthetic receptor; and (2) receptors that target a single residue may bind at multiple sites on the surface of a protein and may not be able to discern between different proteins, thereby limiting selectivity. Moreover, the affinity of synthetic receptors for individual amino acid residues tends to be weak ($K_a \leq 10^6\ M^{-1}$) relative to natural protein complexes.

Studies with cucurbit[*n*]urils have revealed an approach to protein recognition that overcomes these limitations and enables sequence-predictive recognition of proteins. Urbach and coworkers asked whether the selectivity of Qn's for N-terminal aromatic residues in peptides[95] would translate to the context of proteins. They reported a study of the binding of Q7 to insulin, which has an N-terminal Phe residue on its B-chain (Phe^{B1}) as well as several other surface-exposed but nonterminal Phe and Tyr residues.[86] Structure–activity studies by isothermal titration calorimetry revealed that Q7 binds insulin with a K_a value of $1.5 \times 10^6\ M^{-1}$, whereas binding to a $Glu^{B1}Glu^{B27}$ variant (native B27 is Thr) was too weak to be measured by this technique. Both insulin variants have similar structures, and therefore high-affinity binding occurs at Phe^{B1}. Q7 bound to model tripeptides containing an N-terminal Phe (Phe-Gly-Gly) with similar affinity as native insulin and showed measurable binding to Gly-Phe-Gly and Gly-Tyr-Gly, which were models of the other possible aromatic sites on insulin. It was interesting that Q7 bound to nonterminal Phe and Tyr in the model tripeptides but not in the context of the mutant insulin. A crystal structure of the Q7·insulin complex (Figure 6.20) shows binding at Phe^{B1}, in which the aromatic side chain is bound within the cavity of Q7, and the N-terminal ammonium group is proximal to carbonyl oxygens on Q7. Superposition of the bound and unbound insulin molecules in the asymmetric unit of the crystal reveals that the terminus of the B-chain unfolds to accommodate the binding of Q7. By unraveling, the terminus becomes fully solvent exposed and flexible, like a short peptide. This feature helps to explain why this binding motif translates from peptides to proteins. The lack of steric crowding at the surface may explain why binding to the N-terminal Phe *vs.* nonterminal sites is more selective in the context of proteins than with peptides. Moreover, the binding interface between Q7 and protein was ~200 $Å^2$, which is extraordinarily small compared to a typical protein–protein interface (≥600 $Å^2$).[28] Therefore, a small interface composed of a single residue is sufficient for strong and selective binding by synthetic

View Online

Published on 15 November 2016 on http://pubs.rsc.org | doi:10.1039/9781782626626-00172

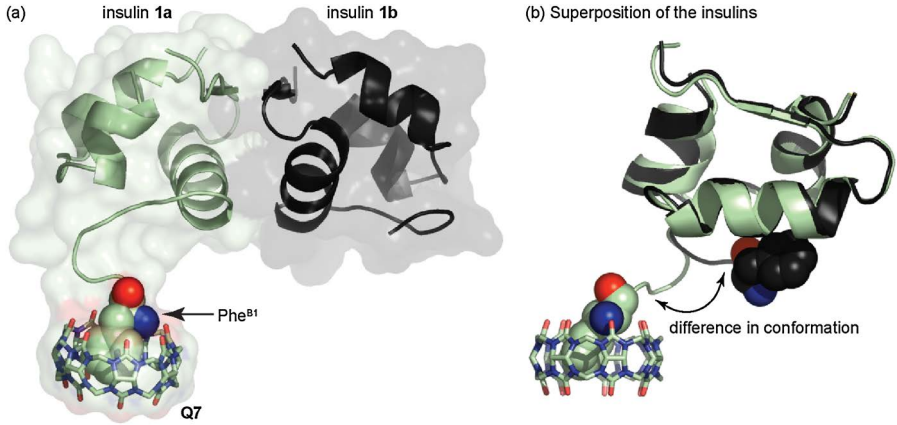

Figure 6.20 Crystal structure of the Q7·insulin complex (PDB: 3LEB).[86] (a) Asymmetric unit of the crystal, with the two molecules of insulin, 1a (green) and 1b (black), rendered as ribbons and the associated Q7 as sticks. The solvent-accessible surface is shown as semi-transparent to reveal the overall shape of the complex. The Phe^{B1} position of 1a, which is bound inside Q7, is rendered as space-filling, with carbon in green, oxygen in red, and nitrogen in blue; the N-terminal nitrogen is the blue sphere. (b) Superposition of the two insulins illustrates the strong homology between 1a and 1b with clear divergence at the N-terminus of the B-chain. In this image, the Phe^{B1} position of both insulins is rendered as space-filling for comparison. Reprinted by permission from ref. 86, © 2011 American Chemical Society.

receptors. This study demonstrates the unique properties of a protein terminus that enable recognition at a single site and that is predictive on the basis of the identity of the terminal residue and therefore on the basis of the amino acid sequence.

The interaction between a Qn and an N-terminal Phe residue has been used as an engineered recognition site in recombinant proteins. Applications include using Q8 to induce the dimerization of fluorescent proteins,[115] to control enzyme activity,[116] to build protein nanowires,[112] and to attach proteins and cells to a surface.[128,129] The reported binding constants for Qn–protein interactions correlate well to those with short peptides (Table 6.12). These studies illustrate the value of this approach to protein recognition for applications in biochemistry, biosensing, and biomaterials. They also further support the high selectivity of protein recognition enabled by targeting the terminal residue.

The selective recognition of proteins by Q7 and Q8 at an N-terminal aromatic residue reveals important design principles for synthetic receptor–protein interactions, but this phenomenon is not unique to synthetic systems. Pathways that abide by the N-end rule of protein degradation,[130] which is highly conserved in prokaryotes and eukaryotes, use a similar recognition strategy. Natural N-recognins, such as the adaptor protein ClpS, recognize a specific amino acid residue at the N-terminal position of a protein (*i.e.*, the

View Online

Table 6.12 Thermodynamic binding data of Qn-protein complexes.[86,112,115,116]

Protein	Sequence	Receptor	K_a (M^{-1})	K_{ter} (M^{-2})
Insulin	Phe-B1	Q7	$1.5 \times 10^{6\,b}$	—
CFP·YFP	FGG[a]	Q8		$1.0 \times 10^{13\,c}$
Caspase-9	FGG[a]	Q8	—	$2.7 \times 10^{12\,d}$
GST	FGG[a]	Q8	—	$2.9 \times 10^{12\,e}$

[a]Recombinant protein tags.
[b]Determined by isothermal titration calorimetry at 300 K in 10 mM sodium phosphate, pH 7.0.[86]
[c]ITC, 10 mM sodium phosphate, pH 7.0, 303 K.[115]
[d]Q8-dependent enzyme activation, 25 mM HEPES, 100 mM NaCl, 4 mM $MgCl_2$, 2 mM TCEP, pH 6.5, 310 K.[116]
[e]ITC, 20 mM sodium phosphate, 1 mM EDTA, pH 7.4, 298 K.[112]

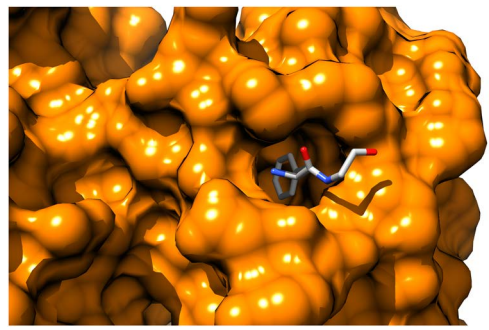

Figure 6.21 Crystal structure of peptide FGG bound in the hydrophobic cavity of ClpS (PDB: 3GW1).[134] The protein is rendered to show the solvent-exposed surface in orange, and the peptide is shown as a stick model.

Published on 15 November 2016 on http://pubs.rsc.org | doi:10.1039/9781782626626-00172

degron) in order to deliver the protein to a protease for degradation.[131] ClpS is a bacterial N-recognin that recognizes N-terminal aromatic residues.[132] Crystal structures reported by two independent groups of ClpS in complex with peptides containing N-terminal aromatic residues (Figure 6.21) reveal the molecular basis of recognition.[133–135] Like the synthetic N-recognin Q7, ClpS encapsulates the aromatic side chain of the disordered peptide in a hydrophobic pocket while forming electrostatic contacts with the N-terminal ammonium group. This homologous strategy for the recognition of N-terminal aromatic residues, found in both biological and synthetic receptors, demonstrates that protein recognition can be achieved *via* the unique properties of the terminal residue, and that studies on short peptides can translate to folded proteins while maintaining selectivity.

6.10 Lessons Learned and Challenges

The work described in this chapter illustrates several important lessons. It is clear that aromatic functional groups have unique properties that enable several types of intermolecular interactions and extensive binding interfaces.

View Online

Published on 15 November 2016 on http://pubs.rsc.org | doi:10.1039/9781782626626-00172

These properties help to explain why aromatic amino acid residues are found so commonly at important interaction sites in the natural complexes of proteins and peptides.

While protein receptors may recognize aromatic residues within deep hydrophobic cavities or *via* large clusters that form hydrophobic surfaces, synthetic receptors are limited in size and therefore can typically bind only one residue at a time. Thus, synthetic receptors need efficient ligands. Aromatic residues meet this need.

The binding of synthetic receptors to individual residues on the surface of peptides or proteins can be specific for a certain type of residue, but specificity for a single site or a specific target can be difficult to achieve. This limitation can be overcome by targeting the terminal residue, which presents a small, unique, and solvent-accessible epitope, as demonstrated in particular with cucurbit[*n*]uril recognition of N-terminal aromatic residues. This approach enables the prediction of binding based on the amino acid sequence. Moreover, increasing the size of the binding site to include two residues can substantially improve binding affinity and selectivity.

Protein termini are also less mechanically constrained than other positions in the polypeptide chain. The terminus can unravel in order to accommodate binding by a receptor, as demonstrated by the synthetic receptor Q7 and the natural receptor ClpS. In this respect, the terminus behaves like a small, solvent-exposed peptide. Therefore, it is possible to recognize proteins based on the unique properties of the terminal residue, thus providing a predictive approach based on the amino acid composition.

The principles of aromatic recognition discussed in this chapter serve as a foundation for future studies. The recognition of insulin and Phe-Gly-Gly-modified proteins at the N-terminus by cucurbit[*n*]urils suggests that other native proteins could also be targets for recognition. Moreover, studies on specific protein recognition have largely been carried out in simple media with few, if any, other proteins as competition. It would be valuable to know more about the selectivity in more complex media, including biological mixtures. The work of Rotello and coworkers on measuring the most abundant proteins in serum leads in this direction.[136]

The recognition of N-termini is made challenging by the presence of methionine as the starting amino acid in protein expression. Methods exist to modify the terminus *via* treatment with an endopeptidase or the inclusion of an intein sequence,[137] but it is more straightforward to design recombinant proteins with a desired C-terminal residue. Toward this end, it would be interesting to see if designed receptors for carboxylate groups, such as the guanidinium-based receptors developed by Schmuck and coworkers, could be applied to the recognition of C-terminal aromatic residues.

The study of peptide and protein recognition has been active for some time, and there are still many challenges to be met in order to gain control over natural systems. Much of this chapter focuses on selectivity because it is so difficult to achieve. In order to be relevant in physiological media, where the concentrations of target proteins and peptides are often in the

View Online

subnanomolar range, it would also be necessary to achieve high binding affinity. Although there are a few reports of peptide and protein recognition with both high affinity and high selectivity, we anticipate much more progress in the years to come.

Published on 15 November 2016 on http://pubs.rsc.org | doi:10.1039/9781782626626-00172

Acknowledgements

The authors wish to acknowledge support from the Welch Foundation (W-1640) and the National Science Foundation (CHE-1309978).

References

1. M. W. Peczuh and A. D. Hamilton, *Chem. Rev.*, 2000, **100**, 2479.
2. R. Langer and D. A. Tirrell, *Nature*, 2004, **428**, 487.
3. G. L. Patrick, *An Introduction to Medicinal Chemistry*, Oxford University Press, New York, NY, 5th edn, 2005.
4. D. A. Uhlenheuer, K. Petkau and L. Brunsveld, *Chem. Soc. Rev.*, 2010, **39**, 2817.
5. *Molecular Diagnostics: Current Research and Applications*, ed. J. Huggett and J. O'Grady, Horizon Press, Norfolk, UK, 2014.
6. J.-C. Janson, *Protein Purification: Principles, High Resolution Methods, and Applications*, Wiley, Hoboken, USA, 3rd edn, 2011.
7. *Synthetic Receptors for Biomolecules: Design Principles and Applications*, ed. B. D. Smith, Royal Society of Chemistry, Cambridge, 2015.
8. R. Kubota and I. Hamachi, *Chem. Soc. Rev.*, 2015, **44**, 4454.
9. E. A. Meyer, R. K. Castellano and F. Diederich, *Angew. Chem., Int. Ed.*, 2003, **42**, 1210.
10. M. L. Waters, *Biopolymers*, 2004, **76**, 435.
11. L. M. Salonen, M. Ellermann and F. Diederich, *Angew. Chem., Int. Ed.*, 2011, **50**, 4808.
12. A. K. Tewari, P. Srivastava, V. P. Singh, P. Singh and R. S. Khanna, *Res. Chem. Intermed.*, 2012, **39**, 2925.
13. A. S. Mahadevi and G. N. Sastry, *Chem. Rev.*, 2013, **113**, 2100.
14. S. E. Wheeler and J. W. G. Bloom, *J. Phys. Chem. A*, 2014, **118**, 6133.
15. K. A. Wilson, J. L. Kellie and S. D. Wetmore, *Nucleic Acids Res.*, 2014, **42**, 6726.
16. C. R. Martinez and B. L. Iverson, *Chem. Sci.*, 2012, **3**, 2191.
17. L. M. Salonen, M. Ellermann and F. Diederich, *Angew. Chem., Int. Ed.*, 2011, **50**, 4808.
18. C. Chothia, *J. Mol. Biol.*, 1976, **105**, 1.
19. A. Radzicka and R. Wolfenden, *Biochemistry*, 1988, **27**, 1664.
20. W. C. Wimley and S. H. White, *Nat. Struct. Biol.*, 1996, **3**, 842.
21. C. A. Hunter, K. R. Lawson, J. Perkins and C. J. Urch, *J. Chem. Soc., Perkin Trans. 2*, 2001, **5**, 651.

View Online

Published on 15 November 2016 on http://pubs.rsc.org | doi:10.1039/9781782626626-00172

22. K. V. R. Kishan, M. E. Newcomer, T. H. Rhodes and S. D. Guilliot, *Protein Sci.*, 2001, **10**, 1046.
23. M. M. Rahman, Z. T. Muhseen, M. Junaid and H. Zhang, *Curr. Protein Pept. Sci.*, 2015, **16**, 502.
24. L. M. Espinoza-Fonseca, *Mol. BioSyst.*, 2012, **8**, 237.
25. M. Huber, O. Y. Ovchinnikova, A. K. Schütz, R. Glockshuber, B. H. Meier and A. Böckmann, *Biomol. NMR Assignments*, 2014, **9**, 7.
26. T. Clackson and J. A. Wells, *Science*, 1995, **267**, 383.
27. I. S. Moreira, P. A. Fernandes and M. J. Ramos, *Proteins*, 2007, **68**, 803.
28. A. A. Bogan and K. S. Thorn, *J. Mol. Biol.*, 1998, **280**, 1.
29. B. Ma, T. Elkayam, H. Wolfson and R. Nussinov, *Proc. Natl. Acad. Sci. U. S. A.*, 2003, **100**, 5772.
30. O. Keskin, B. Ma and R. Nussinov, *J. Mol. Biol.*, 2005, **345**, 1281.
31. I. S. Moreira, J. M. Martins, R. M. Ramos, P. A. Fernandes and M. J. Ramos, *Biochim. Biophys. Acta*, 2013, **1834**, 404.
32. T. V. Borchert, R. Abagyan, R. Jaenicke and R. K. Wierenga, *Proc. Natl. Acad. Sci. U. S. A.*, 1994, **91**, 1515.
33. K. Maithal, G. Ravindra, G. Nagaraj, S. K. Singh, H. Balaram and P. Balaram, *Protein Eng., Des. Sel.*, 2002, **15**, 575.
34. L. M. Espinoza-Fonseca, C. Wong-Ramírez and J. G. Trujillo-Ferrara, *Arch. Biochem. Biophys.*, 2010, **494**, 46.
35. S. S. Velanker, S. S. Ray, R. S. Gokhale, S. Suma, H. Balaram, P. Balaram and M. R. Murthy, *Struct. Folding Des.*, 1997, **5**, 751.
36. The UniProt Consortium, *Nucl. Acids Res.*, 2015, **43**, D204.
37. P. H. Kussie, S. Gorina, V. Marechal, B. Elenbaas, J. Moreau, A. J. Levine and N. P. Pavletich, *Science*, 1996, **274**, 948.
38. S. M. Picksley, B. Vojtesek, A. Sparks and D. P. Lane, *Oncogene*, 1994, **9**, 2523.
39. A. Athanasiadis, G. Anderluh, P. Macek and D. Turk, *Struct. Folding Des.*, 2001, **9**, 341.
40. G. Anderluh, A. Razpotnik, A. Podlesek, P. Maček, F. Separovic and R. S. Norton, *J. Mol. Biol.*, 2005, **347**, 27.
41. N. Rojko, M. D. Serra, P. Maček and G. Anderluh, *Biochim. Biophys. Acta, Biomembr.*, 2016, **1858**, 446.
42. G. Robin, Y. Sato, D. Desplancq, N. Rochel, E. Weiss and P. Martineau, *J. Mol. Biol.*, 2014, **426**, 3729.
43. W. Ma, C. Tang and L. Lai, *Biophys. J.*, 2005, **89**, 1183.
44. S. Antonczak, G. Monard, M. Ruiz-Lopez and J. L. Rivall, *J. Mol. Model.*, 2000, **6**, 527.
45. B. Malfroy and J. C. Schwartz, *Biochem. Biophys. Res. Commun.*, 1985, **130**, 372.
46. D. Sanfelice and P. A. Temussi, *Front. Mol. Biosci.*, 2014, **1**, 14.
47. K. M. Vasquez and P. M. Glazer, *Q. Rev. Biophys.*, 2002, **35**, 1.
48. P. B. Dervan and B. S. Edelson, *Curr. Opin. Struct. Biol.*, 2003, **13**, 284.
49. C. Escude and J. S. Sun, *Top. Curr. Chem.*, 2005, **253**, 109.

View Online

Published on 15 November 2016 on http://pubs.rsc.org | doi:10.1039/9781782626626-00172

50. M. K. P. Jayatunga, S. Thompson and A. D. Hamilton, *Bioorg. Med. Chem. Lett.*, 2014, **24**, 717.
51. M. Blind and M. Blank, *Mol. Ther.–Nucleic Acids*, 2015, **4**, e223.
52. *Monoclonal Antibodies, Methods and Protocols*, ed. N. Fischer and V. Ossipow, Humana Press, New York, 2014.
53. E. S. Istvan and J. Deisenhofer, *Science*, 2001, **292**, 1160.
54. S. Bhattacharya, H. Zhang, A. K. Debnath and D. Cowburn, *J. Biol. Chem.*, 2008, **283**, 16274.
55. D. Oberthür, J. Achenbach, A. Gabdulkhakov, K. Buchner, C. Maasch, S. Falke, D. Rehders, S. Klussmann and C. Betzel, *Nat. Commun.*, 2015, **6**, 6923.
56. R. E. McGovern, H. Fernandes, A. R. Khan, N. P. Power and P. B. Crowley, *Nat. Chem.*, 2012, **4**, 527.
57. *Supramolecular Chemistry*, ed. J. W. Steed and J. L. Atwood, John Wiley & Sons, Chichester, 2nd edn, 2009.
58. *Synthetic Receptors for Biomolecules: Design Principles and Applications*, ed. B. D. Smith, Royal Society of Chemistry, Cambridge, 2015.
59. F. Biedermann, W. M. Nau and H.-J. Schneider, *Angew. Chem., Int. Ed.*, 2014, **53**, 11158.
60. T. T. Goodnow, M. V. Reddington, J. F. Stoddart and A. E. Kaifer, *J. Am. Chem. Soc.*, 1991, **113**, 4335.
61. M. E. Bush, N. D. Bouley and A. R. Urbach, *J. Am. Chem. Soc.*, 2005, **127**, 14511.
62. P. Rajgariah and A. R. Urbach, *J. Inclusion Phenom. Macrocyclic Chem.*, 2008, **62**, 251.
63. J. Kim, I.-S. Jung, S.-Y. Kim, E. Lee, J.-K. Kang, S. Sakamoto, K. Yamaguchi and K. Kim, *J. Am. Chem. Soc.*, 2000, **122**, 540.
64. H. J. Kim, J. Heo, W. S. Jeon, E. Lee, J. Kim, S. Sakamoto, K. Yamaguchi and K. Kim, *Angew. Chem., Int. Ed.*, 2001, **40**, 1526.
65. M. Hariharan, S. C. Karunakaran and D. Ramaiah, *Org. Lett.*, 2007, **9**, 417.
66. J. Szejtli, *Chem. Rev.*, 1998, **98**, 1743.
67. A. R. Hedges, *Chem. Rev.*, 1998, **98**, 2035.
68. R. Challa, A. Ahuja, J. Ali and R. K. Khar, *AAPS PharmSciTech*, 2005, **6**, E329.
69. J. M. Adam, D. J. Bennett, A. Bom, J. K. Clark, H. Feilden, E. J. Hutchinson, R. Palin, A. Prosser, D. C. Rees, G. M. Rosair, D. Stevenson, G. J. Tarver and M.-Q. Zhang, *J. Med. Chem.*, 2002, **45**, 1806.
70. X. Cai, W. Liu and S. Chen, *J. Agric. Food Chem.*, 2005, **53**, 6744.
71. H.-J. Buschmann and E. Schollmeyer, *J. Cosmet. Sci.*, 2002, **53**, 185.
72. M. V. Rekharsky and Y. Inoue, *Chem. Rev.*, 1998, **98**, 1875.
73. C. Kahle and U. Holzgrabe, *Chirality*, 2004, **16**, 509.
74. K. Lagona, P. Mukhopadhyay, S. Chakrabarti and L. Isaacs, *Angew. Chem., Int. Ed.*, 2005, **44**, 4844.
75. E. Masson, X. Ling, R. Joseph, L. Kyeremeh-Mensah and X. Lu, *RSC Adv.*, 2012, **2**, 1213.
76. K. I. Assaf and W. M. Nau, *Chem. Soc. Rev.*, 2014, **44**, 394.

View Online

Published on 15 November 2016 on http://pubs.rsc.org | doi:10.1039/9781782626626-00172

77. S. J. Barrow, S. Kasera, M. J. Rowland, J. del Barrio and O. A. Scherman, *Chem. Rev.*, 2015, **115**, 12320.
78. H.-J. Buschmann, E. Schollmeyer and L. Mutihac, *Thermochim. Acta*, 2003, **399**, 203.
79. S. Liu, C. Ruspic, P. Mukhopadhyay, S. Chakrabarti, P. Y. Zavalij and L. Isaacs, *J. Am. Chem. Soc.*, 2005, **127**, 15959.
80. H. Cong, L. L. Tau, Y. H. Yu, F. Yang, Y. Du, S. F. Xue and Z. Tao, *Z. Acta Chim. Sin.*, 2006, **64**, 989.
81. J. Lagona, B. D. Wagner and L. Isaacs, *J. Org. Chem.*, 2006, **71**, 1181.
82. M. V. Rekharsky, T. Mori, C. Yang, H. K. Young, N. Selvapalam, H. Kim, D. Sobransingh, A. E. Kaifer, S. Liu, L. Isaacs, W. Chen, S. Moghaddam, M. K. Gilson, O. Kim and Y. Inoue, *Proc. Natl. Acad. Sci. U. S. A.*, 2007, **104**, 20737.
83. D. M. Bailey, A. Hennig, V. D. Uzunova and W. M. Nau, *Chem.–Eur. J.*, 2008, **14**, 6069.
84. L. A. Logsdon, C. L. Schardon, V. Ramalingam, S. K. Kwee and A. R. Urbach, *J. Am. Chem. Soc.*, 2011, **133**, 17087.
85. L. M. Heitmann, A. B. Taylor, P. J. Hart and A. R. Urbach, *J. Am. Chem. Soc.*, 2006, **128**, 12574.
86. J. M. Chinai, A. B. Taylor, L. M. Ryno, N. D. Hargreaves, C. A. Morris, P. J. Hart and A. R. Urbach, *J. Am. Chem. Soc.*, 2011, **133**, 8810.
87. G. McMahon, S. O'Malley, K. Nolan and D. Diamond, *ARKIVOC*, 2003, **vii**, 23.
88. B. Mokhtari, K. Pourabdollah and N. Dallali, *J. Radioanal. Nucl. Chem.*, 2010, **287**, 921.
89. S. B. Nimse and T. Kim, *Chem. Soc. Rev.*, 2013, **42**, 366.
90. C. S. Beshara, C. E. Jones, K. D. Daze, B. J. Lilgert and F. Hof, *ChemBioChem*, 2009, **11**, 63.
91. G. A. E. Garnett, M. J. Starke, A. Shaurya, J. Li and F. Hof, *Anal. Chem.*, 2016, **88**, 3697.
92. H.-J. Buschmann, L. Mutihac and E. Schollmeyer, *J. Inclusion Phenom. Macrocyclic Chem.*, 2003, **46**, 133.
93. M. A. Hortalá, L. Fabbrizzi, N. Marcotte, F. Stomeo and A. Taglietti, *J. Am. Chem. Soc.*, 2003, **125**, 20.
94. W. C. Still, *Acc. Chem. Res.*, 1996, **29**, 155.
95. A. R. Urbach and V. Ramalingam, *Isr. J. Chem.*, 2011, **51**, 664.
96. M. Maletic, H. Wennemers, D. Q. McDonald, R. Breslow and W. C. Still, *Angew. Chem., Int. Ed.*, 1996, **35**, 1490.
97. R. Breslow, Z. Yang, R. Ching, G. Trojandt and F. Odobel, *J. Am. Chem. Soc.*, 1998, **120**, 3536.
98. M. Mammen, S. K. Choi and G. M. Whitesides, *Angew. Chem., Int. Ed.*, 1998, **37**, 2754.
99. M. A. Hossain and H.-J. Schneider, *J. Am. Chem. Soc.*, 1998, **120**, 11208.
100. S. Tashiro, M. Tominaga, M. Kawano, B. Therrien, T. Ozeki and M. Fujita, *J. Am. Chem. Soc.*, 2005, **127**, 4546.
101. S. Tashiro, M. Tominaga, Y. Yamaguchi, K. Kato and M. Fujita, *Chem.–Eur. J.*, 2006, **12**, 3211.

View Online

Published on 15 November 2016 on http://pubs.rsc.org | doi:10.1039/9781782626626-00172

102. C. Dolain, Y. Hatakeyama, T. Sawada, S. Tashiro and M. Fujita, *J. Am. Chem. Soc.*, 2010, **132**, 5564.
103. S. Tashiro, M. Kobayashi and M. Fujita, *J. Am. Chem. Soc.*, 2006, **128**, 9280.
104. M. V. Rekharsky, H. Yamamura, C. Inoue, M. Kawai, I. Osaka, R. Arakawa, K. Shiba, A. Sato, Y. H. Ko, N. Selvapalam, K. Kim and Y. Inoue, *J. Am. Chem. Soc.*, 2006, **128**, 14871.
105. M. V. Rekharsky, H. Yamamura, Y. H. Ko, N. Selvapalam, K. Kim and Y. Inoue, *Chem. Commun.*, 2008, 2236.
106. G. Ghale, V. Ramalingam, A. R. Urbach and W. M. Nau, *J. Am. Chem. Soc.*, 2011, **133**, 7528.
107. F. Biedermann, U. Rauwald, M. Cziferszky, K. A. Williams, L. D. Gann, B. Y. Guo, A. R. Urbach, C. W. Bielawski and O. A. Scherman, *Chem.–Eur. J*, 2010, **16**, 13716.
108. L. C. Smith, D. G. Leach, B. E. Blaylock, O. A. Ali and A. R. Urbach, *J. Am. Chem. Soc.*, 2015, **137**, 3663.
109. J. J. Reczek, A. A. Kennedy, B. T. Halbert and A. R. Urbach, *J. Am. Chem. Soc.*, 2009, **131**, 2408.
110. S. Sonzini, S. T. J. Ryan and O. A. Scherman, *Chem. Commun.*, 2013, **49**, 8779.
111. X. Tan, L. Yang, Y. Liu, Z. Huang, H. Yang, Z. Wang and X. Zhang, *Polym. Chem.*, 2013, **4**, 5378.
112. C. Hou, J. Li, L. Zhao, W. Zhang, Q. Luo, Z. Dong, J. Xu and J. Liu, *Angew. Chem., Int. Ed.*, 2013, **52**, 5590.
113. M. J. Rowland, E. A. Appel, R. J. Coulston and O. A. Scherman, *J. Mater. Chem. B*, 2013, **1**, 2904.
114. M. J. Rowland, M. Atgie, D. Hoogland and O. A. Scherman, *Biomacromolecules*, 2015, **16**, 2436.
115. H. D. Nguyen, D. T. Dang, J. L. J. van Dongen and L. Brunsveld, *Angew. Chem., Int. Ed.*, 2010, **49**, 895.
116. D. T. Dang, H. D. Nguyen, M. Merkx and L. Brunsveld, *Angew. Chem., Int. Ed.*, 2013, **52**, 2915.
117. V. Ramalingam, S. K. Kwee, L. M. Ryno and A. R. Urbach, *Org. Biomol. Chem.*, 2012, **10**, 8587.
118. D. T. Dang, R. P. G. Bosmans, C. Moitzi, I. K. Voets and L. Brunsveld, *Org. Biomol. Chem.*, 2014, **12**, 9341.
119. O. A. Ali, E. M. Olson and A. R. Urbach, *Supramol. Chem.*, 2013, **25**, 863.
120. G. Grigoryan and A. Keating, *Curr. Opin. Struct. Biol.*, 2008, **18**, 477.
121. M. L. Waters and W. J. Cooper, *Curr. Opin. Struct. Biol.*, 2006, **16**, 514.
122. H. Yin and A. D. Hamilton, *Angew. Chem., Int. Ed.*, 2005, **44**, 4130.
123. S. Fletcher and A. D. Hamilton, *Curr. Opin. Chem. Biol.*, 2005, **9**, 632.
124. R. Mout and V. M. Rotello, *Isr. J. Chem.*, 2013, **53**, 521.
125. D. Bier, R. Rose, K. Bravo-Rodriguez, M. Bartel, J. M. Ramirez-Anguita, S. Dutt, C. Wilch, F.-G. Klärner, E. Sanchez-Garcia, T. Schrader and C. Ottmann, *Nat. Chem.*, 2013, **5**, 234.

View Online

126. R. E. McGovern, B. D. Snarr, J. A. Lyons, J. McFarlane, A. L. Whiting, I. Paci, F. Hof and P. B. Crowley, *Chem. Sci.*, 2015, **6**, 442.
127. F. L. Aachmann, D. E. Otzen, K. L. Larsen and R. Wimmer, *Protein Eng., Des. Sel.*, 2003, **16**, 905.
128. S. Sankaran, M. de Ruiter, J. J. L. M. Cornelissen and P. Jonkheijm, *Bioconjugate Chem.*, 2015, **26**, 1972.
129. S. Sankaran, M. C. Kiren and P. Jonkheijm, *ACS Nano*, 2015, **9**, 3579.
130. A. Varshavsky, *Cell*, 1992, **69**, 725.
131. D. A. Dougan, D. Micevski and K. N. Truscott, *Biochim. Biophys. Acta, Mol. Cell Res.*, 2012, **1823**, 83.
132. R. Schmidt, R. Zahn, B. Bukau and A. Mogk, *Mol. Microbiol.*, 2009, **72**, 506.
133. K. H. Wang, G. Román-Hernández, R. A. Grant, R. T. Sauer and T. A. Baker, *Mol. Cell*, 2008, **32**, 406.
134. G. Román-Hernández, R. A. Grant, R. T. Sauer and T. A. Baker, *Proc. Natl. Acad. Sci. U. S. A.*, 2009, **106**, 8888.
135. V. J. Schuenemann, S. M. Kralik, R. Albrecht, S. K. Spall, K. N. Truscott, D. A. Dougan and K. Zeth, *EMBO Rep.*, 2009, **10**, 508.
136. M. De, S. Rana, H. Akpinar, O. R. Miranda, R. R. Arvizo, U. H. F. Bunz and V. M. Rotello, *Nat. Chem.*, 2009, **1**, 461.
137. N. H. Shah and T. W. Muir, *Chem. Sci.*, 2014, **5**, 446.

Published on 15 November 2016 on http://pubs.rsc.org | doi:10.1039/9781782626626-00172

Published on 15 November 2016 on http://pubs.rsc.org | doi:10.1039/9781782626626-00214

CHAPTER 7

Cation–π Interactions in Biomolecular Recognition

AMBER L. KOENIG[a] AND MARCEY L. WATERS*[a]

[a]Department of Chemistry, University of North Carolina at Chapel Hill, CB 3290, Chapel Hill, NC 27599, USA
*E-mail: mlwaters@email.unc.edu

7.1 The Nature of the Cation–π Interaction

Cation–π interactions arise from an electrostatic interaction between a positively charged ion and the partial negative on the face of an aromatic ring, which results from the quadrupole moment of the aromatic ring (Figure 7.1).[1] This quadrupole moment arises from the difference in electronegativity of the sp^2-hybridized carbons and hydrogens in the aromatic ring. While these interactions are often seen with aromatic rings, it should be noted that the aromaticity is not a necessity for this interaction, rather just the Coulombic interaction between a partial negative π surface and a cation is necessary.[3]

Computational studies in the gas phase first demonstrated that the interaction between metal cations and benzene was stronger than their interaction with water. The ΔH for K^+ and benzene was calculated to be −19.2 kcal mol^{-1}, while the interaction with water was −17.9 kcal mol^{-1}.[4] This difference was also observed with trimethylammonium ions, with values of −9.4 kcal

Monographs in Supramolecular Chemistry No. 20
Aromatic Interactions: Frontiers in Knowledge and Application
Edited by Darren W. Johnson and Fraser Hof
© The Royal Society of Chemistry 2017
Published by the Royal Society of Chemistry, www.rsc.org

View Online

Published on 15 November 2016 on http://pubs.rsc.org | doi:10.1039/9781782626626-00214

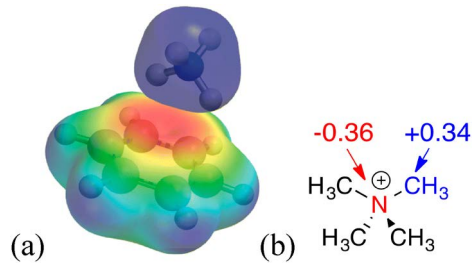

Figure 7.1 (a) Electrostatic potential map of the cation–π interaction between benzene and ammonium. (b) Location of partial charges on an ammonium cation. Adapted from ref. 1. Copyright 2013 American Chemical Society.

mol^{-1} with benzene and −9.0 kcal mol^{-1} with water.[5] In aqueous solution, which is the relevant environment for cation–π interactions in biomolecular recognition, desolvation of the cation plays a significant role. For example, interactions of benzene with other cations in the gas phase follow traditional electrostatic trends with $Li^+ > Na^+ > K^+ > Rb^+$.[4,6–8] In water, however, the trend changes due to differences in desolvation costs, with the interaction of benzene with K^+ becoming more favorable than with Na^+.[8] In biomolecules, nitrogen cations are the most commonly observed cations. In the case of quaternary ammonium ions such as the protonated amine sidechain in lysine, the ε-methylene is most commonly packed against the aromatic ring rather than the NH_3 group.[1] This is because the positive charge is distributed over the carbon and hydrogens rather than being localized on the nitrogen (Figure 7.1(b)).

Other forces, such as van der Waals forces and hydrophobic interactions (in water), also contribute to cation–π binding energies, resulting in a net interaction energy equal to the sum of these forces. However, the variations in the strengths of the interactions arise from differences in the electrostatic component of the interaction.[9]

Electrostatic potential maps of the aromatic group provide a good model for the variance in the interaction energies.[10] Substitution with electron withdrawing groups reduces the negative electrostatic potential in the center of the ring. This correlates well with the gas phase calculations of cation–π energies with Na^+.[10] The resonance effects of the substituents do not influence the cation–π energies, thus these energies correlate best with the σ-meta Hammett parameter.[9,11]

Recently, computational studies have provided a different model for the role of substituents in cation–π interactions.[3,12–14] These studies suggest that the destabilizing effects observed from electron withdrawing substituents are primarily a result of through space effects with the substituent, with π-polarization playing a more minor role.[12,13] In the gas phase, ion–π interactions can be explained by this interaction without any changes to the aromatic π system.[13,14]

View Online

7.2 Model Systems for Cation–π Interactions in Aqueous Solution

Published on 15 November 2016 on http://pubs.rsc.org | doi:10.1039/9781782626626-00214

Many synthetic models have been developed that utilize cation–π interactions in molecular recognition to study the nature of these interactions. One of the first systems that pointed to the potential utility of cation–π interactions are cyclophane receptors, which contain what would traditionally be described as aromatic, hydrophobic binding pockets.[15,16] These receptors were found to preferentially bind alkyl ammonium cations over neutral isosteric guests in aqueous solutions, despite the significantly larger desolvation cost of the cation.[17] Resorcinarene and calixarene based receptors have also been shown to bind various cations *via* cation–π interactions.[18–25] Some of these systems have been utilized in the binding and recognition of cationic amino acid residues.[26,27] Molecular tweezers, U-shaped receptors composed of aromatic rings, have been reported and shown to bind to cationic amino acids as well.[28,29] A variety of mercaptophanes (*i.e.* cyclophanes linked with disulfide bonds), discovered *via* dynamic combinatorial chemistry, have been developed to bind alkyl ammonium cations[30] including methylated derivatives of lysine and arginine residues.[31–35]

Synthetic small molecules capable of folding and unfolding have demonstrated the cation–π interaction between indole and an ammonium cation in water.[36] X-Ray analysis demonstrated the folding of the molecule placing an ammonium group near the indole ring, while replacement of the ammonium with a neutral *tert*-butyl group caused the molecule to adopt an unfolded confirmation (Figure 7.2). As these groups are sterically comparable, the observed difference can be ascribed to electrostatic differences, demonstrating the preference for the cationic group to interact with the indole ring.

This approach of comparing a nitrogen cation with a neutral isostere has proven to be particularly useful in determining the contribution of the electrostatic interaction to the net binding interaction in aqueous solution. Through multiple studies from host–guest interactions, protein–peptide, protein–inhibitor, and protein–nucleotide interactions, a value of about

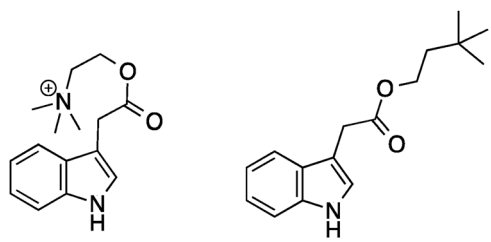

Figure 7.2 Indole linked to cationic ammonium group adopted a folded conformation, while the neutral analog remained unfolded.[36]

View Online

Published on 15 November 2016 on http://pubs.rsc.org | doi:10.1039/9781782626626-00214

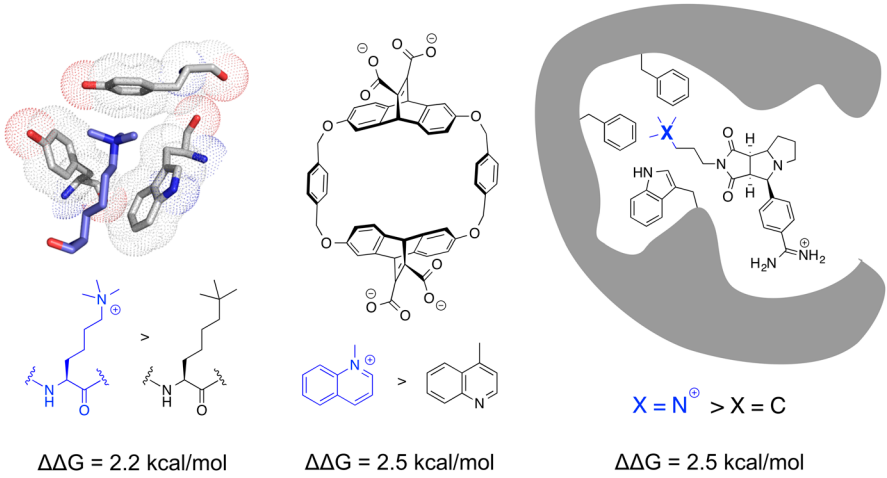

Figure 7.3 Neutral isosteres used to determine electrostatic contributions of cation–π interactions. Interactions between reader proteins and trimethyllysine (left), macrocycle and guest (center), and inhibitor of factor XA (right), are examples of systems studied with observed $\Delta\Delta G$ values around 2.5 kcal mol^{-1}. Adapted from ref. 16, 36–38.

2.5 kcal mol^{-1} has been measured for the contribution of the electrostatic component (Figure 7.3).[17,37–39]

Peptidic model systems relying on cation–π interactions have also been developed to study cation–π interactions.[40] Incorporation of aromatic and cationic residues into α-helices has been shown to increase stability. Specifically, the Arg–Trp pair in the *i*, *i* + 4 positions contributed −0.4 kcal mol^{-1}.[41] Sidechain interactions between Phe and either Lys or Arg were weaker, around −0.1 to −0.2 kcal mol^{-1}, but interaction with the shorter sidechain of diaminobutyric acid (Dab) increases the interaction energy to −0.4 kcal mol^{-1}, indicating that entropic costs influence the observed magnitude of the interaction.[42,43] Cross strand cation–π interactions between cationic and aromatic amino acids in β-hairpins have been used to measure these interactions and study their contribution to folding.[44–46] The contributions ranged from −0.2 to −0.5 kcal mol^{-1}, with the Arg–Trp pair again being the strongest.[46] Molecular dynamics studies have also demonstrated the cation–π stabilization of these β-hairpins.[47] Studies of the interaction of methylated Lys and Arg with Trp in these β-hairpins demonstrate that methylation increases the magnitude of the interaction, presumably by decreasing the desolvation cost and increasing the surface area for interaction.[48–50] Nonetheless, methylation of Lys resulted in distinctly different interactions with Trp than the isosteric carbon analog of trimethyl lysine (KMe3), which exhibited no preference for interaction with the face of Trp relative to other accessible amino acids in the β-hairpin. Recently, a 19 residue mini-protein was stabilized *via* a network of cation–π interactions, demonstrating the ability of cation–π interactions to influence protein structure.[51]

View Online

Published on 15 November 2016 on http://pubs.rsc.org | doi:10.1039/9781782626626-00214

7.2.1 Applications of Synthetic Systems that Mediate Cation–π Interactions

Recently, several groups have demonstrated the ability of synthetic systems that utilize cation–π interactions to influence or report on biomolecular recognition, as highlighted by a few key examples here. Hof has demonstrated that modified calixarenes can disrupt protein–protein interactions between KMe3 reader proteins and KMe3 in proteins *via* direct binding to KMe3.[52,53] The Hof group has also recently reported the use of calixarenes in affinity chromatography to enrich histone digests in peptides containing methylated Lys.[54] Nau also used calixarenes to develop an indicator displacement assay to monitor the activity of lysine methyltransferases. A dye, which is bound to the calixarene and quenched, is displaced by the methylated lysine product, resulting in a fluorescence response used to measure enzyme activity.[55] This work was also expanded to develop an indicator displacement assay for acetylcholine that functioned in cells.[56] Hof also used these indicator displacement assays with calixarenes to develop a sensor array to identify different methylation states of Lys and Arg.[57] Kool has recently reported a fluorogenic probe for demethylation of 1-methyladenine that incorporates a cation–π interaction between *N*-1-methyladenine and pyrene.[58] The 1-methyladenine quenches the pyrene fluorescence. Demethylation by ALKBH3, an enzyme that is a potential diagnostic marker for some types of cancer, results in turn-on fluorescence. These are just a few highlights of potential applications of synthetic systems that mediate cation–π interactions in biomolecular recognition.

7.3 Cation–π Interactions in Proteins

Cation–π interactions are prevalent in proteins, both in structure and their intermolecular interactions. Within proteins, positively charged lysine and arginine residues interact with the aromatic sidechains of phenylalanine, tyrosine, and tryptophan residues.[59] Analysis of proteins in the PDB shows an estimated one cation–π interaction present for every 77 amino acid residues.[1] To exclude other potential non-covalent interactions, geometry and spacing were important in classifying an interaction as cation–π. Interactions where the cation was positioned over the center of the aromatic ring, as well as a distance of less than 10 Å, were used for the initial search, however, most accepted interactions had a distance of less than 5 Å.[60] Based on these metrics, approximately 26% of tryptophan residues are involved in cation–π interactions, while the most common pair is arginine with tyrosine.[60] Cation–π interactions are also found to be important at the interface of various protein–protein interactions. About half of all complexes and one-third of homodimers were found to have a cation–π interaction.[61]

One of the most well studied examples of cation–π mediated protein–ligand interactions is the recognition of acetylcholine (ACh), a neurotransmitter containing a quaternary ammonium cation. A variety of biomolecules

View Online

Published on 15 November 2016 on http://pubs.rsc.org | doi:10.1039/9781782626626-00214

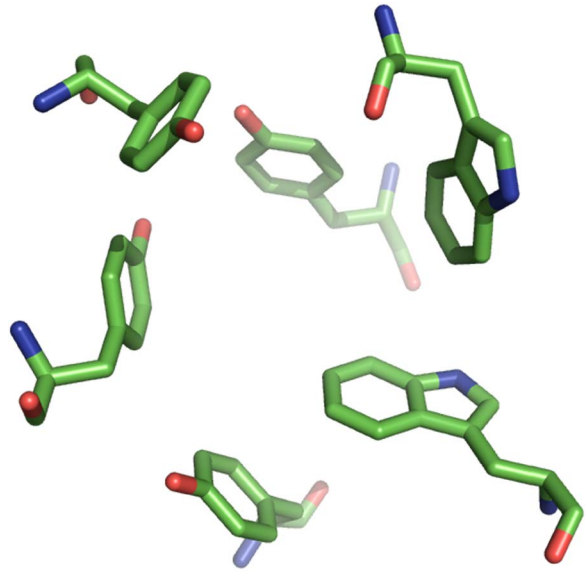

Figure 7.4 Aromatic residues in the binding region of an acetylcholine binding protein (PDB: 1I9B).[62]

have been shown to interact with ACh, including ACh esterases (AChE), receptors, and gated ion channels. Many of these targets contain binding regions where many aromatic residues are present (Figure 7.4)[62] and thought to participate in cation–π interactions with the ammonium group of ACh.[63]

The nicotinic acetylcholine receptor (nAChR) has been extensively studied, and its interactions with both acetylcholine and nicotine are well characterized.[8,62,64–67] While there are no crystal structures available of the membrane-bound protein, it is thought to adopt a structure similar to other AChE binding proteins (Figure 7.4).[62,65] By incorporating unnatural amino acid mutations in the binding pocket, the ability of the aromatic residues to participate in cation–π interactions could be tuned, and important cation–π interactions were revealed.[65] Amino acid derivatives containing various degrees of fluorine substitution around the aromatic ring were used to systematically tune the electronics of each residue. The effect of the mutation on ion channel function was then measured. Using this method, it was found that only one residue, a tryptophan, demonstrated a linear correlation between calculated cation–π energies and function of the ion channel. This relationship indicates this residue participates in a cation–π interaction that is important for function, and therefore binding, of the ACh ligand. This interaction is also seen with nicotine in the nicotinic acetylcholine receptors found in the brain. However, in muscle receptors, the cation–π interaction is absent and the affinity to nicotine is significantly lower. Without this weakened interaction, nicotine would stimulate the muscle receptors in addition

View Online

Published on 15 November 2016 on http://pubs.rsc.org | doi:10.1039/9781782626626-00214

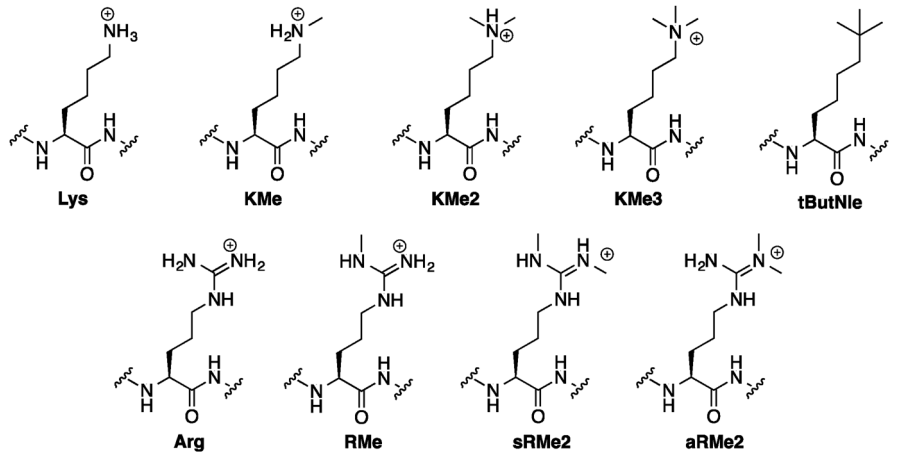

Figure 7.5 Various methylation states of lysine (top) and arginine (bottom) and neutral lysine analog (*t*ButNle). Dimethyllysine can be methylated symmetrically (sRMe2) or asymmetrically (aRMe2).

to those in the brain, leading to detrimental consequences. This study provides important mechanistic insight into the mechanism of nicotine addiction and the mechanism of selectivity between neuronal and muscle-type ACh receptors.

Other ligand gated ion channels that rely on cation–π interactions have been characterized as well.[68] GABA,[69] glycine,[70] and 5-HT_3 [71] receptors have all been shown to participate in cation–π interactions with neurotransmitters using similar methods. The characterization of these interactions have led to the development of antagonists of these receptors and allowed for further biochemical studies of these receptors.[72–74]

Another class of proteins that utilizes cation–π interactions is the "reader" proteins for methylated lysine and arginine.[75] Both residues can be methylated posttranslationally to various degrees and are important modifications in the epigenetic control of gene expression (Figure 7.5).[76,77] Reader proteins recognize these modifications with a high selectivity for both the modification and surrounding sequence, leading to gene expression, gene silencing, or regulation of other epigenetically important modifications, depending on the location of the modification and the reader protein that is recruited. Domains involved in recognition of these modifications include the tudor, chromo, MBT, and PWWP domains and are known as the "royal family". Cation–π interactions with aromatic cages of these proteins are thought to be an important mode of recognition for many of these proteins.

At neutral pH, both unmethylated lysine and arginine are positively charged, but the cation is very well solvated. As the methylation state increases, the cation–π interaction becomes more energetically favorable. While the charge of the ammonium does not change upon methylation, the desolvation cost of the cation decreases, leading to this effect. Upon increasing methylation,

View Online

Published on 15 November 2016 on http://pubs.rsc.org | doi:10.1039/9781782626626-00214

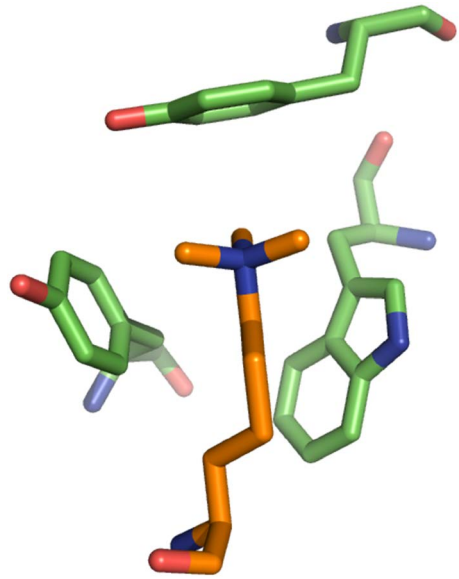

Figure 7.6 Aromatic binding pocket of HP1 (green) bound to trimethyllysine (orange) (PDB: 1KNE).[78,79]

the cation becomes less solvated, and participating in a cation–π interaction becomes more energetically favorable.[48]

The contribution of cation–π interactions to this class of proteins was first studied in the chromodomain of heterochromatin 1 (HP1). Its X-ray structure exhibits an aromatic cage consisting of two tyrosine residues and a tryptophan residue surrounding the trimethylammonium cation of trimethyllysine (Figure 7.6).[78,79] Mutation of these residues to an alanine leads to a significant loss in binding affinity.[80] Further, binding of HP1 to a *tert*-butyl norleucine, a neutral isostere of trimethyllysine (Figure 7.5), is 30-fold weaker, demonstrating the importance of the cation in the binding interaction, as opposed to a purely hydrophobic interaction.[81] Similar studies used the same neutral analog in other histone sequences and measured binding to various reader proteins both experimentally and computationally. Again, a significant reduction in binding affinity to the neutral analog demonstrated the necessity of the cation, and the presence of a cation–π interaction.[82]

Crystal structures of several tudor domains show binding of the methylated guanidinium of arginine in an aromatic box (Figure 7.7),[83] involving stacking of the guanidinium moiety between two aromatic rings as well as CH–π interactions between the methyl groups and aromatic residues on the sides of the box. A hydrogen bond between an NH on the Arg sidechain and an Asn or Asp sidechain usually completes the box. Interestingly, while Arg–π interactions have been shown to be stronger than Lys–π interactions in model systems, the binding of methylated Arg in these reader proteins is quite weak, with reported binding affinities from 5–200 μM.[83–85] These interactions are often

View Online

Published on 15 November 2016 on http://pubs.rsc.org | doi:10.1039/9781782626626-00214

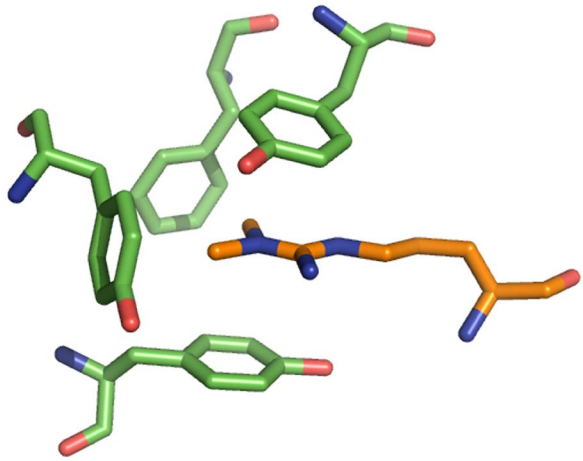

Figure 7.7 Binding of asymmetric dimethyl arginine (orange) by an aromatic box of TDRD3 (green) (PDB: 2LTO).[83]

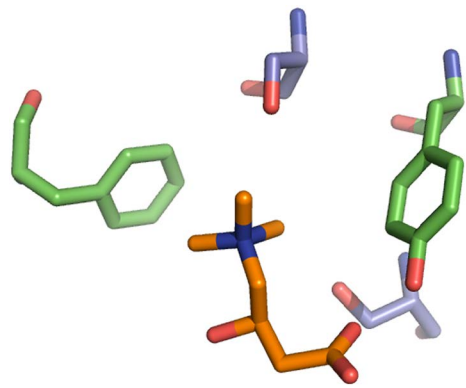

Figure 7.8 Structure of a composite box of an acetyltransferase with aromatic residues (green) and polar residues (blue) (PDB: 1S5O).[88]

important in the regulation of RNA metabolism, while methyllysine reader proteins are often associated with chromatin regulation.[86]

Enzymes have also been shown to utilize cation–π interactions in the recognition of their substrates. Many of these enzymes contain an aromatic box capable of binding a quaternary ammonium ion.[87] Enzymes involved in acetylcholine and phosphocholine reactions and biosynthesis often have aromatic binding regions that recognize the choline moiety. Unlike receptor aromatic boxes, which often contain three or four aromatic rings interacting with a quaternary ammonium, these enzymes have composite aromatic boxes containing only one or two aromatic rings in addition to polar or charged residues (Figure 7.8).[88] It has been proposed that the decreased desolvation

View Online

Published on 15 November 2016 on http://pubs.rsc.org | doi:10.1039/9781782626626-00214

required for binding in a less hydrophobic pocket aids in faster dissociation times needed for efficient catalysis by enzymes.[89]

Mutation studies of the aromatic residues of acetylcholinesterase (AChE) were used to study a potential cation–π interaction between a tryptophan residue of the enzyme active site and the choline group in order to orient the acetylcholine. Mutation of tryptophan 86 to alanine resulted in a 660-fold decrease in binding affinity to acetylcholine, but showed no effect on the affinity of the enzyme to a neutral, *tert*-butyl analog of the neurotransmitter.[90] Further, binding of mutant AChE enzymes where the tryptophan was replaced with tyrosine, phenylalanine, and alanine to transition state analog inhibitors was measured, and a linear free energy relationship was observed.[91] Additionally, computational methods have been developed to identify and quantify cation–π interactions of the active site of an acetylcholinesterase with *ortho*-7, a drug designed to reactivate an enzyme inhibited by organophosphorus.[92,93] Organophosphorus compounds, used in both pesticides and nerve agents in chemical warfare, inhibit the enzyme by phosphorylating the serine residue in the catalytic active site of AChE. This leads to the build-up of acetylcholine and continuous stimulation throughout the nervous system, which ultimately can be fatal.[93]

An inhibitor of an arginine methyltransferase (PRMT5) takes advantage of a cation–π interaction with *S*-adenosylmethionine (SAM) in the enzyme active site (Figure 7.9). SAM, the cofactor that acts as the methyl donor, contains a sulfonium ion positioned near the aromatic face of a phenyl ring in the active inhibitor. Binding constants between the enzyme and inhibitor were measured in the presence of SAM and SAH (lacking the methyl group, and therefore neutral). The K_d's were found to be <1 nM and 171 nM respectively, indicating a significant drop in affinity upon loss of the ability of the inhibitor to participate in a cation–π interaction with SAM. The interaction was estimated to contribute at least 3 kcal mol^{-1}.[94]

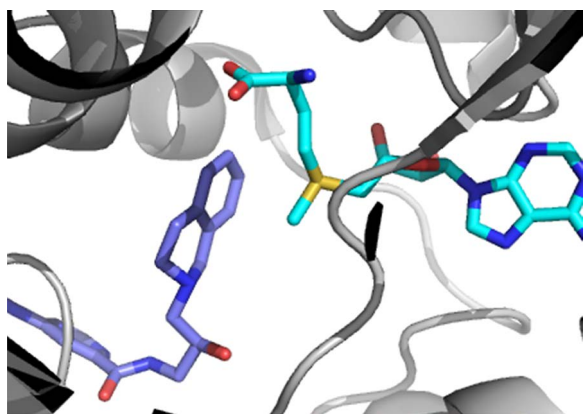

Figure 7.9 PRMT5 with SAM (cyan) and inhibitor (blue) bound in the active site and participating in a cation–π interaction (PDB: 4X61).[94]

View Online

Published on 15 November 2016 on http://pubs.rsc.org | doi:10.1039/9781782626626-00214

Serine hydroxymethyltransferase (SHMT), an enzyme that catalyzes the interconversion between serine and glycine, contains an important cation–π interaction in its active site. In this enzyme, arginine 235 and tyrosine 55 form a cation–π interaction that is highly conserved among SHMT homologs (Figure 7.10).[95] The tyrosine hydroxyl group functions as a proton donor in general base catalysis. The participation in a cation–π interaction with arginine is proposed to increase the acidity of this proton, and aid in the positioning of this side chain.[96]

Factor XA, a serine protease involved in blood coagulation, contains three aromatic residues, Trp, Tyr, and Phe, proposed to be involved in cation–π interactions with inhibitors.[97] Binding to an inhibitor containing a trimethyl ammonium was measured and compared to the same inhibitor containing the neutral *tert*-butyl group in place of the ammonium. The cation–π interaction was determined to contribute 2.8 kcal mol^{-1} to binding,[98] which is similar in magnitude to that of KMe3 with the HP1 chromodomain as determined by the same method of replacing the trimethylammonium with a *tert*-butyl group.[81]

Enzymes catalyzing reactions that possess a carbocation intermediate also rely on aromatic residues for stabilization *via* a cation–π interaction. Many enzymes of this type are those involved in the synthesis of terpenes. Squalene-hopene cyclase contains an active site with several aromatic amino acids. Upon mutation of the aromatic residues to alanine, it was proposed that phenylalanines 365 and 605 were both involved in a carbocation stabilizing cation–π interaction. To probe the cation–π interaction, unnatural amino acids were incorporated in place of these phenylalanine residues. When fluorinated phenylalanine residues were incorporated, the enzyme showed decreased activity and formed products that had been prematurely cyclized. The activity of the enzyme inversely correlated with the number of fluorine atoms on the aromatic ring, indicating the importance of the cation–π

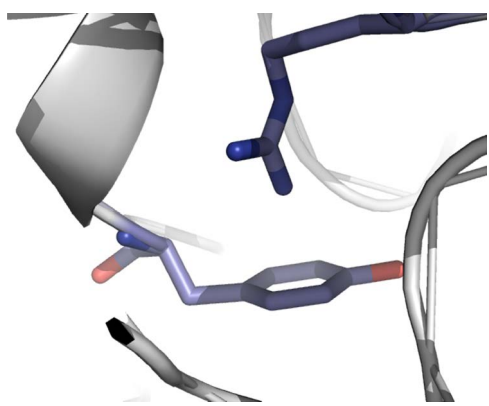

Figure 7.10 Conserved cation–π interaction between Arg 235 and Tyr 55 in SHMT (PDB: 1DFO).[95,96]

View Online

Published on 15 November 2016 on http://pubs.rsc.org | doi:10.1039/9781782626626-00214

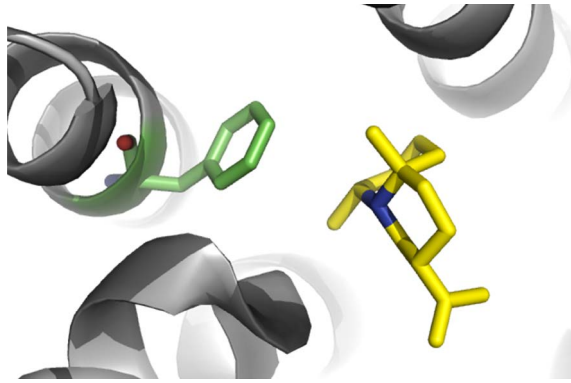

Figure 7.11 Cation–π interaction between a Phe of aristolochene synthase (green) and ammonium transition state analog (yellow) (PDB: 4KVW).[102]

interaction in the stabilization of carbocation intermediates.[99] This method was further used to demonstrate cation–π interactions in the active site of oxidosqualene cyclases.[100]

Similarly, tryptophan 334 of aristolochene synthase was replaced with various *para*-substituted phenylalanine derivatives (Cl, CF_3, and NO_2) to probe a potential cation–π interaction, which led to a substantial decrease in k_{cat} and decrease in overall product formation.[101] A crystal structure of the enzyme with transition state mimics containing ammonium cations in place of the carbocations along the cascade supports the proposed mechanism of cation–π stabilization (Figure 7.11).[102]

In addition to these major classes of proteins that rely heavily on cation–π interactions, there are countless examples of other proteins in the literature with proposed cation–π interactions. For example, photoreceptor UVR8 is proposed to contain several intermolecular cation–π interactions. These interactions are thought to be destabilized upon absorption of UV-B light, leading to dissociation of the homodimer.[103] Several antibodies are also thought to participate in cation–π interactions in binding to their protein antigens.[2] The detailed mechanistic study of these interactions in proteins has led to a better understanding of the role of cation–π interactions in the mechanism of binding and catalysis.

7.4 Cation–π Interactions in Nucleic Acids

Nucleic acids have been shown to participate in cation–π interactions in various ways. As nucleic acids contain aromatic rings, they have the potential to form cation–π interactions with metal or ammonium cations, while positively charged nucleobases often interact with aromatic side chains of protein binding partners.

The recognition of alkylated RNA bases is important for a variety of biological processes, and cation–π interactions have been implicated in their

View Online

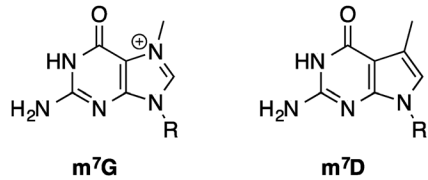

Figure 7.12 Methylated bases for 7-methyl G (m^7G) and neutral analog 7-methyl D (m^7D).

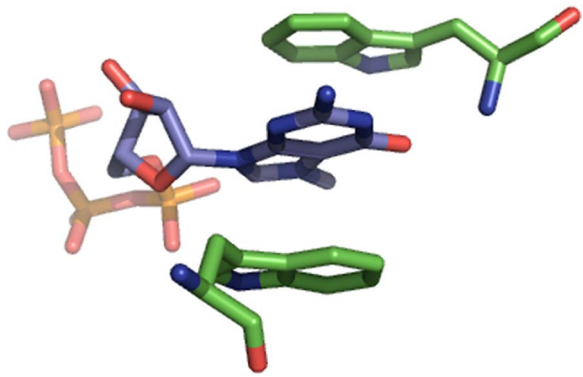

Figure 7.13 Tryptophan residues (green) of eIF4E participation in a cation–π stack with 7-methyl GTP (blue) (PDB: 1IPC).[106]

recognition. Eukaryotic mRNA contains a 5′ cap and a polyA tail that are involved in transcription regulation. This 5′ cap consists of a guanine methylated at the nitrogen at position 7 (Figure 7.12). Proteins with different functions recognize this cap.[104]

Eukaryotic initiation factor 4E (eIF4E) binds to the 5′ cap of mRNA, triggering translation. Crystal structures of eIF4E bound to 7-methyl GDP show that the alkylated base is bound between two highly conserved tryptophan residues in a stacked arrangement (Figure 7.13).[104–106] The positive charge on the methylated GDP is thought to provide an increased affinity of this interaction over simple π–π stacking. Mutation of either tryptophan to a leucine completely eliminates binding, while mutation to phenylalanine decreases binding by 50%. The methyl group on N7 makes van der Waals contact with a third tryptophan residue. Thermodynamic studies of the interaction with this protein and 7-methyl GMP measured large negative values for ΔH° and ΔS°, resulting from the Coulombic character of the cation–π stacking interaction.[107] Computational studies were used to calculate binding affinities of 7-methyl DTP, which cannot participate in cation–π interactions with the tryptophan residues (Figure 7.12). The lack of the cation was calculated to result in a reduction in binding affinity of 2.82 kcal mol^{-1}.[108]

Similarly, virus protein VP39 interacts with the 5′ cap and has been shown to be selective for a positive charge.[109] VP39 is responsible for methylation of the

Published on 15 November 2016 on http://pubs.rsc.org | doi:10.1039/9781782626626-00214

View Online

Published on 15 November 2016 on http://pubs.rsc.org | doi:10.1039/9781782626626-00214

2′-hydroxyl group of the first base, and fails to perform this modification in the absence of the N7 methylation on guanine. Crystal structures of this protein again reveal the methylated base sandwiched between two aromatic residues, in this case tyrosine and phenylalanine. The importance of this "cation–π sandwich" is demonstrated by the dependence on pH. At basic pH levels, the 7-methyl guanine does not contain a positive charge, and binding to VP39 is greatly reduced.[109] This cation–π stacking interaction has subsequently been observed in a variety of other proteins that recognize 7-methyl G.[110]

While nucleic acids frequently interact with metal cations, they are generally bound in the same plane as the base, while the bases are stacked on top of each other, rather than in a cation–π geometry.[111] However, there are some examples where cation–π interactions between metal cations and the aromatic rings of the bases have been suggested.

As nucleic acid bases are often involved in π–π stacking, it has been proposed that cation–π binding to metal cations leads to stabilization of unstacked conformations.[112] Analysis of crystal structures in the nucleic acids database (NDB) shows several examples of potential cation–π interactions between bases and metal cations or cation hydrates. Binding of magnesium hydrates to the major groove of DNA appears to cause cytosine bases to shift from their stacked conformation, making the π system available for cation–π interactions with the magnesium. Additionally, RNA bases in a yeast tRNA appear to be stabilized by several magnesium cations, as was the RNA core of a ribozyme. Crystals grown with Tl^+, a K^+ mimic, showed the ability of Tl^+ cations to bind in cation–π geometries to cytosine bases (Figure 7.14).[113] Among divalent cations, while magnesium was more commonly observed in cation–π geometries, calcium cations were also observed.[114] It was observed that cation–π interactions in the major groove occurred most frequently with cytosine bases, while minor groove cation–π interactions involved mostly purine bases.

In addition to binding metal cations, nucleic acid bases have been observed between positively charged amino acid side chains in protein-DNA and protein-RNA crystal structures. In crystal structures with DNA, cation–π interactions involving arginine occurred 3–4 times more often than other

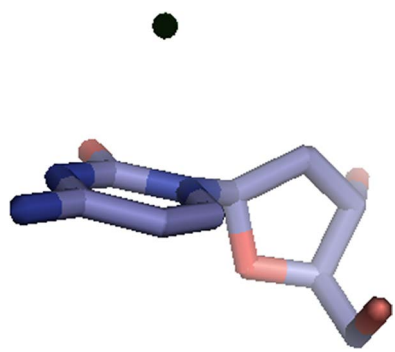

Figure 7.14 Tl^+ cation positioned above a cytosine base (PDB: 1JGR).[113]

View Online

Published on 15 November 2016 on http://pubs.rsc.org | doi:10.1039/9781782626626-00214

charged or partially charged residues, while guanine was the most frequent DNA base involved in cation–π interactions.[115] This Arg–G interaction can be seen in the crystal structure telomere end binding protein, TEBP, which binds and protects telomeric DNA, contributing to chromosome stability (Figure 7.15).[116]

Similar trends were observed in protein–RNA complexes, with calculations suggesting the arginine–guanine cation–π interaction is the strongest of the possible pairs.[117] Crystal structures of muscleblind-like protein (MBNL1) complexed with RNA also demonstrate the Arg–G cation–π interaction (Figure 7.16).[117,118]

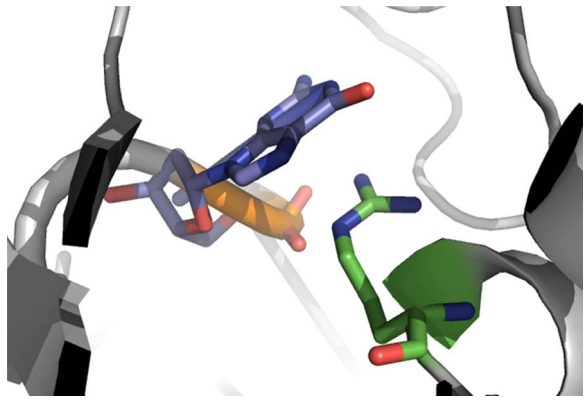

Figure 7.15 Crystal structure of Arg of TEBP (green) engaged in a cation–π interaction with guanine (blue) of a DNA strand.[116]

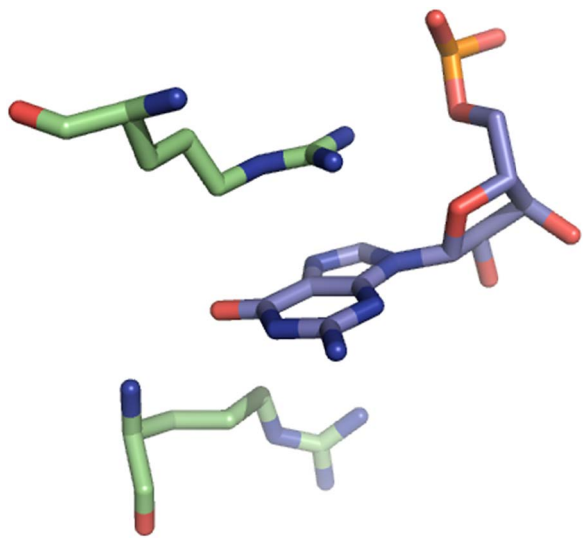

Figure 7.16 Arg residues of MBNL1 (green) participating in cation–π interactions with the G base of an RNA strand (blue) (PDB: 3D2S).[117,118]

View Online

Published on 15 November 2016 on http://pubs.rsc.org | doi:10.1039/9781782626626-00214

7.5 Cation–π Interactions in Lipids

Lipids containing positively charged groups have also been the focus of cation–π studies. A class of lipids, phosphatidylcholines, contains a quaternary ammonium group in addition to the phosphate, forming a zwitterionic head group (Figure 7.17). Phosphatidylcholines (PC) make up a large portion of membranes, and their ammonium provides a cationic handle that can be recognized by cation–π interactions.[119] Proteins that transport these phospholipids between membranes, phosphatidylcholine transfer proteins (PC-TP) crystallized with a PC, reveal a cation–π interaction in a three aromatic residue cage (Figure 7.18).

Additionally, the presence of these lipids in membranes is also important in stabilizing and anchoring other membrane binding proteins. Evidence for cation–π interactions often comes from crystal structure analysis. However, with membrane-bound proteins, these structures in the presence of the lipid bilayer are not readily available, making the study of these interactions somewhat more challenging.

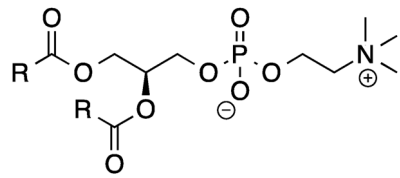

Figure 7.17 General structure of phosphatidylcholines.

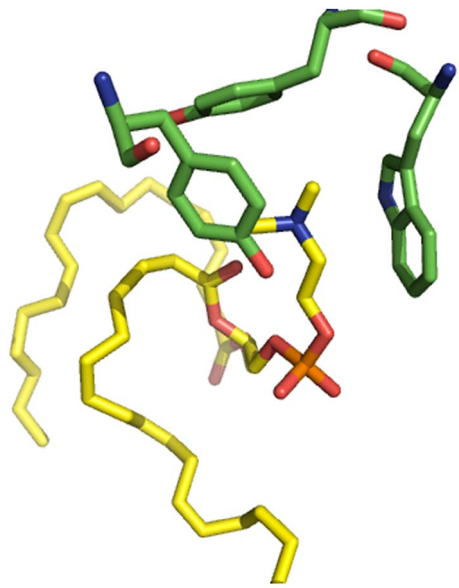

Figure 7.18 PC-TP aromatic residues (green) bound to PC (yellow)[119] (PDB: 1LN1).[119]

View Online

Published on 15 November 2016 on http://pubs.rsc.org | doi:10.1039/9781782626626-00214

Tryptophan residues are often found in membrane-bound proteins, and have been proposed to exhibit cation–π interactions with positively charged ammonium on phosphocholine.[120] To further probe this interaction, linear free energy relationships have been performed between various tryptophan derivatives using a model phosphatidylcholine.[121] Electron withdrawing groups were incorporated at the 5-position on the indole ring of tryptophan. Binding was measured *via* NMR titration by adding the phosphatidylcholine into a solution of the tryptophan derivative and measuring proton shift changes. Instead of exhibiting a linear free energy relationship, an inverted U-shaped relationship was observed, indicating a change in mechanism. It was suggested that cation–π interactions dominated for electron rich indoles, while hydrogen bonding interactions between the indole NH and the lipid carbonyl dominated for electron poor indoles, and both likely play a role in the binding of unsubstituted tryptophan to phosphatidylcholines.

A similar approach was taken to probe the cation–π interactions involved in a phospholipase C that binds poorly to anionic phospholipid membranes, but interacts more strongly with membranes containing phosphatidylcholines. Incorporation of pentafluorophenylalanine and difluoro tyrosine derivatives should increase the hydrophobic interactions while decreasing the cation–π interactions, providing a good probe for the nature of this binding.[122] Several tyrosine residues demonstrated decreased interaction with phosphocholine membranes upon incorporation of fluorinated amino acids, indicating their participation in cation–π interactions, rather than a purely hydrophobic interaction (Figure 7.19).[123] MD simulations and

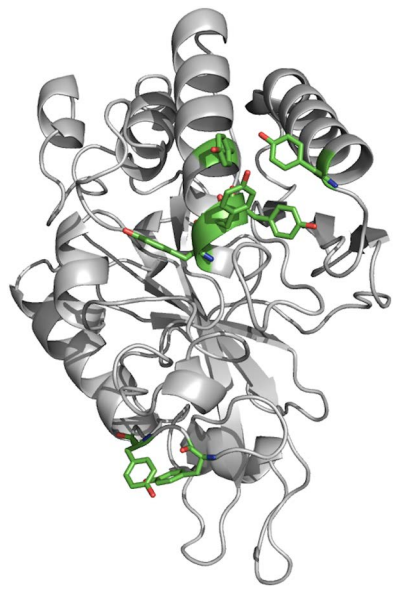

Figure 7.19 Homology model of phospholipase C with tyrosine residues in green (PDB: 1PTG).[122,123]

View Online

Published on 15 November 2016 on http://pubs.rsc.org | doi:10.1039/9781782626626-00214

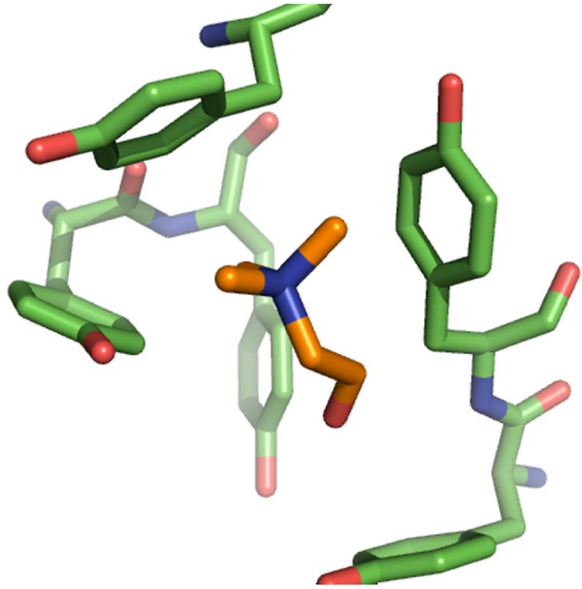

Figure 7.20 Engineered aromatic box (green) bound to choline (orange) (PDB: 4I9O).[125,126]

mutation studies of tyrosine residues in a phospholipase C suggest that cation–π interactions with PC lipids in the membrane are worth as much as 3 kcal mol^{-1}.[124]

In another study, phosphatidylinositol-specific phospholipase C (PI-PLC), a non-PC binding phospholipase C, was engineered to include an aromatic box motif. This engineered protein selectively recognized vesicles containing enriched levels of PC.[125] Crystal structure analysis with PC demonstrated the choline group binding into the engineered aromatic box (Figure 7.20).[126]

Interestingly, an intermolecular cation–π interaction in *Staphylococcus aureus* PI-PLC is proposed to mediate the activity at different pH levels.[127] The enzyme is more active than most enzymes at higher pH values. Crystal structures at basic pHs reveal a similar conformation to other PI-PLC proteins, while at acidic pHs, there is a shift in a loop containing a histidine residue in its protonated state, allowing it to make a cation–π interaction with a phenylalanine residue. A mutant containing a phenylalanine in place of the histidine did not show the same pH dependent shift.

Cation–π interactions have also been proposed to be important in regulating the function of transport proteins.[128] These proteins often rely on conformation flexibility to allow for the passage of substrate through the membrane. One such transport protein for glutamate, Glt_{Ph}, is less active in lipid bilayers containing phosphatidylcholines embedded in the bilayer. Replacement of one tyrosine residue with a serine shows a marked increase in transport rates in the presence of phosphocholine bilayers. A proposed cation–π interaction

View Online

between this tyrosine and the cationic head groups is thought to restrict the conformational flexibility of the protein and decrease transport. Alternatively, cation–π interactions with the lipid bilayer were found to stabilize the active conformation of lyposomal sodium ion channels, where increasing amounts of aromatic residues in side arms aided in higher levels of ion transport.[129]

Published on 15 November 2016 on http://pubs.rsc.org | doi:10.1039/9781782626626-00214

7.6 Conclusions

Since the earliest proposals that cation–π interactions are relevant in biology, these interactions have proven not only to be ubiquitous, but also to have a unique combination of properties that make them both significant and selective in aqueous solution. It is clear that cation–π interactions can no longer be considered a rare occurrence or special case in biomolecular recognition, but are part of the standard biomolecular recognition toolbox that must be considered in biomolecular structure and function as well as inhibitor and probe development.

References

1. D. A. Dougherty, *Acc. Chem. Res.*, 2013, **46**, 885–893.
2. A. S. Mahadevi and G. N. Sastry, *Chem. Rev.*, 2012, **113**, 2100–2138.
3. S. E. Wheeler and J. W. G. Bloom, *J. Phys. Chem. A*, 2014, **118**, 6133–6147.
4. J. Sunner, K. Nishizawa and P. Kebarle, *J. Phys. Chem.*, 1981, **85**, 1814–1820.
5. M. Meot-Ner and C. A. Deakyne, *J. Am. Chem. Soc.*, 1985, **107**, 474–479.
6. R. W. Taft, F. Anvia, J.-F. Gal, S. Walsh, M. Capon, M. C. Holmes, K. Hosn, G. Oloumi, R. Vasanwala and S. Yazdani, *Pure Appl. Chem.*, 1990, **62**, 17–23.
7. B. C. Guo, J. W. Purnell and A. W. Castleman, *Chem. Phys. Lett.*, 1990, **168**, 155–160.
8. R. A. Kumpf and D. A. Dougherty, *Science*, 1993, **261**, 1708–1710.
9. S. Mecozzi, A. P. West and D. A. Dougherty, *J. Am. Chem. Soc.*, 1996, **118**, 2307–2308.
10. S. Mecozzi, A. P. West and D. A. Dougherty, *Proc. Natl. Acad. Sci. U. S. A.*, 1996, **93**, 10566–10571.
11. J. C. Ma and D. A. Dougherty, *Chem. Rev.*, 1997, **97**, 1303–1324.
12. C. D. Sherrill, *Acc. Chem. Res.*, 2013, **46**, 1020–1028.
13. S. E. Wheeler and K. N. Houk, *J. Am. Chem. Soc.*, 2009, **131**, 3126–3127.
14. S. E. Wheeler, *Acc. Chem. Res.*, 2012, **46**, 1029–1038.
15. T. J. Shepodd, M. A. Petti and D. A. Dougherty, *J. Am. Chem. Soc.*, 1986, **108**, 6085–6087.
16. F. Diederich and K. Dick, *J. Am. Chem. Soc.*, 1984, **106**, 8024–8036.
17. M. A. Petti, T. J. Shepodd, R. E. J. Barrans and D. A. Dougherty, *J. Am. Chem. Soc.*, 1988, **110**, 6825–6840.
18. K. Murayama and K. Aoki, *Chem. Commun.*, 1997, 119–120.

View Online

Published on 15 November 2016 on http://pubs.rsc.org | doi:10.1039/9781782626626-00214

19. K. Murayama and K. Aoki, *Chem. Commun.*, 1998, 607–608.
20. A. Shivanyuk and J. Rebek, *Proc. Natl. Acad. Sci. U. S. A.*, 2001, **98**, 7662–7665.
21. K. N. Koh, K. Araki, A. Ikeda, H. Otsuka and S. Shinkai, *J. Am. Chem. Soc.*, 1996, **118**, 755–758.
22. P. Lhoták and S. Shinkai, *J. Phys. Org. Chem.*, 1997, **10**, 273–285.
23. K. D. Daze, T. Pinter, C. S. Beshara, A. Ibraheem, S. A. Minaker, M. C. F. Ma, R. J. M. Courtemanche, R. E. Campbell and F. Hof, *Chem. Sci.*, 2012, **3**, 2695.
24. F. Hof, L. Trembleau, E. C. Ullrich and J. Rebek, *Angew. Chem., Int. Ed.*, 2003, **42**, 3150–3153.
25. M. A. Gamal-Eldin and D. H. Macartney, *Org. Biomol. Chem.*, 2013, **11**, 488–495.
26. R. E. McGovern, B. D. Snarr, J. A. Lyons, J. McFarlane, A. L. Whiting, I. Paci, F. Hof and P. B. Crowley, *Chem. Sci.*, 2015, **6**, 442–449.
27. K. D. Daze and F. Hof, *Acc. Chem. Res.*, 2013, **46**, 937–945.
28. M. Fokkens, T. Schrader and F. G. Klärner, *J. Am. Chem. Soc.*, 2005, **127**, 14415–14421.
29. M. Hardouin-Lerouge, P. Hudhomme and M. Sallé, *Chem. Soc. Rev.*, 2011, **40**, 30–43.
30. P. T. Corbett, J. Leclaire, L. Vial, K. R. West, J.-L. Wietor, J. K. M. Sanders and S. Otto, *Chem. Sci.*, 2006, **106**, 3652–3711.
31. M. R. Gagné, S. Ghosh, L. A. Ingerman, A. G. Frye, S. J. Lee and M. L. Waters, *Org. Lett.*, 2010, **12**, 1860–1863.
32. N. K. Pinkin and M. L. Waters, *Org. Biomol. Chem.*, 2014, 7059–7067.
33. J. E. Beaver, B. C. Peacor, J. V. Bain, L. I. James and M. L. Waters, *Org. Biomol. Chem.*, 2015, **13**, 3220–3226.
34. L. I. James, J. E. Beaver, N. W. Rice and M. L. Waters, *J. Am. Chem. Soc.*, 2013, **135**, 6450–6455.
35. J. E. Beaver and M. L. Waters, *ACS Chem. Biol.*, 2016, **11**, 643–653.
36. K. Aoki, K. Murayama and H. Nishiyama, *J. Chem. Soc., Chem. Commun.*, 1995, **764**, 2221.
37. R. M. Hughes, K. R. Wiggins, S. Khorasanizadeh and M. L. Waters, *Proc. Natl. Acad. Sci. U. S. A.*, 2007, **104**, 11184–11188.
38. T. J. Shepodd, M. A. Petti and D. A. Dougherty, *J. Am. Chem. Soc.*, 1988, **110**, 1983–1985.
39. L. M. Salonen, C. Bucher, D. W. Banner, W. Haap, J. L. Mary, J. Benz, O. Kuster, P. Seiler, W. B. Schweizer and F. Diederich, *Angew. Chem., Int. Ed.*, 2009, **48**, 811–814.
40. M. L. Waters, *Biopolymers*, 2004, **76**, 435–445.
41. Z. Shi, C. A. Olson and N. R. Kallenbach, *J. Am. Chem. Soc.*, 2002, **124**, 3284–3291.
42. C. D. Andrew, S. Bhattacharjee, N. Kokkoni, J. D. Hirst, G. R. Jones and A. J. Doig, *J. Am. Chem. Soc.*, 2002, **124**, 12706–12714.
43. L. K. Tsou, C. D. Tatko and M. L. Waters, *J. Am. Chem. Soc.*, 2002, **124**, 14917–14921.

View Online

Published on 15 November 2016 on http://pubs.rsc.org | doi:10.1039/9781782626626-00214

44. R. M. Hughes and M. L. Waters, *J. Am. Chem. Soc.*, 2006, **128**, 13586–13591.
45. N. H. Andersen, K. A. Olsen, R. M. Fesinmeyer, X. Tan, F. M. Hudson, L. A. Eidenschink and S. R. Farazi, *J. Am. Chem. Soc.*, 2006, **128**, 6101–6110.
46. C. D. Tatko and M. L. Waters, *Protein Sci.*, 2003, **12**, 2443–2452.
47. X. Zheng, C. Wu, J. W. Ponder and G. R. Marshall, *J. Am. Chem. Soc.*, 2012, **134**, 15970–15978.
48. R. M. Hughes and M. L. Waters, *J. Am. Chem. Soc.*, 2005, **127**, 6518–6519.
49. R. M. Hughes and M. L. Waters, *J. Am. Chem. Soc.*, 2006, **128**, 12735–12742.
50. R. M. Hughes, M. L. Benshoff and M. L. Waters, *Chem.–Eur. J.*, 2007, **13**, 5753–5764.
51. T. W. Craven, M.-K. Cho, N. J. Traaseth, R. Bonneau and K. Kirshenbaum, *J. Am. Chem. Soc.*, 2016, **138**, 1543–1550.
52. H. F. Allen, K. D. Daze, T. Shimbo, A. Lai, C. A. Musselman, J. K. Sims, P. A. Wade, F. Hof and T. G. Kutateladze, *Biochem. J.*, 2014, **459**, 505–512.
53. S. Tabet, S. F. Douglas, K. D. Daze, G. A. E. Garnett, K. J. H. Allen, E. M. M. Abrioux, T. T. H. Quon, J. E. Wulff and F. Hof, *Bioorg. Med. Chem.*, 2013, **21**, 7004–7010.
54. G. A. E. Garnett, M. J. Starke, A. Shaurya, J. Li and F. Hof, *Anal. Chem.*, 2016, **88**, 3697–3703.
55. M. Florea, S. Kudithipudi, A. Rei, M. J. González-Úlvarez, A. Jeltsch and W. M. Nau, *Chem.–Eur. J.*, 2012, **18**, 3521–3528.
56. A. Norouzy, Z. Azizi and W. M. Nau, *Angew. Chem., Int. Ed.*, 2015, **54**, 792–795.
57. S. A. Minaker, K. D. Daze, M. C. F. Ma and F. Hof, *J. Am. Chem. Soc.*, 2012, **134**, 11674–11680.
58. A. A. Beharry, S. Lacoste, T. R. O'Connor and E. T. Kool, *J. Am. Chem. Soc.*, 2016, **138**, 3647–3650.
59. S. K. Burley and G. A. Petsko, *FEBS Lett.*, 1986, **203**, 139–143.
60. J. P. Gallivan and D. A. Dougherty, *Proc. Natl. Acad. Sci. U. S. A.*, 1999, **96**, 9459–9464.
61. P. B. Crowley and A. Golovin, *Proteins: Struct., Funct., Bioinf.*, 2005, **59**, 231–239.
62. K. Brejc, W. J. van Dijk, R. V. Klaassen, M. Schuurmans, J. van Der Oost, A. B. Smit and T. K. Sixma, *Nature*, 2001, **411**, 269–276.
63. D. A. Dougherty and D. A. Stauffer, *Science*, 1990, **250**, 1558–1560.
64. P. C. Kearney, M. W. Nowak, W. Zhong, S. K. Silverman, H. A. Lester and D. A. Dougherty, *Mol. Pharmacol.*, 1996, **50**, 1401–1412.
65. X. Xiu, N. L. Puskar, J. A. P. Shanata, H. A. Lester and D. A. Dougherty, *Nature*, 2009, **458**, 534–537.
66. W. Zhong, J. P. Gallivan, Y. Zhang, L. Li, H. A. Lester and D. A. Dougherty, *Proc. Natl. Acad. Sci. U. S. A.*, 1998, **95**, 12088–12093.
67. M. W. Nowak, P. C. Kearney, J. R. Sampson, M. E. Saks, C. G. Labarca, S. K. Silverman, W. Zhong, J. Thorson, J. N. Abelson and N. Davidson, *Science*, 1995, **268**, 439–442.
68. C. L. Padgett, A. P. Hanek, H. A. Lester, D. A. Dougherty and S. C. R. Lummis, *J. Neurosci.*, 2007, **27**, 886–892.

View Online

Published on 15 November 2016 on http://pubs.rsc.org | doi:10.1039/9781782626626-00214

69. S. C. R. Lummis, N. J. Harrison, J. Wang, J. A. Ashby, K. S. Millen, D. L. Beene and D. A. Dougherty, *ACS Chem. Neurosci.*, 2012, **3**, 186–192.
70. S. A. Pless, K. S. Millen, A. P. Hanek, J. W. Lynch, H. A. Lester, S. C. R. Lummis and D. A. Dougherty, *J. Neurosci.*, 2009, **28**, 10937–10942.
71. N. H. Duffy, H. A. Lester and D. A. Dougherty, *ACS Chem. Biol.*, 2012, **7**, 1738–1745.
72. M. Mortensen, F. Iqbal, A. P. Pandurangan, S. Hannan, R. Huckvale, M. Topf, J. R. Baker and T. G. Smart, *Nat. Commun.*, 2014, **5**, 4454.
73. E. B. Van Arnam and D. A. Dougherty, *J. Med. Chem.*, 2014, **57**, 6289–6300.
74. G. Maksay, Z. Bikádi and M. Simonyi, *J. Recept. Signal Transduction Res.*, 2003, **23**, 255–270.
75. S. D. Taverna, H. Li, A. J. Ruthenburg, C. D. Allis and D. J. Patel, *Nat. Struct. Mol. Biol.*, 2007, **14**, 1025–1040.
76. J. Nakayama, J. C. Rice, B. D. Strahl, C. D. Allis and S. I. Grewal, *Science*, 2001, **292**, 110–113.
77. A. J. Ruthenburg, C. D. Allis and J. Wysocka, *Mol. Cell*, 2007, **25**, 15–30.
78. S. A. Jacobs and S. Khorasanizadeh, *Science.*, 2002, **295**, 2080–2083.
79. P. R. Nielsen, D. Nietlispach, H. R. Mott, J. Callaghan, A. Bannister, T. Kouzarides, A. G. Murzin, N. V Murzina and E. D. Laue, *Nature*, 2002, **416**, 103–107.
80. S. A. Jacobs and S. Khorasanizadeh, *Science*, 2002, **295**, 2080–2083.
81. R. M. Hughes, K. R. Wiggins, S. Khorasanizadeh and M. L. Waters, *Proc. Natl. Acad. Sci. U. S. A.*, 2007, **104**, 11184–11188.
82. J. J. A. G. Kamps, J. Huang, J. Poater, C. Xu, B. J. G. E. Pieters, A. Dong, J. Min, W. Sherman, T. Beuming, F. Matthias Bickelhaupt, H. Li and J. Mecinović, *Nat. Commun.*, 2015, **6**, 8911.
83. T. Sikorsky, F. Hobor, E. Krizanova, J. Pasulka, K. Kubicek and R. Stefl, *Nucleic Acids Res.*, 2012, **40**, 11748–11755.
84. K. Liu, Y. Guo, H. Liu, C. Bian, R. Lam, Y. Liu, F. Mackenzie, L. A. Rojas, D. Reinberg, M. T. Bedford, R. M. Xu and J. Min, *PLoS One*, 2012, **7**, 1–8.
85. N. Mathioudakis, A. Palencia, J. Kadlec, A. Round, K. Tripsianes, M. Sattler, R. S. Pillai and S. Cusack, *RNA*, 2012, **18**, 2056–2072.
86. M. M. Müller and T. W. Muir, *Chem. Rev.*, 2015, **115**, 2296–2349.
87. G. N. Nagy, L. Marton, B. Krámos, J. Oláh, Á. Révész, K. Vékey, F. Delsuc, É. Hunyadi-Gulyás, K. F. Medzihradszky, M. Lavigne, H. Vial, R. Cerdan and B. G. Vértessy, *FEBS J.*, 2013, **280**, 3132–3148.
88. L. Govindasamy, T. Kukar, W. Lian, B. Pedersen, Y. Gu, M. Agbandje-McKenna, S. Jin, R. McKenna and D. Wu, *J. Struct. Biol.*, 2004, **146**, 416–424.
89. G. N. Nagy, L. Marton, A. Contet, O. Ozohanics, L. M. Ardelean, Á. Révész, K. Vékey, F. D. Irimie, H. Vial, R. Cerdan and B. G. Vértessy, *Angew. Chem., Int. Ed.*, 2014, **53**, 13471–13476.
90. A. Ordentlichs, D. Baraks, C. Kronmans, Y. Flashners, M. Leitners, Y. Segalls, N. Ariel, S. Cohens, B. Velans and A. Shaffermansll, *J. Biol. Chem.*, 1993, **268**, 17083–17095.
91. D. M. Quinn, S. R. Feaster, H. K. Nair, N. A. Baker, Z. Radić and P. Taylor, *J. Am. Chem. Soc.*, 2000, **122**, 2975–2980.

View Online

Published on 15 November 2016 on http://pubs.rsc.org | doi:10.1039/9781782626626-00214

92. A. K. Pathak and T. Bandyopadhyay, *Biopolymers*, 2016, **105**, 10–20.
93. A. K. Pathak and T. Bandyopadhyay, *Proteins: Struct., Funct., Bioinf.*, 2014, **82**, 1799–1818.
94. E. Chan-Penebre, K. G. Kuplast, C. R. Majer, P. A. Boriack-Sjodin, T. J. Wigle, L. D. Johnston, N. Rioux, M. J. Munchhof, L. Jin, S. L. Jacques, K. A. West, T. Lingaraj, K. Stickland, S. A. Ribich, A. Raimondi, M. P. Scott, N. J. Waters, R. M. Pollock, J. J. Smith, O. Barbash, M. Pappalardi, T. F. Ho, K. Nurse, K. P. Oza, K. T. Gallagher, R. Kruger, M. P. Moyer, R. A. Copeland, R. Chesworth and K. W. Duncan, *Nat. Chem. Biol.*, 2015, **11**, 432–437.
95. J. N. Scarsdale, S. Radaev, G. Kazanina, V. Schirch and H. T. Wright, *J. Mol. Biol.*, 2000, **296**, 155–168.
96. M. Vivoli, F. Angelucci, A. Ilari, V. Morea, S. Angelaccio, M. L. Di Salvo and R. Contestabile, *Biochemistry*, 2009, **48**, 12034–12046.
97. S. Maignan, J. P. Guilloteau, Y. M. Choi-Sledeski, M. R. Becker, W. R. Ewing, H. W. Pauls, A. P. Spada and V. Mikol, *J. Med. Chem.*, 2003, **46**, 685–690.
98. K. Schärer, M. Morgenthaler, R. Paulini, U. Obst-Sander, D. W. Banner, D. Schlatter, J. Benz, M. Stihle and F. Diederich, *Angew. Chem., Int. Ed.*, 2005, **44**, 4400–4404.
99. N. Morikubo, Y. Fukuda, K. Ohtake, N. Shinya, D. Kiga, K. Sakamoto, M. Asanuma, H. Hirota, S. Yokoyama and T. Hoshino, *J. Am. Chem. Soc.*, 2006, **128**, 13184–13194.
100. R. Ito, I. Hashimoto, Y. Masukawa and T. Hoshino, *Chem.–Eur. J.*, 2013, **19**, 17150–17158.
101. J. A. Faraldos, A. K. Antonczak, V. González, R. Fullerton, E. M. Tippmann and R. K. Allemann, *J. Am. Chem. Soc.*, 2011, **133**, 13906–13909.
102. M. Chen, N. Al-Lami, M. Janvier, E. L. D'Antonio, J. A. Faraldos, D. E. Cane, R. K. Allemann and D. W. Christianson, *Biochemistry*, 2013, **52**, 5441–5453.
103. D. Wu, Q. Hu, Z. Yan, W. Chen, C. Yan, X. Huang, J. Zhang, P. Yang, H. Deng, J. Wang, X. Deng and Y. Shi, *Nature*, 2012, **484**, 214–219.
104. J. Marcotrigiano, A. C. Gingras, N. Sonenberg and S. K. Burley, *Nucleic Acids Symp. Ser.*, 1997, **89**, 8–11.
105. C. J. Brown, I. McNae, P. M. Fischer and M. D. Walkinshaw, *J. Mol. Biol.*, 2007, **372**, 7–15.
106. K. Tomoo, X. Shen, K. Okabe, Y. Nozoe, S. Fukuhara, S. Morino, T. Ishida, T. Taniguchi, H. Hasegawa, A. Terashima, M. Sasaki, Y. Katsuya, K. Kitamura, H. Miyoshi, M. Ishikawa and K. Miura, *Biochem. J.*, 2002, **362**, 539–544.
107. A. Niedzwiecka, E. Darzynkiewicz and R. Stolarski, *Biochemistry*, 2004, **43**, 13305–13317.
108. C. R. W. Guimarães, D. J. Kopecky, J. Mihalic, S. Shen, S. Jeffries, S. T. Thibault, X. Chen, N. Walker and M. Cardozo, *J. Am. Chem. Soc.*, 2009, **131**, 18139–18146.
109. G. Hu, A.-L. Tsai and F. A. Quiocho, *J. Biol. Chem.*, 2003, **278**, 51515–51520.
110. M. Wu, P. Nilsson, N. Henriksson, A. Niedzwiecka, M. K. Lim, Z. Cheng, K. Kokkoris, A. Virtanen and H. Song, *Structure*, 2009, **17**, 276–286.

View Online

Published on 15 November 2016 on http://pubs.rsc.org | doi:10.1039/9781782626626-00214

111. J. Sponer, J. Leszczynski and P. Hobza, *Biopolymers*, 2002, **61**, 3–31.
112. L. McFail-Isom, X. Shui and L. D. Williams, *Biochemistry*, 1998, **37**, 17105–17111.
113. S. B. Howerton, C. C. Sines, D. VanDerveer and L. D. Williams, *Biochemistry*, 2001, **40**, 10023–10031.
114. M. Stewart, T. Dunlap, E. Dourlain, B. Grant and L. McFail-Isom, *PLoS One*, 2013, **8**, 1–13.
115. R. Wintjens, J. Liévin, M. Rooman and E. Buisine, *J. Mol. Biol.*, 2000, **302**, 395–410.
116. M. P. Horvath, V. L. Schweiker, J. M. Bevilacqua, J. A. Ruggles and S. C. Schultz, *Cell*, 1998, **95**, 963–974.
117. S. Z. Borozan, B. P. Dimitrijević and S. Đ. Stojanović, *Comput. Biol. Chem.*, 2013, **47**, 105–112.
118. M. Teplova and D. J. Patel, *Nat. Struct. Mol. Biol.*, 2008, **15**, 1343–1351.
119. S. L. Roderick, W. W. Chan, D. S. Agate, L. R. Olsen, M. W. Vetting, K. R. Rajashankar and D. E. Cohen, *Nat. Struct. Biol.*, 2002, **9**, 507–511.
120. K. M. Sanchez, G. Kang, B. Wu and J. E. Kim, *Biophys. J.*, 2011, **100**, 2121–2130.
121. G. Blaser, J. M. Sanderson and M. R. Wilson, *Org. Biomol. Chem.*, 2009, **7**, 5119–5128.
122. T. He, A. Gershenson, S. J. Eyles, Y.-J. Lee, W. R. Liu, J. Wang, J. Gao and M. F. Roberts, *J. Biol. Chem.*, 2015, **290**(31), 19334–19342.
123. D. W. Heinz, M. Ryan, T. L. Bullock, O. H. Griffith and D. W. Heinzl, *EMBO J.*, 1995, **14**, 3855–3863.
124. N. Reuter, *J. Am. Chem. Soc.*, 2012, **135**, 5740–5750.
125. J. Cheng, R. Goldstein, A. Gershenson, B. Stec and M. F. Roberts, *J. Biol. Chem.*, 2013, **288**, 14863–14873.
126. N. Wang, C. Y. Majmudar, W. C. Pomerantz, J. K. Gagnon, J. D. Sadowsky, J. L. Meagher, T. K. Johnson, J. A. Stuckey, C. L. Brooks, J. A. Wells and A. K. Mapp, *J. Am. Chem. Soc.*, 2013, 1–4.
127. R. Goldstein, J. Cheng, B. Stec and M. F. Roberts, *Biochemistry*, 2012, **51**, 2579–2587.
128. B. C. McIlwain, R. J. Vandenberg and R. M. Ryan, *J. Biol. Chem.*, 2015, **290**, 9780–9788.
129. M. E. Weber, E. K. Elliott and G. W. Gokel, *Org. Biomol. Chem.*, 2006, **4**, 83–89.

Published on 15 November 2016 on http://pubs.rsc.org | doi:10.1039/9781782626626-00238

CHAPTER 8

Aromatic Molecules on Metallic Surfaces: Structure and Reactivity

TOMAS MARANGONI[a], RYAN R. CLOKE[a] AND FELIX R. FISCHER*[a,b,c]

[a]Department of Chemistry, University of California Berkeley, Berkeley, California 94720, USA; [b]Materials Sciences Division, Lawrence Berkeley National Laboratory, Berkeley, California 94720, USA; [c]Kavli Energy NanoSciences Institute at the University of California Berkeley and the Lawrence Berkeley National Laboratory, Berkeley, California 94720, USA
*E-mail: ffischer@berkeley.edu

8.1 Introduction

The deposition of molecules featuring an extended conjugated system in thin films, self-assembled monolayers (SAMs) or as molecularly isolated species, on solid supports has emerged as a valuable tool to rationally engineer functional architectures with novel and unprecedented electronic properties.[1–8] Despite the wide variety of techniques available nowadays to deposit molecules on a surface[9–12] (vapor deposition, spin and drop-casting, Langmuir–Blodgett films, *etc.*), the investigation of the intra- and intermolecular interaction of molecules deposited on inorganic surfaces remains

Monographs in Supramolecular Chemistry No. 20
Aromatic Interactions: Frontiers in Knowledge and Application
Edited by Darren W. Johnson and Fraser Hof
© The Royal Society of Chemistry 2017
Published by the Royal Society of Chemistry, www.rsc.org

View Online

Published on 15 November 2016 on http://pubs.rsc.org | doi:10.1039/9781782626626-00238

a very challenging task. In this context, the study of interactions between aromatic molecules in thin films and on surfaces covers a broad field of applications. Given the multitude of possible interactions and the broad range of associated energies, the underlying self-assembly processes are largely treated phenomenologically (*e.g.* 2-D spatial constraint and surface–molecule interactions).

Due to the broad scientific scope and the complexity of self-assembly processes on surfaces, we herein do not attempt to provide an exhaustive review of the literature. We will instead focus our attention on the most important studies investigating the structural characteristics and the reactivity of extended aromatic systems deposited on metal surfaces.

In the last decades, extensive experimental and theoretical efforts have been dedicated to elucidate the interactions of organic molecules with inorganic crystalline solids.[13–17] The interface between organic and inorganic phases in hybrid materials has shown to be responsible for key functions in many types of electronic devices ranging from organic light emitting diodes (OLED) and organic thin film transistors (OTFT) to organic photovoltaics (OPV).[18–24] The key advantages for using organic functional materials as components in electronic devices lie in their light weight, high mechanical flexibility and ease of industrial processing.

The nature and properties of the interface between aromatic organic semiconductors and their inorganic substrates have been shown to play a significant role in the performance of the device, influencing parameters such as the local density of states at the interface or the contact resistance. One of the most crucial factors, which dictates the properties of such interfaces, is the nature of the bond formed between the molecules and the substrate. The two main types of interactions that can occur during the adsorption process at the organic–inorganic interface are chemical (*i.e.* chemisorption) or physical (*i.e.* physisorption) adsorption. The former is generally defined as an adsorption process in which the forces that bind the molecule to the substrate are strong chemical interactions (*e.g.* covalent, ionic, or strong polar bonding), whereas the latter refers to the adsorption of molecules through relatively nonspecific van der Waals or dispersion interactions.[25] Due to the lack of strong interactions with the surface, the physisorbed molecule will largely conserve its structural integrity and orbital structure upon surface adsorption. On the other hand, during chemisorption, the orbital structure of the adsorbed molecule will be altered by the hybridization with the electronic wavefunction of the surface states.

As a first approximation, this simple model describes the absorption process of small molecules. The behaviour and the properties of extended π-conjugated systems on metallic surfaces instead are much less understood. Therefore, the precise characterization of the structures and electronic properties of organic aromatic molecules adsorbed on metal surfaces is critical to understand this fundamental interaction. Initially, this chapter will focus on the most significant developments in the characterization of π-conjugated

View Online

Published on 15 November 2016 on http://pubs.rsc.org | doi:10.1039/9781782626626-00238

molecular systems on metallic surfaces, with a particular emphasis on their direct structural elucidation. In the second part, the focus will be instead shifted to the reactivity of aromatic molecular units on surfaces leading to the rational assembly of complex architectures such as covalent 2D-networks, 1-D polymers and graphene nanoribbons (GNR).

8.2 Structural Investigations of Aromatic Molecules on Surfaces

8.2.1 General Surface Characterization Techniques

Morphological characterization of a substrate can be achieved using microscopic techniques such as transmission electron microscopy (TEM) and scanning electron microscopy (SEM), which enable the acquisition of images with a resolution several orders of magnitude greater than conventional optical microscopy. Furthermore, the constant development of scanning probe microscopy (SPM), such as scanning tunnelling microscopy (STM) or atomic force microscopy (AFM), has provided the possibility to directly visualize the structure of surface-immobilized molecules and nanostructures with molecular and sometimes even sub-molecular resolution (*vide infra*). The elemental composition and chemical state of a material's surface are among the most useful and basic information and can be obtained by X-ray photoelectron spectroscopy (XPS) or energy dispersive X-ray spectroscopy (EDX). Both techniques exploit the interaction of high energy X-ray radiation with a sample surface in order to obtain information about the elemental composition. In particular, XPS spectra can be obtained by exciting the sample with an X-ray source in a high vacuum (or ultra-high vacuum) chamber and measuring the kinetic energy of the electrons that are emitted from a narrow layer (0–10 nm depth) close to the surface of the material. Through XPS, it is possible to obtain important information about the analysed materials, such as elemental composition of the material surface (with part per thousand sensitivity), its empirical formula, the chemical and electronic states of atoms at the surface and the uniformity of the elemental composition.

Another important structural characterization technique is Raman spectroscopy. Excitation with a monochromatic laser can be used to probe characteristic vibrational modes of a molecule adsorbed on a surface. Since these excitations are strictly related to the chemical symmetry and type of bonds present in the material, Raman spectroscopy has been used as an alternative structural characterization method that provides fingerprint spectra by which molecules and materials can be identified. Additionally, having the advantage of being a pure diffractive technique, Raman spectroscopy can also be coupled to optical microscopy to create confocal Raman microscopy that merges the possibility to perform high magnification visualisation of a sample and *in situ* Raman analysis.

View Online

Published on 15 November 2016 on http://pubs.rsc.org | doi:10.1039/9781782626626-00238

8.2.2 Visualization Techniques with Sub-Molecular Resolution: STHM and nc-AFM

With the recent expansion of scanning probe microscopy (SPM), adsorption of organic molecules on inorganic conductive surfaces (*i.e.* metallic) has become one of the most valuable approaches to investigate their structural, chemical and physical properties. Scanning tunnelling microscopy, an imaging technique invented by Binnig and co-workers in 1981, was the first type of SPM technique developed that was able to image inorganic conductive surfaces with atomic resolution.[26] In its classical design, a scanning tunnelling microscope (STM) is composed of an atomically sharp metallic probe (generally made of tungsten or a platinum–iridium alloy), which is scanned along the *xy* plane of a conductive surface at a distance of a few Å, while applying a voltage between the surface and the probe (Figure 8.1).[27,28] The application of a voltage between two conducting materials, separated by a small insulating gap (typically 0.3–1.0 nm), leads to a tunnelling current between the probe and the surface. Since the intensity of the tunnelling current depends on the tip–sample distance, the applied voltage *V* and the tip/sample local density of states (LDOS), even the slightest variation of the sample surface can be detected using this method.

From the experimental point of view, on-surface investigations can generally be performed using two different STM modes. In the first and most intuitive mode, named *constant height* mode, the tip is held at a fixed *z*-position while scanning across the sample surface at a constant bias voltage. In this setting, the variation in the tunnelling current induced by changes in the tip–sample distance is recorded as a function of the tip position and can be used to reconstruct a topographic image of the surface. In the second mode, called *constant current* mode, the distance between tip and sample is continuously adjusted electronically by a feedback loop in order to maintain a constant user-defined tunnelling current. The final STM image is then reconstructed from the feedback signal.

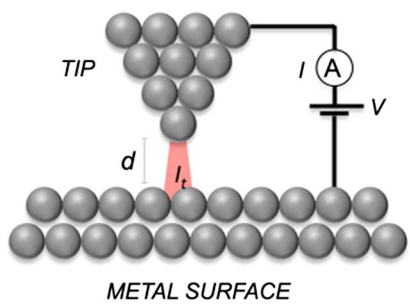

Figure 8.1 Schematic representation of a scanning tunnelling microscope. Tunnelling current between the tip and the metal surface is depicted in red (*d*: distance between tip and sample, I_t: tunnelling current).[28]

View Online

Published on 15 November 2016 on http://pubs.rsc.org | doi:10.1039/9781782626626-00238

From the time of its invention, scanning tunnelling microscopy has been used to investigate the structure and properties of a wide range of molecules and materials, such as isolated organic and bio-molecules, supramolecular systems and 2-D inorganic crystals.[29–33] However, although atomic resolution has been obtained for a wide range of crystalline surfaces, atomic resolution on molecules adsorbed on metallic surfaces has only been achieved very recently. Two SPM techniques able to achieve this kind of spatial resolution are scanning tunnelling hydrogen microscopy (STHM) and non-contact atomic force microscopy (nc-AFM).[33] In both cases, the key to enable the direct visualization of individual bonds and atoms in individual molecules is the functionalization of the probe with diatomic molecules, such as dihydrogen or carbon monoxide for STHM and nc-AFM, respectively.

The first technique, STHM, was developed by Tautz and co-workers.[34,35] Atomic resolution on isolated flat aromatic molecules was obtained when the STM chamber was flooded with molecular dihydrogen or dideuterium (Figure 8.2(A)). High sensitivity of the STM tunnelling junction with molecular hydrogen was achieved by leaking ultrapure hydrogen (99.9999%) into the LT-STM (low temperature STM) chamber at a pressure varying between 10^{-9} and 10^{-7} mbar. Using this technique, Temirov *et al.* were able to obtain

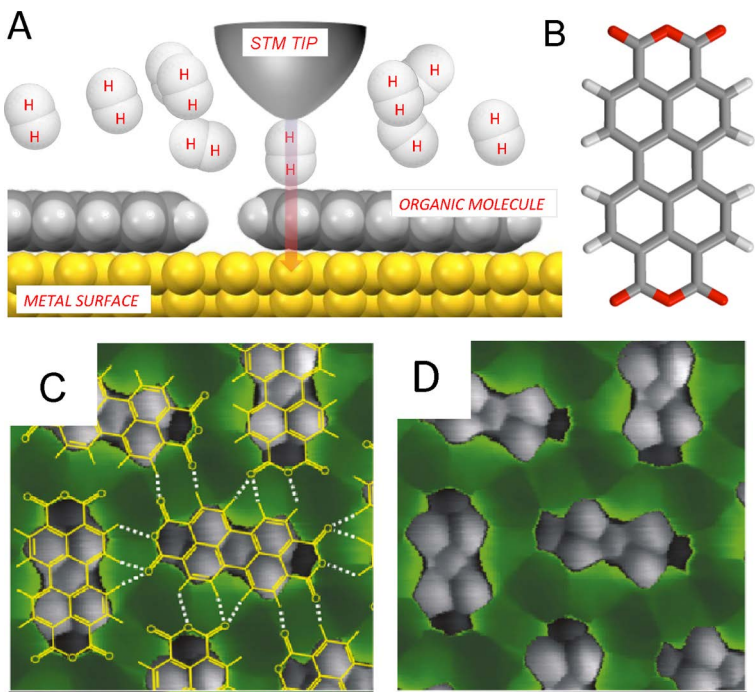

Figure 8.2 Schematic representation (A) of the STHM set-up. Molecular structure (B) of the PTCDA molecule (grey: carbon, white: hydrogen, red: oxygen). STHM images of PTCDA molecules (C and D) on Au(111) in its herringbone phase (image size 2.5 nm × 2.5 nm) (reproduced with permission from ref. 35. Copyright © 2010 American Chemical Society).

View Online

Published on 15 November 2016 on http://pubs.rsc.org | doi:10.1039/9781782626626-00238

sub-molecular resolution images of aromatic molecules such as tetracene and 3,4,9,10-perylene-tetracarboxylic-dianhydride, PTCDA (Figure 8.2(B)). Some representative images of PTCDA as imaged through STHM showing the high level of accuracy are depicted in Figure 8.2(C) and (D). The imaging mechanism of STHM is strictly related to the chemical structure of the molecule itself rather than its electronic molecular states as in conventional STM. The short diatomic molecules (hydrogen or deuterium) act as sensors for short range Pauli repulsion from the surface, behaving as transducers and transforming these forces into a variation of the tunnelling current. The hydrogen/deuterium probe is therefore responsible for a modulation of the tunnelling current over the conventional LDOS contrast.

The second technique is nc-AFM, a powerful method to achieve atomic resolution of organic molecules on surfaces.[36] Contrary to STM, which probes the LDOS of the sample for given energies, non-contact atomic force microscopy probes the force between the probe and the sample during scanning. A sharp probe attached to a piezoelectric quartz crystal resonator is raster-scanned over the sample. The AFM image is then reconstructed measuring either the change in amplitude at a constant frequency (amplitude modulation mode) or measuring the change in resonant frequency at constant resonance amplitude (frequency modulation mode). Atomic resolution can be achieved at low temperatures (~5 K) in UHV (ultra-high vacuum) using a nc-AFM equipped with a qPlus® sensor.[37] The qPlus® system is composed of a quartz tuning fork fixed to a support by one of its prongs while the free-standing prong holds the probe tip. The fork operates in frequency-modulation mode, at high resonance frequency (approx. 30 kHz), and the signal measured is the shift of the resonance frequency Δf caused by the interaction between tip and sample. As for the STHM case, sub-molecular resolution can be achieved when the AFM tip is functionalized with a diatomic molecule, such as CO.

Using this technique Gross and co-workers were able, for the first time, to image with atomic resolution the structure of a planar aromatic molecule deposited on a metallic surface.[38] The functionalization of the AFM tip with a CO molecule enables atomic resolution images of individual pentacene molecules, as deposited on both conductive (*i.e.* Cu(111)) and non-conductive (*i.e.* on a NaCl bilayer on Cu(111)) surfaces. Generally, without tip functionalization, single molecule visualization with AFM is extremely challenging due to the relatively low stability of the system, which is strongly affected by different factors such as the tip structure (*e.g.* its atomic composition and geometrical features) and the occurrence of unintentional molecular manipulation. For this reason, functionalization of the AFM tip apex with a stable molecule adopting a known structure and geometrical orientation (CO is known to bind to the AFM tip by its carbon atom) can both increase the final imaging resolution and facilitate the comparison between experimental results and theoretical calculations. The nc-AFM images of pentacene were obtained using constant height mode while the frequency shift Δf was recorded. Interestingly, all the molecules deposited on Cu(111) displayed local Δf maxima at the edges of the terminal rings near the carbon atom positions and a minima above the central rings of pentacene together with a dark halo completely

View Online

Published on 15 November 2016 on http://pubs.rsc.org | doi:10.1039/9781782626626-00238

surrounding their structures. The origin of this contrast could be explained using DFT simulations that assigned the high contrast to the Pauli repulsion while the long range van der Waals and electrostatic forces contribute only an attractive background force leading to the characteristic dark halo surrounding the molecule.[38,39]

Following the development and consolidation of this technique, Moll and co-workers used nc-AFM with a CO-tip to explore the structure of different types of molecules on metallic surfaces. In a recent work, they investigated the image distortion characteristic of CO-terminated tips and the visualization features of aromatic rings possessing different electronic density.[40] In order to do so, a partially fluorinated oligo-phenylene ethynylene (**OFOPE**) was imaged *via* nc-AFM using a CO functionalized tip (Figure 8.3(A) and (B)).

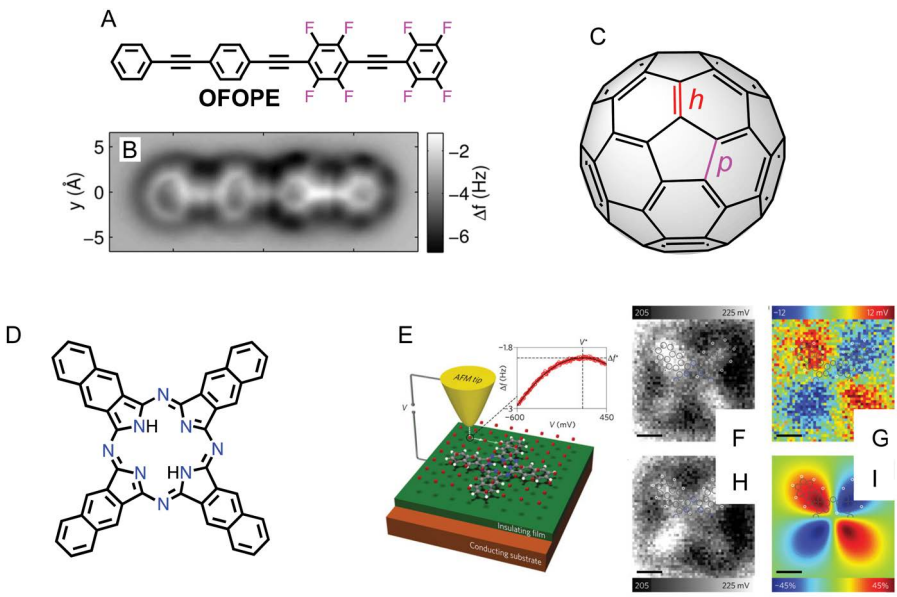

Figure 8.3 Molecular structure (A) of a fluorinated derivative **OFOPE** and its measured constant-height frequency shift Δf image (B) (reproduced with permission from ref. 40. Copyright © 2014 American Chemical Society). (C) Molecular structure of C_{60}, showing the different *h* (fusing two six-membered rings) and *p* (fusing a six- and a five-membered ring) bonds. Molecular structure (D) of naphthalocyanine. Schematic representation (E) of a KPFM measurements method on naphthalocyanine: at each point of the grid (marked with the red points), frequency shifts are recorded as a function of the applied voltage (inset). LCPD mapping of naphthalocyanine as deposited on NaCl/Cu(111) before (F) and after (H) current-induced tautomerisation (scale bars = 0.5 nm). Image obtained after subtracting H from F (G) and DFT calculated asymmetry of the *z*-component of the electric field at 0.5 nm above the naphthalocyanine (I) (reproduced from ref. 44 with permission. Copyright © 2012, Rights Managed by Nature Publishing Group).

View Online

Published on 15 November 2016 on http://pubs.rsc.org | doi:10.1039/9781782626626-00238

This molecule is comprised of two different subsections featuring hydrogen- and fluorine-substituted phenyl rings. When imaged by AFM, the fluorinated rings appear to have a considerably smaller diameter when compared to the non-fluorinated phenyl rings. Kelvin probe force microscopy, STM and nc-AFM, in combination with first principle calculations, revealed that the image distortion of the fluorinated rings can be attributed to their lower charge density in comparison to the hydrogenated ones (a factor 2 smaller as calculated by DFT). This can be rationalized as a consequence of the high electronegativity of the fluorine atoms that seems to influence the π-electrons of the aromatic rings. Additionally, the molecule also appears distorted due to the presence of attractive van der Waals interactions and for low tip height, both Pauli repulsion and van der Waals forces tilt the CO probe in a manner that the bonds of **OFOPE** appear much sharper.

The group of Gross was also able to show that different bond orders of individual carbon–carbon bonds in planar and non-planar polycyclic hydrocarbons can be visualized and characterized using nc-AFM with CO-functionalized tips. Determination of bond order, angle and length can potentially be very useful to predict the reactivity, stability and aromatic character of molecules adsorbed on a surface. In their study, Gross and co-workers elucidated the bond order of three molecules: two extended polycyclic aromatic hydrocarbons (PAH) (namely hexabenzocoronene, HBC, and dibenzo(*cd*,*n*)naphtho(3,2,1,8-*pqra*)perylene, DBNP) and C_{60} fullerene.[41] In the case of C_{60}, the bonds fusing two hexagons (*h*) are structurally different from the bonds fusing a pentagon and a hexagon (*p*) (Figure 8.3(C)). Indeed, both theoretical and experimental investigations by means of neutron, electron and X-ray diffraction have shown that the bond *h* is ~5% shorter than the bond *p*.[42,43] The difference in bond order for *p* and *h* is reflected in the constant height AFM measured with a CO-functionalized tip, which is illustrated by a characteristic bond length alteration corresponding to the cyclohexatriene motif of the C_{60} structure. Two main factors could be deducted. First, the local frequency shift Δf is greater at a position above the *h* bonds. Second, the *h* bond length appears shorter than the corresponding *p* bond. The increase of contrast localized around the *h* bond can be interpreted as a consequence of the higher local electron density associated with this bond, which induces a greater Pauli repulsion. Using Laplace filtered images, it was possible to determine the apparent bond length of $L_h' = 2.0$ Å and $L_p' = 2.7$ Å. Notably, both bonds appear to be much longer than what was previously measured by diffraction techniques with a difference of ~30% in the bond lengths as determined by AFM. DFT simulations indicate that the possible reason for the discrepancy between real and observed bond lengths can be attributed to the tilting of the CO molecule on the AFM tip, which makes the *h* bond appear shifted further away from the molecular center than the *p* ones. Constant height AFM analysis of the other two hydrocarbons HBC and DBNP qualitatively corroborated the bond order related contrast observed in the case of the C_{60} analysis. It is important to point out that the bond length amplification

View Online

Published on 15 November 2016 on http://pubs.rsc.org | doi:10.1039/9781782626626-00238

originating from CO tilting is also the factor that enables the detection of different bond orders, which would otherwise not be visible within the accuracy of the AFM instrument.

Non-contact AFM and STM imaging have also been used in combination with other techniques in order to obtain information about both structure and electronic properties of molecules on surfaces. Kelvin probe force microscopy (KPFM), for example, has been utilized to probe the charge distribution on an isolated naphthalocyanine molecule (Figure 8.3(D)).[44] This technique can be used to measure the local contact potential difference (LCPD) between the tip and the sample, as a function of the charge distribution on the surface. The investigated naphthalocyanine was deposited on a Cu(111) crystal covered with two monolayers (2 ML) of a NaCl island at 5 K. Free-base naphthalocyanine can be adsorbed on the surface as two tautomeric forms (depending on the position of the N–H). The interconversion between the two tautomers (representing a switch) can be triggered by a current pulse. A schematic representation of the KPFM measurement as performed on the naphthalocyanine is depicted in Figure 8.3(E). In this method, a metal-terminated AFM tip is scanned along a grid above the molecule and at each intersection of the grid a Δf (V) spectrum is recorded. The position of the maximum of the parabola gave the LCPD value and the frequency shift at compensated LCPD(Δf) for that point. Upon performing this measurement, Mohn and co-workers observed a striking asymmetry between the lobe parallel (H-lobes) and perpendicular (N-lobes) to the inner hydrogen atoms, which it is remarkably clear when subtracting the LCPD data from the initial state and the switched configuration (Figure 8.3(F)–(I)). Comparison of the electric field generated by the distribution of the total charge to the LCPD has also been performed using DFT simulations. The calculated electric field asymmetry exhibits a similarity to the experimental data obtained by KPFM, leading to the conclusion that the LCPD was indeed reflecting the sub-molecular charge distribution. In the same work, a further increase of the image resolution was obtained by functionalizing the AFM tip with a CO molecule. The contrast of the images in this context was affected strongly by the tip height (z) and as the tip sample distance was decreased, the intramolecular contrast gradually increased. Such drastic increase of resolution in KPFM was ascribed to the close proximity between the tip and the sample. The small oscillation amplitude also contributes to enhance the ability to sense short-range electric fields originating from local charge variations.

Finally, molecular structure resolution using nc-AFM was also recently employed to identify the different components of a very complex mixture of hydrocarbons.[45] Due to its high importance in industry and to its incredible chemical complexity, asphaltene was chosen as a target mixture. In this context, nc-AFM offers the unique capability to identify and characterize isolated units of a very complex mixture, providing precious insight into the interatomic connectivity. For this experiment, a small coverage (<5% monolayer, ML) of asphaltene molecules was obtained on a Cu(111) crystal partially

View Online

Published on 15 November 2016 on http://pubs.rsc.org | doi:10.1039/9781782626626-00238

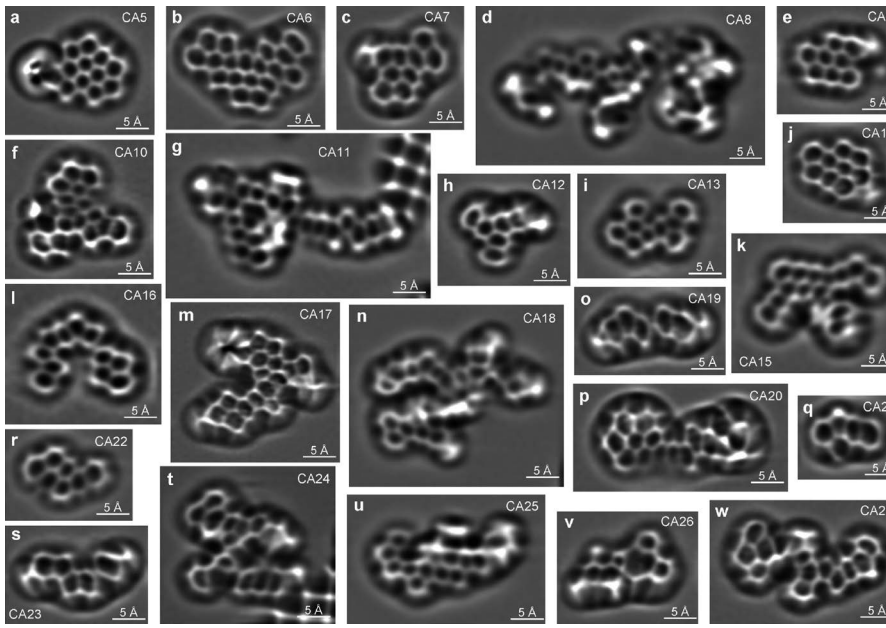

Figure 8.4 Laplace filtered nc-AFM images (a)–(w) of different molecular components observed by depositing coal-derived asphaltenes on Cu(111) or on NaCl(2 ML)/Cu(111) (reproduced with permission from ref. 45. Copyright © 2015 American Chemical Society).

covered with NaCl islands (2 ML) by flash-heating a sample of asphaltene from a silicon wafer.

Using a combination of STM and nc-AFM investigations, the authors found that the main components of asphaltenes are different types of PAHs bearing peripheral alkyl chains. nc-AFM was able to elucidate the structure and the atomic connectivity of a wide range of asphaltene components (Figure 8.4). Upon focusing their attention on asphaltenes of different origins (coal, and petroleum asphaltenes), the authors were able to identify structural differences between their respective components.

8.3 Reactivity of Aromatic Molecules on Metallic Surfaces

The incorporation of functional organic aromatic nanomaterials into electronic devices requires the development of tools to assemble highly extended molecular systems with long-range order and atomic precision. Despite the continuous progress in the field, the synthesis of extended nanomaterials based on traditional solution chemistry presents several challenges and limitations. Indeed, PAH featuring extended surface areas and high molecular weight are often characterized by extremely low solubility and processability,

View Online

Published on 15 November 2016 on http://pubs.rsc.org | doi:10.1039/9781782626626-00238

which can affect the reaction yield, purification and characterization. Additionally, even in the case of a successful synthesis, complicated transfer protocols are usually necessary during the device fabrication process to deposit these compounds on a substrate support. In this context, the exploitation of surface-mediated reactions for the construction of extended organic architectures from reactive small molecules is a promising approach.[46–49] This bottom-up method generally sees the deposition of an appropriate molecular precursor on a metallic surface in UHV and its subsequent inter- or intramolecular reaction is achieved by the application of a secondary stimulus (*e.g.* temperature gradient, light irradiation or electrical stimulation). This strategy possesses several advantages when compared with conventional solution synthesis. The absence of a solvent not only alleviates solubility requirements, but also allows the use of a wider temperature range (from 5 to 600 K) permitting the investigation of reactivity pathways that are not accessible to classical wet chemistry. Furthermore, the metallic surfaces themselves can participate as a catalyst during the chemical reaction. In this section we will discuss the most important types of surface-mediated reactions that have been used so far to construct complex organic architectures starting from aromatic building blocks, highlighting some of the most relevant examples for each specific reaction class.

8.3.1 Surface-Mediated Polymerization

8.3.1.1 Polymerization via *Terminal Acetylene Coupling*

Reactions involving the exploitation of the intrinsic chemical reactivity of terminal alkyne groups are among the most exploited synthetic tools for the construction of both 1-D and 2-D extended organic structures on surfaces.[50,51] Fischer and Crommie recently demonstrated the use of this strategy to assemble a fully conjugated polymer derived from polyacetylene on a metallic substrate.[52] The thermally induced "enediyne cyclization" of a 1,2-bis(2-ethynylphenyl)ethyne precursor **1** gave a diradical intermediate **2**, that polymerizes on the surface *via* a radical step-growth mechanism (Figure 8.5(A)). Deposition of **1** on a Au(111) surface in UHV at room temperature and subsequent thermal annealing at 160 °C induces two C1–C5 radical cyclization reactions as well as the intermolecular radical recombination that leads to the oligo-(*E*)-1,1′-bi(indenylidene) derivative **3**. Using a combination of nc-AFM, STM and Scanning Tunneling Spectroscopy (STS) on individual oligomeric chains, it was possible to shed light on both the structure and the electronic properties of each unit. The molecular connectivity of the oligomer was resolved by nc-AFM (Figure 8.5(B)). Theoretical simulations and dI/dV mapping of the oligomers highlighted the presence of an extended electronic state localized along the center of the conjugated polymer backbone (Figure 8.5(C) and (D)). This electronic structure can be rationalized taking into consideration the electron spatial delocalization caused by the formation of highly extended π-system along the polymer backbone.

View Online

Published on 15 November 2016 on http://pubs.rsc.org | doi:10.1039/9781782626626-00238

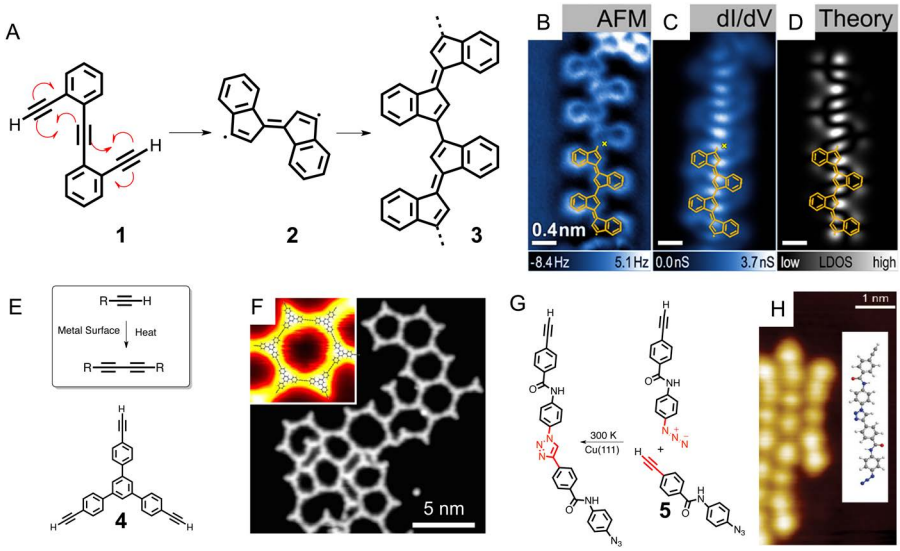

Figure 8.5 The C1–C5 cyclization (A) reaction leading to the formation of the diradical intermediate **2** and its oligomers **3** from polyacetylene precursor **1**. nc-AFM (B), d*I*/d*V* mapping (C) and theoretical simulation (D) of the electronic structure of **3**, showing its atomic connectivity and the presence of an extended electronic state, respectively (reproduced with permission from ref. 52. Copyright © 2014 American Chemical Society). (E) Surface-mediated alkyne dimerization reaction (top) and structure of the trialkyne precursor **4** (bottom). STM image (F) of the 2-D network formed by polymerization of **4** on a Ag(111) surface, inset: 3-D model of the network overlayed to the STM image (reproduced from ref. 55 with permission. Copyright © 2012, Rights Managed by Nature Publishing Group). Surface-mediated "Huisgen-type" cyclization (G) leading to oligomerization of **5** (the functional groups involved in the formation of the triazole ring are shown in red). LT-STM image (H) showing the morphology of the oligomers and their 3D models (inset) (reproduced with permission from ref. 58. Copyright © 2013 American Chemical Society).

Another successful strategy for the preparation of 1-D and 2-D extended aromatic systems in UHV involves the exploitation of the selective reaction of the metallic substrate with functional groups at the metal–vacuum interface. This strategy is inspired by the extensive work performed on transition-metal mediated cross-coupling reactions in solution.[53,54] A representative example is the polymerization of molecular units bearing terminal alkynes. Using this approach, Zhang *et al.* were able to polymerize molecular precursors such as 1,3,5-triethynyl-benzene and 1,3,5-tris(4-ethynylphenyl)benzene **4** through a surface-mediated alkyne homocoupling (Figure 8.5(E)).[55] The polymerization of these tritopic precursors was performed by evaporating the isolated molecules onto a Ag(111) surface, followed by thermal annealing at 300 K. This procedure resulted in the highly selective formation of a new C(sp)–C(sp) single bond between the terminal atoms of the alkyne

View Online

Published on 15 November 2016 on http://pubs.rsc.org | doi:10.1039/9781782626626-00238

functionality, leading to covalently bonded dimers or highly extended reticular networks. The extended porous network formed *via* this route was composed of a heterogeneous distribution of pores featuring different sizes and shapes (*i.e.* pentagon, hexagon, heptagon, Figure 8.5(F)). Such an observation can be attributed to the inherent flexibility of the molecular precursors and to the irreversibility of the homocoupling reaction. Interestingly, when a similar experiment was performed by the group of Fasel using an Au(111) surface, a drastic change in reactivity of the terminal acetylene functionality was observed. Rather than undergoing homocoupling reactions, the terminal alkynes underwent a [2+2+2] cyclotrimerization to form 2-D networks.[56] Further investigations on the reactivity of terminal acetylene showed the possibility to use this group as a partner in a [3+2] cycloaddition reaction with appropriately functionalized azide derivatives.[57,58] Due to the possibility to perform heteromolecular coupling on surfaces, this discovery strongly increases the applicability of these systems, extending the use of this chemistry to the construction of more complex architectures formed by different functional and structural units. Fuchs and co-workers were able to induce the oligomerization of monomer **5** at room temperature by depositing it on Au(111).[58] Exploiting the interaction with the surface, the triple bonds and the azide functionality of **5** reacted in a 1,3-dipolar cycloaddition leading to the exclusive formation of 1,4-substituted triazoles (Figure 8.5(G) and (H)). The success of the coupling reaction and the formation of oligomeric species was confirmed by STM (Figure 8.5(H)) and showed the structure and connectivity of single oligomeric chain.

8.3.1.2 Polymerization of Halogenated Precursors

One of the most common strategies used to assemble extended aromatic systems from small molecular precursors relies on the use of halogenated molecular precursors.[59–63] The coupling of these molecular units is achieved by deposition of the halogenated precursor on a metallic surface followed by subsequent heating of the underlying substrate. The thermal annealing of the surface induces reactions (*e.g.* surface-mediated Ullmann coupling) that link isolated molecules into higher ordered 2-D structures.

One of the most important parameters dictating the reactivity of molecular precursors on surfaces is the type of halogen substituent. Differences in the bond dissociation energies (BDE) of the C–X bond (336 kJ mol^{-1} for $Br–C_6H_5$ and 272 kJ mol^{-1} for $I–C_6H_5$ in the gas phase)[64] are reflected in the reactivity of these groups on surfaces. During the thermal annealing process, iodinated precursors have been shown to react at lower temperatures than brominated analogues. In their pioneering work, Grill and co-workers were able to exploit the difference in reactivity between C–I and C–Br bonds with the goal to produce multiple nanostructures in a hierarchical manner from a tetra-halogenated porphyrin **6**, which bears two iodophenyl and two bromophenyl substituents in the 5, 15 and 10, 20 positions, respectively (Figure 8.6(A)).[65] Deposition of the monomer on a Au(111) surface held at 80 K

View Online

Published on 15 November 2016 on http://pubs.rsc.org | doi:10.1039/9781782626626-00238

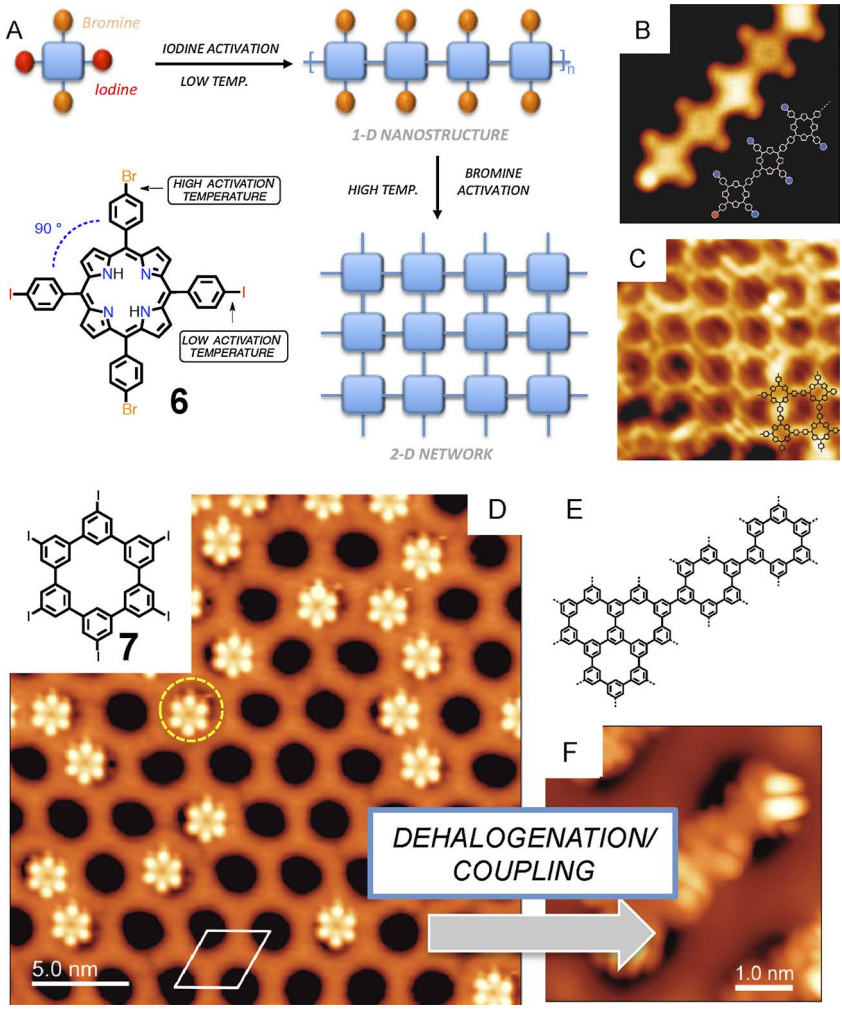

Figure 8.6 Schematic representation (A) of the hierarchic construction of 1-D and 2-D nanostructures starting from the tetrahalogenated porphyrin **6**. Upon selective activation of the C–I bond at 120 °C, the 1-D polymerization of molecule **6** can be triggered. Further increase of the temperature to 250 °C induces the activation of the C–Br bonds and the interconversion of the 1-D nanostructures into extended 2-D networks. LT-STM images of the 1-D oligomers (B) and of the 2-D networks (C) (reproduced from ref. 65 with permission. Copyright © 2012, Rights Managed by Nature Publishing Group). LT-STM image (D) of molecular precursor **7** as deposited on a BN surface (inset: molecular structure of **7**). Generic representation (E) of the structures obtained by the coupling of **7**, and corresponding LT-STM (F) of some of the networks obtained (reproduced with permission from ref. 66. Copyright © 2014 American Chemical Society).

View Online

Published on 15 November 2016 on http://pubs.rsc.org | doi:10.1039/9781782626626-00238

resulted in the adsorption of intact molecular units containing both iodine and bromine atoms. Thermal annealing of **6** at room temperature induced the cleavage of the C–I bond and a radical recombination to give covalently linked dimers of **6**. Further annealing to 120 °C induced an efficient polymerization of **6** by selective and complete activation of the residual C–I bonds. Due to the "*trans*-like" arrangement of the iodine atoms, the polymerization reaction leads to the formation of linear oligomer chains (Figure 8.6(B)). The substantially lower activation temperature of the C–I bond in respect to the C–Br bond allowed the complete preservation of the bromine atoms on the oligomers allowing further growth of this structure. Annealing of the oligomers at 250 °C induces the dissociation of the C–Br bond leading to the growth of a highly regular 2D architecture (Figure 8.6(C)). The same principle has been demonstrated to grow heterogeneous networks formed by multiple types of units. Introduction of a secondary component in the system (*i.e.* a dibrominated oligofluorene) has been shown *via* STM to lead to the formation of hybrid structures composed of interconnected porphyrin and fluorene oligomers.

A further advancement on this technique has been recently demonstrated by the group of Gröning and Dienel, which showed the possibility to perform this coupling on an insulating surface.[66] Since non-conductive surfaces are required as support materials for electronic devices, the investigation of the reactivity of isolated molecules on insulating surfaces remains an important challenge in nanoscience. In their experiments, Gröning and co-workers used an isolating boron nitride (BN) monolayer supported on a Rh(111) surface (Figure 8.6(D)). The reactivity of hexaiodinated precursor **7** on the highly corrugated BN surface during thermal annealing showed a wide temperature range from the start of the dehalogenation process (500 K) to the full dehalogenation and coupling of the isolated molecules (800 K) (Figure 8.6(E) and (F)). This observation is distinctive from the results commonly observed on metallic surfaces and the behaviour of the same molecule in the gas-phase. A combination of STM investigation and DFT simulation showed that the interaction of the BN with the molecule itself governs the dehalogenation process.

8.3.1.3 Polymerization Through Dynamic Covalent Chemistry

In recent years the concepts of dynamic covalent chemistry (DCC) using aromatic building blocks have been successfully applied to the creation of organic architectures on a variety of surfaces.[67–72] The thermodynamic driving force combined with the reversible covalent nature of the interaction paves the way for the assembly of architectures featuring long-range order and higher stability when compared to non-covalent interactions. Among the different reactions that have been developed in this field, imine condensation and the esterification of boronic acid have been exploited the most for the creation of organized networks on surfaces.[73–76]

View Online

Published on 15 November 2016 on http://pubs.rsc.org | doi:10.1039/9781782626626-00238

One example of the use of imine condensation for the creation of 2-D aromatic macrostructures on surfaces is shown in Figure 8.7(A)–(D). Kunitake and co-workers were able to prepare a variety of organic networks by exploiting the condensation reaction between the tetraaminoporphyrin **8** and a library of linear dialdehydes **9**–**11** (Figure 8.7(A)).[77] Simple mixing of molecule **8** (which presents a disposition of its amino group at 90° one from each other) with the appropriate linear dialdehyde under thermodynamic control leads to the formation of various extended networks. Deposition of this aqueous solution onto a Au(111) surface and *in situ* STM indicated the formation of 2-D frameworks with different geometries and pore sizes, strictly dependent on the structural parameters and the configuration of the dialdehyde used (Figure 8.7(B)–(D)).

Another tool that has been exploited for the assembly of 2-D covalent architectures on surfaces is the chemistry of boronic acids. To date, the reversible formation of both boronic esters and cyclic anhydrides (boroxine) has also been used to create extended porous aromatic frameworks on surfaces. In the particular case of boroxine, the general reaction scheme involves the participation of three molecules of boronic acid which, upon condensation and elimination of three H_2O molecules, form a very stable six-membered ring characterized by alternating boron and oxygen atoms (Figure 8.7(E)).

This approach has been successfully used by Abel and co-workers to prepare extended 2-D networks starting from the commercially available 1,4-benzenediboronic acid **13**.[78] Upon sublimation of benzenediboronic acid under ultrahigh vacuum (UHV) conditions onto a clean Ag(111) surface (kept either at room temperature or at 400 K), 2-D extended hexagonal networks were formed (Figure 8.7(G)). The same principle has been used by the authors to couple different types of molecules through an esterification reaction. Indeed, when 1,4-benzenediboronic acid was co-sublimed together with triphenylene derivative **12** on Ag(111), the formation of another 2-D hexagonal network with pores consistently larger than the previous one (29.8 Å *versus* 15.25 Å) was observed. Additionally, the comparison between the two networks shows the presence of fewer local defects in the last one. This can be rationalized considering that the boronic acid esterification is a bimolecular reaction and therefore follows a more favourable kinetic pathway in comparison with the trimolecular boronic acid self-condensation.

A further example that shows the multivalent application of boronic acids on surfaces is the work of Lackinger and co-workers, who were able to obtain a series of isoreticular networks inducing the dehydration of aromatic diboronic acids featuring different lengths on HOPG.[79] By employing a library of diboronic phenyl acids featuring different lengths and structures (diacids **13**–**17**, Figure 8.7(F)), the authors were able to prepare a series of 2-D covalent frameworks in which the lattice parameters and pore sizes could rationally be designed by using the desired type of acid (Figure 8.7(I) and (J)).

Published on 15 November 2016 on http://pubs.rsc.org | d

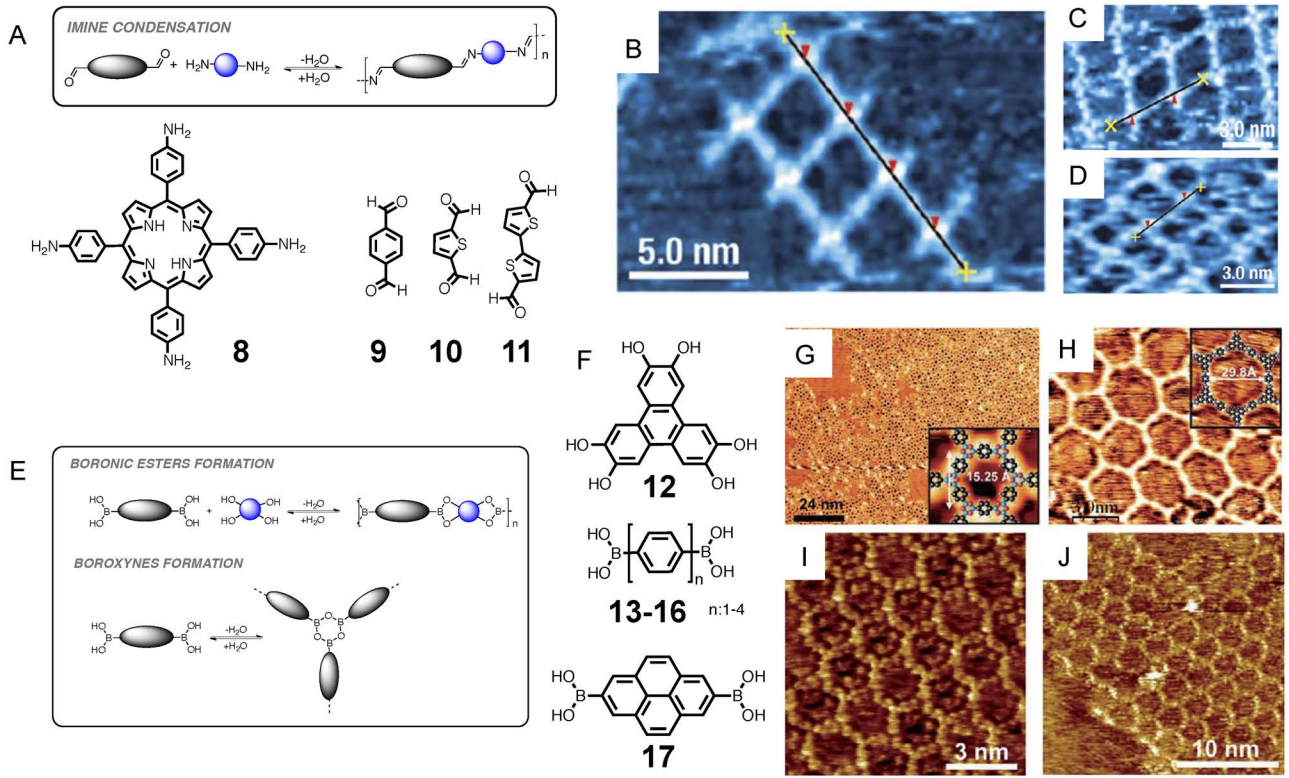

Figure 8.7 (A) The imine condensation reaction (top) and the tetraaminoporphyrin **8** with the partner dialdehydes **9**–**11** (bottom). Representative STM images (B)–(D) of 2-D networks formed by the condensation of **8** with **9, 10** and **11** (reproduced with permission from ref. 77. Copyright © 2011 American Chemical Society). Esterification of boronic acids (E) and their self-condensation into boroxines. Triphenylene derivative **12** and diboronic acids **13**–**17**. STM image (G) of 2D networks formed by self-condensation of **13** on a Ag(111) surface and with triphenylene derivative **12** (H) as obtained by Abel and co-workers (inset: network structure as obtained from DFT) (reproduced with permission from ref. 78. Copyright © 2008 American Chemical Society). Representative STM images (I) and (J) of isoreticular networks that can be formed using different diboronic acids (**13**–**17**) on HOPG, in particular networks obtained by the self-condensation of **14** (I) and **15** (J) are depicted (reproduced with permission from ref. 79. Copyright © 2008 American Chemical Society).

View Online

Published on 15 November 2016 on http://pubs.rsc.org | doi:10.1039/9781782626626-00238

8.3.2 Cyclodehydrogenation Reactions

Cyclodehydrogenation reactions have been extensively used in the last decades in order to obtain synthetic access to extended PAH using solution-based chemistry. Among the different sets of conditions, Scholl and Kovacic reactions, which use Lewis acids/oxidants combinations (such as for example $FeCl_3$, $AlCl_3$, $Sc(TfO)_3$, or TfOH), have proven to be very efficient to induce intramolecular cyclodehydrogenation processes.[80–83] Unfortunately, due to the harsh conditions used, these reactions are generally characterized by a low degree of functional group tolerance and by the presence of undesired side reactions (*e.g.* chlorination, intermolecular coupling and transposition reactions).[81,84–87]

With the advent of STM as a characterization technique, the possibility to induce the cyclodehydrogenation reaction on a metallic surface has also been thoroughly investigated. Over the years, different protocols have been established in order to prepare extended aromatic structures on surfaces, the conditions of which are strictly dependent on the type of metal surface and molecular unit used. One of the most reliable approaches involves the deposition of a geometrically pre-organized molecular precursor on a metallic surface followed by thermal annealing of the substrate at temperatures in the range between 300 and 400 °C. An in-depth investigation of the cyclodehydrogenation process on metal surfaces was performed by Fasel in 2011.[88] In this study, triangular oligophenylene **18** was deposited on a Cu(111) surface and gradually annealed to 200 °C. Through the combined use of STM and *ab initio* DFT simulations, it was possible to identify and characterize the intermediate states leading to the formation of the fully cyclized nanographene **19** (Figure 8.8(A)–(C)). In total, a six-step mechanism featuring five different intermediates was found to be necessary for the complete cyclodehydrogenation of **18**. The authors conceptualize this complex mechanism by dividing it into three consecutive simpler processes: (i) Cu-mediated radical C–H bond breaking, (ii) rotation of the *p*-phenylene towards the neighbouring unit and formation of a new C–C bond by radical addition with consequent loss of the H atom and (iii) recombination of the H atoms. Two of the intermediates composing this mechanism were stabilized by the interaction with the surface and their structural characterization was performed *via* STM. As evidenced by this work, one of the most important advantages of surface-mediated intramolecular cyclodehydrogenation consists of the ability to precisely control the atomic connectivity and the edge structure of the resulting nanostructure by appropriate design of the molecular precursor.

Following the same approach, Fischer and Crommie were able to synthesize peripentacene (**21**), using a thermally-induced cyclodehydrogenation reaction on Au(111).[89] From a structural point of view, peripentacene, which belongs to the class of molecules known as *n*-periacenes, consists of two linear pentacene units fused at the peri-position in a rectangular PAH.

Its characteristic structure exhibits two parallel long edges with a zig-zag configuration and two short armchair edges. Despite several attempts to

Published on 15 November 2016 on http://pubs.rsc.org | d

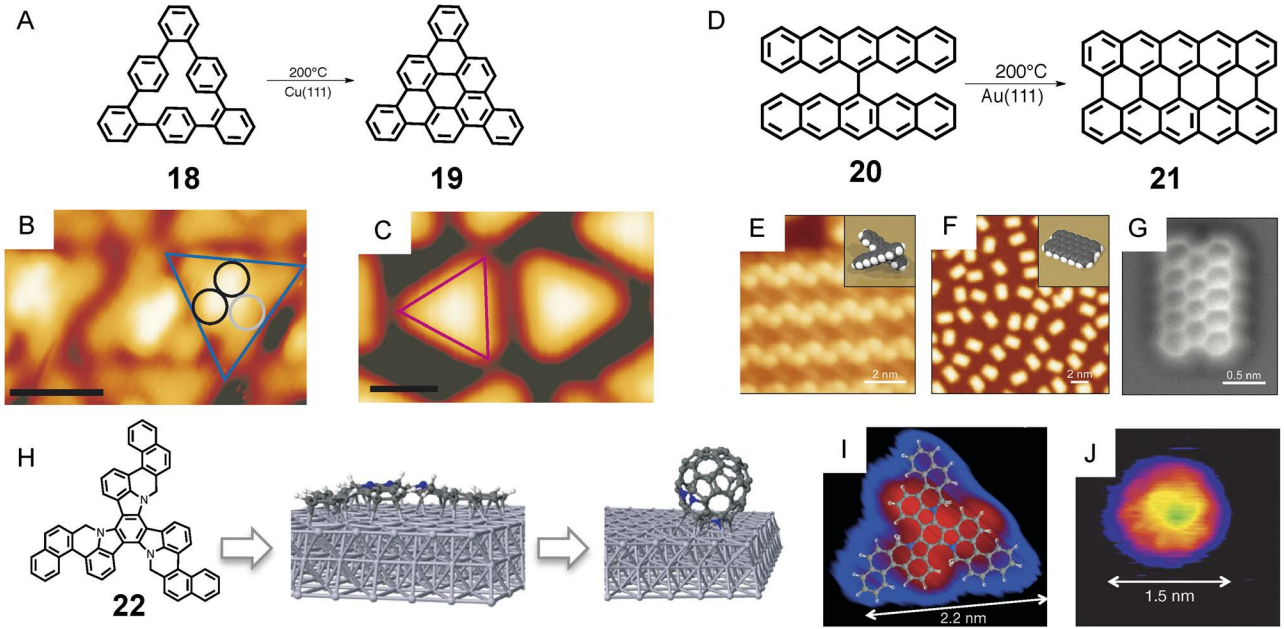

Figure 8.8 Cyclodehydrogenation reaction (A) of **18**, leading to the triangular nanographene **19**. STM images of **18** as deposited on Cu(111) (B) and after heating at 200 °C (C), showing the increase of planarity in the molecule (reproduced from ref. 88 with permission. Copyright © 2010, Rights Managed by Nature Publishing Group). Cyclodehydrogenation process (D) used to obtain peripentacene **21** from 6,6′-bipentacene **20**. LT-STM images of a Au(111) surface showing 6,6′-bipentacene (E) and peripentacenes (F) as obtained from the thermal cyclodehydrogenation reaction. nc-AFM (G) image of a single peripentacene molecule (reproduced from ref. 89 with permission. © 2015 WILEY-VCH Verlag GmbH & Co. KGaA, Weinheim). Cyclodehydrogenation (H) leading to the formation of triazafullerene from molecular precursor **22**. STM image (I) of **22** as deposited on the Pt(111) surface, with its molecular structure superimposed and after annealing (J) the surface at 750 K (reproduced from ref. 94 with permission. Copyright © 2008, Rights Managed by Nature Publishing Group).

View Online

Published on 15 November 2016 on http://pubs.rsc.org | doi:10.1039/9781782626626-00238

synthesize this molecule using traditional solution-based chemistry, fully cyclized peripentacene has been an elusive target and could never be isolated.[90,91] The great difficulty related to its synthesis is strictly connected to a combination of factors, such as its low solubility, its thermal and photochemical instability, and its predicted antiferromagnetic ground state.[92,93] Fischer and Crommie employed a strategy that exploits the direct on-surface-synthesis of peripentacene from the molecular precursor 6,6′-bispentacene **20** *via* a thermally-induced cyclodehydrogenation reaction. Precursor **20** is constituted by two pentacene subunits linked at the C6 position arranged in an orthogonal conformation. Full cyclization into peripentacene **21** from **20** was obtained by thermal annealing at 200 °C on a Au(111) surface (Figure 8.8(D)). LT-STM (7 K) showed the formation of a sub-monolayer of isolated molecular entities featuring rectangular structures with width, length and height comparable to the expected dimensions of peripentacene (Figure 8.8(E) and (F)). The unambiguous structural identification of peripentacene was confirmed by nc-AFM (Figure 8.8(G)), indicating the efficacy of this method to provide access to exotic aromatic compounds that remain inaccessible through conventional solution chemistry.

Surface-mediated cyclodehydrogenation can also be exploited for the construction of 3-D hydrocarbon structures. One of the most remarkable examples in this context is the work performed by Otero and co-workers on the synthesis of C_{60} and *N*-doped C_{60} from molecular precursors.[94,95] In a typical example, deposition of precursor **22** on a Pt(111) surface followed by subsequent sample annealing at 450 °C induced the surface reaction that yields the corresponding triazafullerene (Figure 8.8(H)). STM analysis of precursor **22** shows a triangular shape and a total apparent height of about 0.14 nm (Figure 8.8(I)). Following annealing of the substrate to 450 °C, a drastic change in the morphology of the adsorbate is observed showing the formation of spherical molecules with a height of 0.38 nm and a diameter of 1.5 nm (Figure 8.8(J)). The reduced height of the cyclized compound in combination with XPS data showing a chemisorption process directed by a N–Pt bond indicated a very strong interaction between the fullerene and the Pt(111), which could be at the origin of the high efficiency of this cyclization process.

8.3.3 Metal-Coordination Reactions

Metal coordination reactions are a powerful tool to organize organic aromatic molecules into complex architectures on surfaces. A pivotal prerequisite for the construction of ordered architectures on a metal surface is an appropriate molecular design of the precursor, which, among other things, should take into consideration the type of metal, the binding geometry and the type of ligand to be used. The types of ligands that have been used most extensively so far to construct metal–organic architectures on surfaces are hydroxyl groups, carboxylates, carbonitriles and pyridine moieties. Combination of these functionalities with the appropriate metal centres (generally Cu, Co, Au or Fe), and proper control of the environment conditions and of

View Online

Published on 15 November 2016 on http://pubs.rsc.org | doi:10.1039/9781782626626-00238

the surface used, has originated a wide plethora of 1-D and 2-D nanostructures on surfaces.[96–98]

From a structural point of view, one of the most versatile classes of aromatic molecules that can serve as an organic building block for the construction of extended 1-D and 2-D networks on surface are constituted by the derivatives of benzoic acid. In particular, dibenzoic acids due to their favourable geometry (which can allow the disposition of carboxylic moieties at 60, 120 and 180°) and to their synthetic accessibility and tunability are one of the most useful ligands for the construction of 2-D networks on surfaces. The group of Kern reported a classic example of the molecular organization of organic molecules based on carboxylic acid derivatives. He reported the synthesis of extended two-dimensional metal–organic coordination networks (2-D MOCN) based on the coordination events between 4,4′-di-(1,4-buta-1,3-dynyl)benzoic acid **23** and Fe atoms on both Ag(111) and Au(111) surfaces (Figure 8.9(A)–(C)).[99] LT-STM images showed that when a 1:1 mixture of **23** and Fe atoms was deposited simultaneously through organic molecular beam epitaxy on a Au(111) or Ag(111) surface, the formation of a fully reticulated network was observed (Figure 8.9(B) and (C)). The newly formed 2-D MOCN was homogeneously covering the entire surface, showing a high degree of insensitivity to microscopic surface features such as step-edges, terraces and other defects. High-resolution STM imaging revealed that each network node was comprised of four units of **23** coordinated through their carboxylate functionality to two Fe adatoms. In this configuration, two-carboxylate units bind the iron centres in a symmetric manner while each of the other two axial ligands forms bidentate bonds to one Fe atom.[100] As clearly visible from Figure 8.9(C), the MOCN features a high degree of conformational and geometric flexibility, which originates different types of polygonal assemblies such as squares, triangles and pentagons. Such diversity in orientation and framework structure was ascribed to the high conformational flexibility of the butadyine backbone. The authors consider such flexibility as the crucial factor conferring the high degree of substrate-error tolerance, which enables the construction of these large 2-D architectures.

Porphyrins are another important class of aromatic molecules, which have been extensively used as molecular building blocks for the construction of metal–organic architectures. Indeed, due to their peculiar structural properties (large π-surface, flat structure and high electron density and ease of sublimation) and potential application (*e.g.* light harvesting, catalysis, optics and nanoelectronic components), the possibility to construct porphyrin-based nanoarchitectures has become a field of tremendous investigation.[101] In this respect, several examples have emerged in which porphyrins peripherally decorated with appropriate ligands (such as nitrile and pyridine) have been organized on a metal surface using coordinative interactions.[102–106] In this context, the groups of Barth and Bonifazi were able to synthesize the first example of a 1-D coordination polymer featuring pyridyl-functionalized porphyrins as organic repetitive units.[107] The repetitive unit for this assembly, porphyrin **24**, bears two different types of substituents at its *meso* positions:

Published on 15 November 2016 on http://pubs.rsc.org | d

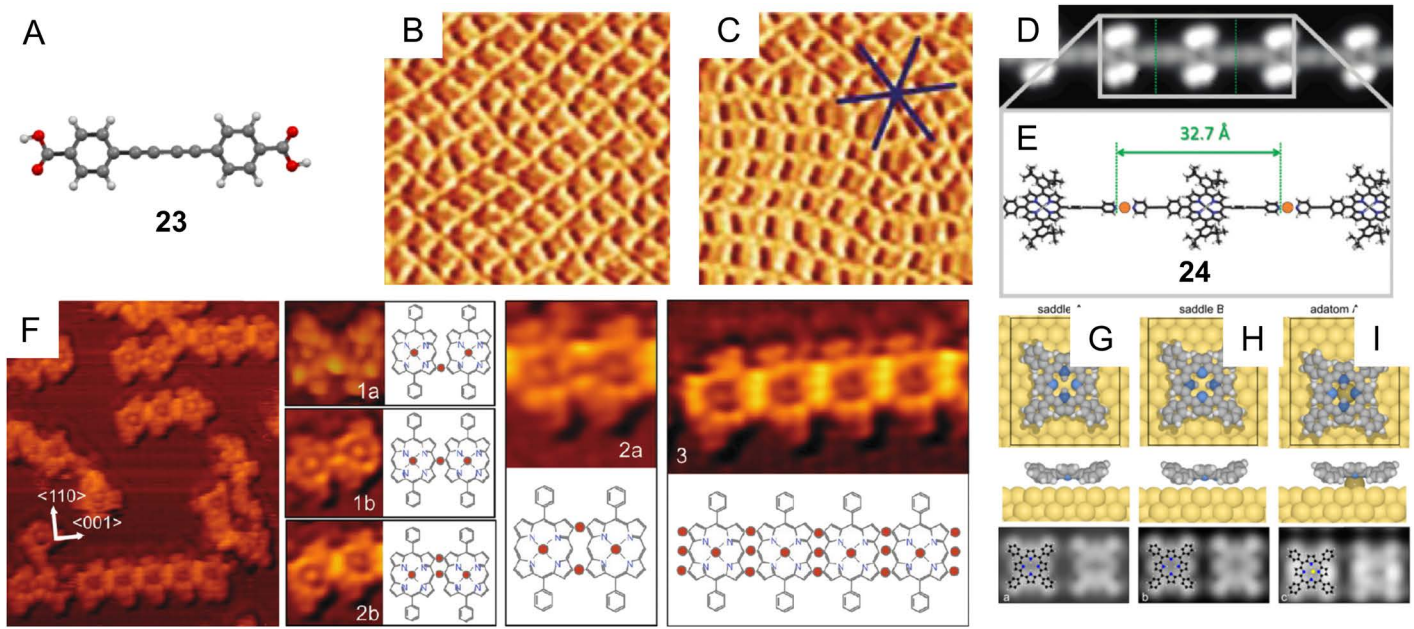

Figure 8.9 Chemical structure (A) of benzoic acid derivative **23** (H, white; C, grey; O, red). Representative STM images (B), (C) of **23**-Fe MOCNs on Au(111). Structural node (B) with the central di-iron binding motif represented and large-scale image (C) showing the different polygonal assemblies composing the network (reproduced with permission from ref. 99. Copyright © 2012 American Chemical Society). STM image (D) of a straight segment of the coordination polymer formed by porphyrin **24** on Cu(111). Graphic representation (E) of the linear pyridyl–Cu–pyridyl arrangement connecting three porphyrins **24** (reproduced with permission from ref. 107. Copyright © 2010 American Chemical Society). Representative STM (F) images showing the variety of linear metal–organic arrays obtained by thermal annealing of diphenylporphyrins on a Cu(110) surface at 620 K (reproduced with permission from ref. 108. Copyright © 2011 American Chemical Society). Calculated adsorption geometries (top and middle) and simulated STM images (bottom) of the two *trans* tautomers of free-base **TPP** (G) and (H) and of a **TPP** molecule (I) featuring a gold adatom in its macrocycle (reproduced with permission from ref. 110. Copyright © 2014 American Chemical Society).

View Online

Published on 15 November 2016 on http://pubs.rsc.org | doi:10.1039/9781782626626-00238

two phen-1,4-diyl-ethynyl-pyridyl (at the position C5 and C15) and two 3,5-di-*tert*-butylphenyl (at the C10 and C20 sites). Such structure leads to a linear alignment of the pyridyl group, which is involved in the coordination event. Additionally, the presence of triple bonds bridging the pyridines to the main porphyrin core allows a certain degree of flexibility. Upon deposition of **24** on Cu(111) or Ag(111) surfaces, the formation of metal–organic polymeric assemblies with a high degree of flexibility was observed by STM imaging (Figure 8.9(D)). Despite not being able to directly visualize the Pyr–Cu–Pyr coupling motif due to electronic effects, a measure of the distance between two N-atoms of subsequent pyridine moieties shows a spacing of 3.6 Å which is in good agreement with the presence of two metal–organic bonding interactions with a Cu–N distance of 1.8 Å (Figure 8.9(D)–(E)). The extreme flexibility that these metal–organic polymers displayed both on Cu(111) and on Ag(111) can be rationalized taking into consideration the enantiomeric conformation that the single units of **24** adopts along the chain. Manipulation experiments performed on isolated oligomeric strands of **24** showed the possibility to move and reversibly relocate the termini of the metal–organic assemblies, proving in this way their great mechanical stability and the high intrapolymer cohesion obtained through the Cu–N bond.

A very recent example of a monodimensional metal–organic architecture formed by porphyrin was provided by the group of Amabilino.[108] Using a library of *meso*-free porphyrins Amabilino and co-workers were able to construct 1-D metal organic co-assemblies by employing a process driven by C–H bond scission and the incorporation of Cu atoms in between the organic components (Figure 8.9(F)). Upon sublimation of the porphyrin on a Cu(110) surface and annealing at 380 °C, long and regular linear chains formed parallel to the [001] symmetry axis of the surface. Combined STM investigations, DFT simulations and temperature programmed desorption (TPD) experiments indicate that up to three Cu atoms are incorporated at the *meso*- free and beta positions on opposite sides of the porphyrin macrocycle, leading to highly regular linear arrays. Interestingly, TPD experiments showed that when free-base porphyrins were used, it was also possible to incorporate Cu atoms into the porphyrin macrocycle leading to an even further degree of structural complexity in the final nanostructure. It is noteworthy that this peculiar surface-mediated reactivity has no precedent in solution-based chemistry and therefore contributes to the development of novel synthetic routes for the construction of organometallic materials.

In the particular case of porphyrins, together with the construction of extended 1-D and 2-D architectures on surfaces, great interest has been dedicated by different groups to the investigation of the porphyrin metallation mechanism upon confinement on metallic surfaces.[109] Indeed, such a process constitutes a valid methodology to selectively tune and modify both the electronic and the structural properties of this family of compounds once deposited on a metallic surface.

In one of the latest efforts on this subject, the group of Grill was able to shed some further light on the interactions between tetraphenylporphyrin

View Online

Published on 15 November 2016 on http://pubs.rsc.org | doi:10.1039/9781782626626-00238

(**TPP**) and the gold adatoms present on an Au(111) surface.[110] Their combined STM-DFT study indicates that the presence of native gold adatoms on the Au(111) surface can induce a characteristic change in the LDOS of the porphyrins if the adatoms adsorb underneath and coordinate to it (Figure 8.9(G)–(I)). Prior to this study, the different appearance of isolated **TPP** molecules on the Au(111) surface was attributed to the difference in conformation adopted by the TPP once adsorbed on the metal surface. However, both DFT simulation and STS on isolated **TPP** molecules indicated that the apparent increase of molecular height (and increase in brightness) of some of the molecules was instead due to an electrostatic shift of the adsorbate-induced electronic states due to the presence of a gold adatom underneath the porphyrin macrocycle. Further experimental evidence of this theory was obtained by creating single adatoms on the Au(111) surface by STM tip-indentation in the proximity of a molecular island of **TPP**. As a consequence of this manipulation, an increase in the number of bright **TPP** molecules was found on the same island. Comparable results were also obtained by lateral manipulation of one of the bright **TPP**, detaching of the Au(111) adatoms in a reversible manner and inducing a drastic change in both the brightness of the porphyrin and in its STS spectra.

8.3.4 Graphene Nanoribbon Synthesis

In the last decade, graphene has risen as one of the most interesting nanomaterials due to its peculiar electronic, magnetic and optical properties.[111–115] Unfortunately, graphene exhibits semimetallic behaviour at room temperature, therefore its applications in semiconductor devices has been so far limited. On the other hand, monodimensional confinement of graphene into narrow ribbons (<10 nm) opens a band gap in graphene.[116–119] Precise manufacturing of graphene nanoribbons (GNRs) has become a topic of tremendous interest. Due to the extremely small width (<10 nm) necessary for a meaningful band gap to emerge in GNRs, surface-mediated bottom-up synthesis from molecular precursors has become one of the most promising synthetic routes.

Both theoretical and experimental works showed that the edge structure and width of GNRs are intimately linked with their electronic structure (Figure 8.10(A) and (B)).[117,120] In this context, straight GNRs featuring armchair edges (AGNRs, Figure 8.10(A)) should exhibit width-dependent semiconductor behaviour. On the other hand, zig-zag GNRs (ZGNR, Figure 8.10(A)) are predicted to possess semimetallic behaviour and spin-polarized edge states.[121–123] Additionally, more complex GNR backbones, such as chevron and cove-type GNRs (Figure 8.10(B)), have been designed and produced by surface-mediated synthesis and have been predicted to have interesting electronic, thermoelectric and optical properties.[124–126] To date, modulation of GNR width, edge structure and geometrical parameters using molecular precursors has been successfully utilized in order to tune their electronic properties.

View Online

Published on 15 November 2016 on http://pubs.rsc.org | doi:10.1039/9781782626626-00238

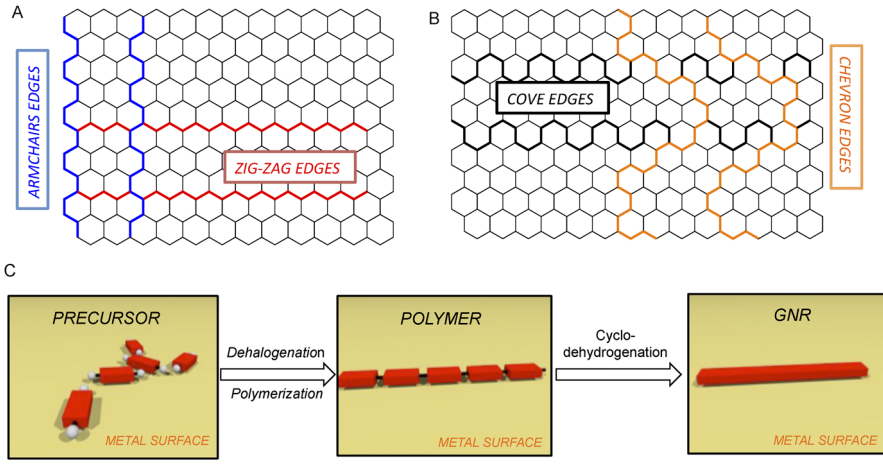

Figure 8.10 Schematic representations (A) and (B) of some of the different edge structures of atomically precise GNRs present in the literature. Schematic representation (C) of the process used for the synthesis of GNR on metal surfaces. A halogenated molecular precursor is deposited on a metal surface (step 1) and thermally annealed to induce C–X bond homolytic cleavage with consequent step growth polymerization (step 2). Finally, thermal cyclodehydrogenation of the resulting polymer (step 3) leads to formation of the GNR.

The typical procedure for the preparation of GNRs through surface-mediated synthesis is depicted in Figure 8.10(C). In the first step, an appropriately designed halogenated precursor is deposited on a metal surface (*e.g.* Au, Ag or Cu) and subsequently heated to induce the homolytic cleavage of the C–X bond. In the following step, the diradical species formed are free to diffuse on the metallic surface and polymerize through a step-growth radical polymerization. Total graphitization of the resulting polymer is then achieved by a thermally-induced cyclodehydrogenation reaction, which leads to the final GNR structure. The first example of atomically precise GNRs produced by surface-mediated synthesis was provided by the groups of Mullen and Fasel in 2009.[127] In their pioneering work, the authors used two different types of halogenated molecular precursors to prepare the very first examples of ultranarrow armchair (AGNRs) and chevron type GNRs. Preparation of 7-AGNRs (where 7 is the number of carbon atoms composing the width of the GNR) was achieved using 10,10′-dibromo-9,9′-bianthryl **25** as a dihalogenated precursor (Figure 8.11(A)–(C)). In a typical experiment (Figure 8.11(A)), deposition of **25** on a Au(111) or Ag(111) surface held at 200 °C induced the homolytic cleavage of its halogen atoms and the formation of surface-stabilized diradical monomers. The biradical species are able to diffuse across the surface and undergo radical step-growth polymerization to form linear polyanthrylene oligomers (***poly*-25**). Finally, a surface-assisted thermal cyclodehydrogenation at 400 °C completes the graphitization of the

View Online

Published on 15 November 2016 on http://pubs.rsc.org | doi:10.1039/9781782626626-00238

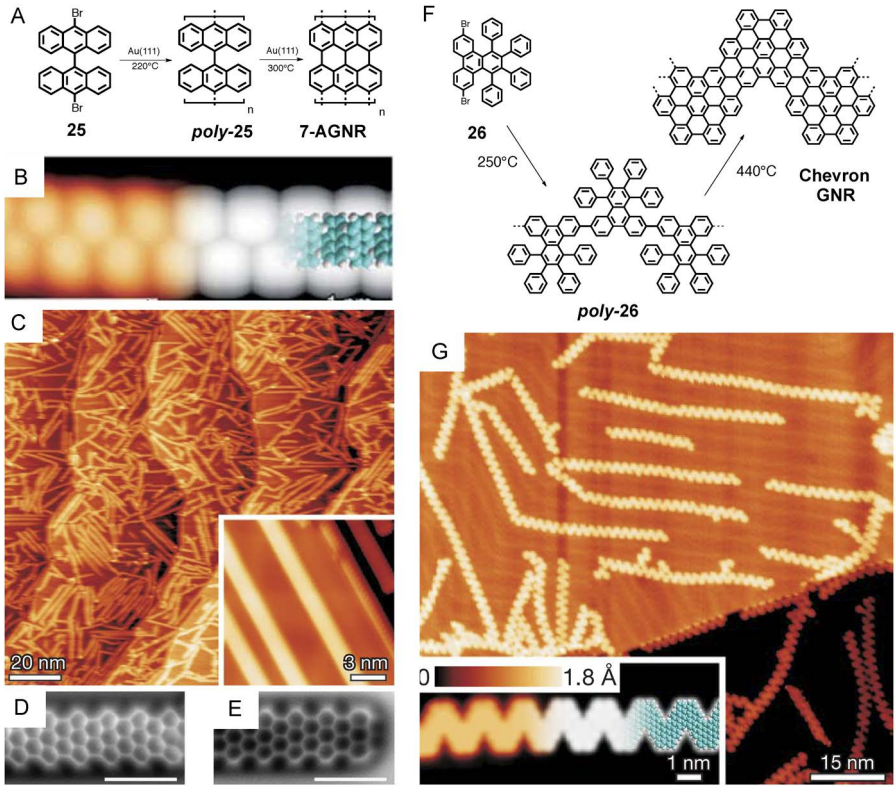

Figure 8.11 Surface-mediated synthesis (A) of **7-AGNR** from precursor **25**. LT-STM topography (B) of an isolated polyanthrylene chain (***poly*-25**) on Au(111), its DFT-based simulation (right) and an overlaid model of the polymer (blue, carbon; white, hydrogen). LT-STM (C) of **7-AGNR** as obtained after cyclodehydrogenation on Au(111) at 400 °C (reproduced from ref. 127 with permission from The Nature Publishing Group). nc-AFM image of the side (D) and the termini (E) of 7-AGNR (reproduced from ref. 135 with permission. Copyright © 2010, Rights Managed by Nature Publishing Group). Surface-mediated synthesis (F) of chevron GNRs from precursor **26**. LT-STM (G) of chevron GNR on Au(111). Inset: STM image of an isolated chevron GNR (left), its DFT simulation (middle) and 3D-model (right) (reproduced from ref. 127 with permission. Copyright © 2013, Rights Managed by Nature Publishing Group).

whole structure, establishing an extended aromatic system. The STM image of the polyanthrylene oligomers obtained (Figure 8.11B) shows alternating protrusions with a periodicity of 0.86 nm, in agreement with the periodicity of the bianthryl core (0.85 nm). Such a configuration of the polymeric chains is dictated by the steric hindrance between the hydrogen atoms in the *peri*-position of adjacent anthracene units, resulting in the periodic tilting of successive anthracene units with respect to the metal surface. 7-AGNR

View Online

Published on 15 November 2016 on http://pubs.rsc.org | doi:10.1039/9781782626626-00238

preparation was then completed by annealing the sample at 400 °C, which induced the intramolecular cyclodehydrogenation of the polymeric chains. STM imaging (Figure 8.11(C)) and simulation revealed that the resulting 7-AGNRs possess half the periodicity of the polymeric chains (0.42 nm) and a consistent reduction of their apparent height of 0.18 nm.

When the same process was applied to tetraphenyltriphenylene precursor **26**, chevron-type GNRs were obtained (Figure 8.11(F) and (G)). In this case, colligation of the dehalogenated monomers on Au(111) was performed at 250 °C, yielding oligomeric chains that were fully cyclodehydrogenated into GNRs by further heating at 440 °C. STM imaging showed that the resulting chevron GNRs possessed a periodicity of 1.70 nm and an armchair edge structure (Figure 8.11(G)).

Inspired by this pioneering work, interest in surface-mediated synthesis of GNRs has greatly expanded.[128–134] **7-AGNRs**' structure and interactions with the metal surface were elucidated by the groups of Swart and Liljeroth.[135] Using a CO-functionalized tip, the authors were able to achieve atomically resolved nc-AFM images of isolated **7-AGNRs**, as obtained from the procedure previously reported by Fasel and co-workers. Consistent with previous STM investigations, constant-height AFM imaging showed GNRs featuring regular armchair edges, alternating rows of two and three fused benzene rings and zig-zag termination at both ends of the GNR (Figure 8.11(D) and (E)). This highly sensitive imaging method was able to resolve structural defects (despite their very low amounts) that were not possible to visualize by conventional STM, underlining the importance of acquiring both STM and AFM data to comprehensively understand the structure of these complex nanomaterials. Additionally, the authors were able to contact an isolated GNR to the gold substrate by single atom chemical bonding. The selective chemical bonding was achieved by removing the hydrogen atom located at one of the zig-zag ends by locally applying a high voltage pulse. Combined nc-AFM and STM showed that the direct GNR–metal bonding was not affecting the bulk electronic structure of the **7-AGNR** but was instead causing a very strong suppression of its electron–vibron (e–v) coupling.

Computational studies have also pointed out the crucial role of the metal surface in the mechanism of GNR formation, especially during the cyclodehydrogenation process.[136] DFT level transition-state calculations on the cyclodehydrogenation reaction mechanism of **7-AGNRs** showed that the Au(111) surface is acting as a catalyst during this crucial step. Indeed, the most favourable reaction pathways calculated showed the concerted transfer of two hydrogen atoms from the anthracene moieties to the gold substrate, followed by a separate desorption in a vacuum and the formation of a new C–C bond. The cyclodehydrogenation reaction was predicted to be most likely to occur initially at one of the termini of the polyanthryl oligomer and to propagate in a domino-like fashion throughout the polymer backbone.

A general strategy, which has been used to tune the electronic structure of GNRs, involves doping GNRs with heteroatoms, leading to the development of GNRs in which carbon atoms have been selectively replaced by

View Online

Published on 15 November 2016 on http://pubs.rsc.org | doi:10.1039/9781782626626-00238

heteroatoms at predetermined positions.[137–140] The most extensively studied class of GNRs subjected to doping investigations is the chevron GNR.[141–144] This is achieved by substitution of the C–H group composing the armchair edges of the ribbon with sp^2 hybridized nitrogen atoms. A typical example of molecular precursors used for the preparation of N-doped chevron GNRs is depicted in Figure 8.12(A). Surface-mediated polymerization of bis-pyrimidine unit **27** followed by cyclodehydrogenation to yield N-doped GNRs was reported both by the group of Sinitskii and by the group of Fasel.[141,142,144] Through the combined use of different microscopy techniques (*e.g.* STM, HR-TEM and optical microscopy), the group of Sinitskii was able to show that substitutional doping with nitrogen atoms was able to trigger a self-assembly process both on metallic surfaces and in the solid state. Whereas undoped chevron GNRs showed no detectable secondary arrangements, nitrogen doped GNRs formed by thermal annealing of **27** on Au(111) showed the formation of 2-D assemblies in which isolated GNRs were arranged edge to edge (Figure 8.12(B)). Such an arrangement could be potentially explained by the formation of multiple hydrogen bond interactions between the nitrogen and the C–H groups of adjacent GNRs. Despite the many examples of doped chevron GNRs, the periodic incorporation of heteroatoms into straight armchair edge GNRs remains a considerable challenge. In very recent work, Fischer and Crommie and independently the group of Kawai published the first example of straight $N = 7$ AGNRs incorporating boron atoms.[145,146] Submitting molecular precursor **28** to the surface-mediated polymerization/cyclodehydrogenation sequence (Figure 8.12(C) and (D)) produced **7-AGNRs** featuring a regioregular pattern of boron atoms along the central backbone of the ribbon. LT-STM (13 K) imaging of a Au(111) sample on which **28** was firstly polymerized at 220 °C and then fully cyclized by further thermal treatment at 330 °C showed the formation of GNRs featuring a characteristic longitudinal stripe pattern with a periodicity corresponding to the distance between the expected position of the boron atoms. First principles calculations, aimed to better understand the effect of the boron doping on the electronic structure of the **7-AGNR**, revealed the presence of a new acceptor band (0.8 eV above the VB maximum), which shows a significant contribution (10%) from the boron atom and an energy comprised in the gap of the undoped **7-AGNR**. As a consequence of the doping, the theoretically predicted band gap (0.8 eV) of the boron doped **7-AGNR** becomes considerably smaller than the one of the undoped **7-AGNRs** (~2.1 eV) calculated with the same method. Experimental confirmation of this predicted electronic structure was obtained through dI/dV mapping, which showed the existence of LDOS along the backbone of the ribbon at an operative voltage V_s = 1.0 V corresponding to the conduction band. Such results, which strongly differ from the mapping of undoped **7-AGNR**, provide additional evidence that the substitution of carbon atoms with trigonal planar boron atoms is introducing a new band in the DOS of the **7-AGNR** modifying drastically its electronic structure.

A further evolution on the construction of GNR-based architecture using both pristine and nitrogen doped GNRs was performed by the groups of Müllen and Fasel.[144] By co-deposition of tetraphenylene unit **26** and the nitrogen

Published on 15 November 2016 on http://pubs.rsc.org | d

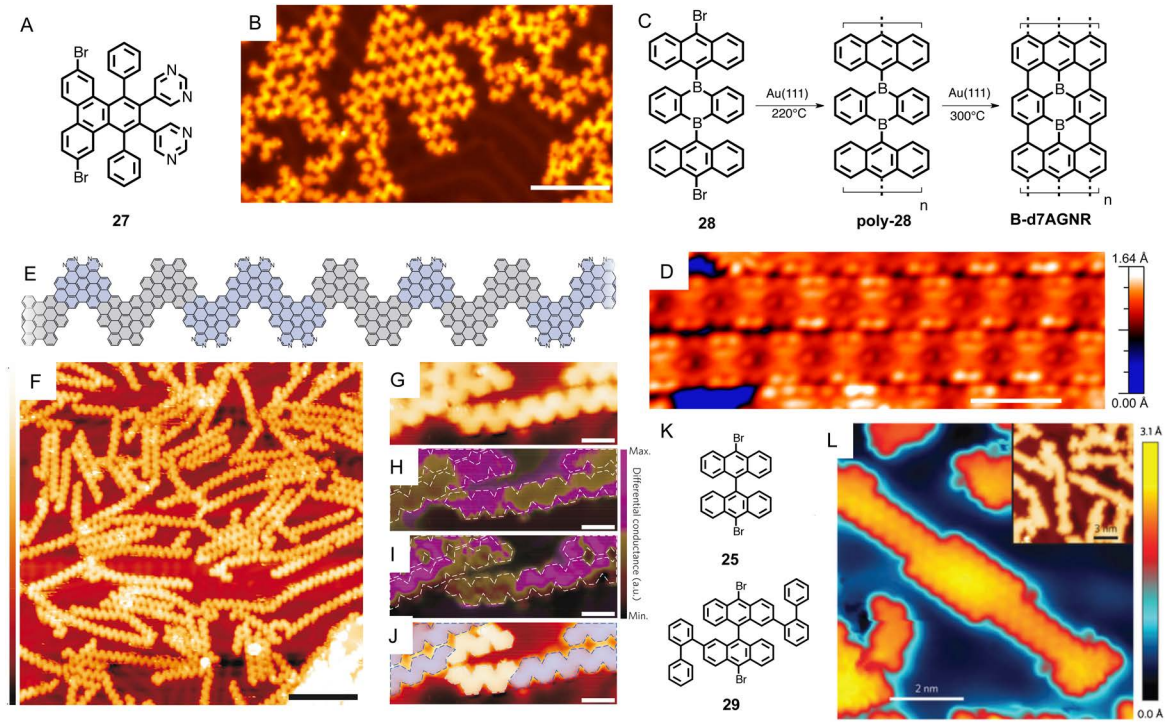

Figure 8.12 Molecular structure (A) of bispyrimidine monomer **27**. LT-STM images (B) of nitrogen doped chevron GNRs obtained from **27** on Au(111) (reproduced with permission from ref. 142. Copyright © 2015 American Chemical Society). Schematic representations (C) of the surface-mediated synthesis of boron doped 7-**AGNR** starting from precursor **28** and its LT-STM topography (D) (reproduced with permission from ref. 145. Copyright © 2015 American Chemical Society). Structural representation (E) of a chevron nanoribbon combining doped (blue) and undoped (grey) segments, and a large scale STM image (F) of the GNR heterostructures on Au(111). Smaller scale (G) STM images of a GNR heterojunction and the corresponding differential conductance dI/dV maps taken at bias voltages of U = −0.35 V (H) and −1.65 V (I) respectively, showing two chemically different ribbon segments (J) which are highlighted in blue (scale bar = 2 nm) (reproduced from ref. 144 with permission. Copyright © 2014, Rights Managed by Nature Publishing Group). Molecular structures (K) of precursors **25** and **29**, used for the construction of 7–13 GNR heterojunction. LT-STM topographic image (L) of a 7–13 GNR heterojunction (inset: larger scale showing the sample composition and multiple GNR heterojunctions) (reproduced from ref. 147 with permission. Copyright © 2015, Rights Managed by Nature Publishing Group).

View Online

Published on 15 November 2016 on http://pubs.rsc.org | doi:10.1039/9781782626626-00238

doped monomer **27** on a Au(111) surface and subsequent thermal polymerization/cyclodehydrogenation synthesis, the authors were able to grow GNR heterostructures composed of both pristine hydrocarbon precursors and their nitrogen-substituted equivalent. LT-STM imaging and dI/dV mapping of the resulting architecture showed the formation of GNRs composed of a statistical mixture of doped and undoped segments (Figure 8.12(E)–(J)). A combination of DFT calculations and dI/dV mapping of this GNR heterostructure showed the presence of a band shift of 0.5 eV at the interface between the doped and undoped section of the chevron GNRs and an electric field of 2×10^8 Vm^{-1}. In particular, DFT computations showed a significant downshift of 0.45 eV and 0.55 eV for the valence band and conduction band as passing from the undoped to the nitrogen doped section of the GNR, indicating a possible staggered band-gap configuration.

Another type of hybrid architecture based on GNRs recently demonstrated by the Fischer and Crommie group exploits the different electronic properties of armchair GNRs featuring different widths.[147] According to their predicted electronic behaviour, armchair GNRs can be classified into three main groups, $N = 3p$, $N = 3p + 1$ and $N = 3p + 2$, where p is an integer and N is the number of carbon atoms across the GNR width.[118,120,148] All families of GNRs are predicted to have a pronounced band gap, which scales inversely with the ribbon width, with $N = 3p + 2$ having the smallest predicted band gaps.[149] Due to the great variation in band gaps between GNRs of different families, the construction of hybrid GNR architectures featuring sections of different widths has the potential to be an extremely promising method to fabricate semiconductor heterostructures that could be used to perform processes such as resonant tunnelling and solar energy conversion.

GNR-based hetero junctions were fabricated by combining two different types of molecular building blocks: bisanthracene derivatives **25** and **29** (Figure 8.12(K)). These molecules, which are precursors for $N = 7$ and $N = 13$ armchair GNRs, were sublimed onto a Au(111) surface and submitted to surface-mediated polymerization at 420 K and to a subsequent cyclodehydrogenation step at 640 K. A typical architecture obtained through this method is depicted in Figure 8.12(L). As expected, LT-STM images show 1-D graphitic structures composed of sections featuring different widths, in which the narrower segments (1.3 ± 0.1 nm in width) are made of covalently bonded monomers of **25** ($N = 7$) and the wider segments (1.9 ± 0.2 nm in width) consist of bonded monomers of **29** ($N = 13$). Interestingly, a sub-nanometer scale investigation of the electronic properties of these heterojunctions by STS and dI/dV mapping, in combination with DFT simulation was able to show that the band alignment in the 7/13-GNR heterojunction can be considered very similar to the one that conventionally is associated with a type I semiconductor junction. Such findings could potentially pave the way to the possible application of this type of junction for the construction of graphene-based quantum dots and band gap-modulated semiconductor junctions smaller than the ones obtainable through lithographic methods.

Very recently, more complex GNR topologies have been developed through surface-mediated synthesis. The group of Mullen has reported

View Online

Published on 15 November 2016 on http://pubs.rsc.org | doi:10.1039/9781782626626-00238

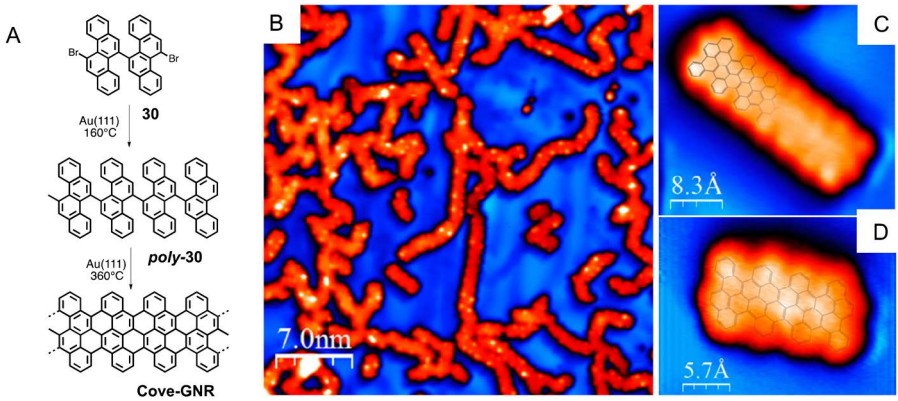

Figure 8.13 Schematic representations (A) of the surface-mediated synthesis of cove-edged GNRs starting from chrysene derivative **30**. Long-range (B) and high-resolution (C) and (D) STM images of cove-edged GNRs as obtained after cyclodehydrogenation of poly-chrysene oligomers (a schematic model is overlayed for clarity) (reproduced with permission from ref. 150. Copyright © 2015 American Chemical Society).

the fabrication of cove type-GNRs through surface-mediated synthesis. In this case, the formation of cove-edged GNR was obtained through surface-mediated polymerization/cyclodehydrogenation of the dibrominated chrysene derivative **30** on Au(111) at 160 °C and 360 °C respectively (Figure 8.13).[150] Interestingly, when similar types of targets were attempted using conventional solution synthesis (Ullmann type polymerization and ($FeCl_3$) or DDQ/trifluoromethanesulfonic acid as the Lewis acid/oxidant), only very short ribbons were obtained (up to octamers). Such a low degree of polymerization can be rationalized taking into consideration the very high steric hindrance during the coupling reaction between the C–H groups in the chrysene "bay-positions" of **30**. On the other hand, using a surface-mediated approach, it was possible to increase the length of the GNRs up to 20 nm. Indeed, monomers on surfaces are confined in just two dimensions (as opposed to the three dimensions of the solution environment), which could potentially increase the statistical probability of monomers reacting with each other to form longer oligomers. In addition, as seen in previous examples, the Au(111) surface could potentially play a role in terms of the catalytic activity necessary to drive the polymerization and cyclodehydrogenation reaction to completion, favouring in this way the formation of longer oligomeric structures.

Very characteristic of this new type of ribbon is the fact that, as highlighted by both X-ray crystal structure of the dimers obtained in solution and DFT simulation, they do not possess a completely planar structure. Indeed, due to steric repulsion, the benzenoid rings in the cove region of the GNR adopt alternating "up–down" conformation, which can deviate from planarity the GNR carbon framework.

View Online

Published on 15 November 2016 on http://pubs.rsc.org | doi:10.1039/9781782626626-00238

8.4 Conclusions

The most important advancements over the last decades regarding structural investigations and reactivity of aromatic molecules on crystalline surfaces have been discussed in this chapter. The invention and the continuing development of scanning probe microscopy techniques allow for the investigation of isolated aromatic molecules adsorbed onto inorganic surfaces with a sub-molecular level of resolution. Techniques such as STM, STHM, nc-AFM and KPFM are extremely valuable for understanding and elucidating the structural and electronic properties of planar aromatic molecules adsorbed on surfaces.

The first section of this chapter introduced the reader to the basic principles behind these types of scanning probe techniques and described their use in the investigations of different aromatic molecules. Applications of different probe techniques for the investigation of important properties such as atomic interconnectivity, bond-order evaluation and sub-molecular charge distribution have been discussed.

In the second part of the chapter, reactivity of aromatic molecules on metallic surfaces was discussed presenting the principal classes of reactions that have been developed. The construction of polymeric systems, 2-D networks, extended polyaromatic hydrocarbons and graphene derivatives (*i.e.* graphene nanoribbons) starting from aromatic molecular precursors have been detailed. Particular emphasis has been placed on the role of the surface during the different reactions and the differences between the reactivity that the same molecules can have if submitted to analogous "solution-based" reactions. Following these many examples, it can be concluded that metal surface mediated synthesis can be efficiently employed to construct highly conjugated organic architectures, which can be investigated with high accuracy by SPM techniques.

References

1. J. M. MacLeod and F. Rosei, *Small*, 2014, **10**, 1038–1049.
2. J. W. Colson, A. R. Woll, A. Mukherjee, M. P. Levendorf, E. L. Spitler, V. B. Shields, M. G. Spencer, J. Park and W. R. Dichtel, *Science*, 2011, **332**, 228–231.
3. S. A. DiBenedetto, A. Facchetti, M. A. Ratner and T. J. Marks, *Adv. Mater.*, 2009, **21**, 1407–1433.
4. E. Goiri, P. Borghetti, A. El-Sayed, J. E. Ortega and D. G. de Oteyza, *Adv. Mater.*, 2016, **28**, 1340–1368.
5. N. Katsonis, M. Lubomska, M. M. Pollard, B. L. Feringa and P. Rudolf, *Prog. Surf. Sci.*, 2007, **82**, 407–434.
6. J. Mendez, M. F. Lopez and J. A. Martin-Gago, *Chem. Soc. Rev.*, 2011, **40**, 4578–4590.
7. H. Klauk, *Chem. Soc. Rev.*, 2010, **39**, 2643–2666.
8. J. K. Gimzewski and C. Joachim, *Science*, 1999, **283**, 1683–1688.

View Online

Published on 15 November 2016 on http://pubs.rsc.org | doi:10.1039/9781782626626-00238

9. P. Sundberg and M. Karppinen, *Beilstein J. Nanotechnol.*, 2014, **5**, 1104–1136.
10. T. Bjornholm, T. Hassenkam and N. Reitzel, *J. Mater. Chem.*, 1999, **9**, 1975–1990.
11. S. R. Forrest, *Chem. Rev.*, 1997, **97**, 1793–1896.
12. D. B. Hall, P. Underhill and J. M. Torkelson, *Polym. Eng. Sci.*, 1998, **38**, 2039–2045.
13. H. Alves, A. S. Molinari, H. Xie and A. F. Morpurgo, *Nat. Mater.*, 2008, **7**, 574–580.
14. K. Norbert, *J. Phys.: Condens. Matter*, 2008, **20**, 184008.
15. G. Vasseur, Y. Fagot-Revurat, M. Sicot, B. Kierren, L. Moreau, D. Malterre, L. Cardenas, G. Galeotti, J. Lipton-Duffin, F. Rosei, M. Di Giovannantonio, G. Contini, P. Le Fevre, F. Bertran, L. Liang, V. Meunier and D. F. Perepichka, *Nat. Commun.*, 2016, **7**, 10235.
16. K. Müller, A. P. Seitsonen, T. Brugger, J. Westover, T. Greber, T. Jung and A. Kara, *J. Phys. Chem. C*, 2012, **116**, 23465–23471.
17. L. Schulz, L. Nuccio, M. Willis, P. Desai, P. Shakya, T. Kreouzis, V. K. Malik, C. Bernhard, F. L. Pratt, N. A. Morley, A. Suter, G. J. Nieuwenhuys, T. Prokscha, E. Morenzoni, W. P. Gillin and A. J. Drew, *Nat. Mater.*, 2011, **10**, 39–44.
18. J. H. Burroughes, D. D. C. Bradley, A. R. Brown, R. N. Marks, K. Mackay, R. H. Friend, P. L. Burns and A. B. Holmes, *Nature*, 1990, **347**, 539–541.
19. K. T. Kamtekar, A. P. Monkman and M. R. Bryce, *Adv. Mater.*, 2010, **22**, 572–582.
20. A. Pogantsch, S. Rentenberger, G. Langer, J. Keplinger, W. Kern and E. Zojer, *Adv. Funct. Mater.*, 2005, **15**, 403–409.
21. L. Zhai, S. I. Khondaker, J. Thomas, C. Shen and M. McInnis, *Nano Today*, 2014, **9**, 705–721.
22. T. W. Kelley, P. F. Baude, C. Gerlach, D. E. Ender, D. Muyres, M. A. Haase, D. E. Vogel and S. D. Theiss, *Chem. Mater.*, 2004, **16**, 4413–4422.
23. C. Reese, M. Roberts, M.-m. Ling and Z. Bao, *Mater. Today*, 2004, **7**, 20–27.
24. S. Z. Bisri, C. Piliego, J. Gao and M. A. Loi, *Adv. Mater.*, 2014, **26**, 1176–1199.
25. K. Oura, V. G. Lifshits, A. A. Saranin, A. V. Zotov and M. Katayama, *Surface Science, An Introduction*, Springer, Berlin, 2003.
26. G. R. Binnig and H. Rohrer, *IBM J. Res. Dev.*, 1986, **30**, 355–369.
27. C. Julian Chen, *Introduction to Scanning Tunneling Microscopy: Second Edition*, Oxford University Press, 2007.
28. A. Della Pia and G. Costantini, in *Encyclopedia of Nanotechnology*, ed. B. Bhushan, Springer, Netherlands, 2012, pp. 2301–2313.
29. S. Kano, T. Tada and Y. Majima, *Chem. Soc. Rev.*, 2015, **44**, 970–987.
30. M. S. J. Marshall and M. R. Castell, *Chem. Soc. Rev.*, 2014, **43**, 2226–2239.
31. H. Arakawa, K. Umemura and A. Ikai, *Nature*, 1992, **358**, 171–173.
32. P. G. Arscott and V. A. Bloomfield, *Trends Biotechnol.*, 1990, **8**, 151–156.
33. L. Gross, *Nat. Chem.*, 2011, **3**, 273–278.

View Online

Published on 15 November 2016 on http://pubs.rsc.org | doi:10.1039/9781782626626-00238

34. R. Temirov, S. Soubatch, O. Neucheva, A. C. Lassise and F. S. Tautz, *New J. Phys.*, 2008, **10**, 053012.
35. C. Weiss, C. Wagner, R. Temirov and F. S. Tautz, *J. Am. Chem. Soc.*, 2010, **132**, 11864–11865.
36. S. Morita, F. J. Giessibl and R. Wiesendanger, *Noncontact Atomic Force Microscopy*, Springer, 2009.
37. F. J. Giessibl, *Appl. Phys. Lett.*, 1998, **73**, 3956–3958.
38. L. Gross, F. Mohn, N. Moll, P. Liljeroth and G. Meyer, *Science*, 2009, **325**, 1110–1114.
39. L. Gross, B. Schuler, F. Mohn, N. Moll, J. Repp and G. Meyer, *Noncontact Atomic Force Microscopy*, Springer, 2015, vol. 3, pp. 223–246.
40. N. Moll, B. Schuler, S. Kawai, F. Xu, L. Peng, A. Orita, J. Otera, A. Curioni, M. Neu, J. Repp, G. Meyer and L. Gross, *Nano Lett.*, 2014, **14**, 6127–6131.
41. L. Gross, F. Mohn, N. Moll, B. Schuler, A. Criado, E. Guitián, D. Peña, A. Gourdon and G. Meyer, *Science*, 2012, **337**, 1326–1329.
42. W. I. F. David, R. M. Ibberson, J. C. Matthewman, K. Prassides, T. J. S. Dennis, J. P. Hare, H. W. Kroto, R. Taylor and D. R. M. Walton, *Nature*, 1991, **353**, 147–149.
43. K. Hedberg, L. Hedberg, D. S. Bethune, C. A. Brown, H. C. Dorn, R. D. Johnson and M. De Vries, *Science*, 1991, **254**, 410–412.
44. F. Mohn, L. Gross, N. Moll and G. Meyer, *Nat. Nanotechnol.*, 2012, **7**, 227–231.
45. B. Schuler, G. Meyer, D. Peña, O. C. Mullins and L. Gross, *J. Am. Chem. Soc.*, 2015, **137**, 9870–9876.
46. Q. Fan, J. M. Gottfried and J. Zhu, *Acc. Chem. Res.*, 2015, **48**, 2484–2494.
47. G. Franc and A. Gourdon, *Phys. Chem. Chem. Phys.*, 2011, **13**, 14283–14292.
48. A. Gourdon, *Angew. Chem., Int. Ed.*, 2008, **47**, 6950–6953.
49. X. Zhang, Q. Zeng and C. Wang, *Nanoscale*, 2013, **5**, 8269–8287.
50. F. Klappenberger, Y.-Q. Zhang, J. Björk, S. Klyatskaya, M. Ruben and J. V. Barth, *Acc. Chem. Res.*, 2015, **48**, 2140–2150.
51. B. Cirera, Y.-Q. Zhang, J. Björk, S. Klyatskaya, Z. Chen, M. Ruben, J. V. Barth and F. Klappenberger, *Nano Lett.*, 2014, **14**, 1891–1897.
52. A. Riss, S. Wickenburg, P. Gorman, L. Z. Tan, H.-Z. Tsai, D. G. de Oteyza, Y.-C. Chen, A. J. Bradley, M. M. Ugeda, G. Etkin, S. G. Louie, F. R. Fischer and M. F. Crommie, *Nano Lett.*, 2014, **14**, 2251–2255.
53. R. Bates, *Organic Synthesis Using Transition Metals*, John Wiley & Sons, Ltd, 2012, pp. i–xv.
54. J. F. Hartwig, *Organotransition Metal Chemistry, from Bonding to Catalysis*, University Science Books, New York, 2010.
55. Y.-Q. Zhang, N. Kepčija, M. Kleinschrodt, K. Diller, S. Fischer, A. C. Papageorgiou, F. Allegretti, J. Björk, S. Klyatskaya, F. Klappenberger, M. Ruben and J. V. Barth, *Nat. Commun.*, 2012, **3**, 1286.
56. J. Liu, P. Ruffieux, X. Feng, K. Mullen and R. Fasel, *Chem. Commun.*, 2014, **50**, 11200–11203.

View Online

Published on 15 November 2016 on http://pubs.rsc.org | doi:10.1039/9781782626626-00238

57. F. Bebensee, C. Bombis, S.-R. Vadapoo, J. R. Cramer, F. Besenbacher, K. V. Gothelf and T. R. Linderoth, *J. Am. Chem. Soc.*, 2013, **135**, 2136–2139.
58. O. Díaz Arado, H. Mönig, H. Wagner, J.-H. Franke, G. Langewisch, P. A. Held, A. Studer and H. Fuchs, *ACS Nano*, 2013, **7**, 8509–8515.
59. J. Eichhorn, D. Nieckarz, O. Ochs, D. Samanta, M. Schmittel, P. J. Szabelski and M. Lackinger, *ACS Nano*, 2014, **8**, 7880–7889.
60. L. Grill, M. Dyer, L. Lafferentz, M. Persson, M. V. Peters and S. Hecht, *Nat. Nanotechnol.*, 2007, **2**, 687–691.
61. M. Bieri, M.-T. Nguyen, O. Gröning, J. Cai, M. Treier, K. Aït-Mansour, P. Ruffieux, C. A. Pignedoli, D. Passerone, M. Kastler, K. Müllen and R. Fasel, *J. Am. Chem. Soc.*, 2010, **132**, 16669–16676.
62. G. Eder, E. F. Smith, I. Cebula, W. M. Heckl, P. H. Beton and M. Lackinger, *ACS Nano*, 2013, **7**, 3014–3021.
63. L. Ferrighi, I. Píš, T. H. Nguyen, M. Cattelan, S. Nappini, A. Basagni, M. Parravicini, A. Papagni, F. Sedona, E. Magnano, F. Bondino, C. Di Valentin and S. Agnoli, *Chem.–Eur. J.*, 2015, **21**, 5826–5835.
64. D. R. Lide, *Handbook of Chemistry and Physics 90th edn*, CRC Press, 2010.
65. L. Lafferentz, V. Eberhardt, C. Dri, C. Africh, G. Comelli, F. Esch, S. Hecht and L. Grill, *Nat. Chem.*, 2012, **4**, 215–220.
66. T. Dienel, J. Gómez-Díaz, A. P. Seitsonen, R. Widmer, M. Iannuzzi, K. Radican, H. Sachdev, K. Müllen, J. Hutter and O. Gröning, *ACS Nano*, 2014, **8**, 6571–6579.
67. Y. Jin, C. Yu, R. J. Denman and W. Zhang, *Chem. Soc. Rev.*, 2013, **42**, 6634–6654.
68. S. J. Rowan, S. J. Cantrill, G. R. L. Cousins, J. K. M. Sanders and J. F. Stoddart, *Angew. Chem., Int. Ed.*, 2002, **41**, 898–952.
69. A. Ciesielski, M. El Garah, S. Haar, P. Kovaříček, J.-M. Lehn and P. Samorì, *Nat. Chem.*, 2014, **6**, 1017–1023.
70. J. Plas, D. Waghray, J. Adisoejoso, O. Ivasenko, W. Dehaen and S. De Feyter, *Chem. Commun.*, 2015, **51**, 16338–16341.
71. X.-H. Liu, Y.-P. Mo, J.-Y. Yue, Q.-N. Zheng, H.-J. Yan, D. Wang and L.-J. Wan, *Small*, 2014, **10**, 4934–4939.
72. L. Xu, X. Zhou, Y. Yu, W. Q. Tian, J. Ma and S. Lei, *ACS Nano*, 2013, **7**, 8066–8073.
73. Y. Yu, J. Sun and S. Lei, *J. Phys. Chem. C*, 2015, **119**, 16777–16784.
74. C.-Z. Guan, D. Wang and L.-J. Wan, *Chem. Commun.*, 2012, **48**, 2943–2945.
75. S. Kandambeth, A. Mallick, B. Lukose, M. V. Mane, T. Heine and R. Banerjee, *J. Am. Chem. Soc.*, 2012, **134**, 19524–19527.
76. S. Clair, M. Abel and L. Porte, *Chem. Commun.*, 2014, **50**, 9627–9635.
77. R. Tanoue, R. Higuchi, N. Enoki, Y. Miyasato, S. Uemura, N. Kimizuka, A. Z. Stieg, J. K. Gimzewski and M. Kunitake, *ACS Nano*, 2011, **5**, 3923–3929.
78. N. A. A. Zwaneveld, R. Pawlak, M. Abel, D. Catalin, D. Gigmes, D. Bertin and L. Porte, *J. Am. Chem. Soc.*, 2008, **130**, 6678–6679.
79. J. F. Dienstmaier, D. D. Medina, M. Dogru, P. Knochel, T. Bein, W. M. Heckl and M. Lackinger, *ACS Nano*, 2012, **6**, 7234–7242.

View Online

Published on 15 November 2016 on http://pubs.rsc.org | doi:10.1039/9781782626626-00238

80. M. Grzybowski, K. Skonieczny, H. Butenschön and D. T. Gryko, *Angew. Chem., Int. Ed.*, 2013, **52**, 9900–9930.
81. B. T. King, J. Kroulík, C. R. Robertson, P. Rempala, C. L. Hilton, J. D. Korinek and L. M. Gortari, *J. Org. Chem.*, 2007, **72**, 2279–2288.
82. P. Kovacic and M. B. Jones, *Chem. Rev.*, 1987, **87**, 357–379.
83. A. T. Balaban, C. D. Nenitzescu and G. A. Olah, *Friedel-Crafts and Related Reactions*, Interscience Ed., New York, 1964, vol. 2, p. 979.
84. X. Dou, X. Yang, G. J. Bodwell, M. Wagner, V. Enkelmann and K. Müllen, *Org. Lett.*, 2007, **9**, 2485–2488.
85. S. L. Skraba-Joiner, E. C. McLaughlin, A. Ajaz, R. Thamatam and R. P. Johnson, *J. Org. Chem.*, 2015, **80**, 9578–9583.
86. J. L. Ormsby, T. D. Black, C. L. Hilton, Bharat and B. T. King, *Tetrahedron*, 2008, **64**, 11370–11378.
87. A. Ajaz, E. C. McLaughlin, S. L. Skraba, R. Thamatam and R. P. Johnson, *J. Org. Chem.*, 2012, **77**, 9487–9495.
88. M. Treier, C. A. Pignedoli, T. Laino, R. Rieger, K. Müllen, D. Passerone and R. Fasel, *Nat. Chem.*, 2011, **3**, 61–67.
89. C. Rogers, C. Chen, Z. Pedramrazi, A. A. Omrani, H.-Z. Tsai, H. S. Jung, S. Lin, M. F. Crommie and F. R. Fischer, *Angew. Chem., Int. Ed.*, 2015, **54**, 15143–15146.
90. L. Zöphel, R. Berger, P. Gao, V. Enkelmann, M. Baumgarten, M. Wagner and K. Müllen, *Chem.–Eur. J.*, 2013, **19**, 17821–17826.
91. X. Zhang, J. Li, H. Qu, C. Chi and J. Wu, *Org. Lett.*, 2010, **12**, 3946–3949.
92. Q. Ye and C. Chi, *Chem. Mater.*, 2014, **26**, 4046–4056.
93. Z. Sun, Q. Ye, C. Chi and J. Wu, *Chem. Soc. Rev.*, 2012, **41**, 7857–7889.
94. G. Otero, G. Biddau, C. Sanchez-Sanchez, R. Caillard, M. F. Lopez, C. Rogero, F. J. Palomares, N. Cabello, M. A. Basanta, J. Ortega, J. Mendez, A. M. Echavarren, R. Perez, B. Gomez-Lor and J. A. Martin-Gago, *Nature*, 2008, **454**, 865–868.
95. A. L. Pinardi, G. Otero-Irurueta, I. Palacio, J. I. Martinez, C. Sanchez-Sanchez, M. Tello, C. Rogero, A. Cossaro, A. Preobrajenski, B. Gómez-Lor, A. Jancarik, I. G. Stará, I. Starý, M. F. Lopez, J. Méndez and J. A. Martin-Gago, *ACS Nano*, 2013, **7**, 3676–3684.
96. Y.-F. Zhang, N. Zhu and T. Komeda, *J. Phys. Chem. C*, 2007, **111**, 16946–16950.
97. U. Schlickum, R. Decker, F. Klappenberger, G. Zoppellaro, S. Klyatskaya, W. Auwärter, S. Neppl, K. Kern, H. Brune, M. Ruben and J. V. Barth, *J. Am. Chem. Soc.*, 2008, **130**, 11778–11782.
98. U. Schlickum, R. Decker, F. Klappenberger, G. Zoppellaro, S. Klyatskaya, M. Ruben, I. Silanes, A. Arnau, K. Kern, H. Brune and J. V. Barth, *Nano Lett.*, 2007, **7**, 3813–3817.
99. C. S. Kley, J. Čechal, T. Kumagai, F. Schramm, M. Ruben, S. Stepanow and K. Kern, *J. Am. Chem. Soc.*, 2012, **134**, 6072–6075.
100. NOTE: An assymetric configuration with monodentates axyal ligands was also observed in some cases.
101. W. Auwarter, D. Ecija, F. Klappenberger and J. V. Barth, *Nat. Chem.*, 2015, **7**, 105–120.

View Online

Published on 15 November 2016 on http://pubs.rsc.org | doi:10.1039/9781782626626-00238

102. T. A. Pham, F. Song, M. N. Alberti, M.-T. Nguyen, N. Trapp, C. Thilgen, F. Diederich and M. Stohr, *Chem. Commun.*, 2015, **51**, 14473–14476.
103. J. I. Urgel, D. Ecija, W. Auwärter, D. Stassen, D. Bonifazi and J. V. Barth, *Angew. Chem., Int. Ed.*, 2015, **54**, 6163–6167.
104. J. I. Urgel, M. Schwarz, M. Garnica, D. Stassen, D. Bonifazi, D. Ecija, J. V. Barth and W. Auwärter, *J. Am. Chem. Soc.*, 2015, **137**, 2420–2423.
105. M. El Garah, N. Marets, M. Mauro, A. Aliprandi, S. Bonacchi, L. De Cola, A. Ciesielski, V. Bulach, M. W. Hosseini and P. Samorì, *J. Am. Chem. Soc.*, 2015, **137**, 8450–8459.
106. Y. Li, J. Xiao, T. E. Shubina, M. Chen, Z. Shi, M. Schmid, H.-P. Steinrück, J. M. Gottfried and N. Lin, *J. Am. Chem. Soc.*, 2012, **134**, 6401–6408.
107. D. Heim, D. Écija, K. Seufert, W. Auwärter, C. Aurisicchio, C. Fabbro, D. Bonifazi and J. V. Barth, *J. Am. Chem. Soc.*, 2010, **132**, 6783–6790.
108. S. Haq, F. Hanke, M. S. Dyer, M. Persson, P. Iavicoli, D. B. Amabilino and R. Raval, *J. Am. Chem. Soc.*, 2011, **133**, 12031–12039.
109. H. Marbach, *Acc. Chem. Res.*, 2015, **48**, 2649–2658.
110. J. Mielke, F. Hanke, M. V. Peters, S. Hecht, M. Persson and L. Grill, *J. Am. Chem. Soc.*, 2015, **137**, 1844–1849.
111. K. S. Novoselov, A. K. Geim, S. V. Morozov, D. Jiang, Y. Zhang, S. V. Dubonos, I. V. Grigorieva and A. A. Firsov, *Science*, 2004, **306**, 666–669.
112. K. S. Novoselov, V. I. Falko, L. Colombo, P. R. Gellert, M. G. Schwab and K. Kim, *Nature*, 2012, **490**, 192–200.
113. A. H. Castro Neto, F. Guinea, N. M. R. Peres, K. S. Novoselov and A. K. Geim, *Rev. Mod. Phys.*, 2009, **81**, 109–162.
114. W. Han, R. K. Kawakami, M. Gmitra and J. Fabian, *Nat. Nanotechnol.*, 2014, **9**, 794–807.
115. A. C. Ferrari, F. Bonaccorso, V. Fal'ko, K. S. Novoselov, S. Roche, P. Boggild, S. Borini, F. H. L. Koppens, V. Palermo, N. Pugno, J. A. Garrido, R. Sordan, A. Bianco, L. Ballerini, M. Prato, E. Lidorikis, J. Kivioja, C. Marinelli, T. Ryhanen, A. Morpurgo, J. N. Coleman, V. Nicolosi, L. Colombo, A. Fert, M. Garcia-Hernandez, A. Bachtold, G. F. Schneider, F. Guinea, C. Dekker, M. Barbone, Z. Sun, C. Galiotis, A. N. Grigorenko, G. Konstantatos, A. Kis, M. Katsnelson, L. Vandersypen, A. Loiseau, V. Morandi, D. Neumaier, E. Treossi, V. Pellegrini, M. Polini, A. Tredicucci, G. M. Williams, B. Hee Hong, J.-H. Ahn, J. Min Kim, H. Zirath, B. J. van Wees, H. van der Zant, L. Occhipinti, A. Di Matteo, I. A. Kinloch, T. Seyller, E. Quesnel, X. Feng, K. Teo, N. Rupesinghe, P. Hakonen, S. R. T. Neil, Q. Tannock, T. Lofwander and J. Kinaret, *Nanoscale*, 2015, **7**, 4598–4810.
116. A. V. Rozhkov, S. Savel'ev and F. Nori, *Phys. Rev. B*, 2009, **79**, 125420.
117. O. V. Yazyev, *Acc. Chem. Res.*, 2013, **46**, 2319–2328.
118. L. Yang, C.-H. Park, Y.-W. Son, M. L. Cohen and S. G. Louie, *Phys. Rev. Lett.*, 2007, **99**, 186801.
119. C.-S. Wu and J.-D. Chai, *J. Chem. Theory Comput.*, 2015, **11**, 2003–2011.
120. K. Nakada, M. Fujita, G. Dresselhaus and M. S. Dresselhaus, *Phys. Rev. B*, 1996, **54**, 17954–17961.
121. Y.-W. Son, M. L. Cohen and S. G. Louie, *Phys. Rev. Lett.*, 2006, **97**, 216803.

View Online

Published on 15 November 2016 on http://pubs.rsc.org | doi:10.1039/9781782626626-00238

122. V. Barone, O. Hod and G. E. Scuseria, *Nano Lett.*, 2006, **6**, 2748–2754.
123. M. Fujita, K. Wakabayashi, K. Nakada and K. Kusakabe, *J. Phys. Soc. Jpn.*, 1996, **65**, 1920–1923.
124. W. Huang, J.-S. Wang and G. Liang, *Phys. Rev. B*, 2011, **84**, 045410.
125. Y. Chen, T. Jayasekera, A. Calzolari, K. W. Kim and M. B. Nardelli, *J. Phys.: Condens. Matter*, 2010, **22**, 372202.
126. S. Wang and J. Wang, *J. Phys. Chem. C*, 2012, **116**, 10193–10197.
127. J. Cai, P. Ruffieux, R. Jaafar, M. Bieri, T. Braun, S. Blankenburg, M. Muoth, A. P. Seitsonen, M. Saleh, X. Feng, K. Mullen and R. Fasel, *Nature*, 2010, **466**, 470–473.
128. P. Han, K. Akagi, F. Federici Canova, R. Shimizu, H. Oguchi, S. Shiraki, P. S. Weiss, N. Asao and T. Hitosugi, *ACS Nano*, 2015, **9**, 12035–12044.
129. K. A. Simonov, N. A. Vinogradov, A. S. Vinogradov, A. V. Generalov, E. M. Zagrebina, G. I. Svirskiy, A. A. Cafolla, T. Carpy, J. P. Cunniffe, T. Taketsugu, A. Lyalin, N. Mårtensson and A. B. Preobrajenski, *ACS Nano*, 2015, **9**, 8997–9011.
130. L. Massimi, O. Ourdjini, L. Lafferentz, M. Koch, L. Grill, E. Cavaliere, L. Gavioli, C. Cardoso, D. Prezzi, E. Molinari, A. Ferretti, C. Mariani and M. G. Betti, *J. Phys. Chem. C*, 2015, **119**, 2427–2437.
131. P. Han, K. Akagi, F. Federici Canova, H. Mutoh, S. Shiraki, K. Iwaya, P. S. Weiss, N. Asao and T. Hitosugi, *ACS Nano*, 2014, **8**, 9181–9187.
132. A. Kimouche, M. M. Ervasti, R. Drost, S. Halonen, A. Harju, P. M. Joensuu, J. Sainio and P. Liljeroth, *Nat. Commun.*, 2015, **6**, 10177.
133. Y.-C. Chen, D. G. de Oteyza, Z. Pedramrazi, C. Chen, F. R. Fischer and M. F. Crommie, *ACS Nano*, 2013, **7**, 6123–6128.
134. P. Ruffieux, J. Cai, N. C. Plumb, L. Patthey, D. Prezzi, A. Ferretti, E. Molinari, X. Feng, K. Müllen, C. A. Pignedoli and R. Fasel, *ACS Nano*, 2012, **6**, 6930–6935.
135. J. van der Lit, M. P. Boneschanscher, D. Vanmaekelbergh, M. Ijäs, A. Uppstu, M. Ervasti, A. Harju, P. Liljeroth and I. Swart, *Nat. Commun.*, 2013, **4**, 2023.
136. J. Björk, S. Stafström and F. Hanke, *J. Am. Chem. Soc.*, 2011, **133**, 14884–14887.
137. Y. Li, Z. Zhou, P. Shen and Z. Chen, *ACS Nano*, 2009, **3**, 1952–1958.
138. H. Kim, K. Lee, S. I. Woo and Y. Jung, *Phys. Chem. Chem. Phys.*, 2011, **13**, 17505–17510.
139. A. E. Torres and S. Fomine, *Phys. Chem. Chem. Phys.*, 2015, **17**, 10608–10614.
140. D. J. Dibble, Y. S. Park, A. Mazaheripour, M. J. Umerani, J. W. Ziller and A. A. Gorodetsky, *Angew. Chem., Int. Ed.*, 2015, **54**, 5883–5887.
141. T. H. Vo, M. Shekhirev, D. A. Kunkel, F. Orange, M. J. F. Guinel, A. Enders and A. Sinitskii, *Chem. Commun.*, 2014, **50**, 4172–4174.
142. T. H. Vo, U. G. E. Perera, M. Shekhirev, M. Mehdi Pour, D. A. Kunkel, H. Lu, A. Gruverman, E. Sutter, M. Cotlet, D. Nykypanchuk, P. Zahl, A. Enders, A. Sinitskii and P. Sutter, *Nano Lett.*, 2015, **15**, 5770–5777.
143. C. Bronner, S. Stremlau, M. Gille, F. Braußе, A. Haase, S. Hecht and P. Tegeder, *Angew. Chem., Int. Ed.*, 2013, **52**, 4422–4425.

View Online

144. J. Cai, C. A. Pignedoli, L. Talirz, P. Ruffieux, H. Söde, L. Liang, V. Meunier, R. Berger, R. Li, X. Feng, K. Müllen and R. Fasel, *Nat. Nanotechnol.*, 2014, **9**, 896–900.
145. R. R. Cloke, T. Marangoni, G. D. Nguyen, T. Joshi, D. J. Rizzo, C. Bronner, T. Cao, S. G. Louie, M. F. Crommie and F. R. Fischer, *J. Am. Chem. Soc.*, 2015, **137**, 8872–8875.
146. S. Kawai, S. Saito, S. Osumi, S. Yamaguchi, A. S. Foster, P. Spijker and E. Meyer, *Nat. Commun.*, 2015, **6**, 8098.
147. Y.-C. Chen, T. Cao, C. Chen, Z. Pedramrazi, D. Haberer, G. de Oteyza Dimas, F. R. Fischer, S. G. Louie and M. F. Crommie, *Nat. Nanotechnol.*, 2015, **10**, 156–160.
148. L. Brey and H. A. Fertig, *Phys. Rev. B*, 2006, **73**, 235411.
149. M. Ezawa, *Phys. Rev. B*, 2006, **73**, 045432.
150. J. Liu, B.-W. Li, Y.-Z. Tan, A. Giannakopoulos, C. Sanchez-Sanchez, D. Beljonne, P. Ruffieux, R. Fasel, X. Feng and K. Müllen, *J. Am. Chem. Soc.*, 2015, **137**, 6097–6103.

Published on 15 November 2016 on http://pubs.rsc.org | doi:10.1039/9781782626626-00238

Published on 15 November 2016 on http://pubs.rsc.org | doi:10.1039/9781782626626-00277

Subject Index

1,9-diarylnaphthalene π-cofacial model, 138–140
β-hairpin peptide cation-π model, 152–153
π–π^+ interactions, 33–34
N-arylimide aromatic stacking balance, 133–137

AFM. *see* atomic force microscopy (AFM)
aliphatic CH–π interactions, 145–150
  Asensio's imine/hemiaminal model, 145–149
  Zondlo's proline tetrapeptide model, 149–150
anion–π interactions, 31–33
  and charge neutral π-systems, 76–82
  in reaction catalysis, 65–74
  solution-phase measurements of, 155–159
    Ballester's calix[4]pyrrole model, 157–159
    Wang's calix[2]arene[2]triazine model, 156–157
  supramolecular chemistry
    aromatic ligands coordinated to metal ions, 83–85
    and ionic liquids (ILs), 74–76
    overview, 39–40
    physical nature, 41–46
    and protonated aromaticss, 86–88
    and synthetic receptors, 46–65
antimony(lp)...π(arene) interactions, 108
arene–arene interactions, 2–3
  nature of, 5–9
  strength of, 9–10
arene (π) interactions
  antimony(lp), 108
  arsenic(lp), 106–108
  bismuth(lp), 108–109
  indium(lp), 102
  lead(lp), 105–106
  selenium(lp), 109–114
  tellurium(lp), 115–116
  thallium(lp), 102–104
  tin(lp), 104–105
aromatic amino acids, 173–175
  synthetic receptors for, 184–192
    recognition by cucurbiturils, 188–189
    recognition by cyclodextrins, 186–187
    recognition by viologen-containing receptors, 184–186
aromatic cation–π interactions, 150–155
  Dougherty's cyclophane model, 151–152

View Online

Published on 15 November 2016 on http://pubs.rsc.org | doi:10.1039/9781782626626-00277

aromatic cation–π interactions (*continued*)
Jacobsen's enantioselective polycyclization model, 153–154
Waters's benzyl pyridinium model, 154–155
Waters's β-hairpin peptide model, 152–153
aromatic edge-to-face interactions, 140–145
Hsung's 4+3 cycloaddition ETF model system, 143–144
Wilcox's ETF molecular torsional balance, 141–143
aromatic interactions
in cooperative catalysis, 31
in non-catalytic reactions, 22–24
and organic reactions
directed by anion–π interactions, 31–33
directed by π–π^+ interactions, 33–34
overview, 18–19
relevance to, 19–22
in organocatalysis, 25–31
solution-phase measurements of
aliphatic CH–π interactions, 145–150
anion–π interaction, 155–159
bimolecular model systems, 125–126
cation–π interactions, 150–155
edge-to-face, 140–145
experiment models, 127–128
interaction energy isolation, 128–129
kinetic approach, 127
lone pair–π interaction, 159–162
overview, 124–125
stacking, 129–140
thermodynamic approach, 126–127
unimolecular model system, 126
in transition-metal catalyzed reactions, 24–25
aromatic molecules, on metallic surfaces
general surface characterization techniques, 240
overview, 238–240
reactivity of, 247–268
cyclodehydrogenation, 255–257
graphene nanoribbon synthesis, 261–268
metal coordination, 257–261
surface-mediated polymerization, 248–254
visualization techniques with sub-molecular resolution, 241–247
aromatic peptides, and synthetic receptors, 192–203
by coordination complexes, 195–197
by cucurbit*[n]*urils, 197–203
early receptors, 193–195
aromatic quadrupole moment, 4
aromatic residues
in biological complexes, 175–180
efficiency of, 182
aromatic sites, and synthetic receptors, 203–205
aromatic stacking interactions, 129–140
Cozzi and Siegel's 1,9-diarylnaphthalene π-cofacial model, 138–140
Hunter's supramolecular zipper model, 130–133

View Online

Published on 15 November 2016 on http://pubs.rsc.org | doi:10.1039/9781782626626-00277

Shimizu's atropisomeric *N*-arylimide balance, 133–137
Swager and Houk's Diels–Alder model system, 137–138
arsenic(lp)...π(arene) interactions, 106–108
atomic force microscopy (AFM), 240

benzyl pyridinium cation–π model, 154–155
bimolecular model systems, 125–126
bismuth(lp)...π(arene) interactions, 108–109

calix[2]arene[2]triazine anion–π model, 156–157
calix[4]pyrrole anion–π model, 157–159
Cambridge Structural Database (CSD), 100
cation–arene interactions, 3–4, 150–155
in lipids, 229–232
model systems, 216–218
nature of, 10–13, 214–215
in nucleic acids, 225–228
in proteins, 218–225
strength of, 13–14
charge neutral π-systems, 76–82
constant current mode, 241
constant height mode, 241
cooperative catalysis, 31
CSD. *see* Cambridge Structural Database (CSD)
cucurbiturils, and aromatic amino acids, 188–189
cycloaddition ETF model system, 143–144
cyclodehydrogenation reactions, 255–257
cyclodextrins, and aromatic amino acids, 186–187
cyclophane cation–π model, 151–152

DCC. *see* dynamic combinatorial chemistry (DCC) *or* dynamic covalent chemistry (DCC)
Diels–Alder model system, 137–138
dynamic combinatorial chemistry (DCC), 145
dynamic covalent chemistry (DCC), 252–254

EDX. *see* energy dispersive X-ray spectroscopy (EDX)
enantioselective polycyclization cation–π model, 153–154
energy dispersive X-ray spectroscopy (EDX), 240
ETF molecular torsional balance, 141–143

gallium (lp)...π(arene) interactions, 102
graphene nanoribbon synthesis, 261–268

halogenated precursors, 250–252

imine/hemiaminal CH-π model, 145–149
indium(lp)...π(arene) interactions, 102
interaction energy isolation, 128–129
ionic liquids (ILs), 74–76

kinetic approach, of aromatic interactions, 127

LCPD. *see* local contact potential difference (LCPD)
lead(lp)...π(arene) interactions, 105–106
ligands, designed, 180–182
lipids, cation–arene interactions in, 229–232
local contact potential difference (LCPD), 246

View Online

Published on 15 November 2016 on http://pubs.rsc.org | doi:10.1039/9781782626626-00277

lone pair–π interaction, 159–162
  Gung's oxygen lp–π triptycene balance, 159–161
  Motherwell's lp–π seesaw balance, 161–162
lone pair–π seesaw balance, 161–162

metal coordination reactions, 257–261
M(lp)...π(arene) interactions
  and antimony, 108
  and arsenic, 106–108
  biological relevance, 116–118
  and bismuth, 108–109
  gallium and indium, 102
  and lead, 105–106
  methodology, 100–102
  overview, 98–100
  and selenium, 109–114
  and tellurium, 115–116
  and thallium, 102–104
  and tin, 104–105

nc-AFM. *see* non-contact atomic force microscopy (nc-AFM)
non-aromatic amino acids, 189–192
non-catalytic reactions, aromatic interactions in, 22–24
non-contact atomic force microscopy (nc-AFM), 241–247
nucleic acids, cation–arene interactions in, 225–228

organic reactions, and aromatic interactions
  directed by anion–π interactions, 31–33
  directed by π–π$^+$ interactions, 33–34
  overview, 18–19
  relevance to, 19–22
organocatalysis, 25–31
oxygen lp–π triptycene balance, 159–161

proline tetrapeptide CH–π model, 149–150
proteins, cation–arene interactions in, 218–225
protonated aromatics, 86–88

scanning electron microscopy (SEM), 240
scanning probe microscopy (SPM), 240, 241
scanning tunnelling hydrogen microscopy (STHM), 241–247
scanning tunnelling microscopy (STM), 240, 241
selenium(lp)...π(arene) interactions, 109–114
SEM. *see* scanning electron microscopy (SEM)
solution-phase measurements, of aromatic interactions
  aliphatic CH–π interactions, 145–150
    Asensio's imine/hemiaminal model, 145–149
    Zondlo's proline tetrapeptide model, 149–150
  of anion–π interactions, 155–159
    Ballester's calix[4]pyrrole model, 157–159
    Wang's calix[2]arene[2]triazine model, 156–157
  bimolecular model systems, 125–126
  cation–π interactions, 150–155
    Dougherty's cyclophane model, 151–152
    Jacobsen's enantioselective polycyclization model, 153–154
    Waters's benzyl pyridinium model, 154–155
    Waters's β-hairpin peptide model, 152–153

View Online

Published on 15 November 2016 on http://pubs.rsc.org | doi:10.1039/9781782626626-00277

edge-to-face, 140–145
Hsung's 4+3 cycloaddition ETF model system, 143–144
Wilcox's ETF molecular torsional balance, 141–143
experiment models, 127–128
interaction energy isolation, 128–129
kinetic approach, 127
lone pair–π interaction, 159–162
Gung's oxygen lp–π triptycene balance, 159–161
Motherwell's lp–π seesaw balance, 161–162
overview, 124–125
stacking, 129–140
Cozzi and Siegel's 1,9-diarylnaphthalene π-cofacial model, 138–140
Hunter's supramolecular zipper model, 130–133
Shimizu's atropisomeric *N*-arylimide balance, 133–137
Swager and Houk's Diels–Alder model system, 137–138
thermodynamic approach, 126–127
unimolecular model system, 126
SPM. *see* scanning probe microscopy (SPM)
STHM. *see* scanning tunnelling hydrogen microscopy (STHM)
STM. *see* scanning tunnelling microscopy (STM)
supramolecular chemistry
aromatic ligands coordinated to metal ions, 83–85
and ionic liquids (ILs), 74–76
overview, 39–40
physical nature, 41–46
and protonated aromaticss, 86–88
and synthetic receptors, 46–65
supramolecular zipper model, 130–133
surface-mediated polymerization, 248–254
and dynamic covalent chemistry (DCC), 252–254
of halogenated precursors, 250–252
and terminal acetylene coupling, 248–250
synthetic receptors, 183–184
for amino acids, 184–192
recognition by cucurbiturils, 188–189
recognition by cyclodextrins, 186–187
recognition by viologen-containing receptors, 184–186
recognition of aromatic peptides by, 192–203
by coordination complexes, 195–197
by cucurbit[*n*]urils, 197–203
early receptors, 193–195
recognition of aromatic sites on proteins, 203–205
recognition of non-aromatic amino acids, 189–192
and supramolecular chemistry, 46–65

tellurium(lp)...π(arene) interactions, 115–116
TEM. *see* transmission electron microscopy (TEM)
terminal acetylene coupling, 248–250

View Online

thallium(lp)...π(arene) interactions, 102–104
thermodynamic approach, of aromatic interactions, 126–127
tin(lp)...π(arene) interactions, 104–105
transition-metal catalyzed reactions, 24–25
transmission electron microscopy (TEM), 240

unimolecular model system, 126

viologen-containing receptors, 184–186

XPS. *see* X-ray photoelectron spectroscopy (XPS)
X-ray photoelectron spectroscopy (XPS), 240

Published on 15 November 2016 on http://pubs.rsc.org | doi:10.1039/9781782626626-00277